

SELECTED ASPECTS OF
TURBULENCE AND COMBUSTION
IN 20-LITRE EXPLOSION VESSELS

Development of Experimental Apparatus
and Experimental Investigation

Trygve Skjold

A thesis submitted in partial fulfilment of the
requirements for the degree of *Candidatus Scientiarum* in
the subject of Physics; Process Safety Technology



Department of Physics
University of Bergen
Bergen, Norway
June 2003

© 2003 by Trygve Skjold

All rights reserved

Table of Contents

Abstract	<i>viii</i>
Sammendrag	<i>ix</i>
Acknowledgements	<i>x</i>
<hr/>	
1 Introduction	1
<hr/>	
1.1 Motivation	1
1.2 Present Work	12
2 Theory and Previous Work	15
<hr/>	
2.1 Definitions and Basic Concepts	15
2.1.1 Explosions	15
2.1.2 Combustion	16
2.1.3 Turbulence	19
2.1.4 Characterization of Particle Laden Flows	25
2.1.5 Turbulent Particle Dispersion	31
2.1.6 Turbulence Modification	31
2.1.7 Turbulent Combustion	33
2.2 Turbulence and Combustion in 20-Litre Vessels	36
2.2.1 Previous Work on the Turbulence in 20-Litre Vessels	36
2.2.2 Characterization of Dispersion Induced Flow in 20-Litre Explosion Vessels	39
2.2.3 The Effect of Particles on the Transient Flow in 20-Litre Explosion Vessels	41
2.2.4 Estimating Burning Velocities in the Inflection Point	44
2.2.5 Aspects of Numerical Modelling of Turbulent Flow and Combustion	46

3	Experiments	48
3.1	Explosion Experiments with Solid Fuels	50
3.1.1	Experimental Procedure for Dust Explosion Tests	50
3.1.2	Experiments with Combustible Dusts	51
3.1.3	Experiments with Explosible Dust	52
3.2	Explosion Experiments with a Gaseous Fuel	53
3.2.1	Experimental Procedure for Tests Involving Gaseous Fuel	53
3.2.2	Experiments with Propane-Air Mixtures	53
3.2.3	Experiments with Propane-Air Mixtures and Inert Dust	53
3.2.4	Experiments with Hybrid Mixtures	54
3.3	Dispersion Experiments	55
3.3.1	Experimental Procedure for LDA Measurements	55
3.3.2	LDA Experiments	55
3.3.3	Experimental Procedure for Measuring Pressure-Time Histories with Piezoelectric Sensors	58
3.3.4	Flow Experiments with Piezoelectric Sensors	59
4	Results and Discussion	60
4.1	Results from Dispersion Experiments	60
4.1.1	Turbulence Decay Measured with LDA	60
4.1.2	Pressure-Time Histories Measured with Piezoelectric Sensors	62
4.1.3	Other Observations Regarding the Dispersion Process	65
4.2	Results from Explosions Involving Gaseous Fuel	73
4.2.1	Propane-Air Explosions	74
4.2.2	Propane-Air Explosions with Inert Dust	81
4.2.3	Hybrid Explosions	83
4.3	Dust Explosions	86
4.3.1	Niacin Amide	86
4.3.2	Spores of <i>Lycopodium</i>	90
4.3.3	Silicon	93
4.3.4	Explosive Dust: RDX	99
4.4	Estimation of Burning Velocity from Pressure Measurements	103
4.4.1	Propane-Air Explosions	103

4.4.2 Dust Explosions	106
4.4.3 Burning Velocity and Rate of Pressure Rise for Explosible Mixtures	109
5 Conclusions	111
References	116

APPENDICES:

A	Arc Generator	A-1
<hr/>		
	A.1 Introduction	A-1
	A.1.1 Motivation	A-1
	A.1.2 Aim of Present Work	A-5
	A.2 Ignition of Dust Clouds and Premixed Gases by Electrical Discharges	A-6
	A.2.1 Characteristics of Electrical Discharges in Air	A-6
	A.2.2 High Voltage Measurement Techniques	A-10
	A.2.3 Discharge Characteristics Influencing the Ignitability of Flammable Mixtures under Turbulent Conditions	A-11
	A.2.4 Reliable Spark Ignition of Dust Clouds	A-17
	A.3 Description of the Arc Generator	A-18
	A.3.1 The Main Circuit	A-20
	A.3.2 Auxiliary Systems	A-23
	A.3.3 Measurement System	A-26
	A.3.4 Energy and Duration of Discharge	A-38
	A.4 Experiments with the Arc Generator	A-42
	A.4.1 Electrical Discharge Experiments	A-42
	A.4.2 Dust Explosion Experiments	A-43
	A.5 Experimental Results and Discussion	A-45
	A.5.1 Characteristics of the Electrical Discharges	A-45
	A.5.2 Incendiary Capabilities of Electrical Discharges for Selected Dusts – Comparison with Chemical Igniters	A-57

A.6 Conclusion	<i>A-67</i>
A.7 Electrical Schematic and Components	<i>A-68</i>
References	<i>A-73</i>
<hr/>	
B Experimental Apparatus	<i>B-1</i>
<hr/>	
B.1 Explosion Vessels and Dispersion Systems	<i>B-1</i>
B.1.1 Standardized Explosion Vessels and Dispersion Systems	<i>B-1</i>
B.1.2 Explosion Vessels and Dispersion System at the 20-Litre Dust Explosion Test Facility at the University of Bergen	<i>B-8</i>
B.2 Auxiliary Components and Equipment	<i>B-15</i>
References	<i>B-18</i>
<hr/>	
C Dust Data	<i>C-1</i>
<hr/>	
C.1 Analytical Methods	<i>C-1</i>
C.2 Inert Dusts	<i>C-4</i>
C.2.1 Aluminium Oxide	<i>C-4</i>
C.2.2 Talc	<i>C-5</i>
C.3 Combustible Dusts	<i>C-8</i>
C.3.1 Niacin Amide	<i>C-8</i>
C.3.2 <i>Lycopodium</i> Spores	<i>C-10</i>
C.3.3 Moisture Content of <i>Lycopodium</i> Spores	<i>C-16</i>
C.3.4 Silicon	<i>C-17</i>
C.3.5 Some Observations on Silicon Oxides	<i>C-21</i>
C.3.6 Polymethyl Methacrylate	<i>C-29</i>
C.4 Explosive Material	<i>C-32</i>
C.4.1 RDX	<i>C-32</i>
References	<i>C-35</i>
<hr/>	

D	Analysis of LDA Data	D-1
	D.1 Data analysis	D-1
	D.1.1 Moving Regression Algorithm	D-2
	D.1.2 Robust Locally Weighted Regression (LOESS)	D-7
	D.1.3 Quality of Analysis Results – An Alternative Approach	D-7
	D.2 Results and Discussion	D-12
	D.2.1 Overall Results with Rebound Nozzle – No Dust	D-12
	D.2.2 Tests with Other Dispersion Nozzles	D-14
	D.2.3 Tests with Dust	D-17
	D.3 Computer Programs	D-24
	D.3.1 The MATLAB Program <i>ldafig.m</i>	D-24
	D.3.2 Other Computer Programs	D-32
	References	D-33

E	CFD Simulations	E-1
	E.1 The CFD-Code FLACS	E-1
	E.1.1 Simulations in FLACS	E-2
	E.1.2 Representing the 20-Litre Cubical Vessel in FLACS	E-2
	E.2 The Dispersion Process	E-6
	E.2.1 Concentration and Mixing	E-5
	E.2.2 Pressure-Time Histories	E-9
	E.2.3 Turbulence	E-11
	E.2.4 Velocity	E-14
	E.3 Explosions	E-18
	References	E-21

Abstract

This thesis describes a critical experimental investigation of selected aspects of the turbulent flow and combustion that takes place in 20-litre explosion vessels during standardized tests. During the initial phase of the present work, a dust explosion laboratory was set up at the University of Bergen. Two 20-litre explosion vessels were constructed, one of the USBM-type and one cubical. The systems for dust-dispersion and pressure-measurement are almost identical with those of the 20-litre Siwek sphere. An electric-arc generator has been developed, and the performance of the arc generator has been characterized under various conditions.

Dispersion-induced turbulence without dust has been measured in the cubical vessel by laser Doppler anemometry. Only the horizontal velocity components were measured. The LDA measurements indicated levels of turbulence during the decay period that was significantly lower than levels reported by others. Pressure measurements during the transient dispersion process show that increased dust loading have significant influence on the pressure measured immediately upstream of the dispersion nozzle, and results in a delay of the pressure-drop in the reservoir.

Explosion experiments with propane-air mixtures illustrated the strong influence turbulence has on both explosion pressure and rate of pressure rise. It has been shown that adding an increasing amount of inert dust to propane-air mixtures, leads to an almost linear reduction in both the explosion pressure and the rate of pressure rise.

Explosion experiments with various dusts (niacin amide, *Lycopodium* and silicon) showed that increased ignition delay time resulted in a dramatic reduction in the rate of pressure rise, but also a significant reduction in the maximum explosion pressure.

The effect of increased ignition delay time was also investigated for the explosive material RDX. It was found that the combustion process continued in the settled dust layers after the flame had passed through the cloud, making the pressure-time curves very difficult to interpret.

Burning velocities estimated from the measured pressure-time curves, from both propane and dusts explosions, were in qualitative agreement with results reported by other workers, indicating a linear increase in burning velocity with increasing root-mean-square velocity. However, inherent limitations associated with explosion experiment performed in closed 20-litre vessels made it difficult to produce quantitative estimates of key parameters, such as burning velocity or flame thickness. It is suggested that the standardized tests in 20-litre vessels are supplemented with alternative experiments, preferably operating at atmospheric and stationary conditions.

...

Keywords: Turbulence decay; Dust explosion; Burning velocity; Arc generator.

Sammendrag

Denne hovedfagsoppgaven beskriver en kritisk eksperimentell undersøkelse av utvalgte aspekter vedrørende strømming og forbrenning i 20-liters eksplosjonskammer. I den innledende fasen av det foreliggende arbeid ble det etablert et støvekspløsjonslaboratorium ved Universitetet i Bergen. To 20-liters eksplosjonskammer ble bygget, ett av USBM-typen og ett kubisk. Systemene for støvdispergering og trykkmåling er tilnærmet identiske med de som benyttes for det kuleformede Siwek-kammeret. En elektrisk lysbuegenerator har blitt utviklet, og yteevnen til generatoren har blitt kartlagt under varierende betingelser.

Turbulensen som genereres under støvdispergeringsprosessen har blitt målt ved hjelp av laser Doppler anemometri i det kubiske kammeret, uten støv. Kun horisontale hastighetskomponenter ble målt. LDA-målingene tyder på at turbulensnivået var betydelig lavere enn tilsvarende målinger rapportert fra et Siwek-kammer. Trykkmålinger under den transiente dispergeringsprosessen viser at trykket umiddelbart oppstrøms av dispergeringsdysen er betydelig påvirket av mengden støv som dispergeres, og at økt støvmengde fører til et forsinket trykkfall i reservoaret.

Ekspløsjonsekspirerenter med propan-luft blandinger viste at turbulensnivået kan ha stor innflytelse på både maksimalt eksplosjonstrykk og trykkstigningshastighet. Tilsetning av økende mengder inert støv til propan-luft blandinger førte til en tilnærmet lineær reduksjon i både eksplosjonstrykk og trykkstigningshastighet.

Ekspløsjonsekspirerenter med diverse brennbare støv, niacinamid, *Lycopodium* og silisium, viste at økt tennforsinkelse medførte en dramatisk reduksjon i trykkstigningshastigheten, men også en betydelig reduksjon i det maksimale eksplosjonstrykket.

Effekten av økt tennforsinkelse ble også undersøkt for det eksplosive støvet RDX. For dette materialet fortsatte forbrenningen i støvlag som hadde dannet seg i bunnen av kammeret, noe som gjorde det svært vanskelig å tolke trykk-tid kurvene fra eksplosjonen.

Forbrenningshastigheter estimert fra de målte trykk-tid kurvene var i kvalitativ overensstemmelse med publiserte resultater: en lineær økning i forbrenningshastigheten for økende u'_{rms} . Iboende begrensninger forbundet med eksplosjonsekspirerenter utført i lukkede 20-liter kammer gjør det vanskelig å generere kvantitative estimater for viktige forbrenningsstørrelser, som forbrenningshastighet og flammetykkelse. Det foreslås at de standardiserte testene i 20-liters eksplosjonskammer blir supplert med alternative tester, fortrinnsvis utført under stasjonære og atmosfæriske betingelser.

...

Nøkkelord: Turbulenshenfall; Støvekspløsjon; Forbrenningshastighet; Lysbuegenerator.

Acknowledgements

I am particular grateful to my supervisor Professor Rolf K. Eckhoff for many interesting discussions concerning the dust explosion phenomenon, and other phenomena. Special thanks are also due to several other people, all of whom have shown personal interest in the project. Werner Olsen (Section for Microelectronics, UoB) provided invaluable help in the development of the arc generator, mostly in his spare time. Kåre Slettebakken, Leif Egil Sandnes, Svein Midtun and Hans Torgilstveit, at the Mechanical workshop (UoB), have made most of the various gadgets that constitute a dust explosion laboratory. The LDA measurements could not have been done without Ivar Øyvind Sand at Christian Michelsen Research AS, who also contributed with many interesting discussions on flow, turbulence and combustion. Everyone at the electronic laboratory at UoB has also been extremely helpful throughout the project. Bjørn J. Arntzen (UoB/GexCon) and the staff at GexCon AS have all been very helpful. My father, Johannes Skjold, took time to trace many of the mechanical drawings, and provided sound scepticism throughout the whole project.

Sponsors

The project could not have been carried through without the aid provided by several sponsors; the following institutions have supported the project financially:

- The Swedish Fire Research Board (BRANDFORSK PROJECT 615-991).
- The Faculty of Mathematics and Natural Sciences, University of Bergen (UoB).
- The Research Council of Norway.
- GexCon AS, Fantoft, Norway.
- Program for Process Technology (UoB).

In addition, dust samples and other products or services have been provided free of charge by the following:

- M. Nybø, R. Hatlenes and A. Damstuen at Elkem Bremanger Smelteverk, Svelgen, provided samples of jet-milled Silgrain, and performed particle size analysis on several dust samples.
- K.P. Mathisen at Norwegian Talc AS, Knarrevik, provided talc samples, and performed particle size analysis on several dust samples.
- T. Engman at Norsk Medisinaldepot ASA provided spores of *Lycopodium*.
- Ø.H. Johansen at DYNØ Defence Products provided samples of RDX.
- Ø. Matre at Norsk Hydro Karmøy provided the aluminium oxide sample.
- K.V. Hovland at SI-Glass AS provided the windows for the cubical vessel.

Last, but not least, special thanks are due to Ngoc Van Nguyen and Tran Hieu Thi for making the stay at the Department of Physics gastronomically bearable.

CHAPTER 1

Introduction

1.1 Motivation

Many materials that are virtually non-flammable in bulk form become highly explosive if dispersed as a fine powder. Hence, dust explosions represent a hazard to both personnel and equipment in all industries that manufacture, transport, process, generate, or use combustible dusts. During normal operation, dust clouds within the explosible concentration range are most likely to occur inside process equipment such as pneumatic conveyors, bucket elevators, grinding mills, dust collectors (e.g. cyclones and filter units) and storage vessels (e.g. silos and hoppers).

Prevention and mitigation of dust explosions

There are two complementary strategies for reducing the risk posed by dust explosions: *prevention* and *mitigation*. Various means of preventing and mitigating dust explosions are described by Eckhoff (2003); they are summarized in Table 1-1.

Table 1-1. Means of preventing and mitigating dust explosions, from Eckhoff (2003).

PREVENTION		MITIGATION
Preventing ignition sources, such as:	Preventing explosible dust cloud:	
<ul style="list-style-type: none">• Smouldering combustion in dust.• Open flames.• Hot surfaces.• Electric sparks/arcs and electrostatic discharges.• Heat from mechanical impact.	<ul style="list-style-type: none">• Dust concentration outside combustible range.• Inerting by adding inert gas (N₂, CO₂, Ar, ...).• Inerting by adding inert dust (e.g. rock dust).• Intrinsic inerting.	<ul style="list-style-type: none">• Pressure resistant equipment.• Venting.• Isolation (sectioning).• Automatic suppression.• Partial inerting.• Good housekeeping (dust removal/cleaning).

Primarily one seeks to prevent the conditions that permit dust explosions to take place; either by eliminating all possible ignition sources, or by avoiding the formation of combustible dust clouds altogether. However, there are situations where the possibility of a dust explosion cannot be ruled out, and measures for minimization of damage has to be considered. In some cases, the enclosure containing a combustible dust-air mixture can be made strong enough to withstand the explosion pressure, and only the maximum attainable explosion pressure is needed as design parameter. More often, however, the enclosure will not be able to withstand the total explosion pressure, and other mitigating measures, such as venting, isolation (e.g. fast closing valves) and automatic suppression, must be implemented in the design. In these cases, safe dimensioning requires adequate knowledge about the burning rate of the dust cloud in the actual process situation.

Constant volume explosion pressure of dust clouds

The simplest way of estimating the rate of energy release during a dust explosion inside a vessel of constant volume is to measure the pressure rise as a function of time during the explosion. It is customary to neglect the volumes of any solid and liquid substances, and assume that the gaseous species obey the ideal gas law:

$$pV_v = n_gRT = \frac{m_g}{\bar{M}_g}RT \quad (1.1)$$

where p , V_v , n_g , m_g , \bar{M}_g , R and T are absolute pressure, volume of explosion vessel, moles of gaseous species, mass of gaseous species, average molecular weight of gaseous species, the universal gas constant and the absolute temperature, respectively. Since the volume is constant, the pressure rise is determined by the change in gaseous species and the net temperature increase due to chemical reactions. The contribution due to change of moles of gaseous species can be both positive and negative, but it is usually far less important than that due to increase in temperature.

Although the maximum constant volume explosion pressure is considered a static explosion parameter, i.e. it can be calculated from stoichiometric and thermodynamic considerations (like adiabatic flame temperature), such parameters are of limited use for combustible dust-air suspensions because reactions are seldom complete (Lee, 1988). Both Kauffman *et al.* (1984) and Dahoe *et al.* (2001c) have found that reducing the turbulence intensity of the dust cloud results in significantly lower constant volume explosion pressures for cornstarch-air mixtures. Several explanations have been suggested for this effect:

- i)* Higher burning velocities at higher turbulence levels lead to increased rates of combustion and reduced heat loss to the walls (Amyotte *et al.*, 1989).
- ii)* A change of composition takes place in the pre-heat zone due to liberation of volatile components (Dahoe, 2000; Dahoe *et al.*, 2001c).
- iii)* Factors associated with the experimental procedure, such as:
 - a. Dust particles settles out of suspension due to gravity.
 - b. Dust particles adhere to all solid surfaces (Bradley *et al.*, 1988).

The true cause is probably a complex combination of several of these factors.

The burning rate of dust clouds

In this context the term *burning rate* should be understood as the rate of energy release caused by the combustion process, it is not necessarily the same as burning velocity. Following Bradley (2002), the key parameters that express burning rate are the turbulent burning velocity and the volumetric heat release rate. The burning velocity, S_w , is the rate of flame propagation relative to the unburnt mixture, whereas the flame speed, S_f , is measured relative to a fixed reference point.

The experimental measurements of burning rates are significantly influenced by turbulence, which is an inherent property of any dust suspension in a gravitational field (Lee, 1988). The burning rate is also determined by various other factors, such as pressure, temperature, scale, etc. Since full scale testing is expensive, the main challenge is to make realistic estimates of the burning rate that will take place under actual process conditions. Such estimates can be based either on small-scale experiments and scaling laws, or on numerical simulations where the development of an explosion is predicted by solving a set of conservation equations. Although burning velocity can be studied in both burners and various arrangements of pipes or ducts, the most frequently used strategy is to estimate a burning rate from measurements of pressure-time histories in constant volume explosions. Whereas the flame front of a laminar flame is usually well defined (at least for gases), that of a turbulent flame is highly wrinkled, and definition of the front can be somewhat arbitrary. Thus, burning velocity is rather difficult both to define precisely and to measure rigorously – even for gaseous flames (e.g. Lipatnikov and Chomiak, 2002). The matter is even more complicated when it comes to combustion of dust-air suspensions, for several reasons:

- i)* It is difficult to determine fundamental properties of laminar dust flames, such as laminar burning velocity, flame thickness, quenching distance, etc. This is mainly due to experimental difficulties in the generation of a quiescent uniform dust suspension, especially under the influence of normal gravity (Jarosinski *et al.*, 1999). Laminar dust flames are difficult to stabilize in burners, and the geometry and flame structure of the stabilized flame are poorly defined (Lee, 1988).
- ii)* Turbulence will generate local variations in dust concentration and/or local particle size distribution due to vorticity (centrifugal effect); hence, uniform dust concentration cannot be achieved in a turbulent dust cloud (Jarosinski and Podfilipski, 1999).
- iii)* In gas flames, the entire heat is released in the flame front; in dust flames, only a small part of the heat is released in the flame front – the remaining part is released far behind it (Jarosinski and Podfilipski, 1999).
- iv)* The presence of a solid fuel in the combustible mixture introduces several additional parameters that has significant influence on flame properties; e.g. particle size distribution, content of volatiles and moisture, uniformity of dust suspension, etc.
- v)* Whereas a flammable gas-air mixture is transparent, combustible dust-air suspensions are rather opaque. Suspended dust also has a tendency to settle on all solid surfaces, including windows. This usually limits visual observation of

the propagating flame front, and makes it inherently difficult to measure turbulence by techniques such as laser Doppler anemometry (LDA).

Thus, experimentally determined burning rates for turbulent dust-air suspensions are usually limited to the information that can be extracted from measurements of the pressure development in constant volume explosions.

Importance of standardized tests

Some of the parameters that influence the ignition sensitivity and explosion violence of a dust clouds are summarized in Table 1-2; note that many of them are related to physical and chemical properties of the particular dust sample. Given the large number of different types of dusts that can represent a hazard in the industry, and all the different combinations of influential parameters such as particle size distribution, particle shape, moisture content, etc. that can exist for each dust type; it is preferable to determine global explosibility characteristics in standardized tests (Cashdollar, 2000). Cost considerations imply that such experiments must be limited in both scale and scope.

The importance of standardized tests was emphasized by Lee (1988), who pointed out that the strong influence of turbulence on dynamic explosion parameters, such as burning rate, implies that all measurements of such parameters are strongly dependent on both apparatus and test procedures. However, criteria for the design of such tests should be established prior to the choice of such standardized tests.

Standardised tests methods – definitions

Although the present ISO standard for determining explosion indices of combustible dust-air mixtures is based on tests performed in a 1-m³ cylindrical vessel (ISO 6184-1, 1985), most tests are performed in the 20-litre Siwek sphere¹. The standardized test procedure for the Siwek sphere is described by Cesana and Siwek (2001), it involves the following steps:

1. A weighted dust sample is placed in a 0.60-litre dust reservoir, and the reservoir is pressurized to 21 bars absolute. The 20-litre sphere is evacuated to 0.40 bars absolute.
2. The outlet valve, separating the reservoir and the vessel, is opened, and the dust follows the flow of air from the pressurized reservoir into the vessel. The transient injection generates intense turbulence that disperses the dust throughout the 20-litre vessel.
3. After a preset ignition delay time, the turbulent dust-air suspension is ignited by two chemical igniters with total energy 10 kJ (5 kJ each).

Typical pressure-time histories from such tests are shown in Figure 1-1 and Figure 1-2; the parameters summarized in Table 1-3 can be determined from the tests.

¹ Design and experimental procedures for some of the most frequently used explosion vessels and dispersion systems are described in Appendix B.

Table 1-2. Some of the parameters influencing the ignition sensitivity and explosion violence of dust clouds. Some parameters are independent of each other – others are not.

MATERIAL DEPENDENT PARAMETERS	Dust = Fuel (Dispersed phase)	Physical	<ul style="list-style-type: none"> ▪ Particle surface area per mass, determined by: <ul style="list-style-type: none"> ○ Particle size distribution. ○ Particle shape, particle porosity. ○ Particle density. ▪ Other relevant physical properties of the dust particles, e.g. specific heat, melting point, boiling point, heat of vaporization, thermal conductivity, oxide layer, ... 	
		Chemical	<ul style="list-style-type: none"> ▪ Chemical composition (overall and surface). ▪ Heat of combustion. ▪ Moisture content, volatiles. ▪ Inert dust content. 	
	Gas = Oxidizer (Continuous phase)	Physical	<ul style="list-style-type: none"> ▪ Initial pressure. ▪ Initial temperature. ▪ Other relevant physical properties of the gas phase, e.g. viscosity, thermal conductivity, ... 	
		Chemical	<ul style="list-style-type: none"> ▪ Chemical composition of gas, including inert gases, oxygen, and gaseous fuels (i.e. hybrid explosions). ▪ Moisture/humidity. 	
	PROCESS DEPENDENT PARAMETERS	Dust cloud (Mechanical suspension)	Dispersion	<ul style="list-style-type: none"> ▪ Degree of dispersion/agglomeration.
			Dust concentration	<ul style="list-style-type: none"> ▪ Nominal and real dust concentration. ▪ Spatial distribution of particle size in cloud.
Flow conditions			<ul style="list-style-type: none"> ▪ Turbulence intensity, turbulent length scales. ▪ Isotropic turbulence? ▪ Homogeneous turbulence? 	
Confinement (Boundary conditions)		Degree of confinement	<ul style="list-style-type: none"> ▪ Unconfined, partially confined (vented) or constant volume explosion? 	
		Geometry of confinement	<ul style="list-style-type: none"> ▪ Volume (scale). ▪ Shape. ▪ Turbulence-generating objects? 	
		Other factors	<ul style="list-style-type: none"> ▪ Heat loss/quenching. ▪ Secondary explosions? Pressure piling? 	
Ignition source		Ignition source	<ul style="list-style-type: none"> ▪ Type of ignition source (see Table 1-1) ▪ Energy of ignition source (power, duration) ▪ Location (and timing) of ignition source. 	

Table 1-3. Parameters that are determined in standardized explosion tests.

The following parameters can be identified directly for each individual test:	
p_d	<i>Expansion pressure:</i> the difference between initial pressure prior to dispersion and pressure at ignition time, it should be close to 0.6 bars.
t_v	<i>Ignition delay time:</i> the time from onset of dispersion to triggering of ignition, the default value is 60 milliseconds in 20-litre vessels.
p_{ex}	<i>Explosion pressure:</i> the difference between the pressure at ignition time and the pressure at the culmination point (W_{cp}).
p_m	<i>Corrected explosion pressure:</i> due to heat loss to the walls and pressure effects caused by the chemical igniters in the 20-litre sphere, the measured explosion pressure p_{ex} has to be corrected to agree with results from the 1-m ³ vessel ¹ .
$\left(\frac{dp}{dt}\right)_m$	<i>Rate of pressure rise:</i> the maximum slope of a tangent through the point of inflexion (W_{ip}) in the rising portion of the pressure versus time curve.
p_{ip}	<i>Inflection pressure:</i> the difference between the pressure at ignition time and the pressure at the inflexion point (W_{ip}).
t_{ip}	<i>Inflection time:</i> time difference between the onset of dispersion and the time when the inflection pressure is reached.
t_1	<i>Duration of combustion:</i> time difference between the activation of ignition and the culmination point (W_{pc}).
t_2	<i>Induction time:</i> time difference between the activation of ignition and the intersection of the inflexion tangent with the 0 bar line.
In addition, the following parameters can be found from a series of tests over a broad range of nominal dust concentrations ² :	
p_{max}	<i>Maximum explosion pressure:</i> the maximum value of p_m determined for tests over a wide range of fuel concentrations.
$\left(\frac{dp}{dt}\right)_{max}$	<i>Maximum rate of pressure rise:</i> the maximum value of $(dp/dt)_m$ determined for tests over a wide range of fuel concentrations.

¹ Formulas for this correction are given in Appendix B. Note that these empirical formulas have been developed for the 20-litre sphere; they should probably be adjusted before they are applied to results from the vessels used in this work. Such adjustments would however require extensive testing of several dusts in both 20-litre vessels and larger vessels, e.g. the 1-m³ ISO sphere. Hence, the parameter p_m will only be used as an approximation of the ‘true’ final pressure when estimating burning velocities in section 4.4, and when comparing results from the Round Robin test CaRo 00/01 in Appendix A.

² Detailed experimental procedures for the determination of these parameters can be found in e.g. Cesana and Siwek (2001). The nominal dust concentration is defined as the weighted amount of dust divided by the volume of the explosion vessel, V_v .

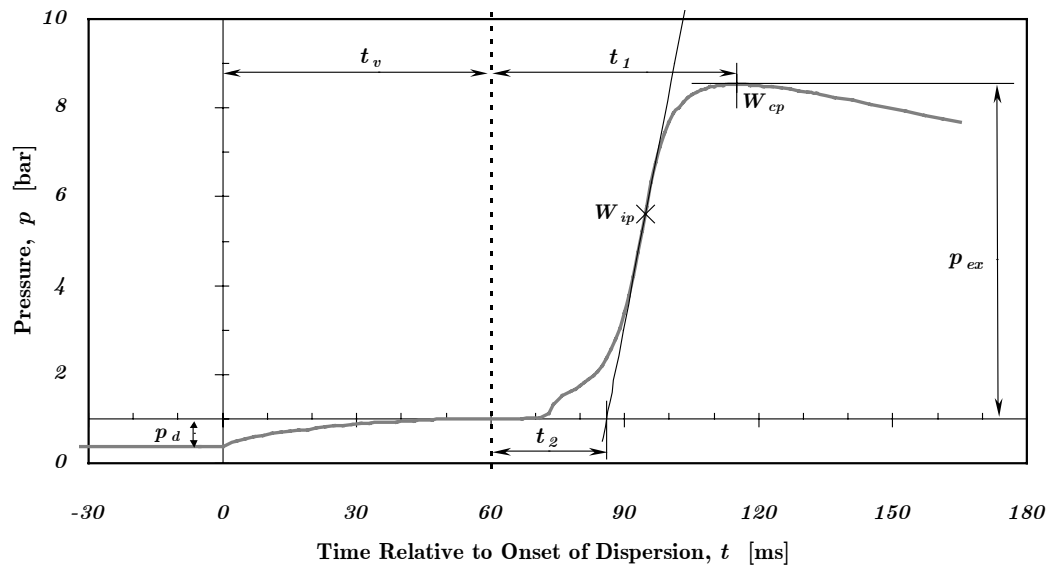


Figure 1-1. Pressure-time history for a typical explosion test in a 20-litre vessel; ignited by two chemical igniters with total energy 10 kJ. Vertical dotted line indicates triggering of the ignition source at the default ignition delay time of 60 milliseconds.

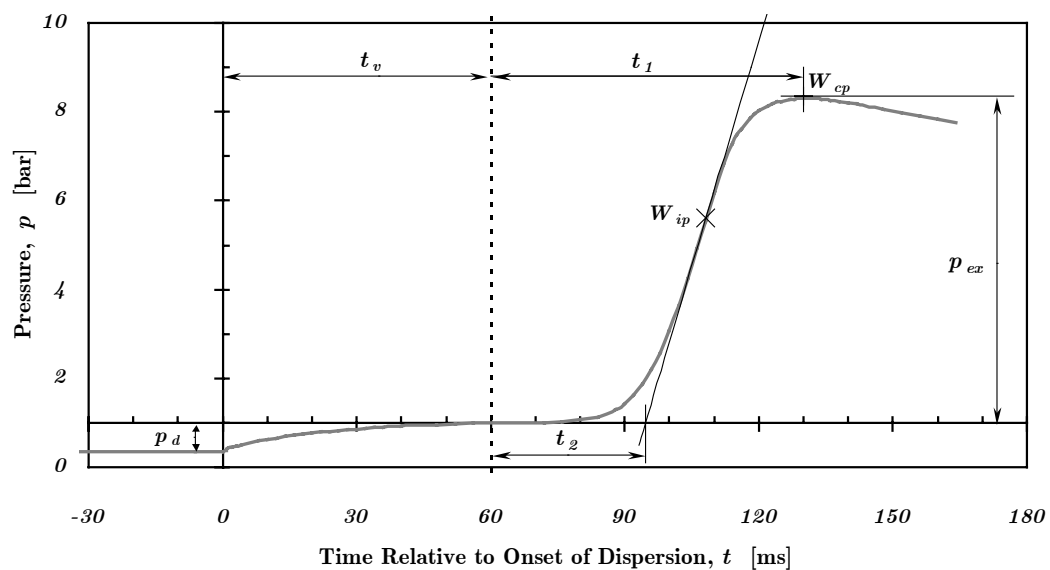


Figure 1-2. Pressure-time history for a typical explosion test in a 20-litre vessel; ignited by a 6 J arc discharge. Vertical dotted line indicates triggering of the ignition source at the default ignition delay time of 60 milliseconds.

There appears to be a growing scepticism towards the use of tests performed in constant volume explosion vessels for the determination of fundamental dust explosion characteristics. Jarosinski and Podfilipski (1999) points out that the cognitive value of such experiments is very limited. However, there are currently no credible alternatives to tests performed in 20-litre vessels. Although experiments performed in e.g. microgravity may reveal fundamental properties of dust flames (e.g. Jarosinski and Podfilipski, 1999; Jarosinski *et al.*, 1999), it is not realistic that the standardized tests used today could be replaced with tests performed in microgravity.

Simple scaling laws for results determined in standardized tests

Since $(dp/dt)_{max}$ depends on the size of the vessel, scaling laws have to be used in order to apply the results from 20-litre vessels on larger enclosures. The most well known scaling law is the *cube-root-law*, the concept was introduced by Bartknecht (1971). The traditional starting point for a theoretical analysis of the cube-root law is central point-ignition of a quiescent, uniform mixture followed by spherical propagation of a laminar flame with negligible thickness (Lewis and von Elbe, 1987; Bradley and Mitcheson, 1976). In the further derivation, it is customary to assume that the fractional pressure rise is proportional to the fractional mass burnt (e.g.: Bradley *et al.*, 1988; Amyotte *et al.*, 1989; Dahoe *et al.*, 1996):

$$\frac{p(t) - p_i}{p_f - p_i} = \frac{m_b(t)}{m_{tot}} = \frac{m_b(t)}{m_{u,i}} \quad (1.2)$$

After some additional simplifications, discussed in section 2.2.4, it is possible to find a relationship¹ between the measured rate of pressure rise, and the burning velocity S_u :

$$\frac{dp}{dt} = 4\pi(p_f - p_i) \frac{\rho_{u,i}}{\underbrace{m_{u,i}}_{V_v^{-1}}} \left(\frac{p}{p_i}\right)^{1/\gamma} \left[\frac{3V_v}{4\pi} \left\{ 1 - \frac{p_f - p}{p_f - p_i} \left(\frac{p}{p_i}\right)^{-1/\gamma} \right\} \right]^{2/3} S_u \quad (1.3)$$

It follows that the rate of pressure rise increases monotonically with p , and the maximum rate of pressure rise, $(dp/dt)_m$, is attained when $p = p_f$, i.e. when the spherical flame reaches the wall of the spherical vessel. Since the experimental value of $(dp/dt)_m$, and consequently $(dp/dt)_{max}$, depends on the size of the explosion vessel, it is normalized with respect to the cube-root of the vessel volume (V_v) to yield a volume-invariant dust explosion severity index:

$$K_{St} \equiv \left(\frac{dp}{dt}\right)_{max} (V_v)^{1/3} \quad (1.4)$$

According to the cube-root law, the rate of pressure rise for the same fuel-air mixture in a larger industrial plant unit (volume V) can be estimated as:

$$\left(\frac{dp}{dt}\right)_{estimated} = \frac{K_{St}}{(V)^{1/3}} \quad (1.5)$$

Bartknecht (1971, 1978, 1987) presented experimental results that indicated that the cube-root-law could be used as a valid scaling relationship for turbulent dust explosions between vessels with volumes larger than 40 litres. Results presented by Siwek (1977, 1988) and Bartknecht (1978, 1987) showed that the 20-litre Siwek sphere could produce K_{St} values that agree with data from the 1-m³ ISO vessel. However, according to e.g. Bradley *et al.* (1988), Dahoe *et al.* (1996, 2001a, 2001b, 2002) and Eckhoff (2003), the cube-root law can only be regarded as an approximation of a single realization of the explosion pressure curve.

¹ The subscripts used in the following equations are i and f for initial and final states; b and u for burned and unburned; v for vessel, and tot for total.

The cube-root-law is only strictly valid as a scaling relationship under hypothetical circumstances:

- i)* The mass-burning rate (i.e. the product of the burning velocity, the flame area, and the density of the unburned mixture) should be the same in both the test vessel and the industrial vessel at the instant when the rate of pressure rise reaches its maximum value (Dahoe *et al.*, 2001b). This condition is only fulfilled when:
 - a. The vessels in question are geometrically similar – they should actually both be spheres. For practical purposes the vessels should also be within a certain size range: the flame may not be fully developed before quenching occurs at the vessel walls if the vessel is very small, and hydrodynamic instabilities can lead to significant deviations from spherical flame propagation in larger vessels (Amyotte *et al.*, 1989).
 - b. The ignition source produces point ignition with negligible energy input at the centre of the vessel, with subsequent spherical flame propagation towards the walls. Zhen and Leuckel (1997) have shown that the energetic chemical igniters that are used in the standardized tests produces volumetric ignition and non-spherical flame spread that are far from the ideal assumption, especially in 20-litre vessels. The concept of central point ignition further illustrates the hypothetical nature of the cube-root law as a credible scaling tool; one may ask what the probability is for ignition taking place in the centre of an industrial enclosure filled with a combustible dust-air suspension?
 - c. The flow properties are identical in both vessels. Both Pu *et al.* (1988) and Dahoe *et al.* (2001b) have pointed out that results from standardized laboratory tests carried out under particular conditions of turbulence are applied to industrial circumstances where different conditions of turbulence exists. This can result in both under-estimation and over-estimation of the actual rate of pressure rise. Not only will the initial (*pre-ignition*) turbulence vary from one process situation to another; the flow of the unburnt mixture ahead of the flame front, caused by the hot expanding combustion products, can also generate considerable turbulence (*post ignition*) – especially in the presence of turbulence generating objects.
 - d. Changes in pressure, temperature and turbulence of the unburnt mixture ahead of the flame have the same effect on the burning velocity in both vessels.
 - e. There is no significant net flow in the vessels at the time of ignition. This would result in a displacement of the growing spherical flame.
- ii)* The thickness of the flame (δ) should be negligible compared to the radius of the explosion vessel (r_v). Theoretically, the highest rate of pressure rise, $(dp/dt)_m$, should occur when the pressure attains its maximum value, p_{ex} ; however, most pressure-time curves for dust explosions in spherical explosion vessels exhibits an inflexion point (W_{ip}), see Figure 1-1. The most accepted explanation for this phenomenon is that the leading edge of the flame reaches the vessel walls, while the remaining part is still propagating through the vessel; hence, it is caused by

either a thick flame or a non-spherical flame/vessel. According to Dahoe *et al.* (1996), the flame thickness of dust flames have been reported to be in the range 15 to 80 centimetres, thus exceeding the radius of the 20-litre vessel – and certainly not negligible compared to the radius of the 1-m³ vessel either. A three-zone model presented by Dahoe *et al.* indicates that significant deviations from the cube-root law can be expected if the relative flame thickness (δ/r_v) exceeds one per cent: the greater the flame thickness and the smaller the vessel size, the greater the relative reduction in the maximum rate of pressure rise.

Several so-called *integral balance models* have been introduced in order to overcome some of the limitations with the cube-root-law, e.g.: Nagy *et al.* (1969, 1971), Bradley and Mitcheson (1976), Nagy and Verakis (1983), Dahoe *et al.* (1996) and Dahoe (2000). Depending on the built-in assumptions in the various models, they should be more or less capable of predicting the entire pressure evolution during an explosion. The effect of parameters such as mixture composition, pressure, temperature and turbulence, on the transient combustion process, can be taken into account in an explicit manner. According to Dahoe *et al.* (1996, 2000), such models can be used in two ways:

- i)* The models can be fitted to experimental pressure-time recordings from dust explosions to determine fundamental properties of the flame propagation, such as burning velocity and flame thickness.
- ii)* When fundamental flame propagation properties are known, the models can be used to predict the pressure development of dust explosions for safety purposes.

However, the application of integral balance models is still limited to explosion prediction in simple geometries, e.g. spheres and enclosures with an aspect ratio close to unity, with central ignition and spherical flame propagation.

Scaling laws for the future – CFD codes

Realistic prediction of flow, flame propagation and pressure build-up in complex geometries can only be accomplished by CFD codes with built-in combustion models that can solve the conservation equations for mass, momentum and energy. If a sufficiently accurate combustion model for turbulent dust clouds could be implemented into an appropriate CFD code, it could turn out to be a valuable tool when mitigating measures are implemented in industrial plants where dust explosions represent a hazard. One such code is currently being developed by GexCon AS. The code, called DESC, will be based on the CFD code FLACS (FLame ACceleration Simulator) for gas explosions. The first version of DESC is expected to be commercially available by the end of the year 2004 (www.gexcon.com). An earlier attempt at simulation dust explosions by the FLACS-code is described by van Wingerden (1996).

A commercial CFD code for dust explosions should be able to describe the development of dust explosions in complex geometries, including pressure piling in interconnected vessels and the effect of turbulence generating objects on flame propagation. It should also be possible to estimate the effect of mitigating measures such as venting and isolation. Similar CFD-codes for gas explosions are currently used by the Norwegian petroleum industry as an integrated part in qualitative risk analysis (QRA); procedures for such calculations can be found in e.g. NORSOK Standard Z-013 (2001).

One of the main challenges in the development of a reliable CFD code for dust explosions will be to develop appropriate combustion models for combustible dust-air suspensions. Combustion models require correlations between fundamental flame properties (such as burning velocity and flame thickness) and characteristic properties of the turbulent flow field (such as turbulence intensity and turbulent length scales). Due to the complexity of the kinetics involved in dust explosions, such correlations must probably be determined by standardized tests. Tamanini (1998) points out that turbulence is the most important factor that needs to be incorporated in a model for dust explosions. Dahoe (2000) suggests that integral balance models can be regressed to experimentally determined pressure-time histories to yield the burning velocity and flame thickness of a particular mixture. This approach may however turn out to be an unnecessary detour when the final goal is to use the results in combustion models for CFD codes anyway. The experimental results can probably just as well be compared directly with CFD simulations of the dynamical flow conditions inside the explosion vessel. A general procedure for such investigations could go through the following steps:

- i)* The initial boundary conditions for the experiments are modelled, including a realistic representation of geometry (e.g. reservoir, outlet valve, dispersion nozzle, and the interior of the explosion vessel) and correct initial conditions (e.g. pressures and temperatures in the pressurized reservoir and the partly evacuated explosion vessel).
- ii)* The dispersion process is simulated for certain amounts of a ‘general’ dust; the state of the transient flow field is saved at selected instants (e.g. 60, 75, 90, etc. milliseconds after onset of dispersion). Because simulations of the dispersion process probably will be much more time-consuming than simulations of the subsequent explosions, it is essential that fundamental combustion parameters of the ‘general’ dust can be adjusted after the dispersion process. Dust properties that may have significant influence on the flow must however be fixed already at this stage, e.g. properties such as particle density, particle size distribution, etc. (depending on how the dispersed phase is modelled).
- iii)* Results from simulations of the dispersion process are compared with experimental results to assure that important features of the flow (e.g. mean velocities and production/decay of turbulence) are reproduced properly. This part of the work may have to be repeated several times to achieve sufficiently good agreement between experimental and simulated results. However, as soon as the dispersion process can be reproduced properly for the experimental equipment in question, one will have a set of initial conditions (at various ignition delay times) for dust explosion simulations that can be used for all dusts with selected flow properties similar to the ‘general’ dust.
- iv)* Dust explosion simulations are started at selected ignition delay times from the set of initial conditions generated in the dispersion simulation. Fundamental combustion parameters such as burning velocity and flame thickness can then be varied in a systematic manner until the simulated results agree with experimental results for that ‘specific’ dust. Initial values must be guessed, or estimated from measured parameters such as $(dp/dt)_m$. The main danger with this approach is that it can turn into an exercise in curve fitting, and result in

physically unrealistic values of the regressed parameters – the same can of course be said for the method of fitting integral balance models to experimental results.

- v) Finally, the resulting model for the ‘specific’ dust must be validated against full-scale experiments in larger and more complex geometries. In time, provided the model is able to reproduce results from full-scale experiments for a broad range of different dusts, it should be possible to perform consequence analyses by CFD simulations solely based on the laboratory tests.

There are several advantages with this approach, compared to e.g. integral balance models. First, the method is less sensitive to the shape of the test vessel. Hence, it could be possible to perform alternative tests (e.g. other vessel shapes) in order to isolate the effect of flame thickness from the effects of non-spherical flame propagation and non-spherical vessel. Second, transient variations in both flow properties (e.g. mean flow, turbulence intensity, turbulent length scales, etc.) and thermodynamic properties (temperature, pressure) that will take place during flame propagation in the currently used standardized tests, can be taken into account. Third, based on computational reproduction of standardized tests, the combustion model for a ‘specific’ dust is ‘generated’ with the same CFD code that will be used for the full-scale experimental verification. This iterative process of model evaluation against experiments for various dusts, and in various geometries, can in itself turn out to yield increased understanding of the dust explosion phenomenon.

However, the method will require that all significant parameters determining the burning rate of combustible mixtures can be first identified, and then modelled sufficiently well. This includes the two-way interaction between chemical reactions and turbulence parameters in particle-laden flows. The transient nature of the flow in the 20-litre vessel tests currently used makes this task particularly challenging.

1.2 Present Work

Safe construction of industrial equipment containing combustible dust clouds will require dimensioning parameters determined in standardized tests, at least in the foreseeable future. Economical considerations and present standardization dictates that the only realistic alternative test method currently available is the 20-litre explosion vessel. Due to their inherent limitations, simple scaling laws like the cube-root law are likely to be replaced by CFD codes with built-in combustion models for combustible dust clouds. A major factor in determining the success, or lack of success, of such codes, will be how well suited the results from the standardized test methods are in revealing the fundamental combustion characteristics of a dust cloud. Thus, the present work contains a critical experimental investigation of selected aspects of both the turbulent flow conditions during the transient dispersion process, and of the subsequent combustion process.

The approach chosen in this work can be summarized in the following points:

- In order to avoid the volumetric and energetic ignition source provided by the currently used chemical igniters, an arc generator capable of providing central point ignition with negligible energy input was developed; this work is documented in Appendix A. Since the main part of this thesis only presents results obtained with arc ignition, Appendix A also includes some results obtained with chemical igniters. This includes the results from the Calibration-Round-Robin Test CaRo 00/01, arranged by Adolf Kühner AG, for both of the vessels used in this work.
- Two 20-litre explosion vessels have been constructed. The main vessel is of the USBM type, having a large top lid providing easy access to the interior of the vessel, for cleaning, etc. In addition, a cubical 20-litre vessel was made, primarily because this geometry is very easy to implement in CFD codes utilizing a Cartesian coordinate system. Both vessels are fitted with the same dispersion system, and the same control and measurement system, used with the Siwek sphere. Unfortunately, it was not possible to extract the numerical values for the pressure-time data in a straightforward way; hence, any further analysis of these data was restricted to estimates made in selected points. Explosion vessels, dispersion nozzles, and some other experimental equipment are documented in Appendix B.
- Special emphasis has been put on documenting the various dusts used in this work. Particle size distributions, combustion mechanisms, SEM pictures and other interesting information are summarized for all dusts in Appendix C.
- The turbulent flow field generated by the transient dispersion process in the cubical vessel is measured by laser Doppler anemometry (LDA). Thus, it is possible to estimate the root-mean-square of the turbulent velocity fluctuations (u'_{rms}) as a function of time after onset of dispersion. However, these measurements could only be done with no dust added to the flow. The expected effect of particles on the flow is to some degree analysed theoretically; some simple pressure measurements at various positions in the flow path during the injection process can also give an indication of the effect of dust on the flow. The analysis of LDA data is described in Appendix D.
- Turbulent combustion of various combustible mixtures has been studied experimentally. The following fuels, or combinations of fuels, have been tested:
 - o flammable gas (propane),
 - o flammable gas and inert dust (propane and aluminium oxide or talc),
 - o flammable gas and combustible dust (hybrid mixtures of propane and *Lycopodium* spores),
 - o combustible dusts (niacin amide, *Lycopodium* spores and jet-milled silicon), and
 - o explosive dust (RDX).

The explosion pressure, p_{ex} , and the rate of pressure rise, $(dp/dt)_m$, have been determined over a broad range of fuel-air concentrations, and also for various ignition delay times for selected concentrations.

- The burning velocity (S_u), evaluated in the inflexion point (W_{ip}), has also been estimated for some of the combustible mixtures.
- Since no CFD code for dust explosions were available, and the present investigation were primarily of an experimental nature, the method of simulating the whole dispersion process and subsequent explosions at selected ignition delay times could only be demonstrated for gaseous fuels. The results are presented in Appendix E. However, since the combustion models used were not optimised for constant volume combustion, and due to the significant uncertainty concerning the level of turbulence, the simulations should only be regarded as a simple illustration of the method.

It should be emphasized that the transient nature of the standardized tests in 20-litre explosion vessel, combined with the inherently complex phenomena of particle-laden flow and heterogeneous combustion, makes it particularly challenging to extract quantitative information from dust explosion tests.

Aim

The main objective of this study is to conduct a critical experimental investigation of selected aspects of the turbulent flow and combustion that takes place in the 20-litre explosion vessels during standardized tests. Although by far not answered, the following questions have guided most of the work presented in the main part of this thesis:

- To what extent is the generation and decay of turbulence during and after the transient dispersion process influenced by the presence of dust?
- To what extent can fundamental mechanisms of flame propagation through combustible dust-air suspensions be explored in 20-litre vessels?
- To what extent are results from standardized tests in traditional 20-litre explosion vessels suited as input for CFD codes that aspire to predict the propagation of flames through turbulent dust-air suspensions in complex geometries?

To the extent that the above questions cannot be answered, it is hoped that the present work can indicate directions for further work.

CHAPTER 2

Theory and Previous Work

Some definitions and basic concepts are introduced. The particle-laden flow involved in dust explosions is characterized in order to clarify whether or not any influence of the particles on the flow can be predicted. Previous work on the dispersion process in 20-litre combustion vessels is briefly reviewed. For a more general overview of dust explosion phenomena, the reader should consult some of the available textbooks, e.g. Bartknecht (1981, 1993) or Eckhoff (2003).

2.1 Definitions and Basic Concepts

2.1.1 Explosions

Explosions are usually associated with a rapid increase in pressure. In order for an explosion to occur, there must be a local accumulation of energy at the site of the explosion, which can be suddenly released to produce a pressure wave. Akhavan (1998) classifies explosions according to the origin of the released energy: *physical* (e.g. bursting of a pressurized vessel), *chemical* (e.g. rapid combustion) or *nuclear* (fusion or fission). Only chemical explosions are considered in this work.

Disregarding explosives and chemically unstable substances, there are five basic requirements for a chemical explosion to take place:

- i)* *Fuel* – any flammable gas, vapour or mist, or combustible dust.
- ii)* *Oxidizer* – usually air.
- iii)* *Combustible mixture* of fuel and oxidizer.
- iv)* *Confinement*. Some degree of confinement is usually necessary for pressure build-up, but this will depend on the rate of the chemical reactions. The violence of an explosion is determined by the rate of energy release due to chemical reactions, relative to the degree of confinement and heat losses (Cashdollar,

2000). Explosions can be classified according to the degree of confinement: *unconfined*, *partially confined* and *constant volume*.

v) *Ignition source*.

This work is mainly concerned with constant volume explosions in which the fuel is either a flammable gas or a combustible dust, and the oxidizer is air. The released energy stems from *combustion*. A *dust explosion* can be defined as the rapid combustion of a combustible dust cloud, resulting in rapid increase in temperature and pressure. The fuel, or combustible dust, can be any finely divided solid material (typically below 100-200 μm in diameter) capable of reacting rapidly and exothermically with the oxidizer.

2.1.2 Combustion

Definitions

Combustion is a phenomenon that is difficult to define precisely, and many of the classical textbooks simply omit any attempts of a formal definition (e.g. Glassman, 1996; Kuo, 1986; Warnatz *et al.*, 1996). Nevertheless, some of the definitions found in the literature will be given below. The shortest definition of is perhaps the one from Webster's Dictionary (1994), used by e.g. Turns (1996):

"Rapid oxidation accompanied by heat and, usually, light."

In his search for a definition, Williams (1986) include the following definition provided by Frank-Kamenetskii (1969)¹:

"Combustion is the name given to the occurrence of a chemical reaction under conditions of progressive self-acceleration which are brought about by the accumulation of heat or catalysing products of the reaction in the system."

Williams concludes with his own 'working definition':

"Combustion may be considered to be the science of exothermic chemical reactions in flows with heat and mass transfer."

Borghini and Destriau (1998) emphasizes that combustion is usually accompanied by the generation of heat and emission of light in the form of a flame.

¹ Williams (1986) also mentions the following definition, of unknown origin: *"Combustion is based on scientific principles, no one is certain exactly what these scientific principles may be. For a person to become knowledgeable about the burning of fuel, he must personally observe conditions and results to reach reasonable conclusions as to the hows, whats, whys and whens of combustion. But he does so always at the extreme hazard of misinterpretation which may lead him to errors greater than those in the literature"*.

General classification of flames

The following criteria are commonly employed for characterizing combustion phenomena, including flames (Williams, 1986; Kuo, 1986):

- i)* According to the degree of mixing between fuel and oxidizer in the system:
 - a. *Non-premixed combustion.* The reactants are initially separated; continuous mixing takes place in the reaction zone (e.g. the jet flame from a cigarette lighter, a candle's flame, etc.).
 - b. *Premixed combustion.* The reactants are intimately mixed before combustion begins (e.g. gas explosions and the flame in a Bunsen burner).
 - c. Intermediate systems, such as *partially premixed combustion* and *premixed combustion with non-premixed substructures* (e.g. dust explosions).
- ii)* According to the phases present:
 - a. *Homogeneous combustion*, i.e. only one phase present (e.g. the combustion of flammable gases in air).
 - b. *Heterogeneous combustion*, i.e. more than one phase present (e.g. combustion of a cloud of droplets or particles).
- iii)* According to the flow conditions:
 - a. *Laminar combustion.*
 - b. *Turbulent combustion.*

Further subdivision can be done based on the speed of the combustion wave: *deflagrations* are subsonic and *detonations* are supersonic.

Theoretical analysis of combustion and flame propagation mechanisms is never trivial, but it is always significantly more difficult for:

- Combustion of intermediate systems, compared to combustion of pure premixed or non-premixed systems (e.g. Williams, 1986).
- Heterogeneous combustion, compared to homogeneous combustion (e.g. Bardon and Fletcher, 1983).
- Combustion of particles, compared to combustion of droplets (e.g. Bardon and Fletcher, 1983).
- Turbulent combustion, compared to laminar combustion.
- Transient conditions (e.g. explosions), compared to stationary conditions (e.g. a stabilized flame).

Thus, transient flame propagation through a turbulent dust-air suspension is among the most complicated combustion processes that can be studied.

Classification of laminar dust flames

A dust cloud is a *mechanical suspension*, i.e. a system of fine particles dispersed by agitation – not by the molecular motion in the surrounding medium (as in a colloidal suspension). Thus, dust flames are rarely laminar. According to Bardon and Fletcher (1983), studies of laminar dust flames are usually conducted at two levels: either the microscopic level (combustion of single particles) or the macroscopic level (combustion of an entire cloud of particles).

In the study of the burning of single particles, a distinction is traditionally made between two types of dust flames (Cassel, 1964):

- i. *Nusselt flames.* Pure heterogeneous combustion at the surface of individual particles is sustained by the diffusion of oxygen towards the particles surface; this includes combustion of materials such as:
 - a. Carbon particles, but also and the remaining char in e.g. coal particles after the volatiles have been consumed in a volatile flame (Bardon and Fletcher, 1983).
 - b. Refractory metals such as zirconium and hafnium (Goroshin and Lee, 1999).
- ii. *Volatile flames.* Vapours, volatiles and/or pyrolysis gases, produced when the solid fuel is heated, mixes with air prior to local homogeneous combustion. Depending on the nature of the solid, Bardon and Fletcher (1983) distinguishes between three different mechanisms for the combustion of single particles in volatile flames:
 - a. *Coal and similar carbonaceous materials:* devolatilisation and burning of volatiles, followed by combustion of the solid residue (Nusselt flame).
 - b. *Plastics:* melting followed by evaporation and subsequent vapour phase burning (e.g. PMMA, but also sulphur).
 - c. *Metals.* The classical model described by e.g. Cassel (1964) suggests vaporization of metal through a solid oxide shell followed by combustion of the vapour outside the shell (e.g. Mg and Al). Altman (1999) describes the ‘gas-phase’ combustion of metals particles as a process in three sequential steps: ¹metal vaporization, ²oxidation of the metal vapour with the formation of intermediate gaseous products of combustion, and ³condensation of the gaseous oxide with the formation of ultra-fine oxide particles (Mg, Al, Ti, Fe and Zr). According to Meinköln (1999), the metal oxide may be grouped in two fractions: oxide outside the flame envelope condenses into μm -size smoke particles, while oxide between the flame envelope and the particle mostly condenses on the particle surface forming a layer.

The combustion rate of a solid fuel particle in a gaseous oxidizer can be limited by either reaction kinetics or by the molecular transport of the oxidizer to the particle surface (Goroshin and Lee, 1999). The mechanisms for the propagation of a flame in a laminar dust clouds have not been well established, but conflicting evidence suggests that there may be several mechanisms involved for various materials (Bardon and Fletcher, 1983):

- Contact between burning gases in the flame front and volatiles released by the heated particles ahead of the flame front (e.g. coal dust).
- Ignition is more a solid/oxidant reaction (e.g. carbon black).
- Flame propagation due to burning particles thrown ahead of the flame front.
- Heat transfer by radiation is probably important for flame propagation through dust clouds, especially when the flame temperature is high (e.g. Al, Mg, etc.).

Han *et al.* (2000, 2001) studied laminar flame propagation in *Lycopodium* dust clouds, and found that the reaction zone showed a double flame structure, consisting of enveloped diffusion flames of individual particles and diffusion flames surrounding some particles. The effect of particle size and agglomeration on flame propagation introduces further complications. Although it seems clear that reduced average particle size generally results in more favourable conditions for ignition and flame propagation, the effect of the actual particle size distribution is much more complex. No general rule for the ‘averaging’ of particle sizes in application to dust flames has been established (Goroshin and Lee, 1999). The explosible concentration range for dust suspensions is much wider than for gaseous mixtures; Bardon and Fletcher (1983) suggests the flame proceeds through paths provided by small particles, while largely bypassing the large ones.

2.1.3 Turbulence

Turbulence is an inherent property of dust explosions. Turbulence is needed for dispersing the dust, and turbulence will be generated when the cloud burns. Without turbulence, the dust cloud will settle down as a dust layer.

Phenomenon

Turbulence is a property of the flow – not a property of the fluid. Often referred to as ‘the last great unsolved problem of classical physics’, turbulence is not easy to define; it is, however, possible to identify several characteristic properties of turbulent flows (Tennekes and Lumley, 1972; Hinze, 1975; Tsinober, 2001):

1. *Continuum.* Turbulence is a continuum phenomenon, and turbulent flows are governed by equations of continuum (fluid) mechanics. Even the smallest scales of turbulent motion are much larger than molecular length scales (e.g. mean free path).
2. *Structures, scales, eddy.* Turbulent flows contain structures. *Turbulent eddies*, or simply an *eddy*, is a conceptual idea rather than a physical definition used to refer to rotating structures; each turbulent eddy has an associated length and time scale. Turbulent flows contain an extremely wide range of strongly and non-locally interacting degrees of freedom, or ‘scales’, in both time and space.
3. *Irregularity, intrinsic randomness, chaos.* Because of irregularity, it is impossible to describe the motion in all details as a function of time and space coordinates. Intrinsic randomness means that there is no necessity for external random forcing either in the interior of the fluid flow or at its boundaries. Chaos is manifested in the sensitive dependence on initial conditions; the development of the system is essentially unpredictable after some finite time.

4. *Vorticity and vortex stretching.* The *vorticity* is defined as the curl of a fluid field (i.e. a measure of circulation). Without vorticity, there is no turbulence. Vortex stretching causes large eddies to break up into smaller eddies, which in turn breaks up into even smaller ones, until the smallest eddies disappear due to viscosity (*eddy cascade hypothesis*).

5. *Three-dimensionality.* Vorticity and vortex stretching are three-dimensional phenomena.

6. *Diffusivity and mixing.* Turbulence increases rates of momentum, heat, and mass transfer. In turbulent flows, the increase in the transport of scalar quantities is primarily a convective phenomenon brought about by the ‘stirring’ action of the turbulent eddies. In addition, depending on the nature of the scalar (e.g. temperature or species concentration), further mixing occurs due to diffusion of the scalar through the medium. In the case of small solid particles, the mixing (‘dispersion’) occurs only due to convection of these particles.

7. *Dissipation.* Turbulence is a dissipative phenomenon; there is a transfer of kinetic energy from the flow to the molecular motion (internal energy) through the deformation work performed by viscous (shear) stresses. A source of energy is required to maintain turbulence; if no energy is supplied, turbulence decays rapidly.

Basic equations

The basic equations that govern the motion of a Newtonian fluid (one phase, both laminar and turbulent) are (Ertesvåg, 1999; Tsinober, 2001):

1. The continuity equation (conservation of mass):

$$\frac{\partial \rho}{\partial t} + \frac{\partial}{\partial x_j}(\rho u_j) = 0 \quad (2.1)$$

2. The Navier-Stokes equations (conservation of momentum); μ is the dynamic molecular viscosity; μ_B is the bulk viscosity (Stokes hypothesis: $\mu_B=0$):

$$\begin{aligned} \frac{\partial}{\partial t}(\rho u_i) + \frac{\partial}{\partial x_j}(\rho u_i u_j) &= -\frac{\partial p}{\partial x_i} + \frac{\partial \tau_{ij}}{\partial x_j} + \rho f_i \\ \tau_{ij} &= \mu \left(\frac{\partial u_i}{\partial x_j} + \frac{\partial u_j}{\partial x_i} \right) + \left(\mu_B - \frac{2}{3}\mu \right) \frac{\partial u_k}{\partial x_k} \delta_{ij} \end{aligned} \quad (2.2)$$

3. The energy equation with respect to conservation of e.g. specific enthalpy h (can also be expressed as specific internal energy e or temperature T ; note that $\alpha=\lambda/(\rho c_p)$ is the thermal diffusivity; S_h is a source term due to e.g. chemical reactions):

$$\frac{\partial}{\partial t}(\rho h) + \frac{\partial}{\partial x_j}(\rho h u_j) = \frac{\partial}{\partial x_j} \left(\rho \alpha \frac{\partial \rho}{\partial x_j} \right) + S_h \quad (2.3)$$

4. A thermal equation of state (e.g. ideal-gas law):

$$pV = nRT, \quad (2.4)$$

5. A caloric equation of state:

$$e = c_v T \text{ or } h = c_p T \quad (2.5)$$

6. In a mixture of N different substances, there will also be an equation for the mass fraction Y_k (or concentration, c_k) of $N-1$ of the substances (the N^{th} mass fraction is given from $\sum_k Y_k = 1$):

$$\frac{\partial}{\partial t}(\rho Y_k) + \frac{\partial}{\partial x_j}(\rho Y_k u_j) = \frac{\partial}{\partial x_j} \left(\rho \mathcal{D} \frac{\partial Y_k}{\partial x_j} \right) + R_k \quad (2.6)$$

The diffusion coefficient, \mathcal{D} , in Fick's law is assumed the same for all substances; R_k is a source term (due to e.g. chemical reactions). Within the continuum approximation the experimentally determined boundary condition is that there is no slip between the fluid (velocity u_i) and a solid boundary (velocity v_i) at the interface:

$$u_i = v_i \quad (2.7)$$

For further discussion of the properties and limitations of the Navier-Stokes equations, refer to e.g. Tsinober (2001) or Foias *et al.* (2001).

Common assumptions regarding turbulence

Several simplifying assumptions are often imposed on turbulent flows, e.g.:

- Turbulent flows are *homogeneous* if all statistical properties/parameters of the turbulent flow are invariant to translations in space. All real flows are inhomogeneous.
- Turbulence flows are *isotropic* if all statistical properties/parameters of the turbulent flow are invariant to rotations and reflections. All isotropic flows are homogeneous.
- Turbulence flows are *stationary* or *statistically steady* if all statistical properties/characteristics of the turbulent flow are invariant to translations in time.
- Turbulence flows are *incompressible* if the density ρ is constant with respect to variations in the pressure p .

The particular significance of homogeneous and isotropic flows is that they are free from external influences, like mean shear, centrifugal forces (rotation), buoyancy, magnetic fields, etc., which usually act as an organizing factor, favouring the formation of so-called (large scale) coherent structures (Tsinober, 2001). According to Hinze (1975) and Bradshaw (1976), there is a distinct difference between turbulence generated by friction forces at fixed walls (*wall turbulence*, i.e. flow through conduits, flow past bodies) and turbulence generated by the flow of fluid layers with different velocities past one another (*free turbulence*, i.e. jets and plumes, wakes, mixing layers).

Turbulent scales and the turbulent energy spectrum

Several different scales (both length and time) can be present in the simplest of turbulent flows. Large structures in turbulent flows generally depend on the geometry of the system; smaller scales feature more universal properties.

The distribution of length scales at any position in the flow is often characterized by a two-point correlation $R_{i,j}(\vec{r}, t)$ between simultaneous velocity measurements in the positions \vec{x} and $\vec{x} + \vec{r}$ (e.g. Hinze, 1975; Peters, 2000; Ertesvåg, 2000). A Fourier transform of this correlation yields the tensor for three-dimensional energy spectrum $E_{i,j}(\vec{\kappa}, t)$ as a function of the wave number vector $\vec{\kappa}$ and time:

$$R_{i,j}(\vec{r}, t) \equiv \overline{u'_i(\vec{x}, t)u'_j(\vec{x} + \vec{r}, t)} \xrightarrow{\mathcal{F}} E_{i,j}(\vec{\kappa}, t) \quad (2.8)$$

For homogeneous isotropic turbulence the position \vec{x} is arbitrary and \vec{r} may be replaced with its absolute value $r = |\vec{r}|$; also, $R_{i,j}(\vec{r}, t)$ and $E_{i,j}(\vec{\kappa}, t)$ becomes $R(r, t)$ and $E(\kappa, t)$, respectively. The wave number $\kappa = |\vec{\kappa}|$ can be thought of as the reciprocal of length scale, and $E(\kappa, t)$ is the density of kinetic energy per unit wave number κ ; hence:

$$\int_0^\infty E(\kappa, t) d\kappa = \frac{1}{2} \overline{u'_i u'_i} = k(t) \quad (2.9)$$

A normalized two-point velocity correlation can be defined as:

$$f(r, t) = \frac{R(r, t)}{u'^2(t)} \quad (2.10)$$

A typical energy spectrum for the hypothetical situation of fully developed, physically restricted, homogeneous isotropic turbulence at high Reynolds numbers is shown in Figure 2-1; the spectrum is constructed from the formulas presented by Skrbek and Stalp (2000). Kolmogorov's 1941 theory for homogeneous isotropic turbulence assumes that there is a steady transfer of kinetic energy from the large scales to the small scales, and that this energy is being consumed at the small scales by viscous dissipation (*the eddy cascade hypothesis*). At sufficiently high Reynolds numbers, there is a range of high wave numbers (*the universal equilibrium range*) where the turbulence is statistically in equilibrium and uniquely determined by the parameters ε and ν .

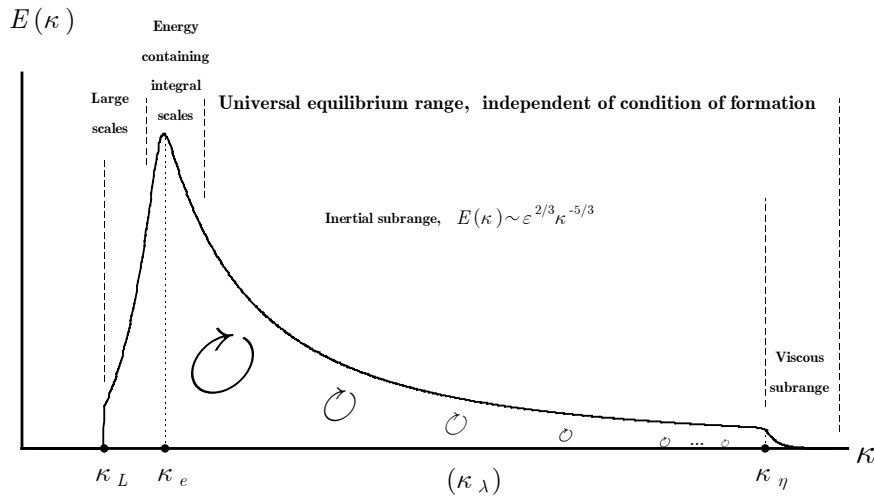


Figure 2-1. Turbulent energy spectrum, showing the energy cascade, left to right. For a detailed discussion, refer to Hinze (1975) or Skrbek and Stalp (2000).

The wave numbers indicated in the Figure 2-1 corresponds to various length scales that are frequently used to characterize turbulent flows:

- The *maximum spatial length scale* ($L = \kappa_L^{-1}$) is determined by the physical boundary conditions (geometric constraints).
- The *integral length scale* ($\ell_e = \kappa_e^{-1}$) is a characteristic length scale for eddies containing most of the kinetic energy; it is defined on the basis of the normalized two-point velocity correlation in (2.10):

$$\ell_e(t) = \int_0^\infty f(r,t)dr \quad (2.11)$$

- The *Kolmogorov length scale* ($\eta = \kappa_\eta^{-1}$) represents the smallest eddy size found in any turbulent flow; its definition follows from dimensional reasoning:

$$\eta = \left(\frac{\nu^3}{\varepsilon} \right)^{1/4} \quad (2.12)$$

- The *Taylor micro scale* ($\lambda = \kappa_\lambda^{-1}$) is an intermediate scale between the integral length scale and the Kolmogorov scale. Several definitions can be found in the literature (Ertesvåg, 2000); i.e.:

$$\lambda^2 = 10\nu \frac{k}{\varepsilon} \xrightarrow{\text{ISOTROPIC}} \lambda^2 = 15\nu \frac{u_{rms}^{\prime 2}}{\varepsilon} \quad (2.13)$$

For each length scale, it is possible to define a corresponding Reynolds number:

$$\text{Re}_L = \frac{u_{rms}' L}{\nu} \quad (2.14)$$

$$\text{Re}_e = \frac{u_{rms}' \ell_e}{\nu} \quad (2.15)$$

$$\text{Re}_\eta = \frac{u_\eta \eta}{\nu} \approx 1 \quad (2.16)$$

$$\text{Re}_\lambda = \frac{u_{rms}' \lambda}{\nu} \quad (2.17)$$

The following time scales can be associated with the length scales defined above, they are sometimes termed ‘turnover time of eddy’ or ‘eddy lifetime’:

$$\tau_L = \frac{L}{u_{rms}'} \quad (2.18)$$

$$\tau_e = \frac{\ell_e}{u_{rms}'} \approx \frac{k}{\varepsilon} \quad (2.19)$$

$$\tau_\eta = \frac{\eta}{u_\eta} = \left(\frac{\nu}{\varepsilon} \right)^{1/2} = \frac{\eta^2}{\nu} \quad (2.20)$$

$$\tau_\lambda = \frac{\lambda}{u_{rms}'} \quad (2.21)$$

According to Hinze (1975), relations amongst the various length, time and velocity scales, can be derived from the following expressions for the dissipation of kinetic turbulence energy in isotropic turbulence (A is a numerical constant close to unity):

$$\varepsilon = 15\nu \frac{u_{rms}^{\prime 2}}{\lambda^2} = A \frac{u_{rms}^{\prime 2}}{\ell_e} \quad (2.22)$$

Further details can be found in e.g. Hinze (1975), Ertesvåg (2000) or Tsinober (2001).

Decay of homogeneous isotropic turbulence

The decay of homogeneous and isotropic turbulence is one the most extensively explored problems in fluid dynamics (see e.g. Hinze, 1975); nevertheless, a general theory describing the decay of such turbulence have not yet been developed from first principles (Skrbek and Stalp, 2000).

Most of the experimental work on the decay of homogeneous and isotropic turbulence is related to turbulence generated by a grid in wind tunnels, where the turbulence is studied as it decays downstream (direction x_1) of a grid with mesh spacing M . The first extensive measurements of turbulence downstream of a grid was done by Batchelor and Townsend (1947, 1948a, 1948b); they divided the process into the following stages:

- i) The *initial build-up* period: turbulence develops from a highly inhomogeneous and anisotropic flow, through the production of turbulence energy, into a more homogeneous and isotropic flow (last up to $x_1/M \sim 20$).
- ii) Three consecutive *decay* periods, increasingly further downstream of the grid (depending on the initial value of the Reynolds number); the decay in turbulence intensity can be described by equations on the form¹:

$$\frac{\overline{u'^2}}{u_0'^2} = \left(\frac{t}{t_0}\right)^{2n} \Rightarrow \frac{u'_{rms}}{u_{rms}^o} = \left(\frac{t}{t_0}\right)^n \quad (2.23)$$

The exponent n is different in the three decay periods:

- a. In the *initial* period of decay, predominantly determined by the decay of the energy containing eddies, n is found to be -0.5 .
- b. In the *transition* period, the exponent changes gradually from $n = -0.5$ to $n = -1.25$.
- c. In the *final* period of decay, dominated by viscous effects, $n = -1.25$.

Figure 2-2 illustrates how the turbulent energy spectrum for homogeneous isotropic turbulence evolves in time as the turbulent energy decays. The spectrum is naturally truncated by the wave numbers κ_L and κ_η , corresponding to the maximum spatial length scale, L , and the Kolmogorov length scale, η , respectively. From the initial time t_0 , the energy containing length scale ℓ_e grows until it reaches the size of the channel or vessel (L) at time t_s , and saturates. However, the Kolmogorov length scale grows faster than the energy containing length scale, causing the inertial subrange to shrink as the turbulence decays. At some stage of this process, the concept of a dissipation length (e.g. the Kolmogorov length scale) is no longer applicable (Skrbek and Stalp, 2000).

Modelling of turbulence

Bradshaw is often quoted for commenting that his favourite definition of turbulence is the general solution of the Navier-Stokes equations². However, it is presently not possible to obtain analytical or numerical solutions (except under idealized conditions)

¹ Note that time has been introduced as $t = x_1/\overline{u_1}$ in order to describe the idealized problem of decay of strictly homogeneous turbulence.

² “*My favorite definition of turbulence is that it is the general solution of the Navier-Stokes equations. This is the perfect answer by a government servant to an inquiry by a Congressman or Member of Parliament: it is brief, it is entirely true, and it adds nothing to what was known already. [...] When people regret that we do not ‘understand’ turbulence they are really regretting that we are not able to integrate the Navier-Stokes equations in our heads: for that, one would need a Cray in the cranium*” (Bradshaw, 1994).

for the general Navier-Stokes equations, which are thought to constitute an (almost) exact model of turbulent flow (Tsinober, 2001). The most common procedure used to overcome the time and spatial resolution problem in numerically solving the Navier-Stokes equations is to time-average the equations. Such an average procedure results in fluctuating quantities, or time-dependence component of the property averaged, that must be modelled separately.

The most frequently used turbulence models for practical applications are the so-called second-order closure models, e.g. the k - ε model. Further details on second-order closure models can be found in e.g. Laufer and Spalding (1974), Laufer (1989), Hanjalic (1994), Chen and Jaw (1998) and Ertesvåg (1999).

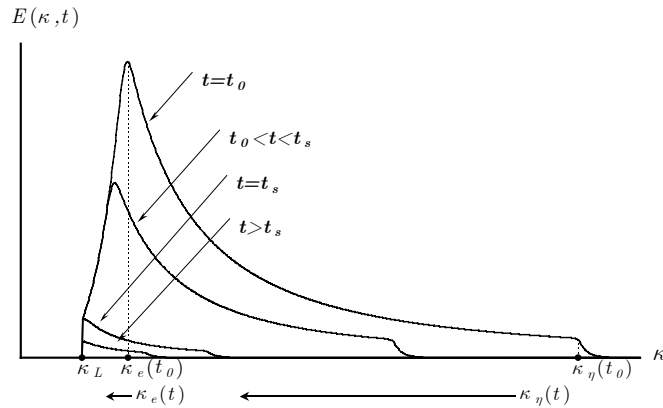


Figure 2-2. Evolution over time of the energy spectrum function $E(\kappa, t)$ for decay of homogeneous isotropic turbulence according to Skrbek and Stalp (2000).

2.1.4 Characterization of Particle-Laden Flows

This section introduces some aspects of multiphase flows relevant for dust explosions, i.e. particle-laden gas flows with only two distinguishable phases:

- i)* The *dispersed phase*, also called *particle phase*.
- ii)* The *continuous phase*, also called *carrier phase* or *fluid phase* (usually air).

However, due to the vast amount of literature on this topic, the account that can be given here is bound to be limited. The emphasis will be on physical phenomena – not mathematical modelling. Introductions to the topic of particle-laden flow can be found in books (e.g.: Clift *et al.*, 1978; Crowe *et al.*, 1998), and in various review articles such as Hinze (1972), Beér *et al.* (1984), Elghobashi (1994), Shirolkar *et al.* (1996), Peirano and Leckner (1998), Gouesbet and Berlemont (1999) and Loth (2000).

After introducing some fundamental definitions and concepts concerning multiphase flows, the two mechanisms of two-way interaction between turbulence and dispersed solid particles will be discussed separately:

- i)* Particle dispersion, i.e. the effects of carrier-phase turbulence on the particles (section 2.1.5).
- ii)* Turbulence modification (or modulation), i.e. the effect of the presence of particles on turbulence (section 2.1.6).

Fundamentals of fluid-particle interactions

Several fluid and particle properties can be identified as important in predicting turbulent particle interaction for a single particle in an isotropic, homogeneous turbulent flow field (e.g.: Hinze, 1972; Kulick *et al.*, 1994; Shirolkar *et al.*, 1996):

- i)* The particle size relative to turbulent length scales in the flow.
- ii)* The particle density relative to the density of the fluid.
- iii)* The fluctuating velocity of the fluid surrounding the particle.
- iv)* The particle relaxation time.
- v)* The eddy lifetime and the particle Lagrangian time scale.
- vi)* The crossing trajectory effect.
- vii)* The proximity of a solid surface.
- viii)* Gravity.

In addition, a couple of other factors becomes important when more than one particle is involved:

- ix)* The particle volume fraction (or dust concentration):
 - a. For very low concentrations, the problem reduces to that of a single particle in a flow field (one-way coupling).
 - b. For moderate concentrations, properties of the carrier-phase are modified by the presence of particles (two-way coupling).
 - c. For higher concentrations, particle-particle interactions become important (four-way coupling).
- x)* Particle size distribution.

Some considerations concerning the various parameters listed above will be discussed briefly in the following.

Particle size

The size of the particle, d_p , relative to the eddy size is an important parameter in determining the outcome of the eddy-particle interaction (Hinze, 1972). It is convenient to classify the particles, in general, into two categories, based on their characteristic dimension (diameter) with respect to the smallest length scale available in a given turbulent field. A particle is referred to as *small* if its diameter is smaller than the Kolmogorov scale ($d_p < \eta$) and *medium* if the diameter lies between the Kolmogorov scale and the integral length scale ($\eta < d_p < \ell_e$).

Relative density

Particles with densities different from that of the fluid tend to segregate due to centrifugal forces. Dense particles (i.e. $\rho_p > \rho_f$, where ρ_p and ρ_f are particle and fluid densities, respectively) are flung out of the vortices and concentrate in regions that are (relatively) stagnant, or do not rotate. Particle segregation depends on time scales for particle motion compared with time scales of the turbulent fluctuations.

Particle relaxation time

Small particle will remain trapped inside an eddy for a certain time; the maximum time is the lifetime of that eddy. The particle will see a uniform velocity field during its

residence time within the eddy; if the particle is dense, the particle will have less fluctuating velocity as compared to that of the fluid. This reduction in the particles root mean square fluctuating velocity ($v'_{rms} = \sqrt{v_p'^2}$) is known as the *inertia effect*, characterized by a time scale called the *particle relaxation time* or *particle response time*. The particle relaxation time, τ_p , is defined as the rate of response of particle acceleration to the relative velocity between the particle and the carrier fluid (Crowe *et al.*, 1998):

$$\tau_p = \frac{24}{C_D \text{Re}_p} \cdot \frac{\rho_p d_p^2}{18\mu_f} \quad (2.24)$$

where d_p is the particle diameter, μ_f is the fluid viscosity, C_D is the particle drag coefficient, and Re_p is the particle Reynolds number defined as (Crowe *et al.*, 1998):

$$\text{Re}_p = \frac{\rho_f |\vec{v}_p - \vec{u}_f| d_p}{\mu_f} = \frac{\rho_f |\vec{u}_d| d_p}{\mu_f} \quad (2.25)$$

where \vec{v}_p , \vec{u}_f and \vec{u}_d are the particle velocity, fluid velocity and drift velocity vectors, respectively. The particle Reynolds number characterizes the flow around the particle; small Reynolds numbers corresponding to attached laminar flow and large Reynolds numbers corresponding to fully turbulent particle wakes. In the limits of low Reynolds numbers ($\text{Re}_p < 0.1$, called Stokes flow), the particle drag is linearly related to the relative velocity:

$$C_D = \frac{24}{\text{Re}_p} \quad \text{Re}_p < 0.1 \quad (2.26)$$

where C_D is the particle drag coefficient. Hence (2.24) reduces to:

$$\tau_p = \frac{\rho_p d_p^2}{18\mu_f} \quad \text{Re}_p < 0.1 \quad (2.27)$$

Several other expressions for the drag coefficients of particles can be found in the literature – depending on the flow conditions. Clift *et al.* (1978) provides the following expression:

$$C_D = \left(\frac{24}{\text{Re}_p} \right) (1 + 0.15 \text{Re}_p^{0.687}) \quad \text{Re}_p < 10^3 \quad (2.28)$$

The particle relaxation time as a function of particle diameter according to (2.27) is plotted in Figure 2-3 for various particle densities; note that equation (2.27) should be modified for both particle Reynolds numbers larger than about 0.1 and deviations from spherical particle shape. The figure nevertheless suggests that the particle relaxation time spans over about four orders of magnitude for typical particle sizes and particle densities involved in dust explosions: τ_p is in the order of 5 μs for a 1 μm particle, and in the order of 50 ms for a 100 μm particle.

Stokes number

Traditionally, the time constant is presented non-dimensionally as a Stokes number, defined as the ratio of the particle relaxation (or response) time to a characteristic time scale of the fluid (Rogers and Eaton, 1991; Crowe *et al.*, 1998). Particles with small Stokes numbers (< 0.01) will follow the flow exactly and will not affect the turbulence

except to the degree that they modify the fluid properties. Particles with large Stokes numbers (>100) will not respond significantly to turbulent velocity fluctuations. According to Koch (1990), the particle Stokes number is greater than one for particles larger than a few μm , indicating that the inertia of the particles is significant.

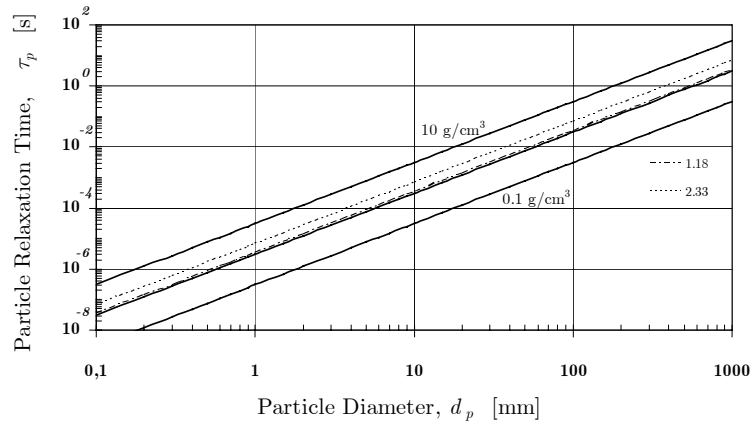


Figure 2-3. Particle relaxation time as a function of particle diameter according to (2.27) for various values of particle densities: 0.1, 1.0 and 10 g/cm^3 . The solid-drawn lines indicate particle densities of 0.1, 1.0 and 10 g/cm^3 ; two typical values for ρ_p for dusts used in this work are also indicated: 1.18 g/cm^3 (*Lycopodium clavatum*, PMMA, aluminium oxide) and 2.33 (silicon).

Particle Lagrangian time scale

If the initial particle velocity is viewed as the velocity of the particle in one particular eddy just before the particle migrates to another eddy, it is comparatively more difficult to change a trajectory or velocity of a particle that has higher inertia than that of a particle that has lower inertia. The correlated time interval described above is known as the *particle integral time scale*, or *particle Lagrangian time scale* (τ_{pL}). The integral time scale is roughly the time over which a particle maintains its initial velocity before it undergoes a turbulent ‘collision’ and changes its velocity (Shirolkar *et al.*, 1996).

The interaction of a medium-sized particle with an eddy larger than itself is the same as that of a small particle. However, the interaction of a medium particle with an eddy that is smaller or of comparable size is very different. When a medium particle interacts with a smaller or comparable sized eddy, it can either completely dissipate the eddy or change the structure of the eddy, depending of the nature of the impact. As in the case of a small particle, a dense particle is less sensitive to turbulent fluctuations because of the inertia force at the fluid particle interface (Shirolkar *et al.*, 1996).

Crossing trajectory effect

A particle may or may not remain trapped inside an eddy for the entire lifetime of that eddy. The phenomenon of migration of a particle from one eddy to another due to turbulence of the original eddy is known as the *crossing trajectory effect*. To estimate this interaction time, a particle drift velocity ($\vec{v}_d = \vec{v}_p - \vec{u}_f$) is used to determine the time a particle would take to cross a given eddy. The minimum time (t_c) a particle would take to cross an eddy with characteristic dimension ℓ is $t_c = \ell/|\vec{v}_d|$. If this minimum crossing time is smaller than the eddy lifetime, the particle will jump to another eddy (Shirolkar *et al.*, 1996).

Gravity

Gravity will cause the solid particles that are in suspension to descend through the fluid, continuously converting their potential energy into kinetic energy, thus augmenting the component of turbulence energy in the gravity direction (Truesdell and Elghobashi, 1994).

Classification of particle-laden flows based on particle volume fraction (α_p)

The mechanics of a gas-solid flow depends significantly on the particle volume fraction, defined by:

$$\alpha_p = \frac{N_p \bar{V}_p}{V_{total}} = \frac{V_{p,total}}{V_{total}} \quad (2.29)$$

N_p is the number of particles, \bar{V}_p is the average volume of a particle, $V_{p,total}$ is the total volume of particles, and V_{total} is the total volume occupied by particles and fluid. The average distance between the particles in the suspension (*particle spacing*, L_p) can be expressed as a function of the particle volume fraction (Crowe *et al.*, 1998):

$$\alpha_p = \frac{\pi d_p^3}{6 L_p^3} \Rightarrow \frac{L_p}{d_p} = \left(\frac{\pi}{6 \alpha_p} \right)^{1/3} \quad (2.30)$$

Elghobashi (1991) classified particle-laden flows according to the particle volume fraction (α_p) and some characteristic time scale ratios of the flow (Stokes numbers): the particle relaxation time (τ_p) divided by either the Kolmogorov time scale (τ_η) or the turnover time for large eddies (τ_e). A modified version of the classification map, from Elghobashi (1994), is shown in Figure 2-4; the vertical coordinates (τ_p/τ_e and τ_p/τ_η) are related via the turbulent Reynolds number $Re_e = u'_{rms} \ell_e / \nu$ since $\tau_e/\tau_\eta = Re_e^{0.5}$, the coordinates shown are for $Re_e = 10^4$.

One-way coupling – very dilute suspensions

For very low values of the particle volume fraction ($\alpha_p < 10^{-6}$), the interaction between the particles and turbulence is called a *one-way coupling*. The particle dispersion is governed by the turbulent motion of the continuous phase, but the particles have negligible effect on the turbulent motion of the continuous phase (the momentum transfer from the particles to the fluid has insignificant effect on the flow).

The behaviour of particles in turbulent flows with one-way coupling is reasonably well understood according to Elghobashi (1994) – mainly limited by the incomplete understanding of turbulence itself even in particle-free flows. Flows in the two-way and four-way coupling regimes are “*still at the infancy stage of understanding*”.

Two-way coupling – dilute suspensions

When the particle volume fraction is increased, $10^{-6} < \alpha_p < 10^{-3}$, the momentum transfer from the particles is large enough to alter the turbulence structure; however, particle-particle interactions, such as collisions and coalescence, can be neglected. This is called *two-way coupling*, and the resulting flow regime are often referred to as a *dilute suspension*. Two-way coupling has been observed experimentally, e.g. by Gore and Crowe (1989).

Four-way coupling – dense suspensions

For higher particle volume fractions, say $\alpha_p > 10^{-3}$, the relative distance between particles is small enough so that particles collide. This is called *four-way coupling*, and the flows are referred to as *dense suspensions*.

Loth (2002) mentions two separate mechanisms for particle-particle interactions:

- i) Particle-particle collisions, whereby the particles can rebound, shatter, or coalesce after impinging on each other.
- ii) Particle-particle fluid dynamic interactions, i.e. when the proximity of the particles affects their fluid dynamic forces.

Granular flow

As α_p approaches unity, we obtain so-called *granular flow*, which has no relevance for dust explosions.

Modelling of turbulent particle-laden flows

Strategies and methods for the modelling of turbulent particle dispersion are not treated here; however, several extensive review papers exist, e.g. Elghobashi (1994), Shirolkar *et al.* (1996) and Loth (2002).

Elghobashi (1994) emphasizes two main challenges facing the attempts of numerically predicting particle-laden flows:

- i) The very wide spectrum of important length and time scales; ranging from the microscopic physics of the dispersed phase, to the fine and large structures of turbulence.
- ii) The incomplete understanding of the physics of turbulence, defining the ‘upper limit’ for the understanding of the more complex particle-laden turbulent flows.

A few results from direct numerical simulations of particle-laden flows will be included in the discussion of turbulent particle dispersion (2.1.5) and turbulence modification (2.1.6).

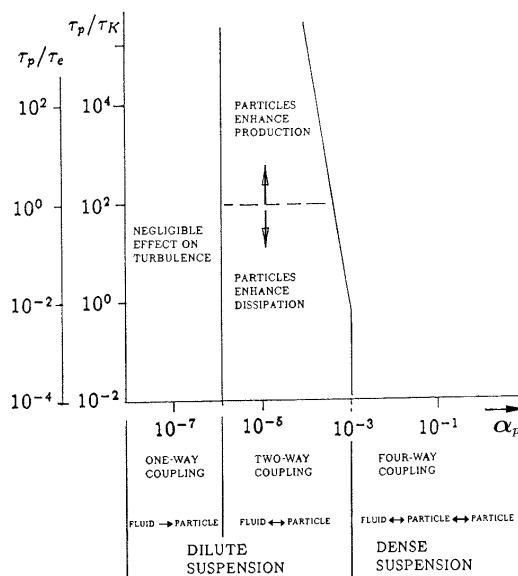


Figure 2-4. Map of regimes of interaction between particles and turbulence (Elghobashi, 1994).

2.1.5 Turbulent Particle Dispersion

The interaction between turbulent eddies and immersed small particles is referred to as *turbulent particle dispersion* because of the observed dispersive effect on particles that originated in the same point. The influence of turbulence, on small, immersed particles, is a convective transport phenomenon that leads to an apparently random spread of the particles through the flow field (Shirolkar *et al.*, 1996). However, Loth (2002) emphasizes that turbulent dispersion can be separated into two different aspects:

- i)* *Mean diffusion* characterises only the overall mean (time-averaged) spread of particles caused by the turbulence.
- ii)* *Structural dispersion* characterises the details of the non-uniform particle concentration structures generated by local instantaneous features of the flow, e.g. heavy particles evacuating eddy cores and migrating towards eddy edges.

Direct numerical simulation of particle dispersion in isotropic turbulence indicates that dense particles collect preferentially in regions of low vorticity and high strain rate (Squires and Eaton, 1990).

2.1.6 Turbulence Modification

The direct influence of discrete particles on turbulence quantities such as the turbulent kinetic energy (k) and its rate of dissipation (ε), is known as turbulence modification (or modulation). The mere presence of a particle locally modifies the turbulence (there is no flow field inside the particle); however, this kind of local modification is expected to be negligible if the particle diameter is much smaller than the Kolmogorov scale ($d_p/\eta \ll 1$). Global turbulence modification by particles occurs when the particles are present in sufficiently large concentrations (i.e. dilute suspension, dense suspensions, etc.) such that the momentum loss or gain to the turbulence by the particles is no longer negligible. In general, small particles tend to attenuate turbulence while large particles augment turbulence.

Mechanisms responsible for turbulence modification

According to Peirano and Leckner (1998), the two dominating mechanisms of turbulence modification in dilute suspensions (for a given value of α_p) are:

- i)* *Vortex shedding.* Increased particle relaxation time, τ_p , enhances turbulence (e.g. bigger particles for the same particle material and fluid viscosity). When $Re_p > 20$ there is an evident wake behind the particle, and when $Re_p > 400$ vortices are shed behind the particles at a frequency which is a function of Re_p (Clift *et al.*, 1978). As both the wake behind the particle and the vortex shedding contributes to the velocity disturbance by the particle, they can both be considered as sources of turbulence production (Yuan and Michaelides, 1992). As can be seen from Figure 2-5, high drift velocities or large particle sizes are required for producing high particle Reynolds numbers. Koch (1990) points out that for particles of radii less than about 100 μm in air at atmospheric conditions, Re_p will usually be of the order one, indicating that inertial effects in the gas are small. However, Elghobashi and Truesdell (1993) points out that experimental evidence presented by Hardalupas *et al.* (1989) from particle-laden jets indicates

that particles without wakes (small Re_p) may also increase the turbulence energy.

- ii) *Work done by eddies.* Lowering the particle relaxation time, τ_p , dampens turbulence (e.g. smaller particles for the same particle material and fluid viscosity) because the increased surface area of the particulate phase increases the dissipation rate of turbulence energy. There is no vortex shedding, and energy is dissipated due to the work done by eddies in accelerating particles.

According to Yuan and Michaelides (1992), the following four mechanisms is probably of minor importance in determining the turbulence modulation:

- iii) Fluid moving with the particles as added fluid mass to the particles.
- iv) Increase of the apparent (turbulent) viscosity due to the presence of particles.
- v) Enhancement of the velocity gradient between two particles.
- vi) Deformation of the dispersed phase.

The six mechanisms mentioned above are not independent of each other; mechanisms *iv*) and *v*) are of minor importance in very dilute flows, and *vi*) is not applicable to particulate flows (without chemical reactions or phase transitions).

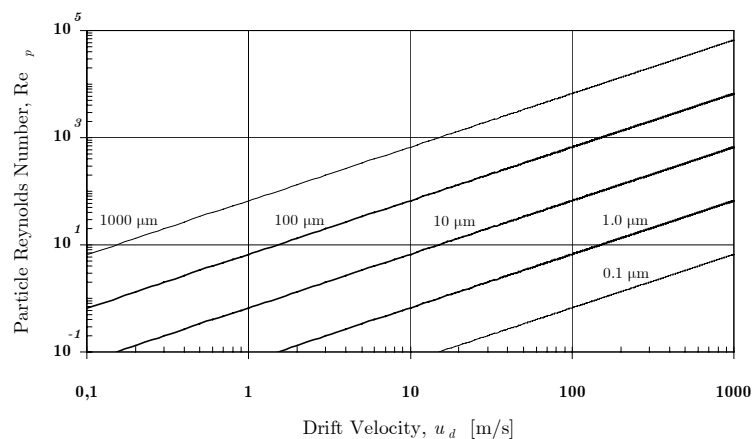


Figure 2-5. Particle Reynolds number for various particle diameters, according to (2.25), as a function of drift velocity ($u_d = |\vec{u}_d| = |\vec{v}_p - \vec{u}_f|$). The following values have been used for the density and viscosity of ambient air: $\rho_f = 1.2 \text{ kg/m}^3$ and $\mu_f = 1.8 \text{ Ns/m}^2$, respectively.

Experimental investigations of turbulence modification

Turbulence modification in particle-laden flows has been experimentally investigated by many researchers, e.g. Lee and Durst (1982), Tsuji *et al.* (1982, 1984) and Kulick *et al.* (1994).

Gore and Crowe (1989) examined available experimental data of turbulence modification in pipe and jet flows. They classified two-way coupling as a function of the ratio of the particle diameter to the integral Eulerian length scale. Below a certain value of d_p/ℓ_e , 0.1 according to Gore and Crowe, turbulence is attenuated, whereas above this value turbulence is enhanced. Rogers and Eaten (1991) pointed out that the correlation by Gore and Crowe were unable to predict the level of turbulence modification. Elghobashi and Truesdell (1993) presented results from direct numerical simulations indicating that turbulence intensity increases for $d_p/\ell_e \approx 10^{-3}$, thus contradicting the results of Gore and Crowe. Kulick *et al.* (1994) commented: “the

degree of turbulence modification does not seem to depend in any obvious fashion on any simple set of parameters”.

Direct numerical simulation of turbulence modification

According to Squires and Eaton (1990), laboratory measurements of turbulence modification by particles are difficult to obtain in the presence of a large concentration of dispersed particles. In addition, changes in the mean flow caused by the particles can cause changes in the turbulence properties, masking the effect of the particle cloud on the turbulence. Elghobashi and Truesdell (1993) found that small particles ($d_p < \eta$ and $\tau_p \approx \tau_\eta$), in the absence of gravity, transfer their momentum to the high wave-number motion of the carrier fluid, thus increasing the energy content of the small length scales. This increase of energy is accompanied by an increase of the viscous dissipation rate, and, hence, increased rate of energy transfer from the large-scale motion. Thus, depending on the conditions at particle injection, the fluid turbulence kinetic energy may increase initially. However, in the absence of external sources (shear or buoyancy), the turbulence energy will eventually decay faster than in the particle-free turbulence. This enhanced decay of energy increases the growth rate of the integral length scale and reduces the Kolmogorov length scale.

Druzhinin (2001) summarized much of the work done on direct numerical simulation of particle-laden flows, and investigated the influence of particle inertia on the two-way coupling and modification of isotropic decaying turbulence by ‘microparticles’ ($d_p < \eta$ and $\tau_p < \tau_\eta$). It was found that there occurs a ‘qualitative transition’ in the two-way coupling effect of particles on isotropic turbulence as the particle response time is increased from $\tau_p \ll \tau_\eta$, in the limit of microparticles, to $\tau_p \simeq \tau_\eta$, for particles with finite inertia:

- When $\tau_p \leq 0.4\tau_\eta$, the particles add kinetic energy to the fluid motion, i.e. both the turbulent kinetic energy, $k(t)$, the dissipation, $\varepsilon(t)$, and the spectral transfer of fluid kinetic energy, are increased by the two-way coupling as compared to the particle-free case – the increase is more pronounced for smaller τ_p .
- Particles with sufficiently high inertia ($\tau_p \geq 0.8\tau_\eta$), low particle Reynolds number ($Re_p < 1$), and small diameter ($d_p < \eta$), reduced the turbulent kinetic energy of isotropic turbulence as compared to the one-way coupling case. The turbulent energy spectrum, $E(\kappa)$, is reduced at low wave numbers and enhanced at high wave numbers.

Thus, turbulence modification is a complex phenomenon, and no simple method for predicting the degree of turbulence modification seems to exist.

2.1.7 Turbulent Combustion

The interaction between turbulence and combustion work both ways: combustion affects turbulence, and turbulence affects combustion. There are many ways in which combustion can affect the physics of turbulence, e.g. the production of density variations, buoyancy, dilatation due to heat release in chemical reactions, influence on molecular transport properties, etc. The effects of turbulence on combustion include fluctuating characteristics in heat and mass transfer, and particularly in chemical reactions.

Turbulent burning velocity

Turbulent burning velocity, $S_{u,T}$, by analogy with the laminar burning velocity ($S_{u,L}$), is assumed to be a basic characteristic of premixed turbulent combustion. Lipatnikov and Chomiak (2002) points out that the following qualitative trends have been found for the turbulent burning velocity at moderate turbulence levels:

- i) $S_{u,T}$ increases for higher values of u'_{rms} .
- ii) $S_{u,T}$ and $dS_{u,T}/du'_{rms}$ increases for higher values of $S_{u,L}$.
- iii) $S_{u,T}$ increases for higher pressure, despite the fact that $S_{u,L}$ decreases for higher pressures.

Both experimental and theoretical analysis suggests the following relationship between the turbulent and laminar burning velocities (Veynante and Vervisch, 2002):

$$\frac{S_{u,T}}{S_{u,L}} = 1 + \alpha \left(\frac{u'_{rms}}{S_{u,L}} \right)^\beta \quad (2.31)$$

where α and β are two model constants. However, since various physical mechanisms of premixed turbulent combustion can dominate, depending on initial conditions, it is not realistic to expect such simple relations to be valid for all flow conditions (Lipatnikov and Chomiak, 2002). Thus, turbulent combustion models have to be developed for, and evaluated against, certain flow conditions.

Scales and diagrams for turbulent combustion

In addition to the various lengths, time and velocity scales describing turbulent flow, turbulent combustion involves scales that describe the chemical reactions. For turbulent premixed flames, the chemical time scale (τ_c) can be estimated as the time a laminar flame requires to propagate over a distance equal to its own thickness (δ_L):

$$\tau_c = \frac{\delta_L}{S_{u,L}} \quad (2.32)$$

If the turbulent time scale is estimated from the integral time scale (2.19), the Damköhler number can be defined as the ratio:

$$Da = \frac{\tau_e}{\tau_c} = \frac{\ell_e}{\delta_L} \frac{S_L}{u'_{rms}} \quad (2.33)$$

Fast chemical reactions ($Da \gg 1$) results in a thin reaction zone (flame front), the turbulent structures wrinkle and strain the flame surface. The internal structure of the flame is not strongly affected by turbulence and may be described as a laminar flame element called a ‘flamelet’. The reaction rate is limited by turbulent mixing. When the chemical reactions are slow ($Da \ll 1$), reactants and products are mixed by turbulent structures before reaction.

If the turbulent time scale is estimated from the Kolmogorov time scale (2.20), the Karlovitz number can be defined as the ratio:

$$Ka = \frac{\tau_c}{\tau_\eta} = \frac{\delta_L}{\eta} \frac{u_\eta}{S_L} \quad (2.34)$$

There exist several diagrams for classifying turbulent premixed flames based on various dimensionless groups, e.g. the Damköhler number, the Karlovitz number and a

Reynolds number. One such diagram, presented by Veynante and Vervisch (2002), is shown in Figure 2-6. The following turbulent premixed flame regimes are indicated:

- The *thin wrinkled flame regime*, or *flamelet regime* ($Ka < 1$). The basic physical mechanism for the influence of turbulence on combustion is the increase in the flamelet surface area by turbulent eddies. A further subdivision of this regime is proposed based on the velocity ratio u'_{rms}/S_L :
 - *Wrinkled flames* ($u'_{rms}/S_L < 1$), large turbulent structures are unable to wrinkle the flame surface up to flame front interactions; hence, laminar flame propagation dominates.
 - *Corrugated flames* ($u'_{rms}/S_L > 1$), large turbulent structures are able to wrinkle the flame surface up to flame front interactions; leading to the formation of ‘pockets’.
- The *thickened wrinkled flame regime*, or *thin reaction zone* ($1 < Ka < 100$). Turbulent motion are able to affect and to thicken the flame preheat zone; however, the reaction zone remains thin.
- The *thickened flame regime*, or *well-stirred reactor* ($100 < Ka$). Both preheat and reaction zones are strongly affected by small-scale high-intensity turbulent motion; no laminar flame structure can be identified. The hypothetical limiting region characterized by $\mathcal{L}_e/\delta_L < 1$ is termed *thick flames*.

Such classifications should only be considered as qualitative descriptions of the turbulent combustion; nevertheless, they may prove to be helpful when developing or choosing combustion models for specific applications. Both Veynante and Vervisch (2002) and Lipatnikov and Chomiak (2002) points out that diagrams such as the one in Figure 2-6 are order of magnitude estimations constructed for an ideal academic case; it is assumed:

- Homogeneous and isotropic turbulence, unaffected by heat release;
- Single step irreversible chemical reactions;
- A Lewis number of unity, $Le = \kappa/\mathcal{D} = k/\{\rho c_p \mathcal{D}\} = 1$, where κ , \mathcal{D} and k are the thermal diffusivity, mass diffusivity and thermal conductivity, respectively;
- The molecular diffusivity is the same for all reactants.

In addition, some quantities are not clearly defined. The laminar flame thickness δ_L can for instance be based on the thermal thickness or the diffusive thickness.

The interaction between turbulence and propagating dust-air flames can be classified according to three characteristic time scales (van der Wel, 1993): a turbulent time scale, the particle burning time (τ_b), and the particle relaxation time (τ_p).

Beér *et al.* (1984) points out that turbulence can alter the mechanism of coal particle combustion; not only the heat and mass transfer processes. The stoichiometric relations, and hence the total combustion rate, will be significantly influenced by where and how the oxidation takes place – outside the boundary layer, or within it.

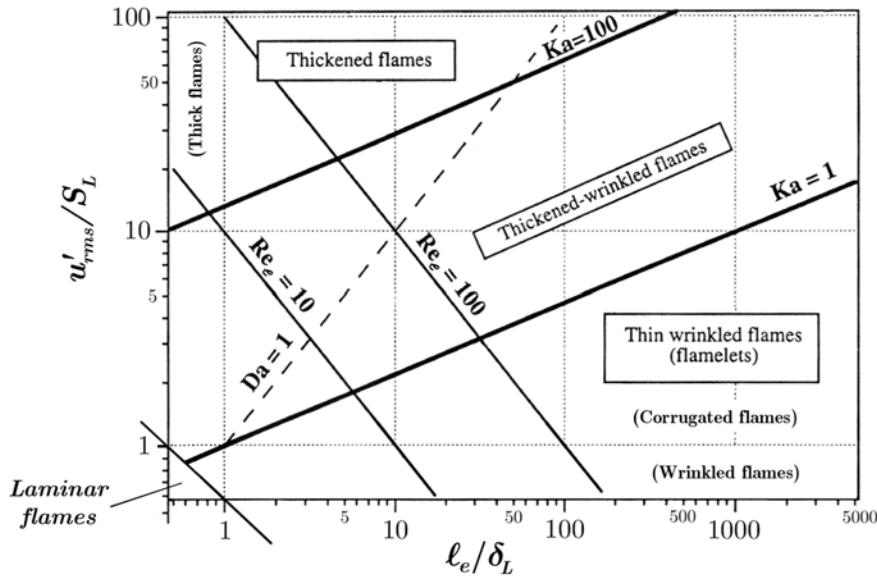


Figure 2-6. Regimes of premixed turbulent combustion; simplified version of diagrams presented by Veynante and Vervisch (2002) and Lipatnikov and Chomiak (2002).

2.2 Turbulence and Combustion in 20-Litre Explosion Vessels

Whereas the previous section introduced general aspects of turbulence and combustion, this section describes the processes that take place in closed explosion vessels. The focus will be on 20-litre vessels fitted with dispersion systems of the kind used with the standardized Siwek sphere.

2.2.1 Previous Work on the Turbulence in 20-Litre Vessels

The sudden discharge of compressed air from a dust reservoir into the initially evacuated explosion vessel results in a short period of turbulence build-up, followed by a much longer period of turbulence decay. This phenomenon has been investigated by e.g. Pu *et al.* (1988, 1989, 1990), van der Wel (1993), Zhen and Leuckel (1995a, 1995b, 1996), Dahoe (2000) and Dahoe *et al.* (2001a, 2001b).

Pu *et al.* (1988) measured the root-mean-square of the fluctuating velocity and the integral length scale in three different vessels (6, 26 and 950 litres), all fitted with pneumatic dispersion systems typical for laboratory scale dust explosion testing. It was found that u'_{rms} and l_e varied within the ranges 0.1-3.3 m/s and 0.4-1.6 cm, respectively. The burning velocity in methane-air and cornstarch-air mixtures was found to be a linear function of the initial value of u'_{rms} . Pu *et al.* pointed out that this high-intensity and small-scale turbulence is very different from expected natural conditions of accidental explosions in industry.

Pu *et al.* (1989, 1990) measured u'_{rms} and ℓ_e in a 20-litre sphere fitted with a dispersion ring. The integral length scale in the 20-litre vessel increased from about 1 cm immediately after onset of dispersion, to about 2.5 cm after 0.6 seconds. The root-mean-square velocity reached a maximum value of about 3 m/s after a very short time, and decayed to 10% of the initial value in 150-400 ms. The turbulent burning velocity of aluminium-air and cornstarch-air mixtures was found to be a linear function of the initial value of u'_{rms} in the range from 0.25 to 3.0 m/s.

Van der Wel (1993) measured power density spectra by hot wire anemometry in both the 20-litre Siwek sphere (fitted with the dispersion ring) and the 1-m³ ISO vessel. He found that an ignition delay time of 165 ms in the 20-l vessel would result in similar conditions of turbulence that exists in the 1-m³ vessel during standardised tests. Hence, the turbulence conditions in the 20-litre sphere, at the default ignition time of 60 ms, are considerably more intense those in the 1-m³ vessel at the standard time of ignition. Estimates of the Kolmogorov time (τ_η) scale in the 20-litre sphere indicated a linear increase from about 0.1 ms to about 0.8 ms in the period from 50 to 300 ms after onset of dispersion (a value of 0.4-0.5 ms was indicated for the 1-m³ vessel). The burning velocity in stoichiometric methane-air mixtures and in various dust-air mixtures (500 g/m³ *Lycopodium*, 1000 g/m³ potato starch, 500 g/m³ activated carbon – all ignited with 10 kJ chemical igniters) was found to be a linear function of the initial value of u'_{rms} . Both Pu *et al.* (1990) and van der Wel pointed out the transient nature of the decay process in the smaller 20-litre vessels, compared to the larger 1-m³ vessel.

Hauert *et al.* (1994) measured the transient flow field in both the standard 1-m³ ISO vessel and in a pneumatically or mechanically fed 12-m³ silo. It was concluded that u'_{rms} measured in the ISO vessel was at least 2.5 times higher than the values measured in the silo.

Zhen and Leuckel (1995a) investigated the influence of u'_{rms} on the turbulent burning velocity of methane-air and cornstarch-air mixtures in a 1-m³ cylindrical vessel, and found a general relation on the form:

$$\frac{S_{u,T}}{S_{u,L}} = 1 + 1.65 \frac{\sqrt{u'_{rms}}}{S_{u,L}} \quad (2.35)$$

Zhen and Leuckel (1995b, 1996) investigated the dynamic features of dispersing dust by air discharging from pressurized reservoirs through a nozzle. Their measurements in a 1-m³ vessel showed that the discharge process is strongly affected by the dust loading and initial supply pressure in the reservoir. The dispersion process was characterized as two successive discharges, dust loading and residual air. Increased dust loading resulted in a decreased rate of pressure decrease in the reservoir, and an increased total discharge time. This resulted in higher turbulence intensity at a given time in the dispersion process (after the dust had been completely injected).

Dahoe (2000) and Dahoe *et al.* (2001a, 2001b) investigated the transient flow inside a plastic replica of the 20-litre Siwek sphere, fitted with the standardized dispersion system (three different nozzles were used: rebound, perforated ring, and 'Dahoe' nozzle). Although the injection process in the 20-litre vessel only lasts for about 50 milliseconds, turbulence build-up was found to be restricted to the first 10 milliseconds. This phenomenon was explained by considering the various mechanisms of turbulence

generation that can be active during the air blast. The three main mechanisms responsible for the turbulence production inside the 20-litre vessel during the transient dispersion process are:

- i) The baroclinic effect.
- ii) Turbulence generated by wall friction during the injection process.
- iii) Turbulence generated in shear layers.

According to Dahoe and Dahoe *et al.*, the most important mechanism during the first milliseconds will be the baroclinic effect in the region where air at high and low pressure is initially separated¹. The vorticity is the curl of the velocity vector:

$$\omega_i = \varepsilon_{ijk} \frac{\partial u_j}{\partial x_k}$$

A transport equation for the vorticity can be found by taking the curl of the Navier-Stokes equations (2.2):

$$\frac{\partial \omega_i}{\partial t} + u_j \frac{\partial \omega_i}{\partial x_j} = \omega_j \frac{\partial u_i}{\partial x_j} + \nu \frac{\partial^2 \omega_i}{\partial x_j^2} - \omega_i u_i + \underbrace{\frac{1}{\rho^2} \varepsilon_{ijk} \frac{\partial \rho}{\partial x_i} \frac{\partial p}{\partial x_j}}_{\text{Baroclinic term}} e_k \quad (2.36)$$

According to Dahoe *et al.*, the initial vorticity production rate at the onset of the dispersion process will be governed by the so-called *baroclinic term* in this equation. Although there is still a net inflow from the reservoir up to about 50 milliseconds, turbulence will start to decay. Turbulence production by other mechanisms, i.e. wall friction and shear turbulence, is insufficient to counteract the decay of turbulence generated by the baroclinic effect during the first 10 milliseconds.

Dahoe *et al.* found that with no dust present, the root-mean-square of the velocity fluctuations from $t_0 = 60$ ms and up to about $t = 200$ ms could be described by an equation on the form:

$$\frac{u'_{rms}}{u'_{rms}^o} = \left(\frac{t}{t_0} \right)^n \quad (2.37)$$

i.e. on the same form as the equation describing the decay of homogeneous and isotropic turbulence downstream of a grid. Measured values of $u'_{rms}^o = u'_{rms}(t_0)$ for the three nozzles perforated dispersion ring, rebound and ‘Dahoe’ were found to be 2.68 m/s, 3.75 m/s and 2.79 m/s, respectively; the values of the exponent n were estimated to (-1.49) , (-1.61) and (-1.52) , i.e. significantly lower than for both the initial ($n \approx -0.5$) and the final ($n \approx -1.25$) period of decay in grid-generated turbulence (section 2.1.3).

¹ Assuming ideal gas law and an average molecular weight of 28.97 g/mol for air, the compressed air (21 bara) in the reservoir has a density of 25 kg/m³, while the air inside the vessel (0.4 bara) has a density of 0.47 kg/m³.

2.2.2 Characterization of Dispersion Induced Flow in 20-Litre Vessels without Dust

This section aims at describing some aspects of the flow that can be expected to take place inside 20-litre explosion vessels during the transient dispersion process when no dust is present. It will be assumed that the results presented by Dahoe (2000) and Dahoe *et al.* (2001a, 2001b), for the decay of turbulence inside a 20-litre sphere fitted with the rebound nozzle, is representative for such tests. After estimating some fundamental length and time scales of the dust-free flow in this section, the nature of the particle-laden flow will be briefly discussed in section 2.2.3.

Decay of turbulent kinetic energy (k) without dust

Assuming isotropic turbulence, an empirical equation for the turbulent kinetic energy can be found from (2.37):

$$k(t) = \frac{3}{2} u_{rms}^{\prime 2}(t) = \frac{3}{2} \left\{ u_{rms}^{\prime o} \left(\frac{t}{t_0} \right)^n \right\}^2 = \frac{3}{2} \underbrace{(u_{rms}^{\prime o})^2}_{k_0} \left(\frac{t}{t_0} \right)^{2n} = k_0 \left(\frac{t}{t_0} \right)^{2n} \quad (2.38)$$

The decay of both the root-mean-square of the velocity fluctuations and the turbulent kinetic energy, in the period from 60 to 200 milliseconds, is illustrated in Figure 2-7 for the measured values reported by Dahoe *et al.* ($u_{rms}^{\prime o} = 3.75 m/s$ and $n = -1,61$). According to Dahoe *et al.*, the decay of turbulence in the 20-litre sphere occurs faster than anyone has ever observed in the turbulent flow field behind a grid.

Dissipation rate of turbulent kinetic energy (ε) and Kolmogorov scales without dust

In order to qualitatively describe the particle-fluid interactions that can be expected to take place inside 20-litre explosion vessels, it will be of interest to estimate the Kolmogorov length scale in the transient flow. However, according to (2.12), this requires an estimate of the dissipation rate for turbulent kinetic energy (ε). Two different strategies will be pursued.

The first method for estimating the rate of dissipation relies on simplifying the modelled transport equation for the turbulent kinetic energy¹, used in e.g. the k - ε model, for the simple case of isotropic decaying turbulence:

$$\frac{\partial}{\partial t}(\rho k) + \underbrace{\frac{\partial}{\partial x_j}(\rho k \bar{u}_j)}_{\text{Gradient} \approx 0} = \frac{\partial}{\partial x_j} \left\{ \left(\mu + \frac{\mu_t}{\sigma_k} \right) \underbrace{\frac{\partial k}{\partial x_j}}_{\text{Gradient} \approx 0} \right\} + \underbrace{\mu_t \left(\frac{\partial \bar{u}_i}{\partial x_j} + \frac{\partial \bar{u}_j}{\partial x_i} \right) \frac{\partial \bar{u}_i}{\partial x_j}}_{\text{Production: } \rho P_k \approx 0} - \rho \varepsilon \quad (2.39)$$

When neglecting the terms containing space gradients of averaged values (should vanish in isotropic turbulence), and the production term ρP_k , equation (2.39) reduces to:

$$\frac{dk}{dt} \approx -\varepsilon \quad (2.40)$$

¹ This equation can be derived from the Navier-Stokes equations by introducing averaging and applying several simplifying assumptions, e.g. introducing the turbulence viscosity μ_t ; for further details refer to e.g. Ertesvåg (1999).

Thus, an empirical estimate for ε can be found by differentiating (2.38):

$$\varepsilon(t) \approx -2n \underbrace{\left\{ \frac{3}{2} (u'_{rms})^2 \left(\frac{t}{t_0} \right)^{2n} \right\}}_{k(t)} t^{-1} = -2n \frac{k(t)}{t} \quad (2.41)$$

The resulting estimated Kolmogorov scales for length and time in the period from 60 to 200 milliseconds is illustrated in Figure 2-8.

The second method for estimating the rate of dissipation, again assuming local isotropic turbulence, is to use the equation:

$$\varepsilon = A \frac{u_{rms}^3}{\ell_e} \quad (2.42)$$

where A is a numerical constant of the order of unity (Hinze, 1975). However, in the case of the transient flow inside 20-litre vessels, the integral length scale is not known – and it is not constant. From the discussion of the decay of isotropic homogeneous turbulence in section 2.1.3, and Figure 2-2 especially, one would expect ℓ_e to increase during the decay period, and eventually approach dimensions comparable with the vessel (~ 10 cm). Nevertheless, a constant value for ℓ_e of 1 cm will be used here, assuming the integral length scale in the flow during this phase of the decay process is still strongly influenced by the dimension of the inlet, rather than having adapted to the geometry of the vessel. The value chosen for the constant A was 0.2 (Ertesvåg, 1999). The resulting estimated Kolmogorov scales for length and time in the period from 60 to 200 milliseconds is included in Figure 2-8, together with the estimated Kolmogorov time scale reported by van der Wel (1993).

Although the results presented in Figure 2-8 are based on a series of assumptions that are highly questionable for the present case (e.g. isotropic decaying turbulence, and equilibrium between the energy supplied from the large structures of the flow and energy dissipated in the fine structures of the flow), the following trends are indicated:

- The Kolmogorov length scale η increases linearly from about 40 μm at 60 ms, to about 160 μm at 200 ms; i.e. an increase of a factor four.
- The Kolmogorov time scale τ_η increases at an increasing rate from about 0.1 ms at 60 ms, to about 1-2 ms at 200 ms; i.e. an increase of a factor of more than ten. The results from van der Wel (1993) suggest similar initial values, but a somewhat lower rate of increase.

Although the results presented in Figure 2-7 and Figure 2-8 must be regarded as ‘order of magnitude’ estimates, it seems clear that both the intensity and the structure of the turbulence will change rapidly during the course of an explosion in a 20-litre explosion vessel.

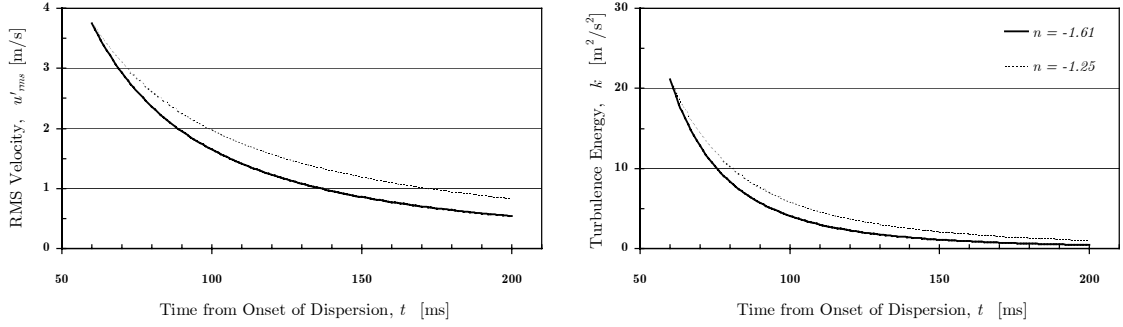


Figure 2-7. Decay of the root-mean square of velocity fluctuations and the turbulent kinetic energy in a 20-litre sphere according to equations (2.37) and (2.38), respectively.

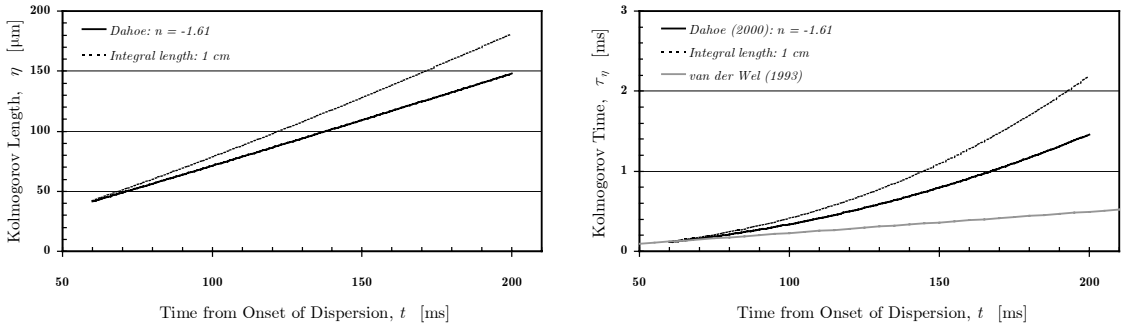


Figure 2-8. Evolution of Kolmogorov length and time scale during decay of turbulence in 20-litre sphere, according to equations (2.12) and (2.20).

2.2.3 The Effect of Particles on the Transient Flow in 20-Litre Explosion Vessels

This section describes the particle-laden flow that exists in typical dust explosion tests in 20-litre vessels, i.e. turbulent dust-air suspensions where the dispersed particles are in the size range from 1 to 100 micrometers and have a density in the order of 1 g/cm³. The main aim is to investigate to what extent the decay of turbulence in a dust-air suspension in the 20-litre vessel will deviate significantly from the behaviour described in 2.2.2.

Particle volume fraction (α_p) and dust concentration (c_d)

It is straightforward to classify the particle-laden flow in combustible dust clouds according to particle volume fraction, as suggested by Elghobashi (1994). The relation between the dust concentration, c_d , assuming perfect and homogeneous dispersion within the volume in question, and α_p is simply:

$$c_d = \frac{m_{p,total}}{V_{total}} = \frac{\rho_p V_{p,total}}{V_{total}} = \rho_p \alpha_p \quad (2.43)$$

The particle volume fraction as a function of dust concentration is plotted in Figure 2-9 for various particle densities; the following should be noted:

- The lower explosion limit (*LEL*) for combustible dust clouds is typically between 20 and 60 g/m³ for a large number of technical dusts (Bartknecht, 1981). For realistic particle densities, this corresponds to particle volume

fractions in the order of 10^{-5} to 10^{-4} ; hence, we have dilute suspensions where two-way coupling should be expected.

- The dust concentration that yields the maximum burning rate is typically in the order of 500 g/m^3 (at least for the combustible dusts used in this work), corresponding to particle volume fractions in the order of 10^{-4} to 10^{-3} . Thus, the particle-laden flow is still within the regime of dilute suspensions and four-way coupling is probably negligible.
- The upper explosion limit (*UEL*), although difficult to determine (Mintz, 1993), is probably in the order of $2\text{-}10 \text{ kg/m}^3$ for many combustible dusts; four-way coupling can be expected.

Thus, two-way coupling should always be expected to take place in combustible dust-air suspensions; for dust concentrations higher than $\sim 1000 \text{ g/m}^3$, four-way coupling cannot be ruled out.

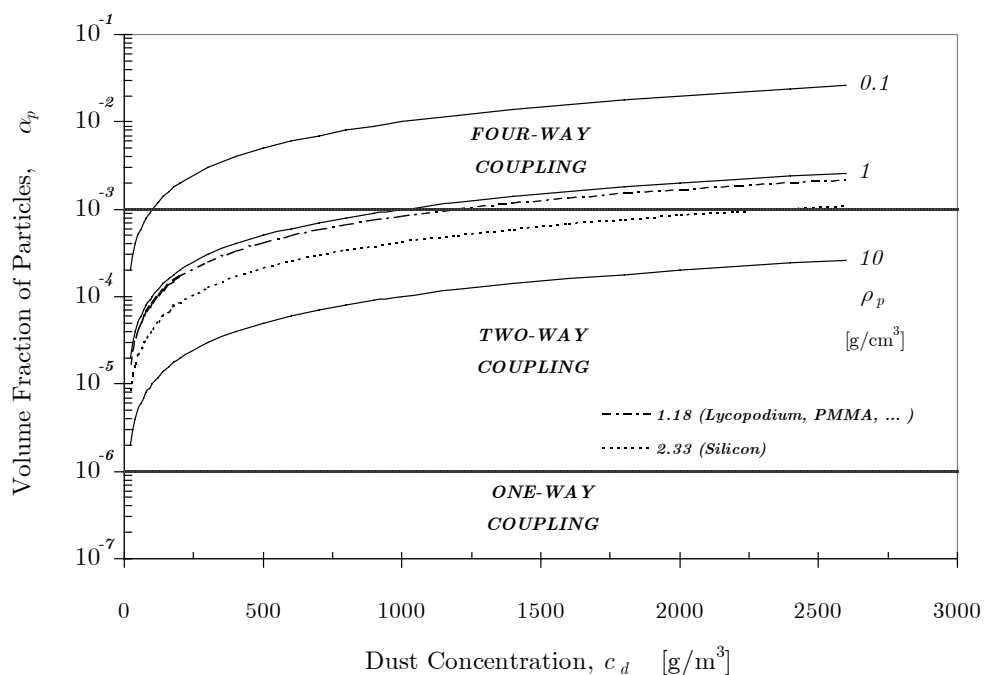


Figure 2-9. Expected flow regimes for turbulent dust clouds as a function of dust concentration for various particle densities according to the classification by Elghobashi (1991, 1994). The solid-drawn lines indicate particle densities of 0.1, 1 and 10 g/cm^3 ; two typical values for ρ_p for the dusts used in this work are also indicated: 1.18 (*Lycopodium clavatum*, PMMA, aluminium oxide) and 2.33 (silicon).

The particle spacing ratio, i.e. the ratio between the average distance L_p between particles of average size d_p in suspension, is shown as a function of the particle volume fraction α_p in Figure 2-10. The two-way coupling regime covers the range from $L_p/d_p \sim 80$ to $L_p/d_p \sim 10$; four-way coupling occurs when $L_p/d_p < 10$. The average particle spacing as a function of dust concentration is also plotted in Figure 2-10, for various particle diameters.

Kolmogorov length scale (η) and particle size (d_p)

In section 2.1.4, particles were defined as small when their size was smaller than the Kolmogorov scale. From Figure 2-8, it follows that this ‘definition’ will change during

the transient dispersion process: from about 40 μm at 60 ms, to about 160 μm after 200 milliseconds. Thus, there will probably be both ‘small’ and ‘medium’ sized particles in most combustible dust clouds encountered in practice at the default ignition delay time of 60 ms, but after 200 ms most of the particles should probably be classified as ‘small’. In most practical flow situations in the industry, the particles should definitely be regarded as ‘small’. Hence, the simple general rule referred in section 2.1.6, that ‘small’ particles tend to attenuate turbulence, while large particles augment turbulence, gives no clear indication of how turbulence will be modified for typical combustible dust clouds during the dispersion process in standardized tests.

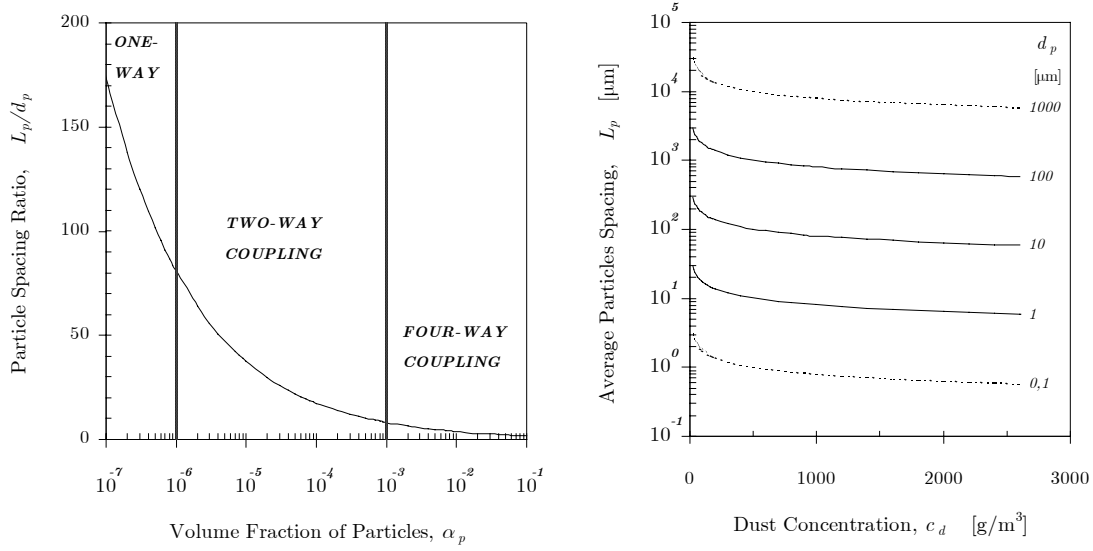


Figure 2-10. Relative particle spacing as a function of α_p according to (2.30) (left); average particle spacing as a function of dust concentration, assuming ρ_p equal to 1 g/cm^3 (right).

Particle density (ρ_p)

As most combustible dust will have particle densities in the order of, or greater than, 1000 kg/m^3 , the particles can safely be regarded as dense (compared with air: $\rho_{\text{air}} \sim 1.2 \text{ kg}/\text{m}^3$). This means that particle segregation will take place; particles with sufficiently high Stokes number will concentrate in regions of low vorticity.

Kolmogorov time scale (τ_η) and particle relaxation time (τ_p)

In section 2.1.4, Figure 1-1, it was found that τ_p is in the order of 0.005 ms for a 1- μm particle, and in the order of 50 ms for a 100- μm particle. Compared with the estimated Kolmogorov time scales for the flow in the period from 60 to 200 milliseconds, Figure 2-8, this results in the following particle Stokes numbers:

- Small particles ($d_p \sim 1 \mu\text{m}$):

$$St_{p,\eta} = \frac{\tau_p}{\tau_\eta} \sim \begin{cases} \frac{0.005 \text{ ms}}{0.1 \text{ ms}} = 0.05 & t = 60 \text{ ms} \\ \frac{0.005 \text{ ms}}{1.6 \text{ ms}} = 0.003 & t = 200 \text{ ms} \end{cases} \quad (2.44)$$

- Large particle ($d_p \sim 100 \mu\text{m}$):

$$St_{p,\eta} = \frac{\tau_p}{\tau_\eta} \sim \begin{cases} \frac{50ms}{0.1ms} = 500 & t = 60ms \\ \frac{50ms}{1.6ms} = 30 & t = 200ms \end{cases} \quad (2.45)$$

As was discussed in section 2.1.4, only particles with small Stokes numbers (<0.01) will follow the flow exactly; particles with large Stokes numbers (>100) will not respond significantly to turbulent velocity fluctuations. Hence, given that the particle Stokes numbers for a dust sample with a broad particle size distribution will cover a range of over five orders of magnitude (10^{-3} to 10^2) during the transient dispersion process in 20-litre vessels, no characteristic particle behaviour can be identified. The mono-sized spores of *Lycopodium* ($d_p \sim 30 \mu\text{m}$, $\rho_p \sim 1.18 \text{ g/m}^3$) will have a particle relaxation time in the order of 10 ms, and Stokes numbers in the order of 100 and 6 at ignition delay times 60 and 200 ms, respectively.

Integral length scale (ℓ_e) and particle size

For particle sizes in the range 1 to 100 μm , assuming an integral length scale of 1 cm, the ratio d_p/ℓ_e becomes 10^{-4} and 10^{-2} , respectively (i.e. significantly lower than 0.1). Hence, the simple classification by Gore and Crowe (1989), described in section 2.1.6, predicts that turbulence will be attenuated. However, the simple relation described by Gore and Crowe was based on experiments performed in far less complicated flow situations than the one in 20-litre vessels, and the result have been questioned by others (see section 2.1.6).

The particle laden flow during standardized tests in 20-litre vessels

From the above discussion, it seems clear that most combustible dust clouds can be characterized as dilute suspensions, and that two-way coupling should be expected to take place. However, it seems impossible to predict to what extent turbulence will be modified by the presence of particles during standardized tests in 20-litre vessels.

2.2.4 Estimating Burning Velocities in the Inflection Point

Point estimates for the burning velocity (S_u) in combustible mixtures

Based on measured pressure-time curves, such as the ones in Figure 1-1 and Figure 1-2, some simple point estimates of the burning velocity, S_u , will be made in section 4.4. Similar derivations are presented by e.g. Bradley *et al.* (1988) and Dahoe *et al.* (1996). The following simplifying assumptions will be used:

- Central point ignition, with subsequent spherical flame propagation
- Ideal gas behaviour of both burnt and unburnt mixture.
- At any given time, the thin spherical flame (with radius r_b and surface area A_b) divides the content of the vessel (volume V_v) in two separate regions:
 - A spherical inner region of completely burnt mixture.
 - An outer region of completely unburnt mixture that undergoes adiabatic compression (i.e. $p\rho^{-\gamma}$ is constant; the specific heat ratio $\gamma=c_p/c_v$ is assumed to have a constant value of 1.4).

As was pointed out in the introduction, it is customary to assume that the fractional pressure rise is proportional to the fractional mass burnt:

$$\frac{p(t) - p_i}{p_f - p_i} = \frac{m_b(t)}{m_{tot}} = \frac{m_b(t)}{m_{u,i}} \quad (2.46)$$

Rearranging and differentiation with respect to time, and using conservation of mass, yields:

$$\frac{dp}{dt} = \frac{p_f - p_i}{m_{u,i}} \frac{dm_b(t)}{dt} = -\frac{p_f - p_i}{m_{u,i}} \frac{dm_u(t)}{dt} \quad (2.47)$$

The mass consumption rate of the unburnt mixture is:

$$\frac{dm_u}{dt} = -A_b \rho_u S_u = -4\pi r_b^2 \rho_u S_u \quad (2.48)$$

Hence:

$$\frac{dp}{dt} = 4\pi \frac{p_f - p_i}{m_{u,i}} r_b^2 \rho_u S_u \quad (2.49)$$

The radius of the flame and the density of the unburnt mixture can be replaced by known variables by using the fact that the volume is constant:

$$V_v = V_b + V_u = \frac{4}{3}\pi r_b^3 + m_u \rho_u^{-1} \quad (2.50)$$

Assuming adiabatic compression of the unburnt mixture:

$$\frac{\rho_{u,i}}{\rho_u} = \left(\frac{p_i}{p}\right)^{1/\gamma} \Rightarrow \rho_u = \rho_{u,i} \left(\frac{p}{p_i}\right)^{1/\gamma} \quad (2.51)$$

Hence:

$$V_v = \frac{4}{3}\pi r_b^3 + m_u \rho_{u,i}^{-1} \left(\frac{p}{p_i}\right)^{-1/\gamma} = \frac{4}{3}\pi r_b^3 + m_u \frac{V_v}{m_{u,i}} \left(\frac{p}{p_i}\right)^{-1/\gamma} \quad (2.52)$$

An equation for $m_u/m_{u,i}$ can be derived by rearranging (2.46):

$$\begin{aligned} \frac{p - p_i}{p_f - p_i} &= \frac{m_b}{m_{u,i}} = \frac{(m_b + m_u) - m_u}{m_{u,i}} = 1 - \frac{m_u}{m_{u,i}} \\ &= \frac{(p_f - p_i) - (p_f - p)}{p_f - p_i} = 1 - \frac{p_f - p}{p_f - p_i} \end{aligned} \quad (2.53)$$

Hence:

$$\frac{m_u}{m_{u,i}} = \frac{p_f - p}{p_f - p_i} \quad (2.54)$$

From (2.52) and (2.54), the following expression is found for the radius of the flame:

$$r_b = \left[\frac{3V_v}{4\pi} \left\{ 1 - \frac{p_f - p}{p_f - p_i} \left(\frac{p}{p_i}\right)^{-1/\gamma} \right\} \right]^{1/3} \quad (2.55)$$

By combining (2.49), (2.51) and (2.55), the rate of pressure rise can be expressed as:

$$\frac{dp}{dt} = 4\pi (p_f - p_i) \frac{\rho_{u,i}}{m_{u,i} V_v^{-1}} \left(\frac{p}{p_i}\right)^{1/\gamma} \left[\frac{3V_v}{4\pi} \left\{ 1 - \frac{p_f - p}{p_f - p_i} \left(\frac{p}{p_i}\right)^{-1/\gamma} \right\} \right]^{2/3} S_u \quad (2.56)$$

Hence, the burning velocity is given by the equation:

$$S_u = \frac{1}{3(p_f - p_i)} \left(\frac{dp}{dt} \right) \underbrace{\left(\frac{3V_v}{4\pi} \right)^{1/3}}_{r_v} \left(\frac{p}{p_i} \right)^{-1/\gamma} \left\{ 1 - \left(\frac{p_f - p}{p_f - p_i} \right) \left(\frac{p}{p_i} \right)^{-1/\gamma} \right\}^{-2/3} \quad (2.57)$$

Definition of the parameters that can be determined in standardized explosion tests in 20-litre vessels were presented in section 1.1, together with typical pressure-time histories from such tests (Figure 1-1 and Figure 1-2). If we assume that the initial pressure is one bar absolute, and that the corrected explosion pressure p_m provides a reasonable estimate of the adiabatic explosion pressure $(p_f - p_i)$; the following empirical equation can be used to estimate the burning velocity at the inflection point (W_{ip}):

$$S_{u,ip} = \frac{1}{3p_m} \underbrace{\left(\frac{dp}{dt} \right)_m}_{K_{st}} V_v^{1/3} \left(\frac{3}{4\pi} \right)^{1/3} \left(1 + \frac{p_{ip}}{1[bar]} \right)^{-1/\gamma} \left\{ 1 - \left(1 - \frac{p_{ip}}{p_m} \right) \cdot \left(1 + \frac{p_{ip}}{1[bar]} \right)^{-1/\gamma} \right\}^{-2/3} \quad (2.58)$$

where p_{ip} is the pressure measured in the inflection point: $p_{ip} = p(t_{ip})$. If we further assume that neither the presence of dust particles, nor the turbulence induced by the explosion, has significant effect on the turbulence level; we can estimate the root-mean-square of the velocity fluctuations at the inflection point by modifying equation (2.37):

$$u'_{rms,ip} = u'_{rms}(t_{ip}) = u'_{rms} \left(\frac{t_{ip}}{t_0} \right)^n \quad (2.59)$$

This requires that n and u'_{rms} can be determined experimentally, and that t_{ip} is within the time range where equation (2.37) is valid, i.e. $60\text{ms} < t_{ip} < 200\text{ms}$. Estimates of burning velocity as a function of root-mean-square velocity for several explosive mixtures, according to (2.57) and (2.59), will be presented in section 4.4.

Lee *et al.* (1987) pointed out that the concept of burning velocity requires a well-defined flame zone, and that the ‘burning velocity’ derived from pressure-time measurements of dust explosions in closed vessels can deviate from the real flame front velocity. The measured $p(t)$ curves represents progressive release of energy, and volumetric combustion can give rise to similar results.

2.2.5 Aspects of Numerical Modelling of Turbulent Flow and Combustion in Closed Explosion Vessels

Successful modelling of combustion by CFD codes is critically dependent on the accuracy of the mathematical models used to describe the key physical processes, including fluid turbulence and the interactions with and between the mixing, heat transfer and chemical reactions. Some of the main challenges are listed below:

- i) The conventional time-averaging procedure that is applied to the Navier-Stokes equations is known as Reynolds averaging; the other popular averaging procedure is mass-weighted averaging, also called Favre averaging. For variable density flows, which include reacting flows, Favre averaging is preferred over Reynolds averaging because the Favre averaged Navier-Stokes equations are simpler. A recent review on the modelling of variable density turbulent flows is given by Chassaing (2001). However, Veynante and Vervisch (2002) point out that Favre averaging is only a mathematical formalism: there is no simple relation between Favre and Reynolds averaging, and comparison between Favre

averaged quantities from numerical simulations and experimental results are not obvious.

- ii)* In many turbulence models (e.g. the k - ε model), the convective mixing due to velocity fluctuations is lumped together with molecular diffusion and modelled as one term using an analogy to Stoke's law; the Boussinesq's hypothesis (Launder and Spalding, 1974). The terms related to diffusion of turbulent quantities also include contributions from pressure diffusion, viscous effects, and triple correlation terms (Tennekes and Lumley, 1972). In combustion, the density changes by a factor of roughly seven; hence, many of the approximations (e.g. the Boussinesq's hypothesis) that are often used in other fluid mechanical situations are not valid (Lumley and Yaglom, 2001).
- iii)* All prevailing turbulence models are based on the assumption that the dissipation, ε (i.e. the rate of transfer of turbulent kinetic energy k from the large eddies to the smallest eddies), is a property of the large eddies rather than the smallest eddies. In rapidly changing turbulent flows the 'equilibrium' argument fail, and the rate of transfer from the energy-containing eddies to the dissipating eddies is not equal to the rate at which energy is being transferred from the dissipating eddies to heat (Bradshaw, 1994).
- iv)* For reacting two-phase flows, e.g. dust explosions and pulverized coal combustion, it is necessary to solve transport equations for both the carrier and dispersed phase. The interaction between turbulence and particles involve exchange of mass, momentum and energy between the two phases. The (coal) particle trajectories determine where the particles burn. In turbulent dust-air flames, several two-phase flow regimes are present due to the wide range of (coal) particle diameters in the dispersed phase (typically 1-200 μm).
- iii)* Turbulent dispersion of particles, i.e. the effects of turbulence on the particles.
- iv)* Modification of the carrier-phase turbulence structure, i.e. the effect of the presence of particles on turbulence. Although much work has been done on particle-laden flows, no simple method seems to exist for predicting the degree of turbulence modification by particles.

As the focus in this work is the experimental investigation, and not modelling, not much more will be said on this topic. However, it should be noted that although there are many complicating factors regarding the modelling of the transient reacting flow that take place in 20-litre explosion vessels, several examples of both experimental investigations and modelling of related problems have been described in the literature. Ouellette and Hill (2000) compared simulation results of turbulent transient gas injection into a large chamber obtained with the k - ε model with experimental results. It is indicated that the computed results become very sensitive to the specified initial values of k and ε , especially when coarse grid resolution was employed (i.e. grid size greater than the radius of the orifice). A discussion of adjustments of some of the coefficients in the standard k - ε model was included.

CHAPTER 3

Experiments

Experiments and experimental procedures are described in this chapter; the results will be presented and discussed in Chapter 4. Note that the order of the presentation is reversed between the two chapters. Experimental apparatus is presented in appendices A and B. Appendix A describes the development and performance of the arc generator used to generate the electrical discharges that has been used as ignition source in all the explosion tests in the main part of this work¹. Appendix B describes the two explosion vessels and the dispersion system used in this work. Data on the various dusts used in this work are given in Appendix C. Details on the analysis of LDA data is described in Appendix D. Appendix E describes some simple CFD simulations, illustrating that such methods could become a useful method for analysing the transient processes that take place inside closed explosion vessels.

Common for all tests

The general procedure for each individual test is more or less the same for all the experiments described in this work; it resembles the procedures described by Cesana and Siwek (2001) for the 20-litre Siwek sphere. The tests are divided into broader categories: *explosion tests* and *dispersion tests*; the explosions are subdivided on the basis fuel type: *solid fuel* or *gaseous fuel*. The various steps involved in each category of tests will be described in detail.

When explaining the experimental procedures, reference will be made to the schematic representation of the 20-litre dust explosion test facility at the University of Bergen (UoB) in Figure 3-1. In the rest of this chapter, numbers in square brackets [**n**] refers to numbered elements in this figure.

¹ Results from a few tests with chemical igniters are included in Appendix A, including the results from the Calibration-Round-Robin Test CaRo 00/01.

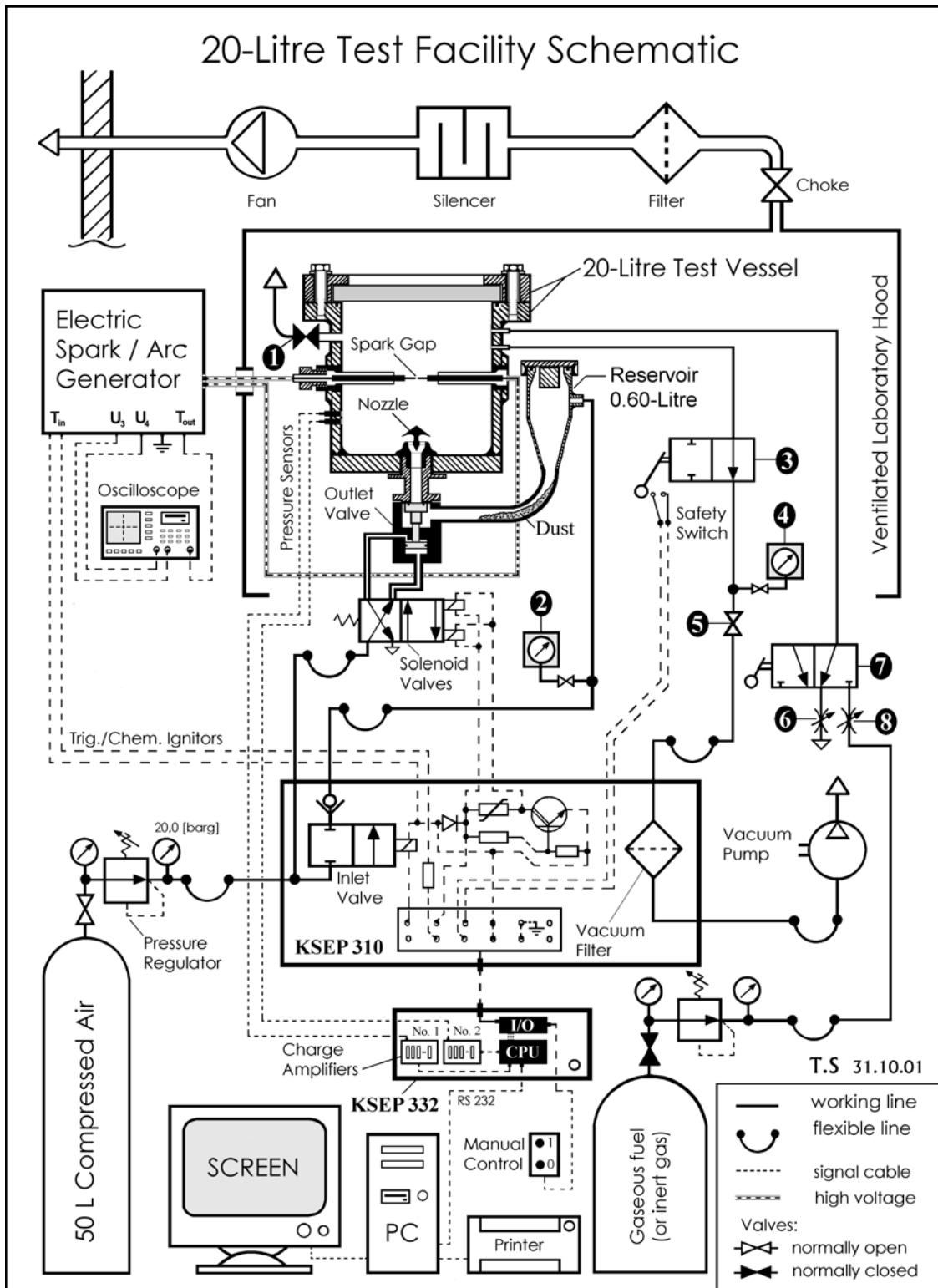


Figure 3-1. Electrical and pneumatic schematic of apparatus in the 20-L Dust Explosion Laboratory at the University of Bergen.

3.2 Explosion Experiments with Solid Fuels

The solid fuels used in this work are various combustible dusts (niacin amide, spores of *Lycopodium casuarinoides*, and various lots of silicon metal), and two lots of the explosible dust (RDX)

3.2.1 Experimental Procedure for Dust Explosion Tests

The sequence of events that take place for each individual dust explosion experiment performed in this work is described in detail.

Preparing the 20-l test vessel

The *20-l test vessel*, either the *modified USBM vessel* or the *cubical vessel* (see Appendix B), is set up in a *ventilated laboratory hood*. The *spark gap* is checked¹ before the lid is sealed, and the *exhaust valve* [1] is closed. The vessel is evacuated to an absolute pressure below 0.4 bars by the *vacuum pump* (LABOPORT, type N86KN.18 from KNF Neuberger GmbH) through the *vacuum filter* (part of the Control Unit KSEP 310). The ball valve [5] is closed, and the pressure in the 20-l vessel is adjusted by adding air through the *throttle valve* [6]. The pressure inside the vessel is monitored with the *digital pressure indicator* [4] (Druck, type DPI 705, pressure range -1 to 1 barg). As soon as the pressure remains stable at -0.600 ± 0.002 barg, the ball valve [3] is closed. The closing of [3] also operates the *safety switch*; this protects the pressure indicator [4] from being subjected to the explosion pressure.

Preparing the reservoir

A weighted dust sample is poured into the *reservoir*² ($V_r = 0.600$ litres), and the reservoir lid sealed. The reservoir is pressurized to 20 barg with air from the *50-l compressed air bottle* by operating the *manual control* (operates the *inlet valve*). The air pressure supplied to KSEP 310 is controlled by a *pressure regulator* (MESSER, type Constant 2000, 0-20 barg). The pressure in the reservoir is monitored with the *digital pressure indicator* [2] (Druck, type DPI 705, pressure range 0-20 barg). After this first pressurizing, the pressure in the reservoir drops slightly over the next few minutes.

Preparing the ignition source

The *electric spark/arc generator* is triggered³ by the *Control Unit KSEP 310*. Before a test sequence can be initiated, the generator has to be switched on manually. A flashing blue warning light indicates that spark ignition is ready to be triggered.

¹ Alternatively, the electrodes may be replaced by chemical igniters.

² In the tests with explosive material (RDX), the dust was placed in the bottom of the RDX nozzle (see Appendix B).

³ When chemical igniters are used, the spark/arc generator is disconnected, and KSEP 310 is coupled directly to the electrode holders.

Dispersion and explosion

The *Measurement and Control Unit KSEP 332* runs the dust dispersion, triggering of the ignition source, and pressure measurements. The sequence of events is initiated from a personal computer (*PC*), connected to KSEP 332 by a *RS-232* connection. The necessary software (KSEP software, version 6.0d) is provided by Adolf Kühner AG. The amount of dust added, the ignition energy, and the desired ignition delay time (t_v) is entered before the test is initiated. First, the inlet valve is opened for about 5 seconds to pressurize the reservoir for the second time, providing an initial reservoir pressure ($p_{r,i}$) of 20.00 ± 0.05 barg. Then the *solenoid valves* are operated, and the *outlet valve* is pneumatically opened by means of an auxiliary piston. Dust and pressurized air flow through the outlet valve and the *dispersion nozzle*, creating a turbulent dust cloud inside the test vessel. The outlet valve is closed, and after a preset ignition delay time (t_v , measured from onset of dispersion), the dust cloud is ignited by an electrical arc discharge. The discharge releases about 6 Joules of energy in about three milliseconds (see Appendix A). Two *piezoelectric pressure sensors* (Kistler Instrumente AG, type 701A) measure the pressure inside the explosion vessel. Two completely independent measuring channels gives good security against erroneous measurements and allows for self-checking. The charge generated by the piezoelectric pressure sensor's is transformed into proportional voltage by means of two charge amplifiers (Kistler Instrumente AG, type 5041) in KSEP 332. The measured values are transferred to the computer, processed, and the pressure-time curve displayed.

Supplementary work

After a test, the spark/arc generator is switched off. The overpressure in the explosion vessel is relieved by opening the exhaust valve [1], and the lid is opened. Residual dust is removed by a vacuum cleaner and a brush, sometimes water and detergents is used. The final pressure in the reservoir ($p_{r,f}$) is usually recorded before the reservoir is opened.

3.2.2 Experiments with Combustible Dusts

The effect of concentration and turbulence (ignition delay time) on explosion pressure and rate of pressure rise has been investigated for three different combustible dusts: niacin amide, spores of *Lycopodium casuarinoides*, and silicon. As the main issue here is the effect of turbulence on dust explosion indices, observations concerning other parameters will be dealt with in appendices. The various dusts are described in Appendix C, including particle size analysis and SEM pictures.

The general procedure has been to determine the dust explosion indices p_{ex} and $(dp/dt)_m$ for each dust (or lot of dust) over a broad range of dust concentrations; and then to investigate the effect of varying the ignition delay time for one specific nominal dust concentration. A nominal dust concentration close to the one that produced the maximum values of the explosion indices is chosen in order to minimize the effect of decreasing actual dust concentration for higher ignition delay times (dust settling out of suspension).

Niacin amide

The niacin amide (or pyridine 3-carboxamide) used in this work was the dust chosen by Kühner for the Calibration-Round-Robin test CaRo 00/01 (Cesana, 2001). Explosion indices were determined in both the modified USBM vessel and the cubical vessel, both fitted with the rebound nozzle, for nominal dust concentrations up to 1500 g/m³. The effect of varying the ignition delay time for a nominal dust concentration of 500 g/m³ was investigated in both vessels with the rebound nozzle, and with the mushroom and pepper nozzles in the cubical vessel.

Results from the Calibration-Round-Robin test CaRo 00/01 for both vessels are included in Appendix A; they illustrate the effect of chemical igniters on dust explosion indices.

***Lycopodium casuarinoides* spores**

Explosion indices were determined for dried spores of *Lycopodium casuarinoides* in the modified USBM vessel fitted with the rebound nozzle, for nominal dust concentrations up to 1500 g/m³. The effect of varying the ignition delay time for a nominal dust concentration of 500 g/m³ was investigated.

A few tests illustrating the effect of chemical igniters are discussed in Appendix A; the effect of moisture content on explosion indices is illustrated in Appendix C.

Silicon

For the three lots J133, J135 and J136, explosion indices were determined in the cubical vessel fitted with the rebound nozzle for nominal dust concentrations up to 2000 g/m³. The effect of varying the ignition delay time for a nominal dust concentration of 500 g/m³ was investigated for all three lots. Some peculiar observations on the colour of the silicon oxide from these tests are included in Appendix C; the observations may provide a rough estimate for the actual dust concentration during combustion.

For all the nine lots described in Appendix C, the effect of particle size distribution on explosion indices were investigated. A nominal dust concentration of 500 g/m³, and the default ignition delay time of 60 milliseconds, was used in all tests. These results are presented in Appendix A, together with a few tests with chemical igniters; the idea is to illustrate the limitations of electrical discharges as ignition source.

PMMA

A large batch of PMMA was purchased, but the dust turned out to be too difficult to ignite with the electrical discharges produced by the spark/arc generator. This is discussed in Appendix C.

3.2.3 Experiments with Explosible Dust

RDX

For both the fine and coarse lot, the effect of varying the ignition delay time for a nominal dust concentration of 1000 g/m³ was investigated in the modified USBM vessel fitted with the RDX nozzle. Lower nominal dust concentration turned out to be very difficult to ignite with the electrical discharges used in this work.

3.3 Explosion Experiments with a Gaseous Fuel

3.3.1 Experimental Procedure for Tests Involving Gaseous Fuel

Tests involving gaseous fuels follow the same general procedure as described for dust, except that the gaseous fuel is added to the 20-l vessel before dispersion. A similar procedure could be used for adding inert gases.

The 20-l vessel is evacuated to e.g. -0.700 barg. The *3-way ball valve* [7] is operated, and gaseous fuel added through the *throttle valve* [8] from a gaseous fuel bottle with pressure regulator. The digital pressure indicator [4] is used to monitor the increase in pressure as the gas enters the vessel. When the desired amount of fuel has been added, the 3-way valve [7] is operated again, and air added through the throttle valve [6] until the pressure reaches -0.600 barg. Air from the pressurized reservoir is then dispersed into the explosion vessel, and the mixture ignited after the desired ignition delay time. The method relies on precise measurements of partial pressure to achieve accurate fuel concentrations. The main uncertainty is whether sufficient mixing can take place in the short time from dispersion to ignition; hence, the concentrations should be considered as nominal concentrations. Results from CFD simulation presented in Appendix E indicate that the mixing may be incomplete for short ignition delay times.

For tests with initially quiescent conditions, the mixture is not ignited during the dispersion process. Instead, the dispersion process is terminated, and after some time the pressure is equalized with the surroundings by opening the throttle valve [6]. The mixture is then ignited directly.

In tests with both gaseous fuel and inert or combustible dust, the dust was added to the reservoir (as described in section 3.2.1), and the gaseous fuel added to the 20-l vessel (as described in section 3.3).

3.3.2 Experiments with Propane-Air Mixtures

Explosion indices for propane-air explosions in the modified USBM vessel fitted with the rebound nozzle have been investigated over a wide range of ignition delay times, and over the entire combustible concentration range. In addition, the effect of varying the ignition delay time for a nominal gas concentration of 4.5 per cent propane by volume was investigated in the cubical vessel for the three dispersion nozzles rebound, mushroom and pepper.

3.3.3 Experiments with Propane-Air Mixtures and Inert Dusts

The effect of inert dust on explosion indices for 4.5 per cent propane in air has been investigated in the modified USBM vessel fitted with the rebound nozzle. Two different inert dusts have been used: *talca* and *aluminium oxide*; the maximum nominal dust concentration was 800 g/m^3 , and two different ignition delay times were used: 60 and 300 milliseconds.

3.3.4 Experiments with Hybrid Mixtures

Hybrid mixtures can be defined as mixtures of fuels and oxidizer in which the fuels are present as both combustible dust and flammable gas (Bartknecht, 1981).

Explosion indices have been determined for hybrid mixtures consisting of propane and dried spores of *Lycopodium casuarinoides* in air. All tests were performed in the modified USBM vessel fitted with the rebound nozzle; ignition delay time 60 milliseconds. Two different approaches have been tried for varying the concentrations of combustible dust and flammable gas: *constant equivalence ratio*, and *constant optimum concentration ratio*.

Constant equivalence ratio

In one series of tests, the concentrations of propane and *Lycopodium* spores was varied in such a way that the sum of the equivalence ratios for the two fuel was kept at unity. The *equivalence ratio* is defined as:

$$\Phi = \frac{\left(\frac{m_{fuel}}{m_{oxidant}}\right)_{\text{actual mixture}}}{\left(\frac{m_{fuel}}{m_{oxidant}}\right)_{\text{stoichiometric}}} = \frac{\left(\frac{n_{fuel}}{n_{oxidant}}\right)_{\text{actual mixture}}}{\left(\frac{n_{fuel}}{n_{oxidant}}\right)_{\text{stoichiometric}}} \quad (3.1)$$

The nominal dust concentration is varied from stoichiometric (120 g/m³) to zero, while the propane concentration is varied from zero to stoichiometric (4.0 per cent by volume), in such a way that:

$$\Phi_{dust} + \Phi_{gas} = 1 \quad (3.2)$$

The major drawback with this approach is that while stoichiometric propane-air mixtures yields explosion indices close to the maximum value, stoichiometric *Lycopodium*-air mixtures results in very low explosion indices. When the relative amount of dust is high, there is also the question of how much dust that will adhere to the walls prior to ignition (i.e. the hybrid mixture will no longer be stoichiometric).

Constant optimum concentration ratio

An alternative approach is to define an *optimum concentration*, defined as the concentration that results in the maximum value of the explosion indices, and to define an *optimum concentration ratio* as:

$$\Psi = \frac{\left(\frac{m_{fuel}}{m_{oxidant}}\right)_{\text{actual mixture}}}{\left(\frac{m_{fuel}}{m_{oxidant}}\right)_{\text{optimum mixture}}} = \frac{\left(\frac{n_{fuel}}{n_{oxidant}}\right)_{\text{actual mixture}}}{\left(\frac{n_{fuel}}{n_{oxidant}}\right)_{\text{optimum mixture}}} \quad (3.3)$$

The concept of optimum concentration is obviously more arbitrary than stoichiometric concentration. For many fuels, the maximum explosion pressure occurs at a different concentration than the maximum rate of pressure rise. In addition, the concentration that yields the maximum explosion pressure and the maximum rate of pressure rise may depend on the turbulence level. Nevertheless, for most fuels an optimum concentration can be estimated within reasonable narrow limits of uncertainty. The values used in this work were found from the results determined for the pure fuels.

The concentrations of propane and *Lycopodium* spores was varied in such a way that the sum of the optimum concentration ratios for the two fuel was kept at unity:

$$\Psi_{dust} + \Psi_{gas} = 1 \quad (3.4)$$

The nominal dust concentration was varied from optimum (500 g/m³) to zero, while the propane concentration varied from zero to optimum (5.0 per cent by volume).

3.4 Dispersion Experiments

The transient dispersion process inside the 20-l cubical explosion vessel has been experimentally investigated in two different ways: turbulence measurements by backward scattering laser Doppler anemometry (LDA), and pressure measurements by piezoelectric sensors at various locations in the flow.

Turbulence decay during injection of air was measured by backward scattering laser Doppler anemometry (LDA). Attempts were also made to measure the effect of dust on the decay of turbulence; however, the dust introduced considerable noise and resulted in a dramatic reduction in sample frequency (for further details refer to Appendix D). This work was done by Ivar Øyvind Sand and the author at Christian Michelsen Research, Fantoft; the work was partly sponsored by GexCon AS.

Pressure measurements with piezoelectric sensors were used to characterize the transient flow during the dispersion process, both with and without dust.

3.4.1 Experimental Procedure for LDA Measurements

The 20-l vessel was flushed with dried air before it was evacuated. This was done to avoid the formation of small water drops by condensation when air was injected. A small amount of tracer particles (0.22 µm TiO₂) was added in the reservoir. The dispersion process commenced as described in 3.2. The LDA measurements were triggered by the same signal used to trigger the ignition, with t_v equal to 1 ms.

LDA system

A photograph of the experimental arrangement, and a schematic of the LDA system used, is shown in Figure 3-2. The LDA system, from TSI Inc., consists of the following items:

- An *argon ion laser* (Spectra Physics Inc., model 2580A) with beam lock system (BEAM LOCK 2060, Model 2060A-06) is used to generate a multi-line laser beam.
- A *Multicolour Beam Separator* (COLORBURST, model 9201) with a Bragg cell separates the three most energy containing wavelengths of the multi-line laser beams into three pairs of monochromatic beams: 476.5 nm (violet), 488.0 nm (blue) and 514.5 nm (green). Only the green beam was used in this work.
- Fibre optical cables transmit two monochromatic laser beams, one frequency shifted and one unshifted, to a *fibre optical probe* (TSI 9253-350, focal length 363 mm, beam spacing 50 mm). The two beams cross at the focal point of the fibre

optical probe. The crossed beams form an interference volume in which a given number of parallel bright and dark planes are located. These planes are normal to the plane formed by the two beams and parallel to the optical axis of the transmitting lens of the fibre optical probe. The fibre optical probe is attached to a 3-D traverse table.

- *Multicolor Receiver* (COLORLINK, model 9230) receives optical signals from the optical probes, generates a 40 MHz electric signal that drives the Bragg cell, and controls the magnitude of the frequency shift (10 MHz was used in this work).
- An *Intelligent Flow Analyzer* (IFA 750 – low pass filter 3 MHz, high pass filter 20 MHz) performs signal processing.
- A *software package* (FIND) from TCI Inc, used for data analysis.
- *Lexel Power Meter*, Model 504 (33 mW), for measuring the intensity of the laser beam.

Most of the experimental set-up is the same as the one used by Kong *et al.* (1993). The procedure was similar to the one described by Dahoe (2000); but he used a spherical 20-l vessel and forward scattering LDA. Further details on LDA measurements can be found in Durst *et al.* (1981), and in Goldstein (1996). Analysis of LDA data is described in Appendix D.

3.4.2 LDA Experiments

Measurements were done in various positions inside the 20-l cubical vessel. In each test one of the two horizontal velocity components, u_x or u_y , were measured. The vertical component (u_z) was not measured due to limited resources; this would have required alterations in the experimental set-up. In most of the tests the vessel were fitted with the rebound nozzle, but a few tests were also done with the mushroom and pepper nozzles. The coordinates defining the position of the measurement volumes assumes a Cartesian coordinate system with origin at the centre of the spark gap, the x-axis parallel to the electrode axis, and vertical z-axis.

In most of the tests, only air with tracer particles was injected; these tests are summarized in Table 3-1.

In some tests, both tracer particles and dust (*Lycopodium casuarinoides*) were injected; see Appendix D.

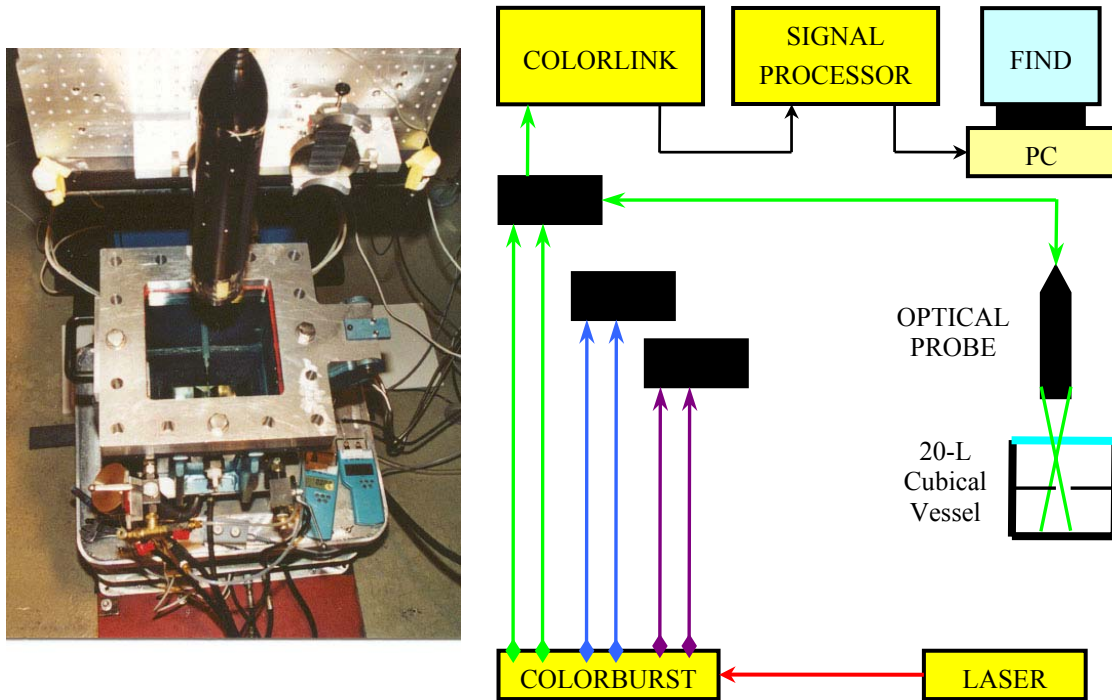


Figure 3-2. Experimental arrangement for LDA measurements of turbulence inside the cubical 20-l vessel during the dispersion process (left) – photograph by I.O. Sand. Schematic of LDA system used (right), modified from Kong et al. (1993).

Table 3-1 LDA measurements performed without dust, only tracer particles. The signal-to-noise ratio was set to “medium”, and the initial data rate was approximately 10 to 15 kHz.

Test No.	POSITION [mm]	Component	Nozzle
19-23	(0,0,0)	u_y	Rebound
24-28	(0, -30,0)		
29-33	(0,30,0)		
35-39	(0,60,0)		
40-44	(0,90,0)		
47-51	(0,0,0)	u_x	
52-56	(0, -30,0)		
57-61	(0,30,0)		
63-67	(0,60,0)		
68-71, 73	(0,90,0)		
74-78	(0,0,90)	u_y	
79-83	(0,0,0)		Mushroom
84-88	(0,0,0)		Pepper
89-93	(0,0,0)		Rebound
94-98	(0,0,0)		
99-103	(0,0,90)		

3.4.3 Experimental Procedure for Measuring Pressure-Time Histories with Piezoelectric Sensors

The basic procedure were the same as described for dust explosion tests, but without ignition. Static pressures were measured at three different locations in the flow; see Figure 3-3:

1. In the reservoir, $p_r(t)$.
2. At the nozzle inlet, $p_n(t)$.
3. Inside the 20-l explosion vessel, $p_v(t)$.

The nozzle and reservoir pressures were measured with piezoelectric pressure transducers (Kistler, type 5041B), charge amplifiers (Kistler, type 5041B) and a digital real-time oscilloscope (Tektronix, TDS 360, 200 MHz, 1 GS/s). The pressure in the 20-l vessel was measured with the built-in pressure measurement system in KSEP 332, see section 3.2.

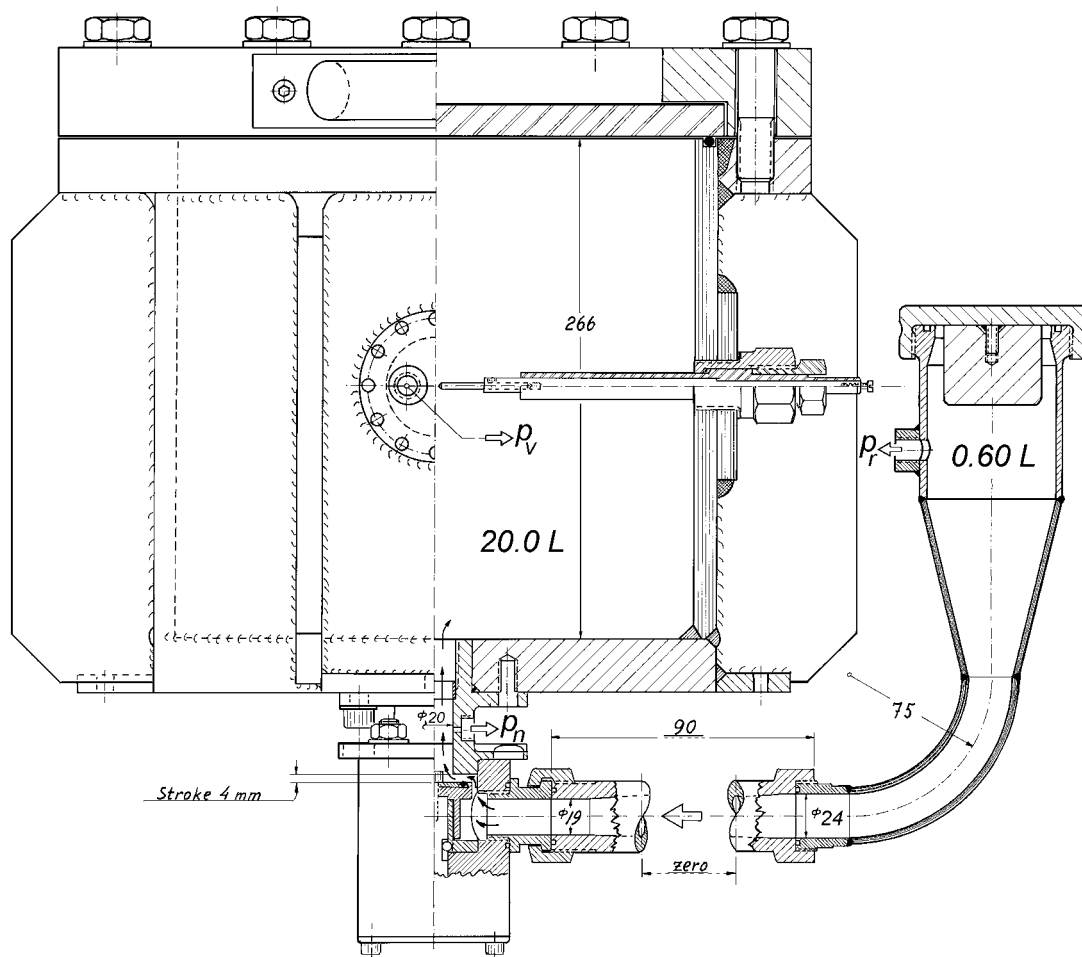


Figure 3-3. Mechanical drawing of the flow path from the reservoir, through the extension piece, outlet valve and adapter flange, and finally into the 20-l cubical vessel. The drawing shows the location of the three pressure measurements: reservoir pressure (p_r), nozzle pressure (p_n) and vessel pressure (p_v). Drawing by J. Skjold.

3.4.4 Flow Experiments with Piezoelectric Sensors

Pressure-time histories were measured with piezoelectric sensors for dispersion experiments in the 20-litre cubical vessel. Four different nozzles were used: *rebound*, *mushroom*, *pepper* and *open*; the various nozzles are described in Appendix B.

For each nozzle the following tests were done:

- To document the characteristic flow, five dispersions with only air were performed.
- The effect of dust was investigated by dispersing various amounts of *Lycopodium casuarinoides* spores; the experiments included two repetitions for each of the following amounts of dust: 2.5, 5, 10 and 20 grams.

Some additional tests were done with the rebound nozzle to illustrate the effect of dust type; including a series of tests with various amounts of jet-milled Silgrain (lot J-136), and a series of tests with 10 grams of various dusts: *L. casuarinoides*, PMMA, and various lots of jet-milled Silgrain (J-133, J-136 and J140).

Experimental Results and Discussion

The experimental results are presented and discussed. In section 4.1 the results concerning the dispersion process are presented. Section 4.2 contains the results from explosions with gaseous fuel, including hybrid explosions. Dust explosion tests, including tests with explosible dust, are presented in section 4.3. Finally, results from both dispersion and explosion experiments are combined in the discussion of burning velocity in section 4.4.

4.1 Results from Dispersion Experiments

The transient dispersion process in the 20-l cubical explosion vessels has been investigated by laser Doppler anemometry, and by measuring the pressure-time history with piezoelectric pressure sensors. Results from both methods are presented below. Some simple CFD-simulation of the dispersion process can be found in Appendix E.

4.1.1 Turbulence Decay Measured with LDA

Analysis of the LDA data is described in Appendix D; within the accuracy of the measurements, the turbulent flow field were found to be *spatially homogeneous*¹ and *directionally isotropic*² for ignition delay times exceeding 60 milliseconds. However, it should be noted that the vertical velocity component were not measured. No significant effect of nozzle type could be identified from the limited number of tests with other nozzles than the rebound nozzle.

¹ The root-mean-square values of the velocity fluctuations measured at different locations converge towards each other.

² The root-mean-square values of the two horizontal components of the velocity fluctuations converge towards each other; however, the vertical component was not measured.

Dispersion of air with tracer particles only

The mean value of the root-mean-square of the fluctuating velocity, for all the results performed with the rebound nozzle (see Table 3-1), is shown in Figure 4-2. The fact that the level of turbulence seems to have reached its maximum value within 10 milliseconds after onset of dispersion, supports the suggestion by Dahoe (2000) and Dahoe *et al.* (2001a, 2001b); i.e. that the turbulence production is dominated by the baroclinic effect. The remaining part of the injection process, from 10 to about 45 milliseconds, is not able to maintain this high level of turbulence.

Results reported by Dahoe *et al.* for a spherical 20-litre vessel fitted with the rebound nozzle, for the time interval from 60 to 200 milliseconds, is indicated in Figure 4-2. As described in both Chapter 2 and Appendix D, Dahoe *et al.* were able to describe the decay of turbulence in this interval by an equation on the same form as the equation used by Batchelor and Townsend (1947, 1948a, 1948b) to describe decay of grid generated turbulence:

$$\frac{u'_{rms}}{u'_{rms}^o} = \left(\frac{t}{t_0} \right)^n \quad (4.1)$$

In this context, the fixed time t_0 is 60 milliseconds, and u'_{rms}^o is the root-mean square of the fluctuating velocity at time t_0 . For the results in this work, u'_{rms}^o and n takes the values 1.93 m/s and -1.70 , respectively; Dahoe *et al.* reported values of 3.75 m/s and -1.61 . Hence, the value of the root-mean-square of the fluctuating velocity measured in the cubical vessel is significantly lower than the value reported by Dahoe *et al.* The main reasons for this discrepancy, provided both measurements are reasonable correct, can be an increased rate of dissipation in the cubical vessel due to its higher surface-to-volume ratio, and the possibility of secondary flow in corners. However, considerable uncertainty is introduced by the arbitrary nature of the smoothing procedures used to define the mean velocity (Appendix A). There may also be minor differences in experimental procedures, or in details of the dispersion systems (e.g. the extension piece and adaptor flange used in this work, see Figure B-8). The lower turbulence level found in this work has some influence on the estimates of Kolmogorov scales in section 2.2.2; see Figure 4-1. However, the estimated increase in the Kolmogorov scales, both length and time, are moderate in light of the ‘order of magnitude’ nature of these calculations.

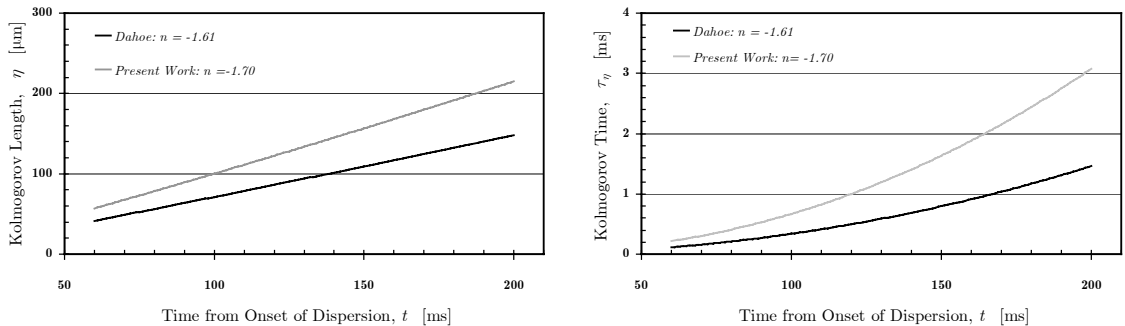


Figure 4-1. Comparison of the evolution of Kolmogorov length and time scale during decay of turbulence in 20-litre sphere, as predicted from the results in this work compared the results by Dahoe *et al.* – according to equations (2.12) and (2.20).

An alternative approach (Appendix A; van der Wel, 1993) is to skip the whole smoothing procedure, and simply define u'_{rms} as the root-mean-square of the measured velocity. The result of applying this simplified method to the data in the present work is illustrated in Figure 4-3 for measurements of both velocity components in the point (0,0,0); the results obtained with smoothing are also included. The spread in the results without smoothing is considerably higher than for the smoothed data, as would be expected. As pointed out in Appendix D, the results obtained without smoothing defines an upper limit for the estimated value of u'_{rms} . Note that the measurements by Dahoe *et al.* are lower than this upper limit; in Figure 4-3 u'_{rms} and n takes the approximate values 4.75 m/s and -1.60 , respectively.

Since the smoothing procedure adopted in this work was the same as the one used by Dahoe (2000), it will be assumed in the following that (4.1), with $u'_{rms} = 1.93$ m/s and $n = -1.70$, represents the decay of turbulence in the cubical vessel in the period from 60 to 200 milliseconds. Although the turbulence in the modified USBM vessel has not been measured, it seems reasonable to expect that the level of turbulence in this vessel will be closer to the values reported for the Siwek sphere by Dahoe; assuming the lower turbulence level measured in this work is due to the shape of the cubical vessel. However, if the low values of u'_{rms} found in this work are primarily caused by discrepancies in the dispersion system, the turbulence level in the modified USBM vessel may be closer to the values measured in the cubical vessel. This will be discussed further in the section 4.4.

Dispersion of air and dust

The LDA measurements performed with dust added to the flow had to low effective data rate to yield meaningful results; either most of the data points were discarded by the measurement system, or the data were infested with disproportionately amounts of noise that could not be removed in an unambiguous way. This is discussed further in Appendix D.

It should be noted that results reported by Dahoe (2000) indicate that the turbulence fluctuations of the gas phase behave more or less independent of the presence of solid particles. However, it is not clear how reliable these results are; e.g. what the efficient sampling rate were in the LDA measurements, the level of noise, etc.

4.1.2 Pressure-Time Histories Measured with Piezoelectric Sensors

Pressure measurements at various positions in the flow have been used to characterize the transient dispersion process for the various nozzles, with and without dust. The main advantages with such measurements is that they can be performed just as easy with dust as with air only, and it is straightforward to compare the results with results from e.g. CFD simulations of the same process.

It should be noted that Zhen and Leuckel (1995a, 1995b, 1996) used similar measurements to estimate an equivalent nozzle diameter and an equivalent exit velocity of the air at the nozzle, and used these parameters to characterize the flow conditions during the dispersion process in a 1-m³ vessel; similar calculations will not be attempted in this work. The analysis of Zhen and Leuckel applies theory for self-similarity of

turbulent free jets, an assumption that probably will be violated by most of the dispersion nozzles used in this work.

Dispersion of air

Results from dispersion tests with air for four different nozzles: *open*, *rebound*, *mushroom* and *pepper* (Appendix B), are given in Figure 4-4; five tests are included for each nozzle.

For the reservoir and vessel pressures, defined in Figure 3-3, there is no significant difference in the pressure-time histories for the various nozzles. The reservoir pressure decreases exponentially, and the vessel pressure increases exponentially; both flatten off at a pressure close to atmospheric.

However, pressure-time histories for the nozzle pressures are significantly different. For the mushroom and pepper nozzles, the nozzle pressure increases rapidly to a maximum value between eight and nine bar gauge in less than 10 milliseconds; it then decreases exponentially towards its final value. The nozzle pressure for the two other nozzles also increases rapidly in the initial phase, but only to a value less than 2 bar gauge. It then decreases steadily, and reaches values that are below the simultaneously measured values for the pressure in both the reservoir and the explosion vessel. Then a sudden ‘jump’ is observed after 30 to 40 milliseconds, before the pressure again decreases towards its final value.

The ‘jump’ phenomenon observed for the nozzles *open* and *rebound* are probably due to a shock in the nozzle, analogous to the classical theory for flow through a converging-diverging nozzle found in most text on gas dynamics (e.g. Shapiro, 1953). Thus, to use terminology from turbulent free jets; the flow from the mushroom and pepper nozzle can probably be characterized as *underexpanded*¹, while the flow from the open and rebound nozzle are *overexpanded*².

Dispersion of air and dust

Results showing the effect of dust loading on the measured reservoir pressure for all off the four nozzles are shown in Figure 4-5 and Figure 4-6. The total mass of dust that was placed in the reservoir varied from 2.5 to 20 gram, corresponding to nominal dust concentrations from 125 to 1000 g/m³. Tests with *Lycopodium casuarinoides* spores were done for all four nozzles; some additional tests with other dusts were performed with the rebound nozzle. The pressure-drop in the reservoir is delayed when dust is introduced in the flow; the delay increases with increasing amount of dust, and there is little difference between the various nozzles. The results with the rebound nozzle for various dusts indicate that the type of dust has little influence on the results, although the finer fractions of silicon dust seems to increase the delay compared to the coarse silicon (and other dusts).

Results showing the effect of dust loading on the measured nozzle pressure for all off the four nozzles are shown in Figure 4-7 and Figure 4-8. The initial pressure peak

¹ A jet is *underexpanded* if the pressure at the exhaust region is less than the exit-plane pressure – the gas velocity is sonic (Shapiro, 1953; Ouellette and Hill, 2000).

² A jet is *overexpanded* if the pressure at the exhaust region is higher than the exit-plane pressure – the gas velocity is supersonic (Shapiro, 1953).

observed for the mushroom and pepper nozzles is lowered by increased amounts of dust; the effect is probably caused by decreased mass flow¹. The subsequent pressure fall is increasingly delayed for higher dust loading, presumably because the remaining reservoir pressure is higher. The much lower initial pressure peak is also reduced slightly with increased dust loading for the open and rebound nozzles; the subsequent overexpanded jet seems to be suddenly interrupted by a period of increased pressure, indicating that the flow is slowed down by dust. This second pressure peak occurs sooner, and lasts longer, with increased dust loading. The open nozzle seems to return to a state of overexpanded jet, before a sudden pressure rise indicates the transition to underexpanded jet. The final pressure jump is increasingly delayed with higher dust loading, presumably due to the higher reservoir pressure. For the rebound nozzle, the second pressure peak decays steadily towards the final pressure; i.e. the flow is in a state similar to an underexpanded jet during the rest of the dispersion period. The main reason for the observed difference between the flow in the open and rebound nozzles is probably due to the reflection plates at the exit of the rebound nozzle. The reflection plates reduce the effective cross section area of the exit slightly compared with the open nozzle, and the momentum change induced on the flow is likely to increase the pressure gradients upstream of the exit.

As pointed out by Zhen and Leuckel (1995a, 1995b, 1996), there can be no doubt that the discharge of pure air from the reservoir undergoes different flow conditions compared with dust-air mixtures. Zhen and Leuckel suggested that delayed inflow due to dust blockage, compared to that of the pure air, would result in higher turbulence intensity at the time of ignition for increased dust loading. However, this effect will probably not apply to standardized tests performed in 20-L vessels, since the outlet valve is closed before ignition takes place. Results presented in the next section indicates that there is not significantly more air left in the reservoir after injection of dust, compared with injection of air only. In addition, it is not clear how the dust will influence on the initial turbulence production by the baroclinic effect discussed in section 4.1.1. Given the significant contribution of this effect on the initial turbulence production, and the fact that the flow seems to be most affected by the presence of dust in this early phase, it may well be that the influence of dust particles on the baroclinic effect is the main source of any significant ‘turbulence modification’ that takes place in 20-litre explosion vessels during standardized tests.

¹ Note in Figure 3-3 that the nozzle pressure is measured in the channel downstream of the piston in the outlet valve. The *throat*, or the narrowest cross-section encountered by the flow in its way from the reservoir to the vessel, is immediately over the piston; where the flow direction changes from horizontal flow inwards towards the centre, to vertical (upward) flow. The Mach number at the throat will be unity; hence, the downstream mass flow will be limited to the mass flow at the throat.

4.1.3 Other Observations Regarding the Dispersion Process

Initial conditions for explosions

It has been pointed out by Mintz (1995) that due to the rapid rate that air enters a 20-litre explosion vessel, the system is not at thermodynamic equilibrium at the time of ignition. According to Mintz, the actual concentration of air is 15 per cent less than indicated by the measured pressure after 60 milliseconds; thus, a significant error is introduced in the determination of explosion pressure. It should be noted that Mintz used a different dispersion system than the one used in this work.

The initial conditions inside the explosion vessel can be estimated if we assume that air behaves as an ideal gas, and that the initial and final temperatures in both reservoir and explosion vessel are equal. If a reservoir with volume 0.6 litres and initial pressure 0.4 bar absolute is emptied into a vessel with volume 20 litres and initial pressure 21 bar absolute, the final pressure in both the reservoir and the vessel will be 1.0 bar, exactly:

$$\begin{aligned}
 p_f &= \frac{(n_{v,i} + n_{r,i})RT}{(V_v + V_r)} \\
 &= \frac{\left(\frac{p_{v,i}V_v}{RT} + \frac{p_{r,i}V_r}{RT}\right)RT}{(V_v + V_r)} \\
 &= \frac{0.4[\text{bar}] \cdot 20[\text{L}] + 21[\text{bar}] \cdot 0.6[\text{L}]}{(20 + 0.6)[\text{L}]} \\
 &= 1.0[\text{bar}]
 \end{aligned}$$

However, the transient dispersion process in the 20-litre explosion vessels is certainly not isothermal, and the outlet valve is closed long before the pressure and temperature can reach equilibrium. The final pressure in the reservoir has been measured throughout all the experiments described in this work; it usually stabilizes at a pressure close to 0.6 bar gauge. For increased amounts of dust, the final reservoir pressure is found to increase, see Figure 4-9. This is reasonable; the results in section 4.1.2 clearly indicate that the inflow is increasingly delayed for higher dust loading. The increase is higher for the mushroom and pepper nozzles.

A final reservoir pressure of 0.6 bar gauge corresponds to a final vessel pressure, assuming the initial and final temperatures are the same, of:

$$\begin{aligned}
 p_{v,f} &= \frac{(n_{v,i} + n_{r,i} - n_{r,f})RT}{V_v} \\
 &= \frac{\left(\frac{p_{v,i}V_v}{RT} + \frac{(p_{r,i} - p_{r,f})V_r}{RT}\right)RT}{V_v} \\
 &= \frac{0.4[\text{bar}] \cdot 20[\text{L}] + (21[\text{bar}] - 1.6[\text{bar}]) \cdot 0.6[\text{L}]}{20[\text{L}]} \\
 &= 0.982[\text{bar}]
 \end{aligned}$$

Thus, the initial concentration of air will only be about 2 per cent below that of ambient conditions for the tests in this work. Observes values of the final pressure in

the reservoir as a function of the final pressure in the explosion vessel for various dispersion tests (and tests that misfired) are shown in Figure 4-10. The theoretical values are calculated from the equation:

$$p_{v,f} = \frac{p_{v,i}V_v + (p_{r,i} - p_{r,f})V_r}{V_v} \quad (4.2)$$

The actual volumes of the two vessels, 19.97 and 20.50 litres for the cubical and modified USBM vessel, respectively, have been used in the calculation of the theoretical values; similar values for a vessel of exactly 20 litres in volume are also indicated. The greater volume of the modified USBM vessel yields somewhat lower final pressures, but this effect is to some extent counteracted by increased inflow from the reservoir due to the decreased backpressure.

Dust deposits

In both vessels, a layer of deposited dust was usually found underneath the lid after dispersion experiments. The deposit had a radius of about five centimetres, extending from the centre of the lid. The most obvious explanation for this phenomenon is that the flow from the dispersion nozzles is directed upwards, but it is also possible that a wake formed by opposing flows could produce favourable conditions for dust deposition. The existence of such a wake is suggested by results from CFD simulations of the dispersion process, see Appendix E.

This phenomenon can be partly responsible for the poor results obtained when measuring particle-laden flow with LDA; unfortunately, the laser beams passed through the window exactly in this position.

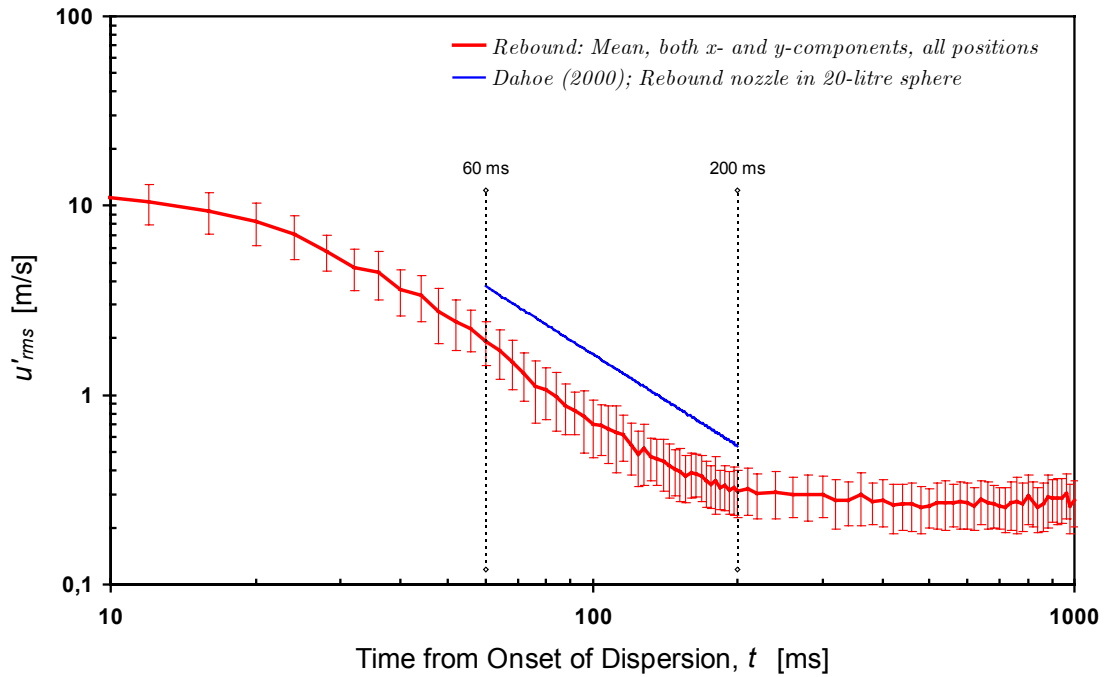


Figure 4-2. Decay of the root-mean-square velocity in the 20-l cubical vessel; the series represents the average value of all the 60 tests with the rebound nozzle (see Table 3-1); error bars indicate one standard deviation above and one standard deviation below the average value. Results from Dahoe (2000) and Dahoe et al. (2001a) are also indicated in the figure.

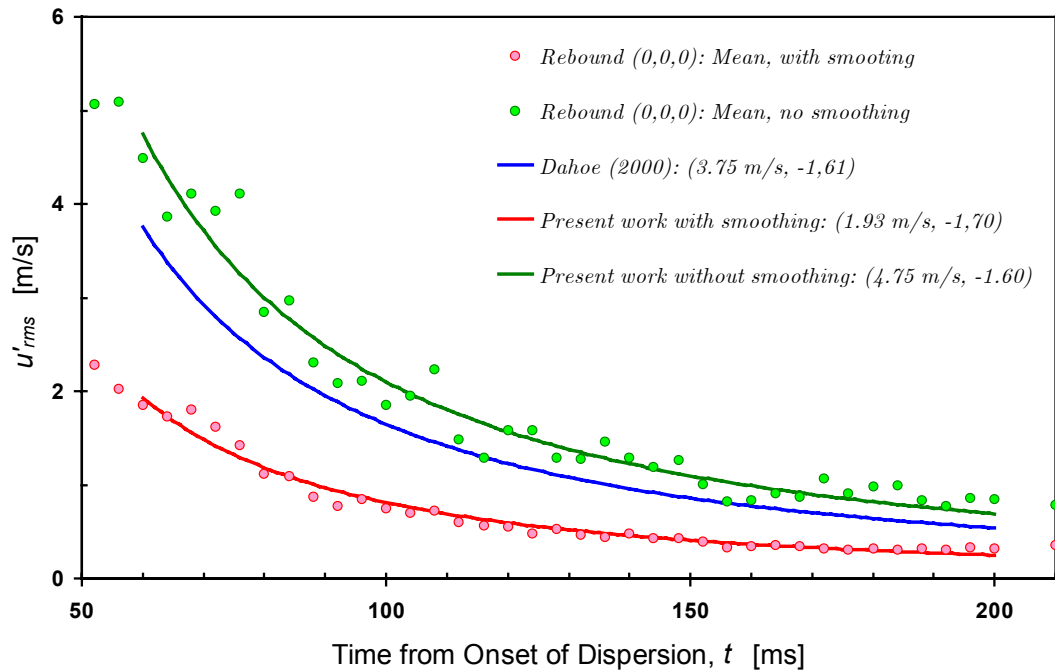


Figure 4-3. Decay of the root-mean-square velocity in the 20-l cubical vessel, with (red) and without (green) smoothing. Each data point is the mean value of all measurements of both velocity components in the point (0,0,0), i.e. ten measurements in total. The value of $u'_{rms}{}^0$ and n are given in parenthesis behind the legend for the fitted curves. Results from Dahoe (2000) and Dahoe et al. (2001a) are also indicated in the figure (blue).

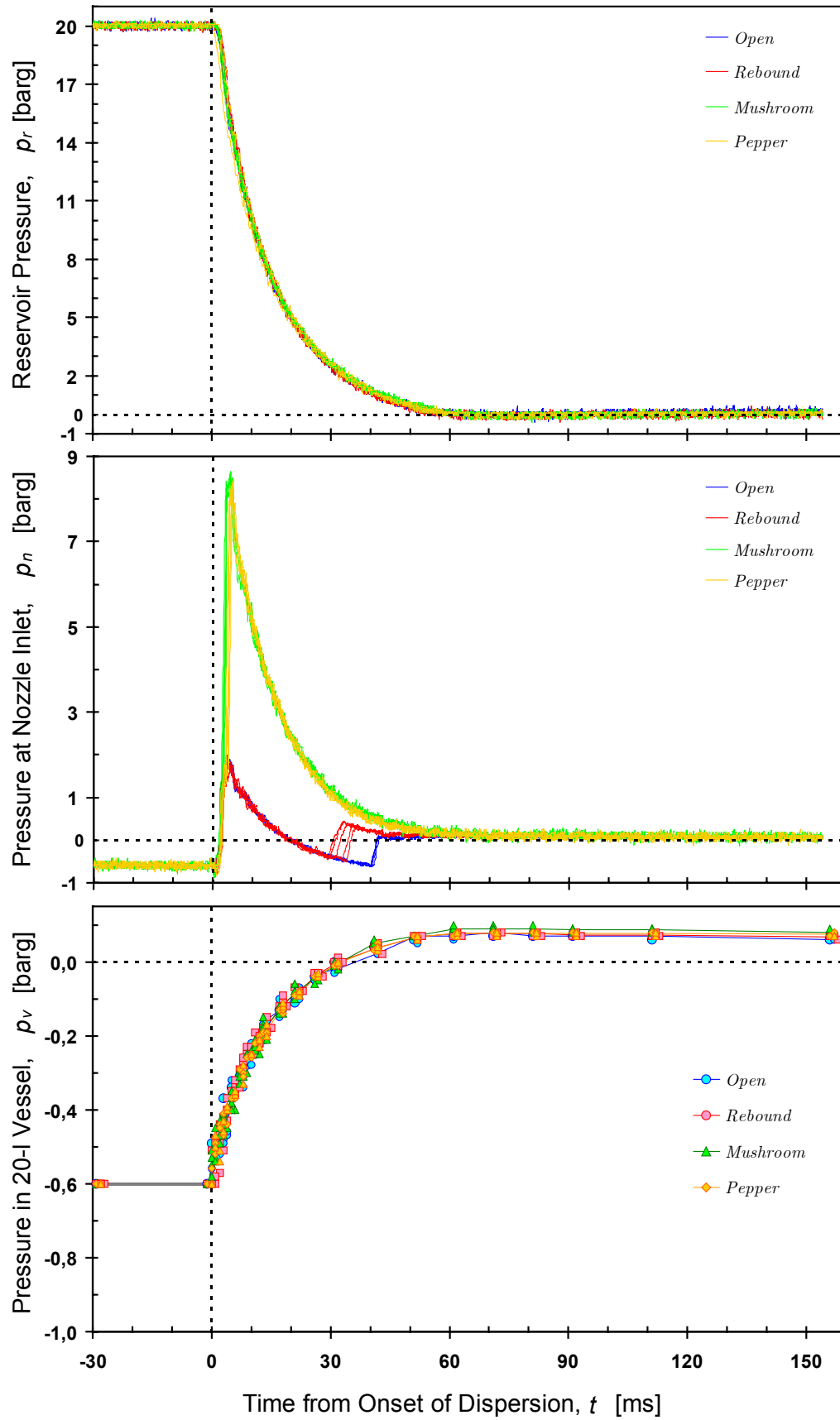


Figure 4-4. Experimental pressure-time histories from dispersion experiments with air only. Five tests are included for each of the four nozzles.

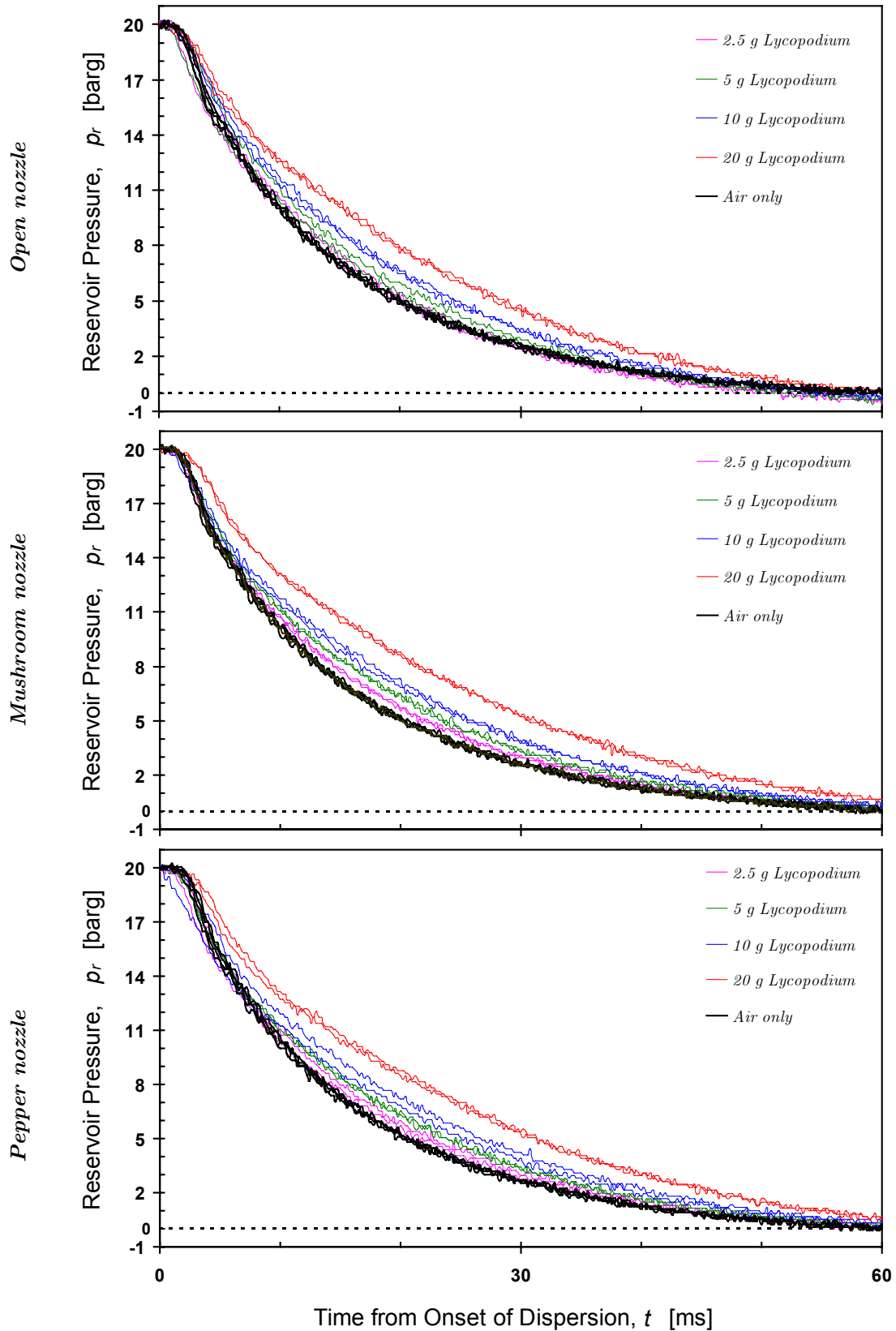


Figure 4-5. Reservoir pressure measured in dispersion experiments with various amounts of *Lycopodium casuarinoides* spores for three of the nozzles: open (top), mushroom (centre) and pepper (bottom). For each nozzle, there are two tests for each amount of dust in addition to the five tests from Figure 4-4 with air only.

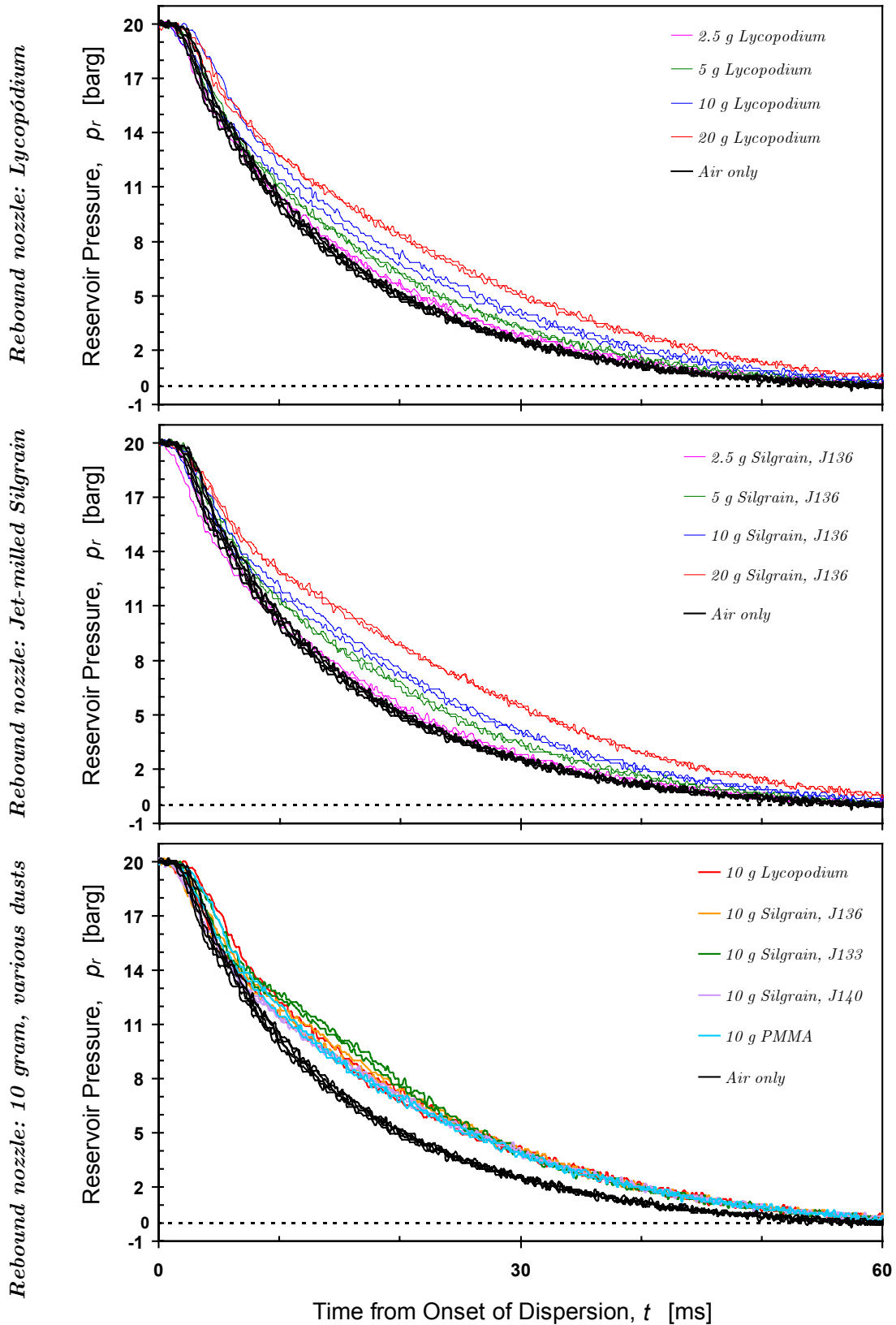


Figure 4-6. Reservoir pressure measured in dispersion experiments with dust for the rebound nozzle: *L. casuarinoides* (top), jet-milled *Silgrain* (middle) and 10 grams of several dusts (bottom). There are two tests for each test with dust, in addition to the five tests from Figure 4-4 with air only.

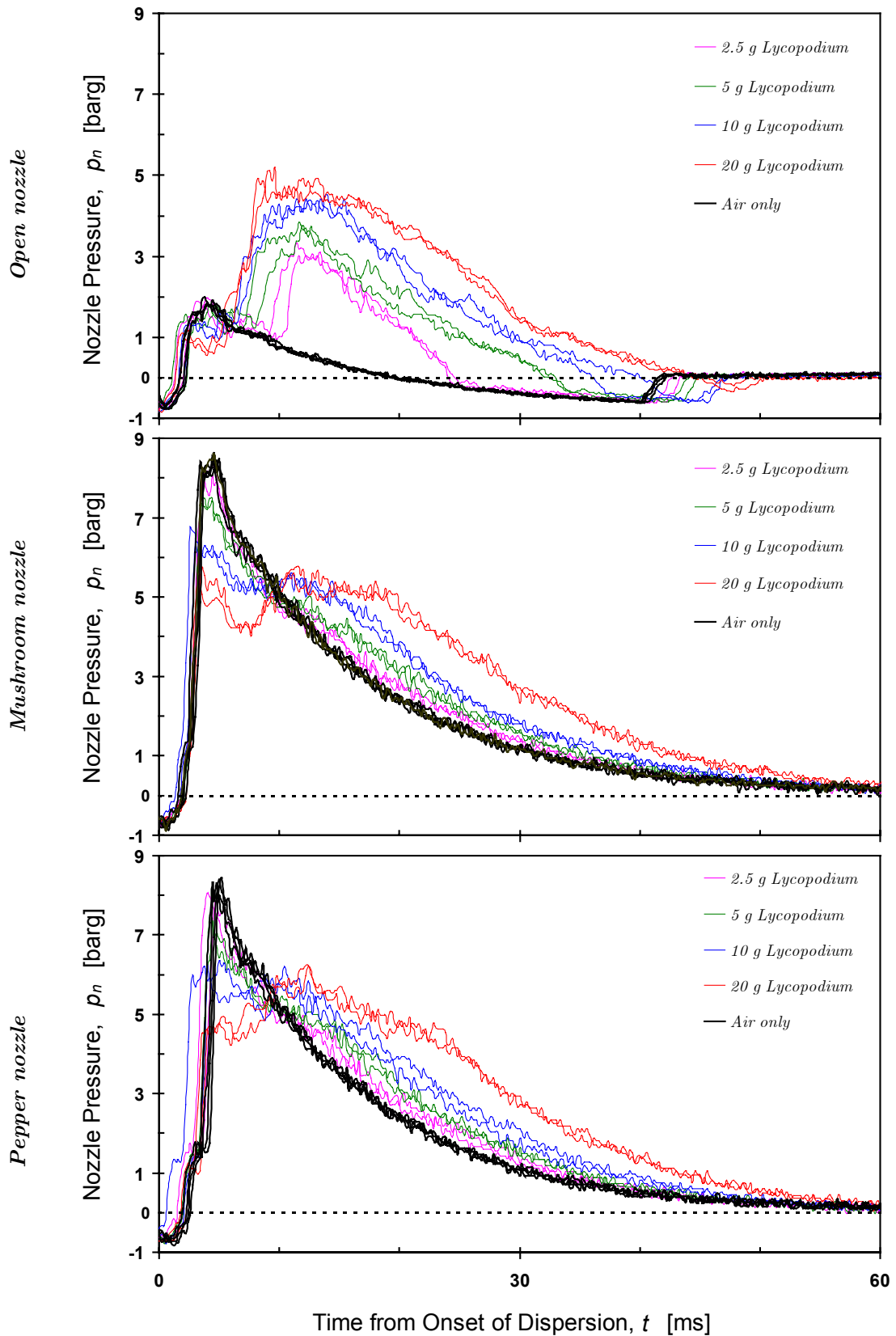


Figure 4-7. Nozzle pressure measured in dispersion experiments with various amounts of *Lycopodium casuarinoides* spores for three of the nozzles: open (top), mushroom (centre) and pepper (bottom). For each nozzle, there are two tests for each amount of dust in addition to the five tests from Figure 4-4 with air only.

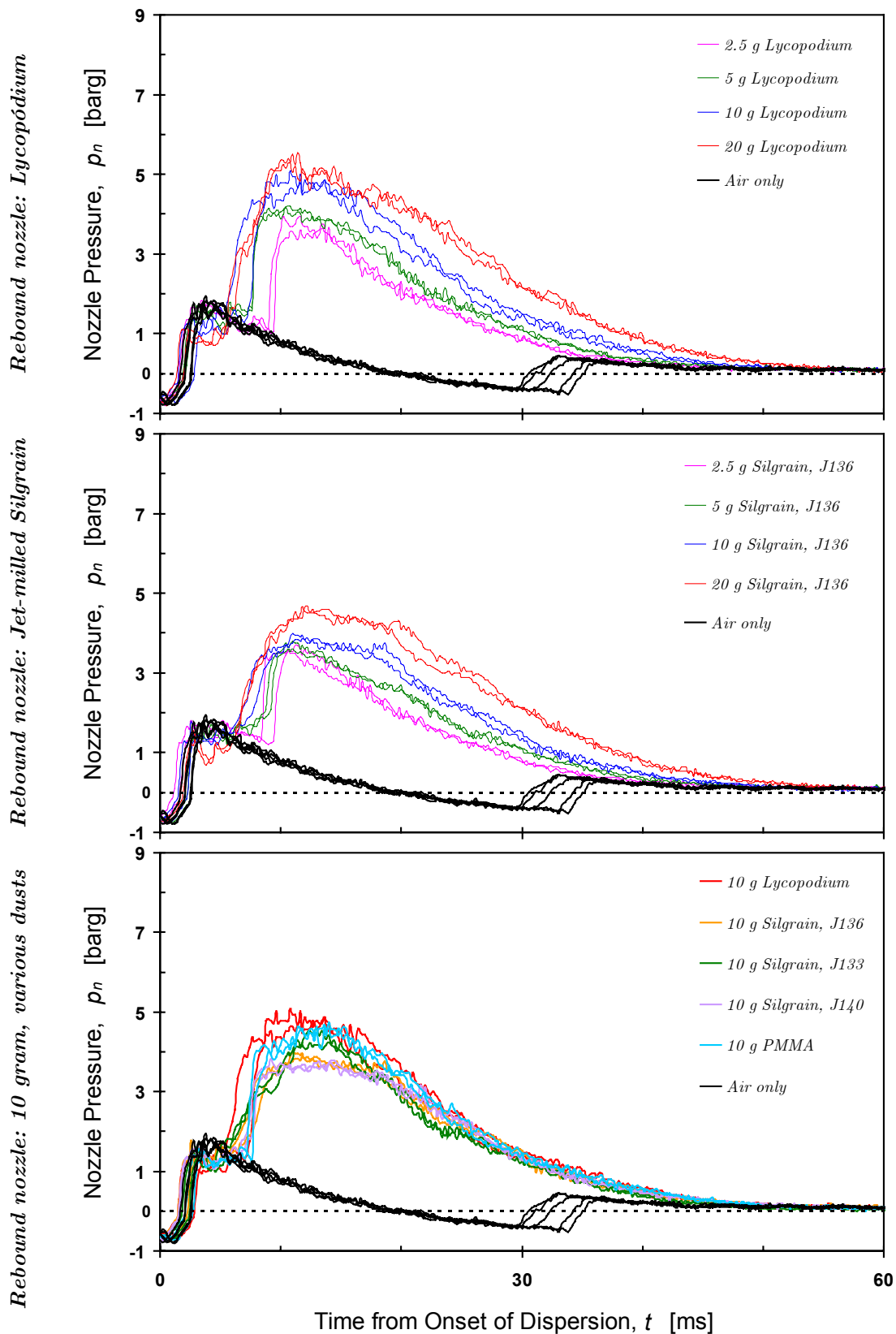


Figure 4-8. Nozzle pressure measured in dispersion experiments with dust for the rebound nozzle: *L. casuarinoides* (top), jet-milled Silgrain (middle) and 10 grams of several dusts (bottom). There are two tests for each test with dust, in addition to the five tests from Figure 4-4 with air only.

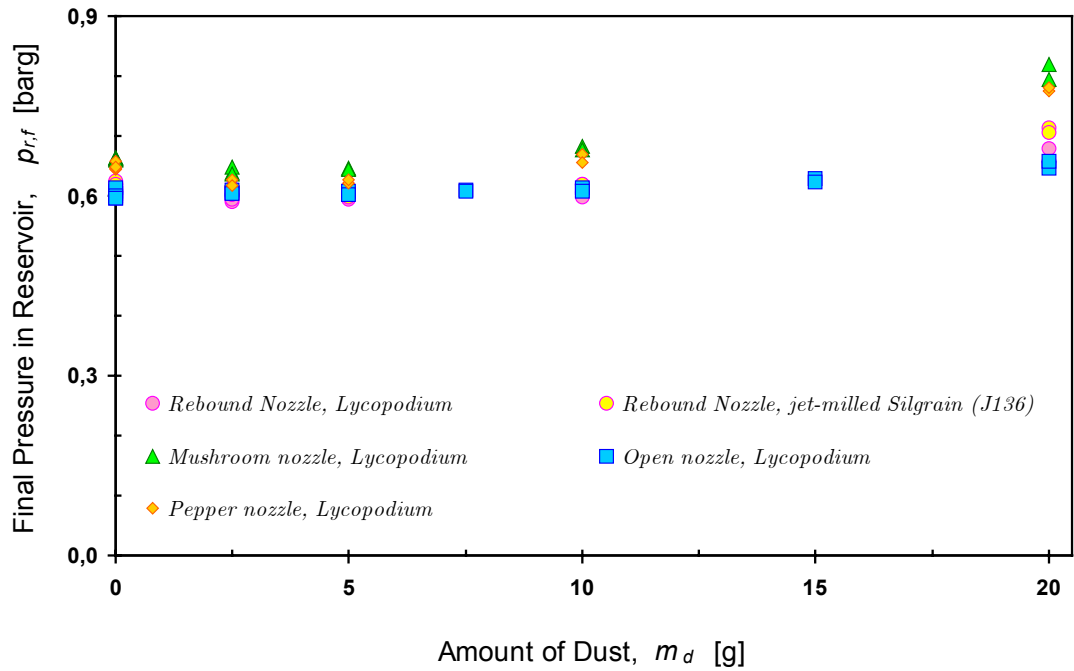


Figure 4-9. The final pressure in the reservoir as a function of dust loading for various nozzles. Although these results are limited to the dispersion results discussed in section 4.1.2, similar results have been measured for all the tests performed in this work.

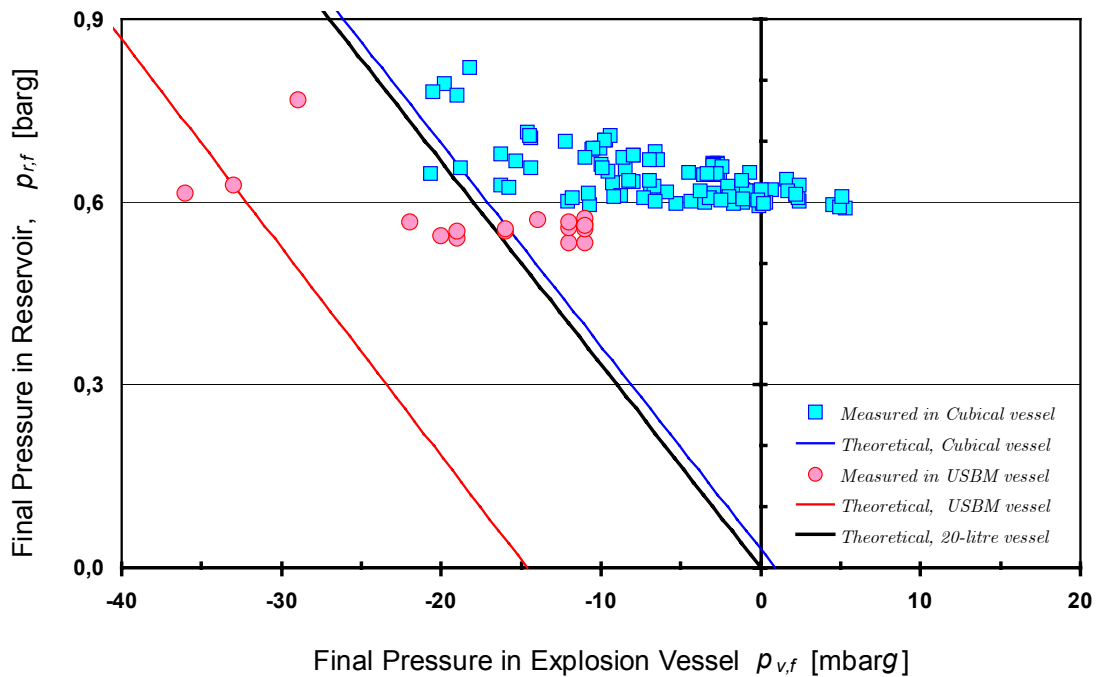


Figure 4-10. Final pressure in the reservoir as a function of dust loading for various nozzles.

4.2 Results from Explosions with Gaseous Fuel

The reason for doing explosion experiments with pure gaseous fuels in the 20-litre apparatus was threefold. First, experimental data obtained with gaseous fuel can serve as a reference when interpreting dust explosion data. Combustion of premixed gaseous mixtures is much better understood than combustion of dust clouds. Second, explosion indices from gas explosions can be used as an indirect measure of the turbulence level at various ignition delay times. In this way, they can be used to illustrate the effect of vessel shape and dispersion nozzle. Third, any CFD code with ambitions of reproducing the standardized tests used to determine explosion indices for dust clouds should be able to reproduce similar tests with gaseous fuel fairly well. However, as is illustrated in Appendix E, it is not straightforward to imitate the initial conditions created by the transient dispersion process; this complicated the validation of the simulation results for the subsequent explosions.

By adding inert or combustible dust to the gaseous fuel, effects that follow from the presence of solid particles in the combustible mixture could be illustrated. Simulations of such experiments can be logical steps towards developing a CFD code for dust explosions from a code developed for gas explosions.

4.2.1 Propane-Air Explosions

Explosion pressure and rate of pressure rise of combustible propane-air mixtures has been measured in the modified USBM vessel fitted with the rebound nozzle; the results for various ignition delay times are presented in Figure 4-11, Figure 4-12 and Figure 4-13.

Quiescent conditions

For initially quiescent mixtures of propane in air, the lower flammability limit (LFL) is found to be between 2.0 and 2.1 %; the upper flammability limit (UFL) was between 10.5 and 11.0% (based on detectable pressure rise). The results are in good agreement with those found by others, e.g. Cashdollar *et al.* (2000).

The observed explosion pressure under quiescent conditions are compared with thermodynamic equilibrium calculations performed with the Chemkin® Collection and STANJAN in Figure 4-11. A comparison between experimentally measured pressures and calculated adiabatic pressures indicate to what extent the reaction has gone to completion, and to what degree the explosion can be said to be adiabatic. For concentrations over 8 per cent, the measured explosion pressure was below one barg, with rate of pressure rise below five bar/s. For concentrations above 9.5 per cent, no visible flame could be observed. The considerable deviations between measured and calculated explosion pressures for rich fuel-air mixtures are probably due to a combination of several factors, e.g.:

- i) Only upward flame propagation is possible for mixtures with more than about 7.5 per cent propane (Cashdollar *et al.*, 2000), hence only a small fraction of the

flammable mixture is consumed. This phenomenon are probably caused by the greater diffusivity of oxygen compared to that of propane (Hertzberg, 1989).

- ii) The considerable formation of soot, i.e. combustion-generated particulates, observed for fuel-rich mixtures is likely to contribute to the reduced pressure; the particulates, an approximate empirical formula of C_8H is suggested by Glassman (1996), must be formed on the expense of gaseous species.

The concentrations that produce the maximum explosion pressure and the maximum rate of pressure rise are about 5.0 and 4.5 per cent by volume, respectively; i.e. slightly higher than stoichiometric (4.03 per cent, see Appendix E). Similar results have been found by others, e.g. Cashdollar *et al.* (2000).

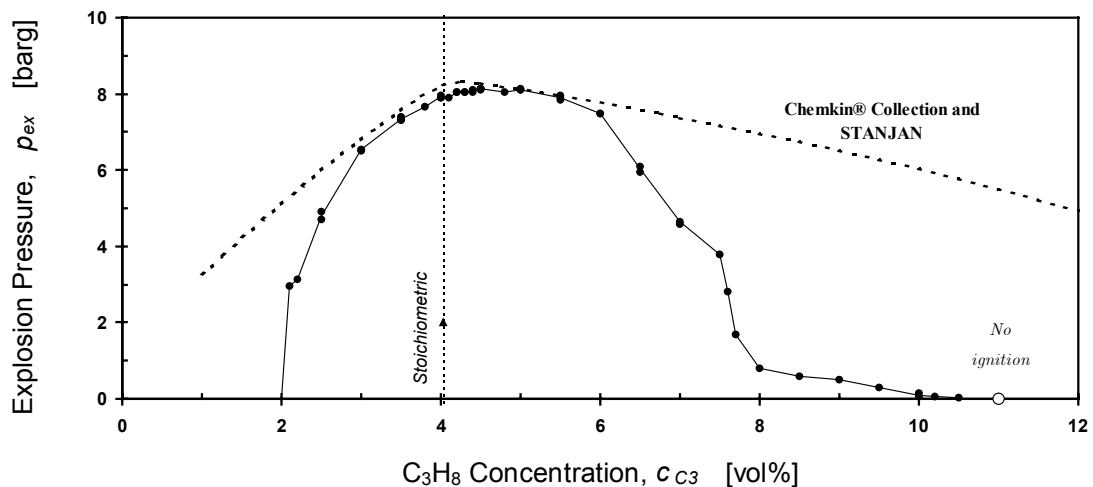


Figure 4-11. Measured and calculated explosion pressure, quiescent conditions. The dotted line represents chemical equilibrium calculations by the Chemkin® Collection and STANJAN; the equilibrium composition, pressure and temperature is found by minimizing Gibbs free energy for a mixture containing the reactants C_3H_8 , O_2 , and N_2 and specified products (CO_2 , H_2O , CO , H_2 , OH , H , O , NO and NO_2); assuming constant volume and constant enthalpy. Note that the equilibrium calculations do not relate to flammability limits.

Turbulent conditions

Measured explosion indices for turbulent conditions are shown in Figure 4-12, the results for quiescent conditions are included for comparison. The main uncertainty in these results is due to the possibility of incomplete mixing during the relatively short ignition delay times.

For concentrations from about three to six per cent propane in air, there is little difference between explosion pressures measured for turbulent conditions and in the quiescent case. The deviation is also moderate for lean mixtures (2-3% C_3H_8); it is probably caused primarily by increased heat loss due to the combustion. The pronounced difference in explosion pressure between quiescent and turbulent condition observed for fuel-rich mixtures (above 6-7%) illustrate the influence turbulence can have on combustion processes. The difference is dramatic even for the longest ignition delay time (900 ms), although the LDA measurements in section 4.1.1 indicate that the turbulence level at this time is very low.

The rate of pressure rise is dramatically increased for decreased ignition delay time over the entire flammable concentration range. Although turbulence increases the burning velocity, this is accompanied by a narrowing of the flammability limits, especially UFL. This effect is well known, and has been documented by e.g. Swett (1956a, 1956b), Ballal and Lefebvre (1974), and Akindele *et al.* (1982). Typical pressure-time histories for mixtures of 4.5 percent propane in air at various ignition delay times are shown in Figure 4-13. The turbulence level will decrease during the time that elapses from ignition to the time where the maximum rate of pressure rise occurs. Note that the rate of pressure decrease after the explosion pressure is reached seems to be independent of the turbulence level in the vessel.

Effect of explosion vessel and dispersion nozzle

Explosion pressure and rate of pressure rise as a function of ignition delay time for 4.5% propane-air mixtures, in both the modified USBM vessel and the Cubical vessel, are presented in Figure 4-14.

The explosion pressure is only moderately affected by increased ignition delay time, as would be expected; the slight reduction observed for longer ignition delay times is probably due to increased heat loss to the walls. Heat loss to the walls are probably also the main reason why the explosion pressure is significantly lower in the cubical vessel, compared to the modified USBM vessel; at least for ignition delay times higher than about 150 milliseconds. For shorter ignition delay times, $t_v < 150\text{ms}$, the spread in the measured explosion pressures are considerable. This can be due to incomplete mixing of fuel and air, but higher levels of turbulence are also likely to increase the stochastic element of uncertainty in the measurements. The low explosion pressure for the single measurement at 45 milliseconds can be caused by both incomplete mixing, and quenching due to intense turbulence; or most likely a combination of the two. The highest explosion pressures at short ignition delay times are found with the mushroom nozzle, indicating that this nozzle yields the fastest mixing of gaseous fuel and air.

The rate of pressure rise measured in the cubical vessel is significantly lower than the rate of pressure rise measured in the modified USBM vessel. The main reason for this is probably a lower level of turbulence in the cubical vessel compared to the modified USBM vessel, for the same ignition delay time. In section 4.1.1, measurements of the root-mean-square of the fluctuating velocity in the cubical vessel was shown to be significantly lower than the measurements presented by Dahoe (2000) and Dahoe *et al.* (2001a) for a spherical vessel (Figure 4-2). Although there are some doubts regarding the quality of these estimates, it seems reasonable to assume that turbulence will decay more rapidly in a cubical vessel compared to a spherical one. Due to similar vessel shape, the turbulence level in the modified USBM vessel is probably closer to the turbulence level in the spherical vessel described by Dahoe *et al.*, for identical dispersion systems. However, it is also possible that lower rates of pressure rise measured in the cubical vessel is a result of other factors, such as:

- i)* The cubical shape of the vessel can cause the flame to interact with the walls of the vessel before the maximum rate of pressure rise is reached. The initially spherical flame will probably become increasingly cubical in shape as it approaches the vessel walls; at the same time, the local flame speed is likely to decrease due to increased heat loss to the wall.

- ii)* Secondary flow in the corners of the cubical vessel, and a different overall flow pattern, can influence the flame propagation.

The type of dispersion nozzle seems to have an effect on the rate of pressure rise, but mainly for very short ignition delay times. This effect can be due to variations in the turbulence generated with the various nozzles, or it can be a result of limited degree of mixing; most likely, it is a combination of both. The pepper nozzle yields especially low values for short ignition delay times, presumably because of its ‘multi-jet’ design; it seems reasonable that the 31 small jets will produce a flow field with different turbulent length scales than the other nozzles.

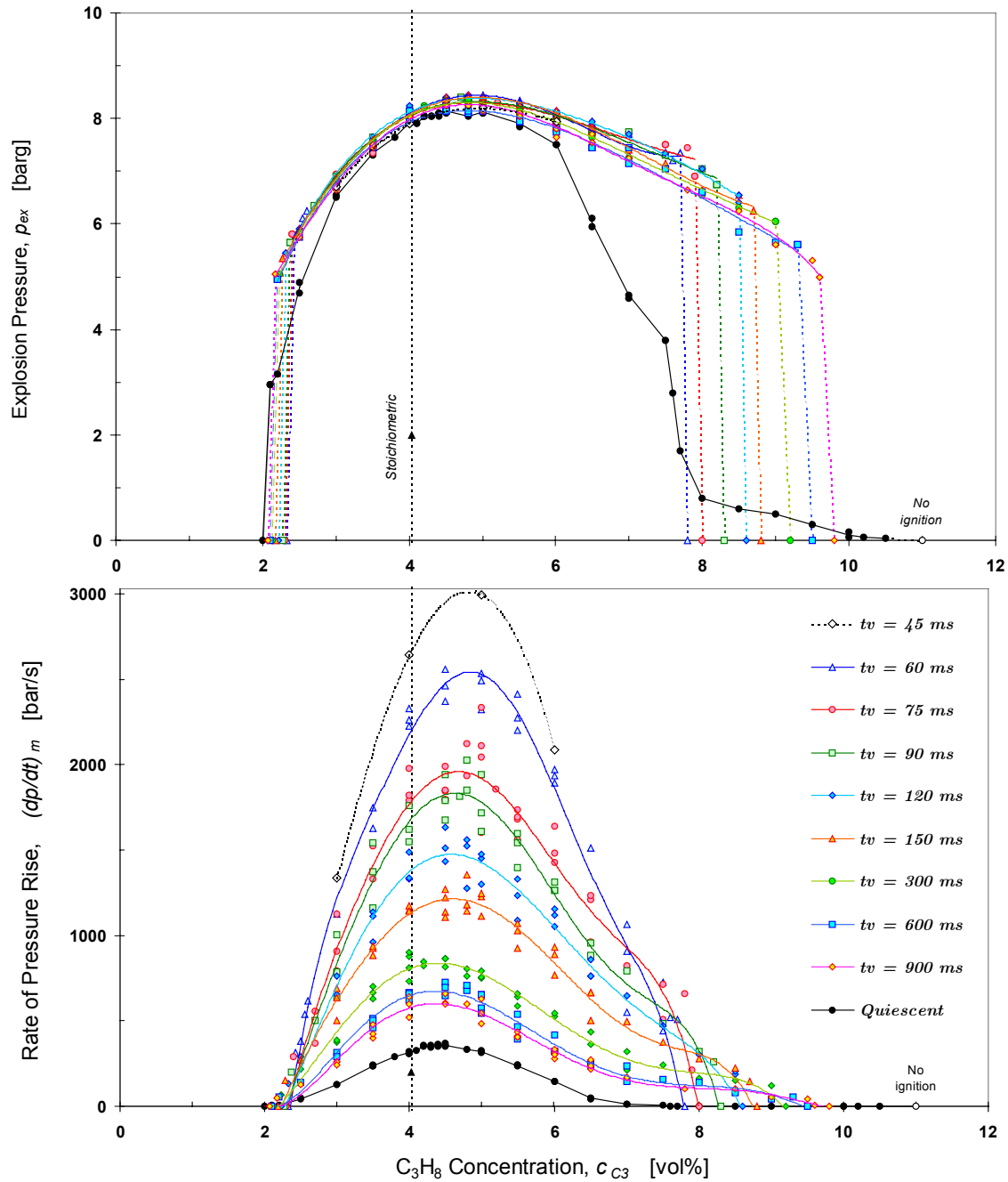


Figure 4-12. Flammability data for propane-air mixtures, tested in the 20-litre modified USBM vessel for a broad range of ignition delay times. Stoichiometric mixture, 4.03 per cent by volume C_3H_8 in air, is indicated by the vertical dotted line. For some of the tests with 45 ms ignition delay time the explosion backfired through the inlet valve and into the reservoir. After each such incident the inlet valve had to be repaired – hence there is only four tests with $t_v = 45$ ms. Ignition source: electric arc, $E_a = 6$ J, $t_a = 3$ ms.

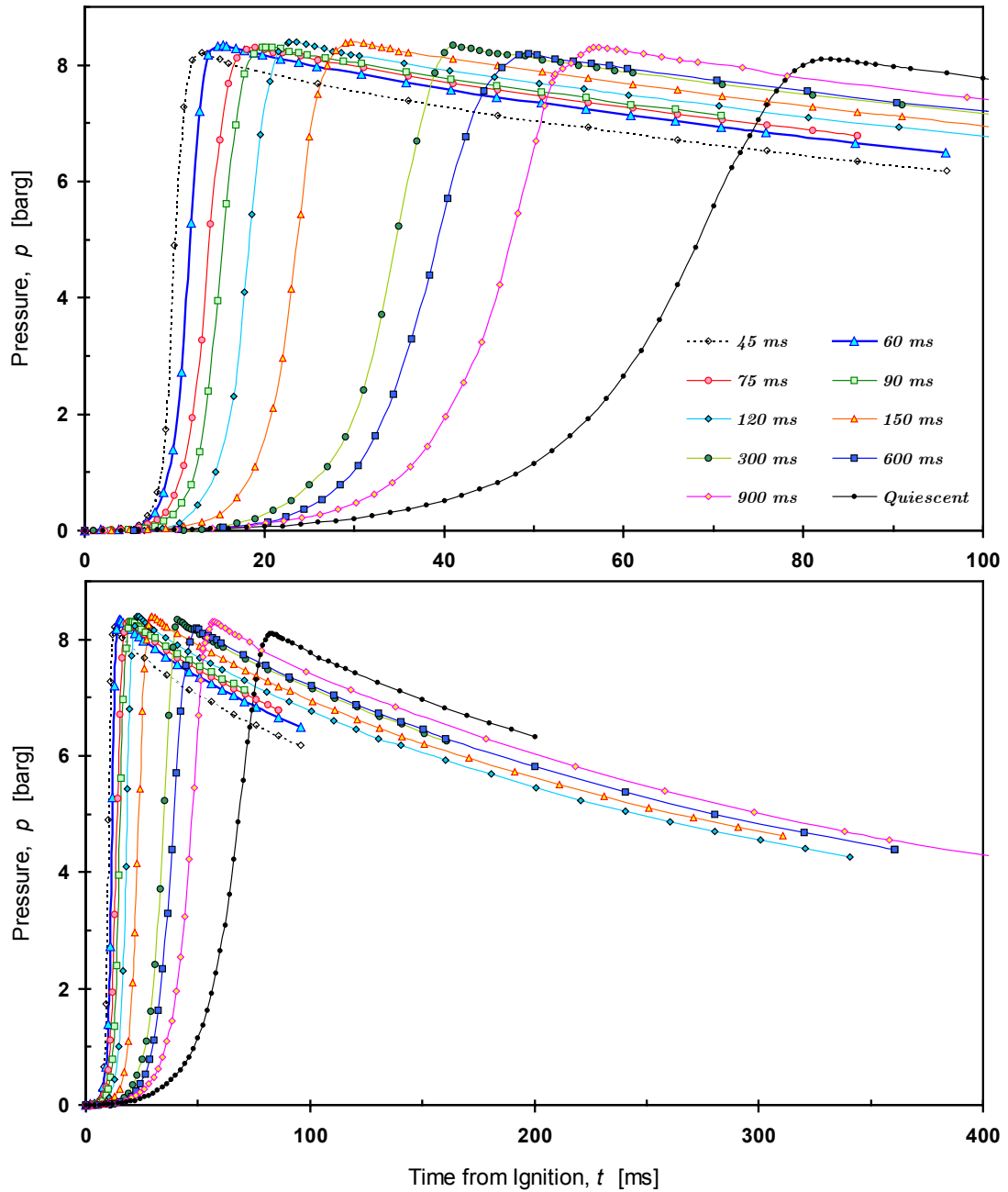


Figure 4-13. Typical pressure-time histories for various ignition delay times; measured in the modified USBM vessel fitted with the rebound nozzle, C_3H_8 concentration is 4.5 per cent by volume in all tests. The presented curves is the same in both figures, the lower figure is included to illustrate the limited effect turbulence seems to have on the rate of pressure decrease after the explosion pressure is reached.

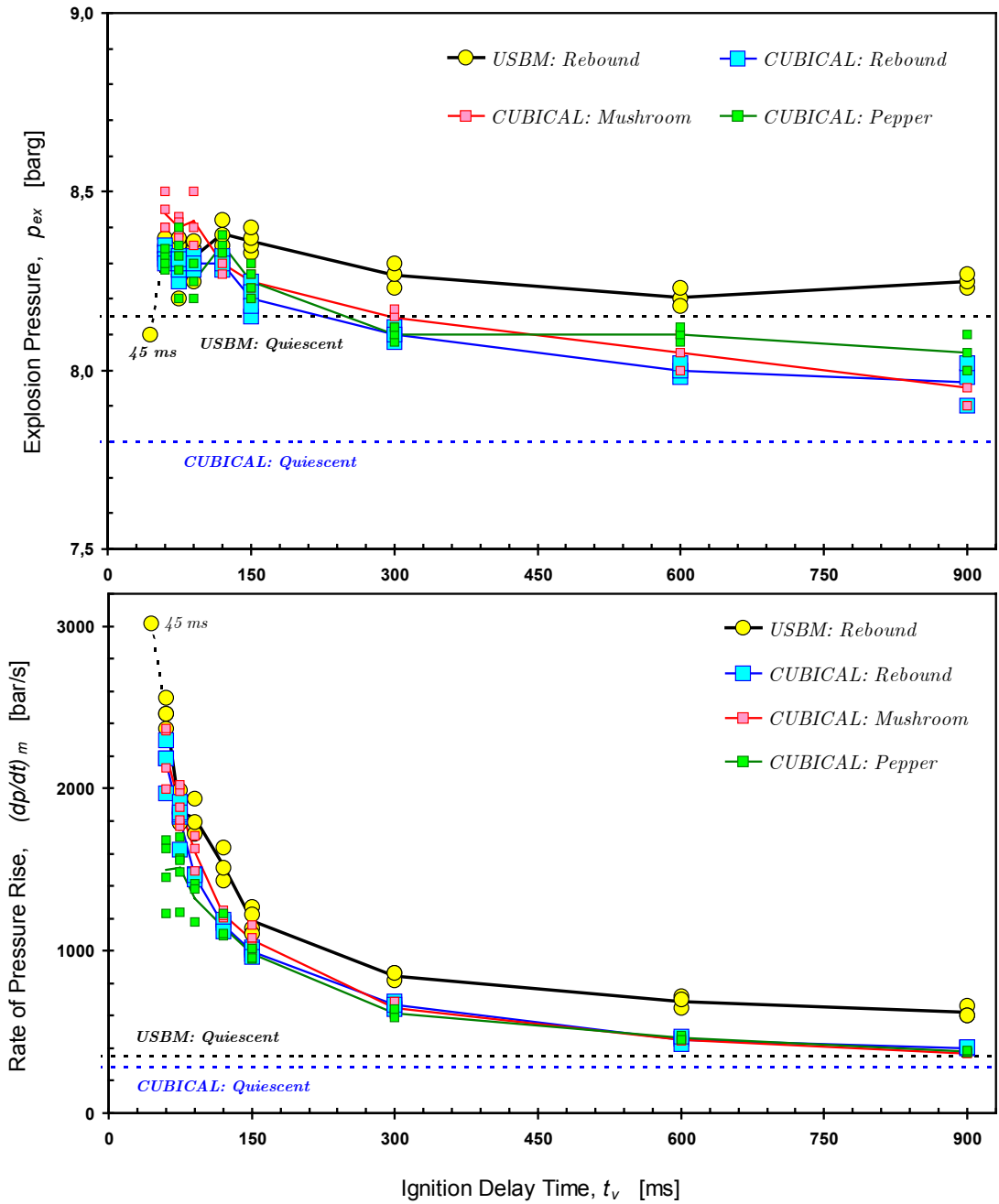


Figure 4-14. The effect of ignition delay time on explosion pressure and rate of pressure rise, both in the modified USBM-vessel and in the Cubical vessel, for a C_3H_8 concentration of 4.5 per cent by volume. The results from the Cubical vessel also include tests with various dispersion nozzles. Results obtained under initially quiescent conditions are indicated by dotted lines. Note the scale on the vertical axis in the upper figure.

4.2.2 Propane-Air Explosions with Inert Dust

The dust concentration that yields the highest values of both explosion pressure and rate of pressure rise are considerably greater than stoichiometric for most combustible dusts; hence, there will usually be a considerable amount of dust present that does not participate in the chemical reactions. However, the excessive dust will consume heat. Apart from the increase in the particles temperature, physical changes like devolatilisation and phase transitions (e.g. melting, vaporization) are also likely to take place for several types of dust. A CFD code for dust explosions should be able to model these effects (heat sinks).

A simple way of illustrating the effect that excessive dust can have on an explosion is to add inert dust to flammable gas-air mixtures. Explosion indices for propane-air mixtures with varying amounts of dispersed inert dust are shown in Figure 4-15.

As the dust represents a heat sink, the explosion pressure decreases almost linearly with increased dust loading. The decrease is smaller for the longest ignition delay time, presumably because a considerable amount of dust has settled out of suspension. The finer talc particles yields slightly lower explosion pressure than the coarser aluminium oxide particles.

The decrease in the rate of pressure rise is also approximately linear, but slightly more rapid for low dust concentrations at an ignition delay time of 60 milliseconds. The relative decrease is much bigger for an ignition delay time of 60 milliseconds than for 300 milliseconds. The main reason for this effect is probably that most of the dust has settled out of suspension after 300 milliseconds.

Goral *et al.* (1988) showed that the flame propagation velocity in a flammable gas-air mixture increased considerably in the presence of neutral particles. No such effect can be observed in Figure 4-15. However, Goral *et al.* did their experiments in a vertical pipe filled with a lean methane-air mixture; sand was added from the top by a dust feeder. The increased flame acceleration reached a maximum for concentrations in the order of 100 g/m^3 ; coarse sand (320-400 μm) resulted in higher flame propagation velocities than fine sand (20-60 μm). The observed effect was attributed to turbulence generated by the falling particles; a measurable increase in flame velocity was even observed when ignition took place some time after the last particles had passed through the pipe. The structure of the flame changed in the presence of particles; the thin methane-air flame with a smooth surface became thick and corrugated when particles were added. Thus, the experiment of Goral *et al.* illustrates that even very low levels of turbulence can have significant effect on the burning rate of flammable gas-air mixtures.

Adding inert particles to a flammable gas-air mixture may also influence the combustion wave travelling through the mixture by increasing the heat transfer due to radiation. Goral *et al.* (1988) found higher values of flame propagation for black sand particles compared to pale. According to Blouquin *et al.* (1997), the presence of inert particles can render non-flammable pre-mixtures flammable.

When a flammable mixture is ignited during the violent and transient dispersion process in the 20 litre explosion vessels, both the effect of the modest turbulence

generated by falling particles, and the effect of radiation, are likely to be negligible compared to the effects of dispersion induced turbulence and rapidly changing dust concentration. However, it is possible that increased flame thickness due to the added particles can be partly responsible for the reduction in the rate of pressure rise at low dust concentrations and high levels of turbulence; particle size does not seem to influence this effect significantly.

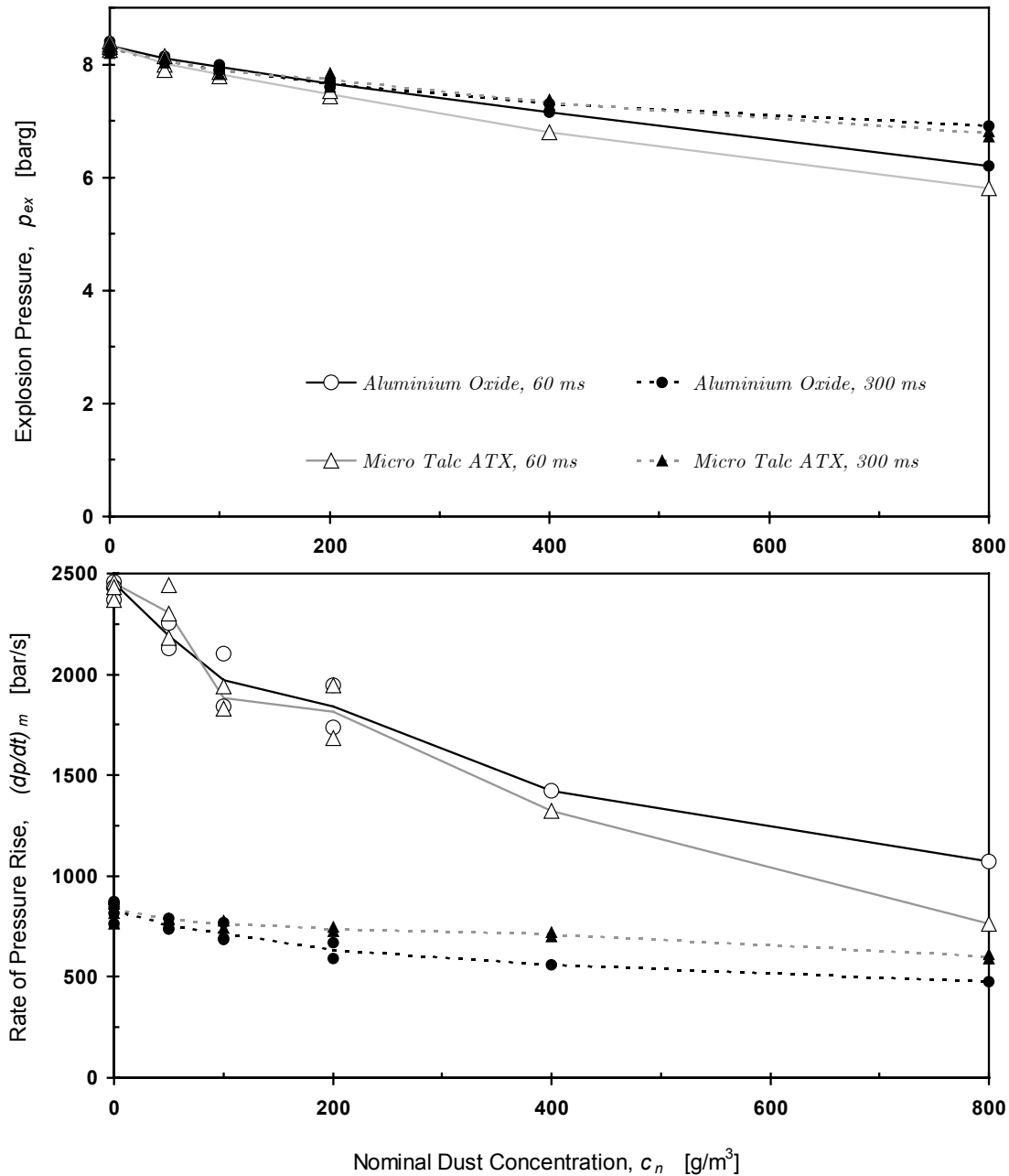


Figure 4-15. Explosion indices for propane-air mixtures with inert dusts, for two different ignition delay times: 60 and 300 milliseconds. 4.5 per cent propane by volume in all tests; ignition source: electric arc, $E_a = 6 \text{ J}$, $t_a = 3 \text{ ms}$.

4.2.3 Hybrid Explosions

Constant equivalence ratio

Figure 4-16 illustrates how the explosion indices for turbulent propane-*Lycopodium*-air mixtures are affected when the relative amounts of solid and gaseous fuel are changed for a constant equivalence ratio of unity.

The explosion pressure increases almost linearly from the value for pure dust to the value for pure gas. A slight deviation from the linear trend can be observed for very low propane concentrations, it may indicate an increased degree of incomplete combustion for lean mixtures where most of the fuel is dust.

The situation for rate of pressure rise is more complicated. As long as the propane concentration is significantly below LFL, the combustion rate is only slightly higher than for pure dust. The process seems to be limited by mechanisms related to the combustion of dust particles (e.g. pyrolysis). For propane concentrations within the flammable range for pure propane-air mixtures, the rate of pressure rise for the hybrid explosions is dominated by the flammable gas.

Constant optimum concentration ratio

Figure 4-17 illustrates how the explosion indices are affected when the relative amounts of solid and gaseous fuel are changed for constant optimum concentration. Note that the equivalence ratio varies from 4.17 for the pure dust-air mixture, to 1.25 for the pure propane-air mixture; i.e. the mixture is always fuel-rich.

The general trends are similar to the ones observed for constant equilibrium ratio, with a few exceptions. There is negligible deviation from linear increase of the explosion pressure, indicating that all the oxygen is consumed. A slight decrease in the rate of pressure rise is indicated for hybrid explosions with low dust concentration (50 g/m^3), compared to pure 4.5% propane in air explosions. It is possible that this effect can be related to the slightly more rapid decrease in the rate of pressure rise observed for propane-air mixtures with moderate amounts of inert dust added (Figure 4-15). This effect can be due an increase in flame thickness; however, it is also possible that the particles can influence the level of turbulence, either through some of the mechanisms discussed in 2.1.6, or by their very presence during the dispersion process.

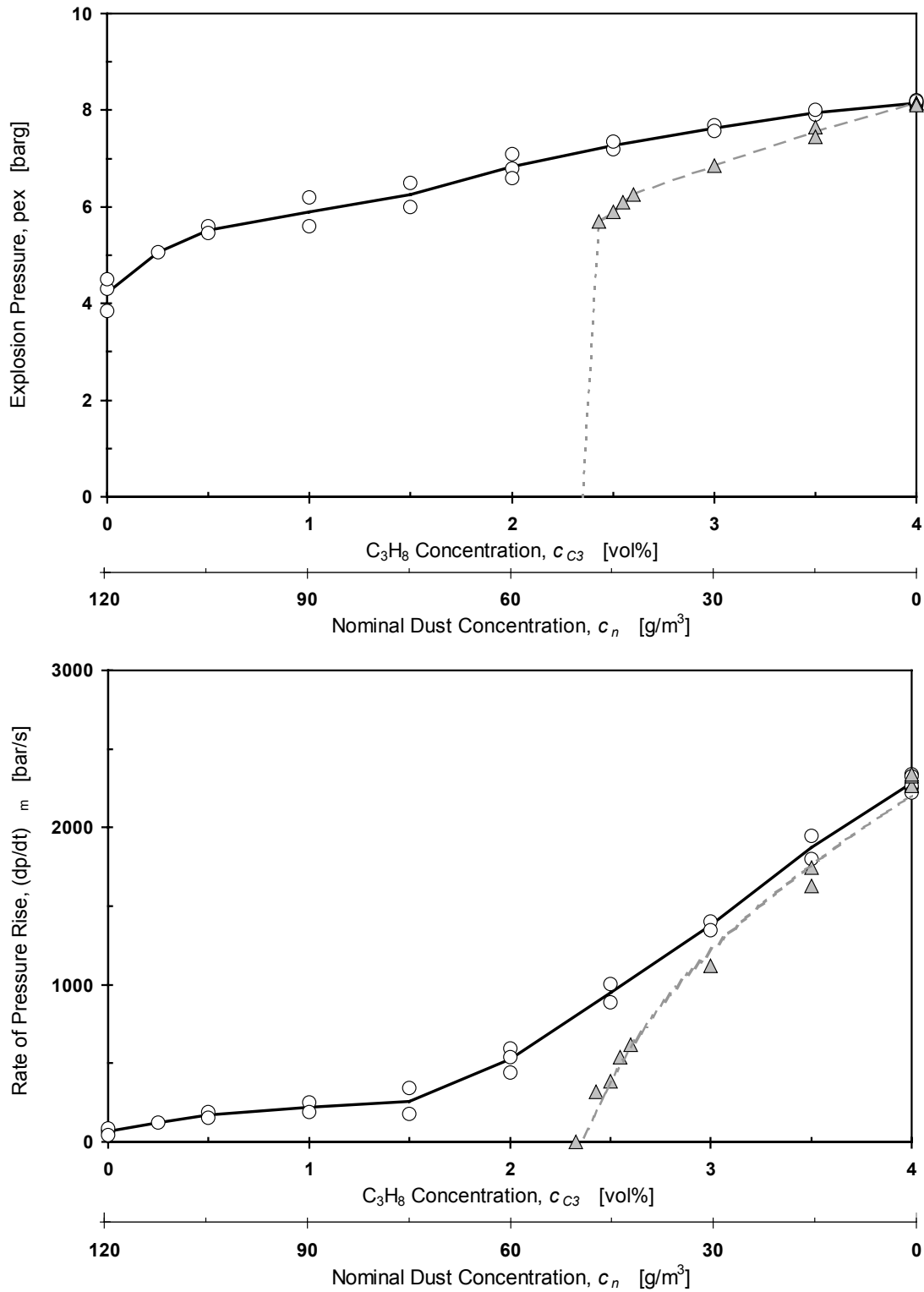


Figure 4-16. Explosion indices for hybrid explosions with constant equivalence ratio; performed in the modified USBM vessel fitted with the rebound nozzle, ignition delay time 60 milliseconds. Ignition source: electric discharges: $E_a = 6$ J, $t_a = 3$ ms. The dotted curve indicates the explosion indices for the pure propane-air explosions at the concentration indicated by the upper horizontal axis (i.e. a part of the 60 ms series in Figure 4-12).

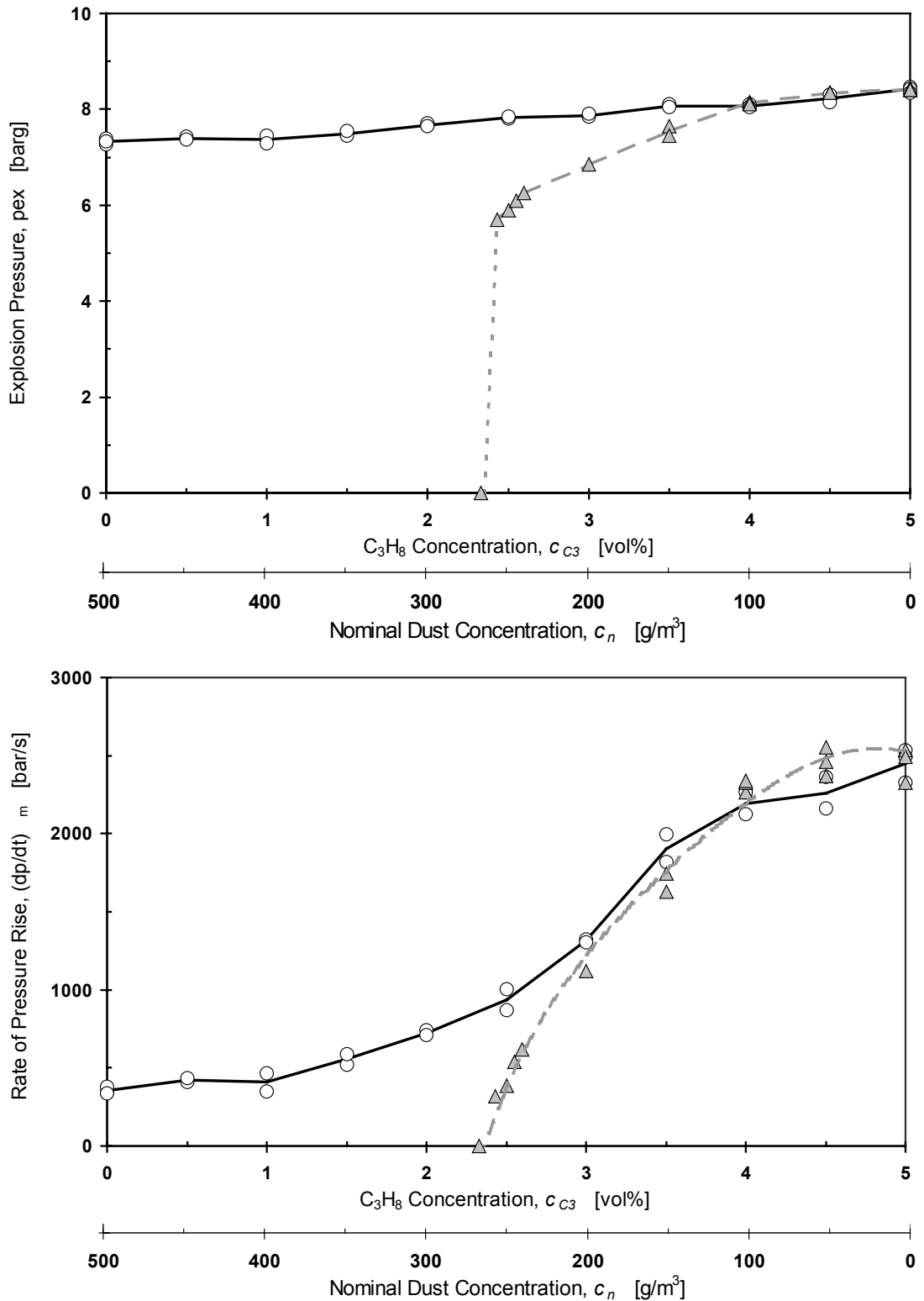


Figure 4-17. Explosion indices for hybrid explosions with constant optimum concentration ratio; performed in the modified USBM vessel fitted with the rebound nozzle, ignition delay time 60 milliseconds. Ignition source: electric discharges: $E_a = 6$ J, $t_a = 3$ ms. The dotted curve indicates the explosion indices for the pure propane-air explosions at the concentration indicated by the upper horizontal axis (i.e. a part of the 60 ms series in Figure 4-12).

4.3 Dust Explosions

Explosion indices, i.e. explosion pressure and rate of pressure rise, have been determined for the following dusts: niacin amide, spores of *Lycopodium casuarinoides*, and silicon. Combustion reactions, particle size distributions, and SEM pictures of characteristic particles, are presented in Appendix C.

4.3.1 Niacin Amide

Niacin amide, or *pyridine 3-carboxamide*, was the dust chosen by Kühner for the Calibration Round-Robin Test CaRo 00/01 (Cesana, 2001). Both of the two 20-l explosion vessels participated in this test. Because chemical igniters were used in the official tests, these results are presented in Appendix A, only tests ignited by electrical discharges are reported in the main part of this work. Unfortunately, the number of tests was limited by the amount of dust available.

Nominal dust concentration

The influence of nominal dust concentration on explosion indices for niacin amide is shown in Figure 4-18. The maximum values for both the explosion pressure and the rate of pressure rise is found for a nominal dust concentration close to 500 g/m^3 , in both vessels. The decrease in the observed explosion indices for higher concentrations is similar to the decrease observed for propane-air explosions with inert dust (Figure 4-15 in section 4.2.2); thus, it is probably caused primarily by heat loss to excessive dust. In both ends of the concentrations range, the explosion indices found in the cubical vessel is higher than those found in the modified USBM vessel. These observations do not support the assumption that the level of turbulence should be higher in the modified USBM vessel, compared to the cubical vessel. For the highest concentrations, this effect could be caused by a more rapid settling of dust; i.e. there is less dust in suspension that can act like a heat sink.

Results from a limited series of tests at an ignition delay time of 300 milliseconds are also indicated in Figure 4-18; the tests were only done in the cubical vessel. The explosion pressure from the tests with late ignition approaches the explosion pressure from the tests with early ignition for higher concentrations, presumably because there is enough dust left in suspension to consume all the oxygen. There is a clear effect of turbulence on the burning rate; the rate of pressure rise is significantly lower over the whole concentration range. However, the main problem is to isolate the effect of turbulence from the effect of concentration – especially since both the actual dust concentration, and the actual turbulence level in the cloud, are unknown.

Ignition delay time and nozzle type

Explosion pressure and rate of pressure rise as a function of ignition delay time are shown in Figure 4-19; all tests are done in the cubical vessel fitted with various nozzles, nominal dust concentration 500 g/m^3 . By choosing a nominal concentration close to the

value that produces the maximum explosion pressure and rate of pressure rise, it was hoped that the effect of dust concentration could be minimized. However, the rapid decrease in explosion pressure indicates that any significant increase in the ignition delay time is accompanied by a reduction in the actual dust concentration.

The decrease in explosion pressure is close to linear for increasing ignition delay times for all the three nozzles. The results for the pepper nozzle deviate from the results with the other two nozzles; the initial explosion pressure is lower, but the rate of decrease is also lower.

The exponential decrease in the rate of pressure rise for increased ignition delay times resembles the results for propane-air mixtures in Figure 4-14. For short ignition delay times, there is a significant difference between the results from the three nozzles; the pepper nozzle yields the lowest values, the rebound nozzle the highest.

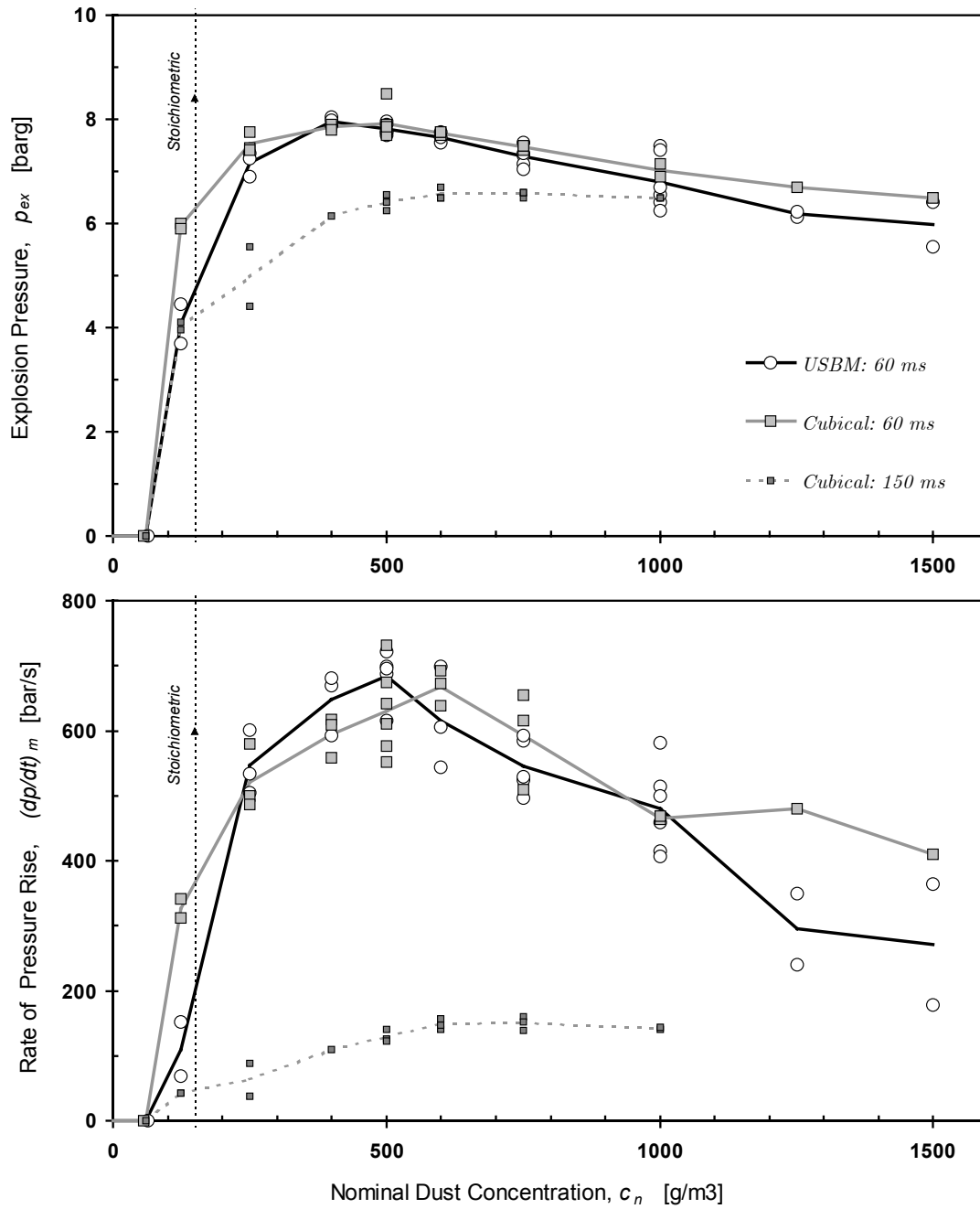


Figure 4-18. Explosion indices for niacin amide. In addition to the tests with the default ignition delay time of 60 milliseconds, in both the USBM and Cubical vessels, there are also some results from the Cubical vessel for an ignition time delay of 150 milliseconds. Dotted vertical line represents stoichiometric concentration (150 g/m³).

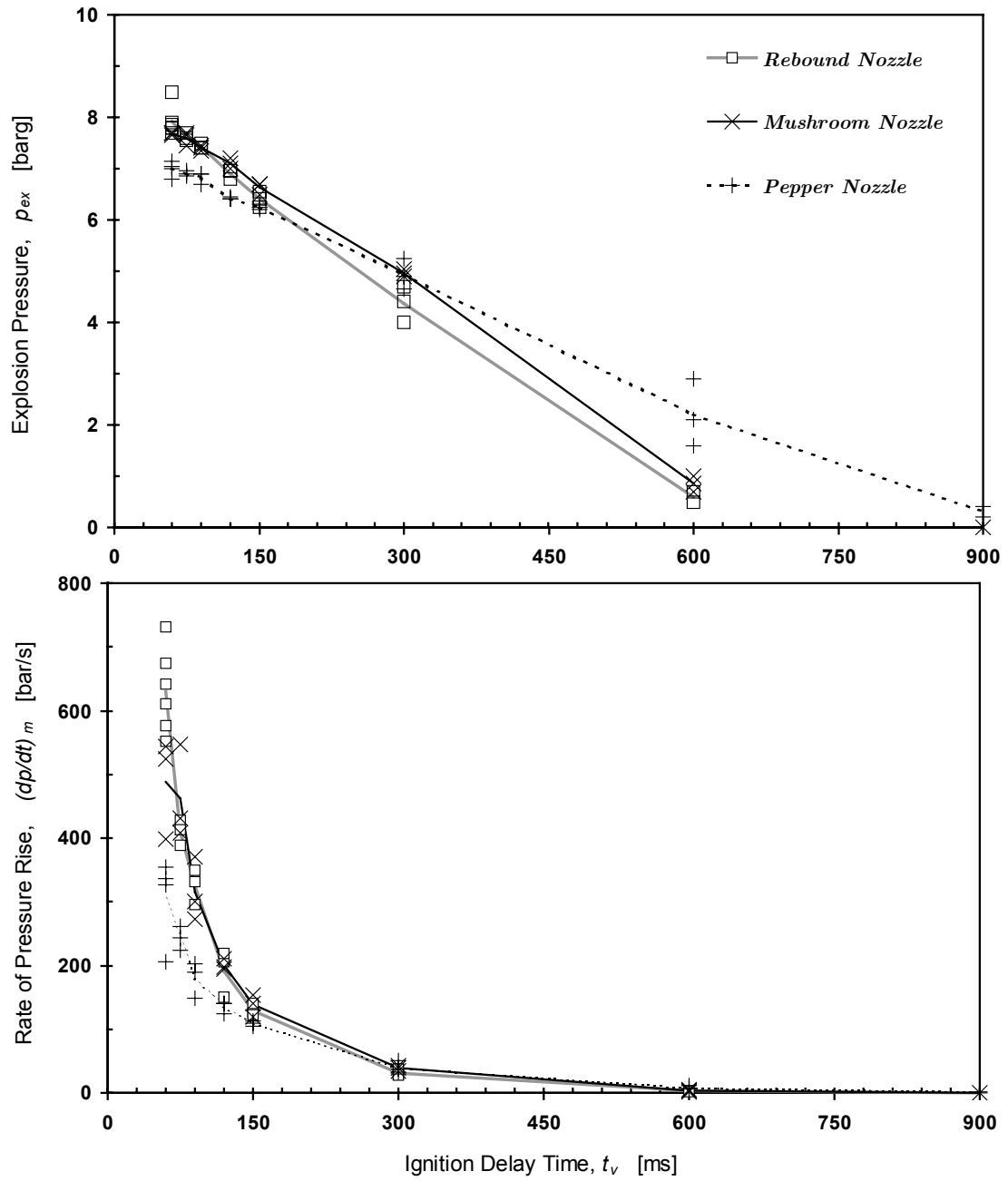


Figure 4-19. The effect of ignition delay time on explosion pressure and rate of pressure rise for niacin amide. Tests done in cubical vessel fitted with various nozzles. Ignition source: electrical arc discharges, $E_a = 6 \text{ J}$, $t_a = 3 \text{ ms}$.

4.3.2 Spores of *Lycopodium*

Spores of *Lycopodium clavatum* have been used for dust explosion research for a long time; however, the spores we received from our supplier were certainly not from the species *clavatum*. The origin of the spores used in this work has been traced to China; they are probably from the species *Lycopodium casuarinoides* (see Appendix B).

Nominal dust concentration

The influence of nominal dust concentration on explosion indices for *Lycopodium* spores is shown in Figure 4-20. The maximum values for both the explosion pressure and the rate of pressure rise is found for a nominal dust concentration close to 500 g/m³. The decrease in the observed explosion indices for higher concentrations is similar to the decrease observed for both propane-air explosions with inert dust (Figure 4-15 in section 4.2.2) and niacin amide explosions (Figure 4-18 in section 4.3.1).

Ignition delay time

Explosion pressure and rate of pressure rise as a function of ignition delay time is shown in Figure 4-21; all tests are done in the modified USBM vessel fitted with the rebound nozzle, nominal dust concentration 500 g/m³. The results resemble those for niacin amide in Figure 4-19, but the additional data for the 45-millisecond ignition delay time alters the appearance somewhat.

Typical pressure-time histories for various ignition delay times for spores of *Lycopodium casuarinoides* are compared to pressure-time histories for propane-air (from Figure 4-13) in Figure 4-22; the main differences are:

- i)* The rate of pressure rise is much higher for the propane-air explosions.
- ii)* For increasing ignition delay time, the explosion pressure decreases much faster for the dust explosions, compared to the propane-air explosions.
- iii)* While the rate of pressure fall that takes place after the explosion pressure has been reached seems to be more or less the same for all the propane-air explosions, there is a significant difference for the dust explosions. The pressure after an explosion with spores of *Lycopodium* in air decreases faster for the shorter ignition delay times. This effect is probably the result of a combination of several factors, e.g.:
 - a. As the ignition delay time is increased, the explosion pressure decreases; hence, the temperature difference between the vessel walls and the gaseous combustion products is reduced, and the rate of heat transfer will decrease. However, if we compare the rate of pressure fall for the ignition delay times 45 and 60 milliseconds, it is clear that the pressure decreases faster for the former even though the explosion pressure is higher for the latter.
 - b. The turbulence level in the vessel will be higher after the explosion with the shortest ignition delay time; this should promote heat transfer. However, no such effect can be identified for the propane-air explosions.
 - c. An isolating layer of settled dust can form on the vessel walls, and heat generation by smouldering combustion in dust layers can produce enough heat to dampen the pressure fall.

- d. Phase transitions may influence the rate of pressure fall for both gas and dust explosions. Water is always found on the vessel walls after a propane-air explosion, and both condensation of water and formation of soot are likely to take place after an explosion with *Lycopodium* spores in air.

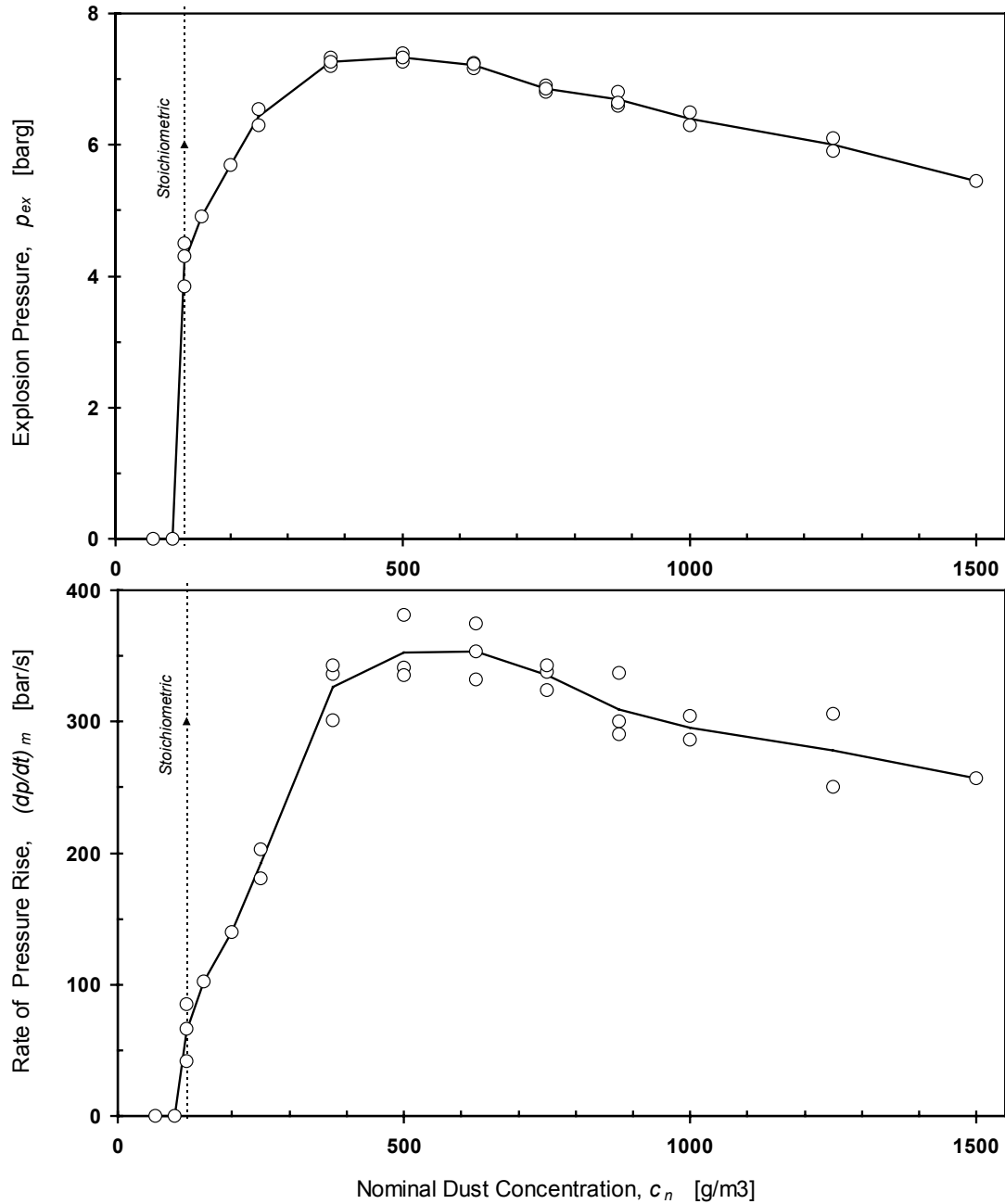


Figure 4-20. Explosion indices as a function of nominal dust concentration for spores of *Lycopodium casuarinoides*; tests in the modified USBM vessel fitted with the rebound nozzle. The dotted vertical line represents stoichiometric concentration (120 g/m³). Ignition source: electrical arc discharges, $E_a = 6$ J, $t_a = 3$ ms.

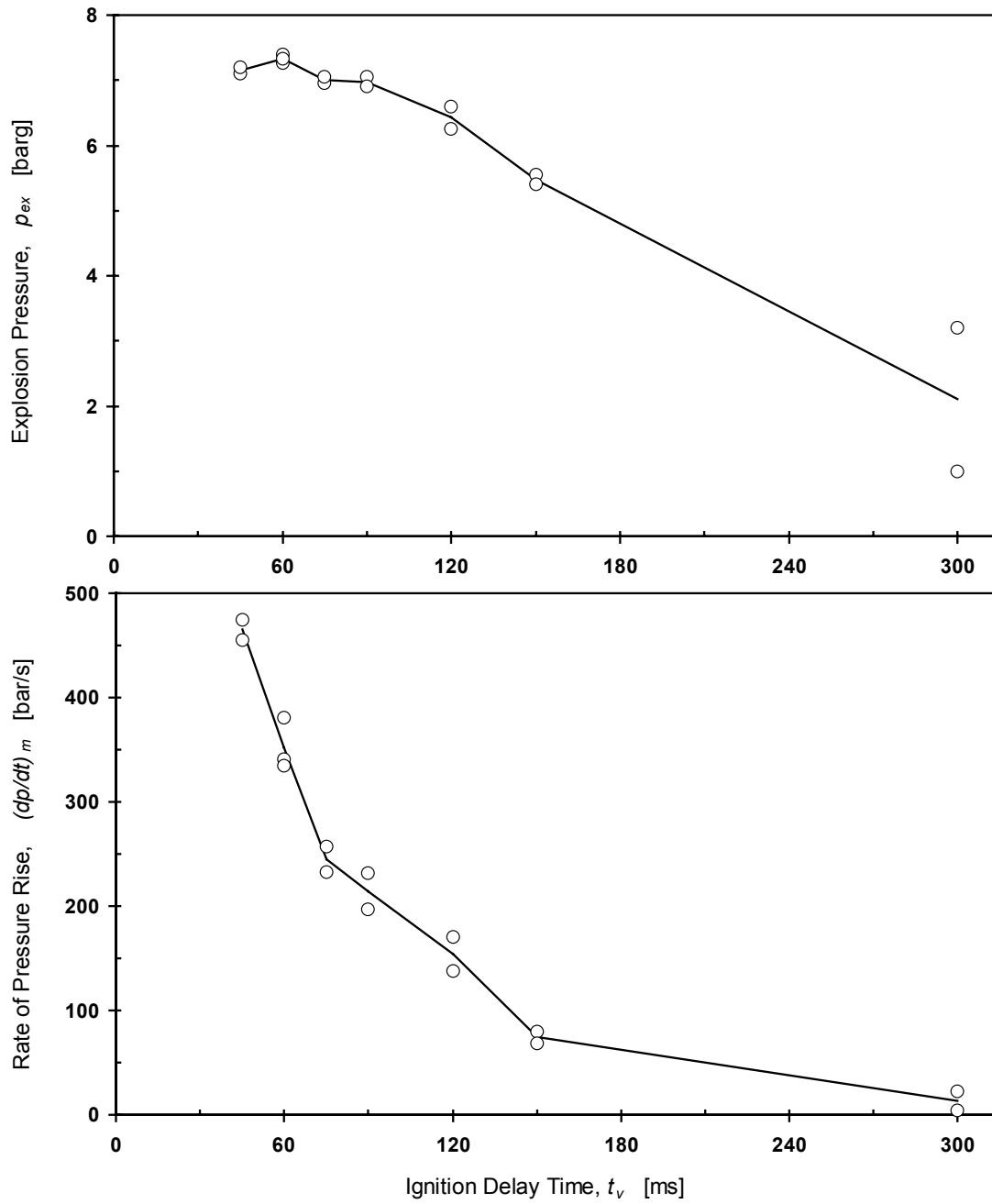


Figure 4-21. The effect of ignition delay time on explosion pressure and rate of pressure rise for spores of *Lycopodium casuarinoides*; determined in the modified USBM vessel fitted with the rebound nozzle. Ignition source: electric arc discharges, $E_a = 6 J$, $t_a = 3 ms$.

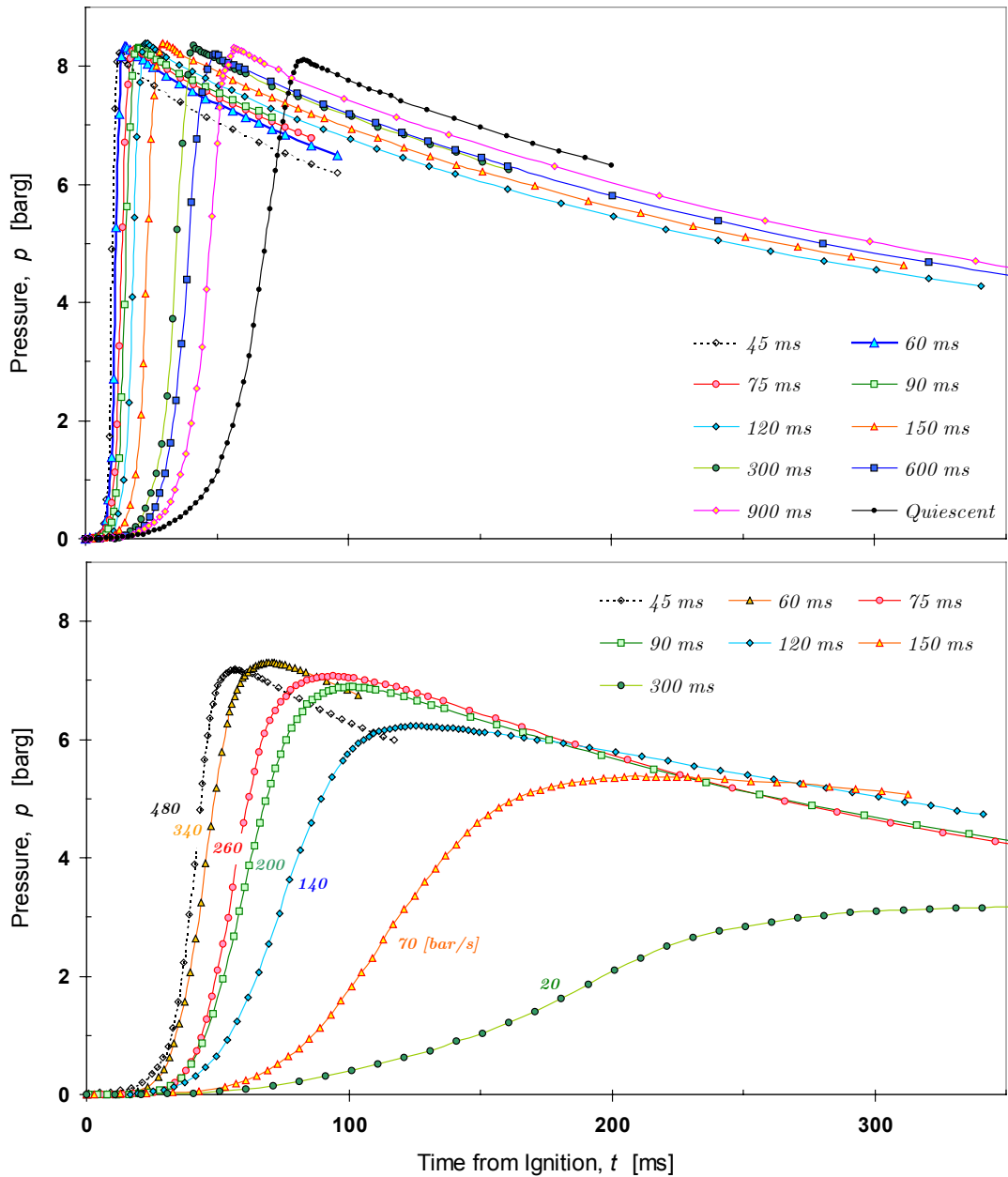


Figure 4-22. Typical pressure-time histories for various ignition delay times; results for 4.5 per cent propane in air (above), and for 500 g/m^3 spores of *Lycopodium casuarinoides* in air (below); measured in the modified USBM vessel fitted with the rebound nozzle. Ignition source: electrical arc discharges, $E_a = 6 \text{ J}$, $t_a = 3 \text{ ms}$.

4.3.3 Silicon

The effect of nominal dust concentration, ignition delay time and particle size have been investigated for nine different lots of jet-milled silicon metal, or Silgrain, from Elkem Bremanger. All the tests were done in the cubical vessel fitted with the rebound nozzle. SEM pictures, particle size analysis, combustion reactions, and some observations regarding the colour of the silicon oxides produced in the reactions, are presented in Appendix C. Similar work have been reported by both Eckhoff *et al.* (1986) and van der Wel *et al.* (1991) for various samples of silicon dust. However, Eckhoff *et al.* used a 1.2-litre Hartmann bomb and electrical discharges with net energy 3.5 Joules and duration 2-3 milliseconds, whereas van der Wel *et al.* used a 20-litre Siwek sphere fitted with the dispersion ring (see Appendix B) and 10 kJ chemical igniters.

Nominal dust concentration and particle size

The influence of nominal dust concentration on explosion indices for three of the lots of Silgrain is shown in Figure 4-23. Maximum values for the explosion pressure for all three lots are found for a nominal dust concentration close to 500 g/m³; the rate of pressure rise increases slightly from 500 to about 750 g/m³. These values are slightly lower than those reported by van der Wel *et al.* (1991).

The particle size data presented in Appendix C reveals that the two finer lots (J133 and J135) have similar particle size distributions, whereas the distribution for the coarser lot (J136) has a significantly different shape. Although almost all measures of particle size ($d_{4,3}$, $d_{3,2}$, ... etc.) indicate that J133 consists of finer particles than J135, both the maximum explosion pressure and the maximum rate of pressure rise is higher for J135 than for J133. It should be noted that the measured difference between the particle size distributions is small, especially when the particles are dispersed in a water solution. Nevertheless, the present results seem to contradict the general assumption that smaller particles always give higher rate of pressure rise. The results from van der Wel *et al.* gave higher K_{St} values for the finer dust samples over the whole concentration range, whereas the results from Eckhoff *et al.* were less clear. The influence of median particle diameter on explosion indices for all the nine lots of Silgrain is shown in Figure 4-24. Both of the finer lots (J133 and J134) yields lower rate of pressure rise than J135, but for all of the coarser lots there is a clear reduction in rate of pressure rise for increased particle size. An augmented inclination towards agglomeration in the finer lots may provide one possible explanation for the observed phenomenon. It should be noted that all of the nine lots have relatively broad particle size distributions; hence, there will always be a certain amount of fine particles present.

The decrease in the rate of pressure rise for higher concentrations is markedly different for the coarser lot (J136), compared to the two finer lots (J133 and J135). Whereas the rate of pressure rise for the fine fractions decreases with increased concentration in a similar manner as other dusts described in previous sections, there is little variation for the coarse fraction in the concentration range from 500 to 2000 g/m³. This effect is most likely related to the fact that the particle size distribution for J136 is significantly different from those of J133 and J135 – similar results were found for

the coarsest sample investigated by van der Wel *et al.* (1991). It is possible that the increased concentration of very fine particles (that can burn faster) outweighs the quenching effect of higher overall concentration (the heat sink effect).

Ignition delay time and particle size

Explosion pressure and rate of pressure rise as a function of ignition delay time for three lots of Silgrain is shown in Figure 4-25.

Initially the explosion pressure decreases steadily with increasing ignition delay time for all three lots. Beyond a certain ignition delay time, the explosion pressure becomes unsteady; both the rate of decrease, and the spread in data, seems to accelerate until ignition no longer is possible. Some observations of the colour of the residue left in the explosion vessel after the tests are summarized in Appendix C; it is suggested that the actual dust concentration may decrease rapidly, and that the unsteady regime indicates that the actual dust concentration is approaching the minimum explosible concentration (for the present ignition source). The fact that the onset of the unsteady regime occurs sooner for the finer lots, suggests that the actual dust concentration decreases faster for these dusts. After tests with the finer lots (J133, J134 and J135) that failed to ignite, the interior of the vessel were covered in a thick fur-like layer of dust; there were not significantly more dust on the bottom of the vessel compared with the walls and underneath the lid. This supports the hypothesis of an augmented inclination towards agglomeration in the finer lots compared with the coarser lots. However, SEM pictures of the residue, presented in Appendix C, indicate that a transition in the mode of combustion of single particles may take place when the level of turbulence is changed.

The rate of pressure rise decreases exponentially with increasing ignition delay time. Note the dramatic increase in rate of pressure rise when the ignition delay time is decreased from 60 to 45 milliseconds.

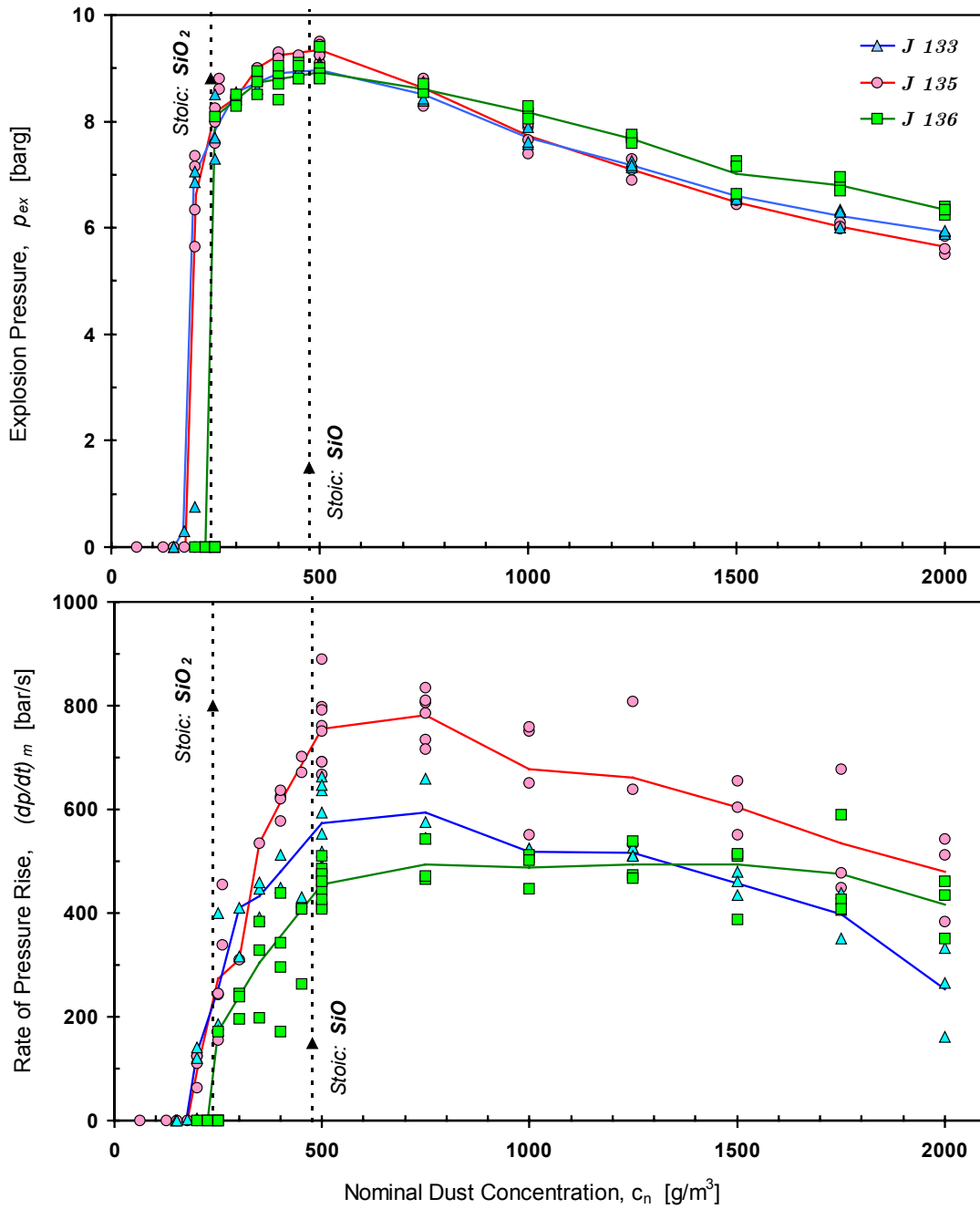


Figure 4-23. Explosion indices for three different lots of jet-milled Silgrain: J133, J135 and J136. The two dotted vertical lines represents stoichiometric concentrations with respect to two different oxides as product: SiO_2 or SiO . Ignition source: electrical arc discharges, $E_a = 6 \text{ J}$, $t_a = 3 \text{ ms}$.

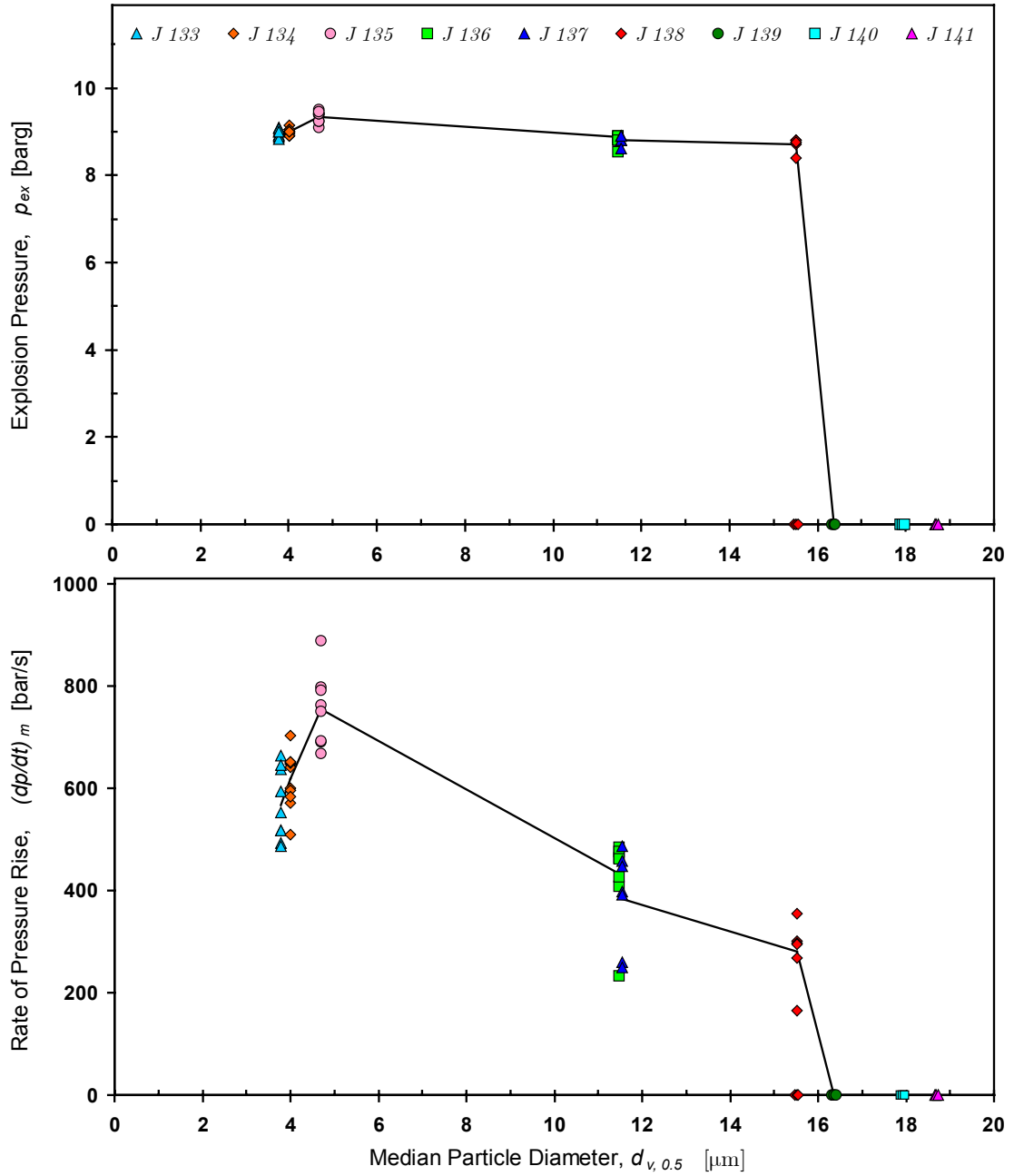


Figure 4-24. Explosion indices for various lots of jet-milled Silgrain as a function of median particle diameter; determined in the cubical explosion vessel fitted with the rebound nozzle. Ignition source: electrical arc discharges, $E_a = 6$ J, $t_a = 3$ ms.

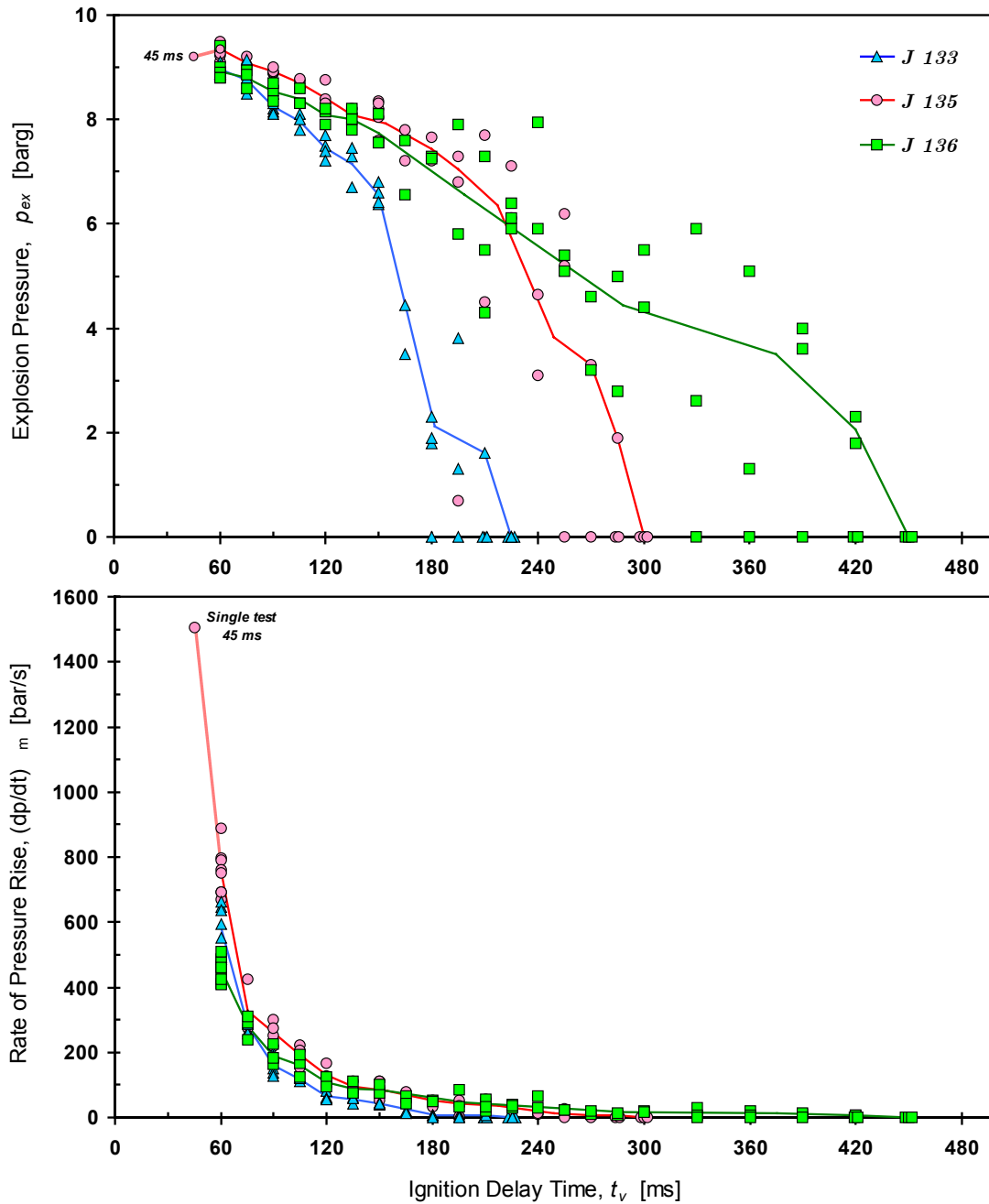


Figure 4-25. The effect of ignition delay time on explosion pressure and rate of pressure rise for three different lots of jet-milled Silgrain: J133, J135 and J136. The nominal dust concentration is 500 g/m^3 in all tests. Ignition source: electrical arc discharges, $E_a = 6 \text{ J}$, $t_a = 3 \text{ ms}$.

4.3.4 Explosible Dust: RDX

The majority of chemical explosives, including RDX, contain oxygen, nitrogen and some elements such as carbon and hydrogen that can be oxidized (fuels) – the oxygen is generally attached to nitrogen in groups such as NO, NO₂ or NO₃ (Akhavan, 1998).

The fact that the oxidizer is chemically bound to the fuel makes it possible for the particles in a cloud of explosive dust to decompose without the supply of oxygen from the air¹. Hertzberg *et al.* (1992) found that clouds of RDX and HMX could propagate a flame even when dispersed in pure nitrogen; however, it is possible that the 5 kJ igniters that were used to ignite the clouds to some extent did overdrive the system (Cashdollar and Chatrathi, 1992). Mitgau (1996) and Mitgau *et al.* (1997) have shown that the burning velocity in particle clouds consisting of an explosive material, *diamino-guanidine-azotetrazole-mono-hydrate* (AGATZ), dispersed in air, decreases when the root-mean-square value of the fluctuating velocity increases. This effect was attributed to a reduction in the rate of the chemical reactions due to increased cooling of the particles in more intense turbulence. The main reason for doing tests with RDX were to see if similar results to those of Mitgau could be produced in the 20-litre vessel.

The effect of increased ignition delay time on explosion indices for two lots of RDX have been investigated in the modified USBM vessel fitted with the RDX nozzle (described in Appendix B). The finer of the two lots had a median particle diameter of 16 µm, the coarser 72 µm; particle size distributions and SEM pictures are presented in Appendix C. Turbulent clouds of RDX particles in air turned out to be inherently difficult to ignite with the electrical discharges produced by the arc generator, especially at low concentrations. At a nominal dust concentration of 500 g/m³, only one out of ten tests resulted in successful ignition. Hence, all the results that are reported in this work are from tests with a nominal dust concentration of 1000 g/m³. It should be noted that the difficulties in igniting the RDX powder could be partly due to the poor performance of the RDX nozzle, see Appendix B.

Explosion pressure and rate of pressure rise as a function of ignition delay time for the two lots of RDX is shown in Figure 4-26. The observed decreases in explosion pressure for increased ignition delay time is much less than for the combustible dusts described in previous sections. The main reason for this is probably that the combustion process continued in the settled dust layers after the flame had passed through the cloud. After each test that misfired, there were thick dust deposits at the bottom of the vessel, and a thin layer of dust underneath the lid. After any successful ignition, both these layers were replaced by a thin layer of solidified RDX. It appears as if a liquid layer do exist at the surface of the burning substance (as has been suggested by Schroeder, 2001), and that the flame is quenched by heat loss to the vessel walls while there is still some melted RDX left. When removed from the vessel

¹ Decomposition reactions for RDX are given in Appendix C. The RDX molecule decomposes readily into CO, H₂O and N₂; complete combustion, to CO₂, H₂O and N₂, requires some additional oxygen from the air.

wall, and ignited, the material that constituted these layers burnt readily. SEM pictures of samples taken from these layers are shown in Figure 4-27.

The rate of pressure rise decreases rapidly with increased ignition delay time, but there is considerable spread in the data even for relatively short ignition delay times. There is no indication of the phenomenon described by Mitgau (1996) and Mitgau *et al.* (1997), i.e. an increase in the burning velocity for lower root-mean square velocity (or increased ignition delay time); there can be several possible reasons for this:

- i) Mitgau used the explosive material *diamino-guanidine-azotetrazole-monohydrate* – not RDX (*cyclotrimethylene-trinitramine*). There is no reason to suspect that substances with so very different molecular structure should have much in common.
- ii) Mitgau used grid-generated turbulence in a flow tunnel; hence, the initial flow was steady – not transient. The variation in pressure during the course of flame propagation will also be negligible in an open channel compared to a closed vessel.
- iii) The dust concentration used by Mitgau was 145 g/m³, i.e. far less than 1000 g/m³. The transient decay of the actual dust cloud concentration in the closed 20-litre vessel is also likely to complicate the matter.
- iv) Mitgau measured the actual propagation of a non-steady flame by a CCD-camera, whereas the rates of pressure rise reported in the present work in reality is a combined measure for energy release and increase in moles of gas. Pressure-time histories from typical RDX explosions are shown in Figure 4-28¹; the deviation from the classical S-shaped curves found for most explosible mixtures increases with increasing ignition delay time. It is evident that many of the pressure-time histories are heavily influenced by the release of heat and gaseous species from the combustion of settled dust layers; however, it is not always clear when the transition takes place.

There is no significant difference between the fine and the coarse lot in Figure 4-26. Hertzberg *et al.* (1992) showed that finer sizes ($d_{v,0.5} < 20 \mu\text{m}$) of explosible dust were substantially less explosible in air than intermediate sizes (40-80 μm); however, these tests were all performed at nominal dust concentrations below 600 g/m³ – and the ignition source were chemical igniters of energy 2.5 kJ.

¹ The only straightforward way to obtain pressure-time data from the KSEP-files in the current version of the Kühner software was to use the individual $p_{ex}(t)$ curves produced by the software; single data points could be found manually, but the process was extremely time consuming. The following applies to all the subfigures in Figure 4-28: ¹⁾Time is given in milliseconds and is relative to onset of test, not relative to onset of dispersion. ²⁾The reported pressure is the measured explosion pressure (p_{ex}), not the corrected explosion pressure (p_m). ³⁾Activation (or triggering) of ignition (t_{ign}) is indicated by a red vertical line; the time (t_m) when the explosion pressure (p_{ex}) is reached, the so-called *culmination point*, is indicated by a plus sign (+). ⁴⁾Note that it was not possible to achieve equal scaling of all axes. ⁵⁾A vector containing key explosion data is placed underneath each subfigure. The elements of the vector are: $\{t_v; p_{ex}; (dp/dt)_m\}$.

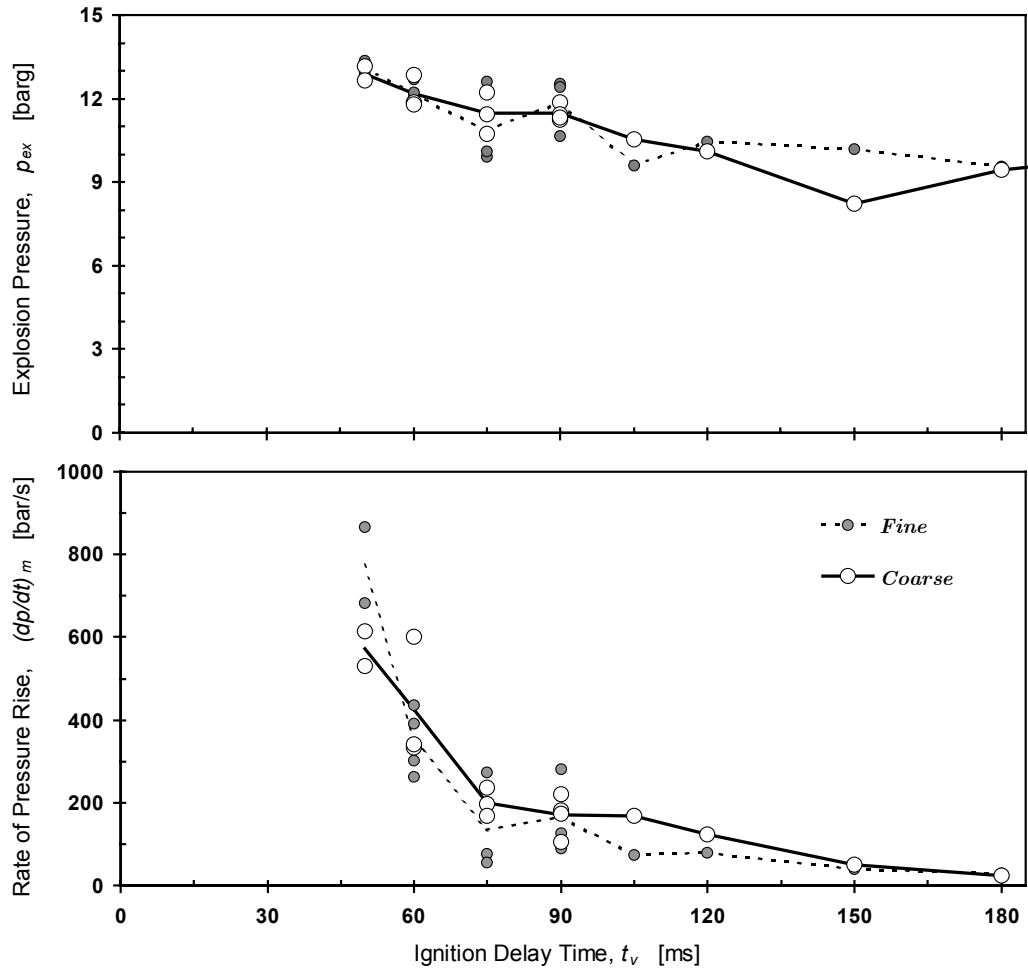


Figure 4-26. The effect of ignition delay time on explosion pressure and rate of pressure rise for two different lots of RDX; nominal dust concentration 1000 g/m^3 .

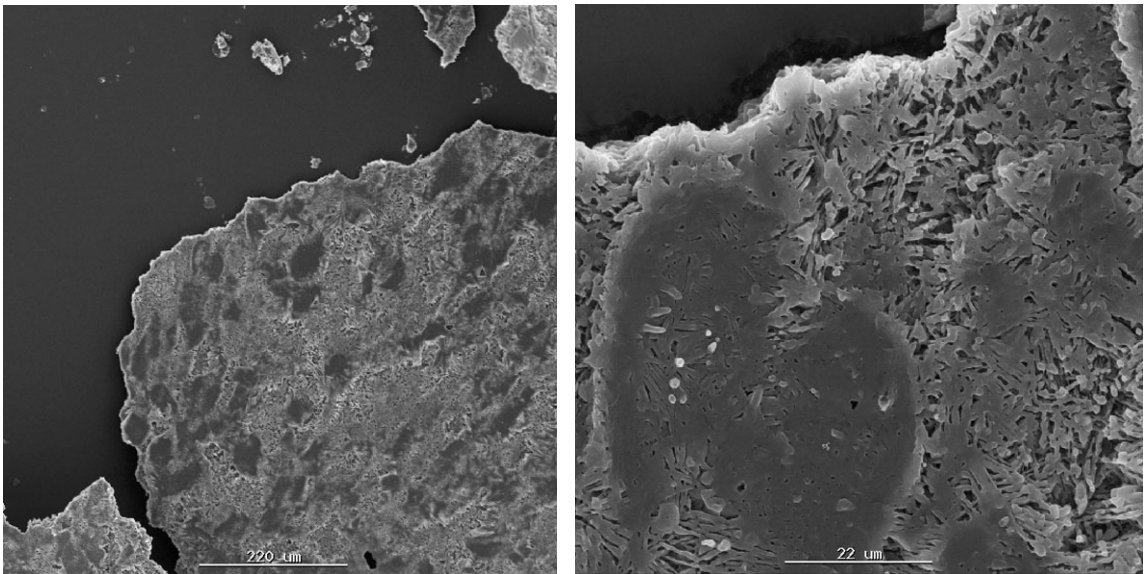


Figure 4-27. Layers of melted RDX that has been quenched by heat loss to the vessel walls. The right picture is a magnified portion of the left.

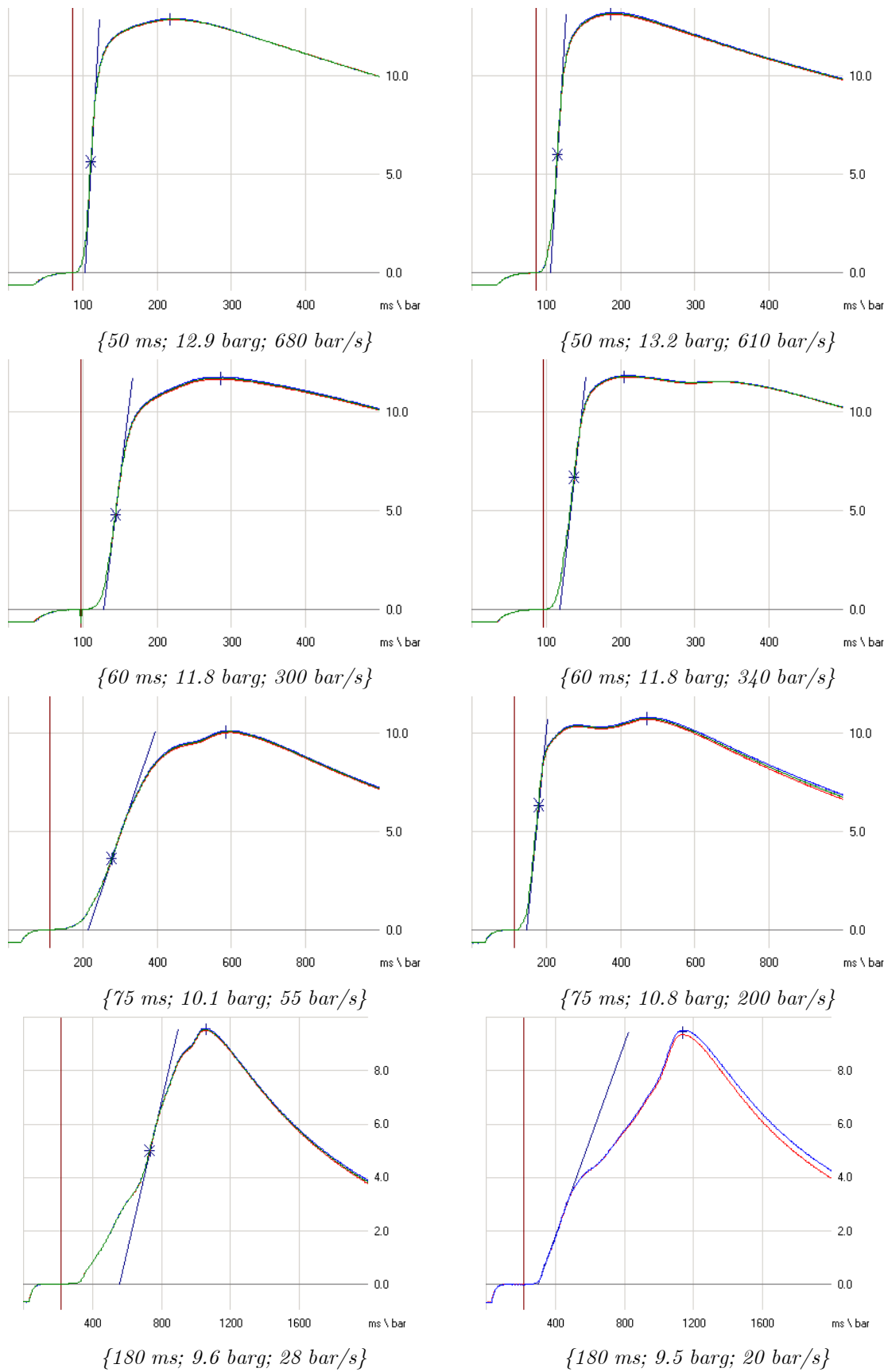


Figure 4-28. Pressure-time histories for representative RDX explosions in the modified USBM vessel fitted with the RDX nozzle; ignited by 6 J electrical discharges, nominal dust concentration 1000 g/m³. Results for both the fine lot (left) and the coarse lot (right).

4.4 Estimation of Burning Velocity from Pressure Measurements

In this section, results from section 4.1, describing the decay of turbulence, are combined with results from 4.2 and 4.3, describing pressure-time histories for explosions with gaseous and solid fuels. For selected tests, a rough estimate of the burning velocity in the inflection point of the pressure-time curve, $W_{ip}=(p_{ip}, t_{ip})$, is found by equation (2.58). The root-mean-square of the velocity fluctuations in the inflection point is estimated by evaluating (2.37) for $t=t_{ip}$; the measured values 1.93 m/s and -1.70 for u'_{rms} and n have been used to describe the decay in the cubical vessel. Since no turbulence measurements have been done for the modified USBM vessel, both the measured values from the cubical vessel, and the values reported by Dahoe (2000) for the 20-litre Siwek sphere, have been used. Note that only tests with ignition delay times shorter than about 90-100 milliseconds can be included, depending on the reactivity of the mixture, because equation (2.37) only describes the interval from 60 to 200 milliseconds.

The estimated burning velocities will be reported without any correction for the temperature or pressure of the unburnt mixture; however, the significant effect that such corrections can have on the result will be illustrated for the laminar burning velocity of propane-air mixtures.

4.4.1 Propane-Air Explosions

Laminar burning velocity

Estimates of laminar burning velocity in initially quiescent propane-air mixtures are presented in Figure 4-30, together with values for laminar burning velocity at atmospheric conditions summarized by Glassman (1996). The figure illustrates the inherent limitations of equation (2.58), e.g. the assumption of spherical flame propagation. The increase in the laminar burning velocity for equivalence ratios higher than about 2 (about 8 per cent propane by volume) is not real; in this concentration range the flame could only propagate upwards, and the measured explosion pressure was typically less than one bar. The measured values are significantly higher than values for atmospheric conditions found in the literature. However, burning velocities estimated at the measured pressure (p_{ip}) and temperature (T_{ip} - assuming adiabatic compression of the unburnt mixture) by an empirical formula found in Turns (1996), is actually a bit higher than the measured values found in this work. The corrections formula given by Turns is on the form:

$$S_{u,L} = S_{u,L,ref} \left(\frac{T_u}{T_{u,ref}} \right)^\gamma \left(\frac{p}{p_{ref}} \right)^\beta \quad (4.3)$$

where both the reference value $S_{u,L,ref}$, and the exponents γ and β , are empirical functions of the equivalence ratio Φ . The differences between measured and corrected results are probably due to a combination of several factors, e.g. deviations from purely

adiabatic and isotropic conditions, deviation from spherical flame shape, inaccuracies in the correction formula, etc.

The main point of this discussion is that the estimated burning velocities found in constant volume explosion vessels has to be corrected for the effect of temperature and pressure in order to be compared with burning velocities determined under atmospheric conditions.

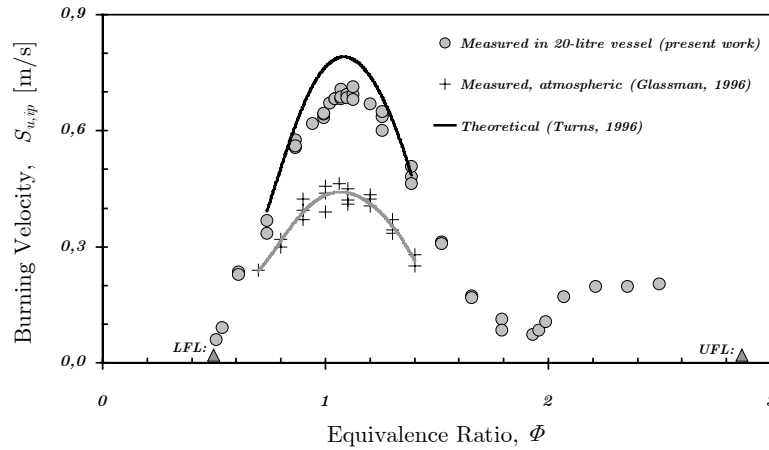


Figure 4-29. Laminar burning velocity for propane-air mixtures as a function of equivalence ratio.

Turbulent burning velocity

Much of the present knowledge about the burning velocity and flame speed in premixed turbulent combustion of gaseous mixtures is summarized in the extensive review article by Lipatnikov and Chomiak (2002); some of the basic trends found for propane-air mixtures are illustrated in Figure 4-30. Although there is to be considerable scatter in the published data, some general trends could nevertheless be found (discussed in Chapter 2). For moderate values of the root-mean-square of the velocity fluctuations (less than about 3 m/s), the increase in the burning velocity with increasing u'_{rms} is close to linear.

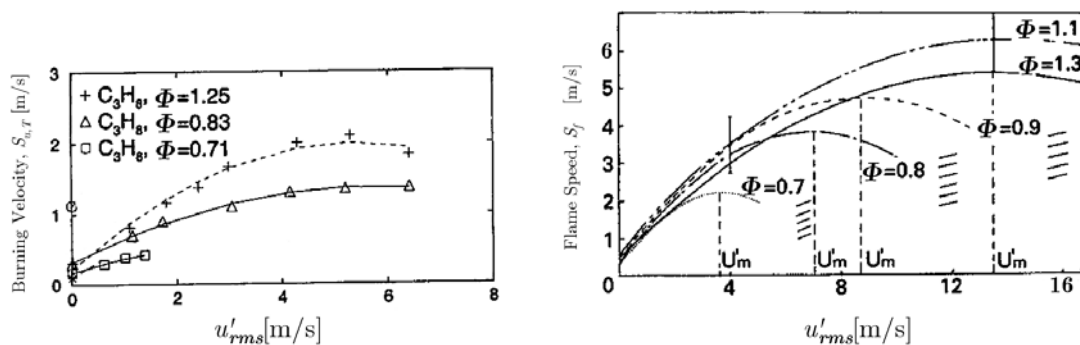


Figure 4-30. Basic trends measured for turbulent burning velocity (left) and flame speed (right) in propane-air mixtures at various equivalence ratios (Φ); slightly modified from Lipatnikov and Chomiak (2002). The burning velocity measurements originate from Karpov and Severin (1980); the flame speed measurements from Abdel-Gayed et al. (1984).

The turbulent burning velocities found by applying equation (2.58) to the results found in this work (section 4.2) are summarized in Figure 4-31; the values of u'_{rms} and n that are used to estimate the level of turbulence are given in parenthesis in the

labels. Although some of the data series could have been better presented by a curved trend line, similar to the ones in Figure 4-30, only linear fits are included in Figure 4-31. For the tests performed in the modified USBM vessel, two data series are included for each set of measurements; one represents the turbulence level measured in the cubical vessel, and one represents the values reported by Dahoe (2000) and Dahoe *et al.* (2001a). The fact that the measurements performed in the cubical vessel¹ more or less coincides with the measurements from the modified USBM vessel, when the turbulence level is based on the measured values from the cubical vessel, suggests that the level of turbulence is more or less the same in both vessels at a given instant during the decay period. However, the same kind of agreement would have been found if the decay in the cubical vessel had been represented by the empirical values found by Dahoe. Hence, provided that other factors that can influence on the estimated burning velocity are assumed to be the same in both vessels, two main possibilities exists:

- i)* The smoothing procedure used in this work to estimate the ‘average velocity’, described in Appendix D, have resulted in considerable over-smoothing compared to the smoothing procedure used by Dahoe (2000) and Dahoe *et al.* (2001a); hence, the real root-mean-square velocity is underestimated. In this case, the real level of turbulence in both vessels is probably closer to the level indicated by Dahoe for the 20-litre sphere. The considerable span in possible values for u'_{rms} , from the low values predicted by the currently used smoothing procedure to the much higher values that results when no smoothing is performed, was illustrated in Figure 4-3. Although the same smoothing procedure was used by Dahoe (2000), it is possible that differences in e.g. the effective data rate, between his measurements and the ones presented in this work, are responsible for much of the observed difference; this possibility is illustrated in Appendix D. It is also a major drawback that the vertical velocity component could not be measured in this work; if any significant anisotropy exists in the flow field inside the 20-litre vessels, the main difference is most likely to be the found between the vertical component, and the two horizontal components.
- ii)* The smoothing procedure used in this work have not resulted in considerable over-smoothing compared to the smoothing procedure used by Dahoe (2000) and Dahoe *et al.* (2001a); hence, the level of turbulence in both of the two explosion vessels used in this work is lower than the level of turbulence in the 20-litre sphere used by Dahoe. Such an effect could be caused by (a combination of) several factors, e.g.:
 - a. Differences between the dispersion system used by Dahoe, and the dispersion system used with both of the two vessels in this work. As was mentioned in section 4.1, the dispersion system used in this work includes an adaptor flange and an extension piece that makes the flow path from the reservoir to the explosion vessel somewhat longer.
 - b. Different vessel shapes.

¹ Measurements in both vessels were only performed for 4.5% propane in air.

- c. Differences in the experimental procedures, e.g. the way the reservoir is pressurized and the vessel evacuated.

Theoretically, a correction of the measured burning velocities for temperature and pressure, and subsequent comparison with published burning velocities for various values of u'_{rms} , could have given some indication of which of the two turbulence levels that are correct. However, this has not been attempted in the present work, for several reasons:

- i) The estimated burning velocities can only be expected to exhibit 'order of magnitude' accuracy in the first place. A spherical flame with zero thickness is assumed to propagate from the centre of the vessel; none of these assumptions is necessarily fulfilled in the experiments. Hence, no correction could possibly remove this inherent uncertainty.
- ii) There exists a magnitude of correction formulas for both pressure and temperature dependencies of measured turbulent burning velocities; reflecting the considerable spread in published experimental data (Lipatnikov and Chomiak, 2002). Hence, it would constitute a separate study just to find a correction formula applicable for the present problem.
- iii) The estimated level of turbulence at the time when the inflection point is reached, is based on the assumption that the level of turbulence in the unburnt mixture is unaffected by the explosion; this is not necessarily true. Post-ignition turbulence can be generated by flow produced by the expanding combustion products. In addition, the kinematic viscosity is likely to increase by a factor of about 3-5 due to the temperature increase caused by adiabatic compression alone; this will have significant influence on the dissipation of turbulent energy (2.22), the turbulent Reynolds numbers (2.14)-(2.17), and the Kolmogorov scales (2.20).

Nevertheless, at least two of the three fundamental qualitative trends that are generally found when studying premixed turbulent combustion can be recognized in the results presented in Figure 4-31: $S_{u,T}$ increases with u'_{rms} , and both $S_{u,T}$ and $dS_{u,T}/du'_{rms}$ increases with u'_{rms} . The high value of the estimated burning velocities also suggests that the third trend is could be confirmed provided the effect of temperature could be isolated: an increase in $S_{u,T}$ with pressure. By comparing Figure 4-30 and Figure 4-31, it follows that the uncorrected measurements from this work overestimate the burning velocity for propane-air mixtures by a factor of 3-5.

4.4.2 Dust Explosions

Estimated burning velocities for the various dust-air mixtures are summarized in Figure 4-32; the nominal dust concentration is 500 g/m³ for all dusts except RDX (1000 g/m³). Generally, there seems to be a linear relationship between the burning velocity and the root-mean-square velocity; similar to the results found by e.g. Pu *et al.* (1988, 1989, 1990) and van der Wel (1993), for various dusts. However, there is every reason to expect that the results are (at least) equally inaccurate, and equally much influenced by both pressure and temperature, as the results presented for propane-air mixtures in

section 4.4.1. Details concerning the various dusts will be briefly discussed in the following.

Niacin amide

Although most of the presented tests were performed in the cubical vessel, the few results from the modified cubical vessel seem to support the findings for 4.5% propane-air mixtures: the turbulence level in the two vessels are not very different. This is also strongly supported by the measured rates of pressure rise, over a broad range of concentrations, which are presented in Figure 4-18.

The results from the Calibration-Round-Robin test CaRo 00/01, presented in Appendix A, gives no reason to suspect that the level of turbulence should be lower in the two 20-litre vessels used in this work. On the contrary, the K_{St} values determined with both vessels were above average when chemical igniters were used as ignition source; the value for the cubical vessel were actually too high to fall within the acceptable $\pm 10\%$ range.

***Lycopodium* spores**

The results for spores of *Lycopodium casuarinoides* are in reasonably good agreement with similar results presented by van der Wel (1993); however, he used probably spores of *Lycopodium clavatum* (see Appendix C). An approximate linear fit to the results presented by van der Wel is: $S_{u,T} = 0.74u'_{rms} + 0.14$; hence, it would fall between the two linear fits shown in Figure 4-32. The results presented by van der Wel was determined for a nominal dust concentration of 500 g/m³ in a 20-litre sphere fitted with the dispersion ring, and the level of turbulence was estimated from the measurements presented by Pu *et al.* (1990). The ignition source was chemical igniters with total energy 10 kJ, and the results were not corrected for temperature and pressure.

A formula on the form $S_{u,T} = Ku'_{rms} + S_{u,L}$, with K equal to 0.37 is referred to by van Wingerden (1996); the formula originates from work in a 1.25 m³ spherical vessel described by Gieras *et al.* (1995). As the original reference was not available, it is not clear whether this formula is corrected for temperature and pressure.

Silicon

The burning velocities for the three lots of silicon all fit on more or less the same line, with the lot J 135 slightly above the other two. The two tests at an ignition delay time of 45 milliseconds seem to fit into the same pattern, although the scatter is increased.

RDX

RDX yields the lowest burning velocities, in spite of relatively high rates of pressure rise. The explanation for this is the fact that the inflection point occurs at relatively low pressures compared to the maximum pressure. The fact that this material probably will burn equally well, or even better, in thick deposits, compared to dust clouds, makes it inherently difficult to interpret the results.

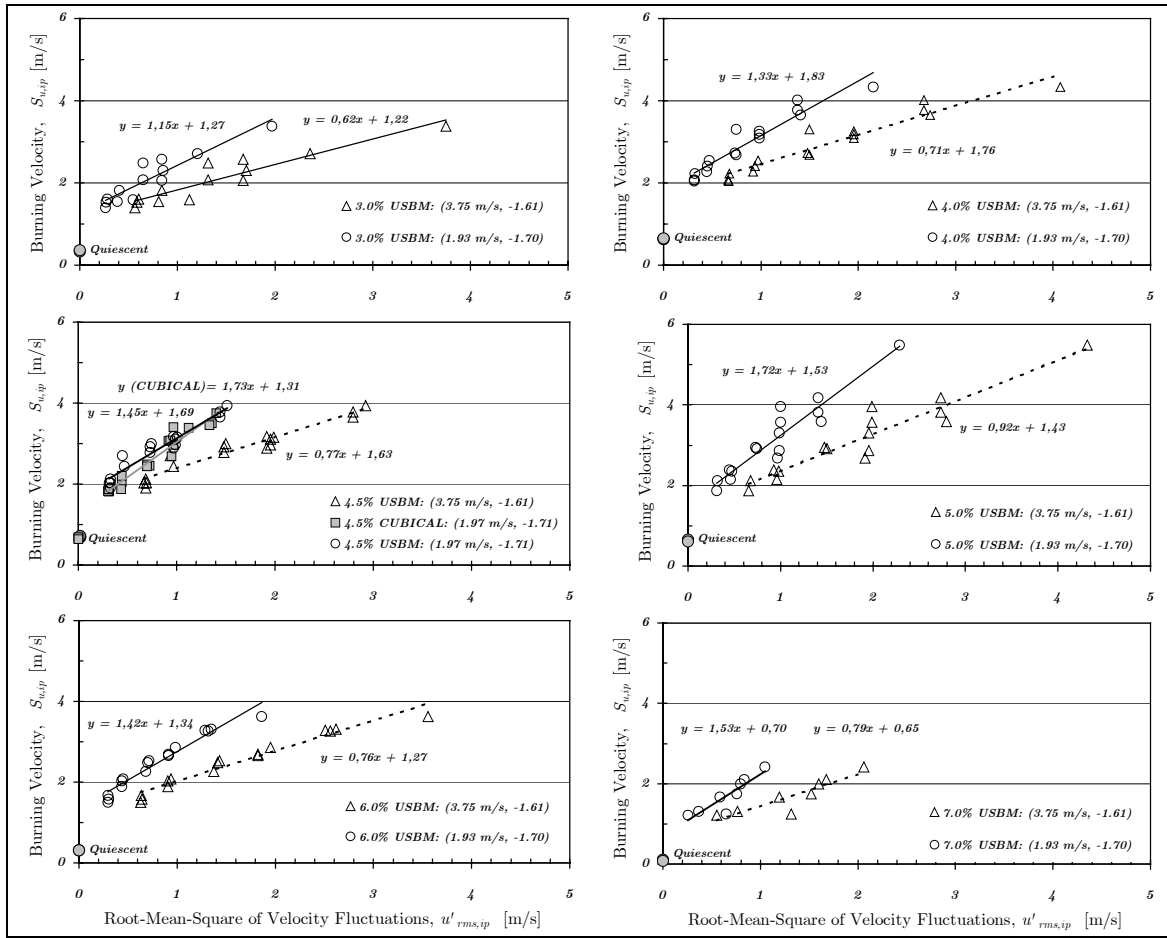


Figure 4-31. Estimated burning velocity for various propane-air mixtures as a function of the root-mean square of the velocity fluctuations, u'_{rms} and n are given in parenthesis.

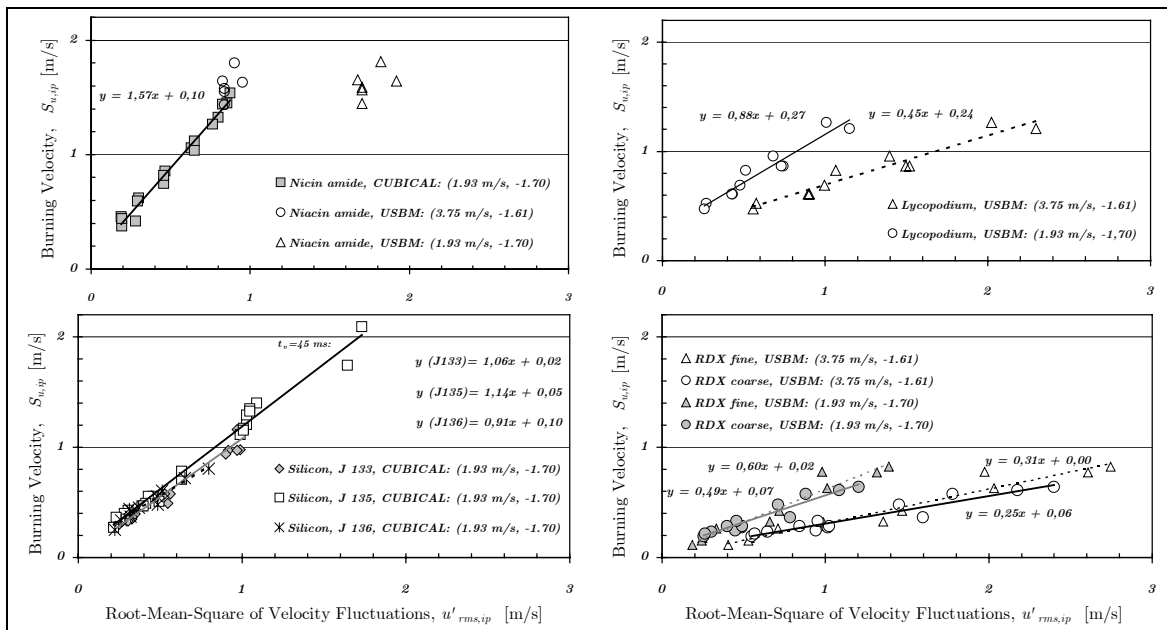


Figure 4-32. Estimated burning velocity for various dust-air mixtures as a function of the root-mean square of the velocity fluctuations, u'_{rms} and n are given in parenthesis.

4.4.3 Burning Velocity and Rate of Pressure Rise for Explosible Mixtures

Whereas the empirical values for the root-mean-square velocities used in Figure 4-32 primarily is determined by the measured value of u'_{rms} , the estimated burning velocity is strongly correlated with the rate of pressure rise – as one would expect.

The strong correlation between $S_{u,T}$ and $(dp/dt)_m$ is illustrated in Figure 4-33. Propane-air mixtures, from 4 to 6 percent by volume fit on a more or less straight line. Compared to this, lean (3.0%) and rich (7.0%) propane-air mixtures, together with *Lycopodium* and niacin amide, yields higher burning velocities for the same rate of pressure rise; silicon and RDX yields lower burning velocities.

The estimated burning velocities as a function of the ratio between the corrected absolute explosion pressure ($p_0 + p_m$), and the absolute pressure in the inflection point ($p_0 + p_{ip}$), are also plotted in Figure 4-33. The figure illustrated that the inflection point occurs at a relatively low pressure for all the dusts, compared to the propane-air mixtures. This is probably a result of the much thicker flames associated with dust-air mixtures, compared to propane-air mixtures. According to Dahoe *et al.* (1996), a greater flame thickness (or a smaller explosion vessel) will result in a greater relative reduction in the measured maximum rate of pressure rise. This effect is due to interactions between the flame and the walls of the vessel. Hence, the burning rates calculated from the rate of pressure rise and the pressure in the inflection point, is likely to be increasingly underestimated for mixtures having a lower value of the pressure ratio described above. Keeping the results for RDX out of the discussion due to the special properties of this material, it follows that the largest underestimation will take place for the three lots of silicon, followed by niacin amide and *Lycopodium* spores. From the results for 4.5% propane in air, there is a tendency towards lower pressure ratios for tests performed in the cubical vessel compared to tests performed in the modified USBM vessel, as would be expected given the difference in shape between the two vessels.

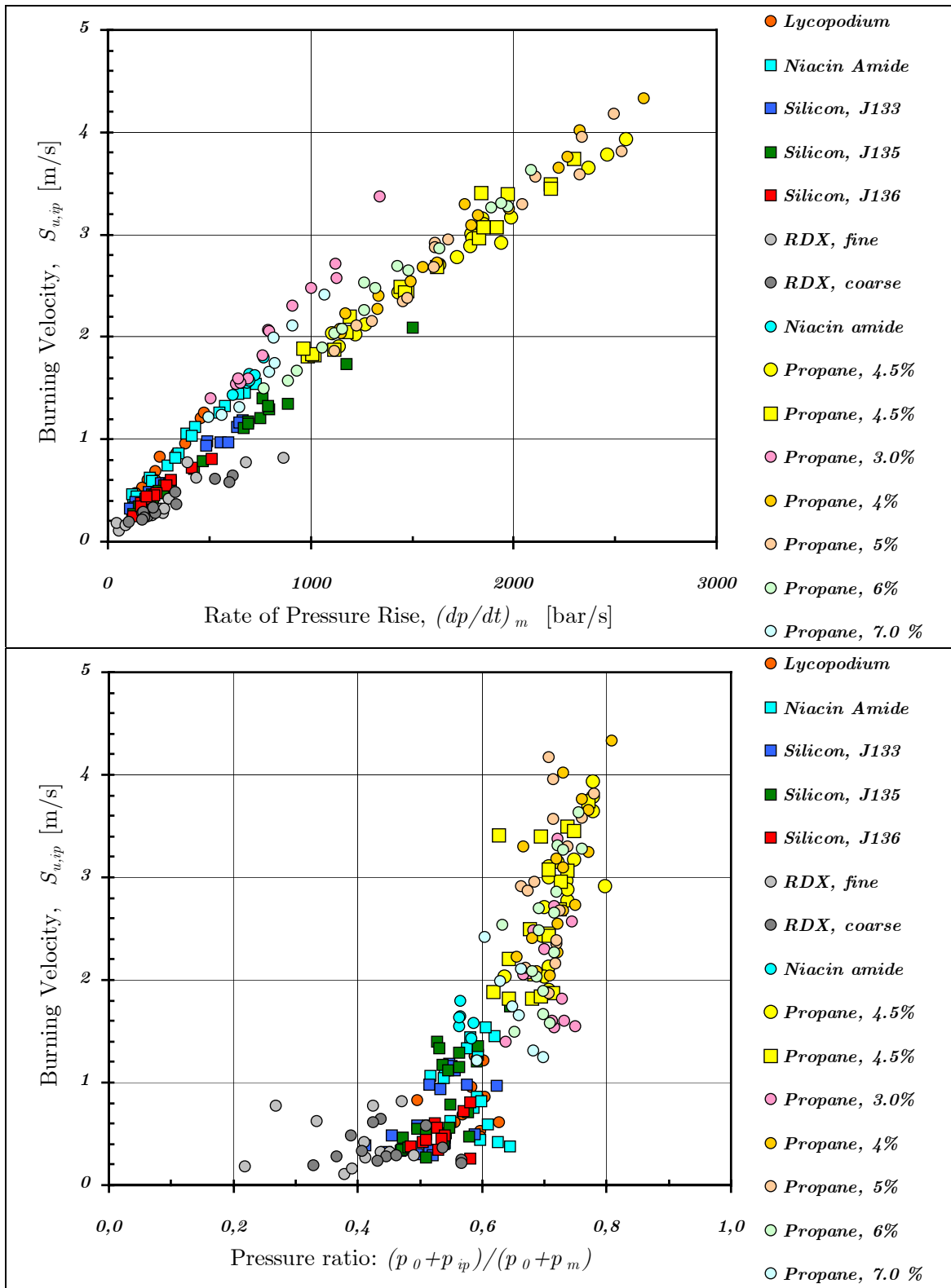


Figure 4-33. The relationship between estimated burning velocity and rate of pressure rise (above), and the relationship between the estimated burning velocity and the ratio between the absolute 'corrected' explosion pressure and the absolute pressure in the inflection point (below); all of the explosive mixtures discussed in sections 4.4.1 and 4.4.2 are included. Tests performed in the cubical vessel are indicated by squares; tests in the modified USBM vessel by circles.

CHAPTER 5

Conclusions

Given the diversity of the results presented in this work, the main conclusions will be briefly stated under separate headings. Suggestions for further work will be included whenever this seems natural.

Apparatus

A dust explosion laboratory has been set up at the University of Bergen. The facility includes two 20-litre explosion vessels, one of the USBM-type and one cubical. The basic systems for dust-dispersion and pressure-measurement are almost identical with those of the 20-litre Siwek sphere. Various dispersion nozzles have been tested, but there does not seem to be any reason for abandoning the traditional rebound nozzle.

Both 20-litre explosion vessels participated in the Calibration-Round-Robin test CaRo 00/01, arranged by Adolf Kühner AG (Cesana, 2001), but only the modified USBM vessel produced results within the acceptable $\pm 10\%$ range; the cubical vessel produced a slightly higher K_{St} value.

An electric-arc generator has been developed, in order to achieve central point ignition of the turbulent dust-air suspensions. The performance of the arc generator has been characterized under various conditions. A typical arc discharge releases about six Joules of energy in about three milliseconds. The arc discharges were found to be a reliable ignition source for most of the dusts tested. The arc generator can be improved by increasing the arc current (thus allowing for higher arc energies) or by making it possible to initiate the arc by an exploding wire, instead of a high voltage spark.

Classification of the particle-laden flows involved in dust explosions

A discussion of the particle-laden flows involved in dust explosions shows that most combustible dust clouds can be characterized as dilute suspensions, i.e. suspensions in which so-called two-way coupling takes place. This means that the momentum transfer from the particles is large enough to alter the turbulence structure. A general trend is that small particles, compared to the Kolmogorov length scale, tend to attenuate turbulence, while larger particles augment turbulence. However, no simple method exists for estimating the amount of turbulence modification. In addition, the transient

flow in standardized 20-litre explosion vessels is far too complex to reliably predict whether turbulence will be attenuated or augmented by the presence of particles.

Dispersion experiments

Dispersion-induced turbulence without dust added has been measured in the cubical vessel by laser Doppler anemometry. Only the horizontal velocity components were measured. The LDA measurements indicated levels of turbulence during the decay period that was significantly lower than levels reported by e.g. Dahoe *et al.* (2001a, 2001b) for a 20-litre spherical vessel fitted with a similar dispersion system as the one used in this work. Turbulence has not been measured in the modified USBM-vessel. Given the similarity in shape between the modified USBM-vessel, and the spherical vessel used by Dahoe *et al.*, it seems reasonable to expect the levels of turbulence should be similar in these two vessels (for the same dispersion system). However, results from explosion experiments indicate that the level of turbulence at a given time during the dispersion process is similar in the two vessels used in this work. The reason for the considerable difference between the results found in this work, and the results reported by Dahoe *et al.*, remains unsolved. It seems clear that there is considerable uncertainty associated with the smoothing procedure used to isolate the ‘mean’ velocity in the LDA data. However, variations in vessel shape, dispersion system, or experimental procedures may also be responsible for the observed discrepancy. A possible way of solving this problem in a future study could be to measure the decay of turbulence in various vessels, using the same dispersion system, the same LDA equipment, the same experimental procedures, and the same procedures for analysing the data.

Attempts have been made at measuring the level of turbulence with dust added to the flow. However, the effective data rate in the LDA measurements was reduced so much that no reliable information could be extracted. Hence, the influence of the presence of dust on the level of turbulence could not be measured.

Pressure measurements at various positions in the flow have been used to characterize the transient dispersion process. Four different nozzles were used (Appendix B), with and without dust added to the flow. For flows without dust, two different flow regimes were identified for the early phase of the dispersion process: the flow in the mushroom and pepper nozzles seemed to be underexpanded (sonic), whereas the flow in the open and rebound nozzles seemed to be overexpanded (supersonic). Increased dust loading had significant influence on the pressure measured immediately upstream of the nozzles, and resulted in a delay of the pressure-drop in the reservoir. However, measurements of the final pressure in the reservoir showed that the dust had negligible effect on the amount of air added to the explosion vessel prior to the closing of the outlet valve.

Propane explosions

Explosion experiments performed in the modified USBM-vessel with propane-air mixtures, over the whole explosible concentration range, illustrated the strong influence turbulence has on both explosion pressure and rate of pressure rise. Tests performed under initially quiescent conditions indicated the following flammability limits, based on detectable pressure rise: LFL between 2.0% and 2.1%, and UFL between 10.5% and 11.0% propane, by volume. In the tests performed under turbulent conditions, the fuel

was added to the vessel, and pure air was injected from the reservoir; thus, there can be some doubts concerning the degree of mixing prior to ignition, especially for short ignition delay times. Nevertheless, shorter ignition delay times, i.e. higher turbulence intensity, resulted in a narrowing of the flammability limits, especially on the fuel-rich side, in accordance with results presented by e.g. Akindele *et al.* (1982). For mixtures that could be ignited, the rate of pressure rise was significantly higher for test performed under turbulent conditions, even for ignition delay timed as high as 900 milliseconds.

Tests performed in the cubical vessel, for a propane concentration of 4.5 per cent by volume, yielded slightly lower values of both p_{ex} and $(dp/dt)_m$ than the tests in the USBM-vessel, for the same fuel concentration. Spread in the results from tests performed with various nozzles at short ignition delay time ($t_0 < 90\text{ms}$) indicated incomplete mixing, especially with the pepper nozzle.

Propane explosions with inert dust and hybrid explosions

It has been shown that adding increasing amount of inert dust to propane-air mixtures leads to an almost linear reduction in both the explosion pressure and the rate of pressure rise. This effect is probably primarily caused by heat loss to the inert particles. However, the relative reduction in the rate of pressure rise was much greater than the reduction in the explosion pressure, especially for very low dust concentrations. This could indicate that the turbulence level is reduced when particles are added to the flow, but it is equally likely that the presence of particles in the combustible mixture is accompanied by an increase in the thickness of the gaseous flame. Small amounts of combustible dust (spores of *L. casuarinoides*) added to propane-air mixtures, also resulted in a noticeable reduction in the rate of pressure rise.

Dust explosions

Explosion experiments with dust-air mixtures, over a broad concentration range, showed that the maximum values of both the explosion pressure and the rate of pressure rise is found for nominal dust concentration close to 500 g/m^3 , for all the three combustible dusts used in the main part of this work: niacin amide, spores of *Lycopodium*, and silicon. For this concentration, the effect of increasing the ignition delay time was a dramatic reduction in the rate of pressure rise, but also a significant reduction in the maximum explosion pressure. There are strong indications suggesting that the actual dust concentration decreases rapidly during the transient decay period.

A limited amount of tests performed with chemical igniters resulted in significantly higher values for the rate of pressure rise, compared with arc ignition, for all the three dusts; the maximum explosion pressure was less affected.

Qualitative observations of the change in colour and particle shape of the residue after silicon explosions performed at various ignition delay times, suggests that a transition is taking place. Two possible explanations have been suggested for this phenomenon:

- i)* A rapid decrease in the actual dust concentration. This explanation is supported by the rapid decrease in explosion pressure, and the failure to ignite at various ignition delay times for the three lots of silicon.

- ii) A transition from a combustion mode where the oxide is formed as μm -sized particles outside the flame envelope (at short ignition delay times), to a combustion mode where the oxide condenses on the particle surface. This explanation is supported by SEM pictures of the residue.

Hence, further work focused on this particular phenomenon could prove to reveal new information on fundamental combustion properties of dust clouds. By measuring the particle size distribution of residues formed at various levels of turbulence, and comparing this with that of the unburnt dust, it could be possible to determine whether or not the oxide condenses on the particle surface during the combustion of single particles.

Spores of *Lycopodium*

Spores of *Lycopodium*, frequently used in dust explosion research, have traditionally been from the species *L. clavatum* (Stag's-horn Clubmoss). However, some rugulose spores have also been sold under the name 'Lycopodium', and it has been claimed that these spores originated from the species *L. alpinum* (Thomas *et al.*, 1991). However, it has been found in this work (Appendix C) that the so-called 'rugulose' spores most likely stem from the species *L. casuarinoides*, and that they should be called 'scabrate' – not 'rugulose' (Wilce, 1972; Zhang, 2003; Øllgaard, 2003).

Explosive dust

The effect of increased ignition delay time on explosion pressure and rate of pressure rise was investigated for two lots of RDX. Mitgau (1996) have shown that the burning velocity in particle clouds consisting of an explosive material, *diamino-guanidine-azotetrazole-mono-hydrate* (AGATZ), dispersed in air, decreases when the root-mean-square value of the fluctuating velocity increases. This effect was attributed to a reduction in the rate of the chemical reactions due to increased cooling of the particles in more intense turbulence. However, no indication of a decreased rate of pressure rise for increased ignition delay time could be identified for RDX. It is quite possible that the phenomenon described by Mitgau does not apply to RDX, since the molecular structure of RDX is very different from that of AGATZ. The experimental procedures used are also very different: Mitgau measured the actual propagation of a non-steady flame through a tunnel with grid-generated turbulence by a CCD-camera, whereas the rates of pressure rise reported in the present work in reality is a combined measure for energy release and increase in moles of gas. For RDX, it was found that the combustion process continued in the settled dust layers after the flame had passed through the cloud, making the pressure-time curves very difficult to interpret.

CFD-simulations

Simple CFD-simulations of propane-air explosions illustrate that the concept of comparing simulation results of standardised tests in 20-litre vessels with experimental results, in order to estimate fundamental parameters such as burning velocity and flame thickness, could work. However, considerable work remains to be done. Combustion models for dust clouds have to be developed/improved, and full-scale experiments have to be performed.

Burning velocity

Burning velocities in selected combustible mixtures have been estimated by the rate of pressure rise, the pressure in the inflection point, and the corrected explosion pressure. The calculations assume a thin flame. The results for both propane-air mixtures, and clouds of the various dusts, were in qualitative agreement with results reported by other workers, indicating a linear increase in burning velocity with increasing root-mean-square velocity.

It is found that the inflection point occurs at a relatively lower pressure for all the dusts, compared to the propane-air mixtures. This is probably a result of the much thicker flames associated with dust-air mixtures, compared to propane-air mixtures. According to Dahoe *et al.* (1996), a greater flame thickness, or a smaller explosion vessel, will result in a greater relative reduction in the measured maximum rate of pressure rise.

Limitations in experimental method

Inherent limitations associated with explosion experiment performed in closed 20-litre vessels make it difficult to produce quantitative estimates of key parameters, such as burning velocity or flame thickness. The propagating flame front is usually not observed, or measured directly. Estimates of burning velocity must rely on measured pressure-time curves that only represent progressive release of energy. Considerable difficulties arise due to the transient nature of the dispersion process, making it difficult to measure both turbulence parameters, and important characteristics of the flame (e.g. flame thickness). Nevertheless, it is possible that results from such tests can prove to be useful input to CFC codes, provided appropriate corrections can be made for the effect of temperature, pressure and flame thickness. However, such correlations will probably require parallel tests performed at atmospheric, and preferably stationary, conditions (e.g. burners). Hence, it is suggested that the standardized tests performed in 20-litre vessels are supplemented with alternative experiments, preferably operating at atmospheric and stationary conditions.

References

- Abdel-Gayed, R.G., Bradley, D., Hamid, M.N. & Lawes, M. (1984). *Lewis Number Effects on Turbulent Burning Velocity*. 20th Symposium (International) on Combustion, The Combustion Institute, Pittsburgh, pp. 505-511.
- Akhavan, J. (1998). *The Chemistry of Explosives*. ISBN 0-85404-563-5. Royal Society of Chemistry, Cambridge.
- Akindele, O.O., Bradley, D., Mak, P.W. & McMahon, M. (1982). *Spark Ignition of Turbulent Gases*. *Combustion and Flame*, **47**, pp. 129-155.
- Altman, I.S. (1999). *On Condensation Growth of Oxide Particles During Gas-Phase Combustion of Metals*. 17th International Colloquium on the Dynamics of Explosions and Reactive Systems, July 25-30, Heidelberg, Germany.
- Amyotte, P.R., Chippett, S. & Pegg, M.J. (1989). *Effects of Turbulence on Dust Explosions*. *Journal of Loss Prevention in the Process Industries*, **14**, pp. 293-310.
- Ballal, D.R. & Lefebvre, A.H. (1974). *The Influence of Flow Parameters on Minimum Ignition Energy and Quenching Distance*. 15th Symposium (International) on Combustion, The Combustion Institute, Pittsburgh, pp. 1473-1481.
- Bardon, M.F. & Fletcher, D.E. (1983). *Dust Explosions*. *Science Progress*, Vol. **68**, No. 272, pp. 459-473.
- Bartknecht, W. (1971). *Brenngas- und Staubeexplosionen*. Forschungsbericht F45, Bundesinstitut für Arbeitsschutz, Koblenz. (In German).
- Bartknecht, W. (1978). *Explosionen: Ablauf und Schutzmaßnahmen*. ISBN 3-540-08675-7. Springer-Verlag, Berlin. (In German, English translation: Bartknecht, 1981).
- Bartknecht, W. (1987). *Staubeexplosionen: Ablauf und Schutzmaßnahmen*. ISBN 3-540-16243-7. Springer-Verlag, Berlin. (In German).
- Bartknecht, W. (1981). *Explosions: Course Prevention Protection*. ISBN 3-540-10216-7. Springer-Verlag, Berlin.
- Bartknecht, W. (1993). *Explosionsschutz: Grundlagen und Anwendung*. ISBN 3-540-55464-5. Springer-Verlag, Berlin. (In German).
- Batchelor, G.K. & Townsend, A.A. (1947). *Decay of Vorticity in the Isotropic Turbulence*. *Proceedings of the Royal Society of London, Series A: Mathematical and Physical Sciences*, **190**, pp. 534-550.
- Batchelor, G.K. & Townsend, A.A. (1948a). *Decay of Isotropic Turbulence in the Initial Period*. *Proceedings of the Royal Society of London, Series A: Mathematical and Physical Sciences*, **193**, pp. 539-558.

- Batchelor, G.K. & Townsend, A.A. (1948b). *Decay of Isotropic Turbulence in the Final Period*. Proceedings of the Royal Society of London, Series A: Mathematical and Physical Sciences, **194**, pp. 527-543.
- Beér, J.M., Chomiak, J. & Smoot, L.D. (1984). *Fluid Dynamics of Coal Combustion: A Review*. Progress in Energy and Combustion Science, Vol **10**, pp. 177-208.
- Blouquin, R., Joulin, G. & Merhari, Y. (1997). *Combustion Regimes of Particle-Laden Gaseous Flames: Influences of Radiation, Molecular Transport, Kinetic-Quenching, Stoichiometry*. Combustion Theory Modelling, **1**, pp. 217-242.
- Borghì, R. & Destriau, M. (1998). *Combustion and Flames: Chemical and Physical Principles*. ISBN 2-7108-0740-8. Éditions Technip, Paris.
- Bradley, D. (2002). *Problems of Predicting Turbulent Burning Rates*. Combustion Theory and Modelling, **6**, pp. 361-382.
- Bradley, D., Chen, Z. & Swithenbank, J.R. (1988). *Burning Rates in Turbulent Fine Dust-Air Explosions*. 22nd Symposium (International) on Combustion, The Combustion Institute, Pittsburgh, pp. 1767-1775.
- Bradley, D. & Mitcheson, A. (1976). *Mathematical Solutions for Explosions in Spherical Vessels*. Combustion and Flame, **26**, pp. 201-217.
- Bradshaw, P. (1994). *Turbulence: The Chief Outstanding Difficulty of Our Subject*. Experiments in Fluids, **16**, pp. 203-216.
- Cashdollar, K.L. (2000). *Overview of Dust Explosibility Characteristics*. Journal of Loss Prevention in the Process Industries, **13**, pp. 183-199.
- Cashdollar, K.L. & Chatrathi, K. (1992). *Minimum Explosible Dust Concentration Measured in 20-L and 1-m³ Chambers*. Combustion Science and Technology, **87**, pp. 157-171.
- Cassel, H.M. (1964). *Some Fundamental Aspects of Dust Flames*. R.I. 6551, U.S. Department of the Interior, Bureau of Mines, Washington.
- Cashdollar, K.L., Zlochower, I.A., Green, G.M., Thomas, R.A. & Hertzberg, M. (2000). *Flammability of Methane, Propane, and Hydrogen Gases*. Journal of Loss Prevention in the Process Industries, **13**, pp. 327-340.
- Cesana, C. (2001). *Final Report: Calibration-Round-Robin CaRo 00/01*. Adolf Kühner AG, Birsfelden, Switzerland (www.kuhner.com/DOCUMENT/B052_172.pdf).
- Cesana, C. & Siwek, R. (2001). *Operating Instructions 20-l-Apparatus 6.0*. Adolf Kühner AG, CH-4127 Birsfelden, Switzerland.
- Chassaing, P. (2001). *The Modeling of Variable Density Turbulent Flows*. Flow, Turbulence and Combustion, **66**, pp. 293-332.
- Chen, C.H. & Jaw, S.Y. (1997). *Fundamentals of Turbulence Modeling*. Combustion: An International Series. ISBN 1-56032-405-8. Taylor & Francis, Washington.
- Clift, R., Grace, J.R. & Weber, M.E. (1978). *Bubbles, Drops and Particles*. ISBN 0-12-176950. Academic Press, New York.
- Crowe, C., Sommerfeld, M. & Tsuji, Y. (1998). *Multiphase Flows with Droplets and Particles*. ISBN 0-8493-9469-4. CRC Press, Boca Raton.

- Dahoe, A.E. (2000). *Dust explosions: A Study of Flame Propagation*. ISBN 90-90-13707-8. Ph.D. Thesis, Technische Universiteit Delft. Delft University Press, Delft.
- Dahoe, A.E., Zavenbergen, J.F., Lemkowitz, S.M. & Scarlett, B. (1996). *Dust Explosions in Spherical Vessels: The Role of Flame Thickness in the Validity of the 'Cube-Root Law'*. *Journal of Loss Prevention in the Process Industries*, **9** (1), pp. 33-44.
- Dahoe, A.E., Cant, R.S. & Scarlett, B. (2001b). *On the Decay of Turbulence in the 20-Litre Explosion Sphere*. *Flow, Turbulence and Combustion*, **67**, pp. 159-184.
- Dahoe, A.E., Cant, R.S., Pegg, R.S. & Scarlett, B. (2001a). *On the Transient Flow in the 20-Litre Explosion Sphere*. *Journal of Loss Prevention in the Process Industries*, **14**, pp. 475-487.
- Dahoe, A.E., van der Nat, K., Braithwaite, M. & Scarlett, B. (2001c). *On the Sensitivity of the Maximum Explosion Pressure of a Dust Deflagration to Turbulence*. *KONA*, No. 19, pp. 178-195.
- Dahoe, A.E., Hanjalic, K. & Scarlett, B. (2002). *Determination of the Laminar Burning Velocity and the Markstein Length of Powder-Air Flames*. *Powder Technology*, **122**, pp. 222-238.
- Druzhinin, O.A. (2001). *The Influence of Particle Inertia on the Two-Way Coupling and Modification of Isotropic Turbulence by Microparticles*. *Physics of Fluids*, Vol. **13**, No. 12, pp. 3738-3755.
- Durst, F., Melling, A. & Whitelaw, J.H. (1981). *Principles and Practice of Laser-Doppler Anemometry*. 2nd Edition. ISBN 0-12-225260-8. Academic Press, London.
- Eckhoff, R.K. (2003). *Dust Explosions in the Process Industries*. Third edition. ISBN 0-7506-7602-7. Gulf Professional Publishing, Amsterdam.
- Eckhoff, R.K., Parker, S.J., Gruvin, B., Hatcher, M. & Johansson, T. (1986). *Ignitability and Explosibility of Silicon Dust Clouds*. *Journal of the Electrochemical Society*, Vol. **133**, No. 12, pp. 2631-2637.
- Elghobashi, S.E. (1991). *Particle-Laden Turbulent Flows: Direct Simulation and Closure Models*. *Applied Scientific Research*, **48**, pp. 301-314.
- Elghobashi, S. (1994). *On Predicting Particle-Laden Turbulent Flows*. *Applied Scientific Research*, **52**, pp. 309-329.
- Elghobashi, S. & Truesdell, G.C. (1993). *On the Two-Way Interaction Between Homogeneous Turbulence and Dispersed Solid Particles. I: Turbulence Modification*. *Physics of Fluids A (Fluid Dynamics)*, **5** (7), pp. 1790-1801.
- Ertesvåg, I.S. (2000). *Turbulent Strøyming og Forbrenning: Frå Turbulensteori til Ingeniørverkty*. ISBN 82-519-1568-6. TAPIR Forlag, Trondheim (in Norwegian).
- Foias, C., Manley, O., Rosa, R. & Temam, R. (2001). *Navier-Stokes Equations and Turbulence*. ISBN 0-521-36032-3. Cambridge University Press, Cambridge.
- Frank-Kamenetskii, D.A. (1969). *Diffusion and Heat Transfer in Chemical Kinetics*. Plenum Press, New York.
- Glassman, I. (1996). *Combustion*. 3rd Edition. ISBN 0-12-285852-2. Academic Press, San Diego.

- Gieras, M., Glinka, W., Klemens, R. & Wolanski, P. (1995). *Investigation of Flame Structure During Laminar and Turbulent Burning in Dust-Air Mixtures*. Conference Dust Explosions, Protecting People, Equipment, Buildings and Environment, pp. 168-224.
- Goldstein, R.J. (1996). *Fluid Mechanics Measurements*. 2nd Edition. ISBN 1-56032-306-X. Taylor & Francis, Washington.
- Goral, P., Klemens, R. & Wolanski, P. (1988). *Mechanism of Gas Flame Acceleration in the Presence of Natural Particles*. Progress in Aeronautics and Astronautics, **113**, pp. 325-335.
- Gore, R.A. & Crowe, C.T. (1989). *Effect of Particle Size on Modulating Turbulent Intensity*. International Journal of Multiphase Flow, **15** (2), pp. 279-285.
- Goroshin, S. & Lee, J. (1999). *Laminar Dust Flames: A Program of Microgravity and Ground Based Studies at McGill*. 5th International Microgravity Combustion Workshop, May 18-20, Cleveland, Ohio.
- Gouesbet, G. & Berlemont, A. (1999). *Eulerian and Lagrangian Approaches for Predicting the Behaviour of Discrete Particles in Turbulent Flows*. Progress in Energy and Combustion Science, **25**, pp. 133-159.
- Han, O-S., Yashima, M., Matsuda, T., Matsui, H., Atsumi, M. & Ogawe, T. (2000). *Behaviour of Flames Propagating Through Lycopodium Dust Clouds in a Vertical Duct*. Journal of Loss Prevention in the Process Industries, **13**, pp. 449-457.
- Han, O-S., Yashima, M., Matsuda, T., Matsui, H., Atsumi, M. & Ogawe, T. (2001). *A Study of Flame Propagation Mechanisms in Lycopodium Dust Clouds Based on Dust Particles' Behaviour*. Journal of Loss Prevention in the Process Industries, **14**, pp. 153-160.
- Hanjalic, K. (1994). *Advanced Turbulence Closure Models: A View of Current Status and Future Prospects*. International Journal of Heat and Fluid Flow, Vol. **15**, No. 3, pp. 178-203.
- Hardalupas, Y., Taylor, A.M.K.P., & Whitelaw, J.H. (1989). *Velocity and Particle-Flux Characteristics of Turbulent Particle-Laden Jets*. Proceedings of the Royal Society of London, Series A: Mathematical and Physical Sciences, **426**, pp. 31-78.
- Hauert, F., Vogl, A. & Radant, S. (1994). *Measurement of Turbulence and Dust Concentrations in Silos and Vessels*. In Deng Xufan and Piotr Wolanski, (Eds.), The Sixth International Colloquium on Dust Explosions, pp. 71-80.
- Hertzberg, M. (1989). *Selective Diffusional Demixing: Occurrence and Size of Cellular Flames*. Progress in Energy and Combustion Science, **15**, pp. 203-239.
- Hertzberg, M., Cashdollar, K.L., Zlochower, I.A. & Green, G.M. (1992). *Explosives Dust Cloud Combustion*. 24th Symposium (International) on Combustion, The Combustion Institute, Pittsburgh, pp. 1837-1843.
- Hinze, J.O. (1972). *Turbulent Fluid and Particle Interactions*. In 'Progress in Heat and Mass Transfer, Volume **6**, Proceedings of the International Symposium on Two-Phase Systems', Hetsroni, G., Sideman, S. & Hartnett, J.P. (Eds.), ISBN 0-08-017035-8, Pergamon Press, Oxford, pp. 433-452.

- Hinze, J.O. (1975). *Turbulence*. 2nd Edition. ISBN 0-07-029037-7. McGraw-Hill, New York.
- ISO 6184-1 (1985). *Explosion Protection Systems – Part 1: Determination of Explosion Indices of Combustible Dusts in Air*. International Organization for Standardization.
- Jarosinski, J. & Podfilipski, J. (1999). *Combustion Mechanism of Dust Clouds in Microgravity*. 5th International Microgravity Combustion Workshop, Paper No. 16, Cleveland, Ohio.
- Jarosinski, J., Podfilipski, J. & Pu, Y. (1999). *Visualisation of Dust Explosions Under Microgravity Conditions*. 17th International Colloquium on the Dynamics of Explosions and Reactive Systems, Paper No. 174, Heidelberg, Germany.
- Karpov, V.P. & Severin, E.S. (1980). *Combustion, Explosions and Shock Waves*, **16**, p. 41.
- Kauffman, C.W., Srinath, S.R., Tezok, F.I., Nicholls, J.A. & Sichel, M. (1984). *Turbulent and Accelerating Dust Flames*. 20th Symposium (International) on Combustion, The Combustion Institute, Pittsburgh, pp. 1701-1708.
- Koch, D.L. (1990). *Kinetic Theory for a Monodisperse Gas-Solid Suspension*. *Physics of Fluids A*, Vol. **2**, No. 10, pp. 1711-1723.
- Kong, D., Sand, I.Ø. & van Wingerden, K. (1993). *Measurements of Turbulent Flow Parameters in the Near-Wake of Cylinders Using Laser-Doppler Anemometry*. Report No. CMR-93-F25053 in Kong (1996), Christian Michelsen Research AS, Bergen.
- Kulick, J.D., Fessler, J.R. & Eaton, J.K. (1994). *Particle Response and Turbulence in Fully Developed Channel Flow*. *Journal of Fluid Mechanics*, Vol. **277**, pp. 109-134.
- Kuo, K.K. (1986). *Principles of Combustion*. ISBN 0-471-62605-8. John Wiley & Sons, New York.
- Lauder, B.E. (1989). *Second-Moment Closure: Present ... and Future?* *International Journal of Heat and Fluid Flow*, Vol. **10**, No. 4, pp. 282-300.
- Lauder, B.E. & Spalding, D.P. (1974). *The Numerical Computation of Turbulent Flows*. *Computer Methods in Applied Mechanics and Engineering*, **3**, pp. 269-289.
- Lee, J. (2001). *Burning Velocity Measurements in Aluminium-Air Suspensions Using Bunsen-Type Dust Flames*. 6th International Microgravity Combustion Workshop, May 22-24, Cleveland, Ohio.
- Lee, J.H.S. (1988). *Dust Explosion Parameters, their Measurement and Use*. VDI BERICHTE, No. 701, pp. 113-122.
- Lee, J.H.S., Pu, Y.K. & Knystautas, R. (1987). *Influence of Turbulence on Closed Volume Explosion of Dust-Air Mixtures*. *Archivum Combustionis*, **7** (3/4), pp. 279-297.
- Lee, S.L. & Durst, F. (1982). *On the Motion of Particles in Turbulent Duct Flows*. *International Journal of Multiphase Flows*, Vol. **8**, No. 2, pp. 125-146.
- Lewis, B. & von Elbe, G. (1987). *Combustion, Flames and Explosions of Gases*. 3rd Edition. ISBN 0-12-446751-2. Academic Press, Orlando.

- Lipatnikov, A.N. & Chomiak, J. (2002). *Turbulent Flame Speed and Thickness: Phenomenology, Evaluation, and Application in Multi-Dimensional Simulations*. Progress in Energy and Combustion Science, **28**, pp. 1-74.
- Loth, E. (2000). *Numerical Approaches for Motion of Dispersed Particles, Droplets and Bubbles*. Progress in Energy and Combustion Science, **26**, pp. 161-223.
- Lumley, J.L. & Yaglom, A.M. (2001). *A Century of Turbulence*. Flow, Turbulence and Combustion, **66**, pp. 241-286.
- Meinköln, D. (1999). *Oxide Layer Effects in Metal Particle Combustion*. 5th International Microgravity Combustion Workshop, 18-20 May, Cleveland, Ohio.
- Mintz, K.J. (1993). *Upper Explosive Limit of Dusts: Experimental Evidence for Its Existence Under Certain Circumstances*. Combustion and Flame, **94**, pp. 125-130.
- Mintz, K.J. (1995). *Problems in Experimental Measurements of Dust Explosions*. Journal of Hazardous Materials, **42**, pp. 177-186.
- Mitgau, P. (1996). *Einfluß der Turbulenzlänge und der Schwankungsgeschwindigkeit auf die Verbrennungsgeschwindigkeit von Aerosolen*. Dissertation, Max-Planck-Institut für Strömungsforschung, Göttingen. (In German).
- Mitgau, P., Wagner, H.Gg. & Klemens, R. (1997). *Einfluß der Turbulenzlänge und der Schwankungsgeschwindigkeit auf die Flammengeschwindigkeit von Stäuben*. In Lenze, B. (Ed.): *Feuerungstechnik, Kaleidoskop aus aktueller Forschung und Entwicklung – Festschrift von Prof. Dr.-Ing. Wolfgang Leuckel zu seinem 65. Geburtstag*. ISBN 3-00-001539-0, Engler-Bunte-Institut, Bereich Feuerungstechnik, Universität Karlsruhe. (In German).
- Nagy, J., Conn, J.W. & Verakis, H.C. (1969). *Explosion Development in a Spherical Vessel*. R.I. 7279, U.S. Department of the Interior, Bureau of Mines.
- Nagy, J., Seiler, E.C., Conn, J.W. & Verakis, H.C. (1971). *Explosion Development in Closed Vessel*. R.I. 7502, U.S. Department of the Interior, Bureau of Mines, Washington.
- Nagy, J. & Verakis, H.C. (1983). *Development and Control of Dust Explosions*. ISBN 0-8247-7004-8. In the series: Occupational Safety and Health, **8**, Marcel Dekker, New York.
- NORSOK Standard Z-013 (2001). *Risk and Emergency Preparedness Analysis*. Rev. 2, Norwegian Technology Centre.
- Ouellette, P. & Hill, P.G. (2000). *Turbulent Transient Gas Injections*. Journal of Fluid Engineering, **122**, pp. 743-753.
- Peirano, E. & Leckner, B. (1998). *Fundamentals of Turbulent Gas-Solid Flows Applies to Circulating Fluidized Bed Combustion*. Progress in Energy and Combustion Science, **24**, pp. 259-296.
- Peters, N. (2000). *Turbulent Combustion*. ISBN 0-521-66082-3. Cambridge University Press, Cambridge.
- Pu, Y.K., Jarosinski, J., Tai, C.S., Kaufmann, C.W. & Sichel, M. (1988). *The Investigation of the Feature of Dispersion Induced Turbulence and Its Effect on Dust Explosions in Closed Vessels*. 22nd Symposium (International) on Combustion, The Combustion Institute, Pittsburgh, pp. 1777-1787.

- Pu, Y.K., Li, Y.C., Kauffman, C.W. & Bernal, L.P. (1989). *Determination of Turbulence Parameters in Closed Explosion Vessels*. The 12th International Colloquium on the Dynamics of Explosions and Reactive Systems, Ann Arbor, Michigan, 23-25 July, pp. 107-123.
- Pu, Y.K., Jarosinski, J., Johnson, V.G. & Kauffman, C.W. (1990). *Turbulence Effects on Dust Explosions in the 20-Liter Spherical Vessel*. 23rd Symposium (International) on Combustion, The Combustion Institute, Pittsburgh, pp. 843-849.
- Rogers, C.B. & Eaton, J.K. (1991). *The Effect of Small Particles on Fluid Turbulence in a Flat-Plate, Turbulent Boundary Layer in Air*. Physics of Fluids A (Fluid Dynamics), **3** (5), pp. 928-937.
- Schroeder, M.A., Fifer, R.A., Miller, M.S., Pesce-Rodriguez, R.A., Mcnesby, C.J.S., Singh, G. & Widder, J.M. (2001). *Condensed-Phase Processes during Combustion of Solid Gun Propellants. II. Nitramine Composite Propellants*. Combustion and Flame, 126, pp. 1577-1598.
- Shapiro, A.H. (1953). *The Dynamics and Thermodynamics of Compressible Fluid Flow*; Vol. I. The Roland Press Company, New York.
- Shirolkar, J.S., Coimbra, C.F.M. & Queiroz McQuay, M. (1996). *Fundamental Aspects of Modeling Turbulent Particle Dispersion in Dilute Flows*. Progress in energy and Combustion Science, **22**, pp. 363-399.
- Siwek, R. (1977). *20-L Laborapparatur für die Bestimmung der Explosionskenngrößen brennbarer Stäube*. Thesis, HTL Winterthur, Switzerland.
- Siwek, R. (1988). *Reliable Determination of Safety Characteristics in the 20-Litre Apparatus*. Proceedings of Conference on Flammable Dust Explosions, November 2-4, St. Louis, Missouri.
- Skrbek, L. & Stalp, S.R. (2000). *On the Decay of Homogeneous Isotropic Turbulence*. Physics of Fluids, Vol. **12**, No. 8, pp. 1997-2019.
- Squires, K.D. & Eaton, J.K. (1990). *Particle Response and Turbulence Modification in Isotropic Turbulence*. Physics of Fluids A (Fluid Dynamics) **2** (7), pp. 1191-1203.
- Squires, K.D. & Eaton, J.K. (1991). *Preferential Concentration of Particles by Turbulence*. Physics of Fluids A (Fluid Dynamics), **3** (5), pp. 1169-1178.
- Swett, C.C. (1956a). *Spark Ignition of Flowing Gases*. NACA Report **1287**, Lewis Flight Propulsion Laboratory, National Advisory Committee for Aeronautics, Cleveland.
- Swett, C.C. (1956b). *Spark Ignition of Flowing Gases Using Long-Duration Discharges*. 6th Symposium (International) on Combustion, The Combustion Institute, Pittsburgh, pp. 523-532.
- Tamanini, F. (1998). *The Role of Turbulence in Dust Explosions*. Journal of Loss Prevention in the Process Industries, **11**, pp. 1-10.
- Tennekes, H. & Lumley, J.L. (1972). *A First Course in Turbulence*. ISBN 0-262-200-19-8. The MIT Press, Cambridge.

- Thomas, G.O., Oakley, G & Brenton, J. (1991). *Brief Communication: Influence of the Morphology of Lycopodium Dust on Its Minimum Ignition Energy*. Combustion and Flame **85**, pp. 526-528.
- Truesdell, G.C. & Elghobashi, S. (1994). *On the Two-Way Interaction Between Homogeneous Turbulence and Dispersed Solid Particles. II: Particle Dispersion*. Physics of Fluids A (Fluid Dynamics), **6** (3), pp. 1405-1407.
- Tsinober, A. (2001). *An Informal Introduction to Turbulence*. ISBN 1-4020-0166-5. Kluwer Academic Publishers, Dordrecht.
- Tsuji, Y. & Morikawa, Y. (1982). *LDV Measurements of an Air-Solid Two-Phase Flow in a Horizontal Pipe*. Journal of Fluid Mechanics, Vol. **120**, pp. 385-409.
- Tsuji, Y., Morikawa, Y. & Shiomi, H. (1984). *LDV Measurements of an Air-Solid Two-Phase Flow in a Vertical Pipe*. Journal of Fluid Mechanics, Vol. **139**, pp. 417-434.
- Turns, S.R. (1996). *An Introduction to Combustion: Concepts and Applications*. ISBN 0-07-114783-7. McGraw-Hill, New York.
- van der Wel, P.G.J. (1993). *Ignition and Propagation of Dust Explosions*. ISBN 90-6275-854-1. PhD Thesis, Delft University Press, Delft.
- van der Wel, P., Lemkowitz, S., Scarlett, B. & van Wingerden, K. (1991). *A Study of Particle Factors Affecting Dust Explosions*. Particle & Particle Systems Characterization, **8**, pp. 90-94.
- van Wingerden, K. (1996). *Simulations of Dust Explosion Using a CFD-Code*. Proceedings of the Seventh International Colloquium on Dust Explosions, Bergen, Norway, pp. 6.42-6.51.
- Veynante, D. & Vervisch, L. (2002). *Turbulent Combustion Modelling*. Progress in Energy and Combustion Science, **28**, pp. 193-266.
- Warnatz, J., Maas, U. & Dibble, R.W. (1996). *Combustion: Physical and Chemical Fundamentals, Modeling and Simulation, Experiments, Pollution Formation*. ISBN 3-540-60730-7. Springer Verlag, Berlin Heidelberg.
- Webster's Encyclopedic Unabridged Dictionary of the English Language (1994). ISBN 0-517-11864-5. Gramercy Books, New York/Avenel.
- Wilce, J.H. (1972). *Lycopod Spores, I. General Spore Patterns and the Generic Segregates of Lycopodium*. American Fern Journal, **62** (3), pp. 65-79.
- Williams, F.A. (1986). *Lectures on Applied Mathematics in Combustion: Past Contributions and Future Problems in Laminar and Turbulent Combustion*. Physica D, Vol. **20D**, No. 1, pp. 21-34.
- Yuan, Z. & Michaelides, E.E. (1992). *Turbulence Modulation in Particulate Flows – A Theoretical Approach*. International Journal of Multiphase Flow, Vol. **18**, No. 5, pp. 779-785.
- Zhang, X.C. (2003). *Personal communication with Professor Xian-Chun Zhang*, President of the Chinese Fern Society, Principal Investigator of Higher Cryptogamic Botany, Institute of Botany, Chinese Academy of Sciences, Beijing, China.

- Zhen, G. & Leuckel, W. (1995a). *Influence of Transient Injection Induced Turbulent Flow on Gas and Dust Explosions in a Closed Vessel*. Loss Prevention and Safety Promotion in the Process Industries, **II**, pp. 257-268.
- Zhen, G. & Leuckel, W. (1995b). *The Dynamic Flow Condition of Dust Dispersion Induced Turbulence*. Proceedings of 10th Symposium of Turbulent Shear Flows, Vol. **3**, Session 25, pp. 7-12.
- Zhen, G. & Leuckel, W. (1996). *Determination of Dust-Dispersion-Induced Turbulence and Its Influence on Dust Explosions*. Combustion Science and Technology, Vols. **113-114**, pp. 629-639.
- Zhen, G. & Leuckel, W. (1997). *Effects of Ignitors and Turbulence on Dust Explosions*. Journal of Loss Prevention in the Process Industries, **10** (5-6), pp. 317-324.
- Ollgaard, B. (2003). *Personal communication with Benjamin Ollgaard*; associate professor at Department of Systematic Botany, Institute of Biological Sciences, University of Aarhus, Denmark.

APPENDIX A

Arc Generator

This appendix describes an arc generator, developed at the Department of Physics, University of Bergen, by Werner Olsen and the author. The main aim has been to produce a reliable ignition source for turbulent dust-air suspensions in closed 20-litre explosion vessels. After a short introduction to electrical discharges and spark ignition, both design considerations and performance are described in some detail.

The effect of gap length, turbulence and dust loading on released energy and duration of the discharge has been investigated. The performance of the arc generator as an incendiary device is described. For a few selected dusts, results obtained with arc ignition are compared with results obtained when chemical igniters are used as ignition source, including the results from the Calibration Round Robin Test CaRo 00/01.

The generator produces arc discharges that release approximately 6 joules of energy in about 3 milliseconds, across a 3-millimeter point-to-point spark gap. Although the arc discharges proved to be reliable ignition sources for several of the dusts used in this work, the frequency of successful ignitions were disappointingly low for some types of dust. The type of ignition source is found to have a significant influence on explosion indices, especially the rate of pressure rise.

A.1 Introduction

A.1.1 Motivation

There are many reasons why a moderately strong but reliable point ignition source is desirable for dust explosion tests in closed explosion vessels of moderate size. Although the ideal ignition source probably never will be found, electric arc discharges may provide one applicable option.

Point ignition

Standardized tests aimed at revealing the explosion violence of dust clouds are usually limited to the determination of explosion indices such as the maximum explosion pressure and the maximum rate of pressure rise (Appendix B). However, the measured pressure-time histories from constant volume explosions can also be used to estimate the burning rate or burning velocity, see e.g. Nagy *et al.* (1969), Bradley and Mitcheson (1976), Dahoe *et al.* (1996) or Dahoe (2000). Type and energy of the ignition source influence both the initiation of a dust explosion, and the subsequent flame propagation. Burning velocities are generally estimated by assuming simple spherical flame front propagation from a central ignition point. Consequently, experimental data from the early stage of the explosion, when the flame is more or less unaffected by the walls of the vessel, are better suited for making such estimates than data originating from the final stage of flame propagation (e.g. explosion pressure, maximum rate of pressure rise, and the K_{St} -value).

An ideal ignition source should provide reliable ignition by releasing energy within a small and well-defined volume of the explosion vessel, without significantly disturbing the early phase of flame propagation unnecessarily.

Timing and duration

Explosion indices for dust clouds are usually determined in constant volume explosion vessels (see Appendix B). In order to generate a combustible dust cloud, dust is dispersed by the transient blast, and highly turbulent flow, generated when air is injected into the explosion vessel from a pressurized container. When dispersion is terminated, turbulence decays rapidly with time. Hence, the initial turbulence level in the dust-air suspension is determined by the time delay (t_v) between onset of dispersion and ignition. As turbulence decays, the dust concentration decreases due to gravitational settling and particles adhering to the walls of the vessel. Ignition cannot occur before enough dust has been dispersed, nor after too much dust has settled. The actual dust concentration inside the vessel is seldom measured, although methods exist for such measurements to be done (e.g.: Cashdollar and Hertzberg, 1985; Cashdollar and Chatrathi, 1992). It is usually assumed that the actual dust concentration is approximately equal to the nominal dust concentration (c_n – i.e., the weighted amount of dust divided by the vessel volume). This assumption can only be justified as long as the dust cloud is ignited while the turbulence intensity is still relatively high, i.e. while most of the dispersed dust is still in suspension.

Well-defined initial conditions with respect to both turbulence and concentration require that ignition can be triggered at a preset time, and that the duration of the energy release is short compared to the duration of the subsequent flame propagation.

Amount of supplied energy

It will be shown in section A.2.3 that reliable ignition of a dust-air suspension under high turbulence intensity conditions requires a rather strong ignition source, especially for coarser particle size distributions. It is generally accepted that ignition by chemical igniters are very efficient for most combustible dust-air suspensions; according to Cesana and Siwek (2001), chemical igniters are currently the only mode of ignition for reliable determination of explosion indices in industrial practice. However, there are several reasons for adopting alternative ignition sources.

Most of the standard test methods for determining explosion pressure and rate of pressure rise for dust clouds, e.g.: ISO 6184-1 (1985), ASTM E1226-94 (1999), prEN 14034-1 (2003), prEN 14034-2 (2003) and Cesana and Siwek (2001), prescribe ignition by chemical igniters. For dust explosion research, the most frequently used chemical igniters are those produced by Fr. Sobbe GmbH in Dortmund. Usually two chemical igniters, each having energy 5 kJ, are used. A 5 kJ chemical igniter has a total mass of 1.2 grams, and consists of 40 percent (by weight) zirconium metal, 30 per cent barium nitrate, and 30 per cent barium peroxide. The igniters are fired by electrical fuse heads. The power supply circuit for the chemical igniters is usually required to be capable of firing the fuse heads in less than ten milliseconds. The fact that chemical igniters are used in literally all standardized tests ensures that test results can be compared between different laboratories.

Zhen and Leuckel (1997) investigated the effect of chemical igniters on methane/air explosions in a 1.16-m³ spherical vessel, and on cornstarch/air explosions in a 1-m³ cylindrical vessel. Both the energy of the igniter and the reactivity of the mixture were found to influence the explosion development. Chemical igniters produced jet-like volumetric and/or multipoint ignition, usually over-estimating the rate of pressure rise. The effect of chemical igniters was most important for the early stage of the explosion, but for methane/air explosions the non-spherical flame spread caused by igniters of moderate energy (75 J, 500 J and 5 kJ) was found to yield reduced rate of pressure rise compared to a 1-J spark. The pressure rise from a 10 kJ chemical igniter alone was measured to 30 mbar in the 1-m³ vessel, corresponding to a flame radius of about 18 cm when assuming spherical flame propagation. Zhen and Leuckel also showed that the influence of turbulence on the burning rate of dust clouds, usually studied by varying the ignition delay time, was coupled with the effect of strong chemical igniters. The interpretation of explosion data measured under turbulent conditions is complicated further because dust concentration may be coupled with the effects of both turbulence and chemical igniters.

In smaller explosion vessels, e.g. the 20-litre vessels used in this work (Appendix B), the effect of chemical igniters is even more significant. When measuring the minimum explosible dust concentration for coal dust in a 20-l vessel, Cashdollar and Chatrathi (1992) found that strong chemical igniters could overdrive the system. Dust burning in the flame of the igniter, with no real propagation beyond the igniter, made it appear as

if tests resulted in an explosion. A 5 kJ igniter by itself produced a pressure rise of about 0.54 barg.

Zhu *et al.* (1988) tested chemical igniters of identical chemical composition and energy, but of different shell design (metal and plastic), in a standardized 20-litre sphere. Blank tests with two igniters (5kJ each) gave approximately 1.5 bar overpressure for both types of igniters, but the time between activation of ignition and the moment when the pressure reached its maximum differed by a factor 6 (5 ms for metal shell, and 30 ms for plastic shell). Tests with two different dusts, aluminium and maize starch (sieved through 37 μm mesh opening, nominal dust concentration 1000 g/m^3) revealed that the effect of the igniters on dust explosion indices was difficult to predict because it varied with both shell design and dust type.

Given the considerable influence chemical igniters can have on flame propagation, and the fact that ignition by chemical igniters is far from the ideal assumption of central point ignition, it is tempting to look for some other ignition source capable of igniting turbulent dust clouds. The main challenge is to produce sufficiently high energy density in a limited well-defined volume at a specified time.

Possible alternatives for a suitable ignition source for turbulent dust suspensions

According to Lüttgens and Wilson (1997), there exist only 13 different types of ignition sources; the same subdivision are used in EN 1127-1 (1997), see Table A-1. This classification may seem arbitrary for several reasons, e.g.:

- i)* *Flames* [2] are *exothermic chemical reactions* [13].
- ii)* *Lightning* [7] is an *electrostatic discharge* [6].
- iii)* *Electrical apparatus* [4] is presented as a separate point, but may include ignition by e.g. *hot surfaces* [1].
- iv)* *Electromagnetic waves/radiation* appears in several categories ([8], [9] and [10]).

Nevertheless, most of the listed ignition sources are not applicable when it comes to igniting turbulent dust clouds inside closed explosion vessels. More relevant are perhaps modifications of some of the *enhanced ignition systems* for spark ignition (SI) engines described by Dale *et al.* (1997), i.e. *composite sparks*, *pulsed lasers*, *plasma jet igniters* or *rail plug igniters*. For ultra-high-speed SI engines, Kumagai and Sakai (1967) explored the possibility of producing a large initial flame kernel by using *triggered spark gaps* or *exploding wires* as ignition source. The exploding wire not only triggers the subsequent arc discharge, but also releases vaporized metal into the flammable mixture.

The approach chosen in this work has been to make a special version of composite sparks, optimised for igniting dust-air suspensions under high-turbulence-intensity conditions. The major part of the energy is released in a DC arc discharge¹.

¹ It has been suggested by von Pidoll (2001) that AC arc discharges may be more efficient ignition sources than DC arc discharges of similar energies.

Table A-1. Classification of ignition sources by EN 1127-1 (1997), and Lüttgens and Wilson (1997).

No.	Ignition Source:	Example:
1	Hot surfaces	Bearing housing, casing of electrical apparatus, exhaust pipe, ...
2	Flames and hot gases	Exhaust gases, autogenous welding, ...
3	Mechanically generated sparks	Abrasive cutting, grinding, impact, ...
4	Electrical apparatus	Electrical sparks at make and break, ...
5	Cathodic corrosion protection, stray electric currents.	Sneak current, short circuit to earth.
6	Static electricity	Spark discharges, brush discharges, propagating brush discharges, cone discharges, ...
7	Lightning	
8	Electromagnetic waves in the frequency range: $9 \text{ kHz} < f < 300 \text{ GHz}$	Induction heating, VHF, UHF, ...
9	Electromagnetic waves in the frequency range: $300 \text{ GHz} < f < 3 \text{ PHz}$	Photoflash, laser, ... (Infrared and visible light)
10	Ionising radiation, i.e. electromagnetic radiation with frequency $f > 3 \text{ PHz}$ and nuclear particles.	UV-rays, X-rays, γ -rays, β -rays, α -rays, ...
11	Ultrasonics, i.e. inaudible acoustic waves: $f > 20 \text{ kHz}$	Ultrasonic cleaning, ultrasonic testing, ...
12	Adiabatic compression, shock waves	Heat of compression, drift wave, ...
13	Chemical reactions	Exothermic chemical reactions, self heating, etc.

A.1.2 Aim of Present Work

The aim of the work described in this appendix has been to make a device that can produce electrical arc discharges capable of igniting most suspensions of combustible dust in air under the high turbulence intensity conditions prevailing in standardized 20-litre dust explosion tests. It should be possible to trigger ignition at a specified time delay after onset of dispersion. The energy should be moderate (~ 10 joules), and its release restricted to a limited time interval (some milliseconds). Finally, the cost per dust explosion test should be low compared to chemical igniters.

A.2 Ignition of Dust Clouds and Premixed Gases by Electrical Discharges

A.2.1 Characteristics of Electrical Discharges in Air

This section is primarily intended to provide a short descriptive introduction to discharge phenomena relevant for spark ignition, i.e. electrical breakdown of short spark gaps in air, and the subsequent glow or arc discharge. Comprehensive treatments of electrical discharges in gases can be found in several books, e.g. Cobine (1941), Meek and Craggs (1953, 1978), Llewellyn-Jones (1957), Penning (1957), Somerville (1959), Raether (1964), von Engel (1965), Beynon (1972), Rees (1973), Howatson (1976), Hirsh and Oskam (1978), Maly (1984), Bazelyan and Raizer (1997), Abdel-Salam *et al.* (2000) and Kuffel *et al.* (2000). Electrostatic discharges are described by e.g. Cross (1987), Lüttgens and Glor (1989), and Lüttgens and Wilson (1997).

Spark

A *spark* can be defined as a disruptive discharge through a single ionisation channel that bridges the gap between two electrodes (e.g. Knowlton, 1949; Lüttgens and Glor, 1998). Loeb (1956) emphasizes the term *spark* refer to the transition mechanism, whereas the term *discharge* applies more specifically to the character of the conducting current mechanism to which the breakdown leads. Sometimes a distinction is made between *electrical sparks* (or *break sparks*) formed by the breaking of a low-voltage high-current circuit, and *electrostatic sparks* formed when charge separation and accumulation creates a sufficiently strong electric field to causes electrical breakdown (Cross, 1987).

Discharge phases

Maly and Vogel (1978) demonstrated that both ignition and the subsequent flame propagation are strongly influenced by the discharge mode and the geometry of the plasma volume, and only to a minor degree by the total energy. Figure A-1 shows the 6 phases of a typical discharge in a technical ignition system for SI engines. Maly (1981) emphasises that the energy actually used in the ignition process is only the fraction transferred to the narrow interface layer at the surface of the plasma, which has a thickness of the order of the flame front. Maly (1984) and Franke (2000) gives a thorough description of the characteristics of each phase, providing representative values of important physical parameters.

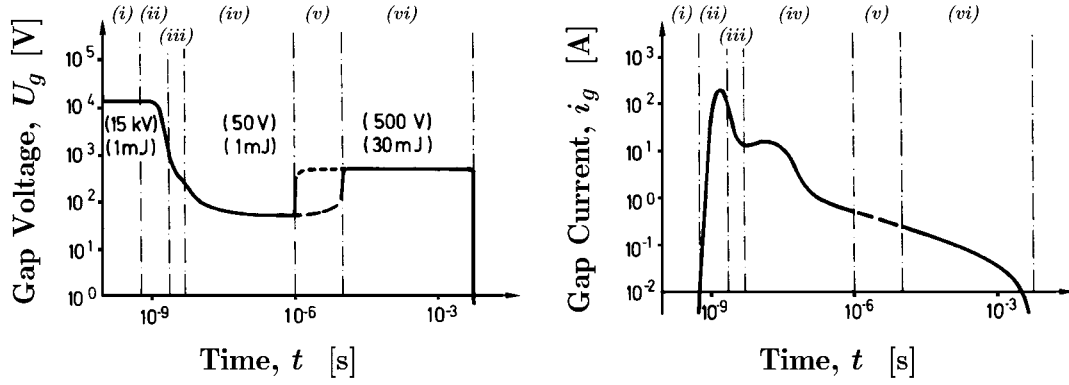


Figure A-1 Schematic diagrams of voltage and current as functions of time during a discharge in a typical technical ignition systems, illustrating the 6 basic discharge phases: (i) pre-discharge, (ii) breakdown, (iii) breakdown/arc transition, (iv) arc, (v) arc/glow transition, and (vi) glow. The actual values depend on the electrical components of the discharge circuit; some typical values are given in parenthesis). From Maly and Vogel (1978).

While referring to Figure A-1, the six discharge phases can briefly be described as follows¹:

- i)* *Pre-breakdown phase.* Initially, the air (or fuel-air mixture) within the electrode gap represents a near perfect insulator². When the spark pulse is applied, producing a rising electric field, free *primary electrons* are accelerated towards the anode. Electrons accelerated by a sufficiently strong electric field ($\sim 50\text{-}100$ kV/cm)³ can ionise neutral gas molecules (*electron collisions*), generating additional *secondary electrons* and ions. Because these initial avalanches are all directed towards the anode, and will extinguish upon arrival, other non-local processes are required to create a conducting channel between the electrodes. Atoms in the gas may become excited to higher states by collisions with electrons of lower energy than the ionisation energy, and when recovering from the excited state (within $\sim 10^{-7}\text{-}10^{-10}$ s) the atom radiates UV radiation ($\lambda < 200\text{nm}$) that can ionise other atoms (*photoionization*). This way the origin of the avalanches can move closer to the cathode. Eventually positive ions are generated sufficiently close to the cathode to be accelerated towards it. When the kinetic energy of the ions exceeds twice the work function of the electrode material, electrons may be liberated from the cathode surface. A positive feedback loop causes the number

¹ When no other reference is provided, numbers in parenthesis in the following summary of the six discharge phases refers to the values provided by Maly (1984) for a 1 mm spark gap in air at atmospheric pressure.

² The conduction in air at low field strength is $\sim 10^{-16}\text{-}10^{-17}$ A/cm², resulting from free electrons generated by cosmic radiation and radioactive substances present in earth and the atmosphere (Kuffel *et al.*, 2000).

³ This field strength is significantly higher than the conventionally quoted breakdown strength for air (30 kV/cm; e.g. Lüttgens and Wilson, 1997), the main reason being the small gap used (Cobine, 1941; Barreto *et al.*, 1974).

of electrons and ions to increase rapidly (*avalanche*), leading to the formation of a leading channel. The pre-breakdown phase last as long as the ionising processes produce fewer electrons than required for rendering the discharge self-sustained – the duration is determined by the rate of rise of gap voltage (a higher over-voltage makes the ionising process more effective). Temperature is practically unchanged, and the mean electron density less than 10^{15} e/cm³, though the density in individual ionising channels (*streamers*) may reach 10^{18} e/cm³. In air an intense N₂ molecule radiation is emitted, atomic radiation is negligible.

- ii) *Breakdown phase.* As soon as enough feedback electrons are produced, the discharge current increases “over-exponentially” (from ~ 10 mA to ~ 200 A in very short time, ~ 1 -10 ns). At the same time, both voltage and electric field strength drops rapidly (from ~ 10 kV to ~ 100 V, and from ~ 30 kV/cm to ~ 1 kV/cm, respectively); hence the term *breakdown*. The impedance of the discharge and the external circuit close to the gap is the only factor limiting the current; there is no inherent current-limiting process. A thin channel (~ 40 μ m) with a slightly higher electrical conductivity develops, carrying more and more of the current flux. The supplied energy is transferred almost without loss to the plasma, being temporarily stored by dissociation and ionisation of the gas molecules inside the channel. Temperature and pressure rises rapidly (to ~ 60000 K and ~ 200 bar, respectively), resulting in the emission of a shock wave. The energy fraction ($\sim 30\%$) carried by the shock wave heats the surrounding gas within a rather small sphere (diameter ~ 1 mm). Due to extremely fast processes, there are almost no losses at all. *Field emission*¹ supplies the electrons, and the cathode remains cold (small heat loss). The energy transfer efficiency of the breakdown phase is high (>80 per cent), it is not affected by flow because of the short duration (flow of 100 m/s moves the channel ~ 1 μ m in 10 ns), but when the energy input is high a fast discharge circuit is required to avoid transition to arc. Larger gaps tend to lengthen the duration of the breakdown phase. Further details on the so-called thermalization process that converts part of the electrical energy stored in the capacitor into thermal energy of the gas can be found in the papers by Barreto *et al.* (1974, 1977), Hill (1975, 1979), Jurenka and Barreto (1982), and Sher *et al.* (1992).
- iii) *Transition region.* Prolonged duration of a high-current flow leads to *thermionic emission*² from hot cathode spots. This indicates the end of the breakdown phase and the start of the arc regime.

¹ Application of a sufficiently strong electric field, in the order of 10^7 - 10^8 V/cm, can cause tunnelling of electrons from the surface of a metal (Kuffel *et al.*, 2000).

² Emission of electrons or ions by substances that are highly heated, the charged particles being called *thermions*. The number of thermions emitted increases rapidly with increased temperature (Kuffel *et al.*, 2000).

- iv) Arc phase.* Electrons emitted from hot *cathode spots* (pools of melted electrode material, 10-40 μm in diameter) are required to sustain the arc, and heavy erosion (evaporation) of the cathode material arises. Material is lost from the electrodes at a more or less regular rate, but often comes off in drops (Cobine, 1941). Arc voltage is very low (~ 50 V), with cathode (~ 15 V) and anode (~ 25 V) falls constituting appreciable fractions of the total voltage drop. Corresponding energy portions are conducted away by the metal electrodes, and considerable losses occur. The equilibrium kernel gas temperature will be limited to ~ 6000 K; electrode temperatures will be close to the melting point of the metal (3410 °C for tungsten). The current may be as high as the impedances of the external circuit permit (from ~ 500 mA to several kA). Only 1 per cent of the particles are ionised, but the degree of dissociation may be quite high in the central region of the discharge. For moderately high currents, the arc phase exhibits a *negative voltage-current characteristic* – similar to the breakdown phase. According to Cobine (1941), the slope of the $U-i$ characteristic flattens out for higher currents (from ~ 40 A), and becomes positive for very high currents ($\sim \text{kA}$). Due to continuous energy losses, temperature and degree of dissociation decrease rapidly with increasing distance from the axis of the discharge channel. The energy transfer efficiency of the arc phase is moderate (~ 30 - 40 per cent), but favoured by flow (up to ~ 50 per cent) because the discharge channel is carried away with the flow and lengthened accordingly. By flow lengthening, the ratio of the plasma voltage to anode/cathode falls rises considerably, and heat losses due to heat conduction to the electrodes drop. Thus, more energy is transferred to the gas, but the energy is distributed over a larger volume.
- v) Arc/glow transition region.* When the cathode fall is building up (the cathode cools down), the glow phase begins. At currents of 100-200 mA, the discharge tends to oscillate between glow and arc. A discharge can be forced into glow mode by deliberately limiting the current from the external circuit.
- vi) Glow phase.* Feedback electrons are liberated from the cathode by *ion impact*. This is very inefficient, and current is less than ~ 100 mA. High cathode fall (~ 400 V), cold cathode, less than 0.01 per cent ionisation, and equilibrium kernel gas temperature ~ 3000 K are typical for the glow discharge. As the cathode-fall region is very close to the cathode surface (< 0.1 mm; or < 1 μm according to Ziegler *et al.*, 1984), almost all the energy input into this layer is conducted into the cathode. As for the arc, the anode fall is approximately equal to the ionisation potential of the gas (~ 15 V). Electrode erosion is due to sputtering but is practically negligible. The glow discharge is very sensitive to flow fields, which can transport the discharge away from the electrodes. For flow velocities up to ~ 15 m/s, the discharge generates enough new electrons and ions to follow the increase in the channel length smoothly (up to ~ 20 gap lengths) and the burning voltage increases proportionally. At higher flow velocities, the channel may attain such a length that the gap voltage rises above the value required for

generating a new spark directly across the electrodes before the energy in the coil has been consumed. This restriking voltage is low ($\sim 2\text{-}3$ kV) since sufficient initial electrons and ions are available at the cathode. Thus the old discharge is interrupted and successive sparks, each starting with a “breakdown” are initiated. The energy transfer efficiency of the glow phase is low ($\sim 5\text{-}10$ per cent), but favoured by flow (up to ~ 30 per cent at ~ 15 m/s).

Any ignition system comprises different combinations of the three discharge modes (breakdown, arc and glow), with individually varying energies and discharge durations. The circuit current is the most decisive factor in controlling the post-breakdown phase: low impedance (e.g. capacitive discharge circuit) favours arc discharge, whereas high impedance (e.g. discharge circuits with series resistance, or inductance) favours glow discharge.

Breakdown voltage and spark gap

Whereas the breakdown voltage U_S of a uniform field is proportional to the product of pressure and gap length for a particular gas and electrode material (*Paschen’s law*), the situation is much more complicated in non-uniform fields where the field strength vary across the gap. Ziegler *et al.* (1984) found that the breakdown voltage for short gaps with thin electrodes where proportional to the square root of the gap length:

$$U_S \sim \sqrt{d_g} \tag{A.1}$$

In non-uniform fields, the streamer mechanism plays an important part, and various luminous and audible *corona discharges* can be observed long before the complete breakdown occurs (Kuffel *et al.*, 2000). The first streamer may lead to breakdown, or it may lead to the establishment of a steady state corona that stabilizes the gap against breakdown. The following non-uniform spark gap configurations are often considered:

- i)* Point anode – point cathode: *point–point gap*
- ii)* Point anode – sphere/plane cathode: *positive corona*
- iii)* Point cathode – sphere/plane anode: *negative corona*

As can be seen from Figure A-2, the static breakdown voltage for a negative corona is generally higher than for a positive corona, but instabilities may occur for very short spark gaps. For an impulse with sufficiently short rise time, the breakdown voltage may be considerably above the static breakdown voltage (Cobine, 1941).

A.2.2 High Voltage Measurement Techniques

General theory of high voltage measurement and laboratory techniques can be found in the books by Craggs and Meek (1954), Schwab (1972), Kind (1978), and Creed (1989). Smith (1993) provides practical guidelines on how to perform high-frequency measurements, and how to deal with noise. An overview of the various methods of generating electric sparks, and considerations concerning measurements relating to electric sparks, are given by Strid (1973).

Methods adopted in this work will be described in section A.3.2. It should be noted that the choice of techniques reflects the financial situation during the early part of the project – the measurement systems were built from scratch by available components, and the performance are far from optimised. However, a few of the most suspect measurements have been checked by commercially available equipment, made available in the final stage of the project.

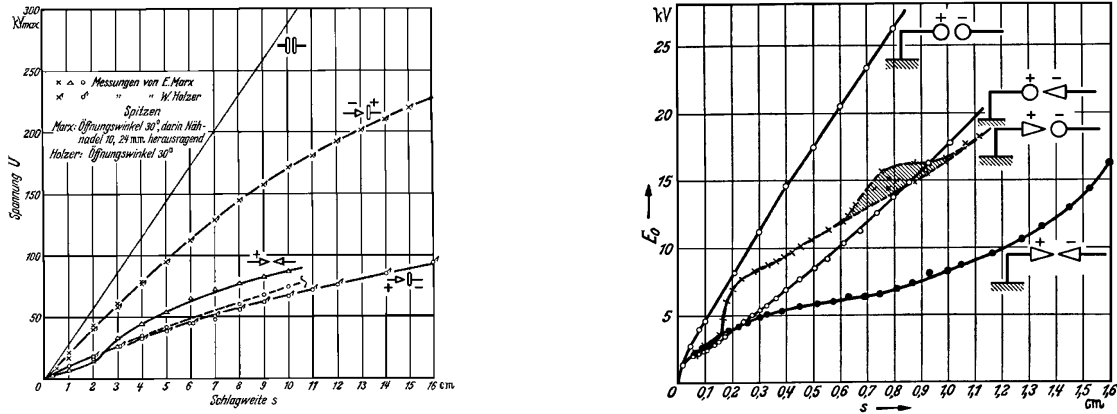


Figure A-2 Static breakdown voltage as a function of gap length and electrode configuration, from Strigel (1955). Very short gap lengths in the right figure are especially relevant for spark ignition, and deserve special attention. Positive corona: Ionisation by electron collision take place in the high field region close to the point, and electrons are readily drawn into the anode due to their high mobility. The positive space charge left behind causes reduction in the field strength close to the anode, and at the same time increase in the field further away. Although this generally favours breakdown ($d_g > 8\text{mm}$), the process can become unstable in short gaps ($1.7\text{mm} < d_g < 8\text{mm}$), resulting in successive quenching and re-ignition of the space discharge. Negative corona: Electrons are repelled into the low field region where they become attached to gas molecules, leaving behind positive space charge. The effect of the resulting space charge distribution is to temporarily terminate ionisation, resulting in pulsed discharges (“Trichel pulses”). Further detail can be found in Kuffel et al. (2000).

A.2.3 Discharge Characteristics Influencing the Ignitability of Flammable Mixtures under Turbulent Conditions

Standardized tests for the determination of minimum ignition energy (MIE) of flammable mixtures are based on spark ignition. Lewis and von Elbe (1987) is the classical reference on spark ignition of flammable gases; Eckhoff (2003) provides an updated account of spark ignition of combustible dust-air suspensions. Although MIE values for dusts are generally higher than for gases, some dusts have been reported to have very low ignition energies¹. Extraordinary complications, and fundamental

¹ MIE values for fine sulphur dust have been reported as low as ~ 0.01 mJ by Bartknecht (1993). Bennett *et al.* (2003) found ignition characteristics for fine sulphur that are similar to ethylene.

contradictions in the experimental requirements, introduce considerable doubt regarding the reliability and relevance of MIE data for dusts (Hertzberg *et al.*, 1984).

The primary aim of this work is reliable ignition, not to explore the limits of ignitability. Nevertheless, valuable information concerning the choice of important discharge parameters can be drawn from work on spark ignition of flammable mixtures under various conditions.

Flame development

The onset of chemical reactions preceding a spark is described by Maly (1984). Chemical reactions (e.g., formation of CN) can be observed a few nanoseconds after spark onset (i.e., during the breakdown phase). These reactions are initiated by the extremely high density of radicals in the breakdown plasma, where all the heavy particles N, O, H, C are present as highly excited atoms and ions. As the kernel temperatures are still much too high to allow stable molecules to exist, these reactions can only take place at the low-temperature end of the plasma surface. However, irrespective of the interior conditions and the expansion velocity of the physical plasma, there will always be a reaction zone at the plasma surface where a sufficient temperature level ($T < 8000\text{K}$) offers ideal conditions for very intense chemical activities. As arc and glow discharges supply heat mainly by heat conduction from the axis, the possible increase in reaction rates is less effective than in breakdown plasmas where radicals carry most of the heat.

At the surface of the plasma channel a layer of highly reactive radicals and atoms is formed at high temperatures, giving rise to a growing *flame kernel*. A few hundred μs after the breakdown the surface temperature is lower than 3000 K (Maly and Vogel, 1978). For this temperature range, the high-temperature chemistry of hydrocarbon combustion applies for the description of the ensuing ignition process (Warnatz *et al.*, 1996). Inflammation from spark ignition is thought to be possible only with formation of a critical flame kernel, or minimum flame sphere to support a combustion temperature. The growth of the flame kernel in spark-ignited propane-air mixtures has been investigated by e.g. Lim *et al.* (1987), Ko *et al.* (1991) and Ishii *et al.* (1992).

Type of discharge

From what has been said in section A.2.1, it is clear that the way in which the total released energy is distributed amongst the three different discharge modes will influence the probability of successful ignition. For a certain electrode configuration (gap length and shape of electrodes), the energy released during the breakdown phase is limited; a certain minimum amount of energy is required to produce a complete breakdown, and transition to arc or glow discharge limits the maximum amount of energy that can be released during the breakdown phase. For a long-duration discharge, the remaining energy has to be released as either an arc or a glow discharge.

According to Ziegler *et al.* (1984), the discharge voltage consists of the cathode fall (U_{CF}), the positive column (U_{PC}), and the anode fall (U_{AF}) – neglecting a small non-uniform part of the positive column. Hence, the total voltage U_g over a gap length d_g is given by:

$$U_g = \frac{U_{CF} + U_{AF}}{U_{fall}} + \left(\frac{\Delta U}{\Delta d} \right) \cdot \frac{d_g}{U_{PC}} \quad (\text{A.2})$$

The voltage gradient $\Delta U/\Delta d$ and the fall voltage U_{fall} can be determined by plotting gap voltage versus gap length. The energy dissipated in the cathode and anode fall is completely lost to the electrodes, whereas the energy of the positive column determines the flame initiation process. The voltage gradients in the positive column, for both glow and arc discharge, can be expressed as a function of the gap current i_g :

$$\frac{\Delta U}{\Delta d} = B \cdot i_g^{-n} \quad (\text{A.3})$$

B and n are empirical constants, determined by discharge type, electrode material, gas, pressure, etc. For a given spark gap, the type of discharge is mainly determined by circuit parameters.

Discharge duration

Duration of electrical discharges influences the minimum ignition energy for both gases and dusts. Considerable work involving composite sparks has been done in relation to lean burning in spark-ignition (SI) engines; e.g. Kono *et al.* (1976, 1984), Maly and Vogel (1978), Maly (1981, 1984), Ishii *et al.* (1992) and Ujiie (1994). It is generally found that composite sparks with high-energy subsequent components show high ignition ability, particularly so for mixtures of high turbulence intensity. Experiments with both quiescent and turbulent gas-air mixtures have verified the existence of the so-called *optimum spark duration*, i.e. the spark duration for which the minimum ignition energy is lowest for a given mixture composition, flow, and electrode configuration (Figure A-3).

For dust clouds, the duration and mode of the electrical discharge has particularly strong influence on the minimum ignition energy. Boyle and Llewellyn (1950) found that the minimum capacitor energy ($E = 0.5 \cdot CU^2$) decreased when a series resistance was introduced in the discharge circuit, in spite of the fact that energy is lost in the resistor. One possible explanation could be that the formation of a flame kernel in a dust cloud relies on relatively slow chemical reactions. The resistance causes an increase in the time constant RC of the discharge circuit and a smaller portion of the energy will be released during the breakdown phase. Line *et al.* (1959) suggested that the blast wave from short duration discharges disturb the dust cloud, creating a dust-free zone around the spark, hence no self-propagating flame kernel can be established. Eckhoff and Enstad (1976) found that the pressure wave from sparks with short discharge times ($\sim 1\mu\text{s}$) could expel particles far beyond the distance at which an object is likely to be ignited by the hot spark channel. The disturbance decreased drastically when the spark discharge time was increased ($\sim 1\text{ms}$).

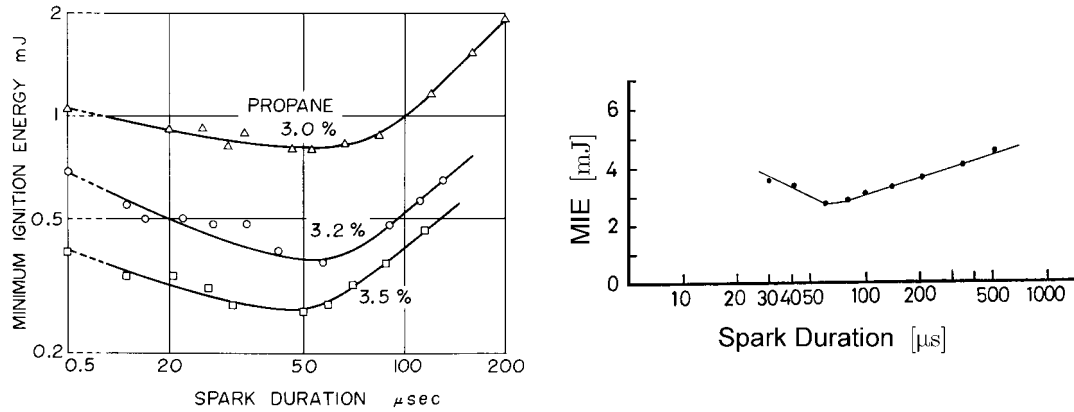


Figure A-3. Effect of spark duration on minimum ignition energy. **Left:** For gap lengths nearly equal to quenching distance in quiescent propane-air mixtures; tungsten electrodes, 30° half-angle cone, diameter 0.3-mm (Kono *et al.*, 1976). **Right:** For *Lycopodium*/air suspension (Matsuda and Naito, 1983).

Spark gap

Several characteristics of the spark gap can influence the ignition process: *gap length*, *electrode diameter*, *electrode configuration* and *electrode material*. This has been investigated by e.g. Swett (1956a, 1956b), Matsuda and Naito (1983), Ziegler *et al.* (1984) and Lewis and von Elbe (1987).

The minimum spark ignition energy is found for an optimum gap length, the *quenching distance*. Increased discharge length beyond the quenching distance increases the ignition energy because the spark plasma volume is unnecessarily large. Large gaps also increase the breakdown voltage; hence less energy can be distributed amongst the other two discharge modes. Gaps shorter than the quenching distance requires higher ignition energy due to heat loss to the electrodes. The quenching distance for dust clouds is generally much larger than those for gas-air mixtures.

Kono *et al.* (1976) found that the electrode configuration can influence the minimum ignition energy of propane-air mixtures, Figure A-3, and suggested that during long duration DC glow discharges the spark kernel is drawn toward the negative electrode by an electrostatic attraction, hence increasing the heat loss. A more precise explanation was suggested by Swett (1956a), and investigated experimentally by Ziegler *et al.* (1984). The energy released in the cathode and anode fall regions is completely lost to the electrodes, and because the cathode fall is considerably higher than the anode fall for a glow discharge, the more efficient heat sink provided by a thick cathode results in higher MIE.

The electrode material is known to influence the electrode fall voltage and the voltage gradient in the positive column, but is usually assumed to have minor influence on minimum ignition energy (see e.g. Ziegler *et al.*, 1984).

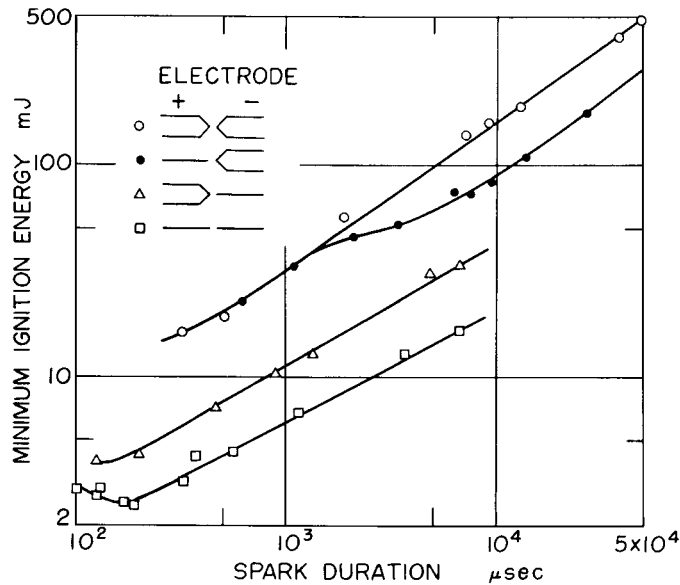


Figure A-4. Effect of spark gap and electrode configuration on minimum ignition energy for various electrode configurations in quiescent propane-air mixture; 3.0 per cent by volume propane, tungsten electrodes (thin electrode: 0.3 mm and 30° half-angle, thick electrode: 3.0 mm and 45° half angle), gap length 1.0 mm (Kono et al., 1976).

Flow conditions and turbulence

Turbulence can make a flammable mixture more difficult to ignite. One of the first documentations of this phenomenon can probably be found in the work by Wheeler (1919) on the influence of turbulence on the burning rate of lean ethane-air mixtures in a 4-litre spherical vessel:

“Strong agitation of a mixture poor in combustible gas renders it difficult to ignite, or, to be precise, renders it difficult for the flame that no doubt occurs during the passage of the discharge to spread away therefrom and travel throughout the mixture. This difficulty increases as the degree of agitation is increased and as the percentage of combustible gas is decreased. When, however, the flame in such an agitated mixture does manage to spread away from the source of ignition it travels rapidly.”

Later work on flammable gases by e.g. Swett (1948, 1949, 1956a, 1956b), de Soete (1971), Ballal and Lefebvre (1974, 1977) and Arkindele *et al.* (1982) has shown that turbulence causes both a narrowing of the flammability limits and an increase in the minimum ignition energy. Figure A-5 shows the increase in minimum ignition energy as a function of turbulence intensity for a propane-air mixture. According to Ishii *et al.* (1992) and Ujiie (1994), adding a subsequent spark to the capacitance one improve the ignition ability (for a given total ignition energy), especially under high-turbulence-intensity conditions (see Figure A-5). Belles and Swett (1957) summarized many aspects of spark ignition related to flight propulsion, emphasizing the inherent physical and chemical limitations in high-speed combustors.

The increase of spark-ignition energy under turbulent flow conditions is mainly contributed to an increase in transport phenomena resulting from turbulent heat diffusivity. According to de Soete (1971) turbulence diffusivity acts in two different manners, both resulting in an increase of ignition energy:

- i) Increased flame front thickness, with corresponding increase in the volume in which the energy is to be released.
- ii) Increased heat dissipation, resulting in a decrease of the efficient fraction of energy available for ignition.

The appearance of long duration discharges may be altered by the flow; Swett (1948) noted that:

“As soon as the spark was established in a moving air stream it began to move downstream as indicated by visual observations and by a rate of current decrease and voltage increase much greater than at zero velocity.” ... “As the velocity was increased the spark moved farther downstream, thereby decreasing the current at a more rapid rate so that the discharge ceased after a shorter time”.

This suggests that the released energy will be distributed over a much larger volume, hence more energy is required to achieve ignition.

Glarner (1983, 1984) and Bartknecht (1993) have shown that turbulence also has a significant effect on the minimum electric spark energies of dust clouds; as can be seen from Figure A-5. The span in minimum ignition energy covers several orders of magnitude as the ignition delay time is varied.

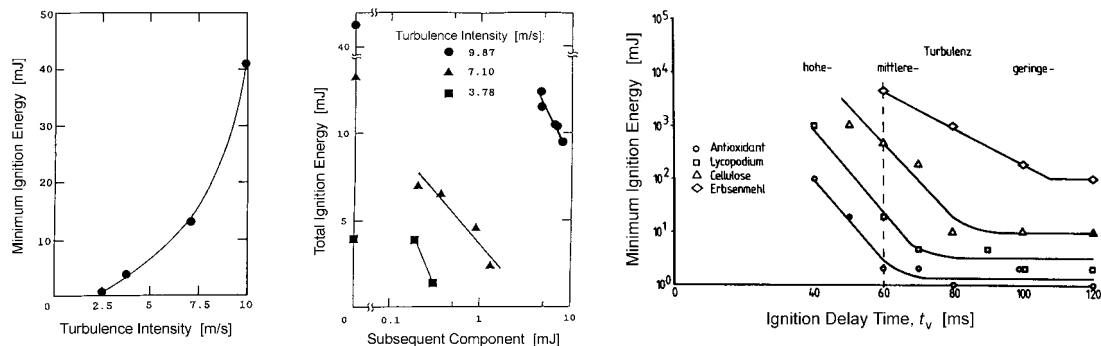


Figure A-5. Minimum ignition energy as a function of turbulence for gases and dusts. **Left:** Exponential increase in the minimum ignition spark energy with increased turbulence intensity, as determined by Ujiie (1994) for 4,7 per cent (by volume) of propane in air. The turbulence was created by mutual collision of injected mixtures in a cylindrical combustion chamber, and ignited by capacitive sparks. **Centre:** Effect of subsequent component on total spark energy under minimum ignition energy conditions (left), from Ujiie (1994). **Right:** Exponential decrease in the minimum ignition spark energy for several dusts with increasing ignition delay time (i.e. decreasing turbulence), from Glarner (1983). The experiments were performed in a 20-l Siwek sphere, and ignited by discharging a bank of capacitors (an inductance of 1.32 mH was included in the discharge circuit).

Influence of particle size on the energy required for igniting a dust cloud

All chemical reactions require the reactants to be mixed on a molecular level. For a dust-air suspension, this implies that there can be no combustion until dust particles reach a temperature where either pyrolysis or evaporation can take place. Theoretically, the minimum ignition energy for spherical particles of uniform size is proportional to the cube of the particle diameter (Kalkert and Schecker; 1979, 1980).

The presence of particles in the spark gap can also reduce the breakdown voltage, the effect is probably most pronounced for conducting particles in homogeneous electric fields (e.g. Cobine, 1941; Dascalescu *et al.*, 1996).

A.2.4 Reliable Spark Ignition of Dust Clouds

From the discussion in section A.2.3 it can be concluded that reliable ignition of combustible dust clouds by an electrical discharge under high-turbulence-intensity conditions will require that the released energy is high, with discharge duration preferably in the order of milliseconds. In this work, this has been achieved by initiating a short-duration arc discharge by a high voltage spark.

A.3 Description of the Arc Generator

The arc generator consists of the following elements:

- The main circuit, will be described in section A.3.1.
- Auxiliary systems, to be described in section A.3.2, including:
 - DC power supply and voltage control system.
 - Triggering system.
 - Circuit protection system.
- The measuring system, will be described in section A.3.3. Procedures for determining the energy and duration of the arc discharges are described in section A.3.4.

The complete circuit diagram for the arc generator is shown in Figure A-6; additional data on the various components can be found in Table A-2, section A.7. A picture of the arc generator is shown in Figure A-7. The whole circuit is built into an aluminium cabinet, situated on top of the ventilated laboratory hood containing the explosion vessel (described in Appendix B).

A.3.1 The Main Circuit

The basic principle of operation of the circuit is to generate a square pulse by discharging a charged *pulse-forming network* through a thyristor. The initial part of the square pulse is passed through a transformer to generate the high voltage necessary to create spark breakdown; the rest of the pulse is redirected through high voltage diodes to sustain an electric arc between the electrodes. Although all the arc energy is supplied by the pulse forming and energy storage network, the circuit has much in common with circuits for *composite sparks*, as described by e.g. Kono *et al.* (1976, 1984), Ziegler *et al.* (1984), Ishii *et al.* (1992) and Ujiie (1994). It also resembles the *CMI Spark Generator*, described by Alvestad (1975) and Eckhoff (1975), used to determine the minimum ignition energy of dust clouds.

Pulse-forming network

A square pulse can be generated by discharging a length of coaxial single-core cable. In practice, the coaxial cable is usually replaced by a *pulse-forming network*, also known as an *artificial transmission line*. The pulse-forming network in this work consists of a series of lumped capacitances and inductances connected as shown in Figure A-8. According to Meek and Craggs (1954), it is found that six or more equal sections of capacitance and inductance are sufficient to give a good approach to the ideal cable condition. The design of the current network was aided by simulations with *AccuSim* (and the *Eldo* simulator) in the *Mentor Graphics* environment, and through

trial and error. A photograph of the actual pulse-forming network is shown in Figure A-8. For further details on pulse-forming networks, refer to Glasoe and Lebacqz (1948).

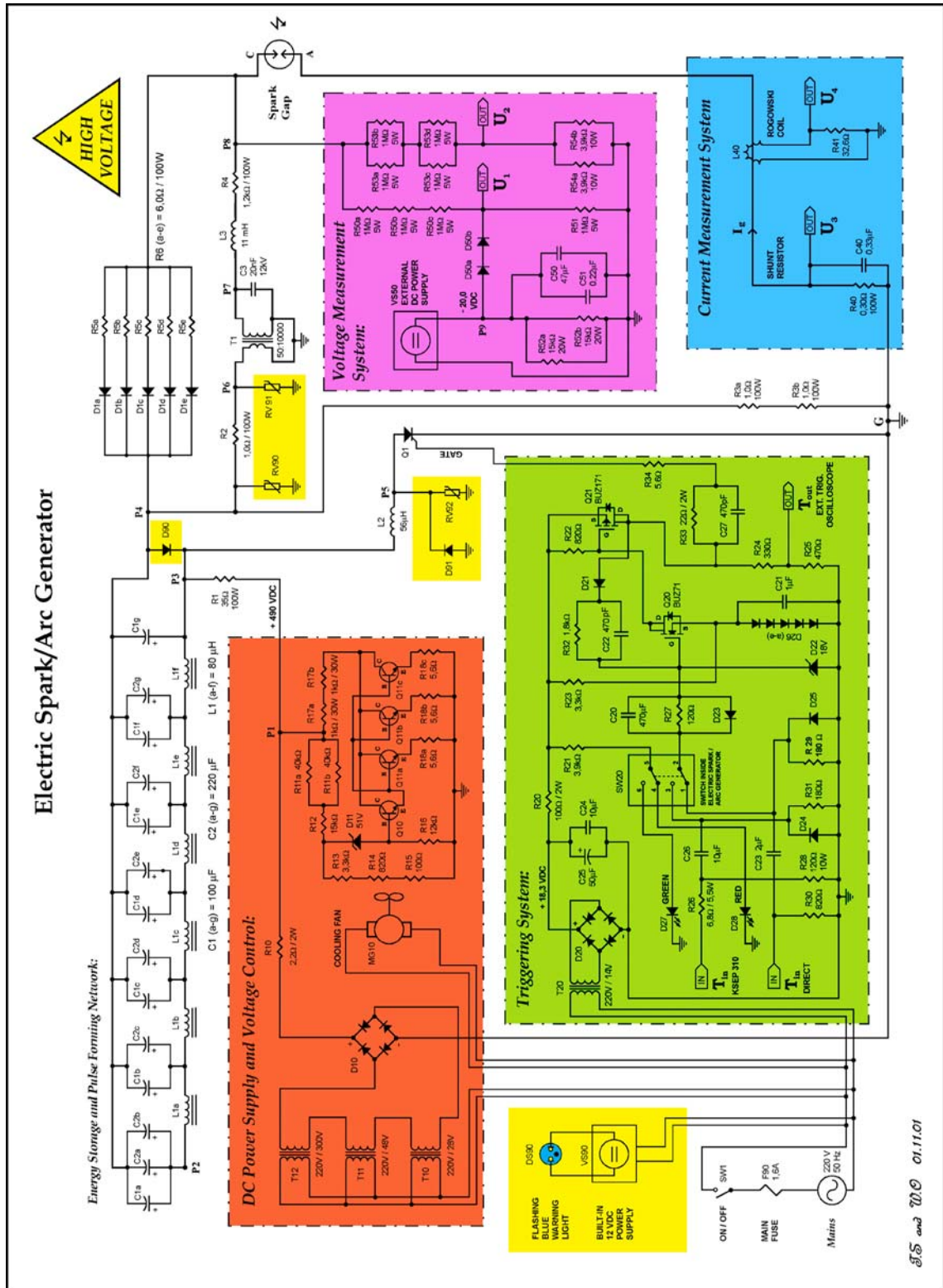


Figure A-6 Complete circuit diagram of the arc generator. Auxiliary and measurement systems have coloured background: dc power supply and voltage control system (red), triggering system for the thyristor (green), current measurement system (blue), voltage measurement system (violet), and circuit protection system (yellow). The components are tabulated in section A.7.

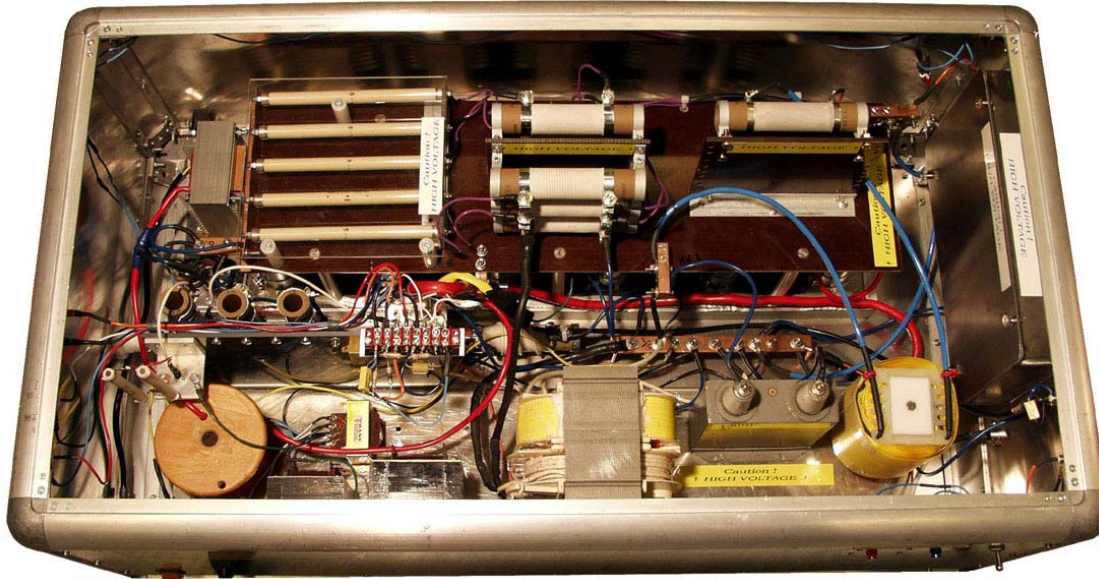


Figure A-7 Arc generator from above, lid removed; dimensions of the cabinet: width 100 cm, depth 55 cm, and height 35 cm.

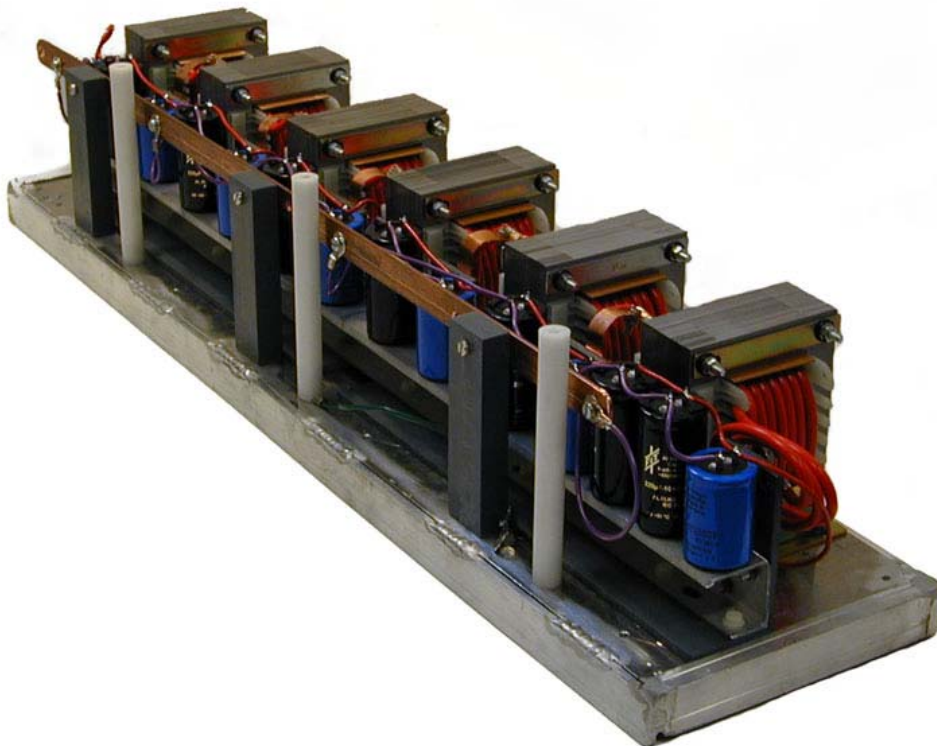


Figure A-8 The energy storage and pulse-forming network used in the arc generator.

Operation of the arc generator

Figure A-9 shows a simplified electrical schematic of the main circuit, including typical sample pulses at various points in the circuit during an electrical discharge. The generation of an electrical discharge passes through the following steps:

- i)* When the switch is turned on, the capacitors in the pulse-forming network are charged through the charging resistor **R1**. The circuit is fully charged and ready to fire after a few seconds (the voltage in **P1**, **P2**, **P3** and **P5** are +490 V).
- ii)* When the thyristor **Q1** is triggered, short circuiting **P5** and ground (**G**), the voltage in **P2** drops to approximately 250 V, and the voltage in **P4** drops to approximately -250 V. These voltage drops lasts for several milliseconds, due to the pulse-forming network.
- iii)* The potential difference between **P6** and **G** introduces a current in the primary windings of the high voltage transformer (**T1**). The induced current in the secondary windings causes a considerable voltage drop in **P7** and **P8**. The voltage continues to drop until breakdown of the spark gap.
- iv)* Breakdown of the spark gap causes the voltage in **P8** to increase rapidly, and a current can flow through the diode **D1** from **P8** to **P4**. This makes it possible to discharge the pulse-forming (and energy-storage) network through the spark gap without having to pass all the energy through the transformer. A stable arc discharge is established between the electrodes, the current is ~100 amperes.
- v)* If turbulent flow should cause the arc to blow out before the pulse-forming network is completely discharged, another breakdown can be initiated through the high voltage transformer. Such consecutive discharges will however contain less energy together than one ordinary discharge, because a considerable part of the stored energy is dissipated in the resistor **R3**.
- vi)* After a test, the switch is turned off. The resistor **R0** provides a leakage path to safely discharge the electrolytic capacitors **C1** (a-g) and **C2** (a-g) when power is removed (in the actual circuit **R0** is a part of the voltage control system).

From time to time, the electrodes should be checked.

Spark gap and electrodes

The spark generator is connected to a spark gap. Both of the two 20-litre explosion vessels used in this work is equipped with spark gaps consisting of two electrode holders with 3.2 millimetre tungsten electrodes, see Figure A-10. The sharp end of the electrodes is ground in a lathe, giving a half-angle cone of 45°. Each pair of newly ground tungsten electrodes can be used for some 20-30 tests.

The tungsten electrodes used are produced by Wolfram Industrie mbH in Traunstein, intended for tungsten inert gas welding (TIG). Electrodes with *red* colour coding (WT 20), which contains between 1.8 and 2.2 per cent thorium oxide (ThO₂) for improves arc starting characteristics, have been used in most of the tests. A few tests with *green* electrodes (WP), i.e. pure tungsten, were made for comparison.

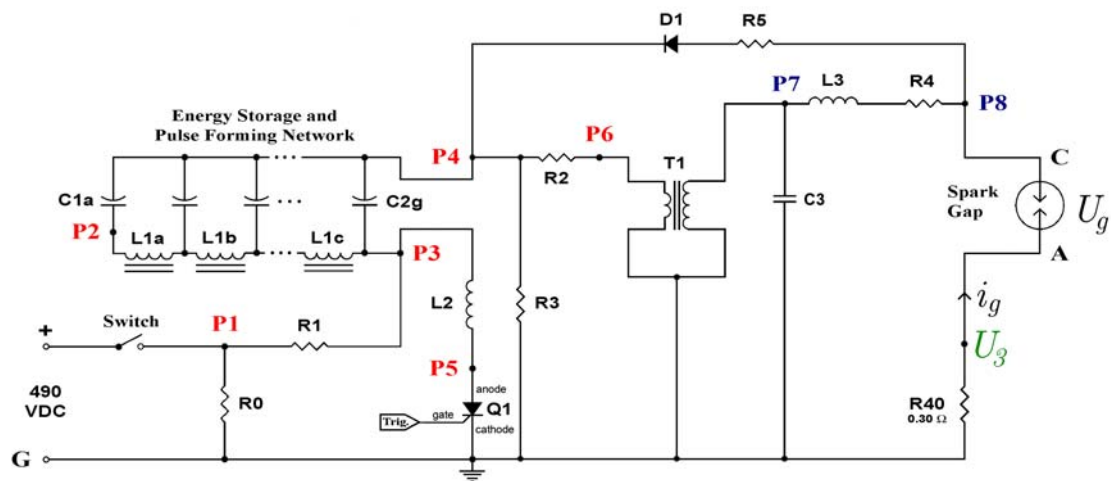
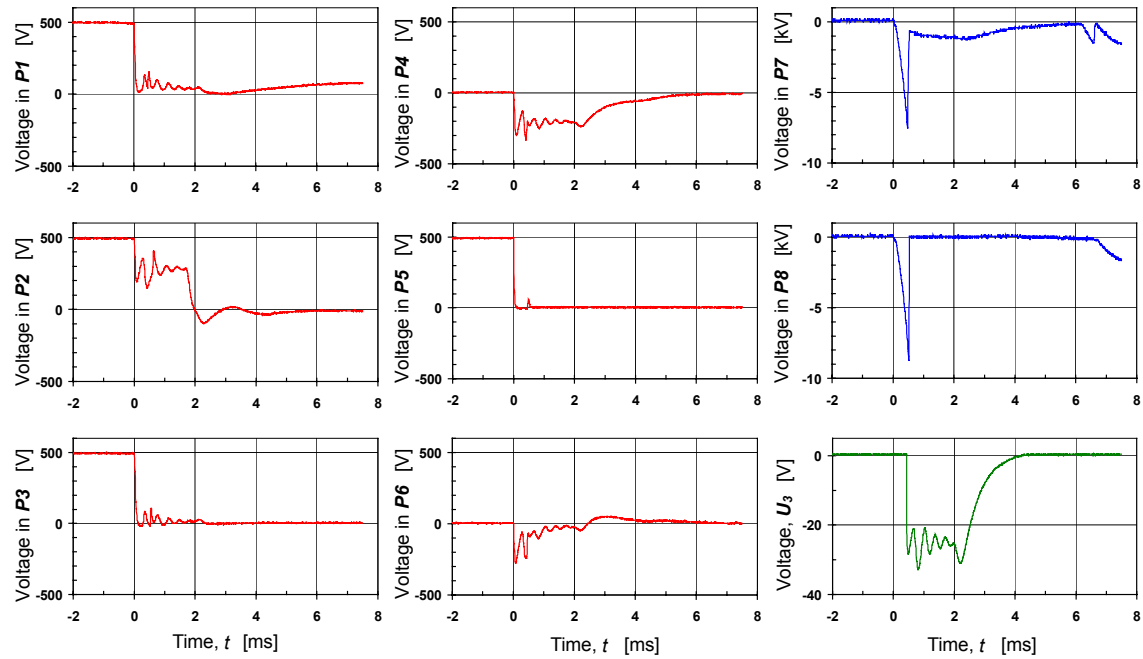


Figure A-9 Simplified electrical schematic of the arc generator, including voltage measurements at various points in the circuit during breakdown, and subsequent arc discharge, over a 3 mm point-to-point spark gap in quiescent air. The pulses are measured with a Tektronix TDS 360 Digital Real-Time Oscilloscope. The voltage in **P1-P6** is measured with a 1:10 voltage divider; the voltage in **P7** and **P8** with the built-in 1:530 voltage divider for measuring breakdown voltage; and U_3 is measured directly. Time is relative to triggering.

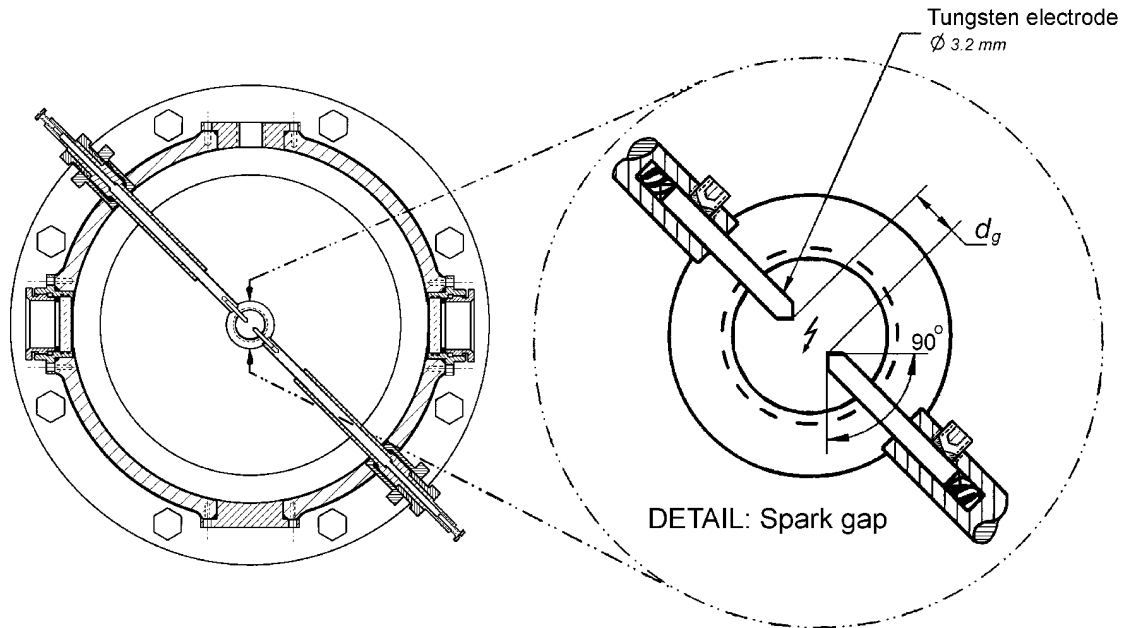


Figure A-10 Horizontal cross section of 20-litre modified USBM vessel, showing electrode holders and spark gap. The cubical vessel has a similar spark gap, see Appendix B. The gap length (d_g) can be varied, but are kept at 3 millimetres in most of the dust explosion tests.

A.3.2 Auxiliary Systems

Auxiliary and measurement systems are shown with coloured background in Figure A-6. The measurement system is described in section A.3.3.

DC power supply and voltage control system

Due to varying mains voltage (220-235 VAC), the resulting rectified voltage (530-570 VDC) from the transformers (**T10**, **T11** and **T12**) and the rectifier bridge (**D10**) had to be stabilized in order to protect the electrolytic capacitors (rated voltage 500 V). When the voltage in **P1** exceeds 490 V, the Zener diode (**D11**) starts to conduct in the blocking direction, triggering the NPN transistor (**Q10**). This triggers the transistors (**Q11**, a-c), allowing current to flow through the dumping resistors (**R17**, a-b), thus lowering the voltage. The stabilized voltage in **P2** is (490 ± 1) V.

Triggering system

The electrical discharge is initiated when the thyristor **Q1** is triggered. A thyristor is a controlled rectifier where the unidirectional current flow from anode to cathode is initiated by a small signal current from gate to cathode.

Reliable operation of a thyristor requires an appropriate gate pulse shape. Immediately after triggering the thyristor, on-state current flows only in the region adjacent to the gate connection. The conducting cross section then spreads quickly to cover the rest of the active area. This time delay imposes a limit on the permissible rate of rise of load current. It is important to provide a trigger pulse large enough and

fast enough to turn the gate on quickly and completely. A trigger circuit should provide pulses that exceed the minimum trigger current (i_{GT}) at least five times. The trigger pulse should have a rate of rise (di_{GT}/dt) of at least 1 A/ μ s, and should last at least 10 μ s (Martin, 1999).

A version of the conventional Schmitt trigger is used to produce suitable trigger pulses for the thyristor. A simplified schematic is shown in Figure A-11. The trigger circuit is capable of transforming slowly changing input signals into sharply defined output signals. The key elements of the switching circuit are two metal oxide semiconductor field effect transistors (MOSFET), one n-channel enhancement mode MOSFET (NMOS) and one p-channel enhancement mode MOSFET (PMOS). The NMOS transistor (**Q20**) is conducting when the gate voltage is positive with respect to the source; the PMOS (**Q21**) transistor is conducting when the gate voltage is negative with respect to the source.

When the gate voltage of **Q21** exceeds a threshold value of 3.1 volts (the forward voltage over the diodes **D26**), current can flow from drain to source. The resulting voltage drop in **T5** makes **Q21** conducting, and a trigger pulse is created at the gate. The process is accelerated by the positive feed back loop from **T6** to **T3** (**D21**, **R32** and the speed-up capacitor **C22**). The purpose of the capacitor **C27** is to compensate for stray capacitance in the thyristor.

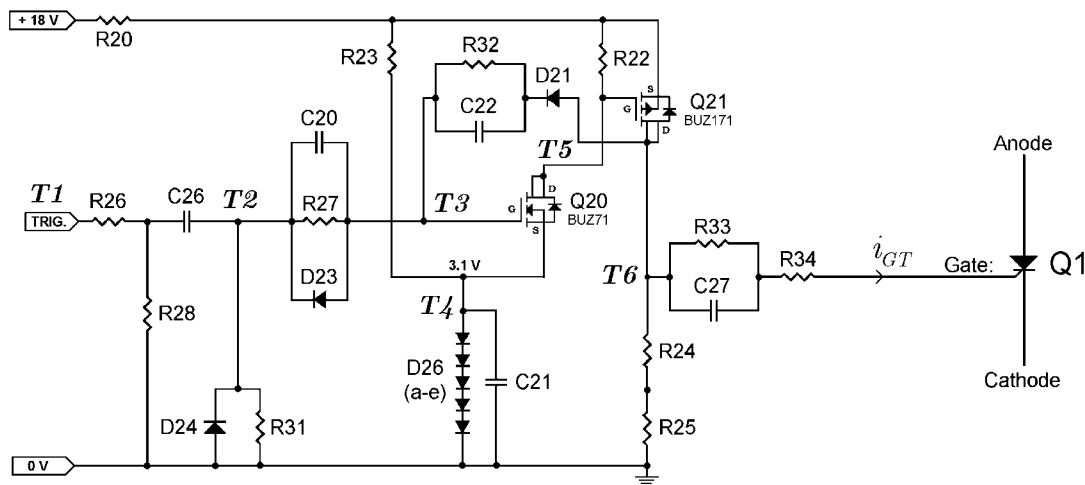


Figure A-11 Principle of triggering system, extracted from the main circuit diagram in Figure A-6.

The device can be triggered by a pulse generator, or the Control Unit KSEP 310 from Adolf Kühner GmbH (see Appendix B). Figure A-12 shows the rate of rise of the gate current provided by this circuit as function of the rise time of the external (incoming) triggering pulse. The rise time $t_{r,in}$ is defined as the time interval required for the signal to rise from 10 to 90 per cent of its maximum value.

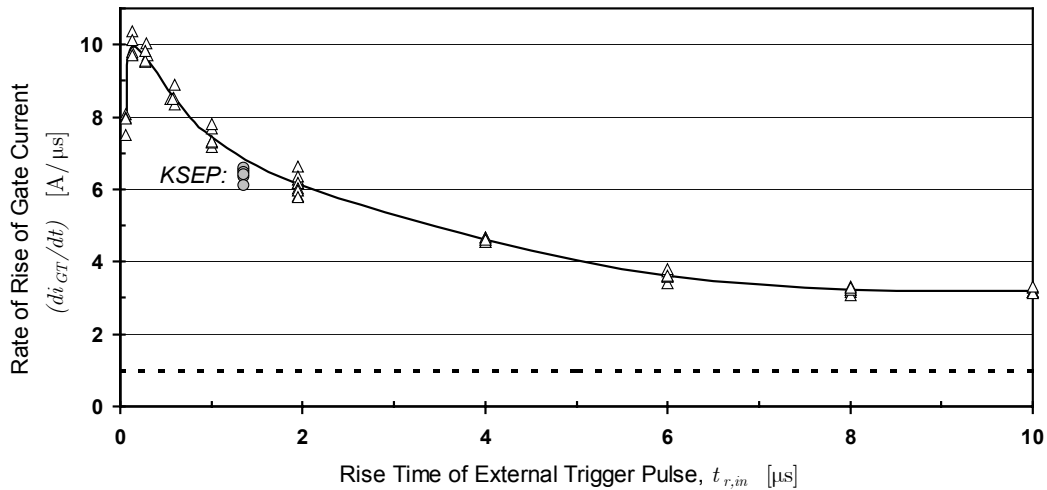


Figure A-12 Rate of rise of gate current as a function of the rise time of the external trigger pulse. The triangular points represents a trigger pulse created with a pulse generator (Phillips, type PM5715); the circular points represents the pulse generated by KSEP 310 (used in all dust explosion tests in this work). The dotted line indicates the recommended minimum value of dI_{Gr}/dt for the thyristor ($1 \text{ A}/\mu\text{s}$).

Circuit protection systems

Several precautions have been taken in order to protect the circuit from destructing loads. Some of the auxiliary systems already mentioned can also be said to have this function. The voltage control system protects the capacitors from being exposed to too high voltage, and provides a safe leakage path for discharging the pulse-forming network when the power is turned off. The triggering system assures reliable triggering of the thyristor, preventing the load current from causing localized burnout near the gate connection.

Several other measures have been taken to prevent damage to the circuit. The main fuse (**F90**) will shut off the voltage supply in case of an internal short circuit. When the switch (**SW1**) is turned on, the strobe light (**DS90**) provides a flashing blue warning light, indicating that the device is ready to fire. The voltage should be switched off immediately after a test, to limit the time the capacitors is exposed to high voltage. The varistors (**RV 90-92**) and diodes (**D 90-91**) prevent high voltage transient pulses originating at the cathode from being transmitted through the entire circuit. The function of the inductor **L2** is to limit the initial current through the thyristor.

A.3.3 Measurement system

The built-in measurement system is primarily intended for estimating breakdown voltage and voltage/current characteristics of the arc discharge. A detailed description of the breakdown phase would require much more sophisticated voltage and current probes. Simultaneous measurements of both the transient breakdown phase (duration ~ 10 ns) and the slowly varying arc phase (duration ~ 4 ms) would also require an additional oscilloscope. However, for the discharges produced by the arc generator, it will be shown in section A.3.4 that only negligible error is introduced by neglecting the energy released during the breakdown and glow phases.

The principle of the built-in current and voltage measurement systems in the arc generator is summarized in Figure A-13. The current and voltage measurement systems had to be calibrated, and some of the data had to be analysed further in order to determine parameters such as arc voltage, released energy, and duration of discharge. All pulses were recorded by a Tektronix TDS 360 Digital Real-Time Oscilloscope; data analysis was done in Excel.

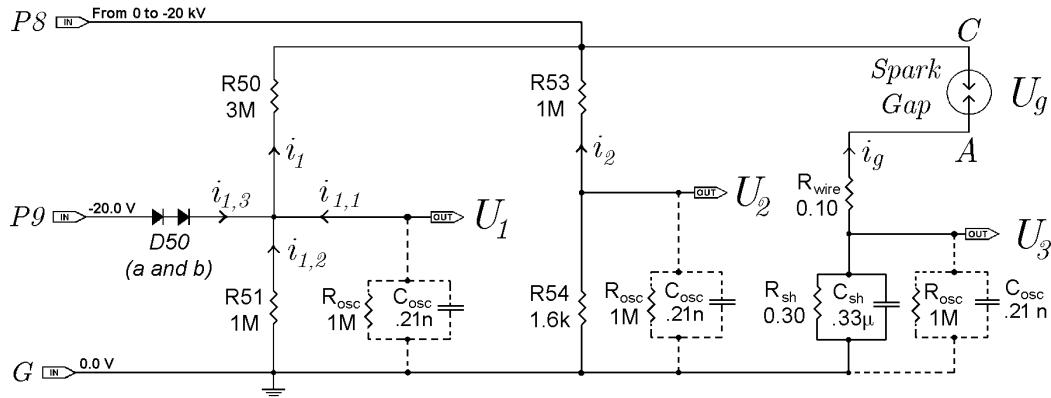


Figure A-13 Principle of current and voltage measurement system. The voltages U_1 , U_2 and U_3 were measured by a digital real-time oscilloscope (Tektronix, TDS 360). The input impedance of the oscilloscope, $1 M\Omega$ ($\pm 1\%$) in parallel with 20 ± 2 pF, is indicated in the schematic. However, the coaxial cables used to connect the outputs from the measurement system to the oscilloscope added some 190 pF to the capacitance.

High voltage measurements

The high voltage at the cathode (U_C) is measured with a 1:530 voltage divider (output U_2 in Figure A-13):

$$U_C(t) = \left(1 + \frac{R_{53}}{R_{54}}\right) \cdot U_2(t) \approx 530 \cdot U_2(t) \quad (\text{A.4})$$

Prior to breakdown there is negligible current passing through the spark gap, e.g. corona, so no correction is necessary for the voltage drop over the shunt resistor. Up to the time of breakdown (t_s), the voltage over the spark gap (U_g) is just the absolute value of the cathode voltage. After breakdown, the voltage drop over the shunt resistor and wires has to be subtracted from the cathode voltage in order to estimate the gap voltage:

$$U_g(t) = \begin{cases} |U_C(t)| & t \leq t_s \\ |U_C(t)| - i_g(t)(R_{wire} + R_{sh}) & t > t_s \end{cases} \quad (\text{A.5})$$

The breakdown voltages (U_S) reported in this work is defined as the maximum of the gap voltage during a single pulse, or the gap voltage at the time of breakdown (t_s):

$$U_S = \max(U_g) = -U_C(t_s) \quad (\text{A.6})$$

Spark gap voltage as a function of time, for several pulses with varying gap length, is plotted in Figure A-14. The fitted curve describing the voltage rise prior to breakdown as a function of time (in milliseconds) is given by:

$$U_g(t)[kV] = \begin{cases} 28.00t^2 + 1.64t + 0.52 & 0 < t < 0.5 \\ 31.29t - 7.29 & 0.5 \leq t < 1 \end{cases} \quad (\text{A.7})$$

The time t_s from the thyristor is triggered until breakdown can be found from current measurements; hence (A.6) makes it possible to estimate the breakdown voltage without occupying one of the a two channel on the oscilloscope. When recording the entire discharge (~ 4 ms) by the digital oscilloscope, the time between each individual measurement is 10 μ s. From (A.7) the rate of rise of gap voltage is 31 kV/ms, hence the resulting uncertainty in the estimated breakdown voltage is:

$$\Delta U_g = \Delta t \cdot \frac{dU_g}{dt} \approx 10\mu s \cdot 31 \frac{kV}{ms} \sim 0.3kV \quad (\text{A.8})$$

The time constant of the 530:1 voltage divider is low (~ 2 μ s) compared with the time between each measurement (10 μ s) when the entire discharge is measured, but much too high to resolve the transient voltage changes during the breakdown phase. This is illustrated in Figure A-15. The considerable overshoot observed for the measurements with the probe is probably due the length of wire (~ 3 meters) from the spark gap to ground. No such overshoot was observed when two such probes was attached directly over the spark gap, see Figure A-16; the capacitance of the probe (3 pF) may however have influenced the measurements. Nevertheless, the duration of the breakdown phase is probably in the order of 10 nanoseconds.

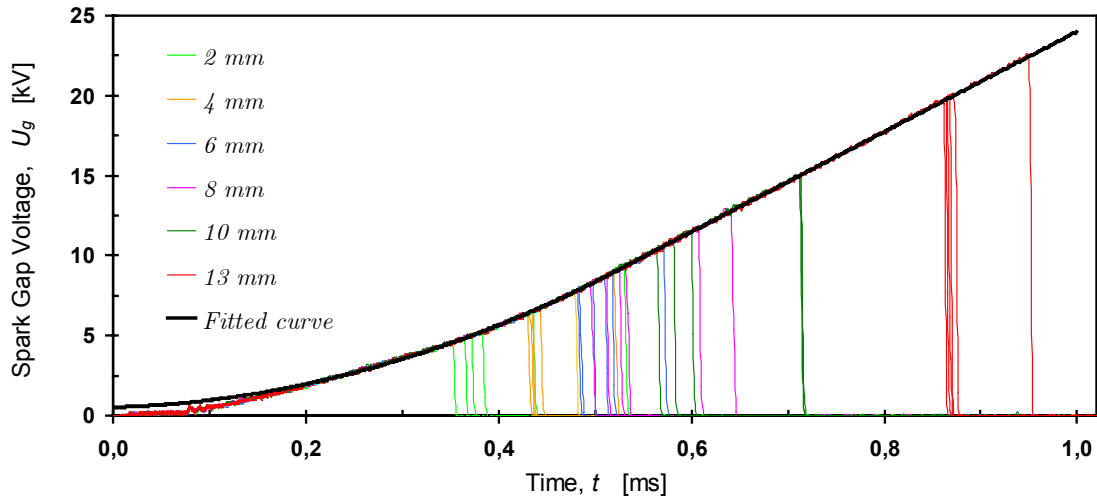


Figure A-14 Absolute value of the voltage over the spark gap as a function of time and gap length, measured with the built-in 530:1 voltage divider. Five tests for each spark gap are included. The fitted curve is described by (A.7).

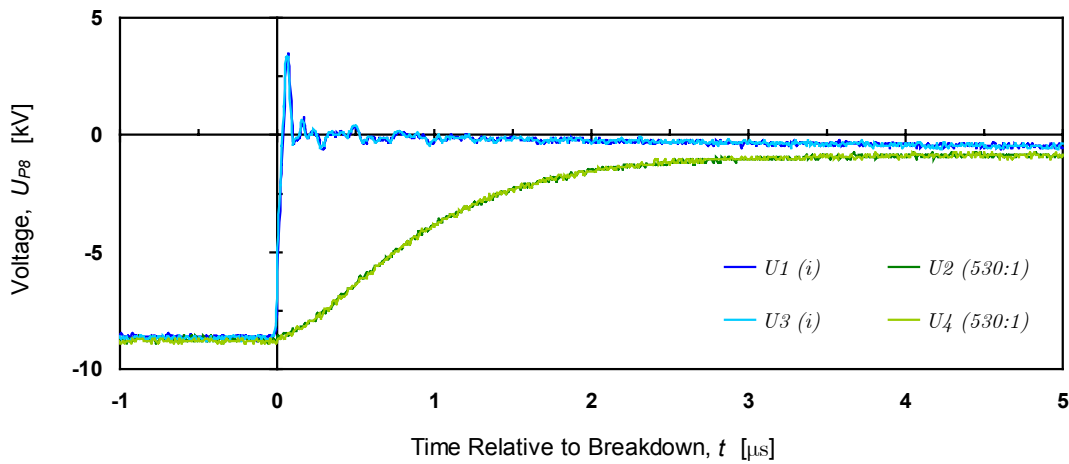


Figure A-15 Voltage in P8 during breakdown phase, measured with both the built-in 530:1 voltage divider (green) and a Tektronix P6015A passive high-voltage probe.

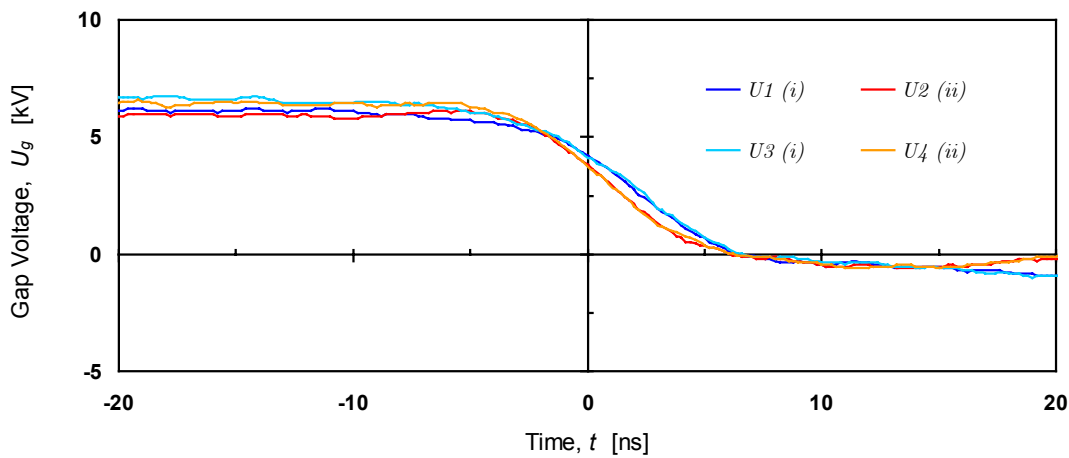


Figure A-16 Voltage measured over a 3 mm spark gap during breakdown, four tests. Two different probes were used: (i) Tektronix P6015A, and (ii) Tektronix P6015 – an older probe.

Arc voltage measurements

Because the breakdown voltage is several orders of magnitude higher than the voltage during the arc phase, $U_2(t)$ from the 530:1 voltage divider could not be used for estimating the arc voltage $U_a(t)$. The resolution in the voltage measurements required for determining the breakdown voltage ($U_s \sim 10$ kV) is typically 100 V, and cannot be used to determine the arc voltage ($U_a \sim 30$ V) with any reasonable accuracy. This is illustrated in Figure A-14. Instead, the measurements were done with a separate voltage divider using clipping diodes biased at a certain voltage, similar to the technique used by Priede (1957). Unfortunately, there are some complications with this method. Additional data analysis is required in order to get accurate results: the considerable time constant for the clipped voltage divider necessitated corrections to the dynamic voltage measurements, a reliable reference level for the voltage measurements had to be found, and the voltage drop over the shunt resistor and wires had to be subtracted from the measured value.

As long as U_i in Figure A-13 is greater than -20 V ($U_C > -140$ V), the two fast-switching diodes **D50** (a and b) is in the non-conducting state, and the resistors **R50**, **R51** and **R_{osc}** form a traditional 7:1 voltage divider. When U_i is less than -20 V ($U_C < -140$ V), the diodes starts to conduct. The forward voltage over the diodes determines the voltage U_i .

$$U_1 = \begin{cases} \frac{1}{7} \cdot U_C & U_C < 150V \\ U_{P9} - 2 \cdot U_F & U_C > 150V \end{cases} \quad (\text{A.9})$$

The clipping diodes made it impossible to use a combined capacitance-resistance voltage divider, as described by e.g. Schwab (1972) or Bazelyan and Raizer (1997), and the measured pulse had to be corrected by numerical methods.

The total resistance of the voltage divider has to be large in order to limit the current i_2 during the high voltage part of the pulse. The built-in capacitance C_{osc} in the oscilloscope and the capacitance in the coaxial cables connecting the oscilloscope to the voltage divider, together with the high resistance in the voltage divider, introduce a rather high time constant ($\tau_a \sim 100$ μ s) for the dynamic voltage measurements. The corrected cathode voltage can be found from U_i with the following corrections (Bentley, 1995):

$$U_C = \left(\frac{R53(R54 + R_{osc})}{R54 \cdot R_{osc}} + 1 \right) \cdot \left(U_1 + \tau_a \frac{dU_1}{dt} \right) \quad (\text{A.10})$$

With the components used in Figure A-13, the amplification constant C_a is equal to 7.0. In order to calibrate the arc measurements, a square pulse from a pulse generator was measured with a voltage divider with very low time constant ($\tau_{ref} \sim 10$ ns), and with the 7:1 voltage divider described in this section. The correction is made according to:

$$U_C = \underbrace{C_a \cdot U_1}_{(I)} + \underbrace{C_a \cdot \tau_a \frac{dU_1}{dt}}_{(II)} \approx U_{ref} \quad (\text{A.11})$$

Results from calibration measurements are shown in Figure A-18. The *measured term (I)* and the *correction term (II)* are plotted separately, and the *corrected pulse (I+II)* is found to agree fairly well with the *reference pulse (U_{ref})*.

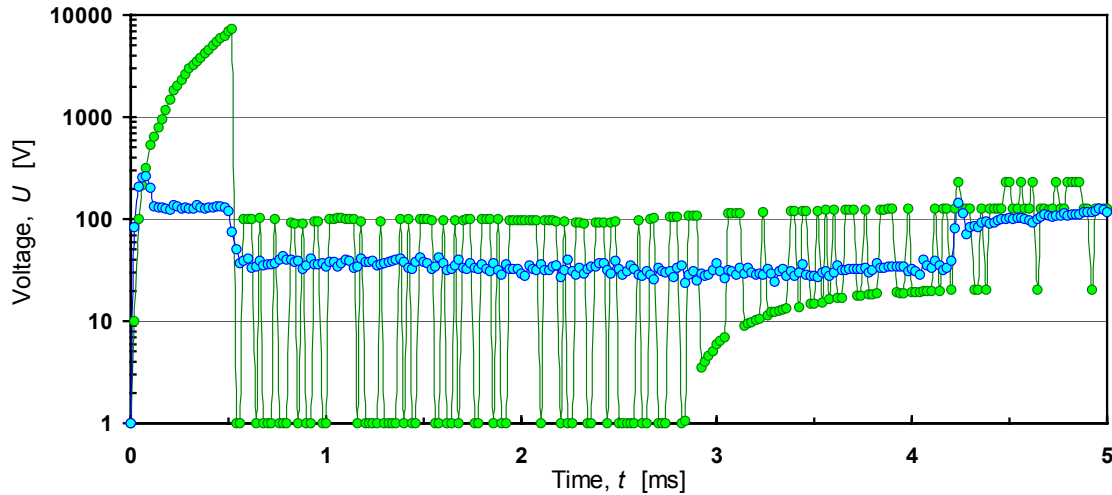


Figure A-17 Gap voltage measurements with the 530:1 voltage divider (green), indicating that these measurements are unsuitable for determining the arc voltage after breakdown. A few negative values have been set to 1 in order to represent the voltage on a logarithmic scale. For comparison the arc voltage measured with the 7:1 voltage divider using clipping diodes is included (blue).

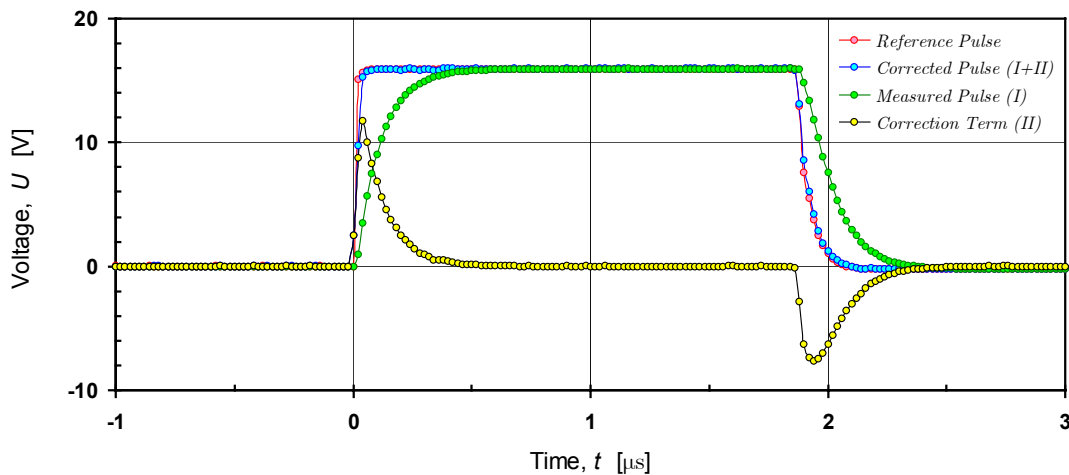


Figure A-18 Calibration of arc voltage measurements. The corrected pulse (blue) is the sum of the measured pulse (green) and the correction term (yellow).

Because the derivative of the measured voltage is included in the correction term in (A.11), and because the resolution of the digital oscilloscope is limited, the measured data had to be smoothed. Smoothing was performed by applying the linear operator described by Shapiro (1970, 1975) to the data. If the 0th estimated value at time t_i is equal to the measured value by definition:

$$\tilde{U}_{1,0}(t_i) \equiv U_1(t_i) \quad (\text{A.12})$$

A general estimate for $U_1(t_i)$ after applying the smoothing operator j times is:

$$\tilde{U}_{1,j}(t_i) = \frac{U_{1,j-1}(t_{i-1}) + 2 \cdot U_{1,j-1}(t_i) + U_{1,j-1}(t_{i+1})}{4} \quad (\text{A.13})$$

Numerical differentiation was done with a three-point formula (Kreyszig, 1979) after applying the smoothing operator 10 times, hence the final estimate for the cathode voltage is:

$$\tilde{U}_C(t_i) = C_a \cdot \left(\tilde{U}_{1,10}(t_i) + \tau_a \frac{\tilde{U}_{1,10}(t_{i+1}) - \tilde{U}_{1,10}(t_{i-1})}{t_{i+1} - t_{i-1}} \right) \quad (\text{A.14})$$

Without any load, the 7:1 voltage divider was significantly influenced by transformer noise. This is illustrated in Figure A-19. In order to find a reliable reference level for the voltage measurements, the value of U_I during the clipping period was estimated from the forward voltage drop over the clipping diodes and the cathode voltage as a function of time (A.7). The relationship between forward current (i_F) and forward voltage (U_F) for the clipping diodes is shown in Figure A-20, the empirical equation ($a_d = 0.0496$, and $b_d = 0.9629$) is:

$$U_F(i_F) = a_d \ln(i_F) + b_d \quad (\text{A.15})$$

Because the voltage in P9 is fixed to -20.0 V, the measured voltage U_I is:

$$U_I = U_{P9} - 2 \cdot U_F(i_F) \quad (\text{A.16})$$

The forward voltage is:

$$\begin{aligned} i_F &= i_{1,3} \\ &= i_1 - i_{1,1} - i_{1,2} \\ &= \frac{U_1 - U_C}{R50} - \frac{U_G - U_1}{R_{osc}} - \frac{U_G - U_1}{R51} \\ &= \underbrace{\frac{-U_C}{R50}}_{(I)} + U_1 \underbrace{\left(\frac{1}{R50} + \frac{1}{R51} + \frac{1}{R_{osc}} \right)}_{(II)} \end{aligned} \quad (\text{A.17})$$

It is impossible to solve (A.17) exactly with respect to i_F since U_I is a function of U_F (A.16), and U_F is a function of i_F (A.15). However, it is possible to find a very good approximation by analysing the variation in the two last terms of (A.17) for typical voltages occurring in the circuit, and with the components specified in Figure A-13. When U_C varies from -1 to -10 KV, the first term (I) varies from 0.3 to 3 mA. During the clipping period U_F is between zero and one volt, consequently U_I will always be in the interval $-20V > U_I > -22V$, and the second term (II) is $(-7.0 \pm 0.3) \mu\text{A}$. The variation in (II) is thus negligible compared to the variation in (I), and can be approximated by a constant value C_{II} (-0.70 mA). By inserting $U_C(t)$ from (A.7), we get:

$$i_F(t) \approx -\frac{U_C(t)}{R50} + C_{II} \quad (\text{A.18})$$

The reference level for U_I that is plotted in Figure A-19 is thus:

$$U_{1,ref}(t) = U_{P9} - 2 \cdot \left(a_d \ln \left(-\frac{U_C(t)}{R50} + C_{II} \right) + b_d \right) \quad (\text{A.19})$$

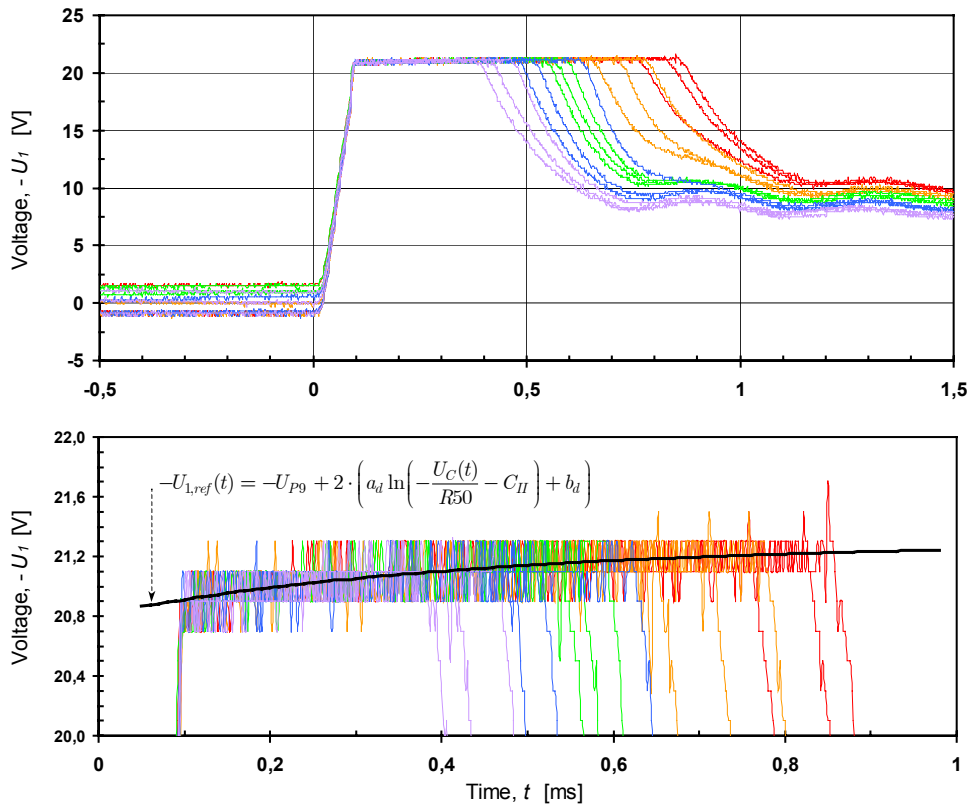


Figure A-19 Measured values of $-U_1(t)$ for several discharges, time relative to triggering. For $t < 0$, the measurements are floating by several volts due to transformer noise etc. After triggering, the voltage increases for about 0.1 milliseconds until the clipping sets in. The voltage is then determined by the forward current through the diodes, until breakdown. During the clipping period, the voltage fits very well to the reference value (black curve); this portion is magnified in the lower figure.

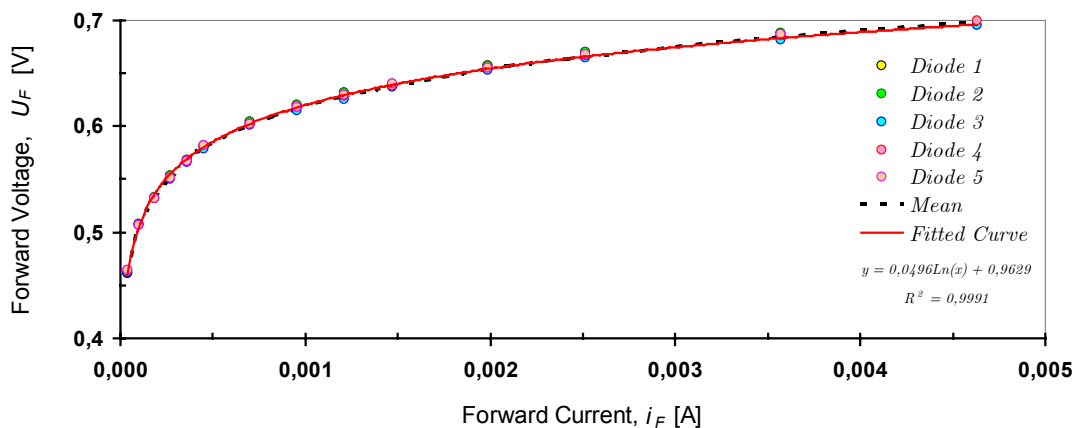


Figure A-20 Forward voltage as a function of forward current for five high-speed diodes (Philips Semiconductors, type 1N4148). The average value and a fitted curve are also included. Two of the diodes were used for clipping in the arc measurement system.

As can be seen in Figure A-19, the measured values are very close to the reference value.

Finally, in order to determine the arc voltage, the voltage drop over the shunt resistor and wires has to be subtracted from the measured cathode voltage.

$$\begin{aligned}
 U_c &= U_g + i_g(R_{wire} + R_{sh}) \\
 &= U_g + U_3\left(\frac{R_{wire}}{R_{sh}} + 1\right) \\
 &\approx U_g + \frac{4}{3}U_3
 \end{aligned}
 \tag{A.20}$$

Setting U_a equal to U_g , and using (A.14) as an estimate for U_c , gives the following expression for the arc voltage:

$$U_a(t_i) = \tilde{U}_c(t_i) - \frac{4}{3}U_3(t_i)
 \tag{A.21}$$

Examples of arc voltage measurements during typical discharge pulses in quiescent air are given in section A.3.4.

Current measurement by shunt resistor

The usual method of measuring transient current pulses is to record the waveform of the voltage developed across a low-resistance shunt by an oscilloscope. The effective impedance of the shunt should be essentially equal to the dc resistance between the tapping-points, and should be constant over the required frequency range (Craggs and Meek, 1954).

The shunt resistor \mathbf{R}_{sh} in Figure A-13 is a $0.30\text{-}\Omega$ wire-wound resistor, with wire wound in the opposite direction to minimize inductance. The current i_g passing through the spark gap is measured by measuring the voltage U_3 over the shunt resistor R_{sh} by a digital oscilloscope:

$$i_g(t_i) = \frac{U_3(t_i)}{R_{sh}}
 \tag{A.22}$$

A capacitor (\mathbf{C}_{sh}) in parallel with the shunt resistor protects the oscilloscope. The impedance of the oscilloscope has negligible effect of the time constant τ_{sh} for the current measurements:

$$\tau_{sh} = R_{sh}C_{sh} \approx 0.30\Omega \cdot 0.33\mu F \sim 0.1\mu s
 \tag{A.23}$$

These measurements are sufficiently fast to describe the arc phase, but cannot be used for the breakdown phase. This is illustrated in Figure A-21. The first two microseconds of the current-pulse measured by the shunt resistance are probably severely distorted due to stray inductance (L_{sh}) in the shunt.

According to e.g. Schwab (1972), the voltage drop across the resistor is the sum of two terms, one resistive (I) and one inductive (II):

$$U_3(t) = \underbrace{R_{sh} \cdot i_g(t)}_I + \underbrace{L_{sh} \frac{di_g(t)}{dt}}_{II}
 \tag{A.24}$$

For the very rapid current variations the inductive component may become many times greater than the resistive component. Other sources of noise are also likely to influence the measurements, e.g. electromagnetic interference and common mode rejection (Smith, 1993).

The error in the discharge energy is magnified by the poor performance of the 530:1 voltage divider, as was shown in Figure A-15. It will be shown in section A.3.4 that the realistic energy release during the first 1-2 microsecond is only a minute fraction of the energy release indicated in Figure A-21.

Examples of current measurements during typical discharge pulses are given in section A.3.4.

Current measurement by Rogowski coil

Attempts were made to measure the initial current by a *Rogowski coil*, i.e. an air-cored coil placed around the conductor carrying the primary current $i(t)$ in a toroidal fashion (Figure A-22). Several single-layer Rogowski coils were made by spinning wire around an 18 mm vacuum hose before bending the hose into a circle; one coil was made from coaxial cable, as described by Murgatroyd *et al.* (1991).

The total magnetic-flux linkage over the whole contour C is then

$$\Psi = \mu_0 n A_t \oint_C \vec{H} \cdot d\vec{l} \quad (\text{A.25})$$

From Ampere's law, the line integral of the flux density (magnetic field) \vec{B} around a closed path C is proportional to the total current that flows through that path:

$$\oint_C \vec{B} \cdot d\vec{l} = \mu_0 \cdot i \quad (\text{A.26})$$

Since there is no magnetic materials present, $\vec{B} = \mu_0 \vec{H}$, and:

$$\Psi(t) = \mu_0 n A_t i(t) \quad (\text{A.27})$$

The electromotive force $\mathcal{E}(t)$ in a loop of wire through which a changing magnetic flux $\Psi(t)$ passes is given by Faraday's law:

$$\mathcal{E}(t) = -\frac{d\Psi(t)}{dt} = -\mu_0 n A_t \frac{di(t)}{dt} \quad (\text{A.28})$$

Introducing the mutual inductance $M = \mu_0 n A_t$ yields:

$$i(t) = -\frac{1}{M} \int_0^t \mathcal{E}(t) dt \quad (\text{A.29})$$

Rogowski coils are linear; an air-cored coil is used to avoid hysteresis and saturation. The only factor limiting linearity is the possibility of electrical breakdown in the winding caused by too high voltage being developed across the ends of the coil (Ramboz, 1996). The major limitation of Rogowski coils is high frequency measurements.

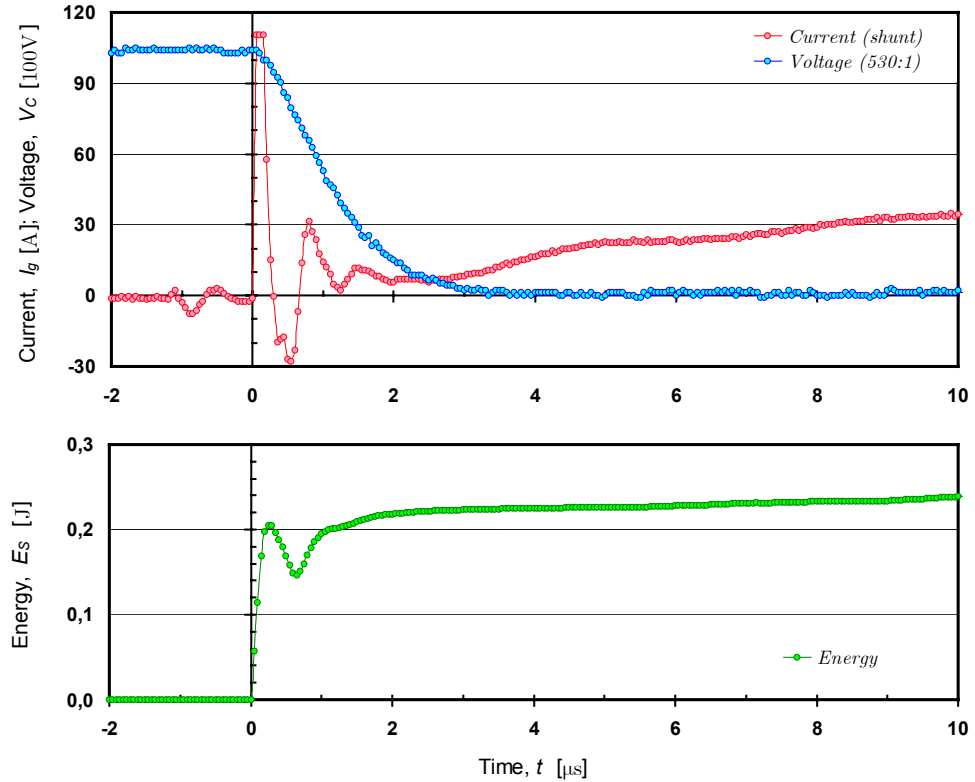


Figure A-21 Gap current and voltage in the initial part of the discharge, measured with the built in shunt resistor and 530:1 voltage divider (above). The resulting energy release, estimated from these voltage and current measurements (below).

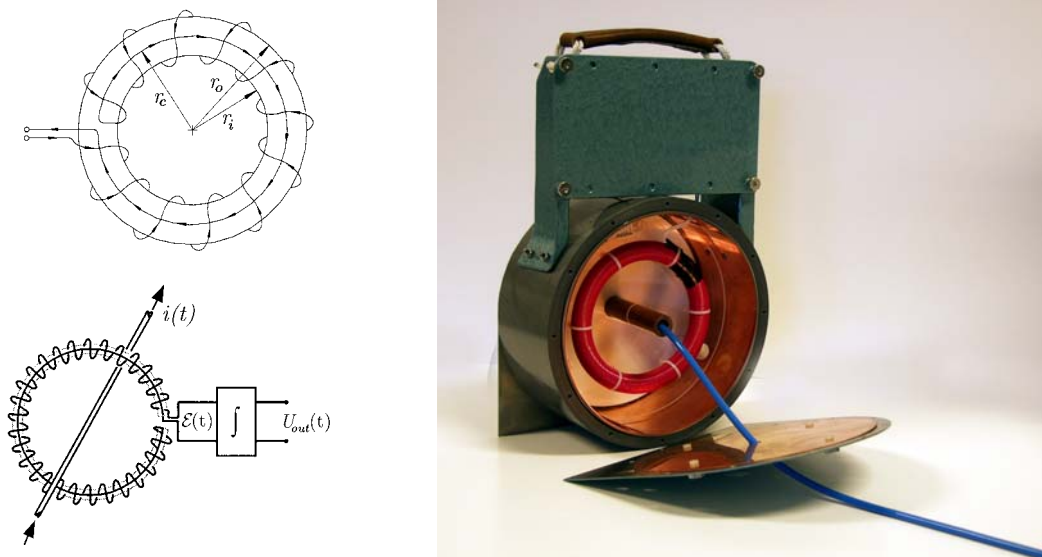


Figure A-22 Schematically drawing (upper left) of a single-layer Rogowski coil with a counter-wound compensation turn (Ramboz, 1996). Schematically representation (lower left) of current measurement with Rogowski coil (Ray and Hewson, 2000). One of the Rogowski coils that has been made and tested in this work (right). The coil is spun on a vacuum hose (dimensions: $r_o - r_i = 18$ mm, and $r_c \approx 62$ mm), and placed inside a Faraday cage. The current to be measured flows in the blue cable (photograph by M. Vabø).

To obtain a measure of the current, the coil's output voltage must be integrated, and then scaled by the reciprocal of the value of mutual inductance (A.29). The integration can be either passive or active, but only passive integration is discussed here. Equivalent circuits for passive integration are shown in Figure A-23.

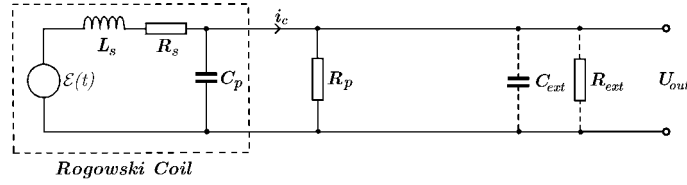


Figure A-23 Equivalent circuit for Rogowski coil and the simple L/R_p integration circuit used in this work. The impedance of the oscilloscope and coaxial cable connecting the coil to the oscilloscope (R_{ext} , C_{ext}) is included for completeness.

By applying Kirchhoff's loop rule to the simple L/R_p integration circuit, we get the following differential equation:

$$L \frac{di_c}{dt} + (R_s + R_p)i_c(t) = \mathcal{E}(t) \quad (\text{A.30})$$

Solving for di_c and integrating with respect to time yields:

$$i_c(t) = \frac{U_{out}(t)}{R_p} = -\frac{R_s + R_p}{L} \int_0^t i_c(t) dt + \frac{1}{L} \int_0^t \mathcal{E}(t) dt \quad (\text{A.31})$$

Thus

$$U_{out}(t) = R_p i_c(t) = -\frac{R_s + R_p}{L} \int_0^t U_{out}(t) dt - \frac{R_p M}{L} i(t) \quad (\text{A.32})$$

Solving for $i(t)$:

$$i(t) = -\left[\frac{L}{R_p M} U_{out}(t) + \frac{L}{R_p M} \cdot \frac{(R_s + R_p)}{L} \int_0^t U_{out}(t) dt \right] \quad (\text{A.33})$$

Introducing the constant k_{rog} :

$$k_{rog} = \frac{L}{R_p M} \quad (\text{A.34})$$

and the time constant τ_{rog} :

$$\tau_{rog} = \frac{L}{R_s + R_p} \quad (\text{A.35})$$

gives the following expression for the current:

$$i(t) = \underbrace{-k_{rog} U_{out}(t)}_{(I)} - \underbrace{k_{rog} \frac{1}{\tau_{rog}} \int_0^t U_{out}(t) dt}_{(II)} = -k_{rog} \left[U_{out}(t) + \frac{1}{\tau_{rog}} \int_0^t U_{out}(t) dt \right] \quad (\text{A.36})$$

Results from the calibration of one of the Rogowski coils are shown in Figure A-25 for a square pulse from a pulse generator. The reference pulse is the current measured over a $5.6\text{-}\Omega$ resistor. The two terms in (A.36), the voltage term (I) and the integrated voltage term (II), are shown separately. The oscillations occur at a frequency of about 7 MHz, corresponding to the resonance frequency:

$$f_{res} = \frac{1}{2\sqrt{LC}} \quad (\text{A.37})$$

Ray and Hewson (2000) analyses this resonance phenomenon in detail. Although the problem is negligible for the calibration pulse in Figure A-24, it escalated when the Rogowski coil was used for measuring the transient spark current. This is illustrated in Figure A-25. Other sources of noise are also likely to influence the measurements, e.g. electromagnetic interference and common mode rejection (Smith, 1993).

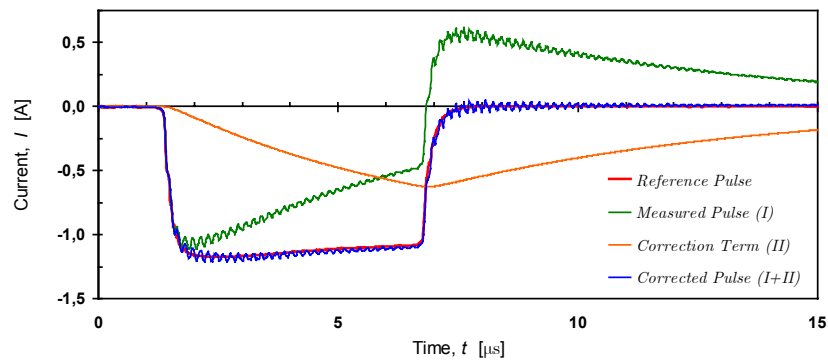


Figure A-24 Calibration of Rogowski coil – the corrected pulse (blue) coincides with the reference pulse (red), except from oscillations at the expected resonance frequency.

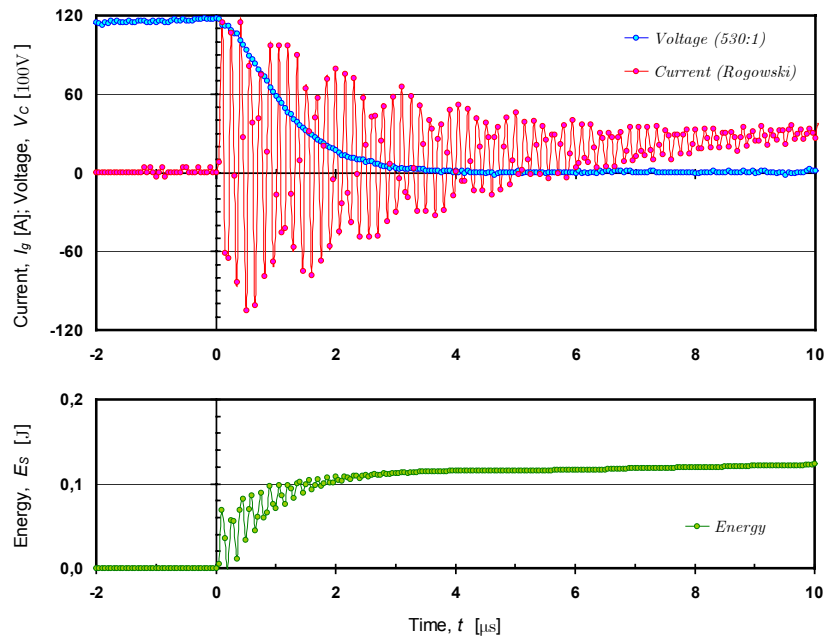


Figure A-25 Gap current and voltage in the initial part of the discharge, measured with Rogowski coil and the 531:1 voltage divider (above). The resulting calculated energy release (below).

A.3.4 Energy and Duration of Discharge

The energy released in the spark gap in the time interval from onset of breakdown (t_s) to the time t is given by the integral:

$$E = \int_{t_s}^t U_g(t) \cdot i_g(t) dt \quad (\text{A.38})$$

The total energy released in each discharge will be assumed equal to the sum of the energy released during each discharge phase: breakdown (E_{bd}), arc (E_a), and glow (E_g):

$$E_{tot} = E_{bd} + E_a + E_g \quad (\text{A.39})$$

Analogous for the duration of the discharge:

$$t_{tot} = t_{bd} + t_a + t_g \quad (\text{A.40})$$

Energy released during the breakdown phase (E_{bd}) – duration of breakdown (t_{bd})

The transient nature of the breakdown phase makes it especially challenging to measure both current and voltage in the initial part of the discharge, and hence to estimate the energy dissipated in the spark gap during this phase. With regards to the first few microseconds of the discharge, the built-in measurement system in the arc generator does not respond fast enough to provide reasonably accurate measurements. This has been illustrated in Figure A-21 and Figure A-25. However, measurements made with better equipment, made available near the end of the project, shows that the energy release in the initial phase is negligible.

The maximum energy released during the breakdown phase is limited by the energy stored in capacitors very close to the spark gap. The capacitance of the spark gap, including wires, has been measured by an *RCL-meter* (Philips, type PM6303):

$$C_g = \begin{cases} \sim 5pF & \text{disconnected from spark/arc generator} \\ 20nF & \text{connected (equal to the high-voltage capacitor } C_3) \end{cases} \quad (\text{A.41})$$

The upper limit for the energy released in the first microseconds is therefore determined by the energy stored in the 20 nF high-voltage capacitor C_3 :

$$E_{bd} \leq \frac{1}{2} C_3 U_{P7}^2 \sim \begin{cases} 0.25 \text{ J} & \text{for } U_S = 5 \text{ kV} \\ 1 \text{ J} & \text{for } U_S = 10 \text{ kV} \\ 2.25 \text{ J} & \text{for } U_S = 15 \text{ kV} \\ 4 \text{ J} & \text{for } U_S = 20 \text{ kV} \end{cases} \quad (\text{A.42})$$

However, the energy stored in the capacitor is discharged through both the air-cored coil **L3** and the resistor **R4**, the resistor alone resulting in a time constant of $R_4 C_3 \approx 24 \mu s$. Consequently, only minute fractions of the energy stored in the high-voltage capacitor can be released during the breakdown phase. Simultaneous measurements of the voltage over the high-voltage capacitor (U7), and over the gap

(US), have confirmed this. As can be seen in Figure A-15, the voltage in **P7** is practically unchanged during the breakdown.

Consequently, the energy released during the breakdown phase can probably be estimated by the energy stored by the gap capacitance C_g :

$$E_{bd} \approx \frac{1}{2} C_g U_{Ps}^2 < \frac{1}{2} \cdot 10pF \cdot (20kV)^2 = 2 \text{ mJ} \quad (\text{A.43})$$

Hence, both the energy and duration of the breakdown phase can safely be neglected when the total energy and duration is estimated.

Energy released during the arc phase (E_a) – arc duration (t_a)

Typical voltage and current measurements during discharges over a 3 mm spark gap in quiescent air are shown in Figure A-27. The power P dissipated in the arc at time t_i is found by multiplying the arc voltage (A.21) with the gap current (A.22):

$$P(t_i) = U_a(t_i) \cdot i_g(t_i) \quad (\text{A.44})$$

The energy released from onset of spark (t_0) to time t_i is then:

$$E(t_i) = \sum_{n=0}^i E(t_i) \quad (\text{A.45})$$

Power and energy release as a function of time for the two discharges in Figure A-27 are shown in Figure A-28. The arc energy E_a will be defined as:

$$E_a = \max\{E(t_i)\} \quad (\text{A.46})$$

The time when the arc phase ends (t_{end}) will be defined as the time when 99 per cent of the energy has been released; because the duration of the breakdown phase is negligible, this will also be used as the *arc duration* t_a :

$$t_{end} \equiv t_i | E(t_i) = 0.99 \cdot E_a \approx t_a \quad (\text{A.47})$$

The end of the arc is indicated in Figure A-27 and Figure A-28.

The *arc voltage* U_a for one particular discharge will be defined as the average arc voltage measured from $t_0 = 10 \mu s$ to $t_N = t_a$:

$$U_a = \frac{1}{\left(\frac{t_N - t_0}{\Delta t}\right)} \cdot \sum_{n=0}^{n=N} U_a(t_i) \quad (\text{A.48})$$

where Δt is the time between each measurement (10 μs). Figure A-29 shows voltage-current characteristic for the two discharges in Figure A-27; the average arc voltage U_a is indicated.

Energy released during the glow phase (E_g) – glow duration (t_g)

When the glow phase sets in, the voltage increases (Figure A-27). This can last for several milliseconds. The current is however very low, less than 100 mA, and the power of the glow discharge is negligible compared to the arc: $P_{arc} \sim 100A \cdot 20V = 2000W$, while $P_{glow} < 100mA \cdot 400V = 40W$.

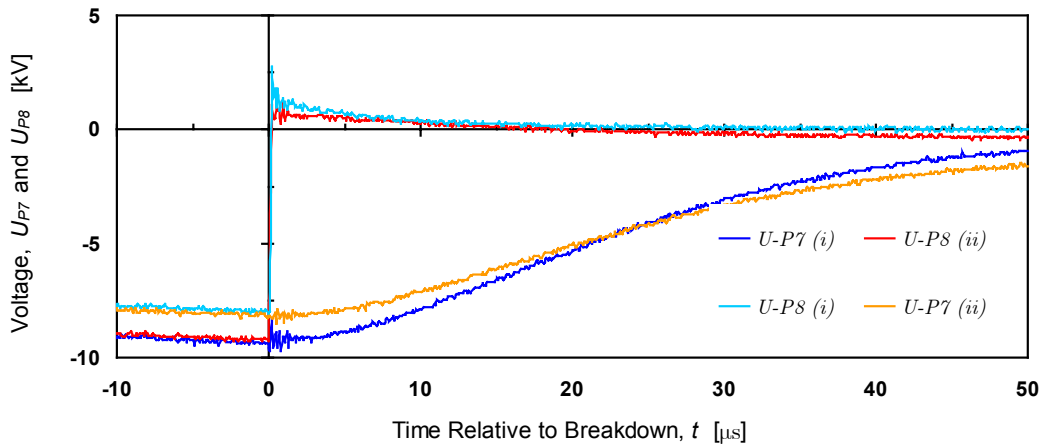


Figure A-26 Voltage at nodes P7 and P8 following a breakdown. The fact that the voltage over the high-voltage capacitor (P7) changes very slowly compared to the voltage over the spark gap (P8) indicates that the capacitor contributes very little to the energy released during the breakdown phase.

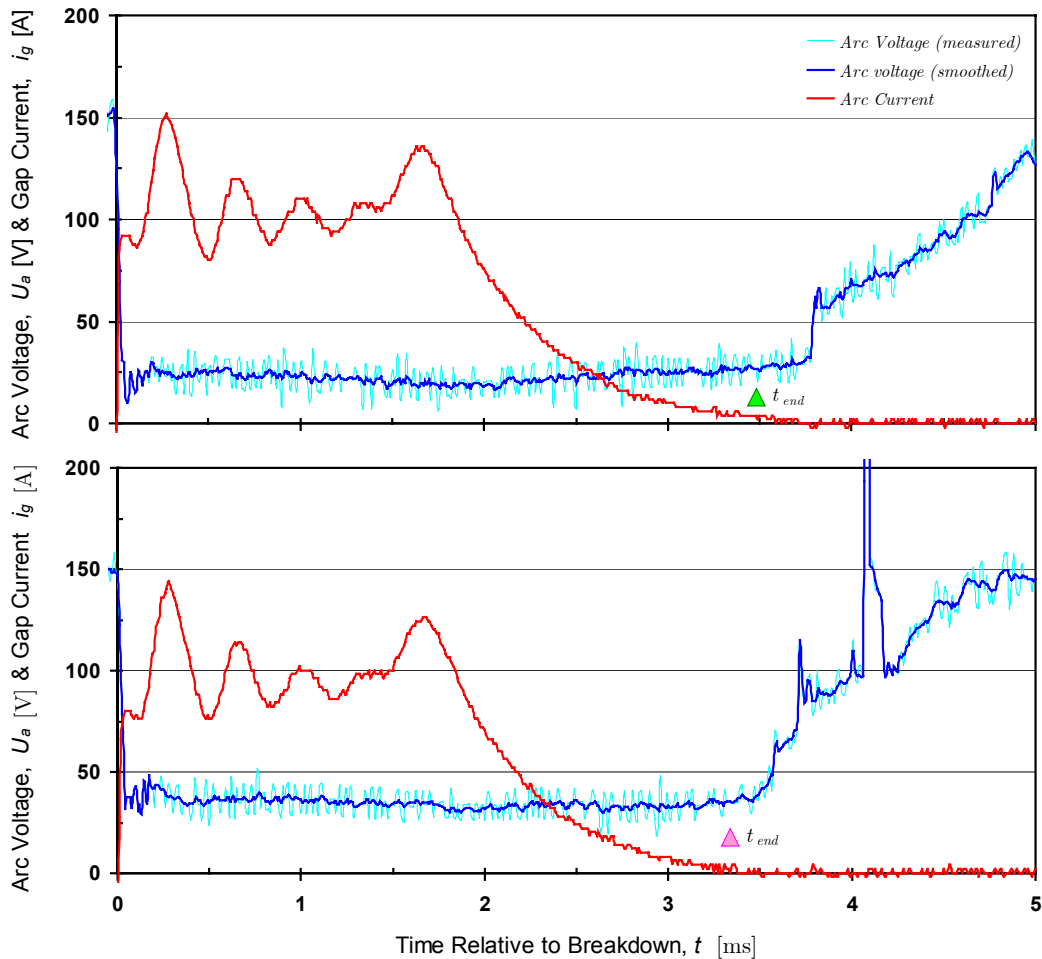


Figure A-27 Arc voltage (blue) and arc current (red) for two typical discharges in quiescent air, gap length: 3 mm (above) and 9 mm (below). The duration of the discharges, defined as the time when 99 per cent of the measured energy has been dissipated, is indicated by pyramids.

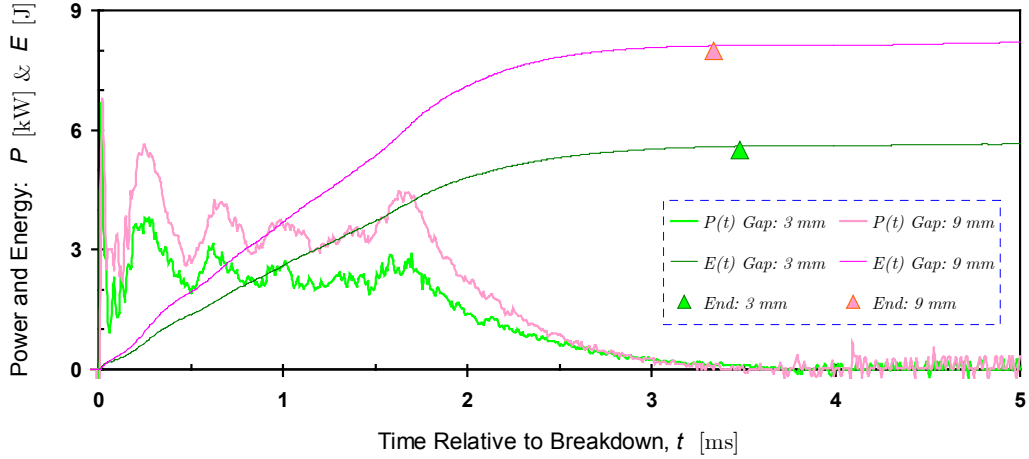


Figure A-28 Power and energy for the two arc discharges in Figure A-27. The duration of the discharges, defined as the time when 99 per cent of the measured energy has been dissipated, is indicated by pyramids.

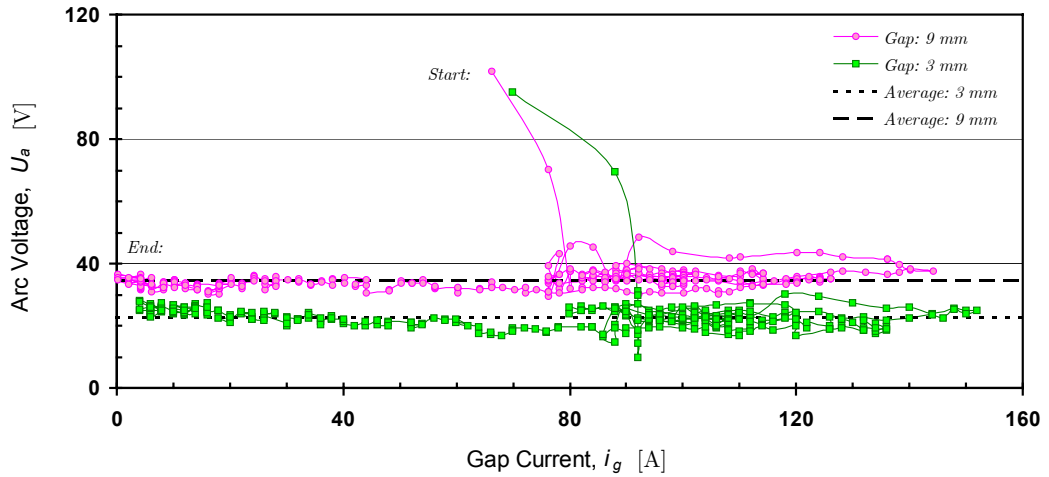


Figure A-29 Voltage-current characteristic for the two discharges in Figure A-27. The average arc voltage U_a is indicated for both discharges.

Since the glow phase follows the arc phase, it is highly unlikely that it will be able to ignite a combustible mixture that has not already been ignited by the arc. Consequently, when considering the energy and duration of the entire discharge, the glow phase can be neglected.

Discharge characteristics

The following discharge characteristics will be reported in this work:

- Breakdown Voltage (U_S), from (A.6),
- Arc Voltage (U_a), from (A.48),
- Arc Duration (t_a), from (A.47), and
- Arc Energy (E_a), from (A.46).

For discharges in quiescent air, the effect of gap length and electrode configuration will be explored.

A.4 Experiments with the Arc Generator

The experiments are subdivided into two main groups: experiments that describe the electrical discharge it selves, and experiments that explore the incendiary capabilities of the arc discharges relative to those of chemical igniters. Experimental results and discussion are given in A.5.

A.4.1 Electrical Discharge Experiments

The characteristics of electrical discharges produced by the arc generator have been measured as described in sections A.3.3 and A.3.4. In most of the tests, the spark gap and electrode configuration were arranged as described in section A.3.1, i.e. point-point gap with 3.2 millimetre tungsten electrodes doped with thorium oxide. All measurements were done with the same oscilloscope (Tektronix TDS 360, Digital Real-Time Oscilloscope, 200 MHz); calculations were done with a spreadsheet (Microsoft Excel).

The general approach for characterizing the electrical discharges consists of three steps:

- i)* Discharge characteristics are determined for various gap lengths in quiescent air.
- ii)* For one selected gap length, discharge characteristics are determined for various ignition delay times.
- iii)* For one selected gap length and one selected ignition delay time, discharge characteristics are determined for various nominal concentrations of selected dusts.

The results are presented and discussed in section A.5.1.

Electrical discharges in quiescent air

The effect of gap length on discharge characteristics was investigated for point-point gaps; the following gap lengths were used: 1, 2, 3, 4, 5, 6, 7, 8 and 10 millimetres. For each gap length, 12 consecutive tests were done with each pair of electrodes (starting with newly ground electrodes). Although the spread in experimental data will increase due to electrode wear, this method is more realistic with respect to the intended use of the arc generator.

A similar series of test with point-point gaps of pure tungsten electrodes were made in order to investigate the effect of electrode material. Only the breakdown voltage was measured, and there were only six tests with each pair of electrodes.

In order to demonstrate how other gap configurations influence the breakdown voltage, some additional measurements with other electrode configurations were performed. Both 8 and 16 mm copper spheres were used as electrodes. In these

experiments only newly ground tungsten electrodes were used in each shot, and the copper spheres were polished for every shot.

Electrical discharges in turbulent air flow

The effect of ignition delay time (t_v) on discharge characteristics was investigated for 3-millimetre gap length. For each ignition delay time, 12 consecutive tests were done with each pair of electrodes (starting with newly ground electrodes). The dispersion was performed as described in Chapter 3.

Electrical discharges in turbulent dust-air suspensions

The effect of nominal dust concentration (c_{nom}) for various dust types on discharge characteristics was investigated for 3-millimetre gap length. The measurements were done during real dust explosion tests with ignition delay time 60 milliseconds.

A.4.2 Dust Explosion Experiments

The incendiary capabilities of the electrical discharges produced by the arc generator have been investigated, and the effects of the arc on dust explosion characteristics are compared to those of chemical igniters. The tests included in this appendix are restricted to a few selected dusts: niacin amide, *Lycopodium casuarinoides*, and various fractions of jet-milled silicon (Silgrain). Data for the various dusts can be found in Appendix C, including SEM pictures and particle size distributions. All tests were done with the rebound nozzle in one or both of the two 20-litre explosion vessels described in Appendix B: the modified USBM vessel and the cubical vessel. Turbulent dust-air suspensions were ignited by either two chemical igniters from Sobbe (5 kJ each), or an electrical discharge from the arc generator (3-millimetre spark gap). Detailed experimental procedures for dust explosion tests are outlined in Chapter 3.

The results are presented and discussed in section A.5.2.

Chemical igniters

A few blind tests were done without dust, just two 5 kJ chemical igniters. The ignition delay times were 60 milliseconds in all these tests. Unfortunately, only a limited number of chemical igniters could be afforded – and most of them were used to ignite the niacin amide dust. However, a few tests were done with spores of *L. casuarinoides* and jet-milled silicon.

Niacin amide

The niacin amide (or pyridine 3-carboxamide) used in this work was the dust chosen by Kühner for the Round-Robin test CaRo 00/01 (Cesana, 2001). Explosion indices for niacin amide have been determined in both explosion vessels – with both chemical igniters and electrical discharges as ignition source – over a wide range of concentrations.

Spores of *Lycopodium casuarinoides*

In a few tests, suspensions of *Lycopodium casuarinoides* spores in air were ignited by chemical igniters for two different ignition delay times: 60 and 300 milliseconds. Results from these tests are compared with data presented in the main part of this thesis for spark-ignited suspensions.

Jet-milled silicon

In order to illustrate the ignition capabilities of the electrical discharges compared to those of chemical igniters, various fractions of jet-milled silicon from Elkem Bremanger were ignited by both ignition sources. For all tests, nominal dust concentration and ignition delay time were 500 g/m³ and 60 milliseconds respectively.

Poly methyl methacrylate (PMMA) and RDX

Some tests with PMMA and RDX were performed in the modified USBM vessel. These tests clearly illustrate the limitations of the electrical discharges as a reliable ignition source.

A.5 Experimental Results and Discussion

A.5.1 Characteristics of the Electrical Discharges

Electrical discharges in quiescent air

The effect of gap length on discharge characteristics for 12 consecutive tests with the same electrodes is shown in Figure A-30. Measurements of voltage and current during typical discharges in quiescent air have been shown in Figure A-27 and Figure A-29.

The increase in breakdown voltage is approximately linear for the investigated gap lengths in Figure A-30. The breakdown voltage for point-point gaps in Figure A-31 is closer in agreement with the data from Strigel (1955), presented in Figure A-1. The breakdown voltages found in this work is somewhat higher than those reported by Strigel, as would be expected since he used sharper electrodes, and measured the static break voltage. The spread in breakdown data is considerable compared to the other discharge characteristics in Figure A-30. This is probably partly due to electrode wear, and partly because of the impulse character of the load.

Although some of the electrode configurations represented in Figure A-31 have little relevance for the work on dust explosions presented in this thesis, it is interesting to note the resemblance with the data from Strigel (1955) in Figure A-1. The breakdown voltage is considerably higher for sphere-sphere gaps than for other electrode configurations, and the high spread in values even for polished copper spheres indicate that the impulse character of the load may be a main factor influencing the results.

The effect of gap length on breakdown voltage for two different types of tungsten electrodes is shown in Figure A-32. Although the spread in data is considerable and the number of tests low, the figure indicates a somewhat higher average breakdown voltage for pure tungsten electrodes compared to the electrodes doped with thorium oxide. This is expected – according to the producer (Wolfram Industrie mbH) the main reasons for using thorium-doped welding electrodes is superior striking characteristics compared to pure tungsten, and that oxide particles counteract the formation of coarse grains at the hot electrode tip (thus reducing electrode consumption).

The increase in arc voltage with increasing gap length is consistent with the model suggested by Ziegler *et al.* (1984). If the linear trend-line in Figure A-30 is compared with (A.2), one finds a combined electrode fall (U_{fall}) of 20.4 V and a voltage gradient of the positive column ($\Delta U/\Delta d$) of 2.2 V/mm. These results are in good agreement with results on welding-arcs presented by Cobine (1941).

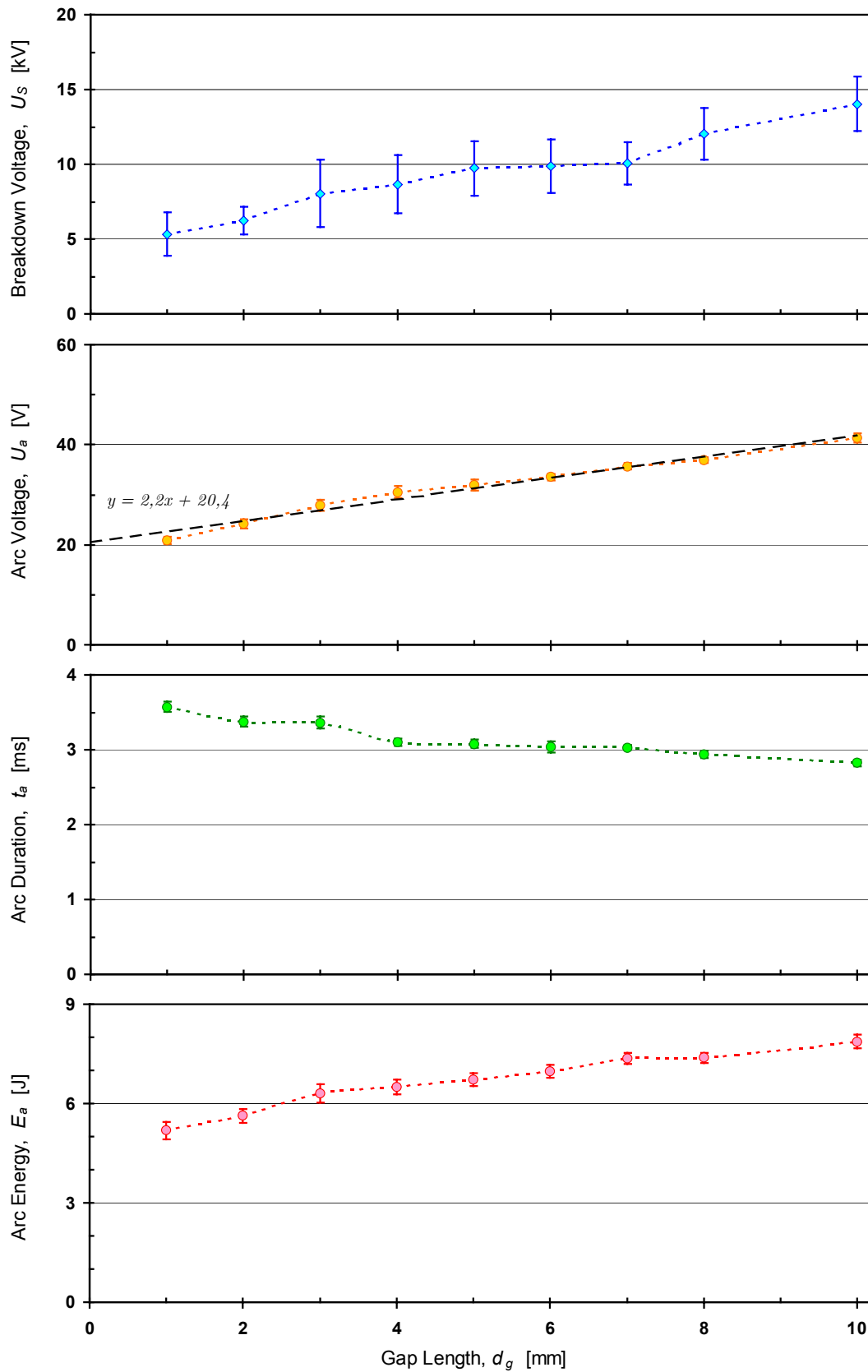


Figure A-30 The effect of gap length on discharge characteristics, tests in quiescent air. Each data point represents the mean value of 12 consecutive discharges, starting with newly ground electrodes. Error bars indicate one standard deviation above, and one standard deviation below, mean.

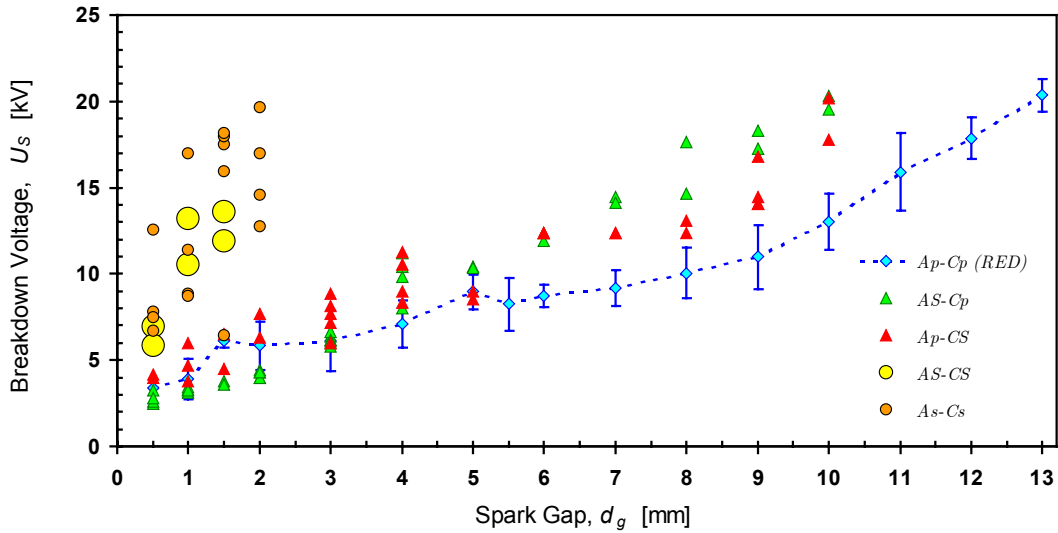


Figure A-31 Breakdown voltage for various spark gap configurations. Only newly ground or polished electrodes were used. The legend uses the following abbreviations: A=anode, C=cathode, p=point electrode (45°, tungsten), S=ϕ16mm copper sphere, s=ϕ8mm copper sphere.

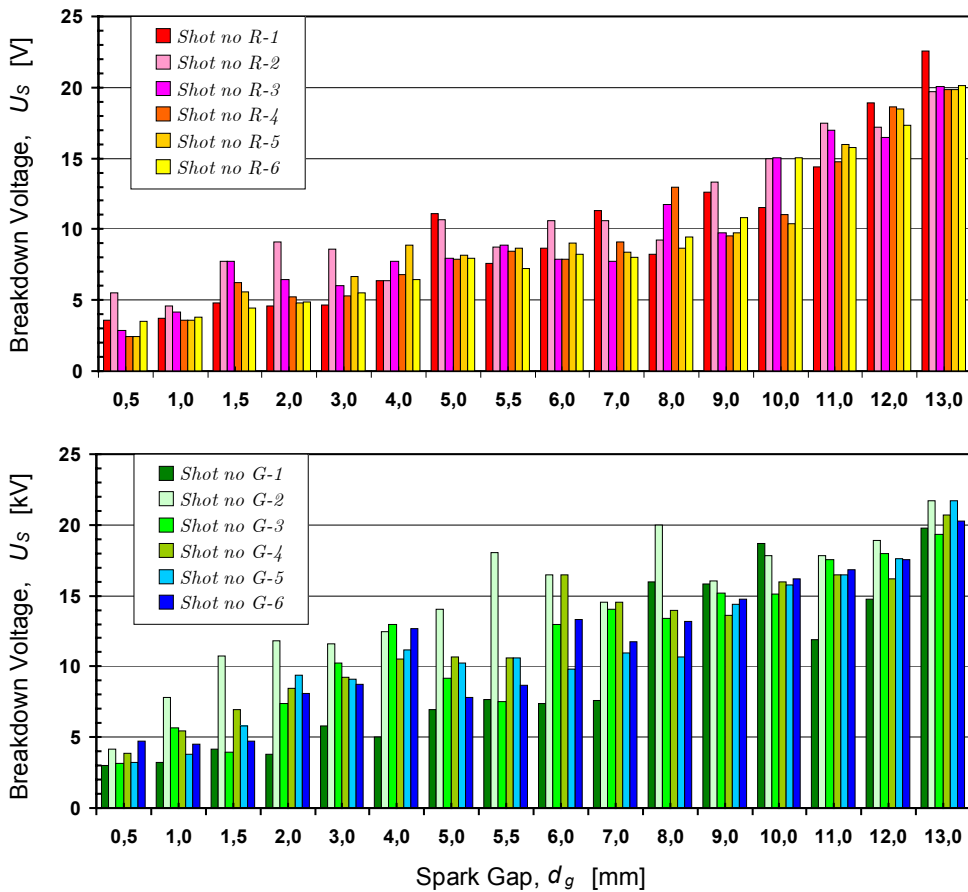


Figure A-32 Breakdown voltage as a function of spark gap for two different electrode materials: thorium oxide doped tungsten (“red”), and pure tungsten (“green”). For each spark gap, the results from six consecutive tests (starting with new electrodes) are included.

The arc duration is reduced for longer spark gaps; the main reasons for this are probably:

- i) A larger fraction of the pulse from the pulse-forming network is used to generate the higher breakdown voltage necessary to produce breakdown – the difference of 8 kV in breakdown voltage between 1 to 10 mm spark gaps shortens the available pulse by $\frac{1}{4}$ millisecond (because the rate of rise of gap voltage prior to breakdown is 31 kV/ms).
- ii) The threshold voltage needed to sustain the arc is higher for larger gaps – hence the arc-glow transition sets in sooner.

Figure A-33 illustrates the variation in arc voltage and arc energy for series of discharges in quiescent air. Although the electrodes are somewhat deformed after 12 consecutive discharges, see Figure A-34, both arc voltage and arc energy remains relatively stable see.

The increase in arc energy with increasing gap length is mainly due to the increased arc voltage. This is illustrated in Figure A-35.

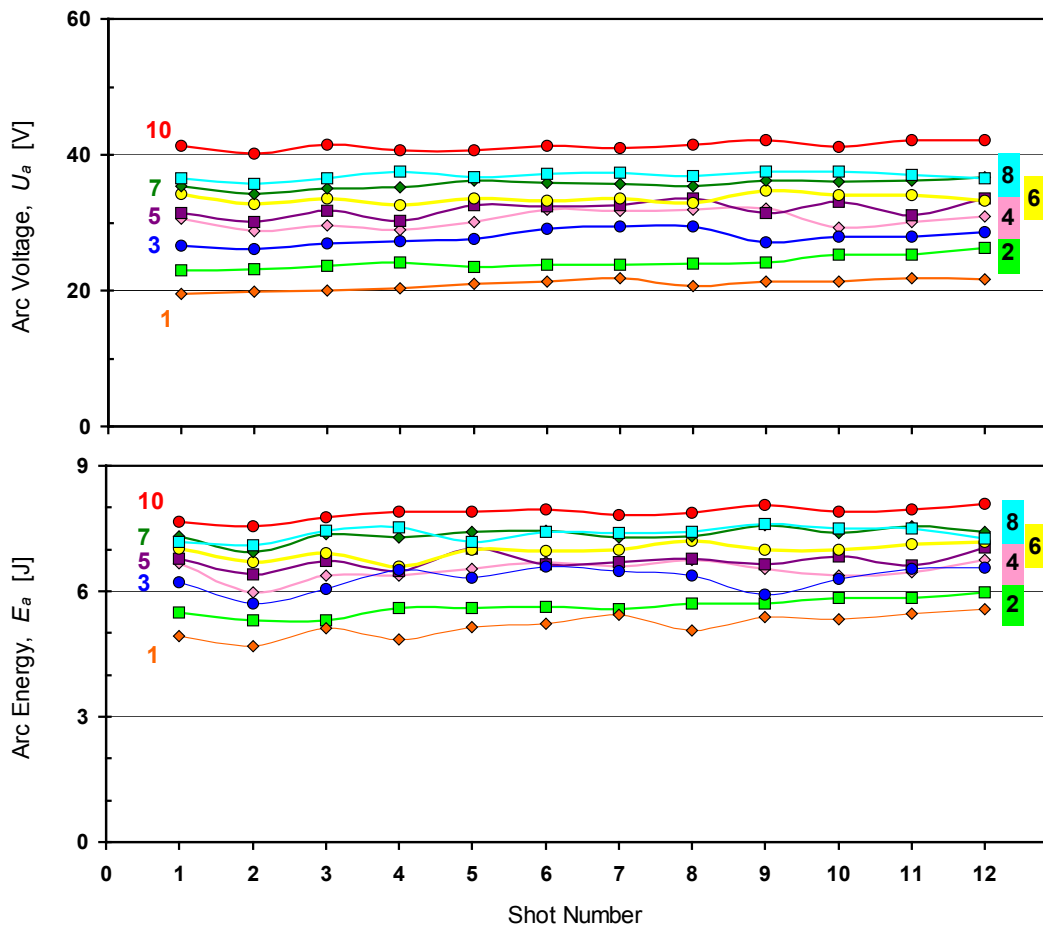


Figure A-33 Arc voltage and arc energy for the 12 consecutive discharges in Figure A-30, illustrating the moderate variation in these values for a given gap length (gap lengths in millimetres are given on the left/right of each series).

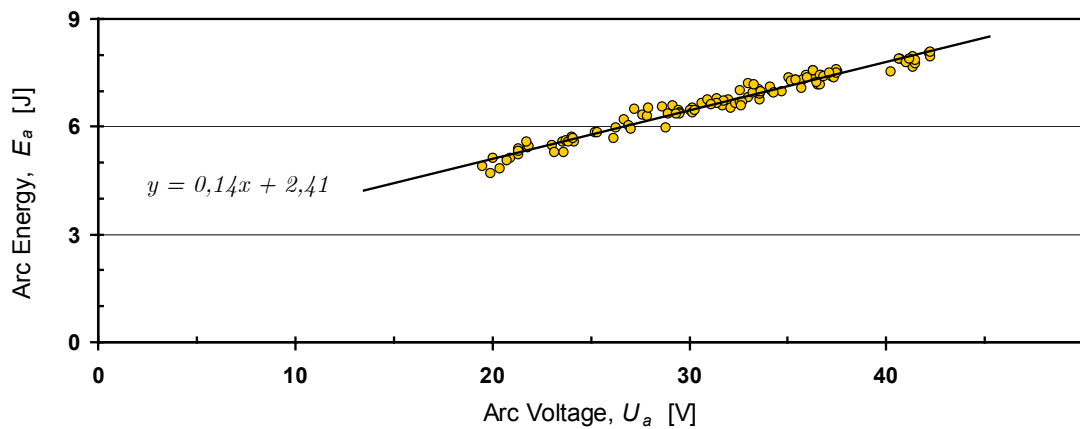
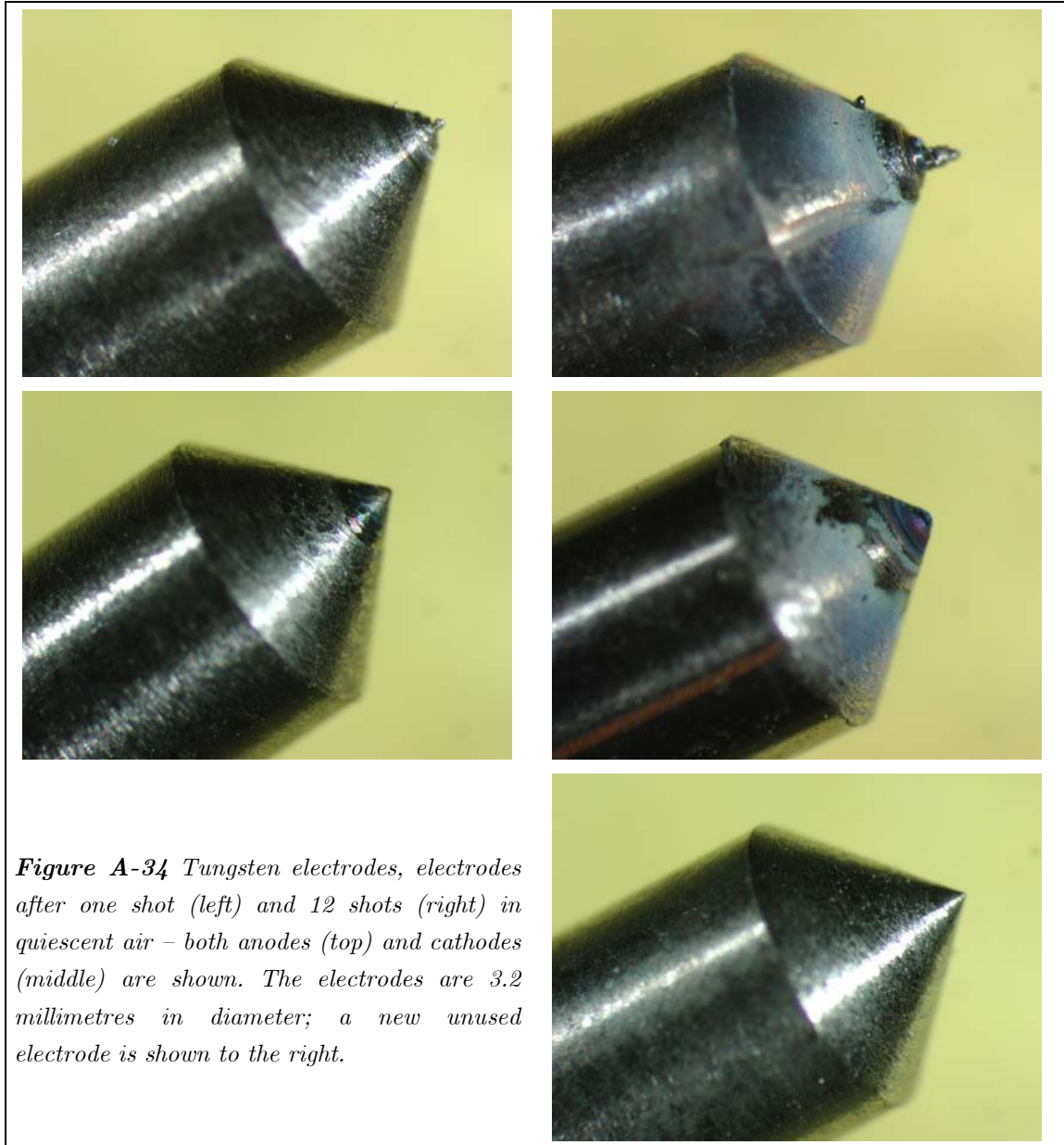


Figure A-35 Arc energy as a function of arc voltage for all the arcs in Figure A-30.

Electrical discharges in turbulent air flow

The effect of ignition delay time (t_v) on discharge characteristics for 3-mm point-point gaps is shown in Figure A-36; the corresponding values in quiescent air from Figure A-30 is indicated to the far right. The relationship between ignition delay time and flow properties inside the 20-litre vessel is described elsewhere (e.g. Appendix D).

The breakdown voltage seems to be slightly influenced by intense flow and turbulence, both the mean and the standard deviation are generally higher for short ignition delay times. It is not clear what causes this effect, but the impact on the total released energy is probably of minor importance.

As was pointed out by Swett (1948, 1949), the arc has a tendency to follow the flow, i.e. the arc is lengthened. This results in higher arc voltage, lower gap current, and shorter duration of the discharge. Measurements of current and voltage during a typical discharge in quiescent air, and a typical discharge at an ignition delay time of 60 milliseconds are shown in Figure A-37; the corresponding voltage-current characteristics are given in Figure A-38. Although the general features of the two discharges are similar, the effect of turbulence is clear; in many ways it resembles the effect of increased gap length that was illustrated in Figure A-27 and Figure A-29. However, a characteristic feature of discharges in turbulent flow is the rapid increase in voltage as soon as the glow phase sets in.

Figure A-36 indicates a dramatic effect of very high turbulence intensity on both arc voltage and arc duration. At an ignition delay time of 30 milliseconds the average arc voltage and the arc duration is about 80 volts and 1.5 milliseconds, respectively – very different from the values in quiescent air. The large variation between individual discharges at short ignition delay times is illustrated for four individual discharges in Figure A-39; commented from top to bottom:

- Some tests exhibit the familiar voltage-current characteristic; while the current oscillates, the voltage remains more or less constant during the main part of the discharge. However, the duration is even more reduced compared to longer ignition delay times, and the voltage increases very rapidly as soon as the current reaches low values. After the main discharge, the remaining part of the pulse from the pulse-forming network causes several short duration discharges. This phenomenon was also observed by Swett (1948, 1949). However, the energy of these subsequent discharges is usually negligible, and only the primary discharge is included in the measured arc energy (E_a).
- Intense flow can cause the voltage to vary in a saw-toothed waveform. It appears as if the discharge is about to be blown out (the voltage increases to ~ 100 V), but the current remains high, and the voltage drops back to its usual level (~ 30 - 40 V); the process then repeats it selves. This phenomenon can probably best be explained as the initial phase of an arc-to-glow transition. A similar saw-toothed voltage pulse has been observed by Kono *et al.* (1984); however, their observations were limited to glow discharges under flowing conditions.

- The primary discharge can be blown out after a short time ($\sim 1\text{ms}$), only succeeded by several short duration discharges of negligible energy.
- When the initial discharge is very short ($\sim 0.5\text{ms}$), it is sometimes succeeded by one or two similar arc discharges.

The considerable variation in the voltage-current characteristics for short ignition delay times shown in Figure A-39 explains the considerable spread in the measurements presented in Figure A-36. The observed increase in the average arc voltage may seem artificial; it may be argued that although the voltage has been measured while the current is relatively high, some of the discharges are not pure arcs – rather a complex mixture between arcs and glow-to-arc transitions. However, for the ignition delay times most relevant with respect to dust explosion research, i.e. higher than 60 milliseconds, the energetic part of the discharges can be regarded as pure arcs.

For most ignition delay times the increased arc voltage seems to add up for the decrease in gap current and arc duration; hence, the measured arc energy is more or unaffected by turbulence. However, because the discharge channel is carried away with the flow, the released energy will be distributed throughout a considerable volume.

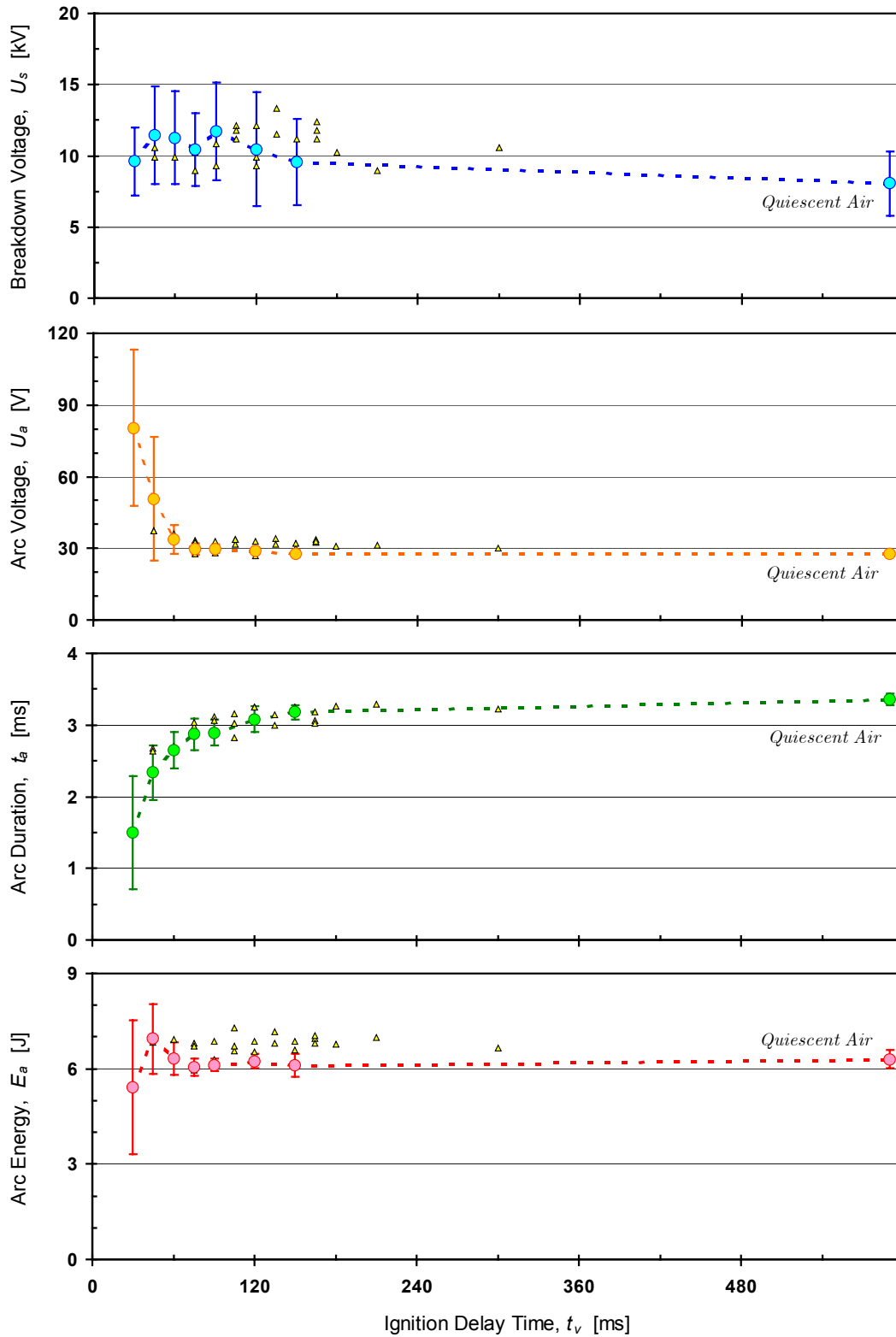


Figure A-36 The effect of ignition delay time on discharge characteristics in air, electrode separation 3 mm. Each data point represent the mean value of 12 consecutive discharges, starting with newly ground electrodes; error bars indicate one standard deviation above mean, and one standard deviation below mean. Some tests with J-135 jet-milled Silgrain, nominal dust concentration $500 \text{ [g/m}^3\text{]}$, are also included (Δ).

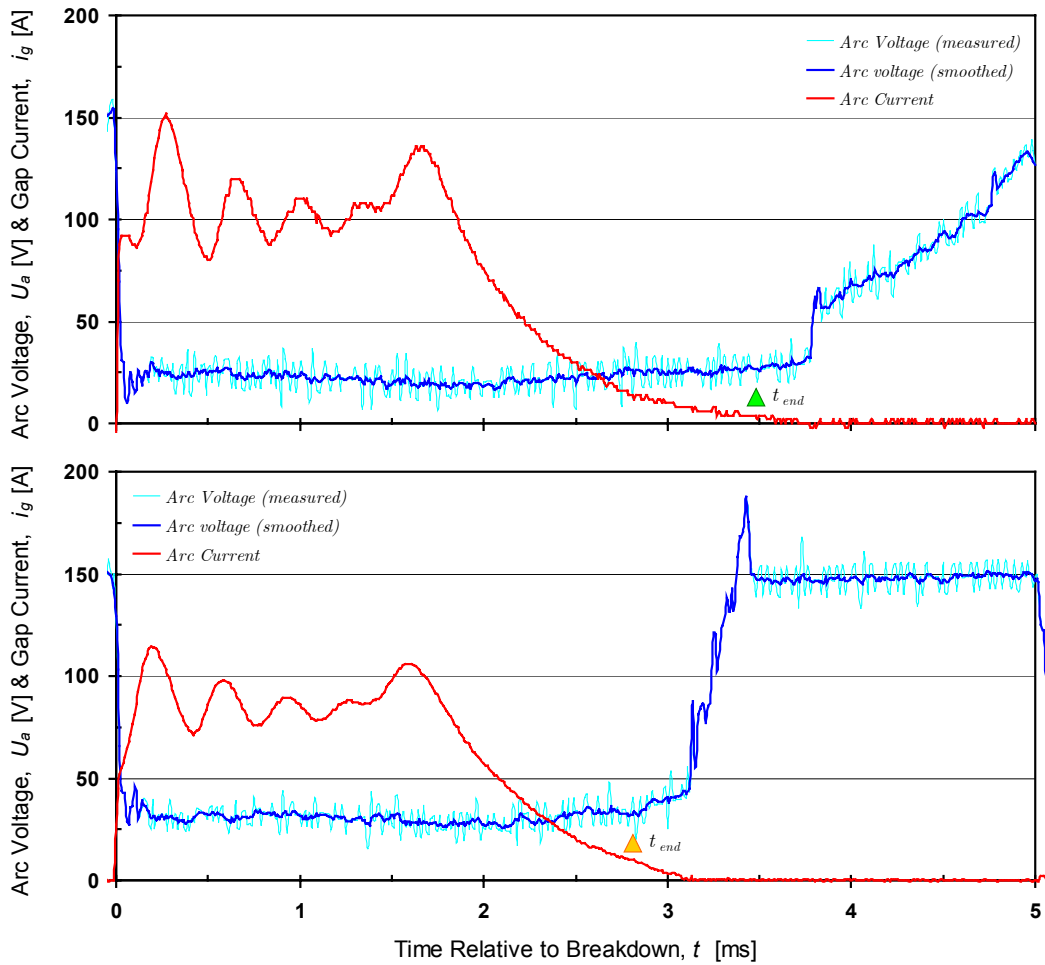


Figure A-37 Arc voltage (blue) and arc current (red) for two typical discharges over a 3-millimetre spark gap: quiescent air (above), and for an ignition delay time of 60 milliseconds (below). The duration of the discharges, defined as the time when 99 per cent of the measured energy has been dissipated, is indicated by pyramids. Note that the voltage measurements are only valid up to about 150 volts due to clipping, see section A.3.3.

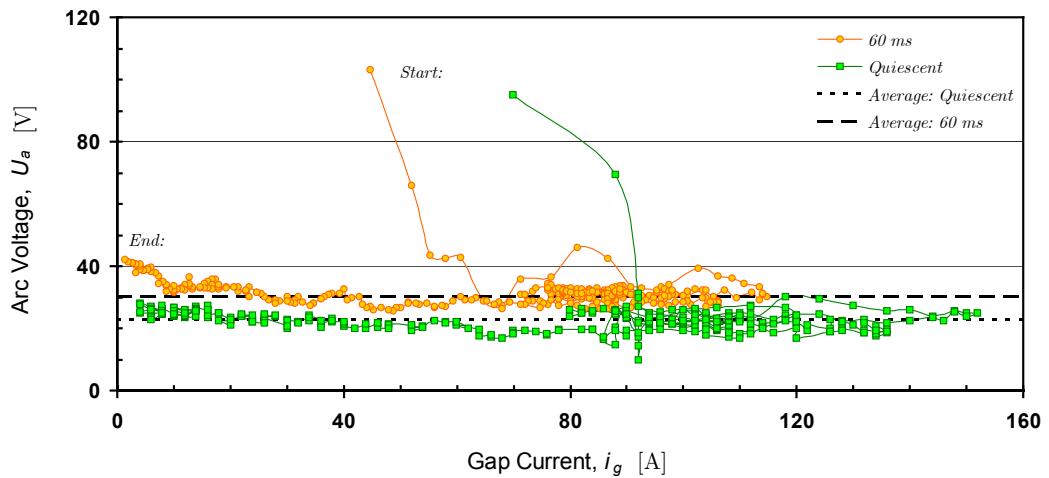


Figure A-38 Voltage-current characteristic for the two discharges in Figure A-37. The average arc voltage U_a is indicated for both discharges.

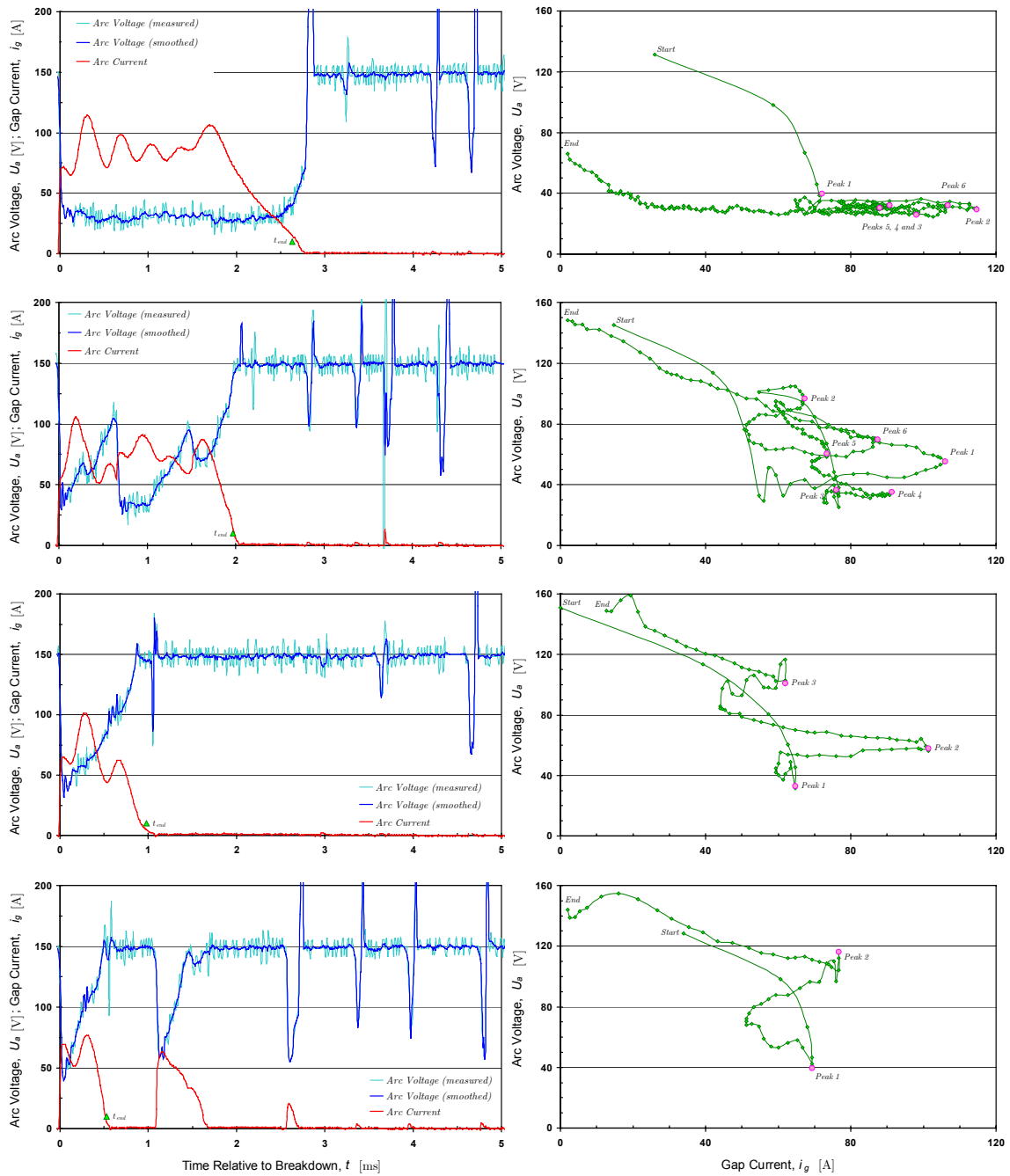


Figure A-39. Arc voltage (blue) and arc current (red) for various discharges at very high turbulence intensity, i.e. an ignition delay time equal to 30 milliseconds (left); corresponding voltage-current characteristics (right). The duration of the discharges, defined as the time when 99 per cent of the measured energy has been dissipated, is indicated by pyramids (green); note that for successive discharges, only the energy for the first discharge is measured. The gap length is 3 millimetres in all the tests. Note that the voltage measurements are only valid up to about 150 volts due to clipping, see section A.3.3.

Electrical discharges in turbulent dust-air suspensions

A few single tests with silicon dust (c_n : 500 g/m³, t_v : 60 ms), for various ignition delay times, are included in Figure A-36. The effect of the dust is not very clear, although there are indications of slightly higher arc energy compared to the tests for pure air. The increased arc energy seems to result from a combination of higher arc voltage and increased arc duration.

The effect of nominal dust concentration for various dust types on discharge characteristics is shown in Figure A-40. There does not seem to be any clear systematic influence from any of the dust types on any of the discharge parameters – although it may appear as if the breakdown voltage and arc energy are slightly influenced by some of the dusts. The breakdown voltage is lower than average for PMMA and silicon, and slightly higher for niacin amide. Most dusts give higher arc energy for high dust concentrations – silicon seems to cause higher arc energies throughout the entire concentration range.

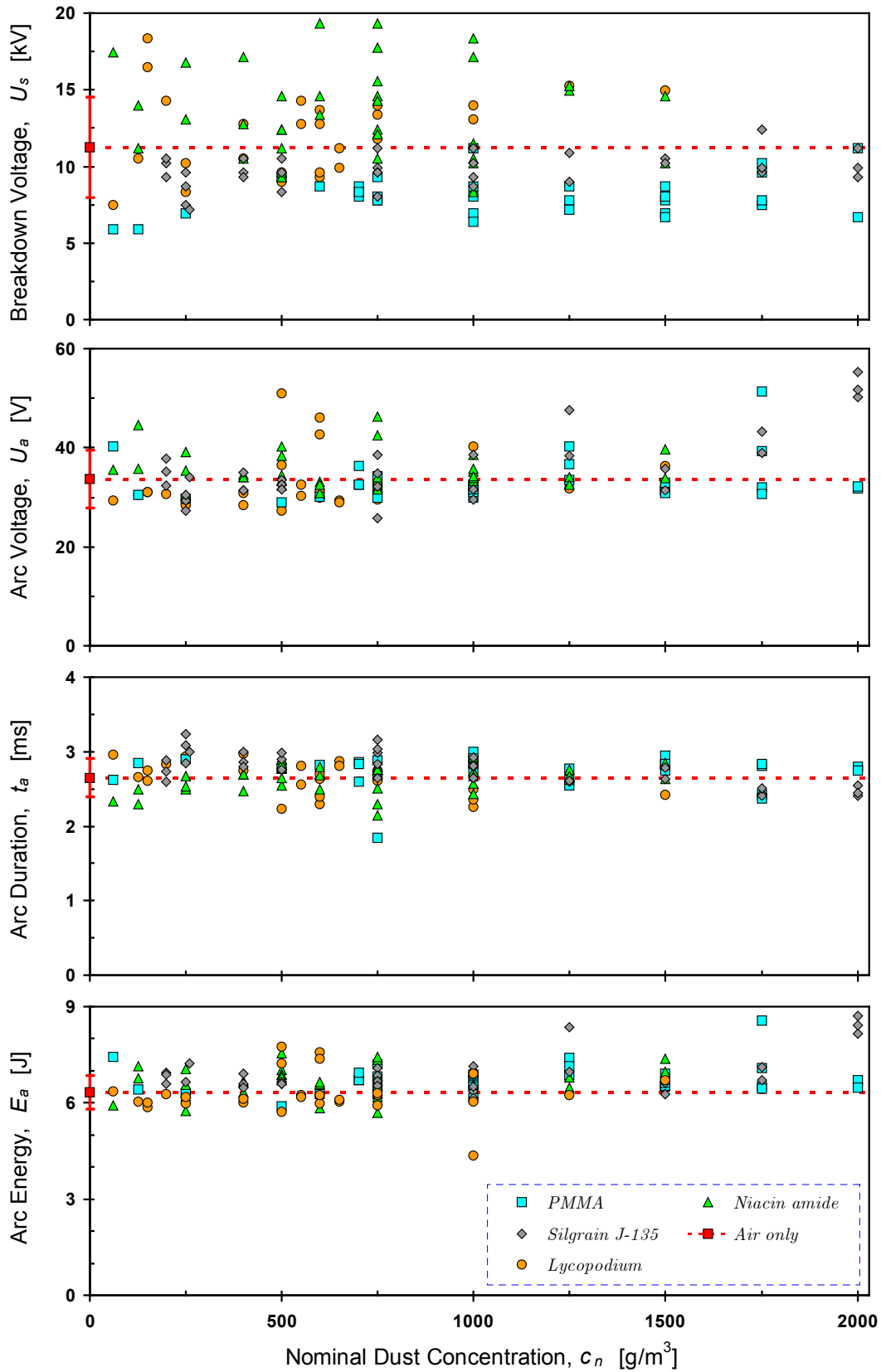


Figure A-40 The effect of dust loading on discharge characteristics for various dusts, 3 mm spark gap and 60 ms ignition delay time in all tests. The corresponding values for pure air from Figure A-36 are represented with a dotted red line, with the mean value and error bar to the left. Each data point represents one single discharge.

A.5.2 Incendiary Capabilities of Electrical Discharges for Selected Dusts– Comparison with Chemical Igniters

Chemical igniters

Pressure-time histories for two typical blind tests with only chemical igniters are shown in Figure A-41. A notable pressure rise sets in about 10 milliseconds after triggering (indicated by the red vertical line), and the maximum overpressure is only 0.8 bar – about half of the “maximum” value indicated by Cesana and Siwek (2000).

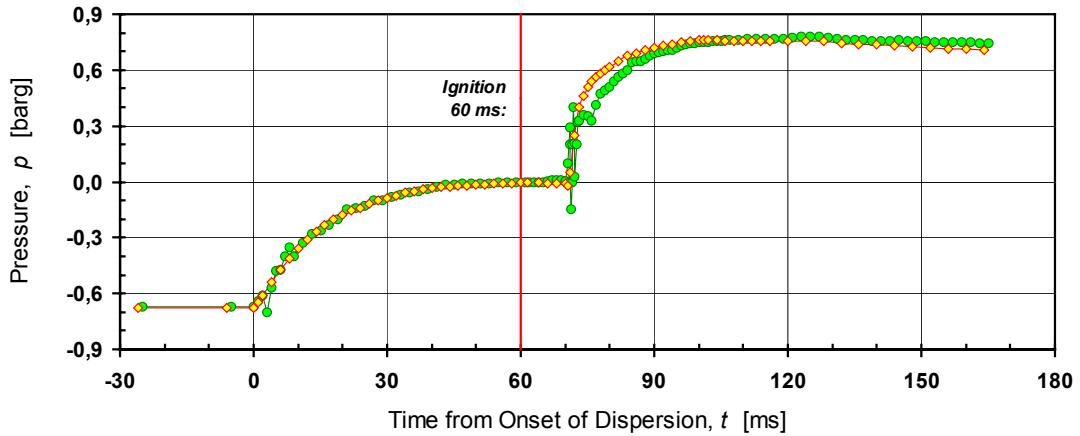


Figure A-41 Pressure-time histories for two tests with chemical igniters only. In each test, two 5 kJ chemical igniters are fired at an ignition delay time of 60 milliseconds.

Niacin Amide and CaRo 00/01

Explosion indices for niacin amide are shown in Figure A-42. The corrected explosion pressure, p_m , and the volume corrected rate of pressure rise, $V_v^{1/3}(dp/dt)_m$, are included to facilitate comparison with the final values for p_{max} and K_{St} from CaRo 00/01 (V_v is the volume of the explosion vessel).

The corrected explosion pressure is a function of measured explosion pressure, Cesana and Siwek (2001):

$$p_m = \begin{cases} \frac{5.5 \cdot (p_{ex} - p_{ci})}{(5.5 - p_{ci})} & \text{when } p_{ex} < 5.5 \text{ barg} \\ 0.775 \cdot p_{ex}^{1.15} & \text{when } p_{ex} > 5.5 \text{ barg} \end{cases} \quad (\text{A.49})$$

where p_{ci} is the pressure due to the chemical igniters alone (i.e. $p_{ci} = 0.8$ barg for two 5 kJ chemical igniters, from Figure A-41). Note that (A.49) is developed for the Siwek sphere, it should probably have been adjusted for the vessels used in this work. The *maximum explosion pressure* p_{max} is defined as the maximum value of p_m determined by tests over a wide range of fuel concentrations.

The K_{St} value is defined as:

$$K_{St} = V_v^{1/3} \left(\frac{dp}{dt} \right)_{\max} \quad (\text{A.50})$$

where $(dp/dt)_{\max}$ is the maximum value of $(dp/dt)_m$ determined by tests over a wide range of fuel concentrations.

Both of the two 20-l explosion vessels participated in CaRo 00/01, but only the USBM-vessel produced results within the acceptable ± 10 per cent range for both p_m and K_{St} . The results are presented in Figure A-42.

Electrical discharges were unable to ignite the niacin amide at a nominal dust concentration of 60 g/m³. However, the low rate of pressure rise observed at this concentration when igniting with two 5 kJ chemical igniters may indicate that the igniters are overdriving the system (Cashdollar and Chatrathi, 1992).

Except from minor deviations at very low concentrations, there is little variation in both observed and corrected explosion pressure throughout most of the concentration range. Although the results for ignition with chemical igniters in the cubical vessel is generally about one bar higher than average, all results lie well within the accepted ± 10 per cent range for p_m from CaRo 00/01. For the cubical vessel, there is also an indication of higher explosion pressure in both the low and high end of the concentration range when igniting with electrical discharges. One possible explanation for a higher explosion pressure in the cubical vessel compared to the modified USBM vessel can be the difference in vessel volume (19.97 and 20.50 litre, respectively), allowing for a higher initial pressure when the air from the dust storage reservoir (having a fixed volume of 0.600 litres) are added. The different shape of the two vessels will inevitably influence the internal flow pattern, and most likely the rate of dust settling.

The difference between ignition by electrical discharges and ignition by chemical igniters is much more pronounced for rate of pressure rise (and the K_{St} value) – the results with chemical igniters are always much higher, see Figure A-42. Both vessels yield K_{St} values below the minus 10 per cent limit from CaRo 00/01 when ignited with electrical discharges, and only the modified USBM vessel is below the plus 10 per cent limit when ignited with chemical igniters. As for explosion pressure, the results for rate of pressure rise (or K_{St} value) is generally higher in the cubical vessel, especially so for high dust concentrations. For higher concentrations, a higher fraction of settled dust in the cubical vessel could explain the increasingly higher explosion pressure in this vessel, compared to the modified USBM vessel.

Representative pressure-time histories for some of the tests in Figure A-42 are shown as subfigures in Figure A-43 (for the modified USBM vessel) and Figure A-44 (cubical vessel). Figure A-45 provides further details on the initial part of the p - t histories for the tests in the USBM vessel, including two tests with nominal dust concentration 1500 g/m³. The $p_{ex}(t)$ data are only available as curves in the current version of the Kühner software; hence, there is one diagram for each individual test. The following applies to all the subfigures in Figure A-43, Figure A-44 and Figure A-45:

-
- i) Time is given in milliseconds and is relative to onset of test, not relative to onset of dispersion.
 - ii) The reported pressure is the measured explosion pressure (p_{ex}), not the corrected explosion pressure (p_m).
 - iii) Activation (or triggering) of ignition (t_{ign}) is indicated by a red vertical line; the time (t_m) when the explosion pressure (p_{ex}) is reached, the so-called *culmination point*, is indicated by a plus sign (+).
 - iv) Note that it was not possible to achieve equal scaling of all axes.
 - v) A vector containing key explosion data is placed underneath each subfigure. The elements of the vector are: $\{c_n; p_m; (dp/dt)_m; t_1\}$, where t_1 is the *duration of combustion*¹.

For the tests in Figure A-43 and Figure A-44 that are ignited by chemical igniters, a characteristic time delay of about 10 milliseconds between activation of ignition and the first measurable pressure rise can be observed. This corresponds with the delayed pressure rise observed for the blind tests in Figure A-41. As soon as the chemical igniter has fired, the pressure increases rapidly.

With arc ignition, a small pressure rise is measured after only a few milliseconds. For moderate dust concentrations, the further increase in pressure is slow but steady – up to the inflection point of the S-shaped curve, it resembles exponential growth. However, increasing dust concentration introduces a time-period where the further pressure rise seems to be halted for some time. For the test with a nominal dust concentration of 1500 g/m³ in Figure A-45, the delay in “normal” pressure rise is in the order of 60 milliseconds. As this phenomena seems to be associated with dust concentrations that are considerably higher than stoichiometric, it is possible that it can be associated with heat loss to particles that cannot participate in the combustion process due to lack of oxygen. The level of turbulence can also be an influential factor.

The effect of dust concentration on the duration of combustion for all the tests from Figure A-42 is illustrated in Figure A-46. The duration of combustion is shorter over the whole concentration range when the ignition source is chemical igniters (compared to electrical discharges), increasingly so for higher concentrations. There is little difference between the two explosion vessels.

¹ The *duration of combustion* (t_1) is defined as the time difference between the activation of ignition and the culmination point (Cesana and Siwek, 2001): $t_1 = t_m - t_{ign}$.

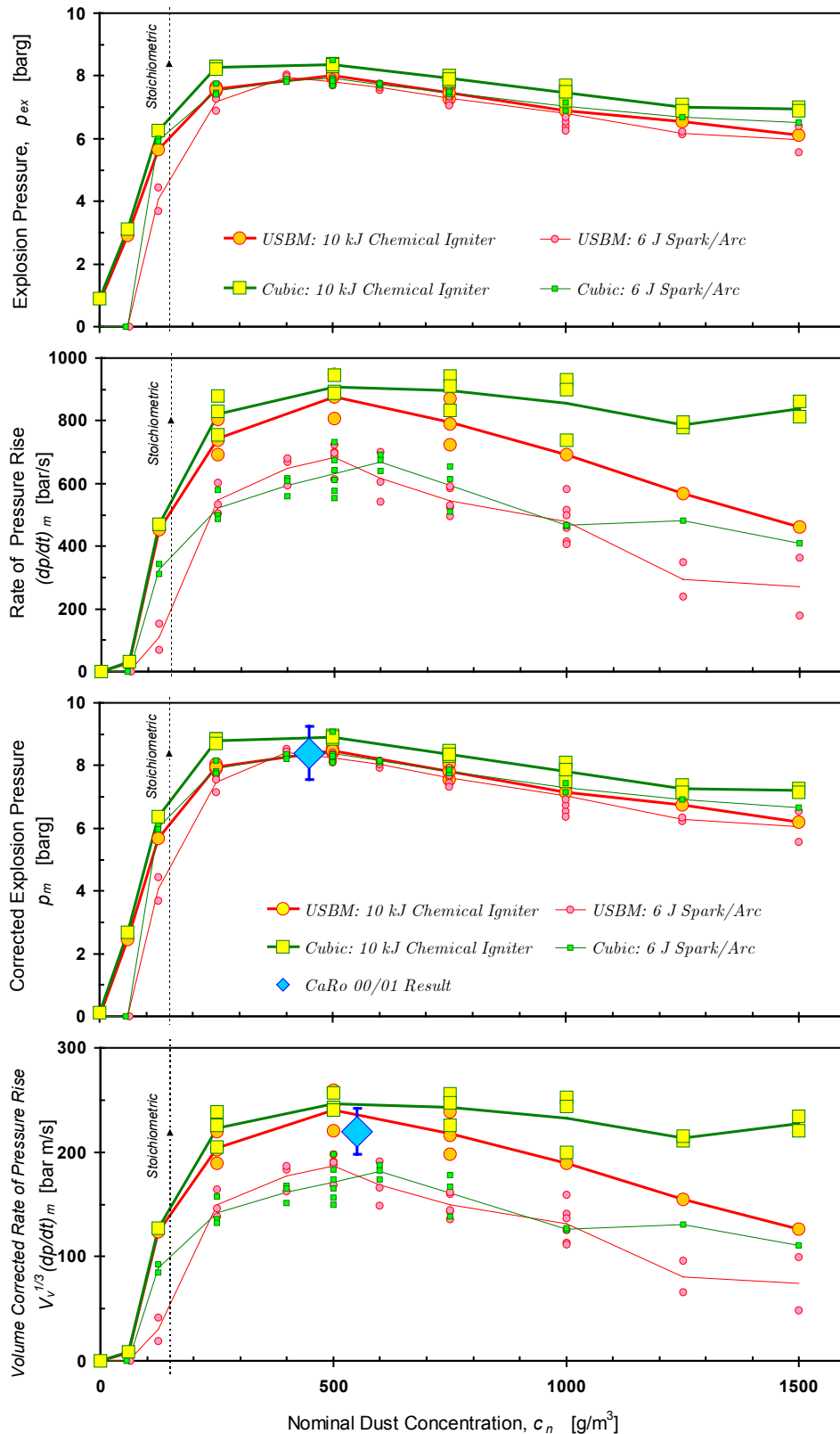


Figure A-42 Explosion indices for niacin amide determined in both the USBM and Cubical vessel, with both an electric arc and two 5 kJ chemical igniters as ignition source. Ignition delay time is 60 milliseconds for all tests. For p_m and $V_v^{1/3}(dp/dt)_m$ the final results for p_{max} and K_{St} from the round-robin test CaRo 00/01 are indicated; data point represents the average value from the 41 vessels that measured explosion indices, and error bars indicate the $\pm 10\%$ range.

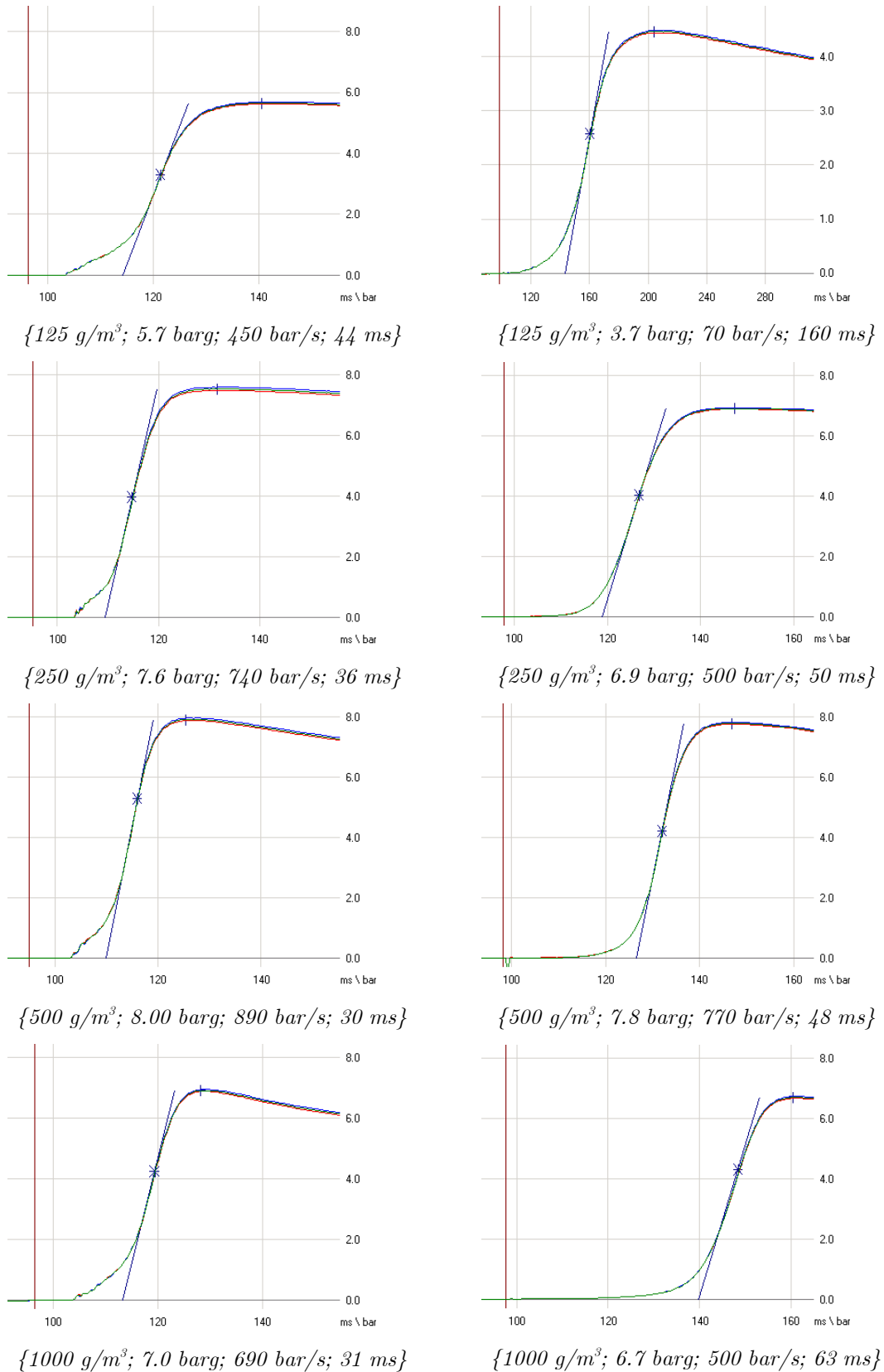


Figure A-43. Pressure-time histories for representative niacin amide explosions in the modified USBM vessel, ignited by two 5 kJ chemical igniters (left) and 6 J electrical discharges (right).

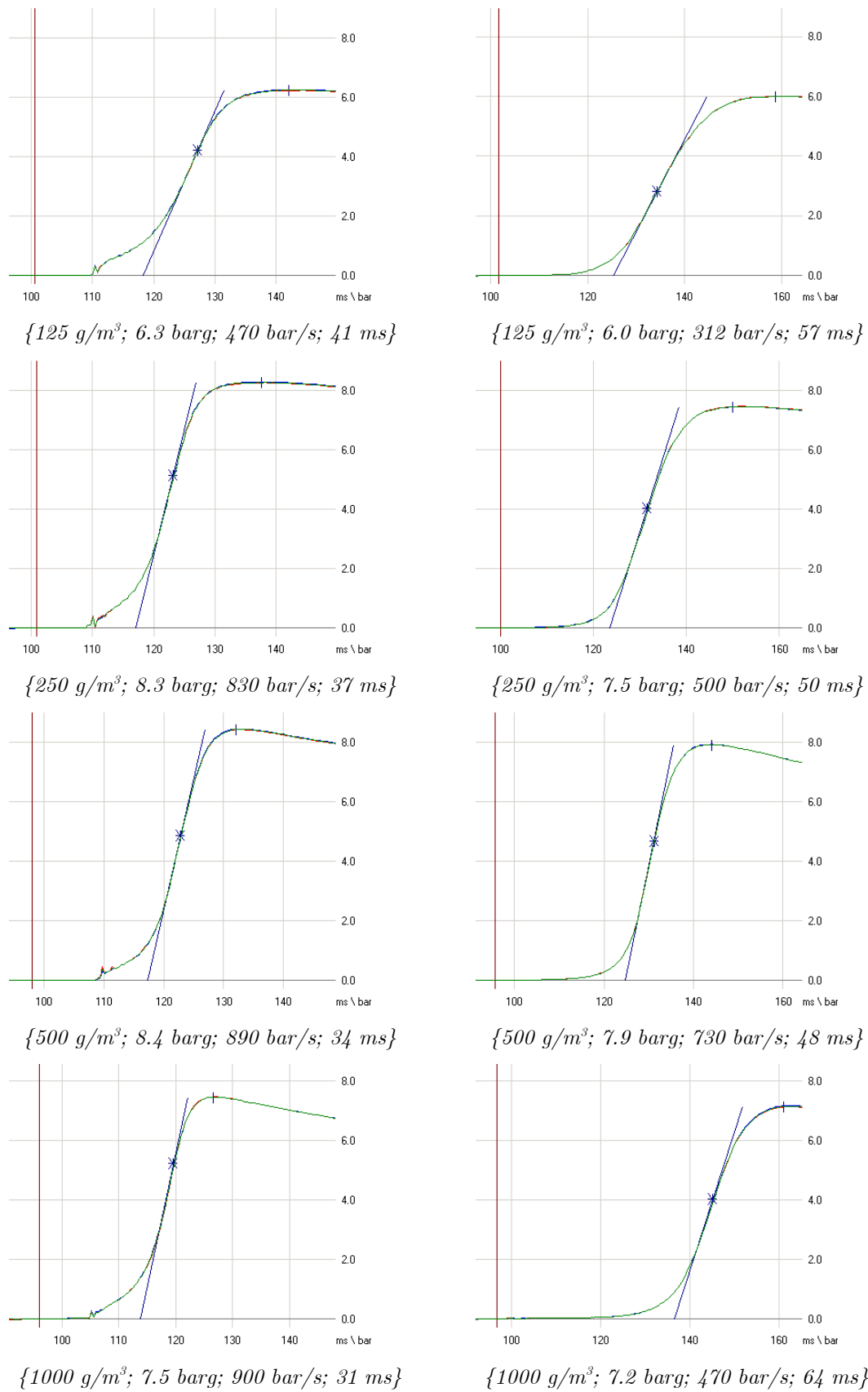


Figure A-44. Pressure-time histories for representative niacin amide explosions in the cubical vessel, ignited by two 5 kJ chemical igniters (left) and 6 J electrical discharges (right).

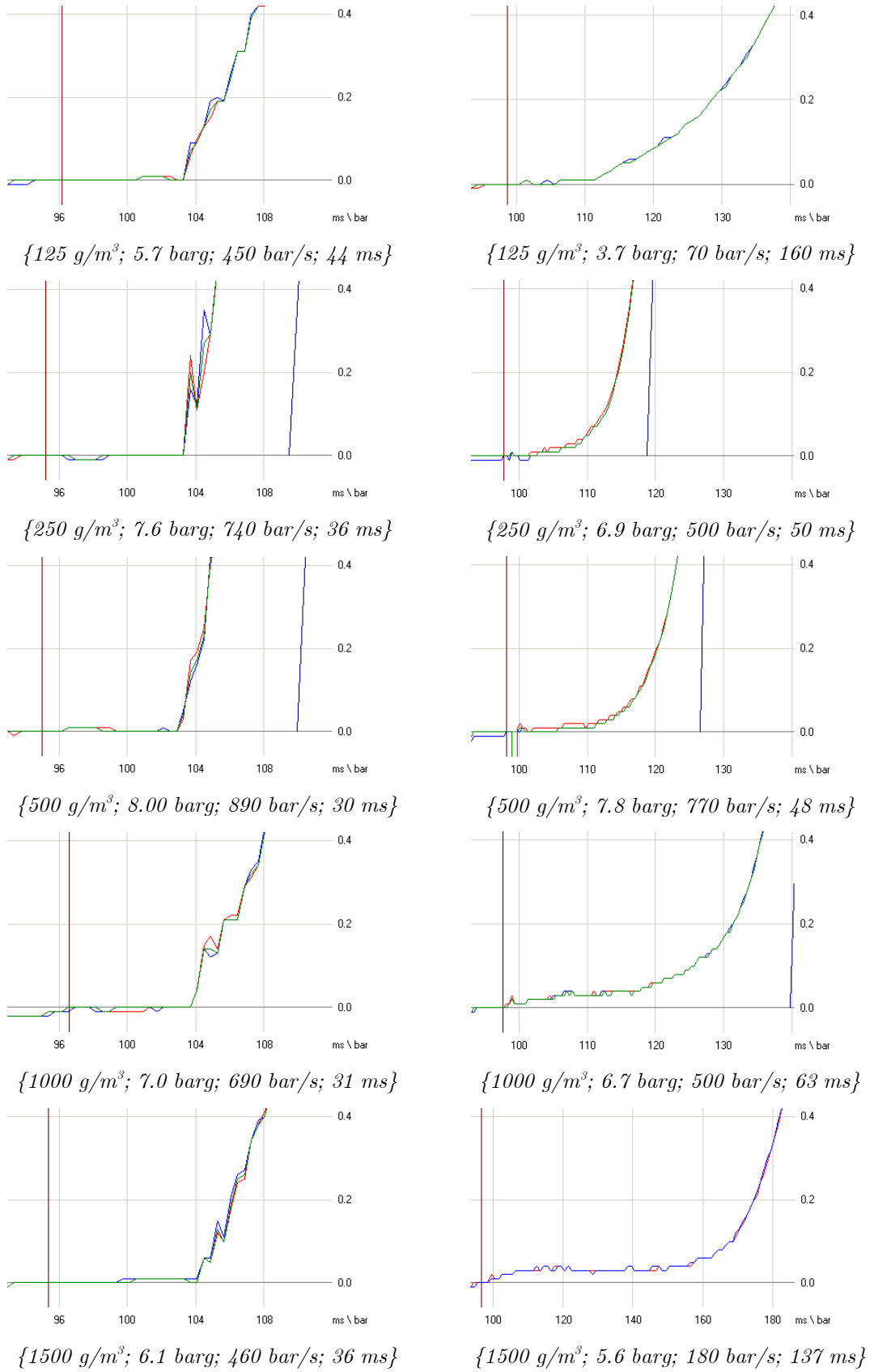


Figure A-45. Initial part of pressure-time histories for representative niacin amide explosions in modified USBM vessel, ignited by two 5 kJ chemical igniters (left) and one 6 J arc discharges (right).

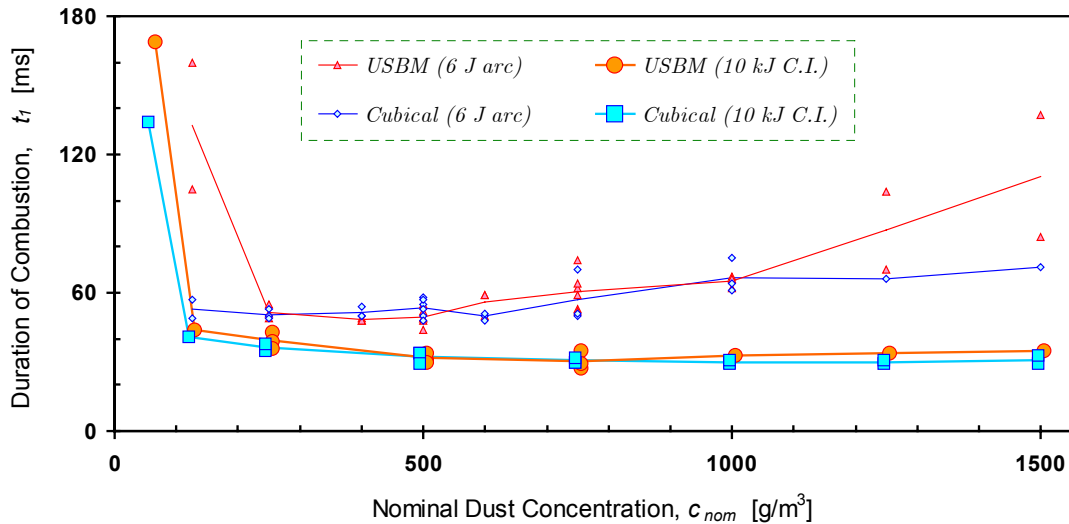


Figure A-46. Duration of combustion as a function of nominal dust concentration and ignition source for niacin amide explosions in both 20-l vessels.

Spores of *Lycopodium casuarinoides*

Three tests where clouds of *Lycopodium casuarinoides* spores are ignited with chemical igniters are shown in Figure A-47, together with the results for ignition with electrical discharges at various ignition delays presented in Chapter 4. For the default ignition delay time of 60 milliseconds, there is little difference in the observed explosion pressures, the corrected explosion pressures calculated from (A.49) actually coincide. As for niacin amide, the rate of pressure rise is considerably lower when electrical discharges are used as ignition source. When the ignition delay time is increased, the explosion pressure decreases steadily when electrical discharges are used as ignition source, the single shot at 300 ms with chemical igniters indicates however a much more moderate decrease. Although it is impossible to draw any conclusions based on one single shot, it may appear as if the blast from the chemical igniter is able to bring settled dust back into suspension. In addition, the volume entrapped by the initial flame created by chemical igniters may trap dust particles that would otherwise have time to settle during the considerable time of flame propagation when the suspension is ignited by electrical discharges. This is illustrated in Figure A-48; with an ignition delay time of 300 ms, the combustion process is terminated after 100 milliseconds when initiated by chemical igniters, and after 300 milliseconds when initiated by the arc discharge.

Jet-milled silicon (Silgrain)

The effects of particle size and ignition source on dust explosion indices for silicon dust are illustrated in Figure A-49. It should be noted that all samples have a broad particle size distribution, see Appendix C. The explosion pressure is practically independent of type of ignition source, whereas the rate of pressure rise is considerably lower when the suspensions are ignited by electrical discharges compared to chemical igniters. The coarser particle fractions could only be ignited by chemical igniters, illustrating the limitations of the electrical discharge as an ignition source.

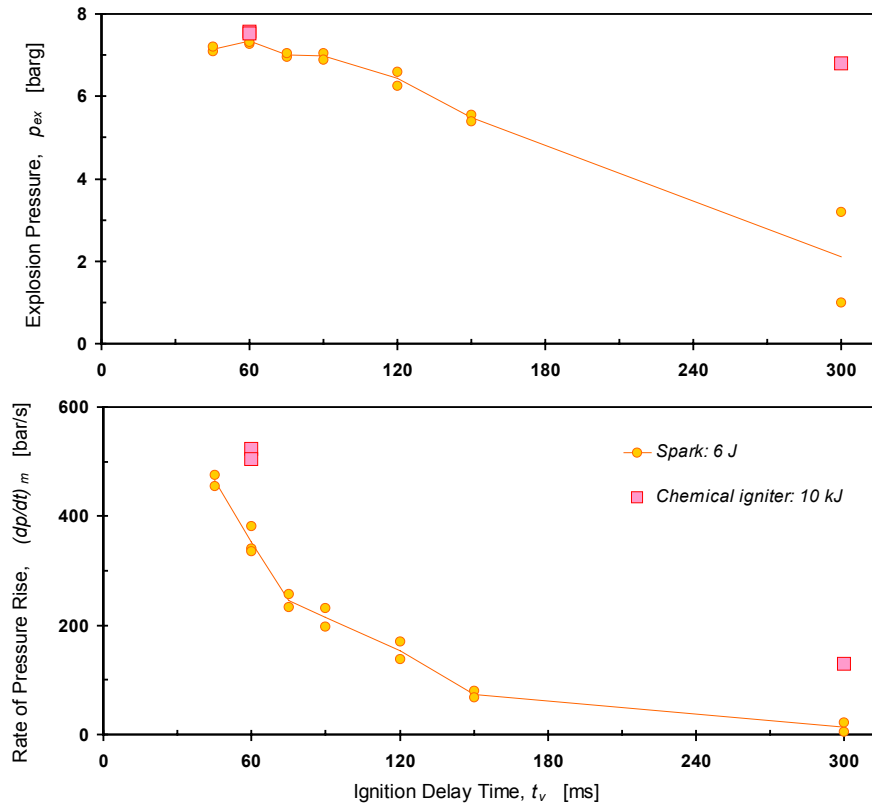


Figure A-47. Effect of ignition delay time and ignition source on explosion pressure and rate of pressure rise for *Lycopodium casuarinoides*, nominal dust concentration 500 g/m^3 .

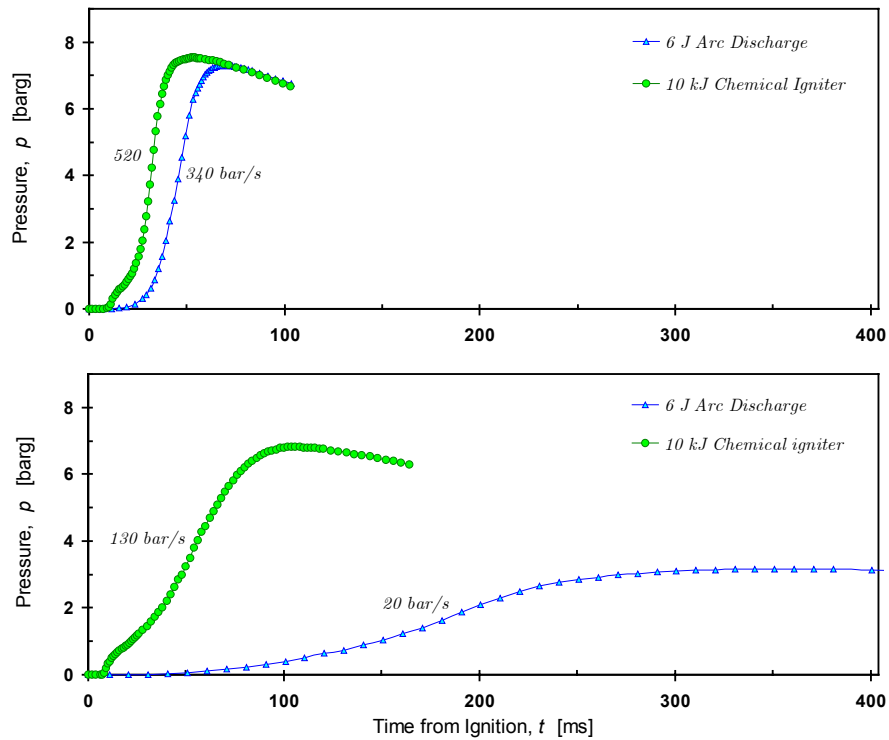


Figure A-48 Effect of ignition source and ignition delay time on pressure-time histories for some of the *Lycopodium casuarinoides* dust explosions in Figure A-47; ignition delay times 60 milliseconds (upper) and 300 ms (lower), nominal dust concentration 500 g/m^3 .

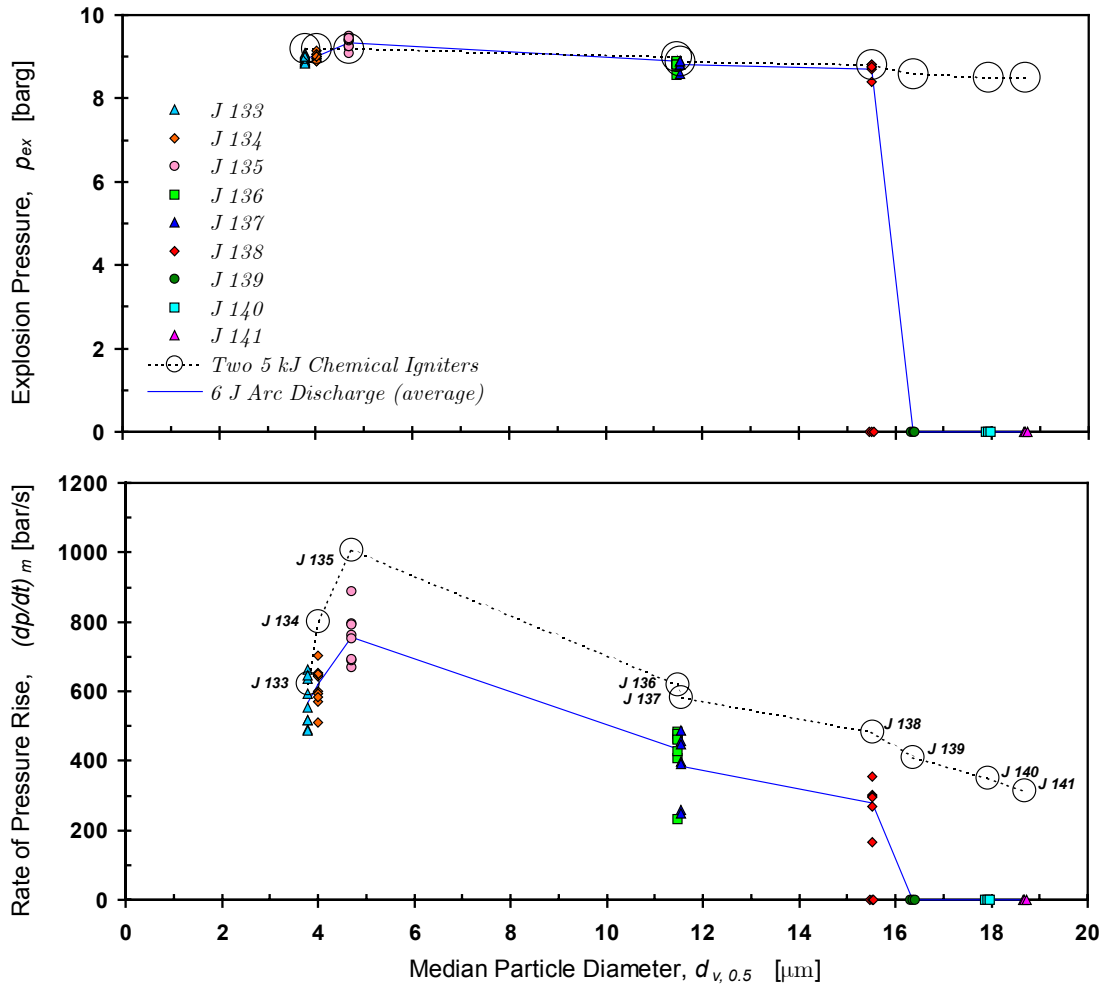


Figure A-49. Effect of median particle diameter on explosion pressure and rate of pressure rise for suspensions of jet-milled Silicon (Silgrain) in air. All tests are done in the modified USBM vessel fitted with the rebound nozzle – nominal dust concentration and ignition delay time is 500 g/m^3 and 60 ms , respectively.

Poly methyl methacrylate (PMMA) and RDX

The PMMA dust proved to be difficult to ignite, only the sieved fraction described in Appendix C could be reliably ignited by the electrical discharges produced by the arc generator.

RDX could only be ignited at relatively high concentrations, and even at a nominal dust concentration of 1000 g/m^3 , one out of four tests misfired.

A.6 Conclusion

An electric arc generator for igniting turbulent dust-air suspensions inside closed 20-litre explosion vessels has been developed. The generator produces arc discharges that releases about six joules of energy in about three milliseconds across a three-millimetre spark gap. Ignition can be triggered by the same signal that fires the chemical igniters in standardized dust explosion tests. Although the electrical discharges are initiated by a spark, they can best be described as short duration arcs because the duration and energy of the breakdown phase is negligible compared to the arc phase.

The effect of the arc discharges on pressure-time histories from explosions is negligible, especially compared to the effect of chemical igniters. Hence, explosion data obtained with arc ignition are well suited for validating models of the early phase of flame propagation. However, the measured rate of pressure rise in explosions ignited by arc discharges is significantly lower than the rate of pressure rise measured with chemical igniters. Thus, results obtained with arc ignition will not be directly comparable with results obtained by the standardized tests in 20-litre explosion vessels. It is possible that correction formula for $(dp/dt)_m$ could be found, similar to (A.49) for p_m , or that comparable results could be obtained by shortening the ignition delay time. However, such corrections would require extensive testing with many different types of dust.

Although the discharges are capable of igniting a variety of combustible mixtures under high turbulence intensity conditions, they were not very efficient for igniting dusts with coarser particle size distributions. The results by Glarner (1983; Figure A-5) show that reliable ignition of turbulent dust-air suspensions can require considerable amounts of energy.

Possible modifications to the arc generator

As it is not desirable to increase the duration of the discharges beyond three milliseconds, and due to the voltage-current characteristic of arc discharges, the only practical way of increasing the arc energy will be to increase the current. The thyristor used in the arc generator can handle currents up to about five kA for short time periods. Hence, it should be possible to produce arc discharges with an output of about $P = U_a i_g \sim 20V \cdot 5kA = 100kW$; i.e. the arc would release 300 J in 3 ms. However, such discharges will increase the electrode consumption considerably.

It should also be possible to initiate the arc by discharging the pulse-forming network over an exploding wire, similar to the method described by Kumagai and Sakai (1967). Hence, the high-voltage part of the circuit could be omitted, and the arc generator would be safer to handle.

A.7 Electrical Schematic and Components

The electrical schematic for the electric arc generator is given in Figure A-6; components are listed in Table A-2.

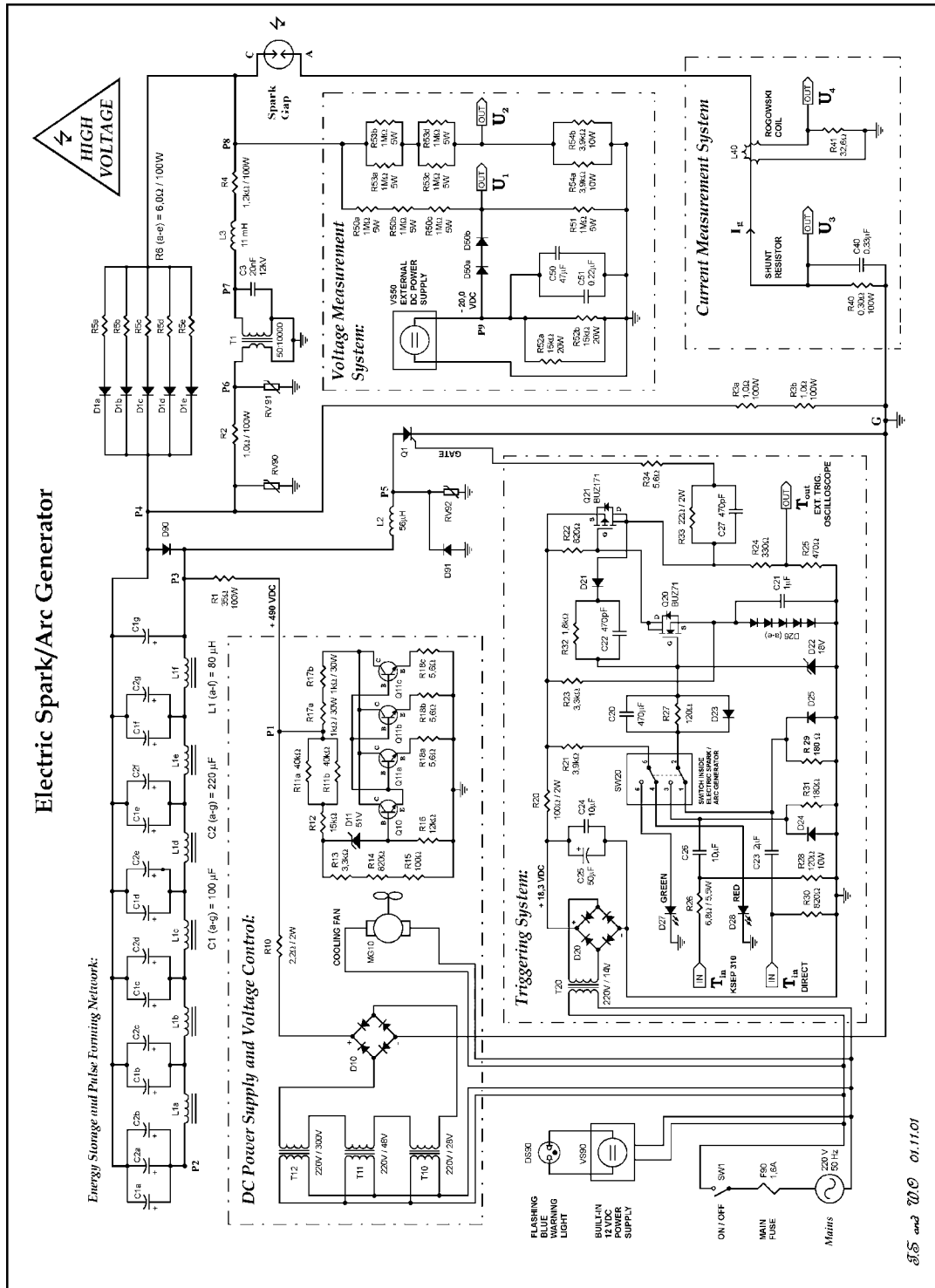


Figure A-50 Complete circuit diagram of the arc generator.

Table A-2 Components used in the electric arc generator. The numbers in the first column refers to Figure A-50.

<i>Circuit Reference</i>	<i>Description</i>	<i>Value, Rating</i>	<i>Manufacturer/Supplier</i>	<i>Type</i>
Main Circuit:				
R1	Wire-wound Resistor	35Ω, 100W	Alnæs Nye AS	–
R2	Wire-wound Resistor	1.0Ω, 100W	Alnæs Nye AS	–
R3 (a-b)	Wire-wound Resistor	1.0Ω, 100W	Alnæs Nye AS	–
R4	Wire-wound Resistor	1.2kΩ, 100W	Alnæs Nye AS	–
R5 (a-e)	Wire-wound Resistor	6.0Ω, 100W	Alnæs Nye AS	–
C1 (a-g)	Electrolyte	100μF, $U_R=500V$	Fisher & Tausche	LF
C2 (a-g)	Electrolyte	220μF, $U_R=500V$	Fisher & Tausche	LF
C3	HV Capacitor	20nF, 20kV	Telegrafia	C82
L1 (a-f)	Iron-cored coils	80μH	Various ¹	–
L2	Air-cored coil	56μH	Author	–
L3	Air-cored coil	11mH	Author	–
D1 (a-e)	HV Rectifier Diodes	$U_{VRMS}=17kV$ $U_{RRM}=40kV$	Semikron GmbH	HSKE 17000/7600-0.3
Q1	Thyristor	See footnote. ²	Westcode	N195PH12
T1	HV Transformer	50:10000, 20kV	Various ³	–
SW1	Main Switch	250VAC, 16A	–	–
D.C. Power Supply and Voltage Control System:				
R10	Resistor	2.2Ω, 2W	–	–
R11 (a-b)	Resistors	40kΩ, 20W	Vitrohm	H

¹ Hand-wound by the author on laminated iron-cores from Os Transformator Fabrikk AS.

² This Converter Grade Stud-Base Thyristor from Westcode Semiconductors Ltd has the following key data: $i_{T(AV)}=226A$, $i_{T(RMS)}=355A$, $U_{RRM}=1.2kV$, $i_{CT}=0.15A$, $U_{GT}=3V$ and $i^2t=131*10^3A^2s$ (10 ms duration). Further details can be found in “Westcode Technical Publication TN195P, Issue 2, October 1995”.

³ Transformer taken from welding apparatus purchased at Clas Ohlson AS. Original secondary coiling (50 windings) used as primary coiling, and new secondary coiling (10000 windings) wound at Os Transformator Fabrikk AS, and embedded in silicone by the author.

<i>Circuit Reference</i>	<i>Description</i>	<i>Value, Rating</i>	<i>Manufacturer/Supplier</i>	<i>Type</i>
R12	Resistor	15k Ω , 20W	Vitrohm	H
R13	Resistor	3.3k Ω , 1W	–	–
R14	Resistor	820 Ω , 20W	–	–
R15	Resistor	100 Ω , 2W	–	–
R16	Resistor	12k Ω , 0.5W	–	–
R17 (a-b)	Resistors	1k Ω , 30W	Dale	RH-50
R18 (a-b)	Resistors	5.6 Ω , 1W	–	–
D 10	Bridge Rectifier	$U_{RRM}=800V$	Semikron GmbH	SKB 30/0.8
D 11	Zener Diode	51V, 1W	–	–
Q10	NPN Transistor	$i_C=8A$, $U_{CES}=1500V$	ST Microelectronics	BU508A
Q11 (a-c)	NPN Transistor	$i_C=8A$, $U_{CES}=1500V$	ST Microelectronics	BU508A
T10	Transformer	220/28VAC	Trans Electric AS	–
T11	Transformer	220/48VAC	Trans Electric AS	–
T12	Transformer	220/300VAC	Trans Electric AS	–
MG10	Cooling Fan	220V, 50Hz, 9W	System Papst	4850 N
<i>Triggering System:</i>				
R20	Resistor	100 Ω , 2W	–	–
R21	Resistor	3.9k Ω , 1W	–	–
R22	Resistor	820 Ω , 1W	–	–
R23	Resistor	3.3k Ω , 1W	–	–
R24	Resistor	330 Ω , 1W	–	–
R25	Resistor	470 Ω , 1W	–	–
R26	Resistor	6.8 Ω , 5.5W	–	–
R27	Resistor	120 Ω , 1W	–	–
R28	Resistor	120 Ω , 10W	–	–
R29	Resistor	180 Ω , 1W	–	–
R30	Resistor	820 Ω , 10W	–	–

<i>Circuit Reference</i>	<i>Description</i>	<i>Value, Rating</i>	<i>Manufacturer/Supplier</i>	<i>Type</i>
R31	Resistor	180Ω, 1W	–	–
R32	Resistor	1.8Ω, 0.5W	–	–
R33	Resistor	22Ω, 2W	–	–
R34	Resistor	5.6Ω, 1W	–	–
C20	Capacitor	470μF, 500V	–	–
C21	Capacitor	1μF, 50V	Wima	–
C22	Capacitor	470μF, 500V	–	–
C23	Capacitor	2μF, 160V	–	–
C24	Capacitor	10μF, 100V	Biltema AS	–
C25	Capacitor	50 μF, 500 V	Schaleco Electrolyte	–
C26	Capacitor	10μF, 100V	Biltema AS	–
C27	Capacitor	470μF, 500V	–	–
D20	Bridge Rectifier	2 A, $U_{RRM}=200V$	Semikron GmbH	SKB 2/0.2
D21	High-speed Diode	0.3A, $U_{RRM}=200 V$	Philips Semiconductor	1N4150
D22	Zener Diode	18V	Philips Semiconductor	1N4150
D23-26	Rectifier Diodes	1A, $U_{RRM}=600V$	Fairchild Semiconductor	1N4005
D27	LED	Green	–	–
D28	LED	Red	–	–
Q20	N-channel MOSFET	$i_D=14A, U_{DS}=50V$	Philips Semiconductor	BUZ71
Q21	P-channel MOSFET	$i_D=-8A, U_{DS}=50V$	Philips Semiconductor	BUZ171
T20	Transformer	220/14VAC	Trans Electric AS	–
SW20	Selector Switch	125VAC, 6A	–	–
<i>Current Measurement System:</i>				
R40	Wire-wound Resistor	0.30Ω/100W	Alnæs Nye AS	–
R41	Resistor	Varies with L40	–	–
C40	Capacitor	0.33μF, 100V	–	–
L40	Rogowski Coil	Various	Author	–

<i>Circuit Reference</i>	<i>Description</i>	<i>Value, Rating</i>	<i>Manufacturer/Supplier</i>	<i>Type</i>
<i>Voltage Measurement System:</i>				
R50 (a-c)	HV-Resistors	1M Ω , 5W, 10kV	–	–
R51	HV-Resistor	1M Ω , 5W, 10kV	–	–
R53 (a-d)	HV-Resistors	1M Ω , 5W, 10kV	–	–
R52 (a-b)	Resistors	15k Ω , 20W	–	–
R54 (a-b)	Resistors	3.9k Ω , 10W	–	–
C50	Capacitor	100 μ F, $U_R=500$ V	Frako	FPF
C51	Capacitor	100 μ F, $U_R=500$ V	–	–
D50 (a-b)	High-speed Diodes	0.45A, $U_{RRM}=75$ V	Philips Semiconductor	1N4148
VS50	External DC Power Supply	-20.0VDC	–	–
<i>Circuit Protection:</i>				
RV90-92	Varistors	$U_{100A}=1815$ VDC $U_{1mA}=680$ VDC	Siemens Matsushita Components	SIOV-S20K680
D90	Rectifier Diode	$i_{FSM}=1000$ A, $U_{RRM}=1.6$ kV	Semikron GmbH	SKR 70/16
D91	Rectifier Diode	$i_{FSM}=1700$ A, $U_{RRM}=1.2$ kV	International Rectifier	85HF120M
F90	Fuse	1.6 A, 220V	–	32x6.3 [mm]
DS90	Strobelight	12 VDC, 0.2A	Clas Ohlson	Blue
VS90	Universal Regulated AC/DC Adaptor	12 VDC, 0.5A	Vanson Electronic Ltd.	RC-48

References

- Abdel-Salam, M., Anis, H., El-Morshedy, A. & Radwan, R. (2000). *High-Voltage Engineering: Theory and Practice*. ISBN 0-8247-0402-9. 2nd Edition. Marcel Dekker, New York.
- Akindele, O.O., Bradley, D., Mak, P.W. & McMahon, M. (1982). *Spark Ignition of Turbulent Gases*. *Combustion and Flame*, **47**, pp. 129-155.
- Alvestad, B. (1975). *An Electric Spark Generator for Determination of Minimum Ignition Energies of Dust Clouds*. CMI-no. 72001-12, Chr. Michelsen Institute, Dept. of Science and Technology, Bergen.
- ASTM E1226-94 (1999). *Standard Test Method for Pressure and Rate of Pressure Rise for Combustible Dusts*. Annual Book of ASTM Standards. ISBN 0-8031-2698-0. Vol. 14.02, pp. 426-436, American Society for Testing and Materials, Pennsylvania, USA.
- Ballal, D.R. & Lefebvre, A.H. (1974). *The Influence of Flow Parameters on Minimum Ignition Energy and Quenching Distance*. 15th Symposium (International) on Combustion, The Combustion Institute, Pittsburgh, pp. 1473-1481.
- Ballal, D.R. & Lefebvre, A.H. (1977). *Ignition and Flame Quenching in Flowing Gaseous Mixtures*. Proceedings of the Royal Society of London, Series A: Mathematical and Physical Sciences, **357**, pp. 163-181.
- Barnett, H.C. & Hibbard, R.R. (1957). *Basic Considerations in the Combustion of Hydrocarbon Fuels with Air*. NACA Report 1300.
- Barreto, E., Reynolds, S.I. & Jurenka, H. (1974). *Ignition of Hydrocarbons and the Thermalization of Electrical Discharges*. *Journal of Applied Physics*, Vol. **45**, No. 8, pp. 3317-3327.
- Barreto, E., Reynolds, S.I. & Jurenka, H. (1977). *The Formation of Small Sparks*. *Journal of Applied Physics*, Vol. **48**, No. 11, pp. 4510-4520.
- Bartknecht, W. (1993). *Explosionsschutz: Grundlagen und Anwendung*. ISBN 3-540-55464-5. Springer-Verlag, Berlin.
- Bazelyan, E.M. & Raizer, Y.P. (1997). *Spark Discharge*. ISBN 0-8493-2868-3, CRC Press, Boca Raton.

- Belles, F.E. & Swett, C.C. (1957). *Ignition and Flammability of Hydrocarbon Fuels*. Chapter III in Barnett & Hibbard (1957), NACA Report 1300.
- Bennett, D., Lunn, G.A., Torrent, J.V., Querol, E. & Fritze, J.P. (2003). *A Test for Electrical Ignitions of Flammable Dust Clouds*. Journal of Loss Prevention in the Process Industries, **16**, pp. 33-40.
- Bentley, J.P. (1995). *Principles of Measurement Systems*. 3rd Edition. ISBN 0-582-23779-3. Longman Singapore Publishers Ltd., Singapore.
- Beynon, J. (1972). *The Conduction of Electricity Through Gases*. ISBN 0-245-50580-6. Harrap, London.
- Boyle, A.R. & Llewellyn, F.J. (1950). *The Electrostatic Ignitibility of Dust Clouds and Powders*. Journal of the Society of Chemical Industry (J.S.C.I.), **69**, pp. 173-181.
- Bradley, D. & Mitcheson, A. (1976). *Mathematical Solutions for Explosions in Spherical Vessels*. Combustion and Flame, **26**, pp. 201-217.
- Cashdollar, K.L. & Chatrathi, K. (1992). *Minimum Explosible Dust Concentration Measured in 20-L and 1-m³ Chambers*. Combustion Science and Technology, **87**, pp. 157-171.
- Cashdollar, K.L. & Hertzberg, M. (1985). *20-L Explosibility Test Chamber for Dusts and Gases*. Review of Scientific Instruments, **56** (4), pp. 596-602.
- Cesana, C. (2001). *Final Report: Calibration-Round-Robin CaRo 00/01*. Adolf Kühner AG, Birsfelden, at: http://www.kuhner.com/DOCUMENT/B052_172.pdf.
- Cesana, C. & Siwek, R. (2001). *Operating Instructions 20-l-Apparatus 6.0*. Adolf Kühner AG, CH-4127 Birsfelden, Switzerland.
- Cobine, J.D. (1941). *Gaseous Conductors: Theory and Engineering Applications*. McGraw Hill, New York.
- Craggs, J.D. & Meek, J.M. (1954). *High Voltage Laboratory Technique*. Butterworths Scientific Publications, London.
- Creed, F.C. (1989). *The Generation and Measurement of High Voltage Impulses*. ISBN 0-944954-00-6. Center Book Publishers Inc., Princeton.
- Cross, J. (1987). *Electrostatics: Principles, Problems and Applications*. ISBN 0-85274-589-3, Adam Hilger, Bristol.
- Dahoe, A.E. (2000). *Dust explosions: A Study of Flame Propagation*. ISBN 90-90-13707-8. PhD Thesis, Technische Universiteit Delft. Delft University Press, Delft.
- Dahoe, A.E., Zavenbergen, J.F., Lemkowitz, S.M. & Scarlett, B. (1996). *Dust Explosions in Spherical Vessels: The Role of Flame Thickness in the Validity of the 'Cube-Root Law'*. Journal of Loss Prevention in the Process Industries, **9** (1), pp. 33-44.
- Dale, J.D., Checkel, M.D. & Smy, P.R. (1997). *Application of High Energy Ignition Systems to Engines*. Progress in Energy and Combustion Science, **23**, pp. 379-398.
- Dascalescu, L., Samulia, A. & Tobazéon, R. (1996). *Dielectric Behaviour of Particle-Contaminated Air-Gaps in the Presence of Corona*. Journal of Electrostatics, **36**, pp. 253-275.

- de Soete de, G.G. (1971). *The Influence of Isotropic Turbulence on the Critical Ignition Energy*. 13th Symposium (International) on Combustion, The Combustion Institute, Pittsburgh, pp. 735-743.
- Eckhoff, R.K. (1975). *Towards Absolute Minimum Ignition Energies for Dust Clouds?* Combustion and Flame, **24**, pp. 53-64.
- Eckhoff, R.K. (2003). *Dust Explosions in the Process Industries*. Third edition. ISBN 0-7506-7602-7. Gulf Professional Publishing, Amsterdam.
- Eckhoff, R.K. & Enstad, G. (1976). *Why Are "Long" Electric Sparks More Effective Dust Explosion Initiators Than "Short" Ones?* Combustion and Flame, **27**, pp. 129-131.
- EN 1127-1 (1997). *Explosive Atmospheres – Explosion Prevention and Protection – Part 1: Basic Concepts and Methodology*. European Standard, version EN 1127-1:1997.
- Franke, A. (2000). *Diagnostics of Electrical Phenomena in Gases for the Monitoring of Spark-Ignited Combustion*. Licentiate Thesis, Lund Institute of Technology, Lund University, Lund.
- Glarner, T. (1983). *Temperatureinfluss auf das Explosions- und Zündverhalten brennbarer Stäube*. Doctorate Thesis No. 7350, ETH, Zurich (in German).
- Glarner, Th. (1984). *Mindestzündenergie – Einfluß der Temperatur*. VDI-Berichte **494**, ISBN 3-18-090494-1, pp. 109-118, VDI-Verlag GmbH, Düsseldorf (in German).
- Glasoe, G.N. Ed. & Lebacqz, J.V. Ed. (1948). *Pulse Generators*. McGraw-Hill, New York.
- Hertzberg, M., Conti, R.S. & Cashdollar, K.L. (1984). *Spark Ignition Energies for Dust-Air Mixtures: Temperature and Concentration Dependences*. 20th Symposium (International) on Combustion, The Combustion Institute, Pittsburgh, pp. 1681-1690.
- Hill, R.D. (1975). *Thermalization of a Spark Channel*. Journal of Applied Physics, Vol. **46**, No. 7, pp. 2910-2914.
- Hill, R.D. (1979). *Ignition of Hydrocarbons by Small Sparks*. Journal of Applied Physics, Vol. **50**, No. 1, pp. 127-131.
- Hirsh, M.N. Ed. & Oskam H.J. Ed. (1978). *Gaseous Electronics: Electrical Discharges*, (Volume 1). ISBN 0-12-349701-9. Academic Press, New York.
- Howatson, A.M. (1976). *An Introduction to Gas Discharges*. 2nd Edition, ISBN 0-08-020575-5. Pergamon Press Ltd, Oxford.
- Ishii, K., Aoki, O., Ujiie, Y. & Kono, M. (1992). *Investigation of Ignition by Composite Sparks under High Turbulence Intensity Conditions*. 24th Symposium (International) on Combustion, The Combustion Institute, Pittsburgh, pp. 1793
- ISO 6184-1 (1985). *Explosion Protection Systems – Part 1: Determination of Explosion Indices of Combustible Dusts in Air*. International Organization for Standardization.
- Jurenka, H. & Barreto, E. (1982). *Study of Electron Waves in Electrical Discharge Channels*. Journal of Applied Physics, Vol. **53**, No. 5, pp. 3481-3490.

- Kalkert, N. & Schecker, H.-G. (1979). *Theoretische Überlegungen zum Einfluß der Teilchengröße auf die Mindestzündenergie von Stäuben*. Chem.-Ing.-Tech. **51**, pp. 1248-1249.
- Kalkert, N. & Schecker, H.-G. (1980). *Einfluß der Kornverteilung auf die Teilchengröße auf die Mindestzündenergie von explosiblen Stäuben*. Chem.-Ing.-Tech. **52**, pp. 515-517.
- Kind, D. (1978). *An Introduction to High-Voltage Experimental Technique*. ISBN 3-528-08383-2. Vieweg, Braunschweig.
- Knowlton, A.E. (Ed.) (1949). *Standard Handbook for Electrical Engineers*. 8th Edition, McGraw-Hill, New York.
- Ko, Y., Anderson, R.W. & Arpaci, V.S. (1991). *Spark Ignition of Propane-Air Mixtures Near the Minimum Ignition Energy: Part I. An Experimental Study*. Combustion and Flame **83**, pp. 75-87.
- Kono, M, Hatori, K. & Inuma, K. (1984). *Investigation on Ignition Ability of Composite Sparks in Flowing Mixtures*. 20th Symposium (International) on Combustion, The Combustion Institute, Pittsburgh, pp. 133-140.
- Kono, M, Kumagai, S. & Sakai, T. (1976). *The Optimum Condition for Ignition of Gases by Composite Sparks*. 16th Symposium (International) on Combustion, The Combustion Institute, Pittsburgh, pp. 757-766.
- Kuffel, E., Zaengl, W.S. & Kuffel, J. (2000). *High Voltage Engineering: Fundamentals*. 2nd Edition. ISBN 0-7506-3634-3. Newnes (An imprint of Butterworth-Heinemann), Oxford.
- Kumagai, S. & Sakai, T. (1967). *Ignition of Gases by High-Energy Sparks*. 11th Symposium (International) on Combustion, The Combustion Institute, Pittsburgh, pp. 995-1001.
- Lewis, B. & von Elbe, G. (1987). *Combustion, Flames and Explosions of Gases*. 3rd Edition. ISBN 0-12-446751-2. Academic Press, Orlando.
- Lim, M.T., Anderson, R.W. & Arpaci, V.S. (1987). *Prediction of Spark Kernel Development in Constant Volume Combustion*. Combustion and Flame, **69**, pp. 303-316.
- Line, L.E., Rhodes, H.A. & Gilmer, T.E. (1959). *The Spark Ignition of Dust Clouds*. Journal of Physical Chemistry, **63**, pp. 290-294.
- Llewellyn-Jones, F. (1957). *Ionization and Breakdown in Gases*. Methuen & Co Ltd, London.
- Loeb, L.B. (1939). *Fundamental Processes of Electrical Discharges in Gases*. John Wiley & Sons, New York.
- Lüttgens, G. & Glor, M. (1989). *Understanding and Controlling Static Electricity*. ISBN -8169-0510-2, Expert-Verlag.
- Lüttgens, G. & Wilson, N. (1997). *Electrostatic Hazards*. ISBN 0-7506-2782-4, Butterworth-Heinemann, Oxford.

- Maly, R. & Vogel, M. (1978). *Initiation and Propagation of Flame Fronts in Lean CH₄-Air Mixtures by the Three Modes of the Ignition Spark*. 17th Symposium (International) on Combustion, The Combustion Institute, Pittsburgh, pp. 821-831.
- Maly, R. (1981). *Ignition Model for Spark Discharges and the Early Phase of Flame Front Growth*. 18th Symposium (International) on Combustion, The Combustion Institute, Pittsburgh, pp. 1747-1754.
- Maly, R. (1984). Spark Ignition: *Its Physics and Effect on the Internal Combustion Engine*. Pages 91-148 in *Fuel Economy in Road Vehicles Powered by Spark Ignition Engines*, edited by Hilliard, J.C. and Springer, G.S., ISBN 0-306-41438-4, Plenum Press, New York.
- Martin, F. (1999). *SEMIKRON: innovation + service, Power Electronics '99*. Semikron International, Nürnberg, Germany.
- Matsuda, T. & Naito, M. (1983). *Effects of a Spark Discharge Duration on Ignition Energy for Dust-Air Suspensions*. Pages 189-198 in *Particulate Systems – Technology and Fundamentals*, by Beddow, J.K. (Ed.), Hemisphere Publishing Corporation, Washington.
- Meek, J.M. & Craggs, J.D. (1953). *Electrical Breakdown of Gases*. Clarendon Press, Oxford.
- Meek, J.M. (Ed.) & Craggs, J.D. (Ed.) (1978). *Electrical Breakdown of Gases*. John Wiley & Sons, Chichester.
- Murgatroyd, P.N. (1991). *Making Rogowski Coils*. Measurement Science and Technology, **2**, pp. 1218-1219.
- Nagy, J., Conn, J.W. & Verakis, H.C. (1969). *Explosion Development in a Spherical Vessel*. R.I. 7279, U.S. Department of the Interior, Bureau of Mines.
- Penning, F.M. (1965). *Electrical Discharges in Gases*. (Reprint of 1st edition 1957). Philips Technical Library, Eindhoven.
- Podlesak, M. (1990). *Rogowski Coil Calibration on a Capacitive Discharge Rig Without the Use of a Current Reference*. Review of Scientific Instruments, **61** (2), pp. 892-896.
- prEN 14034-1 (2003). *Determination of Explosion Characteristics of Dust Clouds – Part 1: Determination of the Maximum Explosion Pressure*. Technical Committee CEN/TC 305 (preliminary version, dated 14.02.2003).
- prEN 14034-2 (2003). *Determination of Explosion Characteristics of Dust Clouds – Part 2: Determination of the Maximum Explosion Pressure Rise of Dust Clouds*. Technical Committee CEN/TC 305 (preliminary version, dated 14.02.2003).
- Priede, T. (1957). *Initiation of Explosions in Gases*. Thesis for the Degree of Doctor of Philosophy, University of London.
- Radun, A. (1995). *An Alternative Low-Cost Current-Sensing Scheme for High-Current Power Electronics Circuits*. IEEE Transactions on Industrial Electronics, **42** (1), pp. 78-84.
- Raether, H. (1964). *Electron Avalanches and Breakdown in Gases*. Butterworths & Co Ltd, London.

- Ramboz, J.D. (1996). *Machinable Rogowski Coil, Design, and Calibration*. IEEE Transactions on Instrumentation and Measurement, Vol. **45**, No. 2, pp. 511-515.
- Ray, W.F. & Hewson, C.R. (2000). *High Performance Rogowski Current Transducers*. IEEE – IAS Conference Proceedings, Rome, September 2000.
- Rees, J.A. (Ed.) (1973). *Electrical Breakdown in Gases*. Macmillan, London.
- Schwab, A.J. (1972). *High-Voltage Measurement Techniques*. ISBN 0-262-19096-6. M.I.T. Press, Cambridge, Massachusetts.
- Shapiro, R. (1970). *Smoothing, Filtering, and Boundary Effects*. Reviews of Geophysics and Space Physics, **8** (2), pp. 359-387.
- Shapiro, R. (1975). *Linear Filtering*. Mathematics of Computation, 29, pp. 1094-1097.
- Sher, E., Ben-ya'ish, J. & Kravchik, T. (1992). *On the Birth of a Spark Channel*. Combustion and Flame, **89**, pp. 186-194.
- Smith, D.C. (1993). *High Frequency Measurements and Noise in Electronic Circuits: A Practical Guide of Successful Techniques for Design, Debugging, and Reducing Noise*. ISBN 0-442-00636-5. Van Nostrand Reinhold, New York.
- Somerville, J.M. (1959). *The Electric Arc*. Methuen & Co Ltd, London.
- Strid, K-G. (1973). *Experimental Techniques for the Determination of Ignition Energy*. Oxidation and Combustion Reviews, **6**, pp. 1-46.
- Strigel, R. (1955). *Elektrische Stoßfestigkeit*. 2nd Edition. Springer-Verlag, Berlin (in German).
- Swett, C.C. (1948). *Investigation of Spark Gaps Subjected to Altitude and Air-Velocity Conditions*. NACA Research Memorandum No. E8117, National Advisory Committee for Aeronautics, Washington.
- Swett, C.C. (1949). *Effect of Gas Stream Parameters on the Energy and Power Dissipated in a Spark and on Ignition*. 3rd Symposium on Combustion and Flame and Explosion Phenomena, The Williams & Wilkins Company, Maryland.
- Swett, C.C. (1956a). *Spark Ignition of Flowing Gases*. NACA Report **1287**, Lewis Flight Propulsion Laboratory, National Advisory Committee for Aeronautics, Cleveland.
- Swett, C.C. (1956b). *Spark Ignition of Flowing Gases Using Long-Duration Discharges*. 6th Symposium (International) on Combustion, The Combustion Institute, Pittsburgh, pp. 523-532.
- Ujiie, Y. (1994). *Spark Ignition Properties of Combustible Mixtures under High-Turbulence-Intensity Conditions*. JSME International Journal, Series B, Vol. **37**, No. 2, pp. 661-617.
- von Engel, A. (1965). *Ionized Gases*. 2nd Edition. Oxford University Press, Oxford.
- von Pidoll, U. (2001). *The Ignition of Clouds of Sprays, Powders and Fibers by Flames and Electrical Sparks*. Journal of Loss Prevention in the Process Industries, **14**, pp. 103-109.
- Ward, D.A. & Exon, J.L.T. (1993). *Using Rogowski Coils for Transient Current Measurements*. Engineering Science and Education Journal, June, pp. 105-113.

- Warnatz, J., Maas, U. & Dibble, R.W. (1996). *Combustion: Physical and Chemical Fundamentals, Modeling and Simulation, Experiments, Pollution Formation*. ISBN 3-540-60730-7. Springer Verlag, Berlin Heidelberg.
- Wheeler, R.V. (1919). *The Inflammation of Mixtures of Ethane and Air in a Closed Vessel: The Effects of Turbulence*. Journal of the Chemical Society – Transactions (British), Vol. **CXV**, part I, article VIII, pp. 81-94.
- Zhen, G. & Leuckel, W. (1997). *Effects of Ignitors and Turbulence on Dust Explosions*. Journal of Loss Prevention in the Process Industries, **10** (5-6), pp. 317-324.
- Zhu, H., Liu, X. & Li, H. (1988). *Influence of Type of Chemical Ignitor on Violence of Maize Starch and Aluminium Dust Explosions in a Closed 20-litre Sphere*. Fire Safety Journal, **13**, pp. 181-183.
- Ziegler, G.F.W., Wagner, E.P. & Maly, R.R. (1984). *Ignition of Lean Methane-Air Mixtures by High Pressure Glow and Arc Discharges*. 20th Symposium (International) on Combustion, The Combustion Institute, Pittsburgh, pp. 1817-1824.
- Zykin, F.A. & Kazakov, M.K. (1998). *A Portable Digital Instrument for Measuring Large Direct Currents*. Electrical Technology Russia, **4**, pp. 87-92.

APPENDIX B

Experimental Apparatus

The arc generator is documented separately in Appendix A; this appendix describes the additional experimental apparatus used the new 20-liter test facility at the University of Bergen (UoB).

B.1 Explosion Vessels and Dispersion Systems

Several different explosion vessels and dispersion systems have been used in dust explosion research throughout the years, a general overview can be found in e.g. Eckhoff (2003). The most frequently used equipment in standardized tests will be described briefly, before the equipment at the dust explosion facility at the University of Bergen is presented.

B.1.1 Standardized Explosion Vessels and Dispersion Systems

The 1-m³ ISO vessel

The International Organisation for Standardization (ISO) provides specifications for the experimental determination of explosion indices of combustible dusts in air (ISO 6184-1, 1985). The standard describes the design and operation of a 1-m³ cylindrical reference chamber. Alternative test equipment and/or procedures can be used provided *“it has been proven that such methodology gives results directly, or by calculation, that are commensurate ($\pm 20\%$) with the results obtained using the 1 m³ apparatus”* for a specified number of dusts in various explosibility ranges. A schematic of the 1-m³ ISO vessel is shown in Figure B-1.

The 20-l Siwek sphere

The most frequently used explosion vessel for the determination of explosion indices for explosible dusts is the Siwek apparatus; a hollow sphere with a volume of 20-litres made of stainless steel. The vessel is designed for a static operating pressure of 30 barg, and a water jacket makes it possible to control the test temperature. A cross-sectional drawing of the Siwek sphere is shown in Figure B-2.

Use of the Siwek apparatus for determining explosion indices in agreement with the ISO reference chamber is given in ASTM E1226-94 (1999). Before a test, the vessel is evacuated to 0.4 bars absolute. The dust is dispersed into the sphere from a pressurized storage chamber ($V_r = 0.6$ litre, $p_{r,0} = 20$ barg) via an outlet valve and a dispersion nozzle. The first vessels were equipped with a *perforated dispersion tube*, similar to the one in the 1-m³ ISO vessel. The so called *rebound nozzle* was introduced later because explosion indices determined with the perforated dispersion tube proved to be significantly lower than those determined by the 1-m³ ISO vessel, especially for dusts with poor flow behaviour (Siwek, 1988). The rebound nozzle is shown in Figure B-2. The ignition source, usually two chemical igniters with total energy of 10 kJ (5 kJ each), is activated after a preset time interval (usually 60 ms) after onset of dispersion. Two piezoelectric pressure sensors measure the pressure development inside the vessel. Two piezoelectric pressure sensors measure the pressure development inside the vessel.

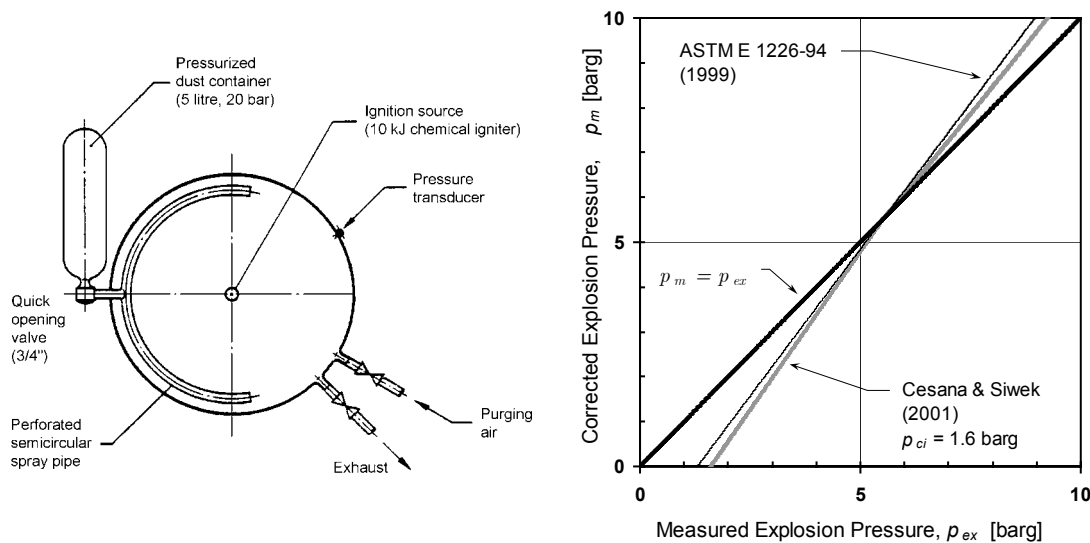


Figure B-1 The drawing to the left is a vertical cross section of the cylindrical reference chamber prescribed by ISO 6184-1 (1985). The explosion chamber has a volume of 1 m³ and aspect ratio 1:1. The diagram (right) shows a comparison between two formulas for making the experimentally determined explosion pressures (p_{ex}) from the 20-l Siwek sphere agree with results from the 1-m³ ISO chamber.

Due to cooling effects from the walls, and the pressure effect caused by the pyrotechnic igniters, the measured explosion pressure p_{ex} has to be corrected in order to agree with results from the 1-m³ vessel. According to Cesana and Siwek (2001) the corrected explosion pressure can be estimated by:

$$p_m = \begin{cases} \frac{5.5 \cdot (p_{ex} - p_{ci})}{(5.5 - p_{ci})} & \text{when } p_{ex} < 5.5 \text{ barg} \\ 0.775 \cdot p_{ex}^{1.15} & \text{when } p_{ex} > 5.5 \text{ barg} \end{cases} \quad (\text{B.1})$$

where p_{ci} is the pressure due to the chemical igniters alone, $p_{ci} < 1.6$ barg for two 5 kJ igniters. The formula described in ASTM E1226-94 (1999), assuming $p_{ci} = 1.3$ barg, is:

$$p_m = \begin{cases} \frac{5.5 \cdot (p_{ex} - 1.3)}{4.2} & \text{when } p_{ex} < 5.5 \text{ barg} \\ 1.3 \cdot p_{ex} - 1.65 \text{ bar} & \text{when } p_{ex} > 5.5 \text{ barg} \end{cases} \quad (\text{B.2})$$

There is little difference in the results from the two correction formulas, as can be seen from Figure B-1. Note that these formulas have been developed for the spherical 20-litre Siwek sphere.

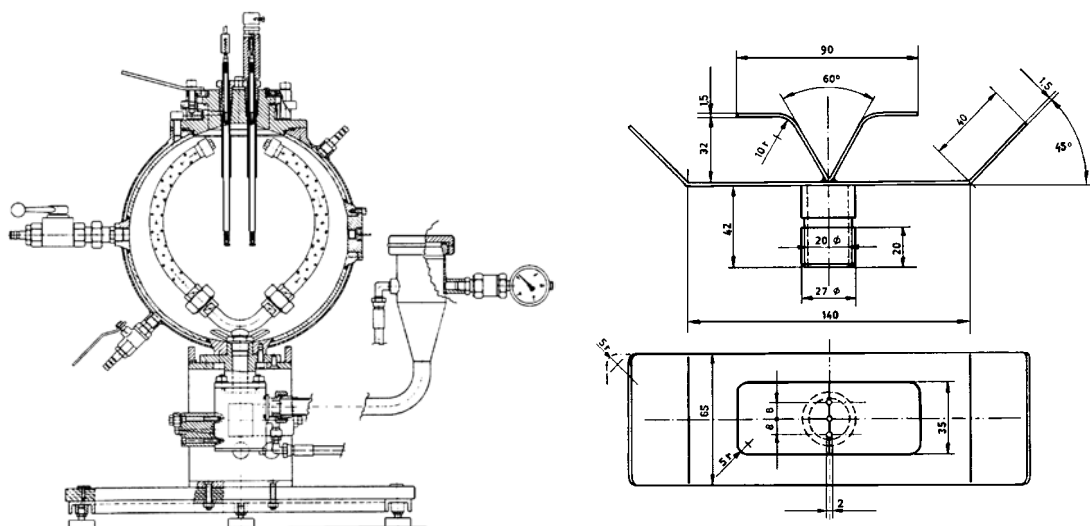


Figure B-2 Siwek 20-l apparatus fitted with the original ring nozzle (left), from ASTM E1226-94 (1999). Rebound nozzle (right), the dispersion nozzle usually used with the 20-l apparatus (from Siwek, 1988).

The 20-l USBM vessel

Another 20-l explosion chamber for the determination of explosion indices for explosible dusts was developed by the US Department of the Interior, Bureau of Mines (USBM). The original vessel, described by Cashdollar & Hertzberg (1985), is equipped with pressure transducers, optical dust probes, an oxygen sensor, and infrared pyrometers. The maximum explosion pressure is 21 barg.

Use of the USBM chamber for experimental estimation of the minimum explosible concentration (MEC), also referred to as the lower explosibility limit (LEL), is described in ASTM E1515-98 (1999). The standard test procedure is to place the dust inside the *dispersion nozzle* (or on top of the nozzle if there is too much dust). An alternate dispersion system, the *cone dispenser*, can also be used. The vessel is evacuated to $p_{v,0} = 0.14$ bara, before a short pulse of air (300 ms, $p_{r,0} = 9$ barg) disperses the dust. The ignition source, either a chemical igniter or an electric spark, is activated 100 milliseconds after the end of the dispersion pulse. The standard also describes how MEC can be estimated with the Siwek sphere. The USBM vessel, with the two dispersion nozzles, is shown in Figure B-3.

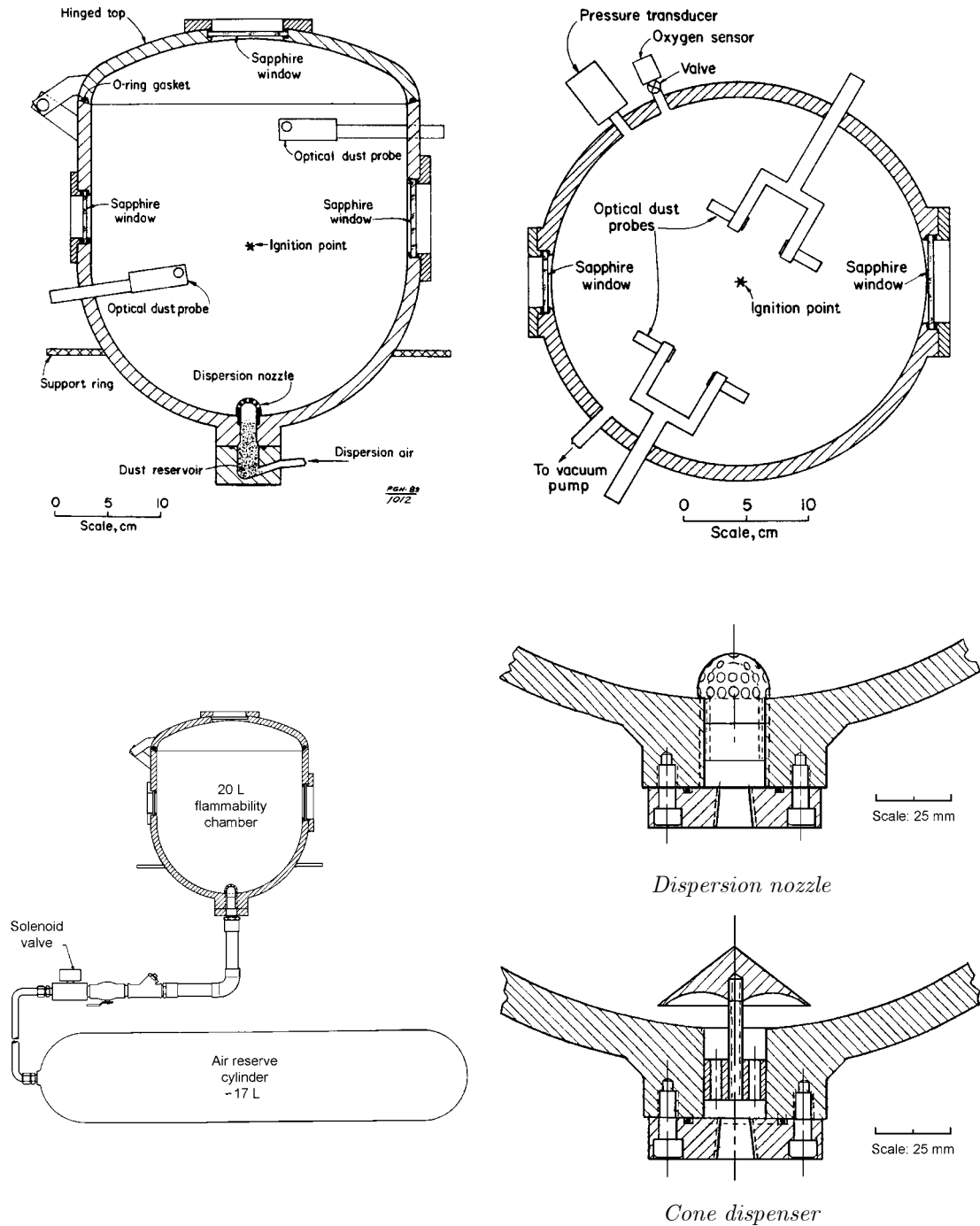


Figure B-3 Vertical (upper left) and horizontal (upper right) cross section of the 20-l USBM explosibility test chamber for dusts and gases (Cashdollar and Hertzberg, 1985). A schematic of the USBM vessel (lower left) showing air reserve cylinder and dispersion plumbing, and the two alternate dispersion nozzles (lower right) used with the vessel (ASTM E1515-98, 1999).

B.1.2 Explosion Vessels and Dispersion System at the 20-Litre Dust Explosion Test Facility at UoB

Two new 20-l explosion vessels have been made; both can be fitted with the same dispersion system. The main vessel is similar in shape to the vessel designed by USBM (described above), and will from here on be referred to as the *modified USBM-vessel*. The other vessel, with cubical internal shape, will be referred to as the *cubical vessel*. The dispersion system is almost identical to the one used by the 20-l Siwek sphere, but some new dispersion nozzles has been tested.

Modified USBM vessel

A drawing of the modified USBM vessel is shown in Figure B-4, photographs in Figure B-5. The modified vessel lacks several of the features of the original vessel, like the sapphire window in the lid, optical dust probes, oxygen sensor and infrared pyrometers; it is however possible to add these features later. An adaptor flange in the bottom of the vessel makes it possible to attach the inlet valve from the Siwek sphere (a product of Adolf Kühner AG) to the vessel, and to fit nozzles with $\frac{3}{4}$ " NPSM threads inside the vessel. The four windows/flanges in the sides of the vessel are also of the same kind as the ones used with the Siwek sphere. The lower part of the vessel can be split in two in a rather thick flange. The original idea was to implement some kind of water-cooling in this area, but this has been postponed. The lid and some of the upper section (down to the welding seam) is a 12" Class 300 T-bolt Horizontal Hinged Closure purchased from Tube Turns Technologies Inc., Kentucky. It is made of 304L stainless steel. The volume of the modified USBM vessel has been determined by water filling to be 20.50 ± 0.02 litres. The vessel is certified to a working pressure of 27 barg by the Norwegian Directorate for Fire and Electrical Safety (Direktoratet for Brann og Eksplosjonsvern, DBE), and participated in the round robin test CaRo 00/01 for p_{max} and K_{St} (Appendix A; Cesana, 2001).

Cubical vessel

The main reason for adopting a cubical geometry is the ease of fitting a Cartesian coordinate system. This facilitates the implementation of the geometrical boundary conditions in commercially available CFD codes such as the FLACS code from GexCon AS; this is illustrated in Appendix E.

Photographs of the cubical vessel are shown in Figure B-6 and Figure B-7. The adaptor flange for the cubical vessel is analogous to the one for the modified USBM vessel, but with the possibility of fitting a piezoelectric pressure transducer for measuring the pressure at the nozzle inlet (p_n) during dispersion. The cubical vessel can be fitted with two alternate lids, one is only suitable for dispersion experiments and the other is used for explosions, see Figure B-6. Machine drawings of the cubical vessel are shown in Figure B-8, Figure B-9 and Figure B-10. The volume of the cubical vessel has been determined by water filling to be 19.97 ± 0.02 litres. The vessel is not certified to any particular working pressure; it participated in the round robin test CaRo 00/01 for p_{max} and K_{St} (Cesana, 2001), but failed to qualify (see Appendix A).

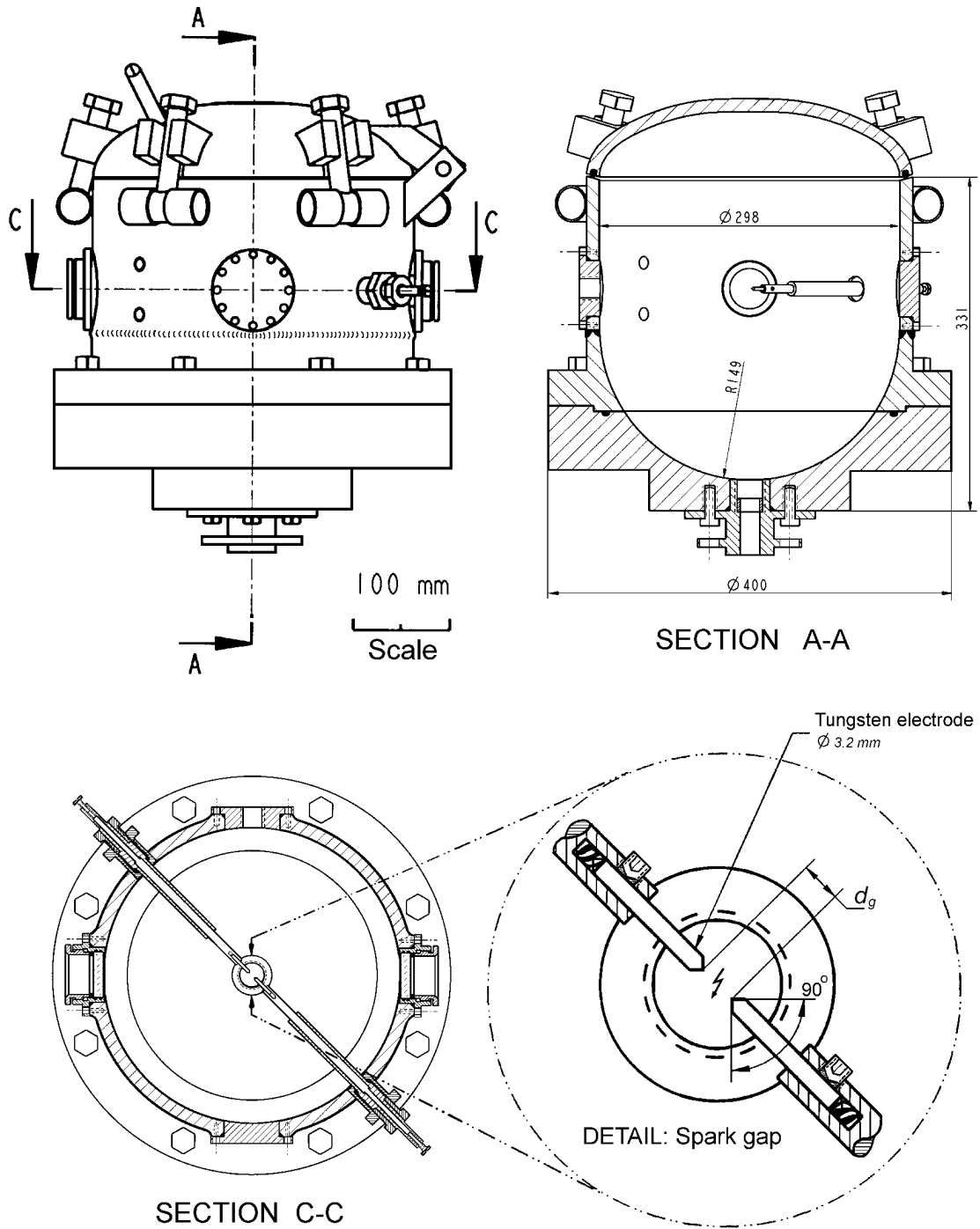


Figure B-4 Drawing of the 20-litre modified USBM vessel, showing windows, flanges and electrode assembly (drawn by R. H. Larsen).

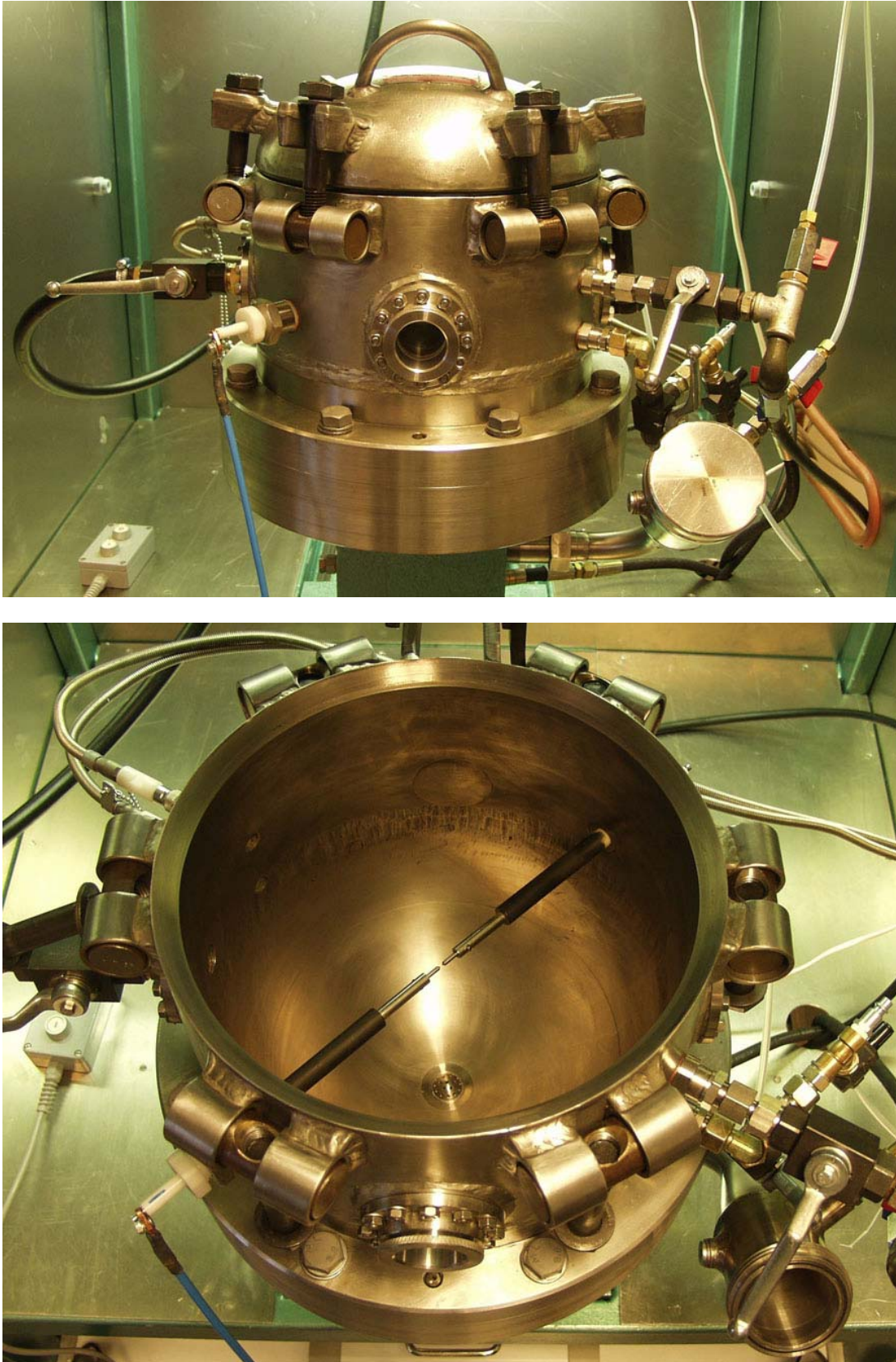


Figure B-5 The modified 20-litre USBM explosion vessels at the dust explosion laboratory at the University of Bergen. The dust cloud is usually ignited by a spark/arc between the two electrodes seen inside the USBM-vessel (lower picture). Photos by M. Vabø.

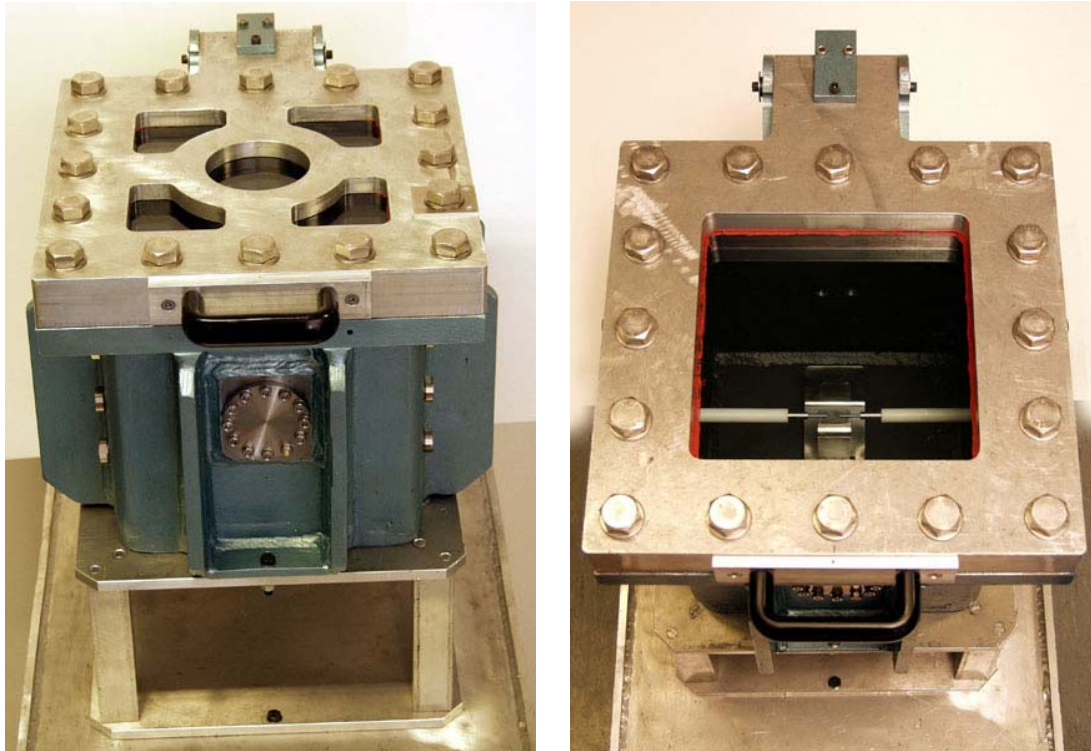


Figure B-6 The 20-litre cubical explosion vessels at the dust explosion laboratory at the University of Bergen. The photographs shows the two different lids, the one used for explosions (left), and the one used for LDA measurements during the dispersion process (right). The photos are taken by M. Vabø.

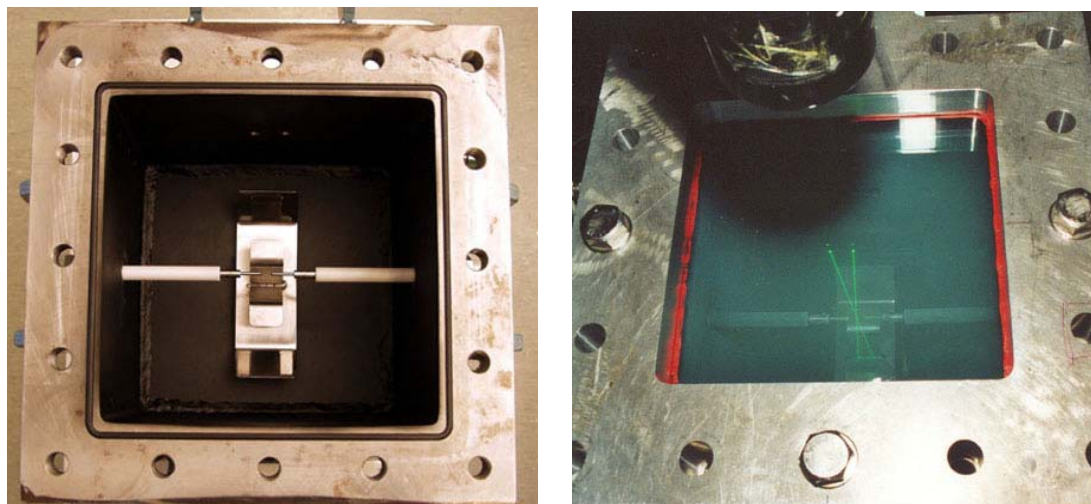


Figure B-7 Top-view of the 20-litre cubical explosion vessels (left) showing the electrodes, rebound nozzle and the o-ring gasket in the top flange (photo taken by M. Vabø). Turbulence measurement with LDA (right), showing the LDA probe and the laser beams inside the vessel (photo taken by I.O. Sand).

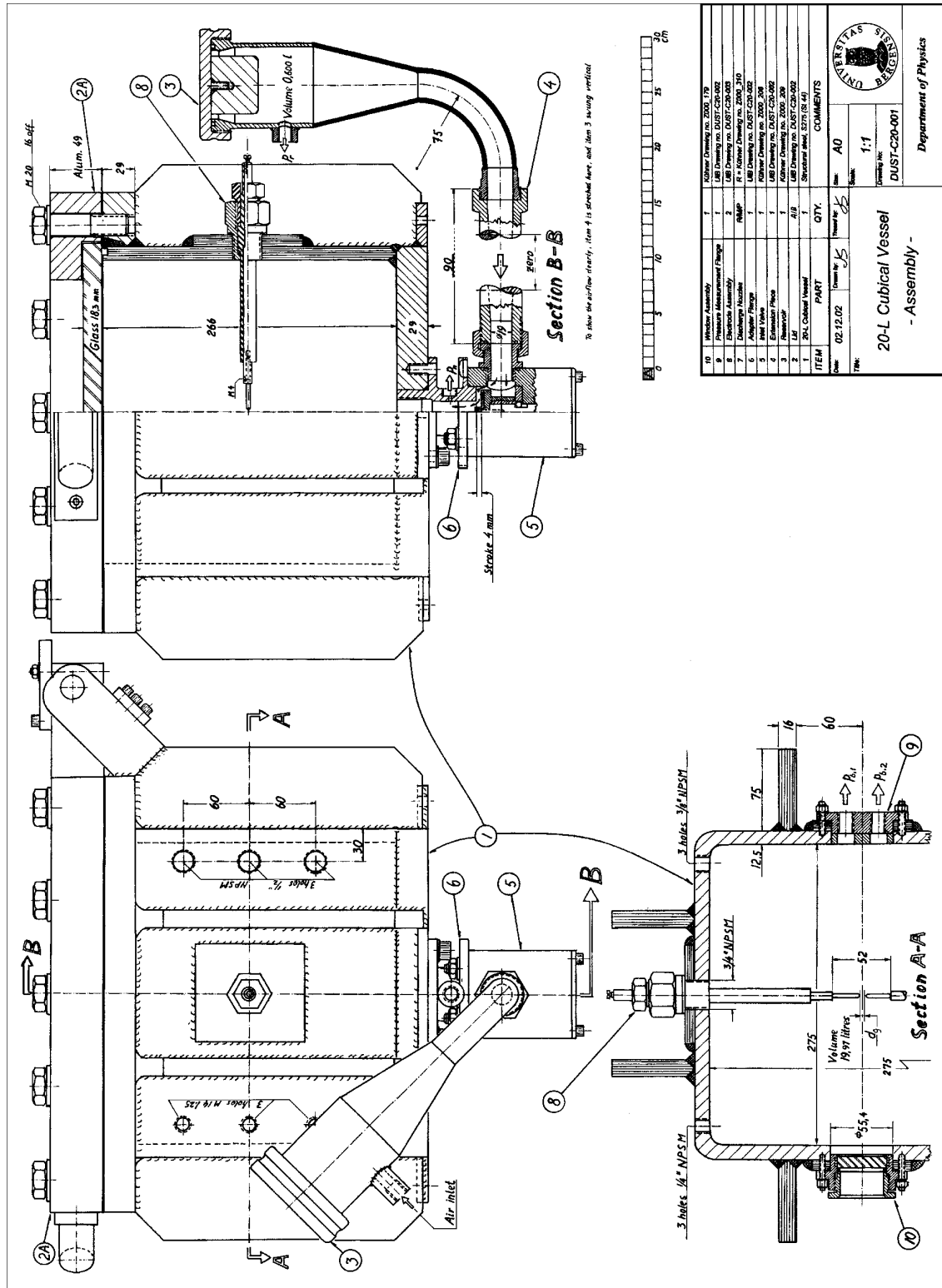


Figure B-8 Machine drawing of the 20-litre cubical explosion vessels at the dust explosion laboratory at the University of Bergen (drawn by J. Skjold).

Dispersion system

The dispersion system is almost identical with the one used for the Siwek 20-l sphere (Cesana & Siwek, 2001). A weighted amount of dust is placed inside the pressurized reservoir (dust storage chamber, $p_{r,i} = 20$ barg) and dispersed into the explosion chamber via an outlet valve and a dispersion nozzle. The outlet valve, separating the reservoir and the explosion vessel, is operated pneumatically by means of an auxiliary piston. A piezoelectric pressure sensor can be fitted to the reservoir to measure the pressure (p_r) during the dispersion process. An extension piece is located between the reservoir and the outlet valve; a nylon cylinder is attached to the reservoir lid in order to compensate for the extra volume. The volume of the reservoir, i.e. the total volume of air that is pressurized to 20.0 barg, has been determined by water filling to be $V_r = 600.0 \pm 0.3$ ml. The outlet valve is the same as the one used with the Siwek sphere, purchased from Adolf Kühner AG. Details of the dispersion system are shown in Figure B-8.

Dispersion nozzles

Several dispersion nozzles have been used. Most of the tests have been done with the rebound nozzle (the nozzle was positioned perpendicular to the electrodes, as shown for the cubical vessel in Figure B-7). Neither of the two dispersion nozzles traditionally used with the USBM-vessel could be used due to their much smaller total flow cross-section area compared to for instance the rebound nozzle (total flow cross section area, A_n , equal to 314 mm²). Two of the new nozzles are adaptations to the nozzles described by Cashdollar and Hertzberg (1985). The *mushroom nozzle* has the same cone as the *cone dispenser*, but the bottom section is modified to give bigger total flow cross section. The *pepper nozzle* is simply an enlarged version of the “*dispersion nozzle*”. An *open nozzle* (basically a short straight pipe) has been used as reference in some of the dispersion tests. Drawings of *mushroom* and *pepper*, and a photograph of the nozzles are shown in Figure B-11.

For tests with explosible materials, the hazard of igniting the dust by mechanical impact inside the reservoir led to the design of jet another nozzle. This nozzle will be called the *RDX nozzle*, named after the explosive dust in question. When using the RDX nozzle, the dust is placed in the recession in the bottom part. The nozzle has two alternate dispersion cones (A and B), as shown in Figure B-12. Explosion indices measured with the RDX nozzle for various ignition delay times are compared with the results obtained with the rebound nozzle in Figure B-13. Although the explosion pressure is more or less the same for both nozzles, the rate of pressure rise is significantly lower for the RDX nozzle. Hence, the RDX nozzle yields lower turbulence intensity, lower degree of mixing, or poorer dispersion, compared to the rebound nozzle.

All nozzles have approximately the same total flow cross-section area (314 mm²).

Spark gap

Both explosion vessels are equipped with electrode holders that are electrically insulated from the main body of the vessel. Pointed wolfram electrodes, 3.2 millimetres in diameter, can be fitted in the holder to create a *spark gap* (Figure B-4). Details of the electrode assembly are shown in Figure B-10.

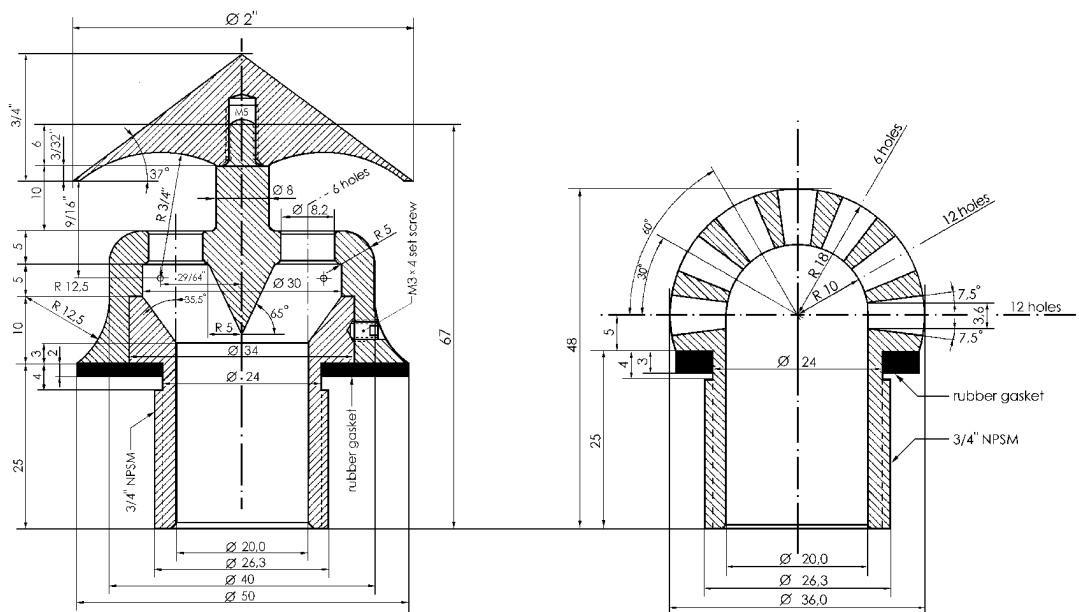
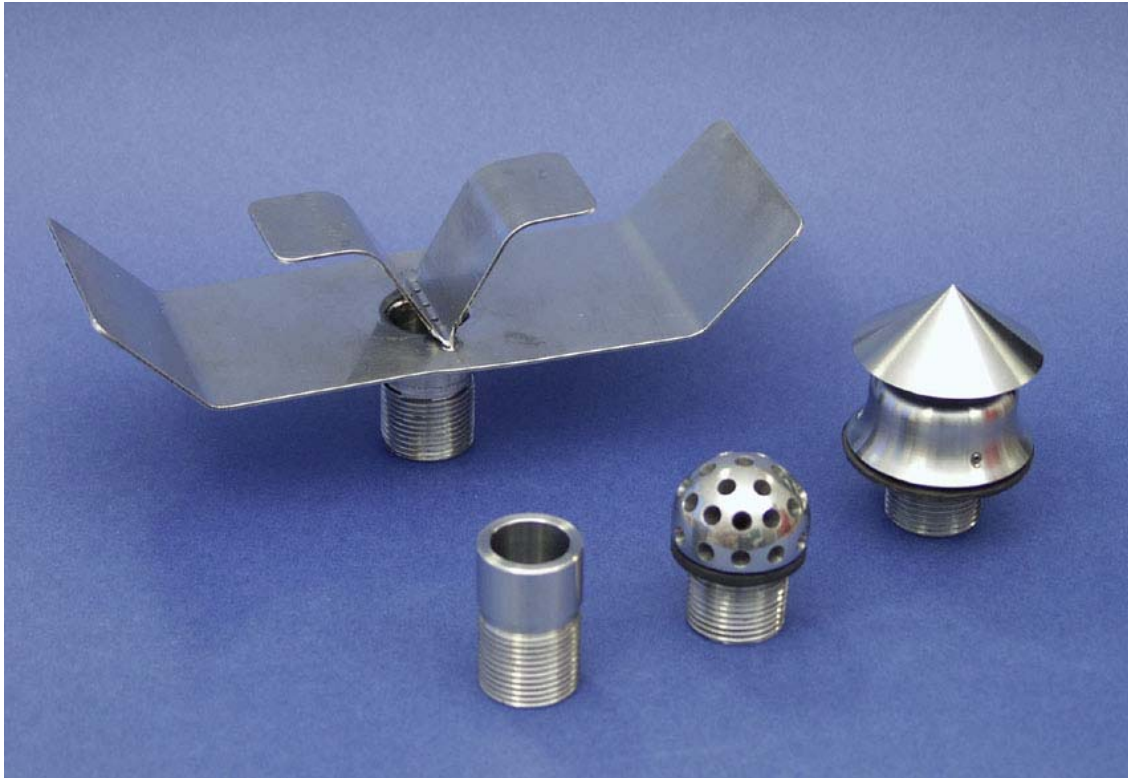


Figure B-11 Dispersion nozzles used with the two explosion vessels at UoB (upper picture): rebound (in the back), open (left), pepper (centre) and mushroom (right); photo by M. Vabø. Vertical cross sections of mushroom nozzle (lower left) and pepper nozzle (lower right).

B.2 Auxiliary Components and Equipment

Ventilated laboratory hood

Figure B-14 shows how the modified 20-l USBM vessel is set up in a ventilated laboratory hood. A schematic representation of all the equipment is given in Chapter 3; together with detailed experimental procedures for the explosion tests.

Measurement and control system

The measurement and control system is the same as the one used with the 20-l Siwek sphere. It consists of two parts: the *Control Unit (KSEP 310)* and the *Measurement and Control System (KSEP 332)*. KSEP 310 and KSEP 332 control the dispersion process, trigger the ignition, and monitor the pressure inside the 20-l vessel. Further detail can be found in Chapter 3, in Cesana and Siwek (2001) and in “*KSEP-332 AN: Technical Appendix*” from Kühner.

Ignition system

The primary ignition source used in this work is electrical arc discharges produced by the *arc generator* described in Appendix A. Alternatively; chemical igniters can be connected to the electrode holders, in a similar way as described by Cesana and Siwek (2001). The ignition is triggered by a signal from KSEP 310 in both cases.

Auxiliary systems

Additional auxiliary systems (*compressed air, ventilation, etc.*) and components (*valves, regulators, sensors, computer, etc.*) necessary for operating the dust explosion facility are described in Chapter 3.

Dust treatment

The laboratory is equipped with an *electronic balance* (Ohaus, type SC2020, 200×0.01g) for weighing the dust, a drying oven (Termaks, type TS 8024), a *desiccator* (Glaswerk Wertheim, 250 mm²) for keeping dust samples dry, and a *sieve shaker* (Cedacería Industrial, type RP-09) for preparing fractioned dust samples. This auxiliary equipment is shown in Figure B-15.

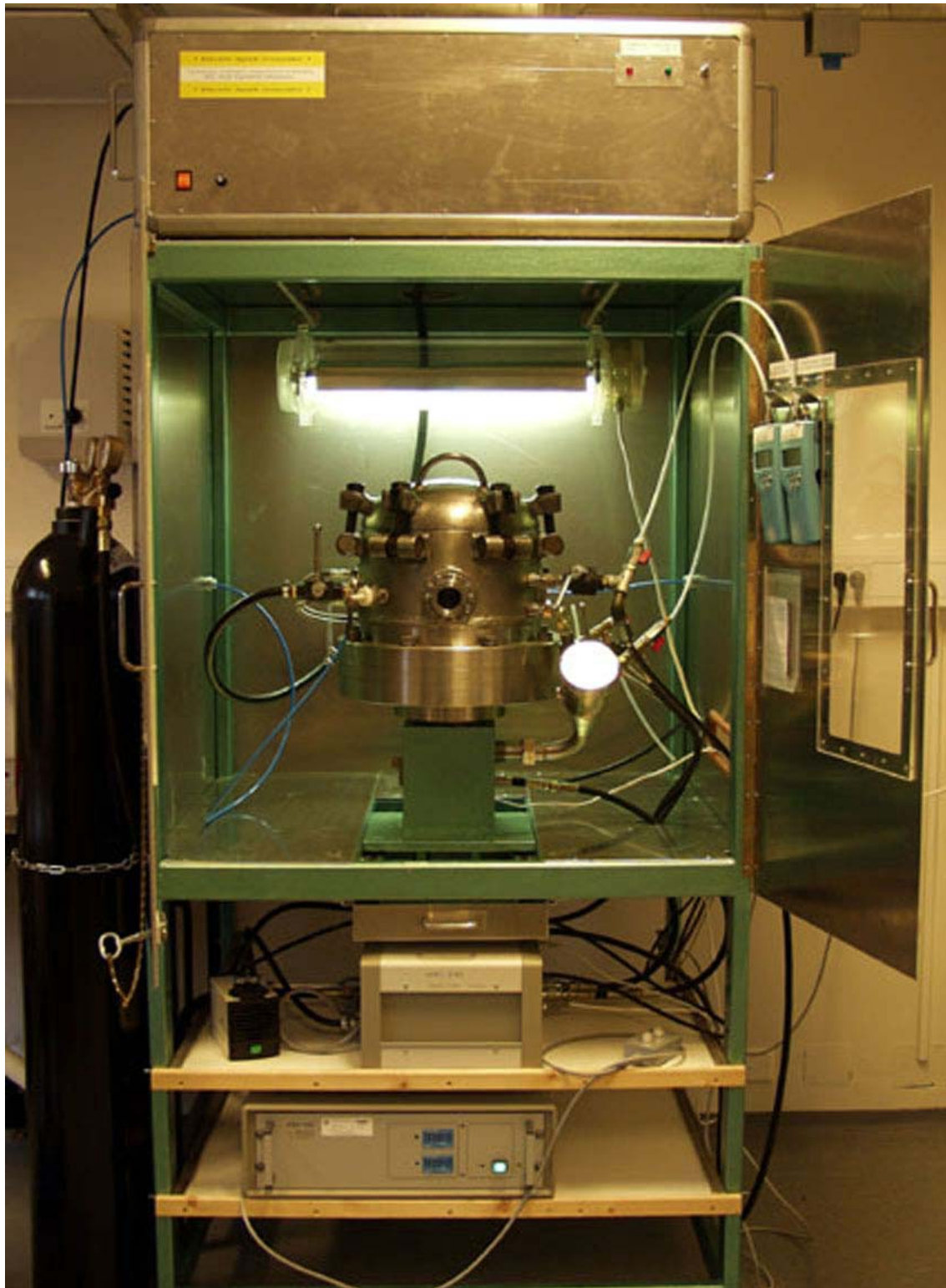


Figure B-14 The ventilated laboratory hood, with the modified USBM vessel inside. The electric spark/arc generator is placed on top of the hood. Underneath there are two shelves, on the upper we see (from left to right) the vacuum pump, the Control Unit KSEP 310 and the manual control for pressurizing/depressurizing the reservoir; on the lower is the Measurement and Control Unit KSEP 332. To the left is the 50-l compressed air bottle with the pressure regulator, and attached to the door on the right side is the Druck pressure sensors.



Figure B-15 The sieve shaker, with a stack of sieves (left); the drying oven (upper right); the desiccator (middle right); the electronic balance, with spoon and spatula (lower right).

References

- ASTM E1226-94 (1999). *Standard Test Method for Pressure and Rate of Pressure Rise for Combustible Dusts*. Annual Book of ASTM Standards. ISBN 0-8031-2698-0. Vol. 14.02, pp. 426-436, American Society for Testing and Materials, Pennsylvania, USA.
- ASTM E1515-98 (1999). *Standard Test Method for Minimum Explosible Concentration of Combustible Dusts*. Annual Book of ASTM Standards. ISBN 0-8031-2698-0. Vol. 14.02, pp. 602-613, American Society for Testing and Materials, Pennsylvania, USA.
- Cashdollar, K.L. & Hertzberg, M. (1985). *20-L Explosibility Test Chamber for Dusts and Gases*. Review of Scientific Instruments, **56** (4), pp. 596-602.
- Cesana, C. (2001). *Final Report: Calibration-Round-Robin CaRo 00/01*. Adolf Kühner AG, Birsfelden, Switzerland, http://www.kuhner.com/DOCUMENT/B052_172.pdf.
- Cesana, C. & Siwek, R. (2001). *Operating Instructions 20-l-Apparatus 6.0*. Adolf Kühner AG, CH-4127 Birsfelden, Switzerland.
- Eckhoff, R.K. (2003). *Dust Explosions in the Process Industries*. Third edition. ISBN 0-7506-7602-7. Gulf Professional Publishing, Amsterdam.
- ISO 6184-1 (1985). *Explosion Protection Systems – Part 1: Determination of Explosion Indices of Combustible Dusts in Air*. International Organization for Standardization.
- Siwek, R. (1988). *Reliable Determination of Safety Characteristics in the 20-Litre Apparatus*. Proceedings of Conference on Flammable Dust Explosions, (November 2-4) St. Louis, Missouri.

APPENDIX C

Dust Data

Origin and preparation of the various dusts used in this work are described. Particle size distributions and scanning electron microscopy (SEM) pictures are presented, and relevant physical and chemical properties of the dusts tabulated. Stoichiometric combustion reactions are provided for the combustible dusts. Special considerations regarding safe handling of the dusts are also included.

Some observations indicating a possible connection between the dust concentration during combustion of silicon metal and the colour of the resulting oxides are also reported.

C.1 Analytical Methods

SEM Pictures

The SEM pictures were produced with a scanning electron microscope (Joel SEM, type 35-S) at *Elektronmikroskopisk felleslaboratorium* (EFL) at the University of Bergen. Preparation of samples included distributing a small amount of dust on double-sided adhesive carbon discs fixed to specimen stubs, and sputter coating with gold/palladium as described by Bozzola and Russel (1999). Carbon adhesive discs are available from Agar Scientific Ltd., Essex.

Particle Size Measurements

Particle size measurements by laser diffraction (low angle light scattering, or LALLS) are provided for most of the dust samples. These measurements was done by various external laboratories:

1. *Elkem, Bremanger Smelteverk, Svelgen, Norway*. Arvid Damstuen performed the analysis on a Malvern Instruments SB.22 (focal length: 100 mm; beam length: 2.2 mm; particles dispersed in air).

2. *Norwegian Talc AS, Knarrevik, Norway.* Kjell P. Mathisen performed the analysis on a Malvern Mastersizer X (Long bed version 2.18; range lens: 100 mm; beam length: 2,40 mm; analysis model: polydisperse; particle were dispersed in water).

3. *Dyno Nobel ASA, Defence Products, Sætre, Norway.* Provided particle size distributions measured with a Malvern Instruments SB.0D for the two RDX fractions.

Some additional particle size data, e.g. sieving analysis and coulter counter data, are taken from laboratory reports provided by the suppliers of some of the dust. Symbols used for derived measures of particle size are summarized in Table C-1.

Combustion data

Stoichiometric combustion reactions are provided for all combustible and explosible dusts. The “stoichiometric” contributions to the explosion pressure are indicated by the ratio of the total number of gas molecules in the reactants to the total number of gas molecules in the products: $n_{g,f}/n_{g,i}$. It is assumed that only water vapour is present in the products. Heat of combustion for some of the reactions is given in Table C-2.

Other data

Additional physical and chemical data on the various dusts are summarized in Table C-2, including CAS numbers¹. Most of the values are mainly found in safety data sheets and laboratory reports provided by the suppliers, but the following references have also been used: Lide (1996), Drysdale (1998), Cardarelli (2000), Walters *et al.* (2000) and Eckhoff (2003).

Although most of the dust samples were used “as received”, some dusts underwent further preparation; procedures for operations such as sieving or drying will be described whenever applicable.

Table C-1 Symbols used for derived particle size measures. All size measures refer to the diameter of equivalent spheres.

$d_{3,2} = \frac{\sum_i d_i^3}{\sum_i d_i^2}$	The <i>surface area moment mean</i> , or <i>Sauter mean diameter</i> (SMD). This value is frequently used in applications where the surface area is important (e.g. catalysis or combustion).
$d_{4,3} = \frac{\sum_i d_i^4}{\sum_i d_i^3}$	The <i>volume moment mean</i> .
$d_{v,0.1}$ $d_{v,0.5}$ $d_{v,0.9}$	<i>Standard percentile readings from sample analysis</i> , i.e. the particle size for which a certain percentage of the sample is below this size (10, 50 and 90 per cent by mass). The most frequently used measure is $d_{v,0.5}$ – the <i>mass median diameter</i> (MMD).

¹ The CAS-RN (Chemical Abstracts Service – Registry Number) uniquely identifies a chemical, but not necessarily the manufacturer or concentration.

Table C-2 Summary of available physical and chemical properties for the dusts used in this work.

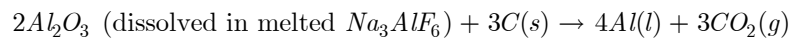
Material Property	Inert dusts		Niacin amide	Combustible dusts			Explosible dust
	Aluminium oxide	Micro Talc AT Extra		<i>Lycopodium spores</i>	PMMA	Silicon	
Molecular Formula	Al ₂ O ₃	Mg ₃ Si ₄ O ₁₀ (OH) ₂ and MgCO ₃	C ₆ H ₆ N ₂ O	(C ₅ H ₈ O ₂) ⁻	Si	C ₃ H ₆ O ₆ N ₆	
CAS RN	1344-28-1	-	98-92-2	7440-21-3	7440-21-3	121-82-4	
Molecular weight [g/mol]	101,96	~ 379.3 / ~84.3	122.13	(17.464)	28.09	222	
Density (particle), ρ _p [kg/dm ³]	3.97	~ 2.7 / ~ 3.2	-	1,18	~ 1.18	1.8	
Melting Point/Range, T _m [°C]	2054	-	128 - 131	-	~ 160	190	
Boiling Point/Range, T _b [°C]	~ 3000	-	224	-	2355	-	
Thermal Conductivity, k [W/(m*K)]	-	-	-	-	-	-	
Heat Capacity, c _p [J/(kg*K)]	-	-	-	14.2	-	-	
Heat of Combustion, -Δh _c [kJ/g]	-	-	-	-	26.8	-	
Heat of Combustion, -Δh _{c,air} [kJ/g(air)]	-	-	-	-	~ 13 (O ₂)	-	
Ignition Temperature, T _{ig} [°C]	-	-	480	-	-	190 - 200	
Bulk Density, ρ _b [kg/dm ³]	0.93 - 1.18	0.37	365	-	-	~ 1	
Acute Oral Toxicity (rat), LD ₅₀ [mg/kg]	-	-	3-53	-	-	100	

C.2 Inert Dusts

Two types of inert dust have been used to illustrate the effect of particles on turbulent propane-air explosions: *aluminium oxide* and *talca*.

C.2.1 Aluminium oxide

Aluminium oxide was provided by Øyvind Matre at Hydro Aluminium Karmøy. The oxide is imported from Jamaica as raw material for aluminium metal production by the Hall-Heroult process (Cardarelli, 2000):



According to laboratory report provided by Hydro, the sample contains almost pure aluminium oxide (98.7 per cent Al_2O_3 by weight). The main impurities are: Na_2O (0.36%), CaO (0.045%), SiO_2 (0.012%) and ZnO (0.010%).

Particle size distributions and key data are given in Table C-3; SEM pictures of aluminium oxide particles in Figure C-2 and Figure C-2.

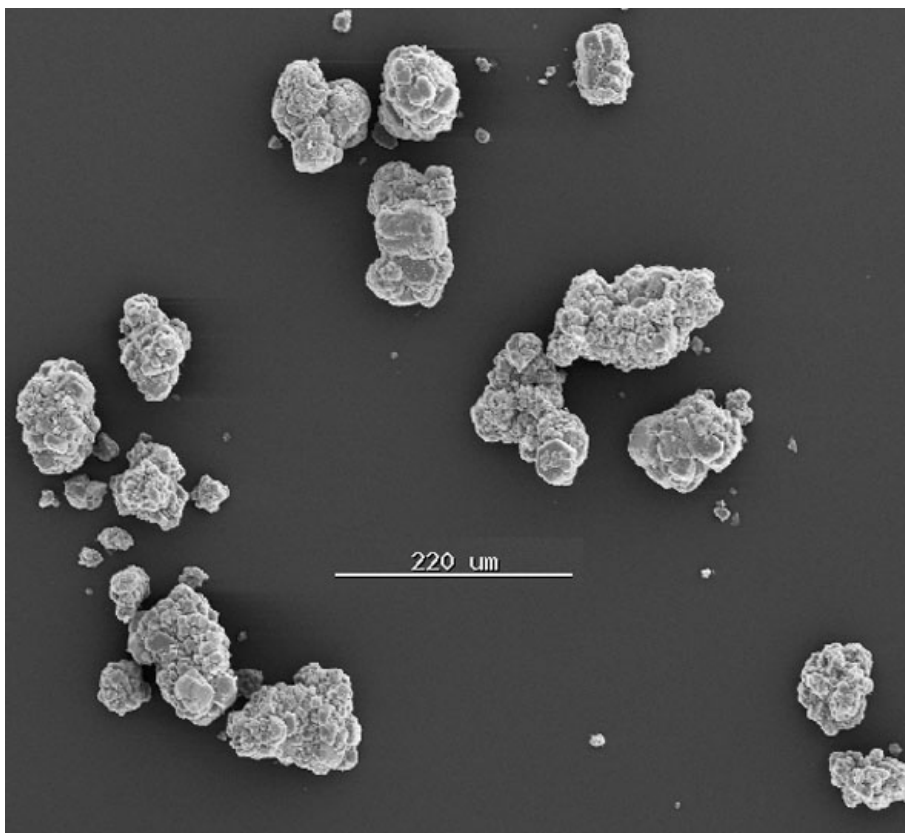


Figure C-1 SEM picture of aluminium oxide particles.

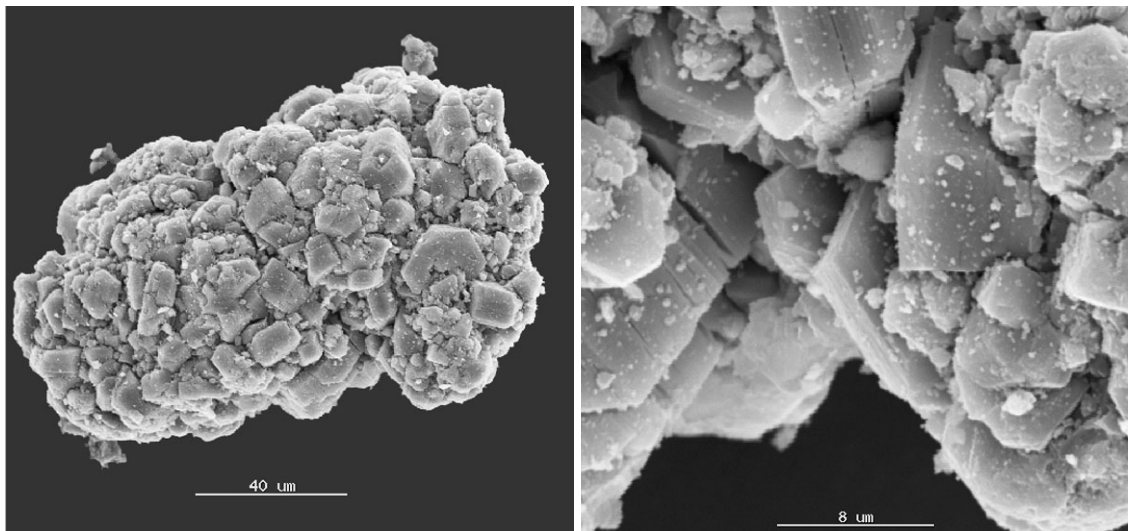


Figure C-2 SEM picture of a typical aluminium oxide particle (left); detailed section from the surface of the same particle (right).

C.2.2 Talc

Talc powder was provided by Kjell P. Mathisen at Norwegian Talc, Knarrevik. According to laboratory report, the actual composition of the talc used in this work is 62 per cent talc, $\text{Mg}_3\text{Si}_4\text{O}_{10}(\text{OH})_2$, and 38 per cent Magnesite, MgCO_3 . The minerals are crushed and grinded to specified particle size at Knarrevik. The product is used in ceramics, paint, paper and plastics.

Particle size distributions and key data are given in Table C-4; SEM pictures in Figure C-3.

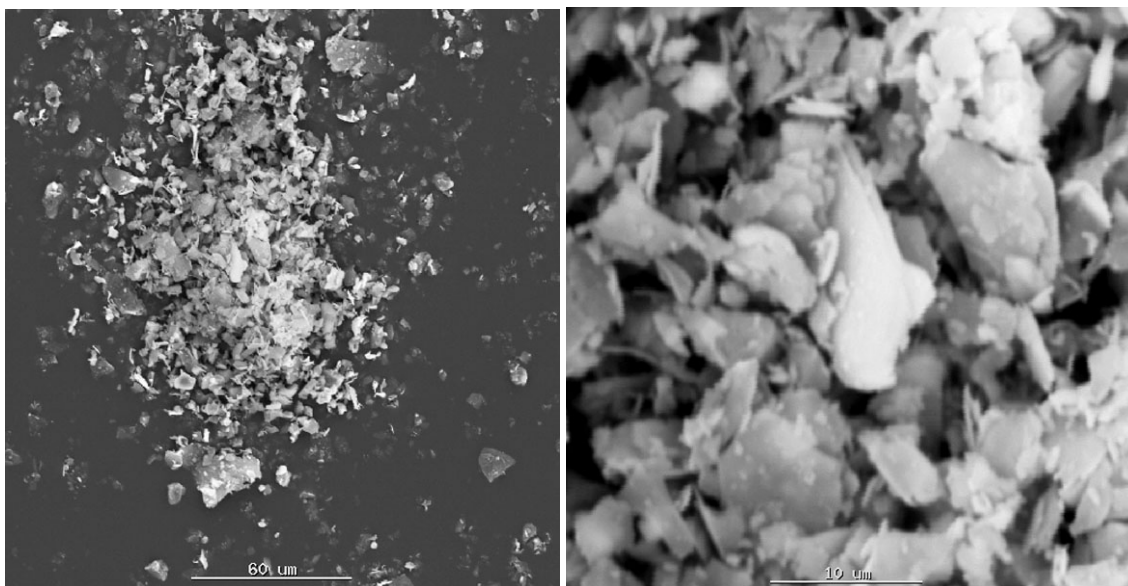


Figure C-3 SEM pictures of talc particles; the picture to the right is a detailed section from the left picture.

Table C-3 Data for the aluminium oxide used in this work; analysis report provided by the works laboratory (“Driftslaboratoriet”) at Hydro Aluminium Karmøy (HAK); document number OKSID-2390 dated 6th of September 2002.

<p>Trade name: Aluminium oxide</p> <p>Manufacturer: Alpart, Port Kaiser, Jamaica</p> <p>Supplier: Hydro Aluminium Karmøy</p> <p>Chemical name: Aluminium oxide</p> <p>Molecular formula: Al₂O₃</p> <p>Appearance: White powder, odourless</p> <p>Specific surface (BET¹): 70-75 m²/g</p> <p>Particle size distributions: Sieving analysis from Hydro Aluminium.</p>	<p>Particle Size Distributions:</p>																								
<p>SIEVING ANALYSIS:</p> <table border="1"> <thead> <tr> <th>Particle Size, x [μm]</th> <th>- 20</th> <th>- 45</th> <th>+ 45</th> <th>+ 63</th> <th>+ 90</th> <th>+ 125</th> <th>+ 180</th> </tr> </thead> <tbody> <tr> <td>Frequency, f [%]</td> <td>1.2</td> <td>5.2</td> <td>9.3</td> <td>31.9</td> <td>39.7</td> <td>12.2</td> <td>0.5</td> </tr> <tr> <td>Cumulative Frequency, F [%]</td> <td>1.2</td> <td>6.4</td> <td>15.7</td> <td>47.6</td> <td>87.3</td> <td>99.5</td> <td>100</td> </tr> </tbody> </table>		Particle Size, x [μm]	- 20	- 45	+ 45	+ 63	+ 90	+ 125	+ 180	Frequency, f [%]	1.2	5.2	9.3	31.9	39.7	12.2	0.5	Cumulative Frequency, F [%]	1.2	6.4	15.7	47.6	87.3	99.5	100
Particle Size, x [μm]	- 20	- 45	+ 45	+ 63	+ 90	+ 125	+ 180																		
Frequency, f [%]	1.2	5.2	9.3	31.9	39.7	12.2	0.5																		
Cumulative Frequency, F [%]	1.2	6.4	15.7	47.6	87.3	99.5	100																		

¹ According to ISO 4652, refers to the method named after *Brunauer, Emmett and Teller*; the surface area of a (ceramic) powder can be calculated from the N₂-isotherm, which is observed at the boiling point of liquid nitrogen. By the analysis of the adsorption curves within the relative pressure ranges $p/p_0 \sim 0,05$ and $p/p_0 \sim 0,2$ the volume V_m is determined, which according to the theory of Brunauer, Emmett and Teller corresponds to the quantity of nitrogen, which is necessary for a monomolecular layer. The surface needed for one nitrogen molecule is 16,2Å². From this value, the specific surface of the sample can be determined in m²/g. The large specific surface area reported for aluminium oxide (compared with e.g. talc), must be due to the porous/composite structure of the individual particles (Figure C-2).

Table C-4 Data for the talc dust used in this work; analysis report provided by Norwegian Talc AS, Knarrevik, document number PRODINFO ATX-01 (version 001, dated 27th of March 2001).

<p>Trade name: Micro Talc AT Extra</p> <p>Manufacturer: Norwegian Talc AS</p> <p>Constituents: Talc (62%) Magnesite (38%)</p> <p>Molecular formula: Talc: $Mg_3Si_4O_{10}(OH)_2$ Magnesite: $MgCO_3$</p> <p>Appearance: White/grey powder, odourless</p> <p>Specific surface (BET): 70-75 m²/g</p> <p>Loss on ignition¹: 20 %</p> <p>Particle size distributions: LALLS from Norwegian Talc.</p>	<p>Particle Size Distributions:</p>		
<p>Particle size measurements:</p> <p>LALLS from Norwegian Talc:</p> <p>Sedigraph 5001 data from Norwegian Talc:</p> <p>Wet sieving data (ISO 787-7) from Norwegian Talc:</p>	<p>Weight% < 2 μm</p>	<p>$d_{v,0.5}$ [μm]</p>	<p>$d_{v,0.98}$ [μm]</p>
	11	5,7	18,5
	39	2,5	10
	99.99 % by weight < 25 μm		

¹ Observed weight loss after heating (according to ISO 3262-1, typically 2 hours at 1000 °C).

C.3 Combustible Dusts

The combustible dusts used in this work are: *niacin amide*, *Lycopodium* spores, various fractions of *jet-milled silicon*, and *polymethyl methacrylate* (PMMA).

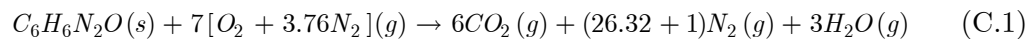
C.3.1 Niacin Amide

Niacin amide (pyridine-3-carboxamide) is the amide of vitamin B-3 (niacin). The dust was provided by Kühner for the calibration round robin test CaRo 00/01.

Particle size distributions and key data are given in Table C-5; only dispersion in air was possible because B-vitamins are water-soluble. SEM pictures of niacin amide particles are shown in Figure C-4.

Combustion of niacin amide

The stoichiometric combustion reaction for niacin amide in air is:



$$\frac{n_{g,f}}{n_{g,i}} = \frac{36.32}{33.32} = 1.090$$

The corresponding stoichiometric dust concentration is 150 g/m³.

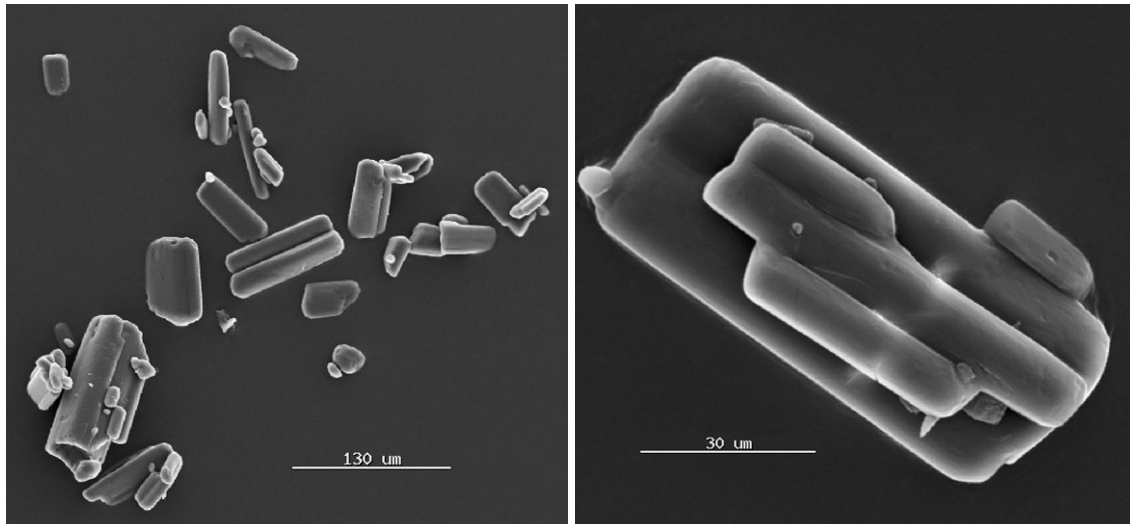
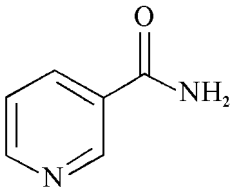
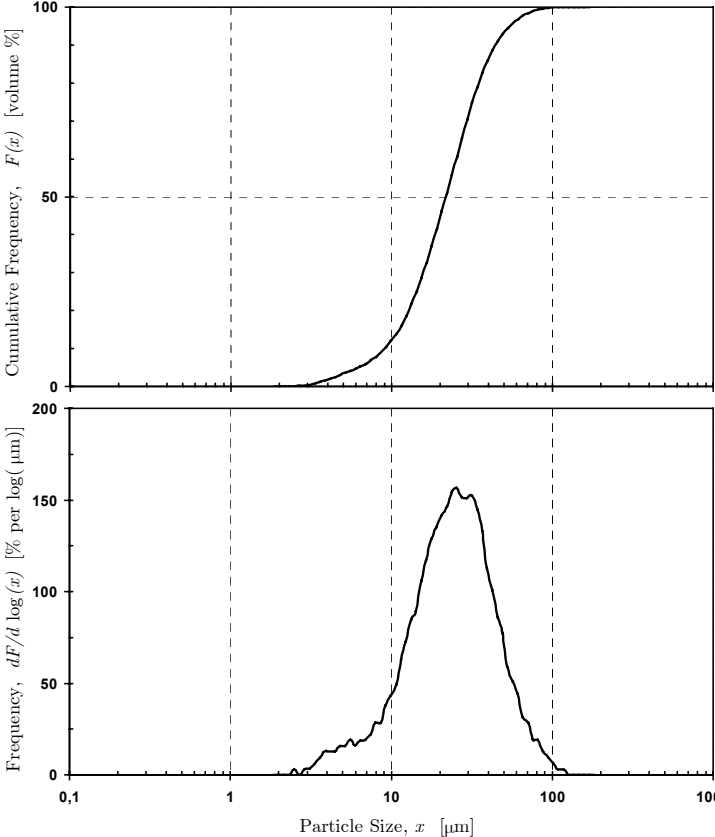


Figure C-4 SEM pictures of typical niacin amide particles.

Table C-5 Data for the niacin amide used in this work (safety data sheet provided by LonzaGroup, version 09.05.2000).

<p>Trade name: Niacin amide USP DC</p> <p>Manufacturer: LONZA AG, CH-4002 Basel</p> <p>Chemical name: Pyridine-3-carboxamide</p> <p>Molecular formula: C₆H₆N₂O</p> <p>Structure:</p>  <p>Appearance: White powder, odourless</p> <p>Particle size distribution: LALLS from Elkem Bremanger.</p>	<p style="text-align: center;">Particle Size Distributions:</p> 				
<p>Particle size measurements, x [μm]:</p>	$d_{4,3}$	$d_{3,2}$	$d_{v,0.1}$	$d_{v,0.5}$	$d_{v,0.9}$
LALLS from Elkem Bremanger.	28	18	10	24	49
Coulter LS Particle Size Analyser, data provided with <i>CaRo 00/01</i> by Adolf Kühner AG (Cesana, 2001).	–	–	14	40	90
<p>Hazard Identification:</p>  <p style="text-align: center;">Xi: Irritant</p>	<p>Risk Phrase(s): <i>R36</i> (Irritating to eyes)</p> <p>Safety Phrase(s): <i>S26</i> (In case of contact with eyes, rinse immediately with plenty of water and seek medical advise)</p>				

C.3.2 *Lycopodium* Spores

Ripe spores from *Lycopodium clavatum* (Stag’s-horn Clubmoss)¹ have been used in dust explosion research for many years. The spores are close to monodisperse, with a mean particle diameter close to 32 µm. The distal surfaces are ornamented with high, narrow ridges (*muri*) that join to form a reticulum, see Figure C-5. However, there are at least 200 different species in the genus *Lycopodium*; and in later years, spores of other species than *L. clavatum* have been received by dust explosion laboratories ordering “*Lycopodium*”². The spores we received from Norsk Medisinaldepot ASA are shown in Figure C-6; they are definitely not *clavatum*. The supplier could not identify the spores; but apparently, they came from China via Germany.

Ornamentation patterns on *Lycopodium* spores

Thomas *et al.* (1991) describes a “rugulose” form of *Lycopodium* spores, with a diameter of about 45 µm. Rugulose spores proved to be more difficult to ignite than reticulate spores (*L. clavatum*), and seemed to burn less violently. Thomas *et al.* claims the rugulose spores are produced by *L. alpinum*, or Alpine Clubmoss. However, according to both Wilce (1972) and Tryon and Lugardon (1991), the spores of *L. alpinum* are actually reticulate – not rugulose.

Wilce (1972) classifies the ornamentation patterns on the walls of *Lycopodium* spores in five main groups:

- i) The *foveolate-fossulate* group, with the two subtypes *selago* and *phlegmaria*.
- ii) The *rugulate* group, with the two subtypes *cernuum* and *carolinianum*.
- iii) The *reticulate* group, with four subtypes: *scariosum*, *clavatum*, *fastigiatum* and *vobibile*. The *clavatum* type comprises at least 18 species, including *L. alpinum* and *L. clavatum*.
- iv) The *baculate* spore, *L. deuterodensum* is the only known species of this type.
- v) The *scabrate* spore, *L. casuarinoides*³ is the only known species of this type.

Only the scabrate spores of *L. casuarinoides* resemble the spores in Figure C-6, and the “rugulose” spores described by Thomas *et al.* (1991). In order to get a more definite

¹ Generic and Latin names are taken from Øllgaard (1993). *Stag’s-horn Clubmoss* (*L. clavatum*) are sometimes called *Running Clubmoss* or *Common Clubmoss*. The scientific name of the genus is derived from the Greek: *Lycos* (wolf) and *pūs* (foot or claw). The name alludes to the paw-like aspect of the creeping shoots of *L. clavatum*, as does the Danish “Ulvefod” (wolf’s paw) and the Norwegian “Kråkefot” (crow’s foot). The Swedish name is “Lummer”; derived from the Latin *lumbricus* (worm), it reflects the use of the plant as vermifuge. *Clavatum* is derived from *clavis* (club), alluding to the shape of the cones.

² The datasheet from Norsk Medisinaldepot ASA describes the product “*Lycopodium*” as “*Witches’ flour (Norwegian: “heksemel”) is ripe spores of Lycopodium clavatum L. and other species of Lycopodium*”. The spores have traditionally been imported from Eastern Europe (Øllgaard, 1993).

³ According to Wikström (2003), the Latin name *casuarinoides* is due to this species resemblance with the tree *Casuarina* (Willow, Whistling Pine).

answer to the problem, pictures like the ones in Figure C-6 was sent to several botanists specializing in the genus *Lycopodium*.

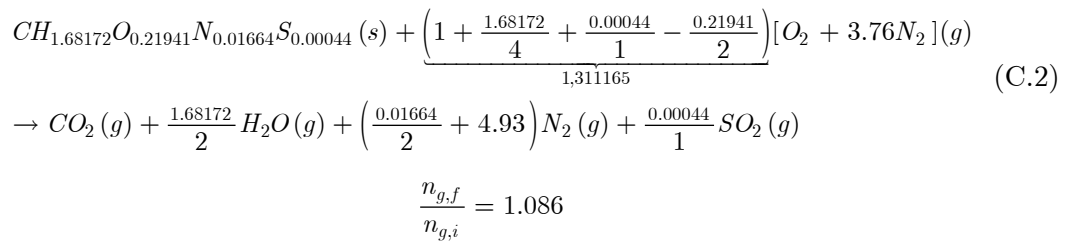
Øllgaard (2003), Wikström (2003) and Zhang (2003) all agree that the spores most likely come from the species *L. casuarinoides*. Professor Øllgaard points out that *L. casuarinoides* is common in South-East Asia including subtropical China; and that the spores of *L. casuarinoides* are formed in large clusters of strobili, making them much easier to harvest than the spores of *L. clavatum*. Dr. Wikström also emphasizes that it would be much easier to gather large quantities of spores from *L. casuarinoides*, compared to *L. clavatum*. Professor Zhang has identified spores from both *L. clavatum* and *L. casuarinoides* in China – the spores were exported to Germany.

Figure C-7 shows spores of *L. casuarinoides* provided by Xian-Chun Zhang from the herbarium at the Institute of Botany, Chinese Academy of Sciences, Beijing; professor Zhang is president of the Chinese Fern Society and Principal Investigator of Higher Cryptogamic Botany at the Institute of Botany in Beijing. The resemblance between the spores in Figure C-6 and Figure C-7 are striking; hence, there can be little doubt that the spores used in this work stem from the species *L. casuarinoides*. It is also highly likely that the “rugulose” spores described by Thomas *et al.* (1991) are spores of *L. casuarinoides* as well.

Particle size distributions and key data for spores of *Lycopodium casuarinoides* are given in Table C-6.

Combustion of *Lycopodium* spores

According to Thomas *et al.* (1991), there is no significant chemical difference between the two species – assuming that the “rugulose” spores are in fact from *L. casuarinoides*. Thus, based on the elemental analysis for *Lycopodium clavatum* given by Line *et al.* (1959), the stoichiometric combustion reaction for *Lycopodium* can be written:



The corresponding stoichiometric dust concentration is 114 g/m³, or 120 g/m³ when adjusted for ash (1.1 wt%) and natural water (3.3-3.7 wt%).

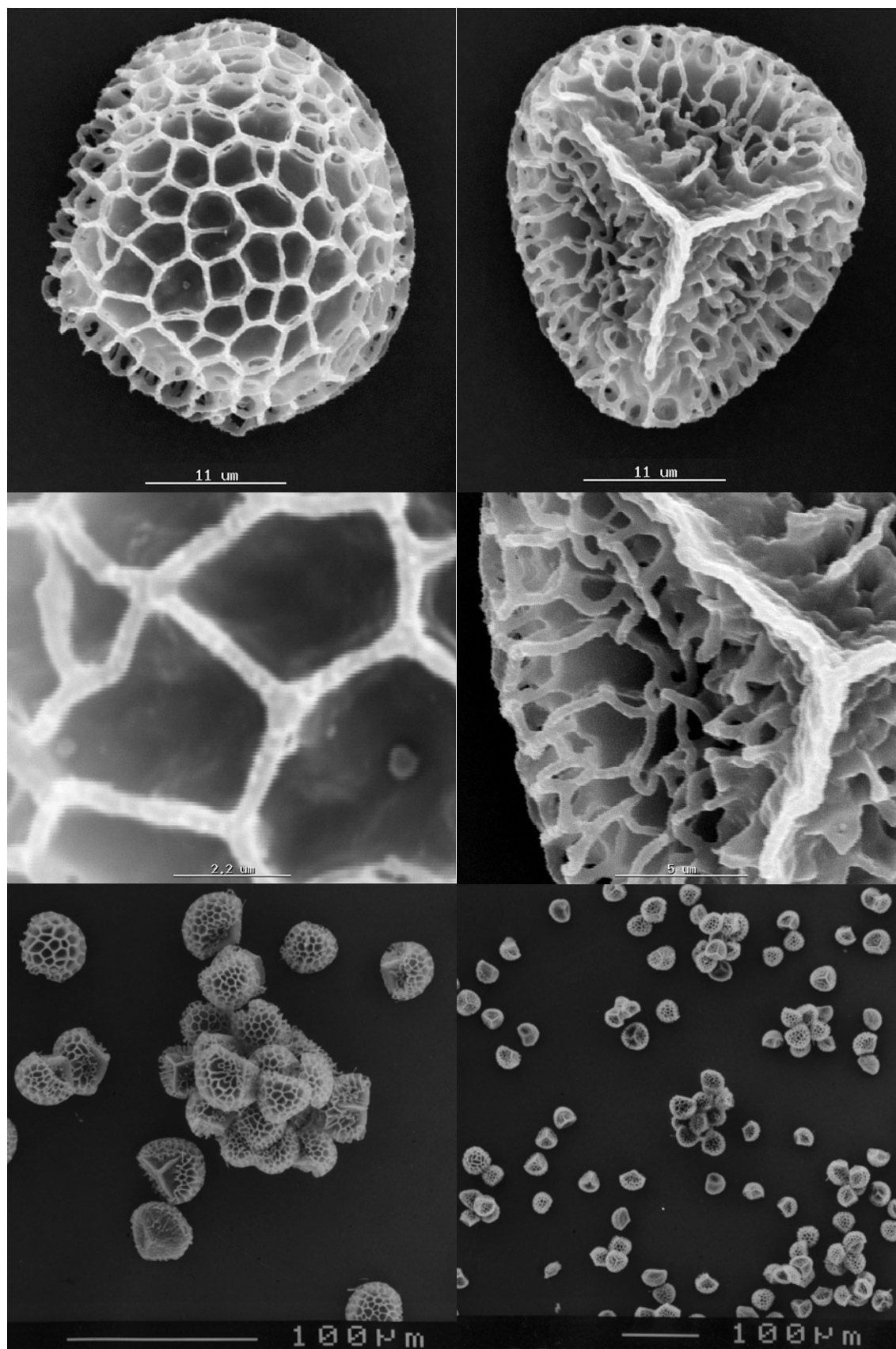


Figure C-5 SEM pictures of spores from *Lycopodium clavatum*, showing the characteristic reticulum formed by muries. The spores are reticulate on both the distal face (upper left) and proximal face (upper right), with a median diameter of approximately 32-35 µm; details (middle) from the surface of the spores above; the spores are nearly monodisperse (below).

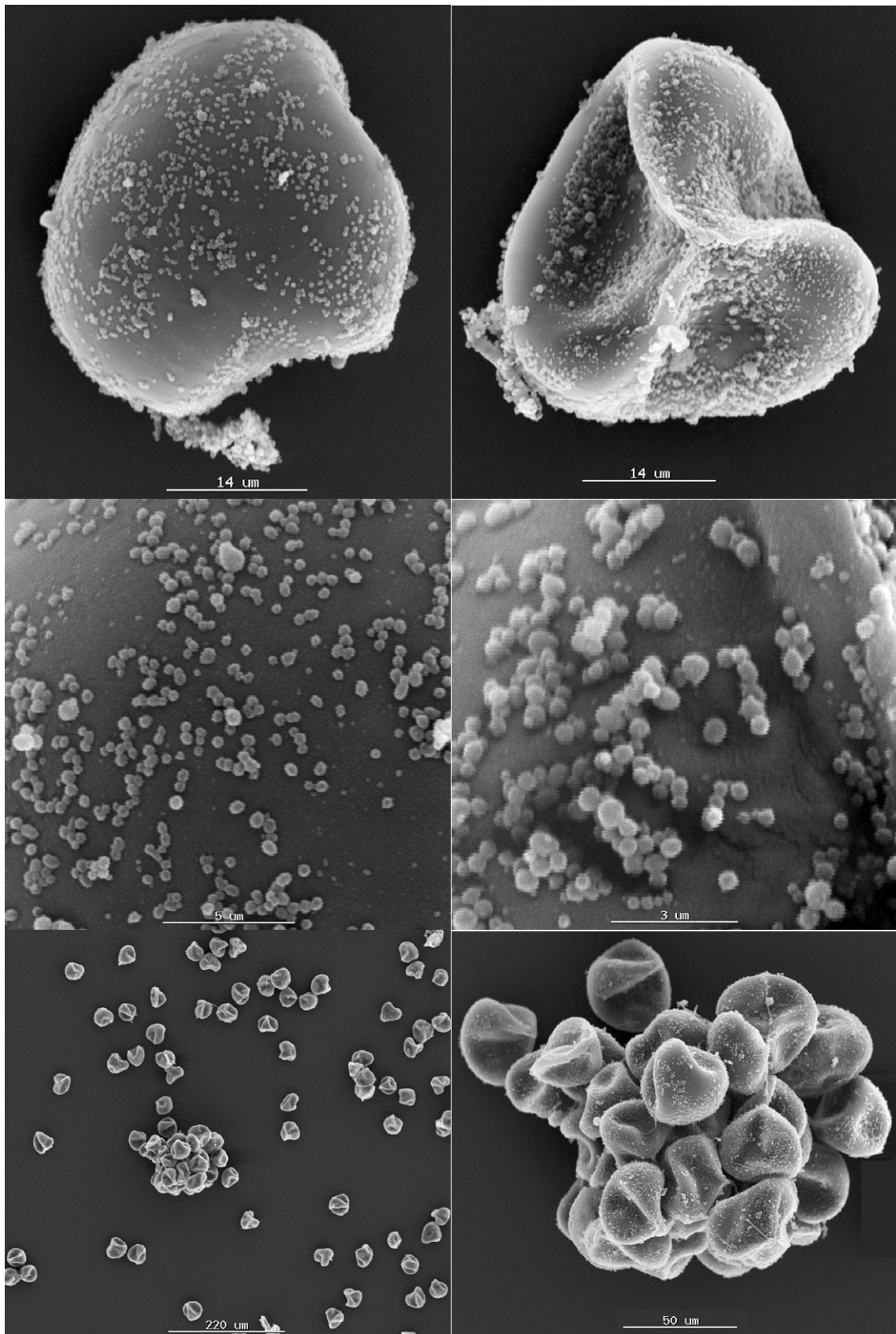


Figure C-6 SEM pictures of the “Lycopodium” spores from Norsk Medisinaldepot ASA. They are irregularly scabrate on both distal (upper left) and proximal face (upper right), with a median diameter of approximately 35-38 µm. Details (middle) from the surface of the spores above; the spores are nearly monodisperse (below).

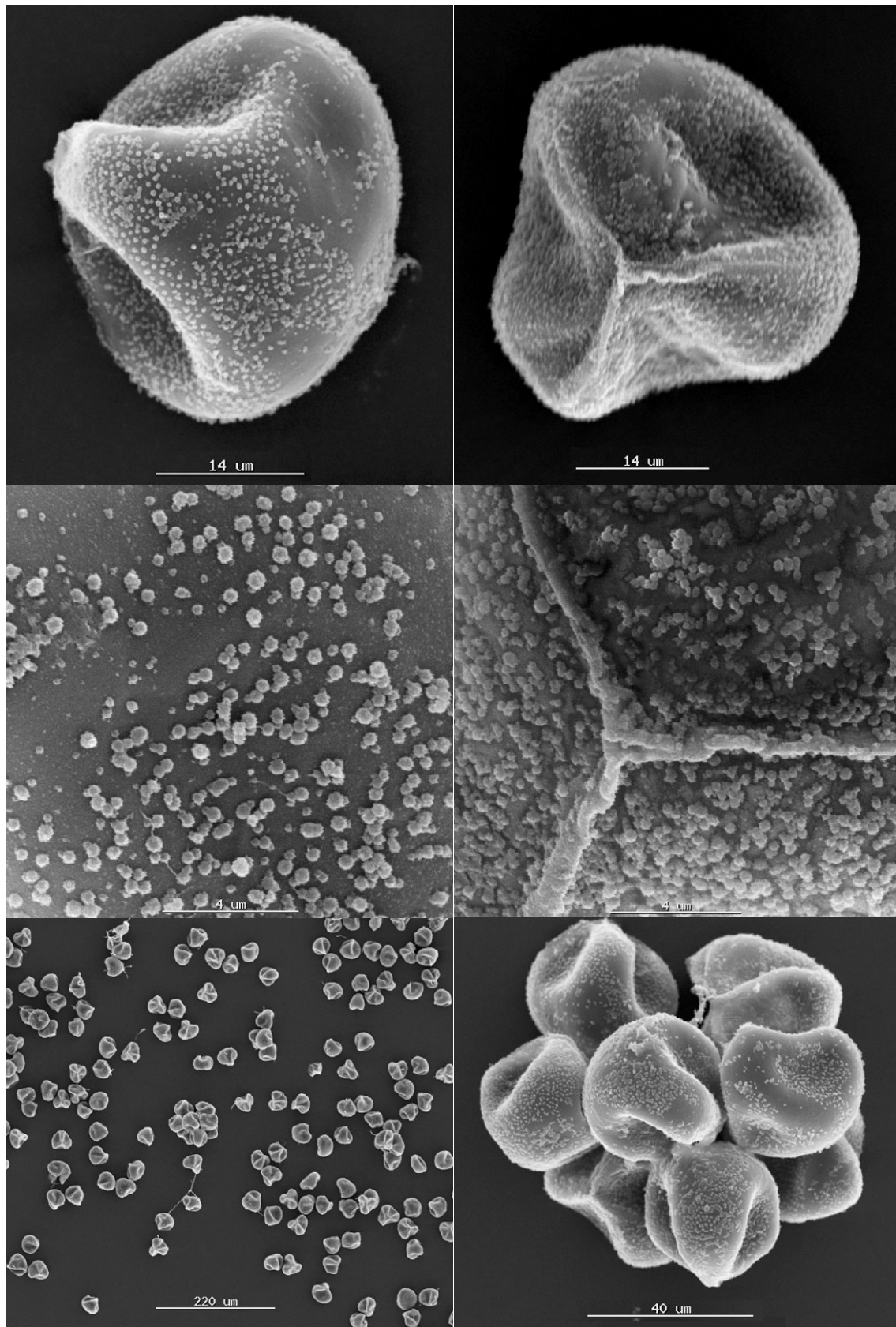


Figure C-7 SEM pictures of *Lycopodium casuarinoides* spores provided by Professor Xian-Chun Zhang, Beijing, China. They are also irregularly scabrate on both distal (upper left) and proximal face (upper right), with a median diameter of approximately 35-38 μm. Details (middle) from the surface of the spores above; the spores are nearly monodisperse (below).

Table C-6 Data for the *Lycopodium* spores used in this work (safety data sheet provided by Norsk Medisinaldepot ASA, no. 195, dated May 1986).

<p>Trade name: <i>Lycopodium</i> (“heksemel”)</p> <p>Manufacturer: Natural product</p> <p>Supplier: Norsk Medisinaldepot ASA</p> <p>Scientific name: <i>Lycopodium</i>, e.g.: <i>L. casuarinoides</i>, <i>L. clavatum</i></p> <p>Atomic composition: $\text{CH}_{1.68172}\text{O}_{0.21941}\text{N}_{0.01664}\text{S}_{0.00044}$</p> <p>Appearance: Yellow powder, odourless</p> <p>Particle size distributions: LALLS from Norwegian Talc. Talc (N.T.) and Elkem Bremanger (E.B.).</p>	<p style="text-align: center;">Particle Size Distributions:</p>				
<p>Particle size measurements, x [μm]:</p>	$d_{4,3}$	$d_{3,2}$	$d_{v, 0.1}$	$d_{v, 0.5}$	$d_{v, 0.9}$
LALLS from Norwegian Talc.	36	19	30	36	42
LALLS from Elkem Bremanger.	38	37	31	37	48
<p>Hazard Identification:</p> <div style="text-align: center;">  <p>F: Highly flammable</p> </div>	<p>Risk Phrase(s): R11 (Highly flammable)</p> <p>Safety Phrase(s): S7 (Keep container tightly closed)</p>				

C.3.3 Moisture Content of *Lycopodium* Spores

The moisture content of the *Lycopodium casuarinoides* spores was measured with a Halogen Moisture Analyser (Mettler Toledo, HG53). The spores had moisture content between 7 and 9 per cent by weight prior to drying, and about 1 per cent after 12 hours of drying at 50 °C. After drying, the spores were stored in a desiccator.

The effect of drying on the explosion indices for *L. casuarinoides* is illustrated in Figure C-8. Whereas the explosion pressure is more or less unaffected, the rate of pressure rise is considerably increased for the dried sample. Heating, and subsequent combustion, of dried particles are likely to proceed faster because there is less water that has to be evaporated. The effective particle size can be smaller for the dried sample because of less agglomeration. Drying will probably reduce the particle density, but it may also cause individual particles to shrink, see the low magnification pictures in Figure C-6. At higher magnifications, some particles were inflated when heated by the electron beam in the microscope. Such shrinking effects are not present in the SEM pictures of *L. clavatum* in Figure C-5, probably because the muries make the spore walls less flexible. Further aspects of the effect of dust moisture on the rate of pressure rise measured in closed explosion vessels are described by Eckhoff and Mathisen (1978).

Only dried samples of *L. casuarinoides* were used in the rest of this work.

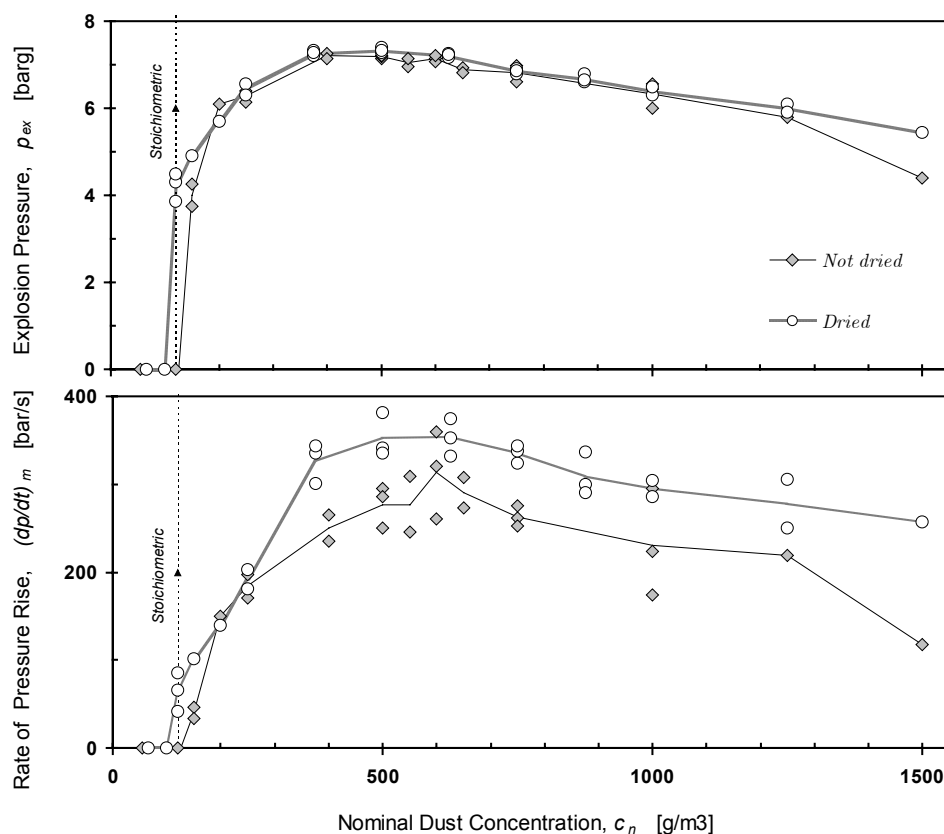


Figure C-8 Effect of moisture content on explosion indices for *L. casuarinoides* dust, determined in the modified USBM vessel fitted with the rebound nozzle. The ignition source was 6 J arc discharges produced by the spark/arc generator described in Appendix A; ignition delay time 60 milliseconds. Dotted vertical line represents stoichiometric concentration.

C.3.4 Silicon

Silicon metal was provided by Martin Nybø at Bremanger Smelteverk, Svelgen. Elkem Bremanger has the world's only facility for the production of silicon metal by a patented hydrometallurgical process. The process removes the impurities in high silicon ferrosilicon by treatment in an iron chloride solution. The product is very pure quality silicon metal, characterized by high homogeneity in chemistry, grain structure and sizing. Refined silicon metal is sold under the trademark Silgrain®, and used in the electronics and aluminium industries. The purest qualities are used for electronic components, solar cells, and ceramic materials. More than 90 per cent of all electronic components are based on silicon, Elkem serves around 50 per cent of the world market (<http://www.silicon.elkem.no/>).

According to laboratory reports provided by Elkem Bremanger, the samples of jet milled Silgrain contains almost pure silicon oxide (99.6 per cent Si by weight). The main impurities are: Al (0.1-0.2%), Fe (0.04-0.14%), Ca (0.01-0.03%) and Ti (0.001-0.01%). Particle size distributions and key data for the various lots of Silgrain used in this work are given in Table C-7 and Table C-8; a SEM picture of jet-milled Silgrain are shown in Figure C-9.

Combustion of silicon

In the combustion of silicon metal, several chemical reactions may be involved. For lean combustion it is probably reasonable to assume that only silicon dioxide (*silica*) are formed, hence the stoichiometric combustion reaction for silicon in air is:

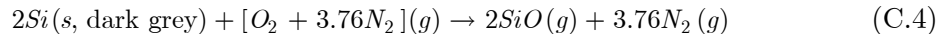


$$\frac{n_{g,f}}{n_{g,i}} = \frac{3.76}{4.76} = 0.79$$

The corresponding stoichiometric dust concentration is 240 g/m³, and the stoichiometric contribution to the pressure rise is a 21 per cent decrease – reflecting that all the oxygen in air has been consumed. The heat of formation for silicon dioxide is (Glassman, 1996):

$$\Delta H_{f,298}^o \approx -900 \frac{kJ}{mol(Si)} = -450 \frac{kJ}{mol(O)}$$

In a fuel-rich mixture, silicon monoxide may be formed according to the reaction:

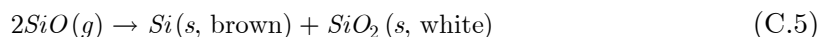


$$\frac{n_{g,f}}{n_{g,i}} = \frac{5.76}{4.76} = 1.21$$

Hence, the stoichiometric dust concentration is doubled, from 240 to 480 g/m³. The heat of formation for silicon monoxide is:

$$\Delta H_{f,298}^o \approx -90 \frac{kJ}{mol(Si)} = -90 \frac{kJ}{mol(O)}$$

However, upon condensation the silicon monoxide is likely to form a diphasic mixture of Si and SiO₂ (Friede and Jansen, 1996; Timms, 2001):



A hypothetical phase diagram of the Si-O system can be found in Rochow (1973); silicon monoxide is stable in the temperature range from 1180 to 2480 °C.

According to Rochow (1973) and Glassman (1996), there is also the possibility of forming silicon nitrides (SiN and Si₃N₄). However, as these reactions consume gaseous nitrogen, it should be possible to detect any significant contributions from (C.5) by measuring the final pressure inside the vessel after silicon-air explosions. In a series of tests, the vessel was left for one hour after each explosion, allowing the vessel temperature to be stabilized with the surroundings. Measured amount of gas consumed in the explosion was equal to the amount of oxygen in air, within the experimental error.

Consequently, the overall reaction for silicon combustion in air can probably best be described by (C.3), but some of the silicon metal can go through the reactions (C.4) and (C.5) – thus experiencing a change in colour from grey to brown. The post-combustion reaction in (C.5) will be used in section C.3.5 as a possible explanation for some observations concerning the relationship between the colour of the precipitated silicon oxides, and the nominal dust concentration during combustion.

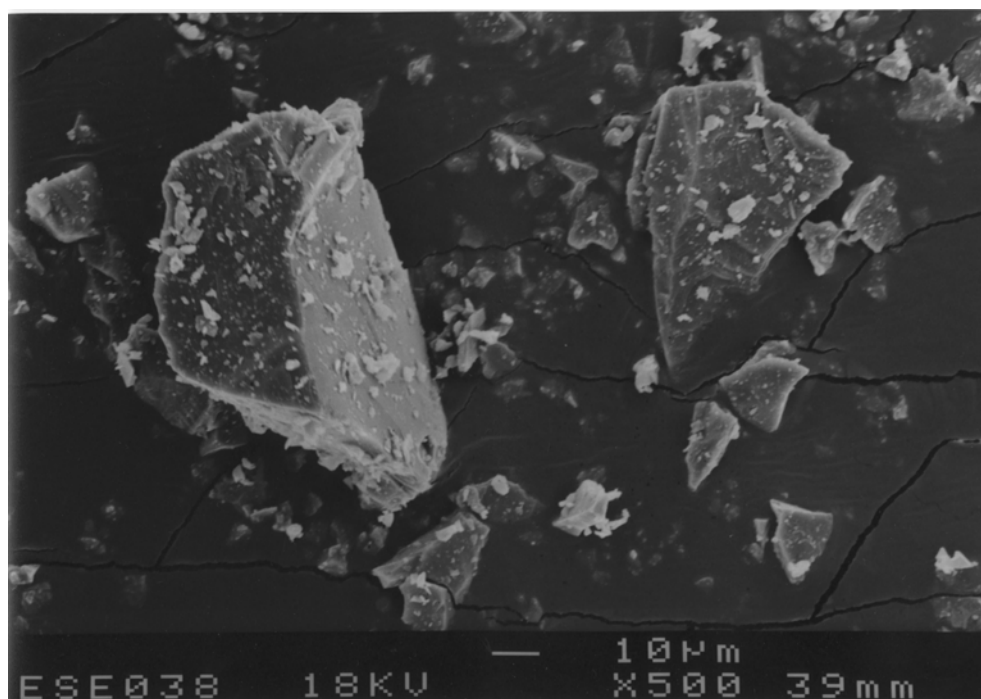


Figure C-9 SEM picture of jet-milled silicon metal (Silgrain).

Table C-7 Data for the most frequently used fractions of silicon dust used in this work (safety data sheet provided by Elkem ASA, revised August 6th 1997).

<p>Trade name: Silgrain</p> <p>Manufacturer: Elkem ASA, Silicon Division Bremanger Smelteverk</p> <p>Chemical name: Silicon Refined</p> <p>Molecular formula: Si</p> <p>Appearance: Dark grey powder, odourless</p> <p>Particle size measurements: LALLS from Norwegian Talc (N.T.) and Elkem Bremanger (E.B.).</p>	<p>Particle Size Distributions:</p>					
Particle size measurements, x [μm]:	<i>Lot no.:</i>	$d_{4,3}$	$d_{3,2}$	$d_{v, 0.1}$	$d_{v, 0.5}$	$d_{v, 0.9}$
LALLS from Norwegian Talc.	<i>J 133</i>	4.3	2.4	1.1	3.5	8.6
	<i>J 135</i>	4.9	2.6	1.2	3.7	7.9
	<i>J 136</i>	12.2	5.5	2.5	11.2	23.5
LALLS from Elkem Bremanger.	<i>J133</i>	4.4	2.5	1.4	3.8	8.8
	<i>J 135</i>	6.2	3.3	1.9	4.7	12.5
	<i>J 136</i>	12.8	6.9	3.4	11.5	23.7

Table C-8 Data for the least used fractions of silicon used in this work (safety data sheet provided by Elkem ASA, revised August 6th 1997)

<p>Trade name: Silgrain</p> <p>Manufacturer: Elkem ASA, Silicon Division Bremanger Smelteverk</p> <p>Chemical name: Silicon Refined</p> <p>Molecular formula: Si</p> <p>Appearance: Dark grey powder, odourless</p> <p>Particle size measurements: LALLS from Elkem Bremanger.</p>	<p>Particle Size Distributions:</p>					
<p>Particle size measurements, x [μm]:</p>	<i>Lot no:</i>	$d_{4,3}$	$d_{3,2}$	$d_{v, 0.1}$	$d_{v, 0.5}$	$d_{v, 0.9}$
<p>LALLS from Elkem Bremanger.</p>	<i>J 134</i>	3.9	2.5	1.3	4.0	6.3
	<i>J 137</i>	12.5	9.0	5.0	11.6	21.0
	<i>J 138</i>	17.7	10.0	4.8	15.5	32.3
	<i>J139</i>	19.5	11.0	5.1	16.4	37.0
	<i>J 140</i>	21.9	10.7	4.9	17.9	43,1
	<i>J 141</i>	24.2	9.9	4.5	18.7	51.6

C.3.5 Some Observations on Silicon Oxides

After silicon dust explosions, the interior of the explosion vessel was covered in a snow-like layer of residue, presumably a mixture of silicon oxides and silicon. The appearance of this residue was observed to be highly dependent on dust concentration, especially so for moderately high concentrations. Low concentrations resulted in a thin white layer, higher concentrations in a thick brown layer. A collection of such samples is shown in Figure C-10. A threadlike white residue were usually found hanging from the electrode holders, see Figure C-11.

Experimental procedure

The basic experimental procedure for the tests is described in Chapter 3; however, in order to collect the oxide samples described here, a small piece of thin cardboard was attached to the bottom of the vessel by Scotch tape prior to each explosion. After the explosion, the tape had melted and the sample could be lifted out with a spatula.

Results

SEM pictures of residue from silicon-air explosions are shown in Figure C-11 and Figure C-12 (white residue), and Figure C-13 (brown residue). White residue consists of small spheres, usually less than 1 μm in diameter; brown residue is a mixture of similar material and larger metal particles that seem to have melted – at least they are very different from the original metal particles shown in Figure C-9.

Based on the dramatic change in oxide colour observed when the nominal dust concentration was changed from $\sim 250 \text{ g/m}^3$ to 500 g/m^3 , an empirical concentration scale has been defined for three different lots of silicon. The *oxide colour dust concentration*, c_{oc} , is determined by comparing the colour of the particular oxide sample from a test with ignition delay time greater than 60 milliseconds, with the colour of samples representing various nominal dust concentrations at 60 milliseconds ignition delay time. This scale has then been used to estimate the actual concentration during combustion at higher ignition delay times. The results are shown in Figure C-14 and Figure C-15, and summarized in Figure C-16.

Discussion

The concept of oxide colour concentration is based on the assumption that the colour of the precipitating oxides reflects the actual dust concentration during combustion. A plausible explanation for such a relationship can be found in the combustion reactions for silicon, described in section C.3.4. For lean combustion, only the white silicon dioxide is formed according to reaction (C.3). As the dust concentration is increased, an increasing fraction of the oxygen will be expected to participate in the silicon monoxide reaction (C.4). This will be consistent with the *principle of Le Châtelier*, which states that any system initially in a state of equilibrium when subjected to a change (e.g., increasing pressure or temperature) will shift in composition in such a way as to minimize the change. As the standard heats of formation per O atom is -90 and -450 kJ/mol for SiO and SiO₂, respectively; higher temperatures are likely to favour reaction (C.4) over reaction (C.3). The effect of (C.3) in counteracting the increase in pressure is probably of minor importance due to (C.5).

Condensation and subsequent cooling of silicon monoxide gas yields an intimate mixture of crystallites of silicon (brown) and silica (white); the colour of this mixture is determined by the relative mass fraction of the two constituents.

Figure C-16 suggests that the decrease in concentration with increasing ignition delay time occurs at a higher rate for the fine powder in lot J 133 than for the coarser lots J 135 and J 136. This is contrary to what one intuitively would expect, namely that the larger particles would settle first. However, the observation is supported by the fact that the coarser lots could be ignited at higher ignition delay times; they also produced higher explosion pressures.

One possible explanation for the rapid decrease in concentration observed for the finest fractions is that the particles adhere to the vessel walls. After tests that misfired with samples of J 133, the interior of the vessel was covered with a rather thick fur-like layer of dust. The particles covered all interior surfaces – there were not significantly more dust at the bottom of the vessel than on other surfaces. The larger surface-to-volume ratio of the cubical vessel, compared to e.g. spherical 20-l vessels, will amplify this effect.

However, the dramatic difference in the appearance of the oxides shown in Figure C-11, Figure C-12 and Figure C-13 also suggests that different flame propagation mechanisms could be active for the individual particles at different turbulence levels. In this case, the fine μm -sized particles of the white residue could be oxide particles condensing outside the flame envelope surrounding the particle, and swiftly being carried away by the intense turbulent flow. The bigger, and apparently melted, particles found in the brown residue could be the result of the mechanism described by van der Wel *et al.* (1991); a solid layer of oxide forms on the surface of the silicon particles, and restricting the further reaction.

It should be noted that the described oxide colour phenomenon might be sensitive to other variables than concentration, e.g. the interaction between chemical reactions and flow properties. Hence, for the time being it should only be considered as a peculiar observation.

Conclusion

If the rapid decrease in concentration suggested by the observed oxide colour variations is real, the results highlight a serious problem with tests performed in closed explosion vessels: after dispersion, both flow and concentration may change very rapidly; hence, there will be great uncertainty concerning the conditions under which a flame propagates.

However, the change in oxide colour could also reflect a gradual transition from a flame where most of the oxide is formed as small spheres outside the flame envelope, to a flame where most of the oxide condenses on the particle surface; or other changes in the flame propagation mechanism caused by the changes in flow conditions.

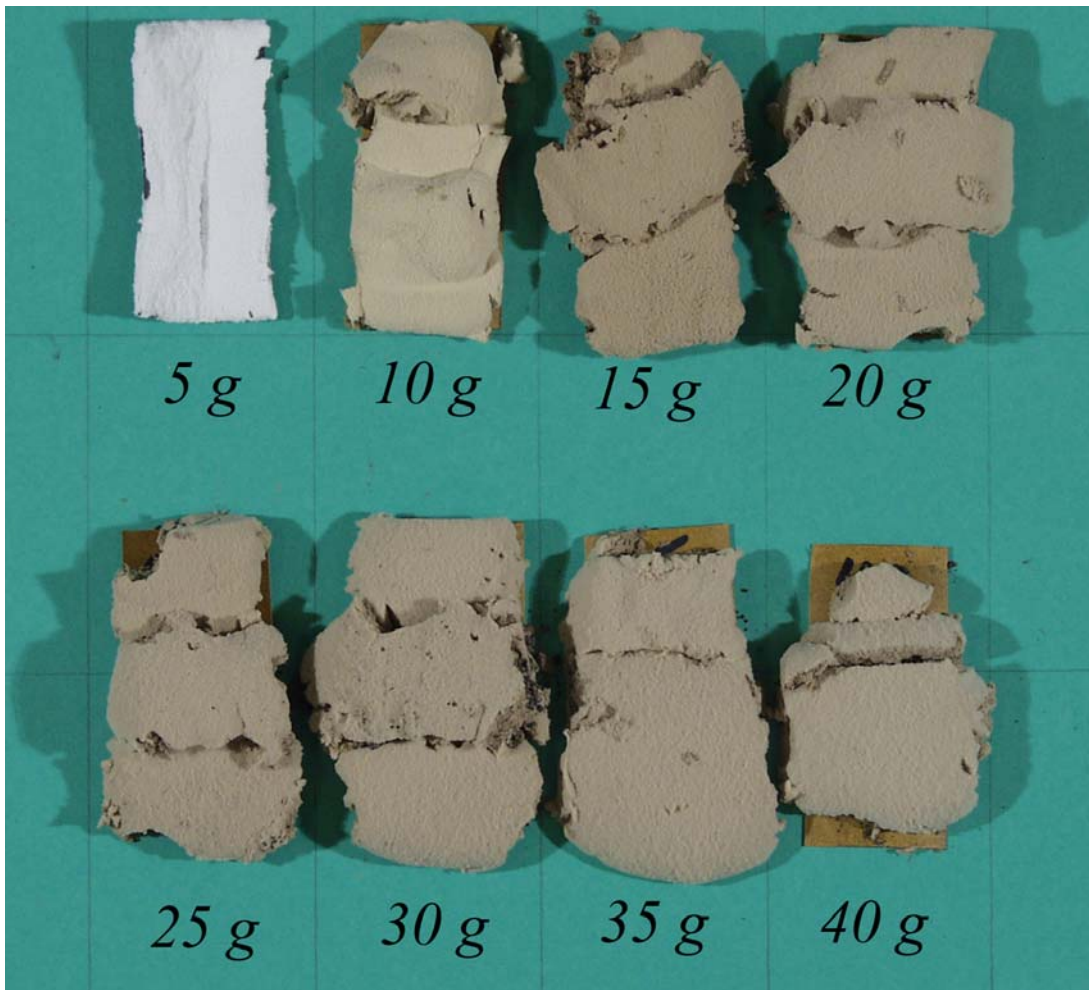


Figure C-10 Residue from the bottom of the 20-l cubical vessel after silicon dust explosions in air. The weighted amounts of dust are given below each sample (i.e. “5 g” corresponds to a nominal dust concentration of 250 g/m^3 , “10 g” to 500 g/m^3 , and so forth). Dimensions of samples: $\sim 30 \text{ mm}$ wide, $\sim 60 \text{ mm}$ long. The ignition delay time is 60 milliseconds in all tests, ignition source is the 6 J electrical discharges described in Appendix A.

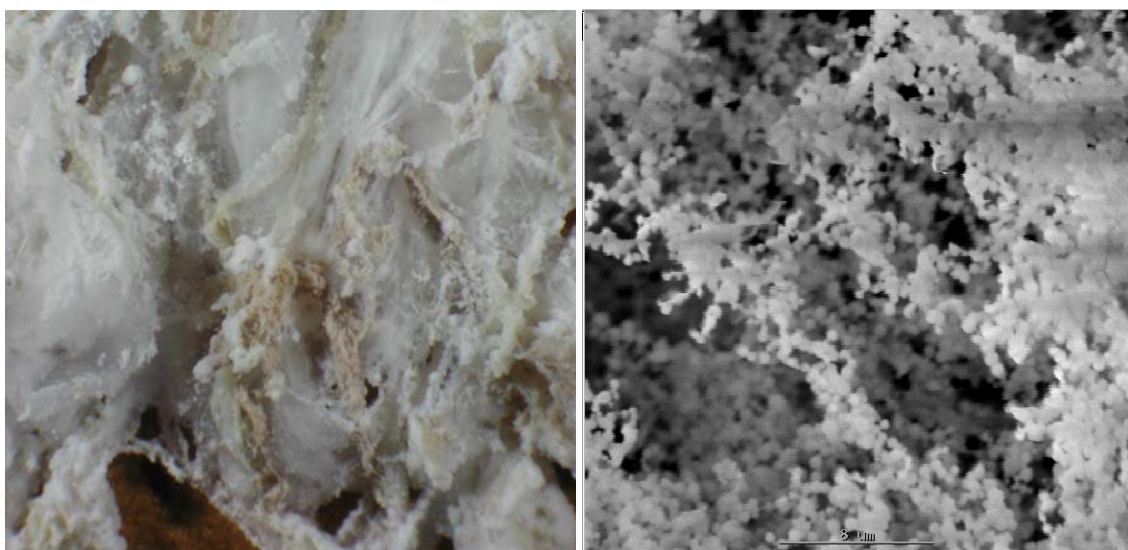


Figure C-11 Threadlike structures found hanging from the electrode holders after silicon-air explosions: light microscope (left), and SEM (right).

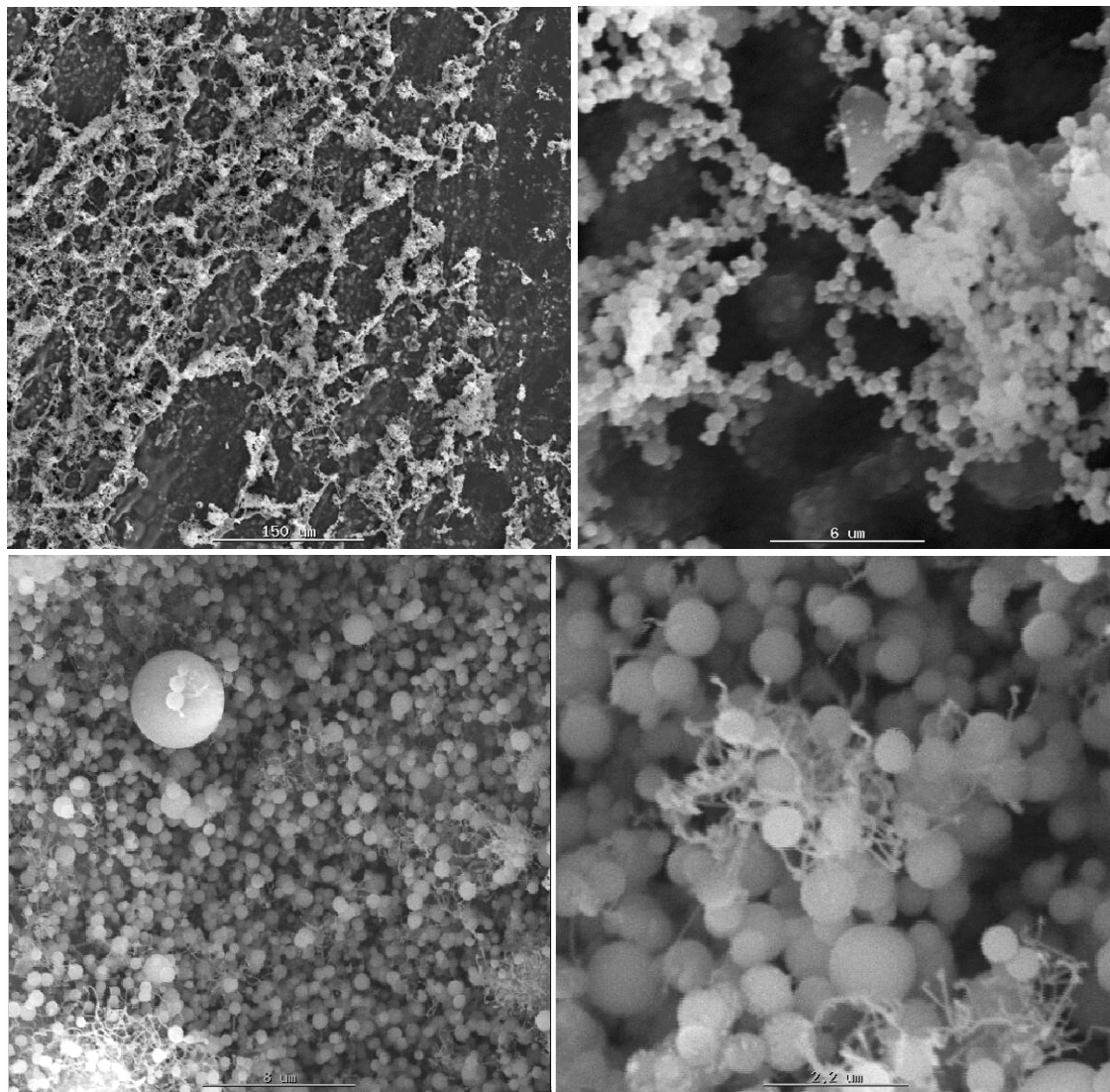


Figure C-12 SEM picture of white residue (silicon oxide) after silicon-air explosions. The pictures on the right are magnified sections from the pictures on the left.

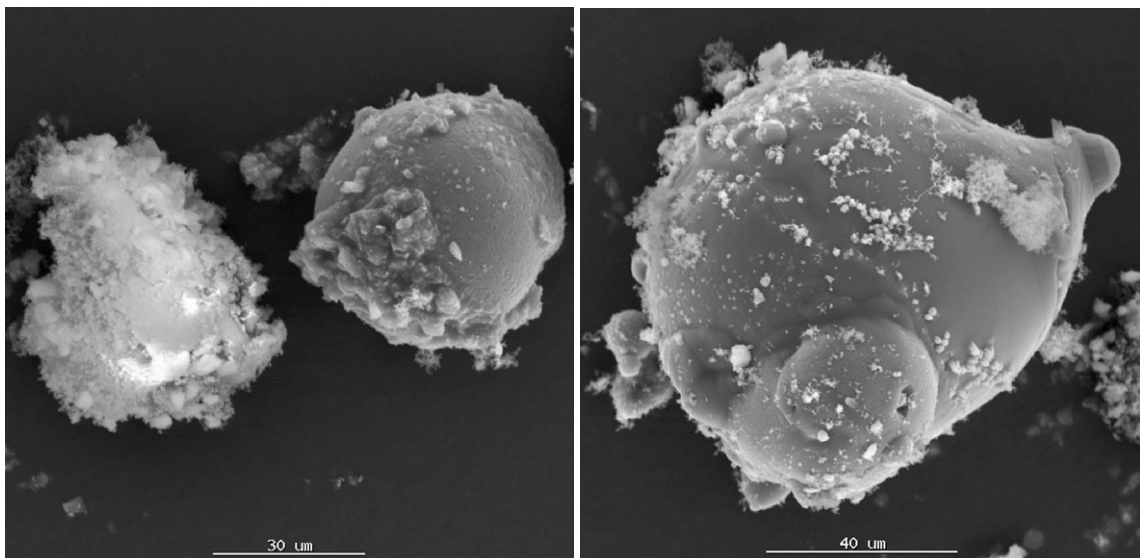
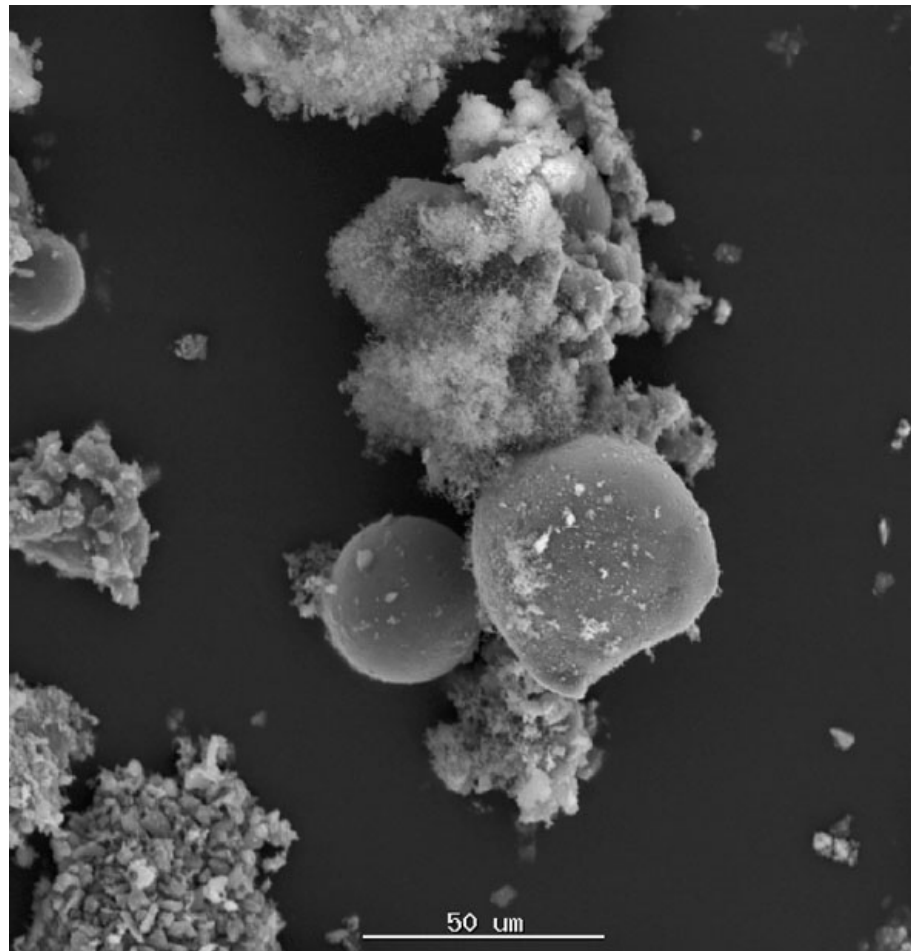


Figure C-13 SEM pictures of brown residue (silicon oxides and silicon metal) after silicon-air explosions. It appears to be a mixture of oxides and melted particles.

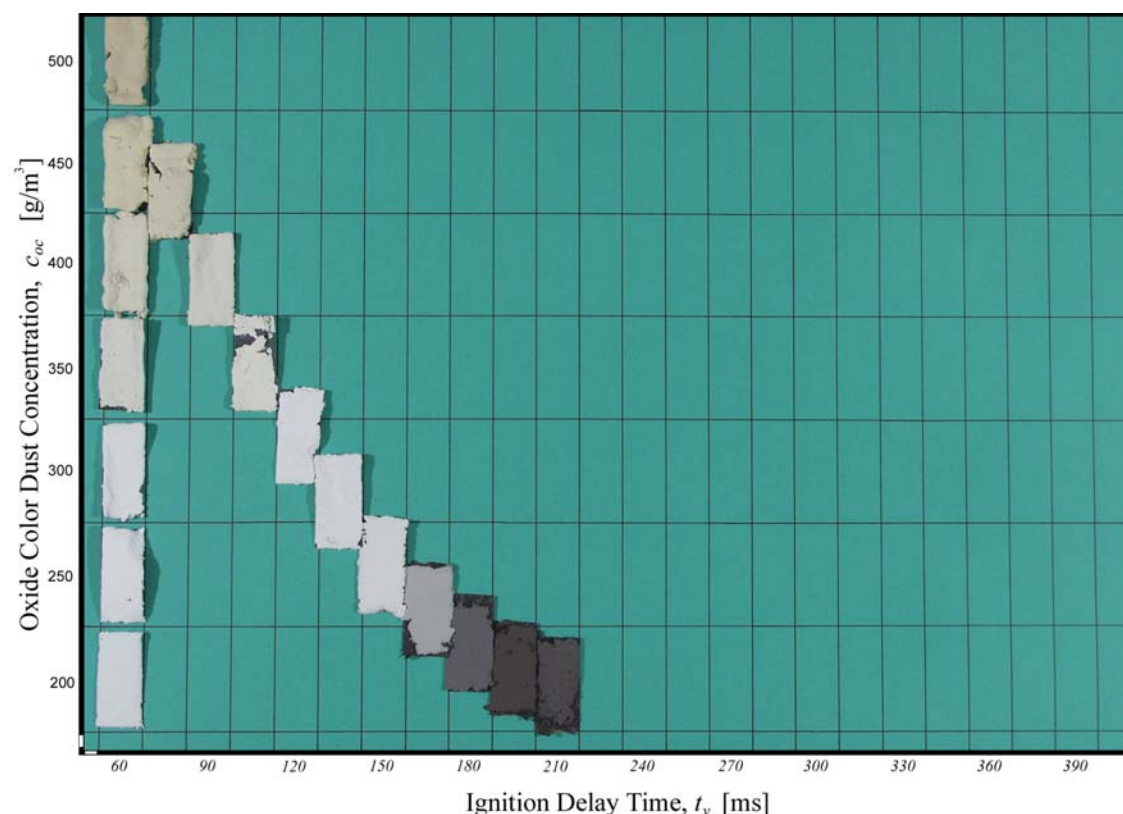


Figure C-14 The oxide colour dust concentration for lot no. J 133 is defined by the vertical column of samples; they cover the concentration range from the lowest concentration that could be ignited by the arc discharges (200 g/m^3), to a nominal dust concentration of 500 g/m^3 . The nominal concentrations for these samples are per definition identical to c_{oc} – they are all taken at an ignition delay time of 60 milliseconds. All the other samples have a nominal dust concentration of 500 g/m^3 , and a vertical position determined by their colour – it should match the oxide colour concentration as close as possible. The ignition delay time is according to the abscissa for all samples. For longer ignition delay times the oxide colour became increasingly dark, until it was almost identical to the colour of the unburnt silicon metal. As the vertical scale could not be used for these samples, the longest ignition delay time that resulted in ignition were assumed to have a concentration equal to the lowest concentration that could be ignited with an ignition delay time of 60 milliseconds. The actual concentration is probably lower because the energy required for igniting the mixture is likely to be reduced for lower turbulence intensities. It should be noted that although the displayed samples represents isolated tests, they have been selected from a collection of 3-5 tests for each set of parameters.

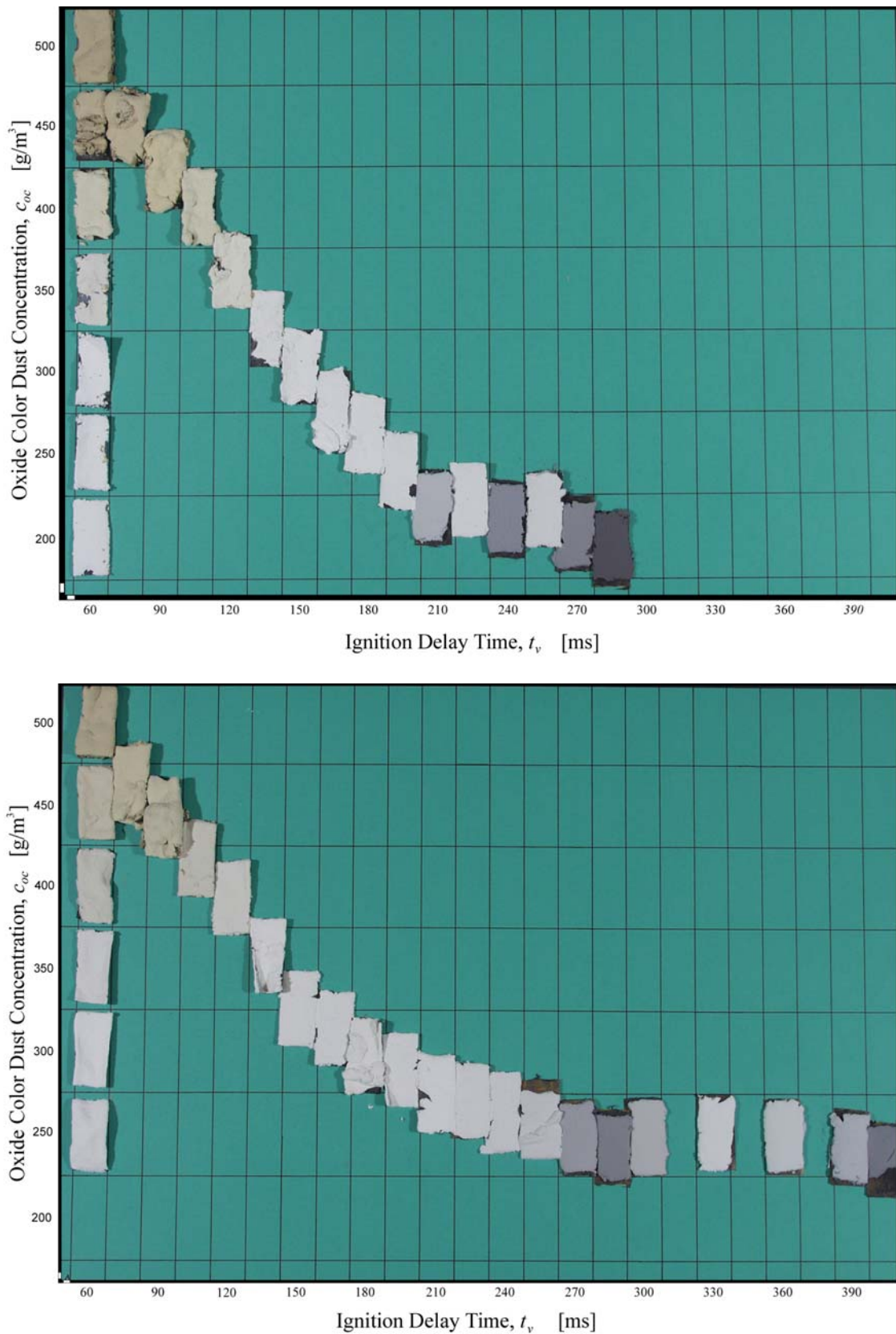


Figure C-15 Oxide colour dust concentrations for lot no. J 135 (above) and J 136 (below). The reasoning behind the placing of samples for these dusts is the same as for the dust in Figure C-14.

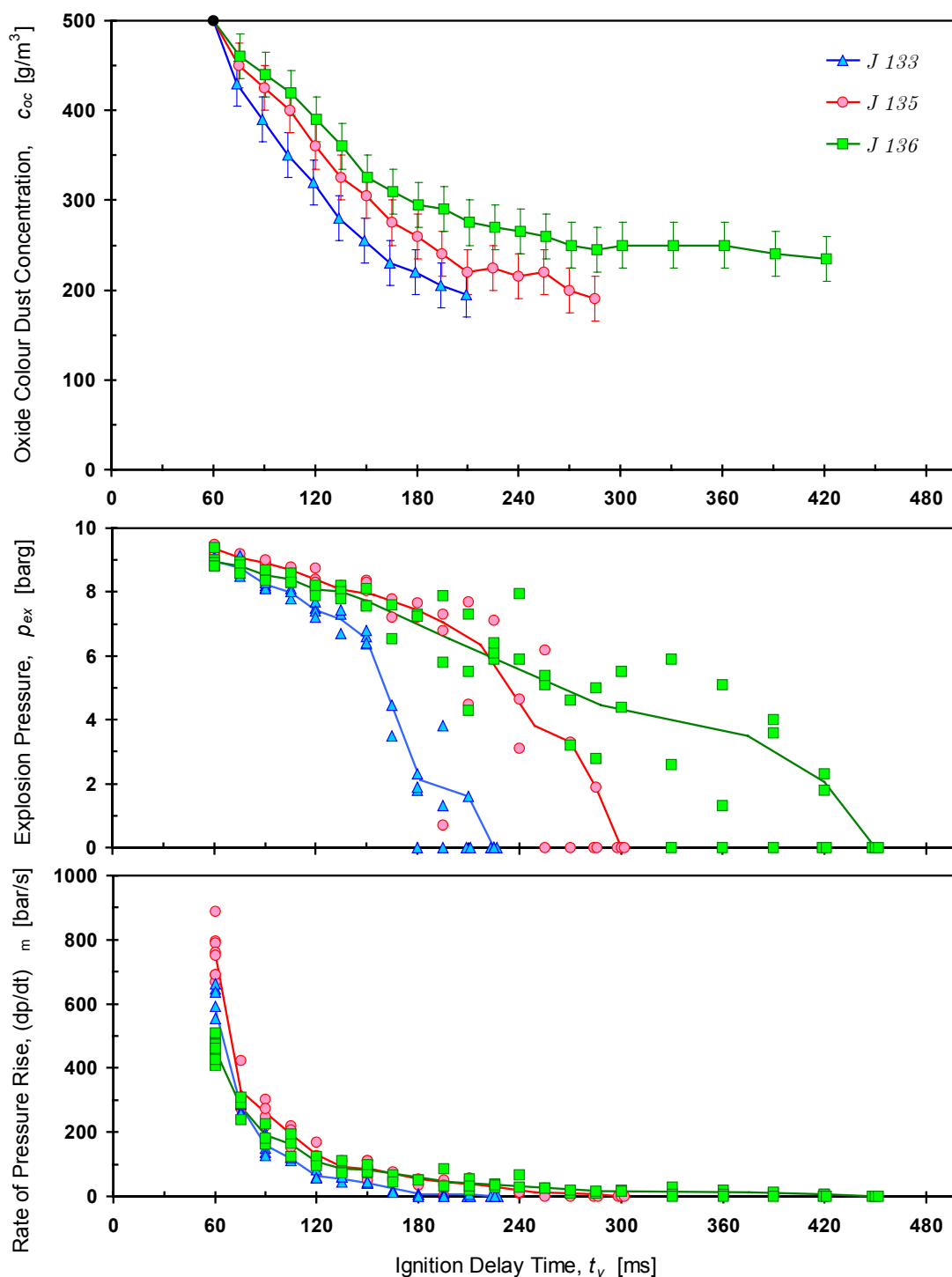


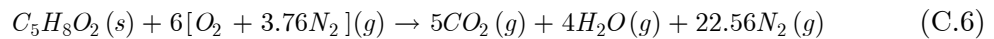
Figure C-16 Summary of oxide colour dust concentrations (upper), explosion pressure (middle), and rate of pressure rise (lower) as a function of ignition delay time for lots J 133, J 135 and J 136. All tests are performed in the 20-l cubical explosion vessel fitted with the rebound nozzle. The plot of oxide colour is based on Figure C-14 and Figure C-15; the results for the explosion indices are repeated here, they have already been discussed in Chapter 4. Nominal dust concentration is 500 g/m^3 in all tests. The error bars in the upper figure indicate the spread in observed oxide colours, not the error in dust concentration. All values of ignition delay time that could be ignited are shown for each lot. At least three consecutive tests without ignition were performed for the next higher ignition delay time before the series were terminated.

C.3.6 Polymethyl Methacrylate

A rather large batch of methyl methacrylate (PMMA) dust was purchased early in the project. However, it proved difficult to ignite the original sample by the electrical discharges produced by the spark/arc generator. Ignition was only accomplished for rather high concentrations and short ignition delay time. An attempt to make finer particle fractions¹ by dry sieving proved to be very time consuming – it only produced enough dust to make five single tests at relatively low concentration after two days of sieving. SEM pictures of PMMA particles are shown in Figure C-17 and Figure C-18; particle size distributions and key data in Table C-5.

Combustion of PMMA

The stoichiometric combustion reaction for polymethyl methacrylate in air is:



$$\frac{n_{g,f}}{n_{g,i}} = \frac{31.56}{28.56} = 1.105$$

The corresponding stoichiometric dust concentration is 143 g/m³. Explosion indices for both original and sieved samples of PMMA are presented in Figure C-19.

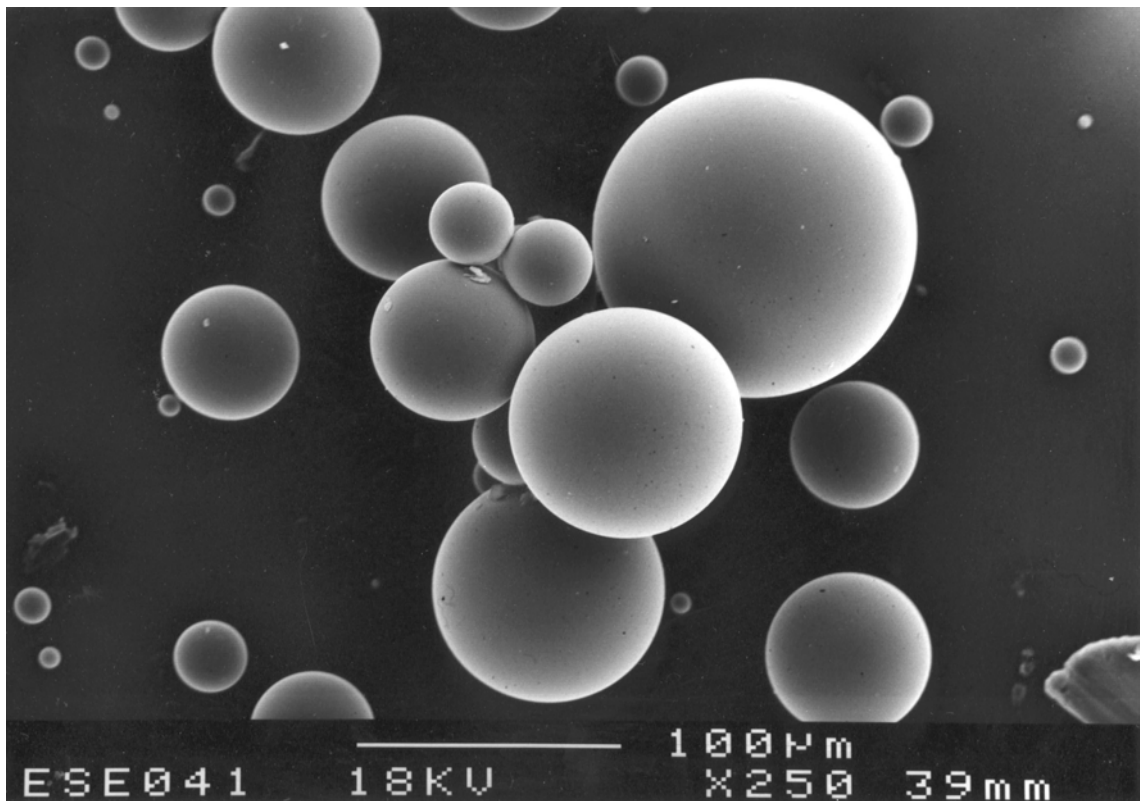


Figure C-17 SEM pictures of PMMA particles.

¹ Reduced particle size generally results in lower minimum explosible dust concentration (Hertzberg and Cashdollar, 1987).

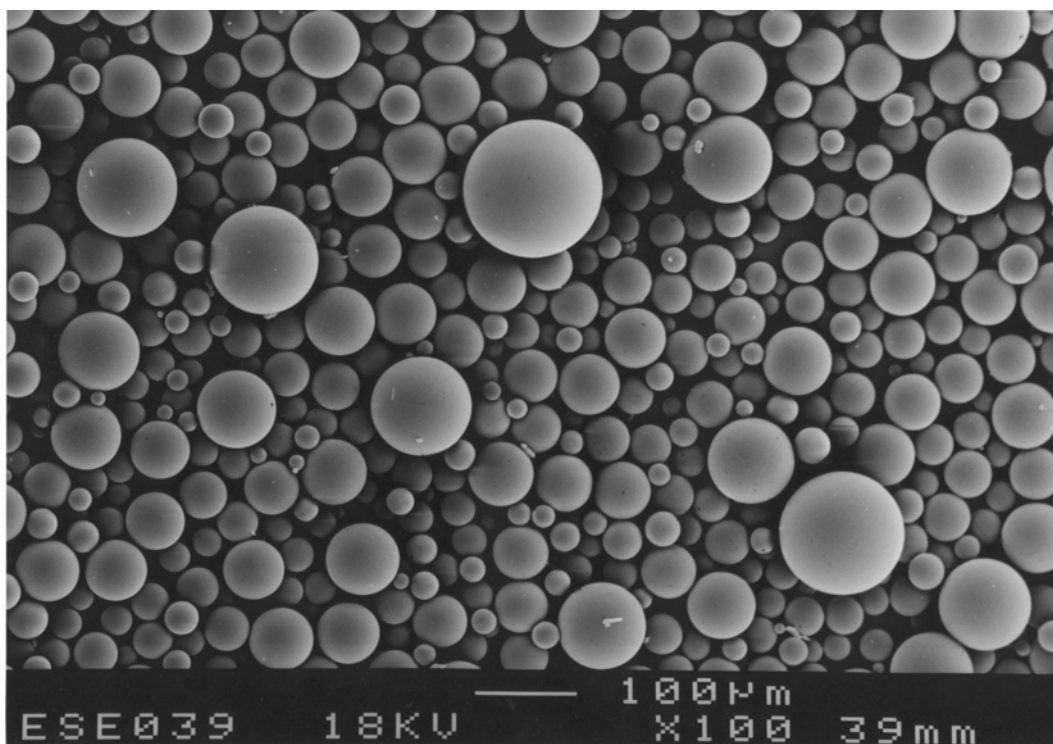


Figure C-18 SEM pictures of PMMA particles.

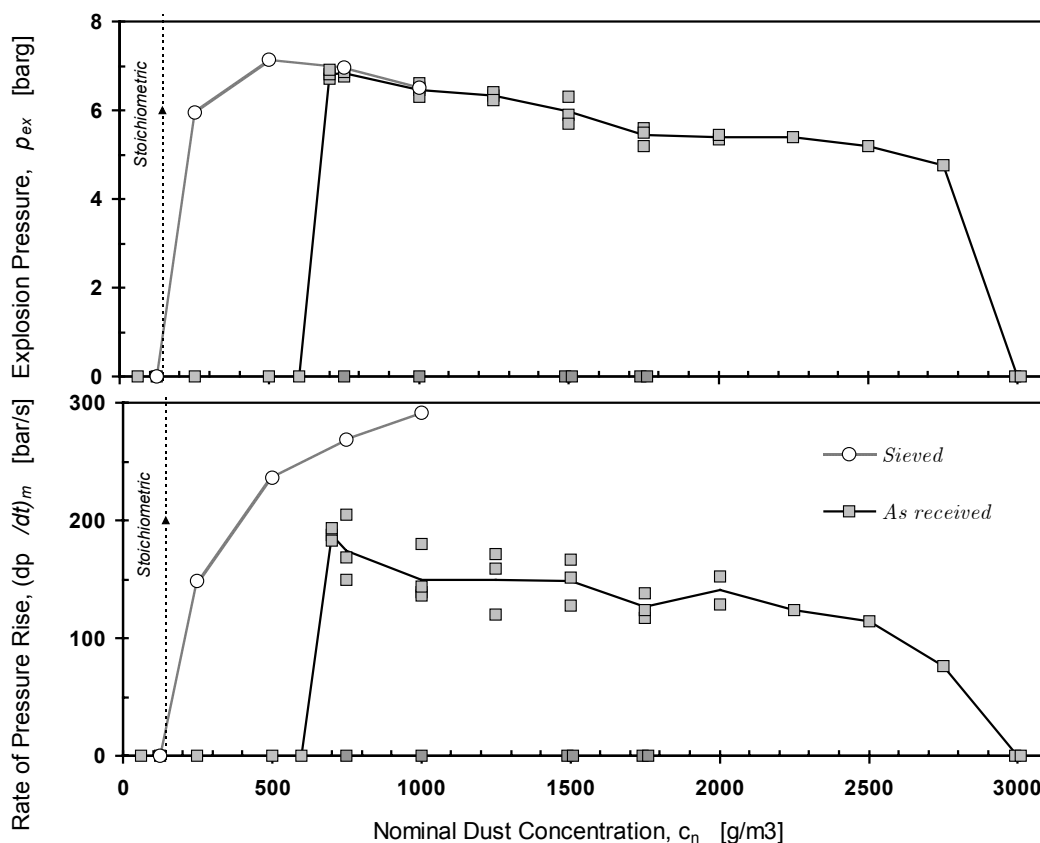


Figure C-19. Explosion indices for PMMA determined in the modified USBM vessel fitted with the rebound nozzle. The ignition source were electrical discharges produced by the spark/arc generator described in Appendix A, ignition delay time 60 milliseconds. Particle size data are presented in Table C-9. Dotted vertical line represents stoichiometric concentration.

Table C-9 Data for the polymethyl methacrylate (PMMA) dust used in this work (safety data sheet provided by Ineos Acrylics Newton Aycliffe Ltd., last revised July 1993).

<p>Trade name: Colacryl DA100P</p> <p>Manufacturer: Ineos Acrylics Newton Aycliffe</p> <p>Chemical name: Polymethyl methacrylate</p> <p>Repeat unit atomic composition: $C_5H_8O_2$</p> <p>Chemical structure:</p> $\left[\text{CH}_2 - \underset{\begin{array}{c} \text{C}=\text{O} \\ \\ \text{O} \\ \\ \text{CH}_3 \end{array}}{\overset{\text{CH}_3}{\text{C}}} \right]_n$ <p>Appearance: White powder, odour mild</p> <p>Particle size measurements: LALLS from Elkem Bremanger.</p>	<p>Particle Size Distributions:</p>				
Particle size measurements, x [μm]:	$d_{4,3}$	$d_{3,2}$	$d_{v,0.1}$	$d_{v,0.5}$	$d_{v,0.9}$
LALLS from Elkem Bremanger, as received:	63.2	50.9	36.5	60.7	86.4
LALLS from Elkem Bremanger, sieved:	40.7	37.8	29.4	37.9	55.4

C.4 Explosive Material

C.4.1 RDX

Two lots of RDX powder were provided by Øyvind H. Johansen at Dyno Nobel Defence Products, Sætre. According to laboratory report, the samples contained 6-7 per cent HMX.

*RDX*¹ is a *secondary explosive*² used for military purposes, it will explode violently if stimulated with a primary explosive. It is stable in storage, and is one of the most powerful of the military high explosives.

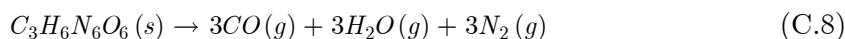
SEM pictures of RDX particles are shown in Figure C-20, particle size distributions and key data are given in Table C-10.

Combustion of RDX

Explosive substances contain both oxidizer and fuel, and the combustion process can be defined as a self-sustaining, exothermic, rapid-oxidizing reaction. The *oxygen balance* Ω for an explosive with the general formula $C_aH_bN_cO_d$ and molecular weight M is defined by the equation:

$$\Omega = \frac{[d - (2a) - (b/2)] \cdot M_{O_2}}{M} \cdot 100[\%] \quad (C.7)$$

For RDX this equation yields an oxygen balance of -21.6 per cent. The decomposition reaction with no additional oxygen present can be found by applying the Kistiakowsky-Wilson rules (Akhavan, 1998):



The stoichiometric combustion reaction for RDX in air is:



$$\frac{n_{g,f}}{n_{g,i}} = \frac{14.64}{7.14} = 2.05$$

The corresponding stoichiometric dust concentration is 1265 g/m^3 .

¹ Commonly called *RDX* (*Royal Demolition eXplosive*; or incorrectly *Research Department eXplosive*, or *Royal Dutch eXplosive*), also called *cyclonite*, or *hexogen*; its formal name is *Cyclotrimethylene-trinitramine*; structural formula: *hexahydro-1,3,5-trinitro-1,3,5-triazine*. *HMX* (*Her Majesty's eXplosive*; or *octogen*, or *cyclotetramethyl-tetranitramine*) is also a secondary explosive, it is a by-product in the production of RDX.

² *Secondary explosives* differ from primary explosives (e.g. lead azide) in that they cannot be detonated readily by heat or shock (Akhavan, 1998). Most secondary explosives are molecular solids consisting of large organic molecules – with large energy barriers to chemical reaction.

Schroeder *et al.* (2001) points out that the thermal decomposition of RDX is a very complex process, and that the detailed mechanisms of the reactions involved are in many cases not very well understood. Their results indicate that a liquid layer does exist on the surface of the burning substance, and that significant bubble formation and chemical reactions take place in this liquid layer.

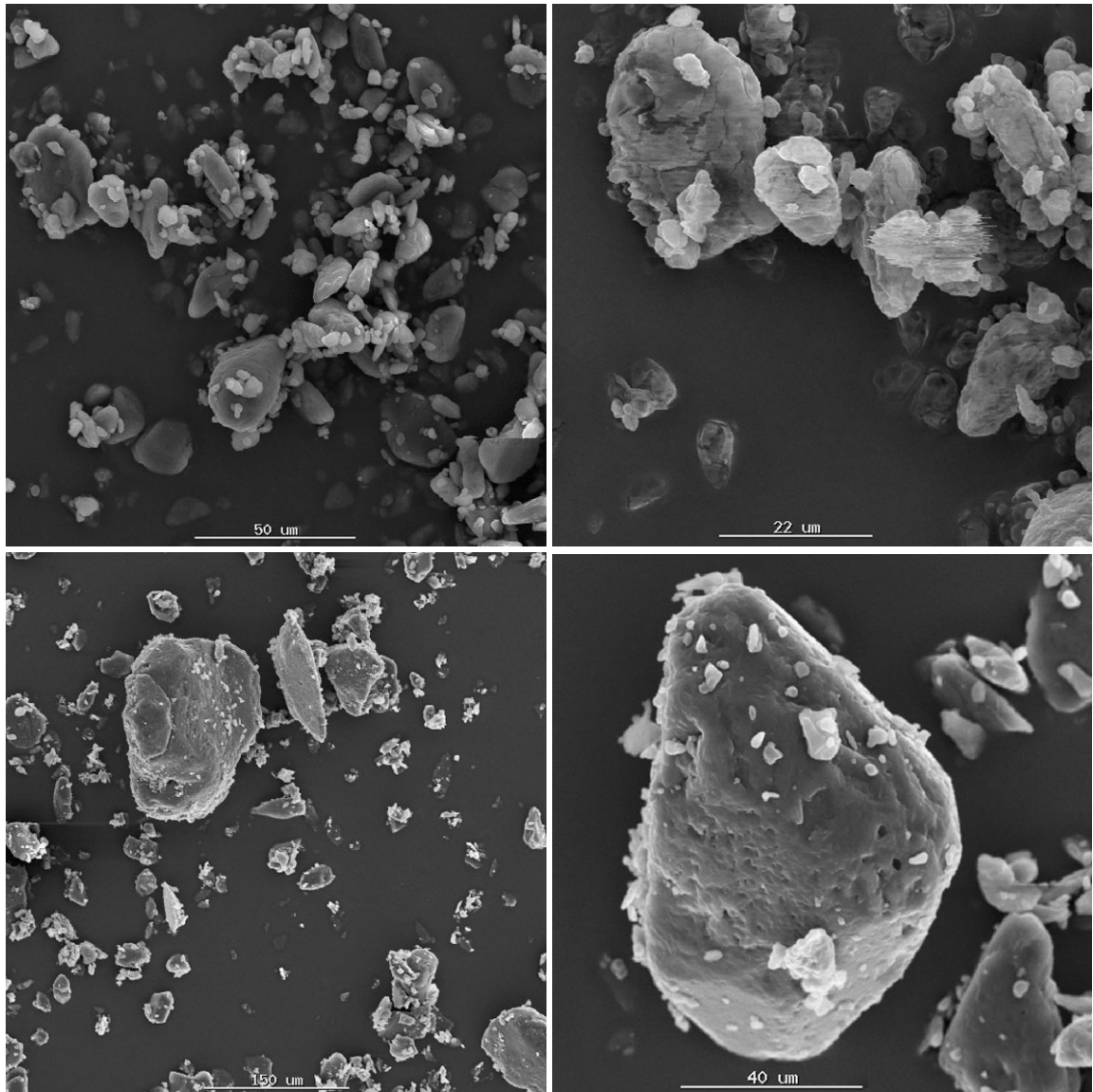
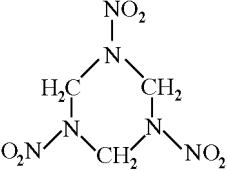
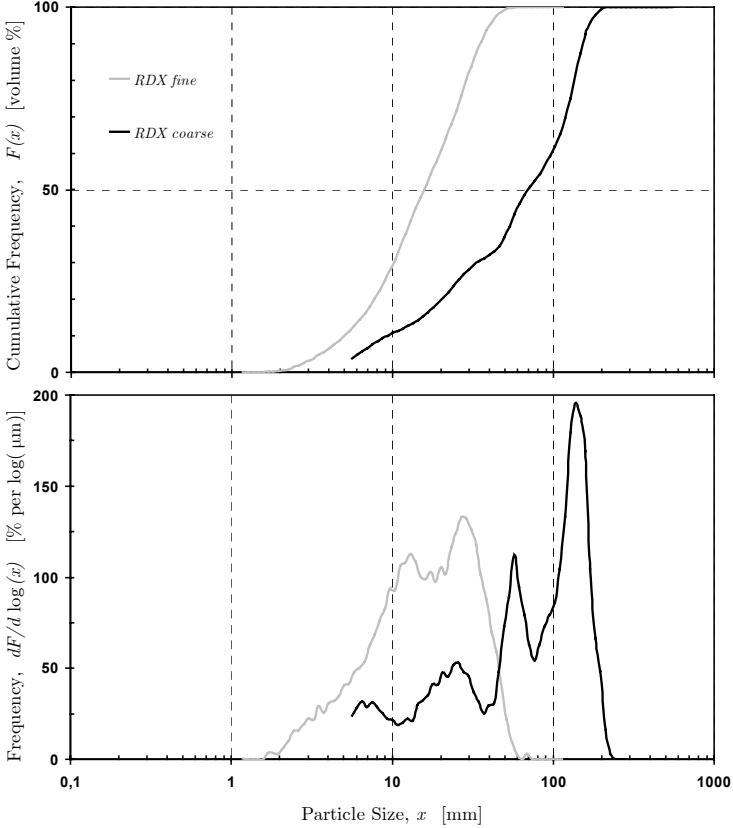


Figure C-20 SEM pictures of RDX particles, fine lot (above) and coarse lot (below).

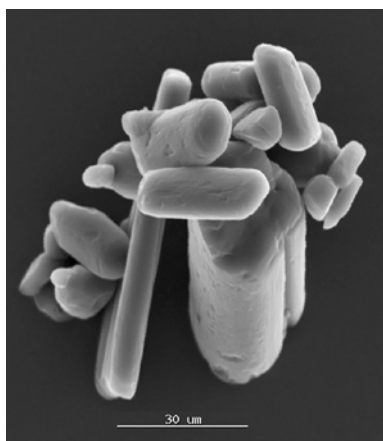
Table C-10 Data for the RDX dust used in this work (safety data sheet provided by Dyno Nobel ASA, Defence Products, dated September 1st 1998).

<p>Trade name: RDX, Type II, Class 5</p> <p>Manufacturer: Dyno Defence</p> <p>Chemical name: Cyclotrimethylene-trinitramine</p> <p>Molecular formula: $C_3H_6O_6N_6$</p> <p>Structure:</p>  <p>Appearance: White crystalline powder, odourless.</p> <p>Particle size measurements: LALLS from Dyno Defence.</p>	<p style="text-align: center;">Particle Size Distributions:</p> 				
<p>Particle size measurements, x [μm]:</p>	$d_{4,3}$	$d_{3,2}$	$d_{v,0.1}$	$d_{v,0.5}$	$d_{v,0.9}$
LALLS from Dyno Defence, fine:	19.0	11.0	5.2	16.2	36.4
LALLS from Dyno Defence, coarse:	81.4	25.0	9.5	71.9	159.9
<p>Hazard Identification:</p>  <p>T: Toxic E: Explosive</p>		<p>Risk Phrases:</p> <p>R2 (Risk of explosion by shock, friction, fire or other sources of ignition)</p> <p>R25 (Toxic if swallowed)</p> <p>Safety Phrases:</p> <p>S22 (Do not breathe dust)</p> <p>S35 (This material and its container must be disposed of in a safe way)</p> <p>S45 (In the case of accident or if one feel unwell, seek medical advise immediately)</p>			

References

- Akhavan, J. (1998). *The Chemistry of Explosives*. ISBN 0-85404-563-5. Royal Society of Chemistry, Cambridge.
- Bozzola, J.J. & Russel, L.D. (1999). *Electron Microscopy*. 2nd Edition. ISBN 0-7637-0192-1. Jones and Bartlett Publishers, Boston.
- Cardarelli, F. (2000). *Materials Handbook: A Concise Desktop Reference*. ISBN 1-85233-043-0. Springer-Verlag, London.
- Cesana, C. (2001). *Final Report: Calibration-Round-Robin CaRo 00/01*. Adolf Kühner AG, Birsfelden, Switzerland, http://www.kuhner.com/DOCUMENT/B052_172.pdf.
- Drysdale, D. (1998). *An Introduction to Fire Dynamics*. 2nd Edition. ISBN 0-471-97290-8. John Wiley & Sons, Chichester.
- Eckhoff, R.K. (2003). *Dust Explosions in the Process Industries*. Third edition. ISBN 0-7506-7602-7. Gulf Professional Publishing, Amsterdam.
- Eckhoff, R.K. & Mathisen, K.P. (1978). *A Critical Examination of the Effect of Dust Moisture on the Rate of Pressure Rise in Hartmann Bomb Tests*. Fire Research, **1** (1977/78), pp. 273-280.
- Friede, B. & Jansen, M. (1996). *Some Comments on the So-Called 'Silicon Monoxide'*. Journal of Non-Crystalline Solids, **204**, pp. 202-203.
- Glassman, I. (1996). *Combustion*. 3rd Edition. ISBN 0-12-285852-2. Academic Press, San Diego.
- Lide, D.R. Ed. (1996). *CRC Handbook of Chemistry and Physics*. 77th Edition. ISBN 0-8493-0477-6. CRC Press, New York.
- Line, L.E., Rhodes, H.A. & Gilmer, T.E. (1959). *The Spark Ignition of Dust Clouds*. Journal of Physical Chemistry, **63**, pp. 290-294.
- Rochow, E.G. (1973). *Silicon*. Chapter 15 in Bailar, J.C., Emeléus, H.J., Nyholm, sir R. & Trotman-Dickenson, A.F. (Eds.): *Comprehensive Inorganic Chemistry*, ISBN 0-08-015655, Pergamon Press, Oxford.

- Schroeder, M.A., Fifer, R.A., Miller, M.S., Pesce-Rodriguez, R.A., Mcnesby, C.J.S., Singh, G. & Widder, J.M. (2001). *Condensed-Phase Processes during Combustion of Solid Gun Propellants. II. Nitramine Composite Propellants*. *Combustion and Flame*, **126**, pp. 1577-1598.
- Thomas, G.O., Oakley, G & Brenton, J. (1991). *Brief Communication: Influence of the Morphology of Lycopodium Dust on Its Minimum Ignition Energy*. *Combustion and Flame* **85**, pp. 526-528.
- Timms, P.L. (2001). *Personal communication with Dr. Peter L. Timms*; Reader in Inorganic Chemistry, School of Chemistry, University of Bristol, Bristol, UK.
- Tryon, A.F. & Lugardon, B. (1991). *Spores of the Pteridophyta: Surface, Wall Structure, and Diversity Based on Electron Microscope Studies*. Springer-Verlag, New York.
- van der Wel, P., Lemkowitz, S., Scarlett, B. & van Wingerden, K. (1991). *A Study of Particle Factors Affecting Dust Explosions*. *Particle & Particle Systems Characterization*, **8**, pp. 90-94.
- Wikström, N. (2003). *Personal communication with Dr. Niklas Wikström*, Department of Systematic Botany, Evolutionary Biology Centre, Uppsala University, Sweden.
- Wilce, J.H. (1972). *Lycopod Spores, I. General Spore Patterns and the Generic Segregates of Lycopodium*. *American Fern Journal*, **62** (3), pp. 65-79.
- Walters, R.N., Hackett, S.M. & Lyon, R.E. (2000). *Heats of Combustion of High Temperature Polymers*. *Fire and Materials*, **24**, pp. 245-252.
- Zhang, X.C. (2003). *Personal communication with Professor Xian-Chun Zhang*, President of the Chinese Fern Society, Principal Investigator of Higher Cryptogamic Botany, Institute of Botany, Chinese Academy of Sciences, Beijing, China.
- Øllgaard, B. (1993). *Scandinavian Ferns: A Natural History of the Ferns, Clubmosses, Quillworts, and Horsetails of Denmark, Norway, and Sweden*. ISBN 87-7245-532-2. Rhodos, Copenhagen.
- Øllgaard, B. (2003). *Personal communication with Benjamin Øllgaard*; associate professor at Department of Systematic Botany, Institute of Biological Sciences, University of Aarhus, Denmark.



¹ SEM: niacin amide particles.

APPENDIX D

Analysis of LDA Data

Measurements of the decay of turbulence inside the 20-litre cubical vessel by laser Doppler anemometry (LDA) are described in Chapter 3; a summary of the main results are presented and discussed in Chapter 4. This appendix describes how the measured LDA data have been analysed, and presents some of the results in more detail.

D.1 Data analysis

The instantaneous velocity u in turbulent flow is traditionally considered to be a sum of the average velocity \bar{u} and the fluctuating velocity u' :

$$u = \bar{u} + u' \quad (\text{D.1})$$

Turbulence decay can be described in terms of the decrease in the *root-mean square of the fluctuating velocity*, u'_{rms} :

$$u'_{rms} \equiv \sqrt{u'^2} = \sqrt{\frac{1}{n} \sum_{i=1}^n (u_i - \bar{u})^2} \quad (\text{D.2})$$

A major problem when analysing LDA data from transient flow measurements is to isolate, or define, the average velocity (\bar{u}) from measurements of the instantaneous velocity; the usual approach is to use some kind of smoothing algorithm to estimate \bar{u} . In the process of smoothing, the smoothed value is obtained from the observations in the immediate neighbourhood of the point, rather than from the whole set of observations. This is an advantage if it is suspected that the form of the underlying curve changes radically from one end of the range to the other (Guest, 1961). However, as pointed out by Bevington (1969):

“The concept of smoothing data is not one which meets with universal approval”.

Provided a realistic estimate for \bar{u} can be found, the decay of turbulence can be calculated by applying (D.2) to separate and sufficiently short time intervals throughout the course of the transient flow.

In this work, the mean velocity has been estimated by two different smoothing methods. The first is a moving regression algorithm, fitting a second order polynomial to a moving point-window of range¹ r equal 35. This point-window size was chosen to facilitate comparison with the work by Dahoe (2000), also described by Dahoe *et al.* (2001). The second method is robust locally weighted regression, or *loess* (Cleveland, 1993). Although both methods produce similar results, there are serious doubts regarding the quality of the results; this is discussed in section D.1.3.

D.1.1 Moving Regression Algorithm

This method is almost identical to the procedure described by Dahoe (2000). A MATLAB program called *ldafig.m* has been written to perform the calculations and display standardized figures of the results; the program code is given in section D.3. The program goes through the following six steps²:

1. Import of the file containing the measured data for one single test. After giving the command *ldafig*, the user is prompted for the test number. The program opens the file containing the LDA data, and starts the calculations (step 2-4).
2. Filtering of outliers, in two steps:
 - i.* In the primary filter, measured instantaneous velocities are compared with an empirical filter criterion³; values exceeding a certain limit defined by the criterion are discarded. This is illustrated in Figure D-1 *a*); the red line defines the filter criterion, and the red stars indicate discarded values. The number of discarded points is indicated in the figure – typically between 10 and 30 with no dust (only tracer particles). This is a small number compared to the total number of measurements, typically 12000. It seems clear that the discarded values must be outliers, especially since they only appear for positive values of velocity – it was not necessary to perform any primary filtering of outliers with negative values.

¹ The size of the moving point-windows will be defined by the *range parameter* r . A point window of range $r = 35$ has 35 points to the left, and 35 points to the right, of the point where the mean velocity is to be estimated; i.e. the total number of points is $(2r+1) = 71$.

² A typical test (no. 23, without dust) will be used as an example throughout the explanation of the regression algorithm.

³ The filter criterion are defined by an equation on the form: $u_{\text{lim}} = (u_0 - u_\infty)e^{-\frac{t}{t_0}} + u_\infty$; the constants u_0 , u_∞ and t_0 are set to 60 m/s, 5 m/s and 50 ms, respectively. Values exceeding u_{lim} are discarded.

- ii. From the remaining measurements, preliminary mean and fluctuating velocities are calculated from a floating winsorized average (Winer, 1971). Absolute values of the fluctuating velocities are compared with a second empirical filter criterion¹; values exceeding the criterion are again discarded. Figure D-1 *b*) illustrates this: the purple line indicates the second filter criterion, purple stars discarded points. This filter usually removes less than ten measurements. The total number of remaining measurements (N_{total}) is given in Figure D-1 *c*), together with a plot of sample frequencies calculated for selected 4-millisecond intervals.
3. A moving regression algorithm is applied to the remaining measurements in order to estimate the mean velocity. For each data point $u_j(t_j)$, ($r < j < N_{total} - r$), a point-window of $(2r+1)$ measurements is selected – the window includes $u_j(t_j)$, and r measurements to each side of point j . For each point-window, a second degree polynomial $P_j(t)$ is fitted to the $(2r+1)$ points by a least square algorithm, and the estimated mean velocity $\bar{u}_j(t_j)$ is defined as $P_j(t_j)$. In this work, r has the value 35; this is the optimal choice according to Dahoe². The estimated mean velocity is shown in Figure D-2 *a*); note that \bar{u} is written as u_m in the figures produced by MATLAB. An estimate for the fluctuating velocity follows directly from equation (D.1); the result is shown in Figure D-2 *b*).
 4. The root-mean-square of the fluctuating part of the velocity is calculated from equation (D.2) in selected 4 ms intervals, see Figure D-2 *c*).
 5. Plotting of results, such as Figure D-1, Figure D-2 and Figure D-3.
 6. Export of results; u'_{rms} in selected 4-millisecond intervals is saved to file.

As pointed out by Dahoe *et al.* (2001), the build up of turbulence as well as the start of decay of turbulence occurs within the first 60 milliseconds. A more detailed description of turbulence decay from 60 to 200 milliseconds is shown in Figure D-3. Dahoe *et al.* were able to describe the decay of turbulence in this interval by an equation on the same form as the equations used by Batchelor and Townsend (1947, 1948a, 1948b) to describe the various stages of decay of grid generated turbulence³:

$$\frac{u'_{rms}}{u'_{rms}^o} = \left(\frac{t}{t_0} \right)^n \quad (D.3)$$

where t_0 is a fixed time (e.g. 60 milliseconds), and u'_{rms}^o is the root-mean square of the fluctuating velocity at time t_0 .

¹ This criterion is in the same form as the first, but with u_0 , u_∞ and t_0 set to 50 m/s, 2.5 m/s and 40 ms, respectively.

² Dahoe (2000) chose r equal to 35 based on “numerical experiments”; however, it is likely that this number will dependent on the sample frequency. Dahoe also comments on a phenomenon known as *velocity bias*: the sample frequency may be dependent on the velocity of the fluid.

³ See Chapter 2 in the main part of this thesis.

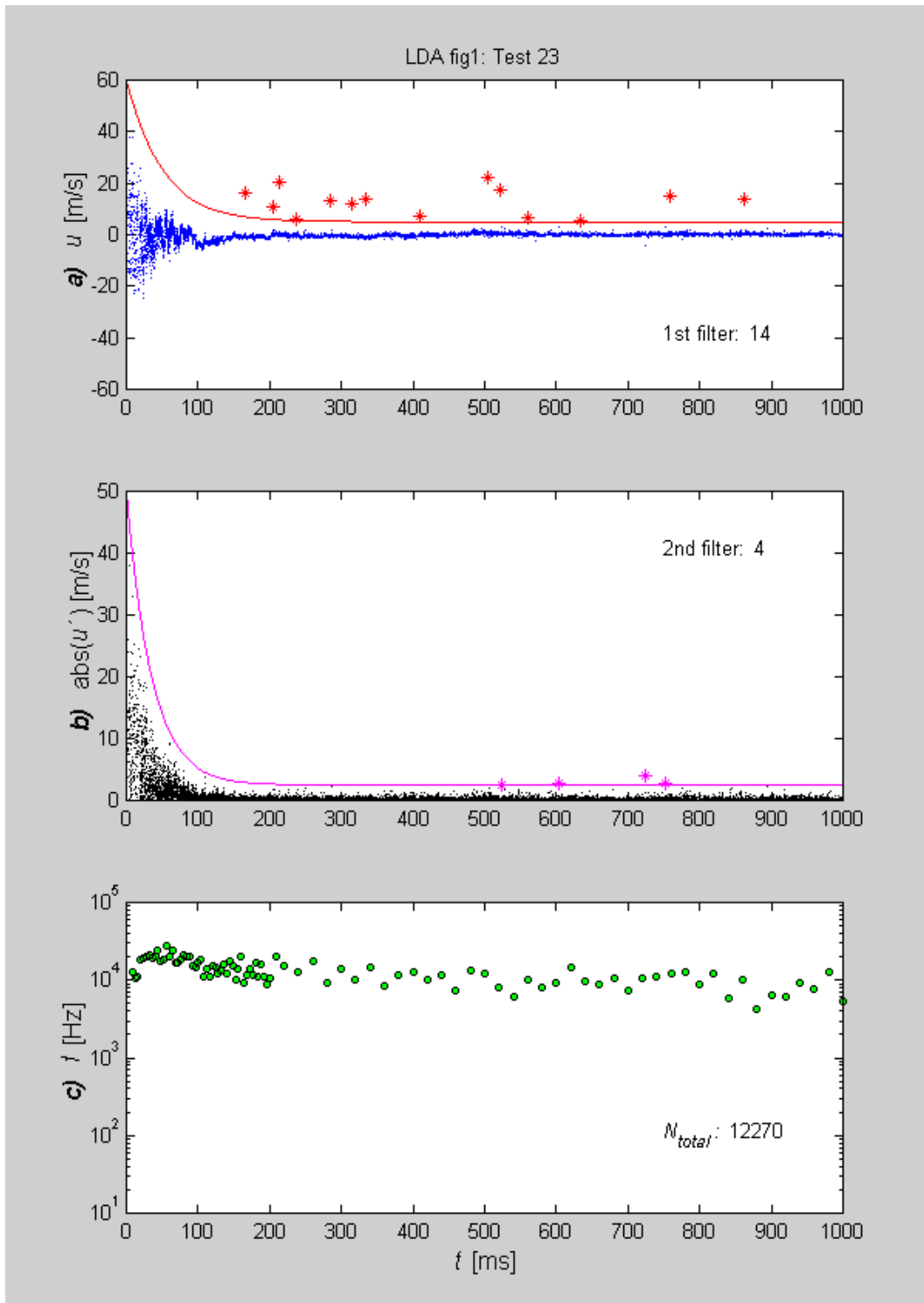


Figure D-1 Analysis of LDA data by moving regression algorithm. The example is for Test No. 23: u_y -component in the point $(0,0,0)$ with rebound nozzle, no dust, S/N is set to medium. a) First filter criterion: measurements of the instantaneous velocity (red stars) exceeding a certain value (red line) are discarded; the number of filtered points is given in the figure. b) Second filter criterion: absolute values of instantaneous velocity components (purple stars) that exceeds a certain value (purple line) are discarded. c) Sample frequency in selected 4 ms intervals, calculated from the data remaining after applying the two filters. N_{total} is the total number of remaining data points. Note that the spacing between the selected 4-millisecond intervals is shorter for $t < 200$ ms than for $t > 200$ ms.

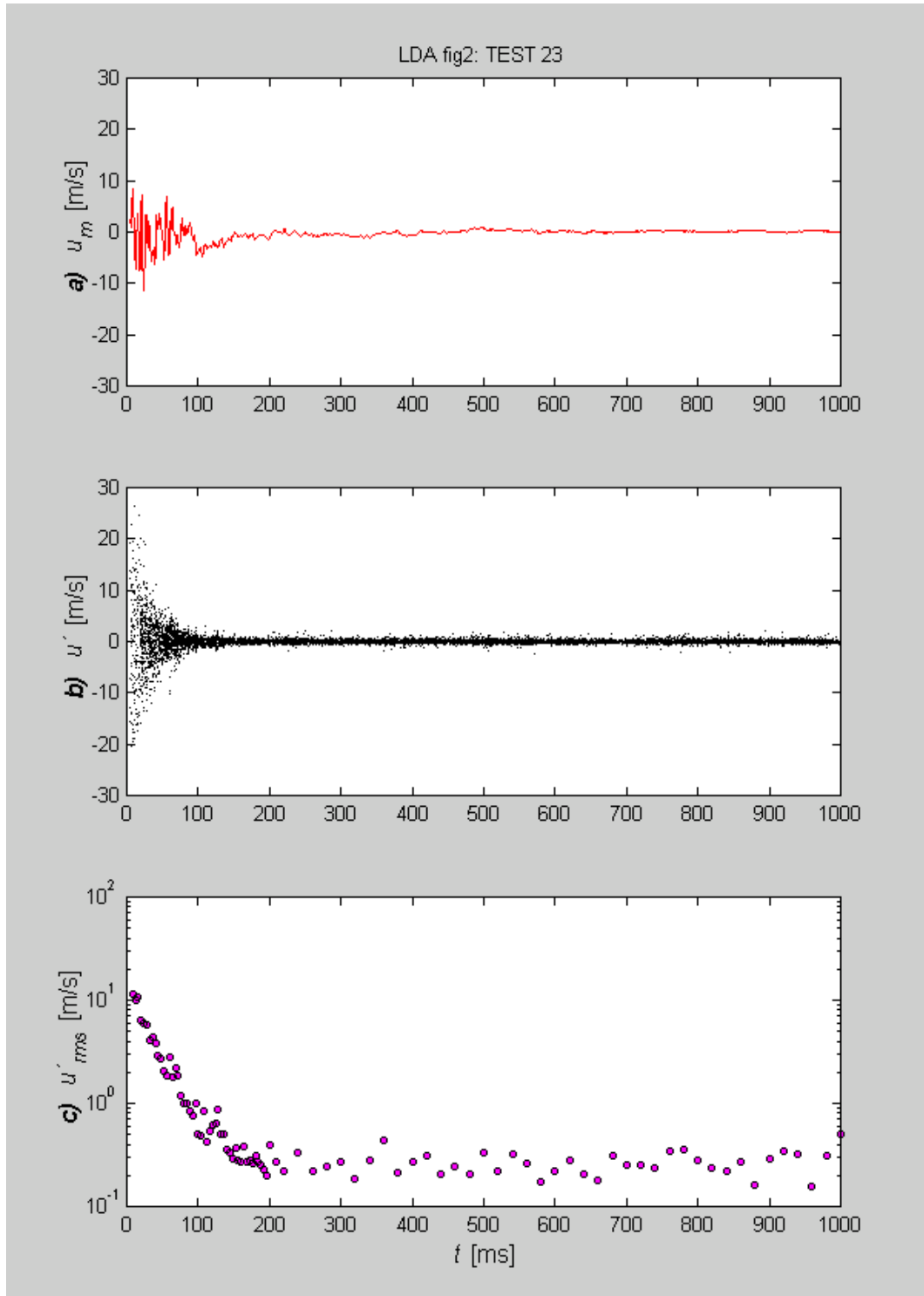


Figure D-2 Analysis of LDA data by moving regression algorithm (continued from Figure D-1): a) Estimated value for mean velocity determined by the moving regression algorithm; b) Fluctuating velocity, defined by equation (D.1); c) Decay of the root-mean-square of fluctuating velocity, calculated from the data in b) over selected 4 ms intervals.

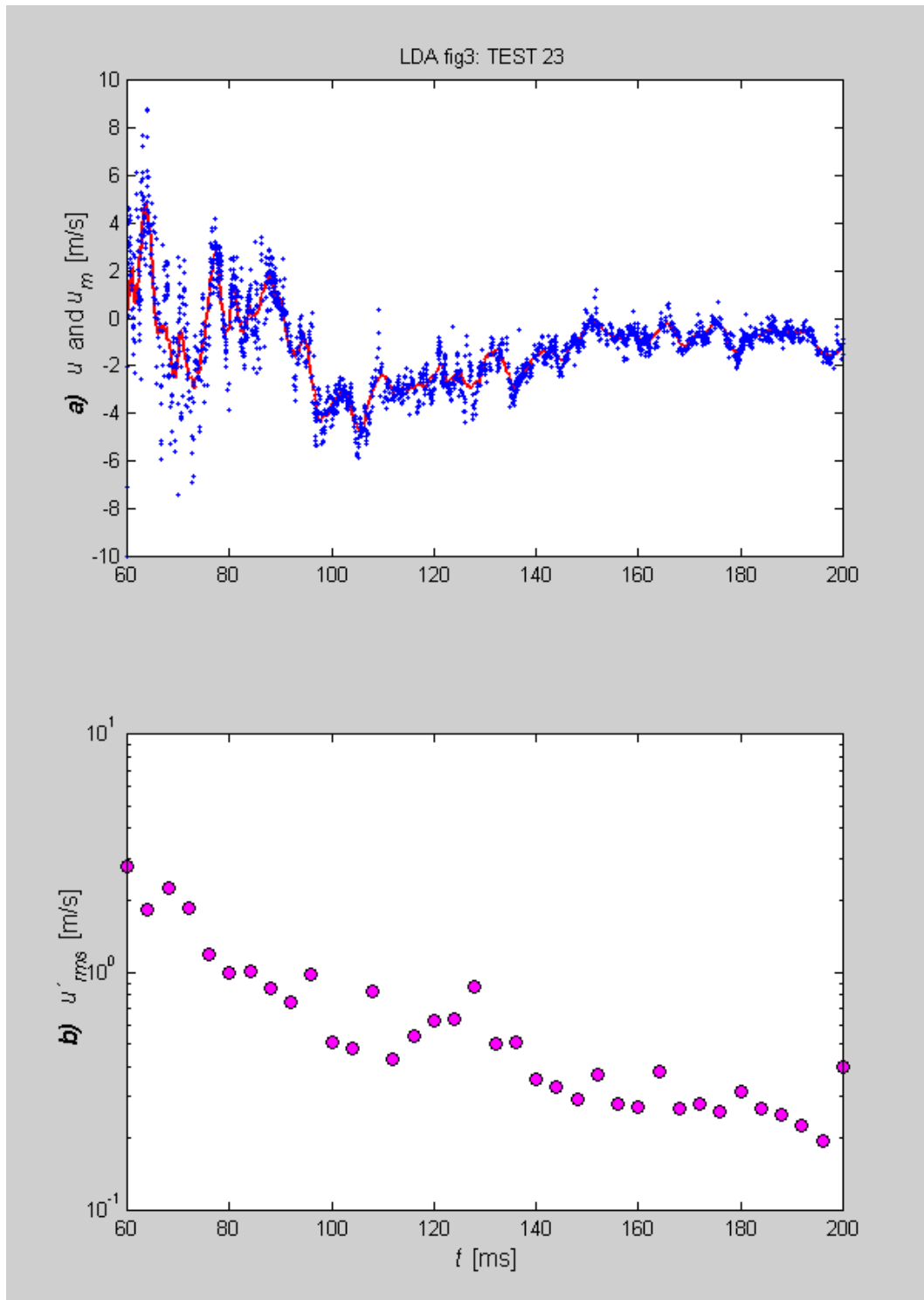


Figure D-3 The time interval from 60 to 200 milliseconds for the test shown in Figure D-1 and Figure D-2; a) mean and fluctuating part of the horizontal velocity component, b) decay of the root-mean-square of the fluctuating velocity.

D.1.2 Robust Locally Weighted Regression (LOESS)

Loess is a powerful but simple strategy for fitting smooth curves to empirical data¹. The method was used by Mercer *et al.* (2001) to smooth the plots of instantaneous velocity versus time data produced by LDA measurements; hence estimating the mean velocity. A detailed description of the loess algorithm can be found in Cleveland (1993); in short, it involves the following steps:

- i) Two loess parameters are chosen: the smoothing parameter f , and the degree λ of the fitting polynomial. As f increases, the fitted curve becomes smoother. Only second-degree polynomials ($\lambda=2$) are used in this work, i.e. *local quadratic fitting*. According to Cleveland, “the choice of the loess parameters must be based on a combination of judgement and of trial and error”.
- ii) For each observation (u_k, t_k) , all the other observations (u_i, t_i) are assigned *neighbourhood weights*, $w_{k,i}(t)$, using a *tricube weight function*. The weight decreases with increasing distance from the point in question.
- iii) A polynomial $P_k(t)$ of degree λ is fitted to the data using *weighted least-squares* with weight $w_{k,i}(t_i)$ at (u_i, t_i) . The fitted value at (u_k, t_k) is simply $P_k(t_k)$.

The overall procedure chosen in this work was to go through the same six steps described in section D.1.1; but the moving regression algorithm in the third step was replaced by the loess algorithm. The smoothing parameter f was chosen in such a way that the results were comparable to those produced by the method in D.1.1; but three different values for the range parameter r were used: 30, 40 and 50.

D.1.3 Quality of Analysis Results – An Alternative Approach

The methods described in the preceding paragraphs have several limitations.

Unevenly spaced data

LDA systems measure the modulated frequency of scattered coherent light from seed particles in the flow; hence, velocity measurements cannot be made continuously because valid data only exists when there is a particle in the measurement volume that scatters sufficient light to be observed by the measurement system. Due to the random intervals between the arrivals of tracer particles in the measurement volume, the measurements of the instantaneous velocity are unevenly spaced in time. This rules out many of the traditional methods for smoothing and curve fitting (Guest, 1961).

¹ The term *loess* is an acronym for **l**ocal **w**eighted **r**egression; the method to which it refers is a generalization of the technique known as *lowess* (**l**ocally **w**eighted **s**catter-plot **s**moother). Loess was introduced by Cleveland (1979); further details on the mathematical properties are provided by e.g. Cleveland and Devlin (1988), Cleveland (1993), and Jacoby (2000).

Outliers

The velocity measurements for turbulent flow regimes obtained with laser Doppler anemometry are affected by random noise arising from laser beam imperfections and the use of electronic equipment. The resulting outliers in the measured data sets can have profound influence on the estimated value of the mean velocity if they are not dealt with properly. Although some false measurements may be mixed with real ones, hence impossible to isolate, it seemed clear that most of the false measurements were concentrated in a separate noise band, characterized by high positive velocity values. If these isolated measurements were real, one would expect to find similar values with opposite sign. The number of outliers were low as long as only air with seed particles were dispersed, and the filters described in section D.1.1 seemed to work very well. However, when dust was added to the flow, the number of outliers increased dramatically (see section D.2.3).

Sample frequency and frequency of turbulence

The distribution density of the seed particles must be large enough to obtain valid velocity measurements at rates at least twice as high as the highest frequency in the flow (Ancimer *et al.*, 1999). However, it was found that too much seed particles yielded fewer valid measurements; it is likely that particles adhering to the inside of the window obstruct the laser beams. The highest achievable data rates were found to be in the order of 10 to 15 kHz; hence, the highest frequencies that can be measured are in the order of five kHz. Dahoe *et al.* (2001) reported data rates up to 25 kHz. As will be discussed in section D.2.3, the sample rate decreased dramatically when dust particles were added to the flow.

Fundamental problems with the smoothing methods

The concept of estimating the “true” average velocity by fitting a smoothed curve to the measured data points is based on the assumption that such a curve really exists – this is not obvious for the situation in question. Furthermore, both the moving regression algorithm described in D.1.1, and the loess algorithm described in D.1.2, rely on a moving point-window of a certain width when the “average” velocity is to be estimated. The frequency of the true average velocity is however likely to change dramatically during the transient dispersion process, and it is not realistic to expect that a point-window of fixed size can resolve the various frequencies equally well. Hence, the results of the analysis should not be regarded as more than crude estimates of the “true” average velocity.

Apart from the size of the point-window (determined by the variable r , defined in D.1.1), the results depend on the choice of the smoothing parameter f , and on the sample frequency. The problem will be illustrated by a simple numerical experiment, in which a known signal of varying frequency is masked by adding random noise; the ability of the loess algorithm to restore the original signal for the various frequencies may be representative for the quality of this kind of calculations. The moving regression algorithm described in D.1.1 will have the same limitations.

First, a hypothetical measurement series $H(t_i)$ is constructed by adding random noise $R(t_i)$ to a function $S(t)$ with time-dependent frequency, $S(t) = \sin(t \cdot 2^t)$. Hence, a hypothetical signal is produced, with the same frequency as $R(t_i)$:

$$H(t_i) = R(t_i) + S(t_i) \tag{D.4}$$

The effect of varying the smoothing parameter f is illustrated in Figure D-4 and Figure D-5; $S(t)$ is the same in both figures (red line in upper subfigures), $R(t_i)$ is represented by green data points (upper subfigures), and $H(t_i)$ is shown as yellow data points (the three lower subfigures). The smoothed estimates $\hat{S}(t_i)$ of the original function are shown for three values of f (0.1, 0.25, and 0.5).

The goal in choosing f is to produce a fit that is as smooth as possible without unduly distorting the underlying pattern in the data; too high f -values result in *lack of fit*, too low f -values result in *surplus of fit* (Cleveland, 1973). For the low data rate in Figure D-4, proper smoothing is only accomplished for higher values of f , and only for the first part of the signal. The high data rate and low f in Figure D-5 b) yields better results for the last part of the signal, but the first part still suffers from surplus of fit.

An alternative approach

Smoothing is not an exact science. The quality of the results is determined by factors such as the effective sample rate during the experiment, the level of noise and the methods chosen to deal with outliers, and not least the experimenters subjective choice of various smoothing parameters (e.g. r , λ and f in this work). In addition, the family of smoothing procedures that relies on moving point (or time) windows of fixed width will inevitably be sensitive to variations in frequency of the underlying signal. Theoretically, some of the smoothing parameters could be made time dependent; however, this would require some *a priori* knowledge of the original signal.

What we consider ‘lack of fit’ or ‘surplus of fit’ will ultimately depend on our definition of ‘fluctuations’ and ‘mean velocity’, or to quote Bradshaw (1976):

“The conventional division into mean and fluctuating components exists for the convenience of technologists. It is not as arbitrary as is sometimes claimed, because it leads to self-consistent equations with useful physical interpretations, but it is artificial because the motion at a given point and time receives no information about mean values, which necessarily depend on averages over large distances or long times.”

An alternative approach to the smoothing procedures described in sections D.1.1 and D.1.2, is to view the system from the viewpoint of an observer positioned outside the closed explosion vessel; as soon as the net inflow is terminated (after 40-50 ms, typically), this observer will see only turbulence – no mean flow. Hence, as soon as all the outliers are removed, all the remaining measurements could be regarded as fluctuations. Thus, the decay of the root-mean square of the fluctuating velocity (u'_{rms}) can be determined without any rigorous procedures for finding/defining a mean velocity; \bar{u} is simply set to zero. This may seem as an oversimplification of the current problem, but at least it can be used as a limiting case.

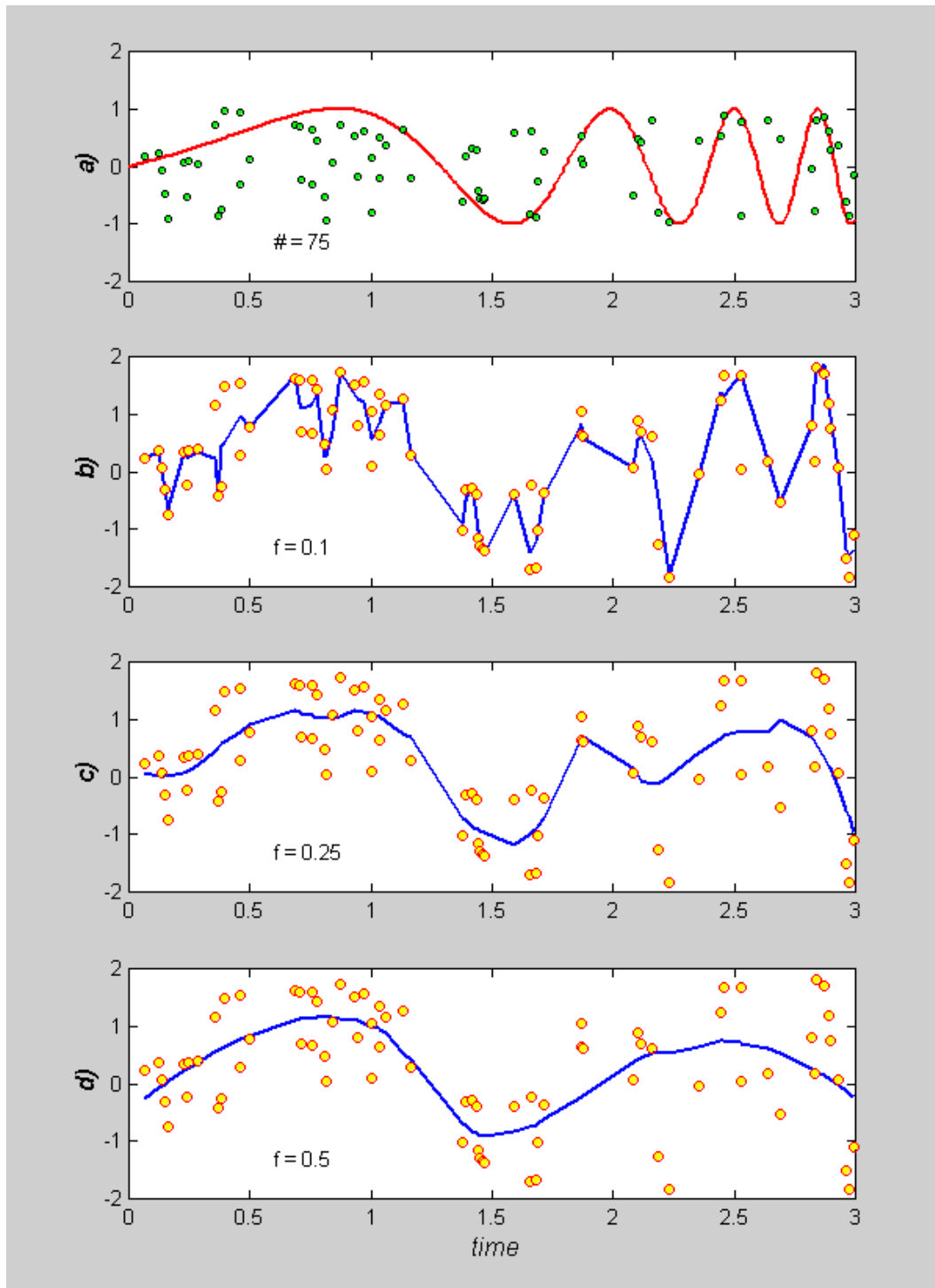


Figure D-4 Restoring a signal by means of loess; low sampling rate. Hypothetical data points, yellow points in b)-d), are created by adding random measurements/noise, green points in a), to a signal with varying frequency, red line in a). The total number of data points is 75, i.e. the sample frequency is 25 measurements per time unit.

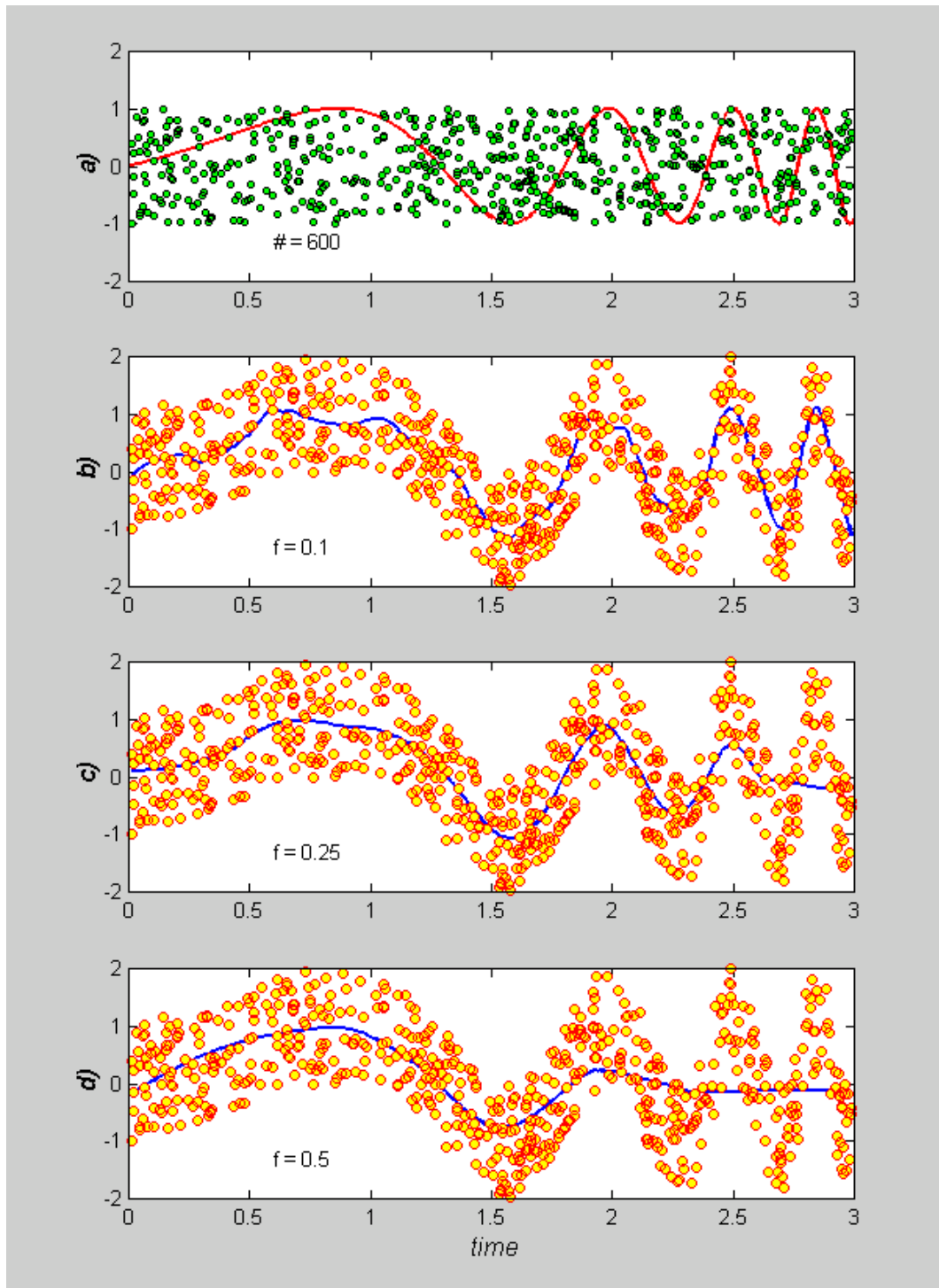


Figure D-5 Restoring a signal by means of loess; high sampling rate. Hypothetical data points, yellow points in b)-d), are created by adding random measurements/noise, green points in a), to a signal with varying frequency, red line in a). The total number of data points is 600, i.e. the sample frequency is 200 measurements per time unit.

D.2 Results and Discussion

The moving regression algorithm described in section D.1.1 was chosen as the main method of data analysis; other methods will be discussed with reference to this method.

D.2.1 Overall Results with Rebound Nozzle – No Dust

A summary of the main results when the average velocity is found by the moving regression algorithm used by Dahoe (2000) and Dahoe *et al.* (2001) is presented in Figure D-6. The red curve represents the average value of all the tests with the rebound nozzle and no dust (except seed particles); i.e. five tests for each of the two horizontal velocity components in all six positions (60 tests in total).

Comparison with results from Dahoe

The turbulence decay from 60 to 200 milliseconds is shown in Figure D-7, together with the results from Dahoe (2000). This interval is of special interest for several reasons:

- i)* The outlet valve is closed, i.e. there is no net flow into the 20-litre vessel.
- ii)* This is the most relevant time interval with respect to dust explosions. Explosions ignited prior to 60 milliseconds have a tendency to backfire into the reservoir; beyond 200 milliseconds, the dust concentration is dramatically reduced.
- iii)* The decay of the root-mean-square velocity can be described by equations like (D.3) in this interval; hence, it is possible to compare the results with those of others.

The curve fitted to the measured decay of the root-mean-square of the velocity in Figure D-7 can be described by the equation:

$$\frac{u'_{rms}}{1.93[m/s]} = \left(\frac{t}{60[ms]} \right)^{-1.70} \quad (D.5)$$

The results reported by Dahoe (2000) in a 20-litre spherical vessel are given by:

$$\frac{u'_{rms}}{3.75[m/s]} = \left(\frac{t}{60[ms]} \right)^{-1.61} \quad (D.6)$$

At 60 milliseconds, the value of the measured root-mean-square velocity in the cubical vessel is only about half of the value reported by Dahoe in a spherical vessel. The rate of decay is also higher in the cubical vessel. As the dispersion system is the same for both systems, the main reason for this discrepancy is probably due to the difference in shape between the two vessels. Increased wall friction due to the higher surface-to-volume ratio of the cubical vessel compared to a spherical vessel will result in decay that is more rapid.

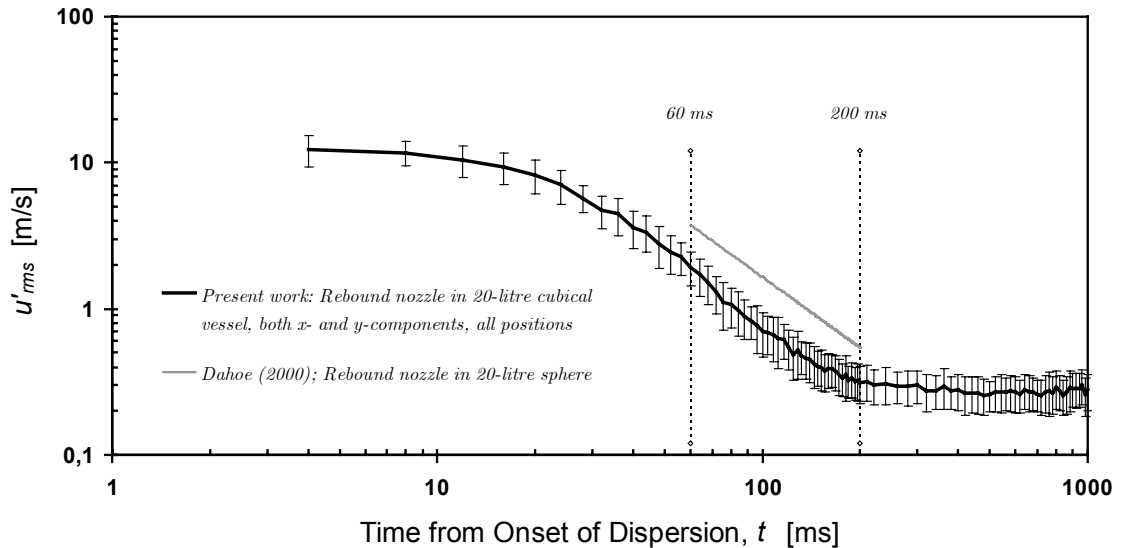


Figure D-6 Decay of the root-mean-square velocity in the 20-l cubical vessel; the series represents the average value of 60 tests in various positions (see table in Chapter 4), all with the rebound nozzle. Error bars indicate one standard deviation above and one standard deviation below the average value. Measurements by Dahoe (2000) are also indicated for $60\text{ms} < t < 200\text{ms}$.

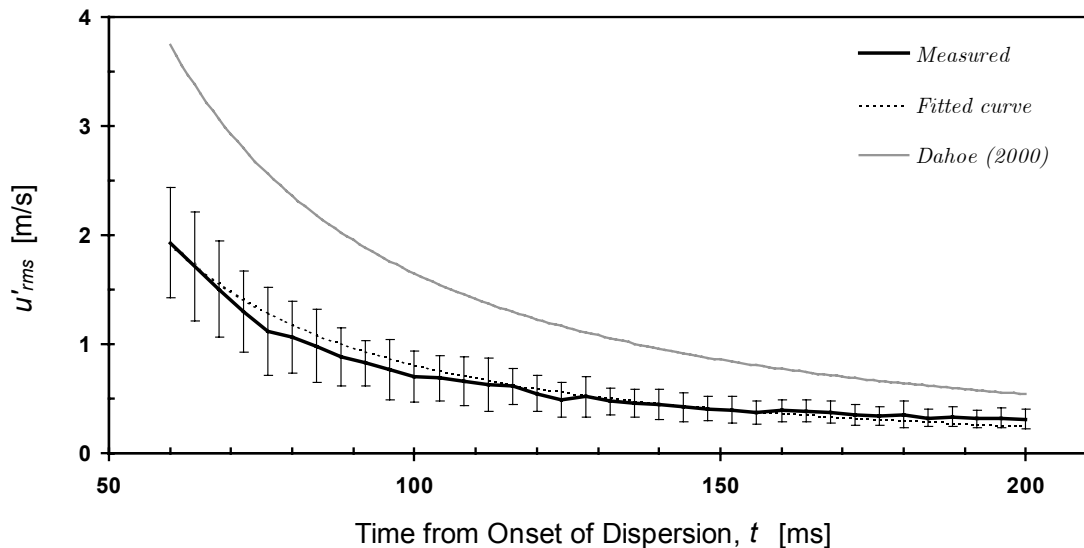


Figure D-7 Decay of the root-mean-square velocity in the time interval from 60 to 200 milliseconds, measured in the 20-l cubical vessel; compared to the results by Dahoe (2000) and Dahoe et al. (2001) measured in a 20-litre sphere. The rebound nozzle is used in all tests.

Effect of position and horizontal velocity component

The root-mean-square of the horizontal velocity fluctuations were measured in various positions (see Chapter 3). Apart from some minor discrepancies in the time interval between 10 and 50 milliseconds, no significant deviations from the overall results could be identified. Hence, the turbulent flow appears to be both spatially homogeneous and directionally isotropic during the time-period that is relevant with respect to dust explosion experiments. It should be noted that the vertical velocity component have not been measured. The number of tests in each point and for each component is also low compared with e.g. Dahoe *et al.* (2001).

Effect of smoothing procedure

Effects of smoothing by the loess algorithm for various sizes of the moving point window are shown in Figure D-8. The results are almost identical to those obtained by the method described by Dahoe (2000) and Dahoe *et al.* (2001), as one would expect since the basic smoothing procedure is the same. A lower value of r results in lower root-mean-square velocity, since a more narrow point window allows for a closer fit between the data-points and the smoothed curve.

The effect of skipping the entire smoothing procedure is illustrated in Figure D-9 for measurements in the point (0,0,0); five measurements of the x-component and five measurements of the y-component are shown. The *red* data-points have been analysed according to the usual smoothing procedure described by Dahoe (2000); no smoothing were done on the *blue* data-points. Although different smoothing procedures can produce a broad range of different results from the same set of measurements, the results produced without smoothing can probably be regarded as the upper limit for this range.

D.2.2 Tests with Other Dispersion Nozzles

The measured root-mean-square velocities measured at position (0,0,0) with various dispersion nozzles (described in Appendix B) are shown in Figure D-10; mean values of five tests from each of the horizontal velocity components are shown separately.

Results with the rebound nozzle follow the overall results from Figure D-6 closely, as would be expected. The results from the mushroom nozzle appears to be somewhat higher than average in the interval from 20 to 100 milliseconds, while the results from the pepper nozzle appears to be somewhat lower than average in the interval from 60 to 100 milliseconds. It seems reasonable that some minor discrepancies will occur since the nozzles are very different in shape. The uncertainties in the current data are high due to the low number of measurements. Dahoe (2000) and Dahoe *et al.* (2001) reported the following equations for the decay of the root-mean-square velocity for various nozzles in a 20-litre spherical vessel:

$$u'_{rms}(t) = \begin{cases} 3.75 [m/s] \left(\frac{t}{60 [ms]} \right)^{-1.61} & \text{for the Rebound nozzle} \\ 2.79 [m/s] \left(\frac{t}{60 [ms]} \right)^{-1.52} & \text{for the Dahoe nozzle} \\ 2.68 [m/s] \left(\frac{t}{60 [ms]} \right)^{-1.49} & \text{for the Perforated Dispersion Ring} \end{cases}$$

Hence, the type of nozzle can have significant effect on the turbulence level.

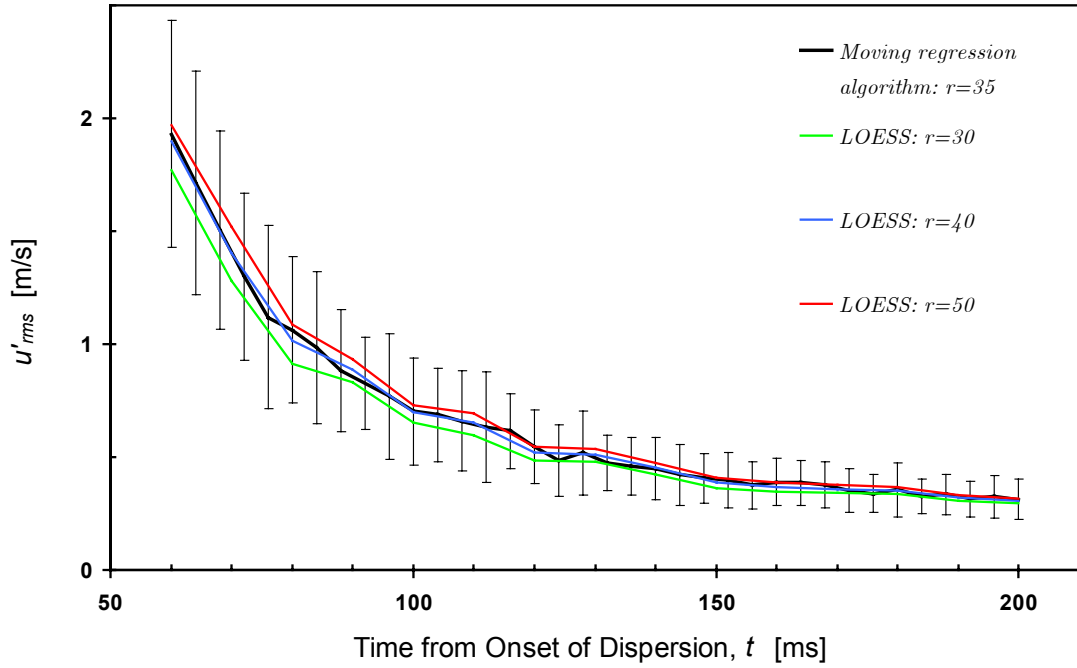


Figure D-8 Decay of the root-mean-square velocity in the time interval from 60 to 200 milliseconds, measured in the 20-l cubical vessel; comparison of smoothing procedures. The rebound nozzle is used in all tests.

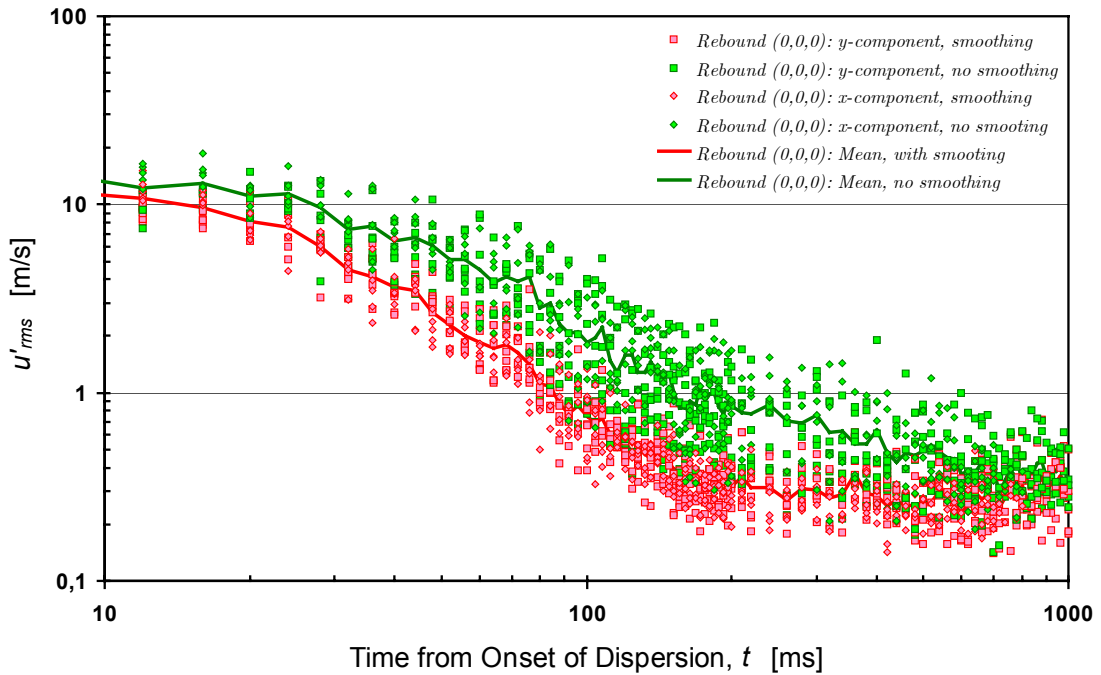


Figure D-9 Decay of the root-mean-square velocity measured at the position $(0,0,0)$ in the 20-l cubical vessel; comparison between results analysed by the smoothing procedure described by Dahoe (red), and results analysed without any smoothing (green). The rebound nozzle is used in all tests.

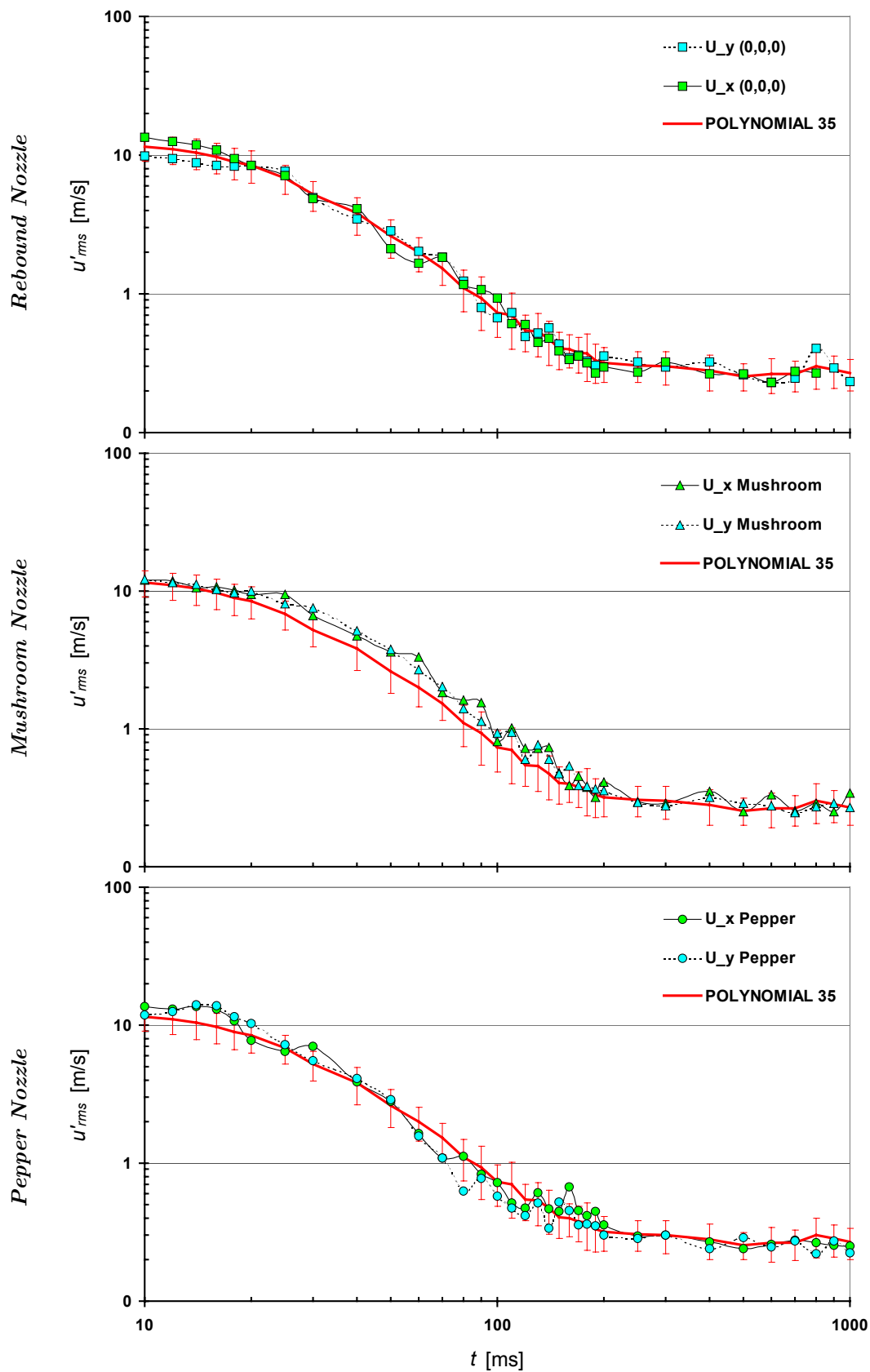


Figure D-10 Decay of the measured rms-velocities (both x-component and y-component) for various dispersion nozzles in the cubical vessel at position (0,0,0); compared to the overall results in Figure D-6 (called “POLYNOMIAL 35” in this figure). Note that there is a miss spelling on the vertical axis, “0” should be “0.1”.

D.2.3 Tests with Dust

Some LDA measurements were done with various amounts of *Lycopodium casuarinoides* spores added to the flow, see Table D-1.

The first test with dust (Test No. 104) proved to yield a very low data rate compared to the tests with only tracer particles; the number of outliers were however low, see Figure D-11, Figure D-12 and Figure D-13.

To increase the data rate, it was decided to change the criteria for Doppler burst detection. The *signal-to-noise ratio* (S/N) in the Intelligent Flow Analyzer (IFA 750) was changed from *medium* to *very low*, and the data rate increased considerably. However, when the data was analysed after finishing the experiments, most of the increased data rate turned out to be due to noise, see Figure D-14, Figure D-15 and Figure D-16. It was very difficult to isolate the noise in an unambiguous way. The effective data rate (after removing obvious outliers and noise) dropped dramatically, from $\sim 10^4$ measurements per second to $\sim 10^2$, making comparison between tests with and without dust highly questionable.

Although all the measurements with dust added to the flow turned out to be useless, it is possible that such measurements could have been done with improved experimental techniques. It was especially unfortunate that the laser beams passed through the centre part of the window in the cubical vessel. Experience has shown that dust particles often adhere to this part of the window, possibly because of a wake formed by opposing flows (see Appendix E).

Table D-1 LDA measurements performed with various amounts of *Lycopodium casuarinoides* spores at position $(0, 0, 90)$ in the 20-litre cubical vessel with rebound nozzle. The signal-to-noise ratio was set to “very low” for all tests, except test number 104 (“medium”).

Test No.	Velocity Component	Concentration, c_{nom} [g/m ³]	Initial Data Rate [kHz]
104	u_y	500	2.5
105		250	7.9
106		125	11.3
107		62.5	14.0
108		500	7.2
109	u_x	62.5	12.5
110		125	10.4
111		250	8.5
112		500	6.1

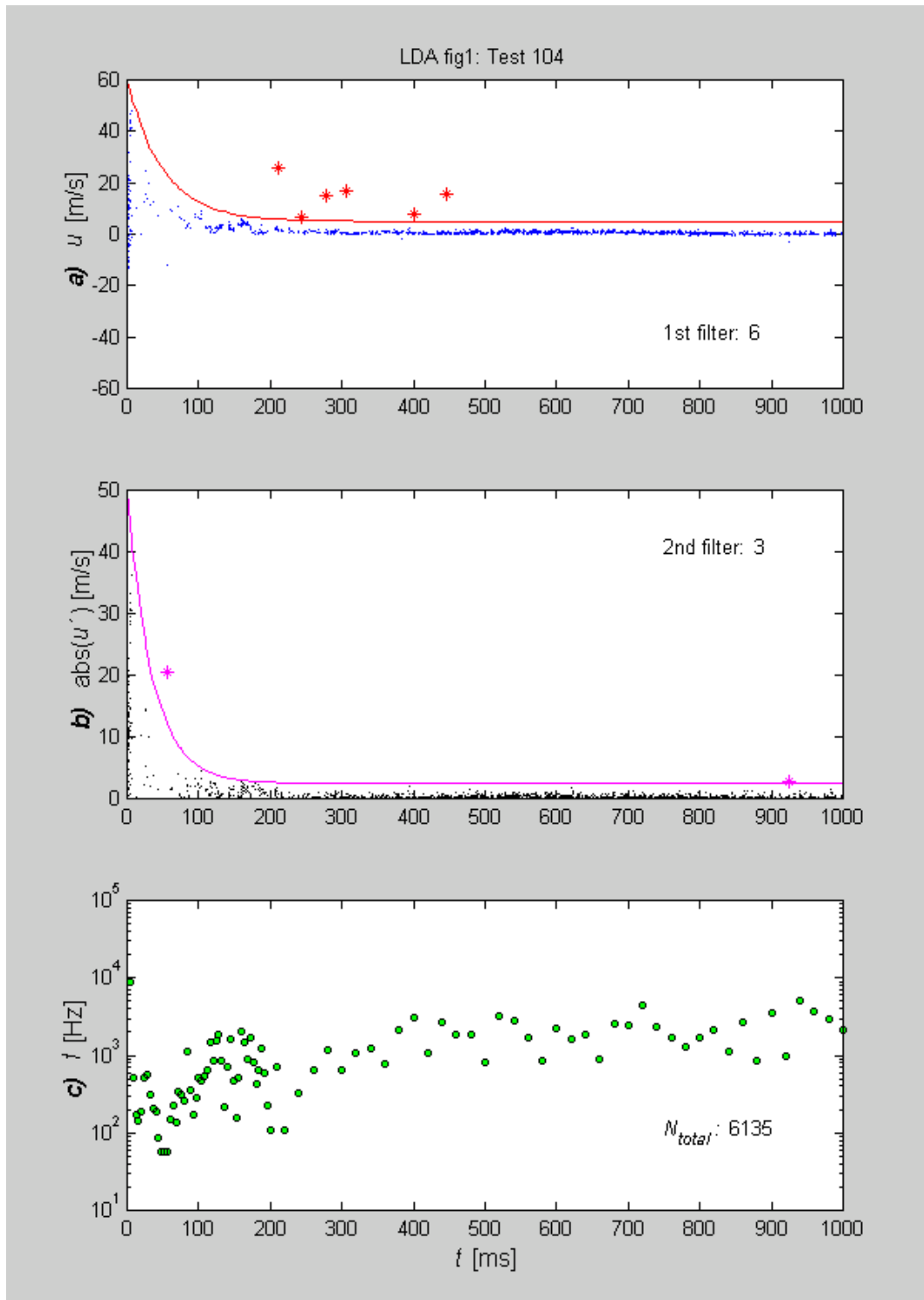


Figure D-11 Analysis of LDA data by the moving regression algorithm for a nominal dust concentration of 500 g/m^3 . The example is for Test No. 104: u_y -component, S/N is set to “medium”. a) First filter criterion: measurements of the instantaneous velocity (red stars) exceeding a certain value (red line) are discarded; the number of filtered points is given in the figure. b) Second filter criterion: absolute values of instantaneous velocity components (purple stars) that exceeds a certain value (purple line) are discarded. c) Sample frequency in selected 4 ms intervals, calculated from the data remaining after applying the two filters. N_{total} is the total number of remaining data points. Note that the spacing between the selected 4-millisecond intervals is shorter for $t < 200 \text{ ms}$ than for $t > 200 \text{ ms}$.

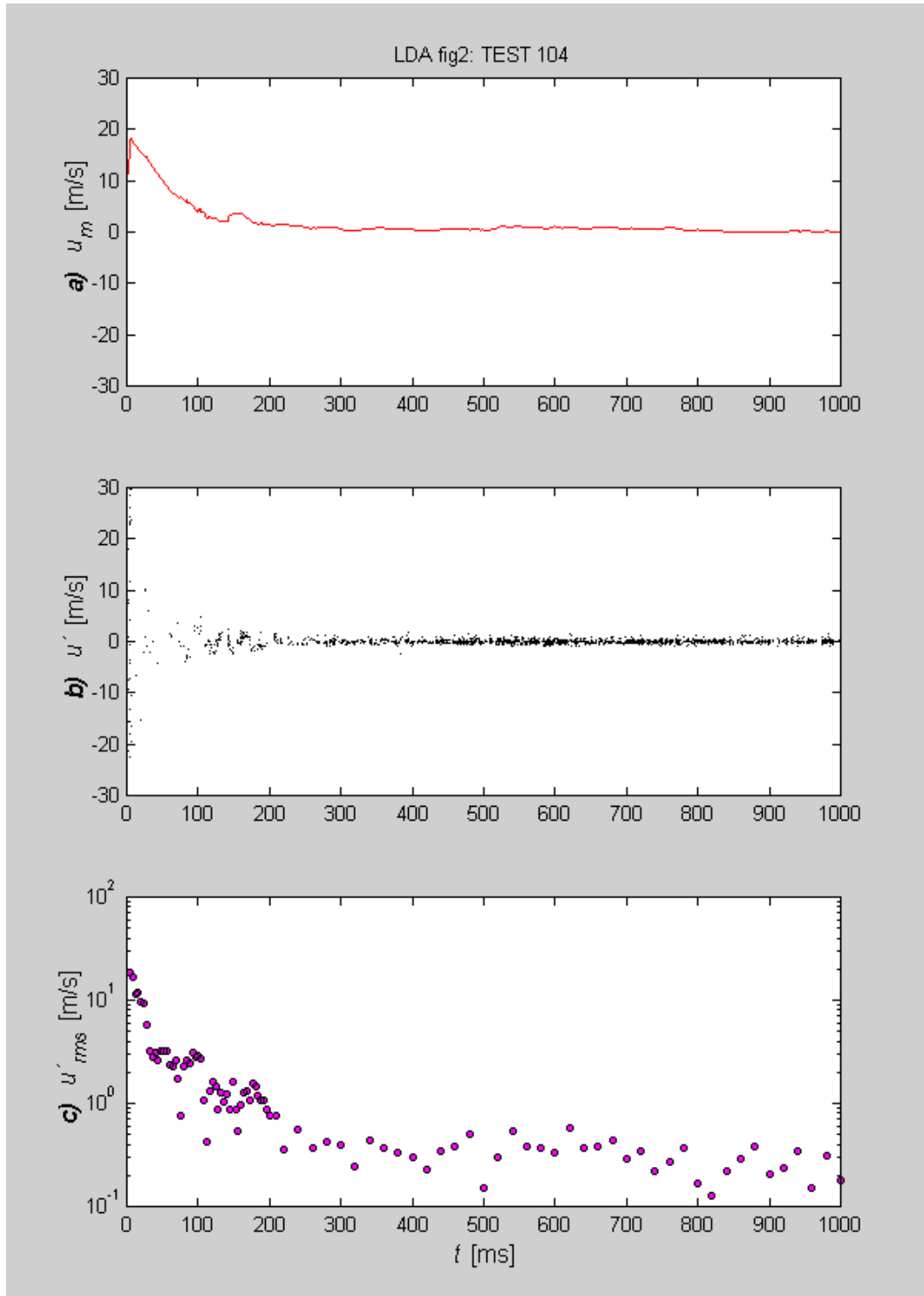


Figure D-12 Analysis of LDA data by moving regression algorithm, nominal dust concentration of 500 g/m^3 (continued from Figure D-11): a) Estimated value for mean velocity determined by the moving regression algorithm; b) Fluctuating velocity, defined by equation (D.1); c) Decay of the root-mean-square of fluctuating velocity, calculated from the data in b) over selected 4 ms intervals.

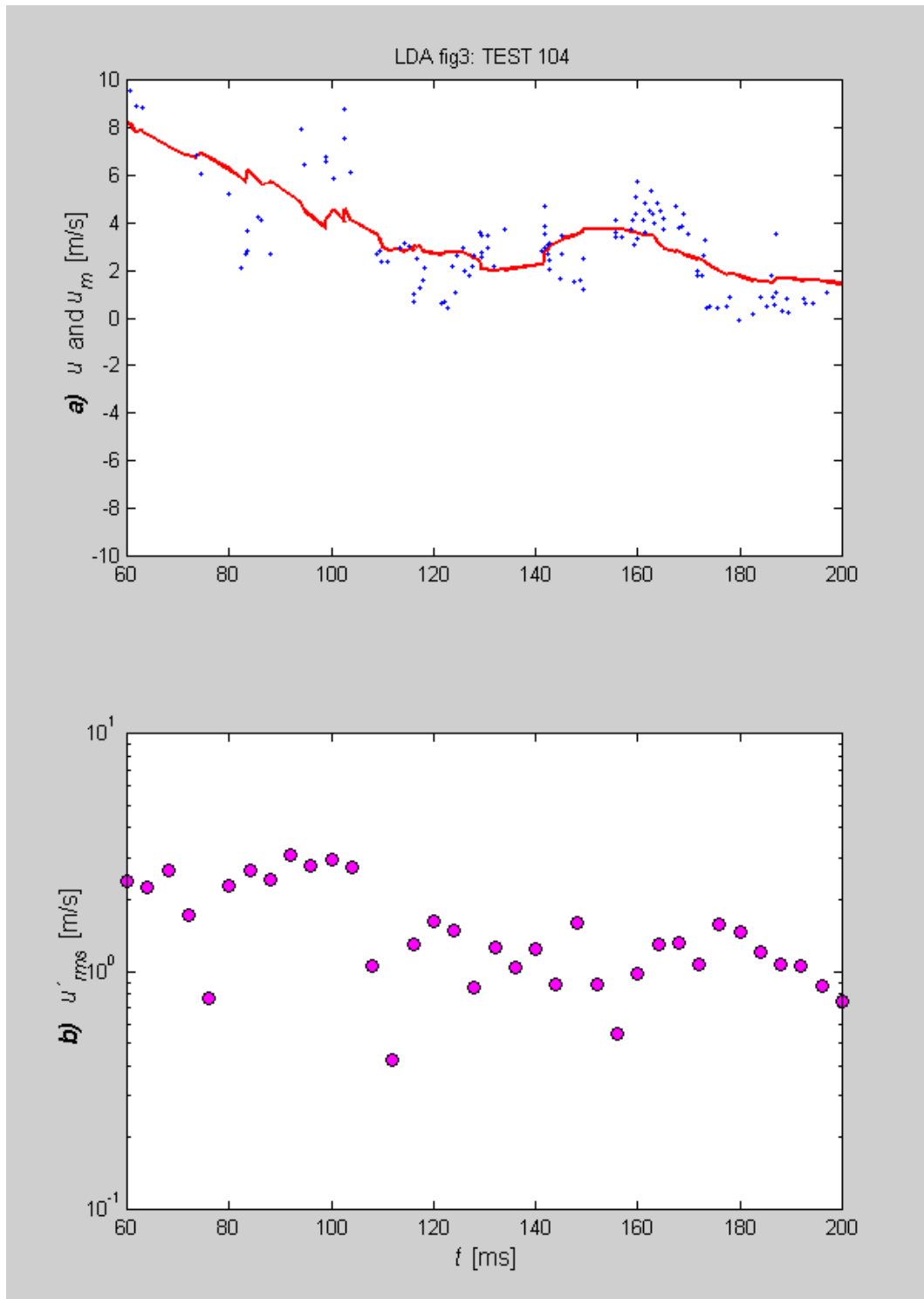


Figure D-13 The time interval from 60 to 200 milliseconds for the test shown in Figure D-11 and Figure D-12; a) mean and fluctuating part of the horizontal velocity component, b) decay of the root-mean-square of the fluctuating velocity.

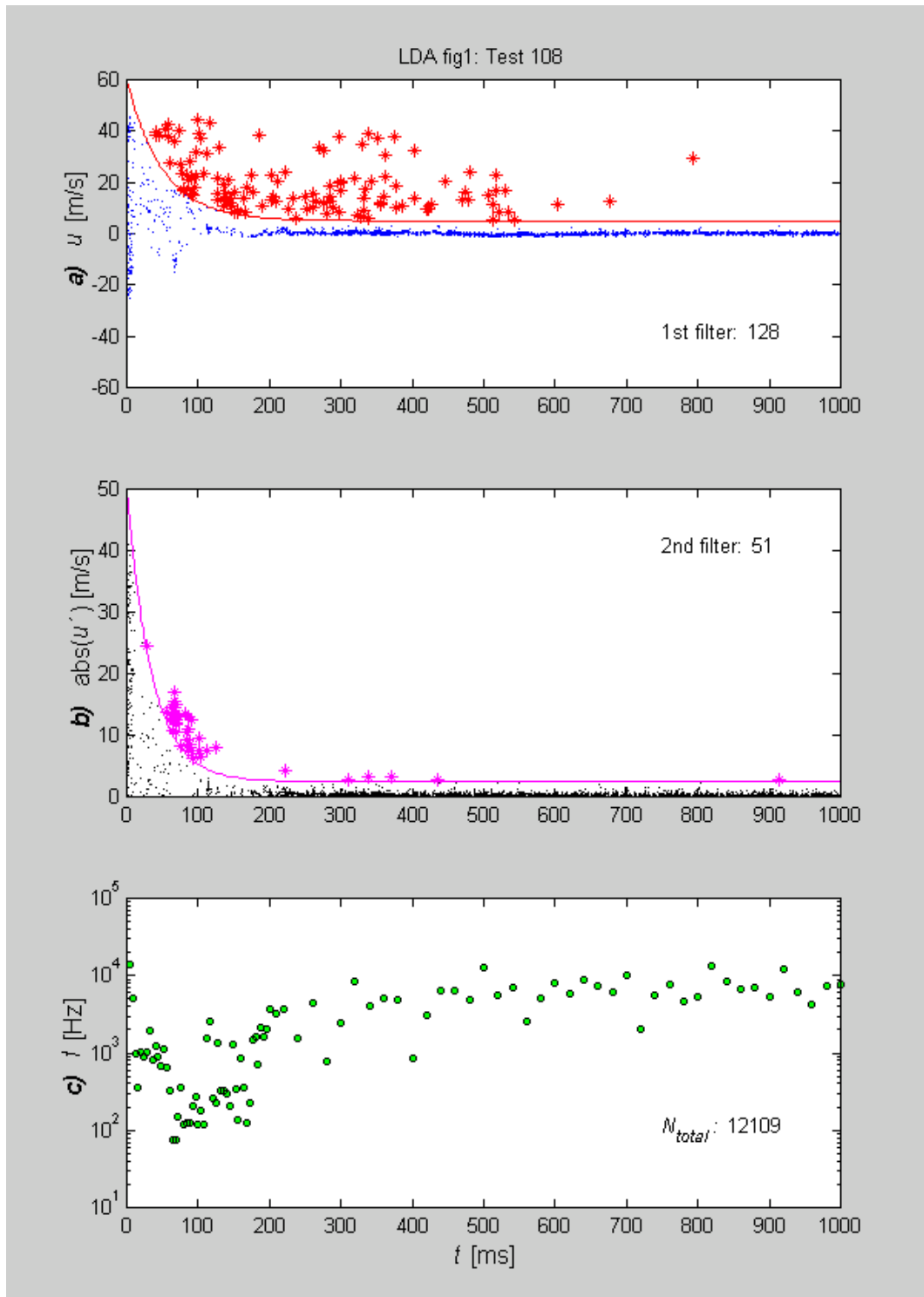


Figure D-14 Analysis of LDA data by the moving regression algorithm for a nominal dust concentration of 500 g/m^3 . The example is for Test No. 108: u_y -component, S/N is set to “very low”. a) First filter criterion: measurements of the instantaneous velocity (red stars) exceeding a certain value (red line) are discarded; the number of filtered points is given in the figure. b) Second filter criterion: absolute values of instantaneous velocity components (purple stars) that exceeds a certain value (purple line) are discarded. c) Sample frequency in selected 4 ms intervals, calculated from the data remaining after applying the two filters. N_{total} is the total number of remaining data points. Note that the spacing between the selected 4-millisecond intervals is shorter for $t < 200 \text{ ms}$ than for $t > 200 \text{ ms}$.

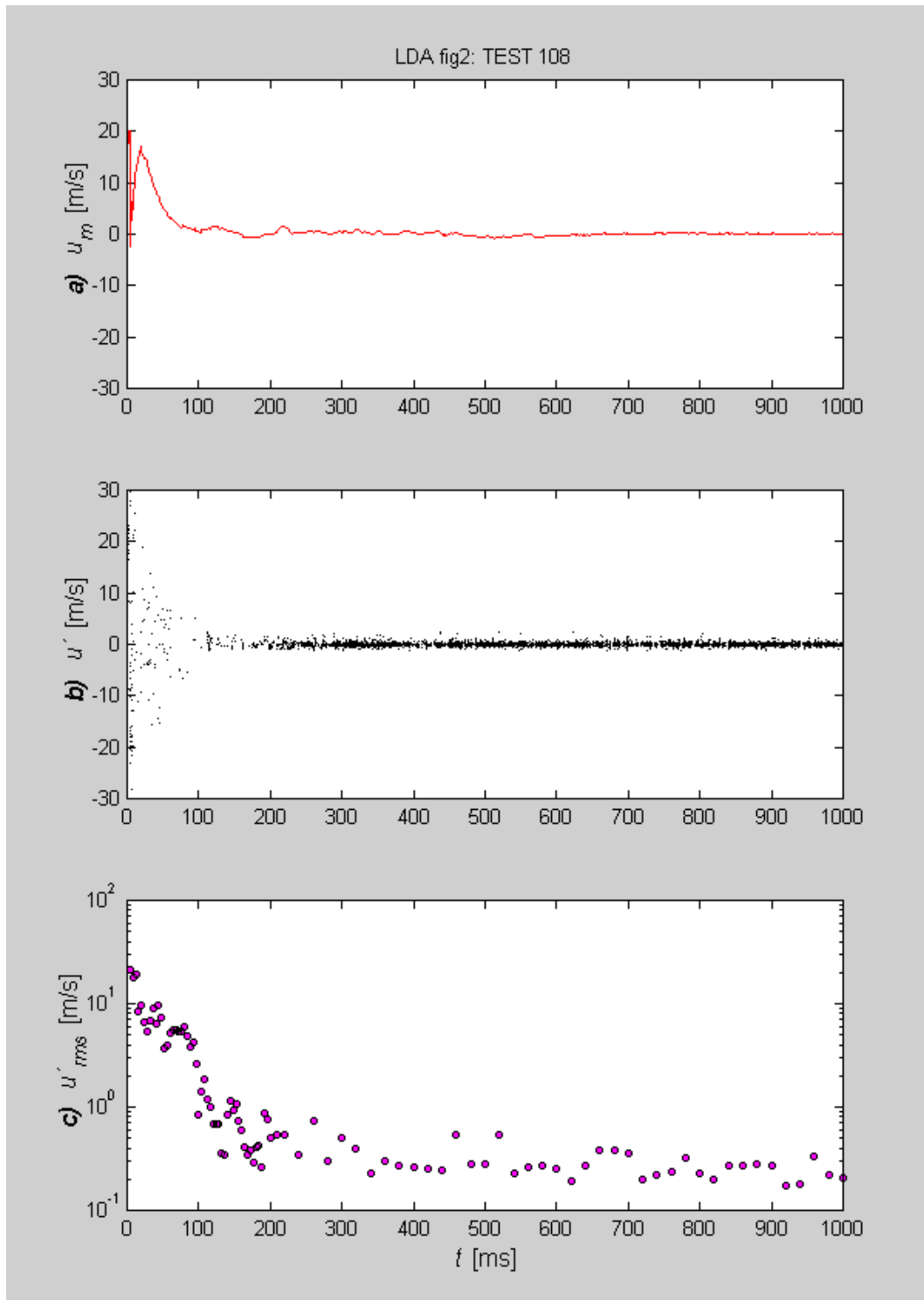


Figure D-15 Analysis of LDA data by moving regression algorithm, nominal dust concentration of 500 g/m^3 (continued from Figure D-14): a) Estimated value for mean velocity determined by the moving regression algorithm; b) Fluctuating velocity, defined by equation (D.1); c) Decay of the root-mean-square of fluctuating velocity, calculated from the data in b) over selected 4 ms intervals.

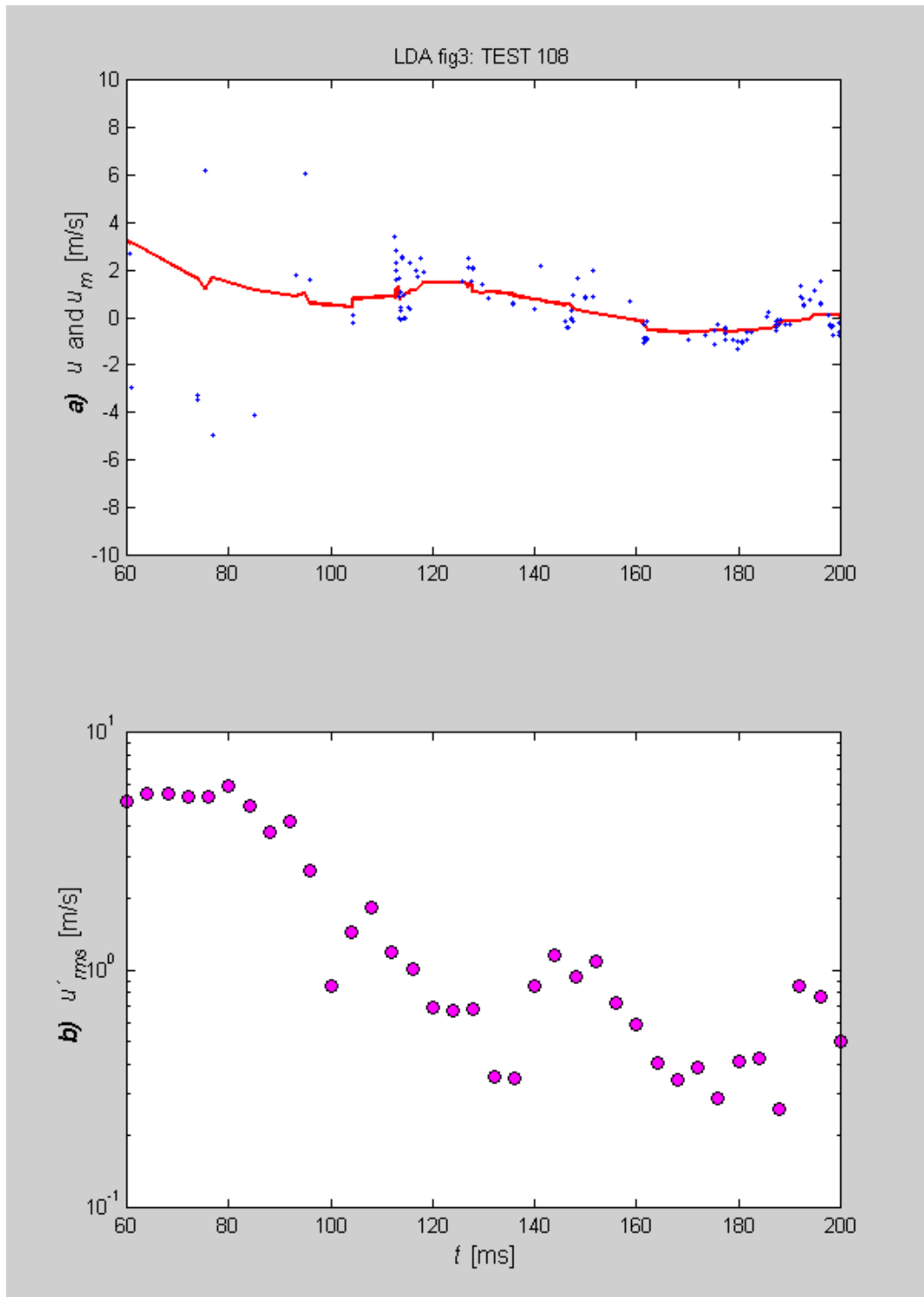


Figure D-16 The time interval from 60 to 200 milliseconds for the test shown in Figure D-14 and Figure D-15; a) mean and fluctuating part of the horizontal velocity component, b) decay of the root-mean-square of the fluctuating velocity.

D.3 Computer Programs

The data analysis was done on a personal computer running MATLAB 5.1.

D.3.1 THE MATLAB Program *ldafig.m*

The program *ldafig.m* takes LDA data as input, and performs data processing in several steps as described in section D.1.1. The program code is given below:

```
function ldafig(r);
% LDAFIG Processes transient LDA data from dispersion experiments.
%%%%%%%%%%%%%%%%%%%%%%%%%%%%%%%%%%%%%%%%%%%%%%%%%%%%%%%%%%%%%%%%%%%%%%%%
%%   LDAFIG(r) processes LDA data and presents the results graphically.   %%
%%   r   "smoothing range" (in each direction).                               %%
%%%%%%%%%%%%%%%%%%%%%%%%%%%%%%%%%%%%%%%%%%%%%%%%%%%%%%%%%%%%%%%%%%%%%%%%
%
%   The processing takes place in several steps:
%
%   STEP 0: Amenities (error messages, setting default values, ... ).
%
%   STEP 1: IMPORT; opens the file "inmatNN.txt", specifications:
%           a. Plain tabulator separated text file.
%           b. No headings.
%           c. Only integers.
%           d. Two columns.
%           e. Velocities [nm/s] in the 1st column.
%           f. Time difference [us] between measurements in the 2nd.
%           Time difference, time and velocity are placed in the following
%           column vectors respectively: DT1, MT1, and MV1.
%
%   STEP 2: Filtering of outliers, in two steps:
%           a. Criteria for maximum u.
%           b. Criteria for maximum abs(u').
%
%   STEP 3: Smoothing by fitting a floating least square 2nd degree
%           polynomial to the fluctuating velocity data.
%
%   STEP 4: Calculating the averaged root mean square (RMS) velocity
%           in selected 4 [ms] time intervals.
%
%   STEP 5: Plotting.
%
%   STEP 6: EXPORT.
%
%%%%%%%%%%%%%%%%%%%%%%%%%%%%%%%%%%%%%%%%%%%%%%%%%%%%%%%%%%%%%%%%%%%%%%%%
%
%           T. Skjold, 2003
%           Revised: 20.02.2003
%           No copyright whatsoever.
```

```

%%%%%%%%%%%%%%%%%%%%%%%%%%%%%%%%%%%%%%%%%%%%%%%%%%%%%%%%%%%%%%%%%%%%%%%%
%
%                               STEP 0: AMENITIES
%%%%%%%%%%%%%%%%%%%%%%%%%%%%%%%%%%%%%%%%%%%%%%%%%%%%%%%%%%%%%%%%%%%%%%%%
%
% Setting default value:
% "r" is by default 35, Dahoe (phd, 2000).
if nargin < 1, r=35; end;
%
% Error statements:
if ceil(r) ~= floor(r); error('Behold; r has to be an integer'); end
if r < 5; error('Behold; r has to be positive integers, at least 5'); end
%
%%%%%%%%%%%%%%%%%%%%%%%%%%%%%%%%%%%%%%%%%%%%%%%%%%%%%%%%%%%%%%%%%%%%%%%%
%                               STEP 1: IMPORT
%%%%%%%%%%%%%%%%%%%%%%%%%%%%%%%%%%%%%%%%%%%%%%%%%%%%%%%%%%%%%%%%%%%%%%%%
%
% Open the file 'inmatNN.txt':
filn1='inmat';filn3='.txt';
testn=input('Give file number:');
if testn < 17 | testn > 112; error('Lost, are we?'); end
testnr=num2str(testn);
fid=fopen(strcat(filn1,testnr,filn3),'rt');
M=fscanf(fid,'%f %f\n',[2 inf]);
fclose(fid);
%
% Placing the time [ms] in MT, and the velocity [m/s] in MV:
DT1=M(:,2)/1e3;
tde=1; % "estimated time delay [ms] due to triggering and opening of valve"
MT1=tde+cumsum(DT1);
MV1=M(:,1)/1e9;
[Mm1 Mn1]=size(M);
tmax=MT1(Mm1);
%
%%%%%%%%%%%%%%%%%%%%%%%%%%%%%%%%%%%%%%%%%%%%%%%%%%%%%%%%%%%%%%%%%%%%%%%%
%                               STEP 2: FILTERING
%%%%%%%%%%%%%%%%%%%%%%%%%%%%%%%%%%%%%%%%%%%%%%%%%%%%%%%%%%%%%%%%%%%%%%%%
%
%                               1st FILTER:
% Setting parameters controlling the 1st filter criterion:
u_01=60;
t_01=50;
u_inf1=5;
ALU=zeros(Mm1,1); % "velocity criterion"
for i=1:Mm1;
    ALU(i)=(u_01-u_inf1)*exp(-MT1(i)/t_01)+u_inf1;
end;
% ALU as function of MT1 <<-----PLOT_1.a
% Making matrix FILM1 for 1st sorting:
FILM1=[MT1,DT1,MV1];
%
nfilt1=0;
for i=1:Mm1;
    if FILM1(i,3)>ALU(i);
        FILM1(i,1)=FILM1(i,1)+tmax;
        nfilt1=nfilt1+1;
    end;
end;

```

```

end
end;
nfilt1
FILM1=sortrows(FILM1,1);
% Making matrix FILD1 for first filtered points:
FILD1=FILM1(Mm1-nfilt1+1:Mm1,:);
% Filtered (1) time and velocity:
TF1=FILD1(:,1)-tmax;
VF1=FILD1(:,3);
% VF1 as function of TF1 <<-----PLOT_1.a
% Making matrix FILM2 for second sorting:
FILM2=FILM1(1:Mm1-nfilt1,:);
[Mm2 Mn2]=size(FILM2);
MT2=FILM2(:,1);
MV2=FILM2(:,3);
% MV2 as function of MT2 <<-----PLOT_1.a
%
%           2nd FILTER:
dw=10; % "degree of winsorization"
% Calculating preliminary mean velocity:
MVM=zeros(Mm2,1); % "winsorized average"
SV=zeros(2*r+1); % "sample"
SSV=zeros(2*r+1); % "sorted sample"
TSS=zeros(2*r-2*dw+1); % "trimmed sorted sample"
for i=r+1:Mm2-r-1;
    SV=MV2(i-r:i+r);
    SSV=sort(SV);
    TSS=SSV(dw+1:2*r-dw+1);
    MVM(i)=mean(TSS);
end;
FLV=MV2-MVM; % "preliminary fluctuating velocity"
ABV=abs(FLV); % "absolute value of fluctuating velocity"
%
% Setting parameters controlling the 2nd filter criterion:
u_02=50;
t_02=35;
u_inf2=2.5;
ABC=zeros(Mm2,1); % "absolute value criterion"
for i=1:Mm2;
    ABC(i)=(u_02-u_inf2)*exp(-MT2(i)/t_02)+u_inf2;
end;
% ABC as a function of MT2 <<-----PLOT_1.b
% Changing matrix FILM2 before 2nd sorting:
FILM2(:,2)=ABV;
nfilt2=0;
for i=1:Mm2;
    if FILM2(i,2)>ABC(i);
        FILM2(i,1)=FILM2(i,1)+tmax;
        nfilt2=nfilt2+1;
    end
end;
nfilt2
Ntot=Mm1-(nfilt1+nfilt2)
FILM2=sortrows(FILM2,1);
% Making matrix FILD2 for 2nd filtered points:

```

```

FILDD2=FILT2(Mm2-nfilt2+1:Mm2,:);
% Filtered (2) time, velocity and absolute velocity fluctuation:
TF2=FILDD2(:,1)-tmax;
VF2=FILDD2(:,3);
ABF2=FILDD2(:,2);
% ABF2 as function of TF2 <<-----PLOT_1.b
% Making matrix FILM - Output of filtering process:
FILM=FILT2(1:Mm2-nfilt2,:);
[Mm Mn]=size(FILM);
AB=FILM(:,2);
% AB as a function of MT <<-----PLOT_1.b
%
%%%%%%%%%%%%%%%%%%%%%%%%%%%%%%%%%%%%%%%%%%%%%%%%%%%%%%%%%%%%%%%%%%%%%%%%%%
%                               STEP 3: SMOOTHING
%%%%%%%%%%%%%%%%%%%%%%%%%%%%%%%%%%%%%%%%%%%%%%%%%%%%%%%%%%%%%%%%%%%%%%%%%%
%
% Fixing a 2nd order polynomial for smoothing:
dp=2;
%
% Filtered time and velocity:
MT=FILM(:,1);
MW=FILM(:,3);
%
% Empty vectors for velocity (POW), polynomial (POL), and time (POT):
LP=Mm-2*r;
POW=zeros(LP,1);
POL=zeros(LP,1);
POT=zeros(LP,1);
% Empty vectors for least square polynomial fit
PT=zeros(2*r+1);
PW=zeros(2*r+1);
% Least square polynomial fitting.
for i=r+1:Mm-r;
    time=MT(i);
    PT=MT(i-r:i+r);
    PW=MW(i-r:i+r);
    p=polyfit(PT',PW',dp);
    U=polyval(p,time);
    POL(i-r)=U;
    POT(i-r)=MT(i); % "time with "POL"-index"
    POW(i-r)=MW(i); % "velocity with "POL"-index"
end
[Pm Pn]=size(POL);
% POL as function of POT <<-----PLOT_2.a
%
%%%%%%%%%%%%%%%%%%%%%%%%%%%%%%%%%%%%%%%%%%%%%%%%%%%%%%%%%%%%%%%%%%%%%%%%%%
%                               STEP 4: CALCULATION
%%%%%%%%%%%%%%%%%%%%%%%%%%%%%%%%%%%%%%%%%%%%%%%%%%%%%%%%%%%%%%%%%%%%%%%%%%
%
% Selecting "test points":
% First 4[ms] interval:
if POT(1)<4;
    mint=4;
    ndel=0;

```

```

elseif POT(1)<8;
    mint=8;
    ndel=1;
elseif POT(1)<12;
    mint=12;
    ndel=2;
elseif POT(1)<16;
    mint=16;
    ndel=3;
elseif POT(1)<20;
    mint=20;
    ndel=4;
elseif POT(1)>24;
    mint=24;
    ndel=5;
end;
ndel
% Last 4[ms] interval:
maxt=min(100*floor(((POT(LP))-2)/100),1000);
maxt
% Choosing the centres of the 4[ms] intervals:
TMP=[mint:4:200 210 220:20:maxt]';
TLP=TMP-2;THP=TMP+2;
[TPm TPn]=size(TMP);
%
% Empty vectors for indexes
ILT=zeros(TPm,1);      %Index low
IHT=zeros(TPm,1);      %Index high
LT=zeros(TPm,1);       %Time low
HT=zeros(TPm,1);       %Time high
% Finding the index ILT(j) of the velocity
% corresponding to the time TLP(j):
for j=1:TPm;
    i=1;
    ILT(j)=i;
    while POT(ILT(j))<TLP(j)&POT(ILT(j)+1)<TLP(j);
        ILT(j)=ILT(j)+1;
    end
    LT(j)=POT(ILT(j));
end;
% Finding the index IHT(j) of the velocity
% corresponding to the time THP(j):
for j=1:TPm;i=1;IHT(j)=i;
    while POT(IHT(j))<THP(j)&POT(IHT(j)+1)<THP(j);
        IHT(j)=IHT(j)+1;
    end
    IHT(j)=IHT(j)+1;
    HT(j)=POT(IHT(j));
end;
% Frequency in the 4 [ms] intervals:
FREQ=1000*(IHT-ILT)./(HT-LT);
% FREQ as function of TMP <<-----PLOT_1.c
% Finding the fluctuating part of the velocity:
FLUC=POW-POL;

```

```

% FLUC as function of POT <<-----PLOT_2.b
it60=1;it200=1;
while POT(it60)<60&POT(it60+1)<60;it60=it60+1;end;it60;
while POT(it200)<200&POT(it200+1)<200;it200=it200+1;end;it200;
HPOW=POW(it60:it200); % <<-----PLOT_3.b
% Smoothing the residuals:
FT=zeros(2*r+1);FW=zeros(2*r+1);
FLUCW=zeros(Mm,1);
FLUCW(1:r)=MW(1:r);
FLUCW(r+1:Mm-r)=FLUC;
FLUCW(Mm-r+1:Mm)=MW(Mm-r+1:Mm);
for i=r+1:Mm-r;
    time=MT(i);
    FT=MT(i-r:i+r);
    FW=FLUCW(i-r:i+r);
    p=polyfit(FT',FW',1);
    FU=polyval(p,time);
    SMUC(i-r)=FU;
end;
% Calculating the square of the fluctuations.
SFLUC=(FLUC.^2);
% Calculating the mean of the squared fluctuations in the 4[ms] intervals.
MSFLUC=zeros(TPm,1);
for j=1:TPm;
    MSFLUC(j)=mean(SFLUC(ILT(j):IHT(j)));
end
% Calculating the square root of the mean of the squared fluctuations
% in each of the 4[ms] intervals.
RMSFLUC=sqrt(MSFLUC);
% RMSFLUC as function of TMP <<-----PLOT_2.c
%
%%%%%%%%%%%%%%%%%%%%%%%%%%%%%%%%%%%%%%%%%%%%%%%%%%%%%%%%%%%%%%%%%%%%%%%%
%
%                               STEP 5: PLOTTING
%
%%%%%%%%%%%%%%%%%%%%%%%%%%%%%%%%%%%%%%%%%%%%%%%%%%%%%%%%%%%%%%%%%%%%%%%%
%
%                               Figure 1
%
%                               FILTRATION OF OUTLIERS AND SAMPLE FREQUENCY
%
%                               0-1000 [ms]
h=1;
figure(h);
set(h,'PaperUnits','centimeters');
set(h,'PaperType','A4');
set(h,'PaperPosition',[3.5 2.5 15 24]);
set(h,'Position',[10 10 600 900]);
zoom on;
%
% 1.a: Instantaneous part of velocity and 1st filtering
subplot(3,1,1);
plot(MT2,MV2,'.b','MarkerSize',5); % Passed 1st filter
t11=testnr;
title(['LDA fig1: Test ',num2str(t11)])
tal='1st filter:_{ }';
ta2=num2str(nfilt1);
tal2=strcat(tal,ta2);
text(750,-40,tal2);

```

```

axis([0 1000 -60 60]);
% y-label;
ylabel('\fontsize{12} \it\bf a}_{ } \rm \itu_{ } \rm[m/s]');
hold on;
plot(TF1,VF1,'*r','MarkerSize',6); % 1st filtered points
plot(MT1,ALU,'-r'); % 1st filter criteria
hold off;
%
% 1.b: Absolute value of fluctuating part of velocity and 2nd filtering
subplot(3,1,2);
plot(MT,AB,'.k','MarkerSize',5); % Passed 2nd filter
tb1='2nd filter:_{ }';
tb2=num2str(nfilt2);
tb12=strcat(tb1,tb2);
text(750,40,tb12);
axis([0 1000 0 50]);
% y-label;
ylabel('\fontsize{12} \it\bf b}_{ } \rm abs(\itu'_{ } \rm) [m/s]');
hold on;
plot(TF2,ABF2,'*m','MarkerSize',6); % 2nd filtered points
plot(MT2,ABC,'-m'); % 2nd filter criteria
hold off;
%
% 1.c: Sample frequency in 4 ms intervals
subplot(3,1,3);
semilogy(TMP,FREQ,'ok','MarkerSize',4,'MarkerFaceColor','g');
tc1='\itN_{total }:_{ } \rm';
tc2=num2str(Ntot);
tc12=strcat(tc1,tc2);
text(750,100,tc12);
axis([0 1000 10 100000]);
% x- & y-label:
xlabel('\fontsize{12} \itt_{ } \rm[ms]');
ylabel('\fontsize{12} \it\bf c}_{ } \rm \itf_{ } \rm[Hz]');
%%%%%%%%%%%%%%%%%%%%%%%%%%%%%%%%%%%%%%%%%%%%%%%%%%%%%%%%%%%%%%%%%%%%%%%%
%
% Figure 2
% Mean, fluctuating and RMS velocity
% 0-1000 [ms]
h=2;
figure(h);
set(h,'PaperUnits','centimeters');
set(h,'PaperType','A4');
set(h,'PaperPosition',[3.5 2.5 15 24]);
set(h,'Position',[310 10 600 900]);
zoom on;
%
% 2.a: Mean part of velocity
subplot(3,1,1);
tb1='Test: ';
tb2=num2str(testnr);
tb12=strcat(tb1,tb2);
text(750,-20,tb12);
plot(POT,POL,'-r') % Mean velocity
t21=testnr;

```

```

title(['LDA fig2: TEST ',num2str(t21)])
axis([0 1000 -30 30]);
% y-label:
ylabel('\fontsize{12} \it\bf a)_{} \rm \itu_{m} \rm[m/s]');
%
% 2.b: Fluctuating part of velocity
subplot(3,1,2);
plot(POT,FLUC,'.k','MarkerSize',5); %           Fluctuating velocity
axis([0 1000 -30 30]);
% y-label:
ylabel('\fontsize{12} \it\bf b)_{} \rm \itu'_{ } \rm[m/s]');
%
% 2.c: RMS of fluctuating part of velocity
subplot(3,1,3);
semilogy(TMP,RMSFLUC,'ok','MarkerSize',4,'MarkerFaceColor','m'); %           RMS
axis([0 1000 0.1 100]);
% x- & y-label:
xlabel('\fontsize{12} \itt_{ } \rm[ms]');
ylabel('\fontsize{12} \it\bf c)_{} \rm \itu'_{rms} \rm[m/s]');
%
%%%%%%%%%%%%%%%%%%%%%%%%%%%%%%%%%%%%%%%%%%%%%%%%%%%%%%%%%%%%%%%%%%%%%%%%
%                               Figure 3
%                               Mean, fluctuating and RMS velocity
%                               60-200 [ms]
h=3;
figure(h);
set(h,'PaperUnits','centimeters');
set(h,'PaperType','A4');
set(h,'PaperPosition',[3.5 2.5 15 24]);
set(h,'Position',[610 10 600 900]);
zoom on;
%
% 3.a: Instantaneous and mean part of velocity
subplot(2,1,1);
tc1='Test: ';
tc2=num2str(testnr);
tc12=strcat(tc1,tc2);
text(750,-20,tc12);
plot(POT,POL,'-r','LineWidth',2) %           Mean velocity
t31=testnr;
title(['LDA fig3: TEST ',num2str(t31)])
axis([60 200 -10 10]);
% y-label:
ylabel('\fontsize{12} \it\bf a)_{} \rm \itu_{ } \rmand \itu_{m} \rm[m/s]');
hold on;
plot(MT,MW,'.b','MarkerSize',6); %           Instantaneous velocity
hold off;
%
% 3.b: RMS of fluctuating part of velocity
subplot(2,1,2);
semilogy(TMP,RMSFLUC,'ok','MarkerSize',6,'MarkerFaceColor','m'); %           RMS
axis([60 200 0.1 10]);
% x- & y-label:
xlabel('\fontsize{12} \itt_{ } \rm[ms]');

```

```

ylabel('\fontsize{12} \it\bf b)_ { } \rm \itu'_{rms } \rm[m/s]');
%
%%%%%%%%%%%%%%%%%%%%%%%%%%%%%%%%%%%%%%%%%%%%%%%%%%%%%%%%%%%%%%%%%%%%%%%%
%
STEP 6: EXPORT
%%%%%%%%%%%%%%%%%%%%%%%%%%%%%%%%%%%%%%%%%%%%%%%%%%%%%%%%%%%%%%%%%%%%%%%%
TOP=[4:4:200 210 220:20:1000]';
[Tm Tn]=size(TOP);
RMSOUT=zeros(Tm,2);
RMSOUT(:,1)=TOP;
for i=1:TPm
    RMSOUT(i+ndel,2)=RMSFLUC(i);
end;
RMSOUT % Time [ms] in 1st column, RMS velocity [m/s] in 4 ms interval in 2nd
%%%%%%%%%%%%%%%%%%%%%%%%%%%%%%%%%%%%%%%%%%%%%%%%%%%%%%%%%%%%%%%%%%%%%%%%
%%%
The end
%%%%%%%%%%%%%%%%%%%%%%%%%%%%%%%%%%%%%%%%%%%%%%%%%%%%%%%%%%%%%%%%%%%%%%%%

```

D.3.2 Other Computer Programs

Some simple MATLAB scripts running variations of the *ldafig.m* program were used to run the analysis automatically. The *loess* calculations were done by incorporating a few *m-files* from the *Data Visualization Toolbox* provided by www.datatool.com into the *ldafig.m* program.

References

- Ancimer, R., Wallace, J. & Jääskeläinen, H. (1999). *Investigation Into the Effect of LDV Seed Particles on the Operating Characteristics of a Spark Ignition Engine*. *Experiments in Fluids*, **27**, pp. 175-180.
- Batchelor, G.K. & Townsend, A.A. (1947). *Decay of Vorticity in the Isotropic Turbulence*. *Proceedings of the Royal Society of London, Series A: Mathematical and Physical Sciences*, **190**, pp. 534-550.
- Batchelor, G.K. & Townsend, A.A. (1948a). *Decay of Isotropic Turbulence in the Initial Period*. *Proceedings of the Royal Society of London, Series A: Mathematical and Physical Sciences*, **193**, pp. 539-558.
- Batchelor, G.K. & Townsend, A.A. (1948b). *Decay of Isotropic Turbulence in the Final Period*. *Proceedings of the Royal Society of London, Series A: Mathematical and Physical Sciences*, **194**, pp. 527-543.
- Bevington, P.R. (1969). *Data Reduction and Error Analysis for the Physical Sciences*. McGraw Hill Book Company, New York.
- Bradshaw, P. Ed. (1976). *Turbulence*. ISBN 0-387-07705-7. Springer Verlag, New York.
- Cleveland, W.S. (1979). *Robust Locally Weighted Regression and Smoothing Scatterplots*. *Journal of the American Statistical Association*, **74** (368), pp. 829-836.
- Cleveland, W.S. (1993). *Visualizing Data*. ISBN 0-9634884-0-6. Hobart Press, New Jersey.
- Cleveland, W.S., & Devlin, S.J. (1988). *Locally Weighted Regression: An Approach to Regression Analysis by Local Fitting*. *Journal of the American Statistical Association*, **83** (403), pp. 596-610.
- Dahoe, A.E. (2000). *Dust explosions: A Study of Flame Propagation*. ISBN 90-90-13707-8. PhD Thesis, Technische Universiteit Delft. Delft University Press, Delft.
- Dahoe, A.E., Cant, R.S. & Scarlett, B. (2001). *On the Decay of Turbulence in the 20-Litre Explosion Sphere*. *Flow, Turbulence and Combustion*, **67**, pp. 159-184.
- Guest, P.G. (1961). *Numerical Methods of Curve Fitting*. Cambridge University Press, Cambridge.

- Jacoby, W.G. (2000). *Loess: A Nonparametric, Graphical Tool for Depicting Relationships Between Variables*. Electoral Studies, **19**, pp. 577-613.
- Mercer, D.B., Amyotte, P.R., Dupuis, D.J., Pegg, M.J., Dahoe, A., de Heij, W.B.C., Zavenbergen, J.F., & Scarlett, B. (2001). *The Influence of Injector Design on the Decay of Pre-Ignition Turbulence in a Spherical Explosion Chamber*. Journal of Loss Prevention in the Process Industries, **14**, pp. 269-282.
- Winer, B.J. (1971). *Statistical Principles in Experimental Design*. 2nd Edition. McGraw Hill Book Company, New York.

APPENDIX E

CFD Simulations

CFD-codes for gas explosions are currently used by the Norwegian petroleum industry as an integrated part in qualitative risk analysis (QRA); procedures for such calculations can be found in e.g. NORSOK Standard Z-013 (2001). Similar codes developed for dust explosions could prove to be valuable tools when mitigating measures are implemented in industrial plants where dust explosions represent a hazard. Such codes should be able to describe the development of dust explosions in complex geometries (e.g. pressure piling in interconnected vessels, effect of turbulence generating objects on flame propagation, etc.); hence, in time they could become a realistic alternative to full-scale experiments – or lack of knowledge.

This appendix illustrates how a commercially available CFD-code can be used to describe certain aspects of the transient dispersion process and subsequent explosion in the 20-litre cubical explosion vessels described in Appendix B. Although only gas explosions could be simulated with the currently available code, similar simulations could prove useful in future evaluation of dust explosion codes.

E.1 The CFD-Code FLACS

The CFD-code used in this work is called FLACS (FLame ACceleration Simulator); FLACS is commercially available from GexCon AS, Fantoft, Norway. The code can be used for modelling ventilation, gas dispersion and vapour cloud explosions in complex geometries. A dust explosion simulator based on FLACS technology is currently being developed at GexCon; the product will be called DESC and is expected to be commercially available by the end of 2004 (www.gexcon.com).

E.1.1 Simulations in FLACS

A typical FLACS simulation can be divided into three separate steps:

- i)* Scenario definition in the program CASD (Computer Aided Scenario Design): boundary conditions¹ and grid are defined, and output options specified.
- ii)* CFD simulation in FLACS. The flow is modelled by the k - ε turbulence model; modified to produce a representative turbulence field in transient reactive flows, independent of grid and initial conditions (Arntzen, 1998). The approach used in this work has been to let one initial dispersion simulation generate initial conditions for several explosion simulations; so-called *dump*-files generated during the dispersion process serves as initial conditions for the explosions. Combustion was modelled by the β flame model (Arntzen, 1998).
- iii)* Post-processing by the graphical presentation program Flowvis, most of the figures presented in this appendix are generated by Flowvis.

For further details, refer to the FLACS *User's Guide*, Bjerketvedt *et al.* (1993), Arntzen (1998), or the GexCon web page (www.gexcon.com).

E.1.2 Representing the 20-Litre Cubical Vessel in FLACS

The main reason for making a cubical 20-litre explosion vessel was the ease of implementing the geometry in CFD-codes based on a Cartesian coordinate system. Figure E-1 shows the cubical vessel, including the reservoir, outlet valve and adaptor flange – the rebound nozzle is shown separately in Figure E-2. Figure E-3 shows how the cubical 20-litre vessel fitted with the rebound nozzle was represented in FLACS.

The grid is shown in Figure E-4; notice the Cartesian coordinate system with origin in the centre of the spark gap. Although a finer grid was used in the central region to improve the representation of the transient inflow from the reservoir, the fine grid does not cover the whole rebound nozzle. The poor representation of the rebound nozzle in the Cartesian coordinate system represents a major source of uncertainty when it comes to modelling the turbulence production during the transient air blast.

¹ The boundary conditions are defined in scenario files (cs-files). Although the notation in this file may seem cryptic to anyone not familiar with the FLACS code, some of the values used in this work will be given here: CFLC=5, CFLV=3 (for dispersions, 0.5 for explosions), WALLF=1, HEAT_SWITCH=1, All boundary conditions were "EULER", and EQUIVALENCE_RATIOS_(ER0_ER9) 3.04 and 0. The temperature on all solid walls were set to 298 K in a separate HEAT-file ('cs010100.HEAT'); a separate set-up file fixed the ambient pressure to 0.4 bars absolute, and defined a high-pressure region of 21 bars absolute to imitate the reservoir.

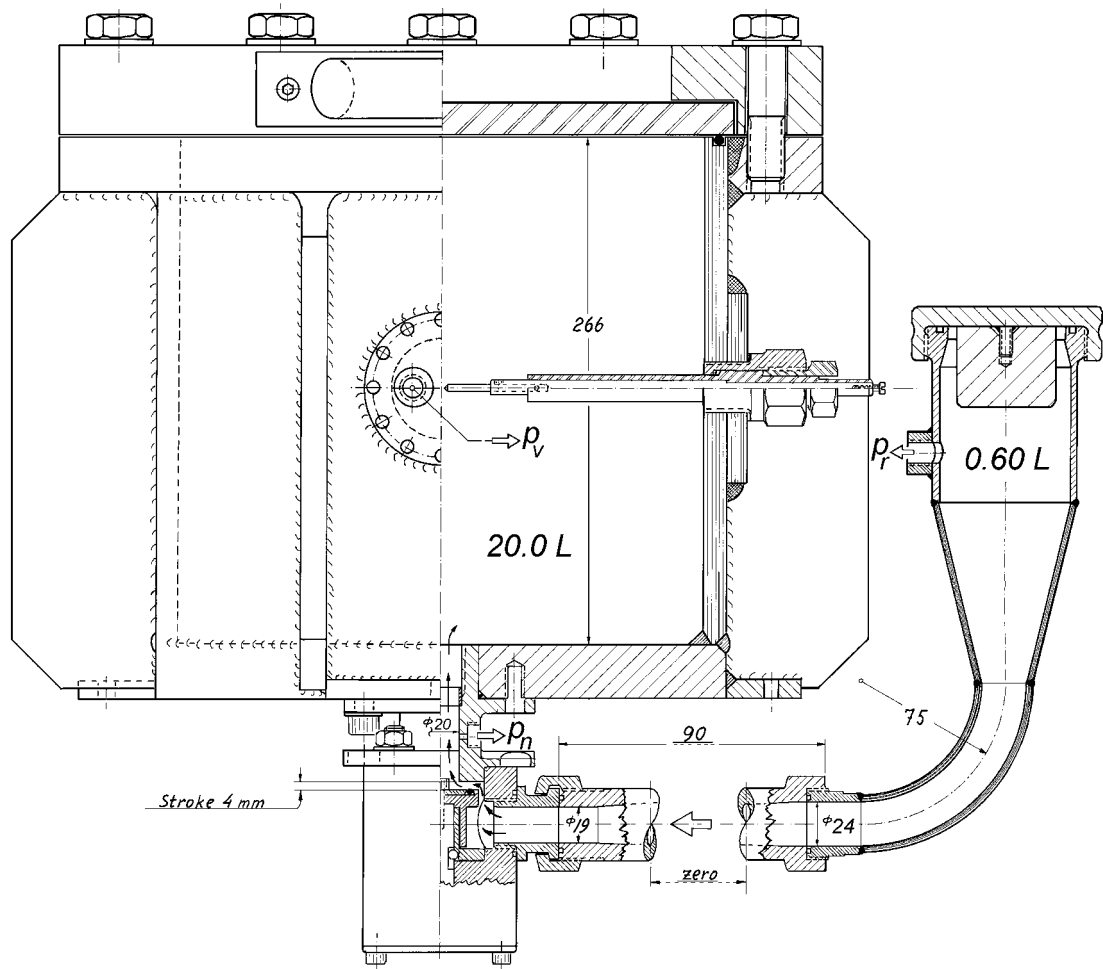


Figure E-1 Mechanical drawing of the flow path from the reservoir, through the extension piece, outlet valve and adapter flange, and finally into the 20-l cubical vessel. The drawing shows the location of the three pressure measurements: reservoir pressure (p_r), nozzle pressure (p_n) and vessel pressure (p_v).

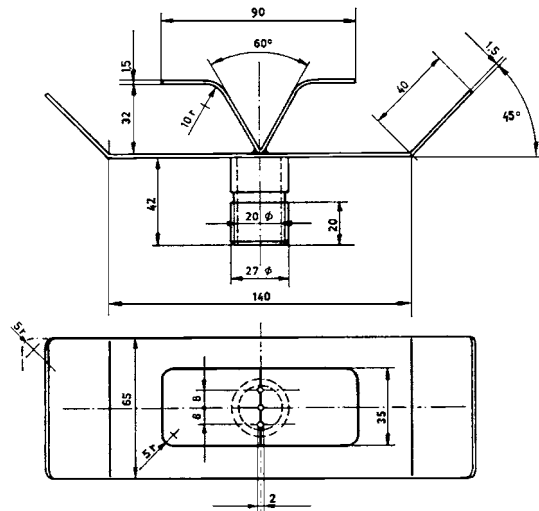


Figure E-2 Mechanical drawing of the rebound nozzle.

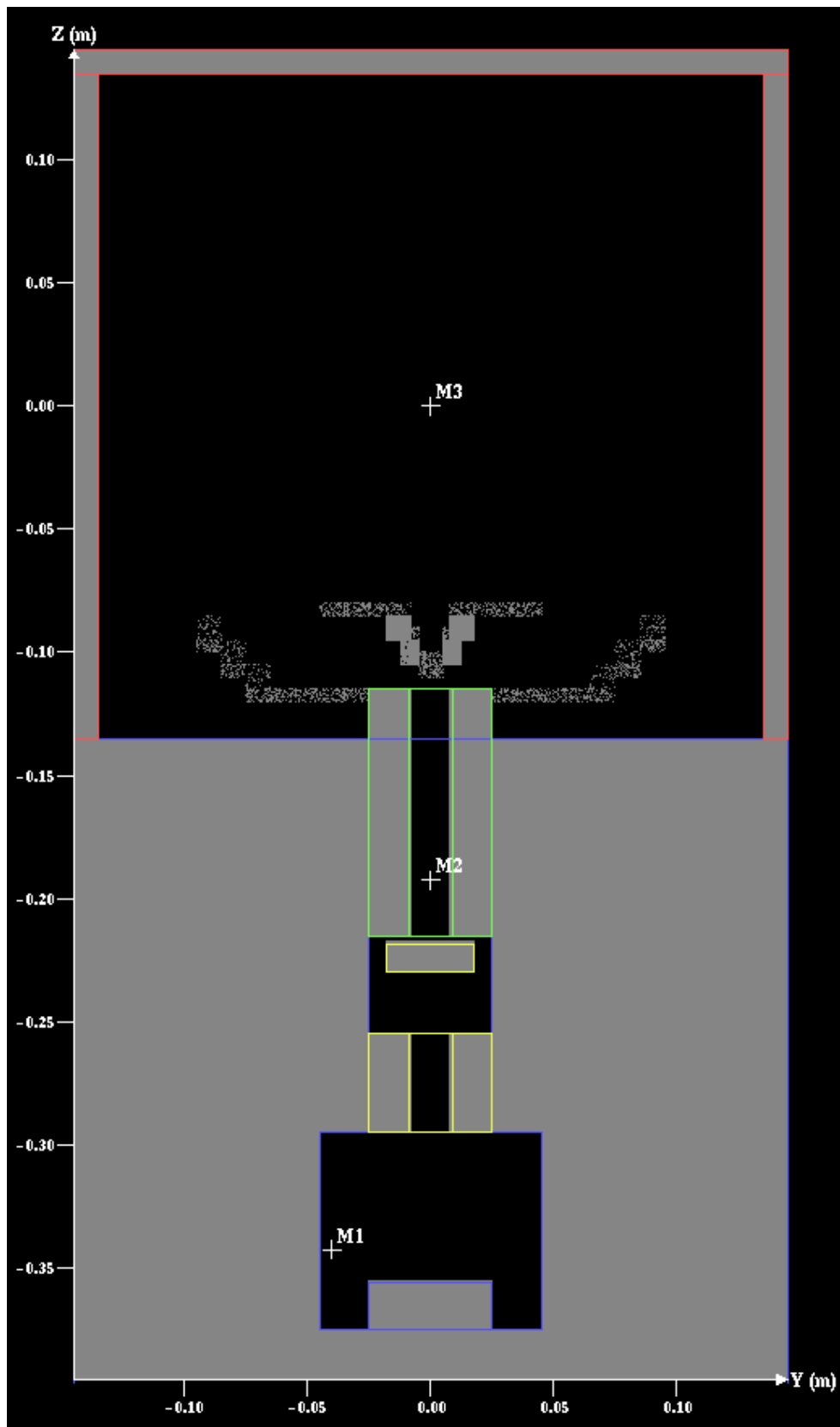
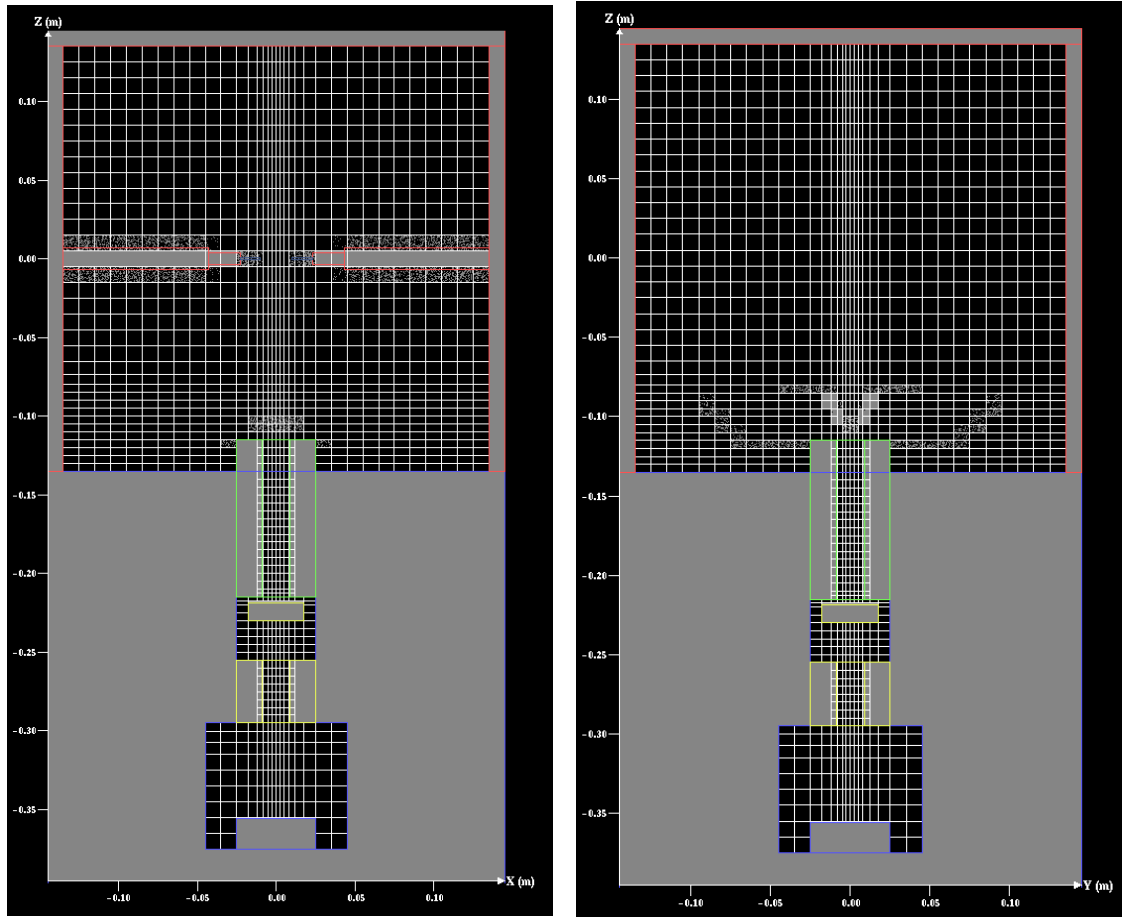
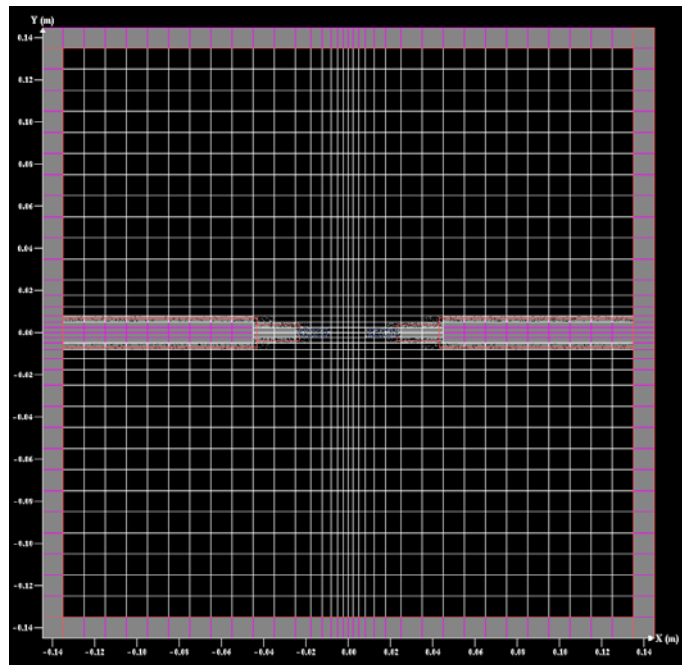


Figure E-3 FLACS-representation of the Cubical 20-l explosion vessel: cross-section in yz-plane, showing how the reservoir, inlet valve and rebound nozzle was modelled, including axes and monitor points for the three pressure measurements: M1 – reservoir pressure (p_r); M2 – nozzle pressure (p_n); M3 – vessel pressure (p_v).



Section: xz -plane, $y=0$

Section: yz -plane, $x=0$



Section: xy -plane, $z=0$

Figure E-4 Cross-sections of the cubical 20-l explosion vessel with rebound nozzle, showing the calculation grid. Cubical grid cells with sides of length 1 cm cover most of the calculation volume, finer grid cells are used close to the outlet valve and rebound nozzle.

E.2 The Dispersion Process

The transient dispersion process when air from the reservoir, initially at a pressure of 20.0 barg, is dispersed into a fuel-rich mixture of propane-air, initially at a pressure of -0.600 barg, has been simulated. The simulations were done both with and without heat transfer between the flowing fluid and solid surfaces. In the non-adiabatic case, all solid surfaces are assumed to have infinite heat capacity and constant temperature of 298 K.

E.2.1 Concentration and Mixing

As outputs from the dispersion simulation were used as input for explosion simulations, the fuel had to be included from the beginning of the simulations. To imitate the experiments as closely as possible, all the fuel are initially mixed with air inside the explosion vessel. One of the main experimental uncertainties concerning the propane-air explosions described in Chapters 3 and 4 is the degree of mixing between injected air from the reservoir and the fuel-rich mixture inside the explosion vessel during the relatively short ignition delay time. To minimize the effect of limited mixing on simulation results, the final concentration should be close to the concentration that yields the highest explosion pressure and rate of pressure rise. In Chapter 4, this concentration was found to be approximately 4.5 per cent propane by volume – i.e. slightly higher than stoichiometric concentration (4.03%). In FLACS, the fuel concentration is given as *equivalence ratio*:

$$\Phi = \frac{\left(\frac{m_{fuel}}{m_{oxidant}}\right)_{\text{actual mixture}}}{\left(\frac{m_{fuel}}{m_{oxidant}}\right)_{\text{stoichiometric}}} = \frac{\left(\frac{n_{fuel}}{n_{oxidant}}\right)_{\text{actual mixture}}}{\left(\frac{n_{fuel}}{n_{oxidant}}\right)_{\text{stoichiometric}}} \quad (\text{D.1})$$

To calculate the initial equivalence ratio inside the partly evacuated 20-litre vessel that produces a propane concentration of 4.5 per cent by volume, one has to keep in mind that only 40 per cent of the final amount of gas are initially inside the vessel, hence the initial equivalence ratio should be:

$$\Phi = \frac{\left(\frac{0.045}{0.355}\right)}{\left(\frac{0.040}{0.960}\right)} = 3.04$$

This is considerably higher than the final equivalence ratio of 1.13, corresponding to 4.5 per cent propane in air. Equivalence ratios at the onset of the dispersion process are shown in Figure E-5. Figure E-6 suggests that the equivalence ratio in the centre of the vessel may be too high for short ignition delay times, e.g. 45 and 60 milliseconds. After 120 milliseconds, the mixing is more or less complete – at least in the cross-section shown.

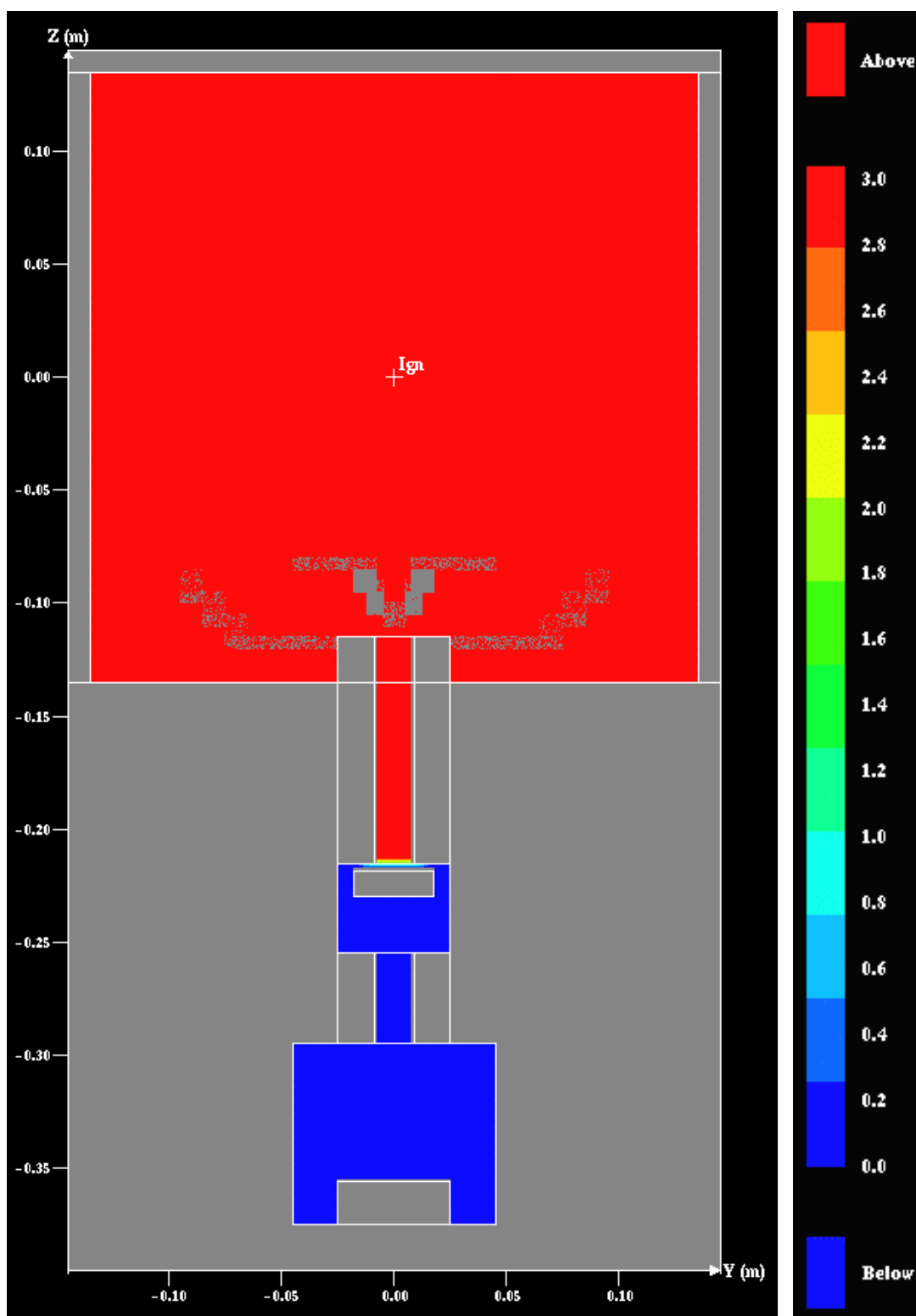


Figure E-5. Equivalence ratio (ER) at the onset of the dispersion process. Blue represents pure air in the reservoir (pressurized to 20.0 barg); red symbolizes the fuel-rich propane-air mixture inside the partly evacuated vessel (ER equal to 3.04, pressure -0.600 barg). The scale at the right is also valid for Figure E-6 on the next page; the scale is linear.

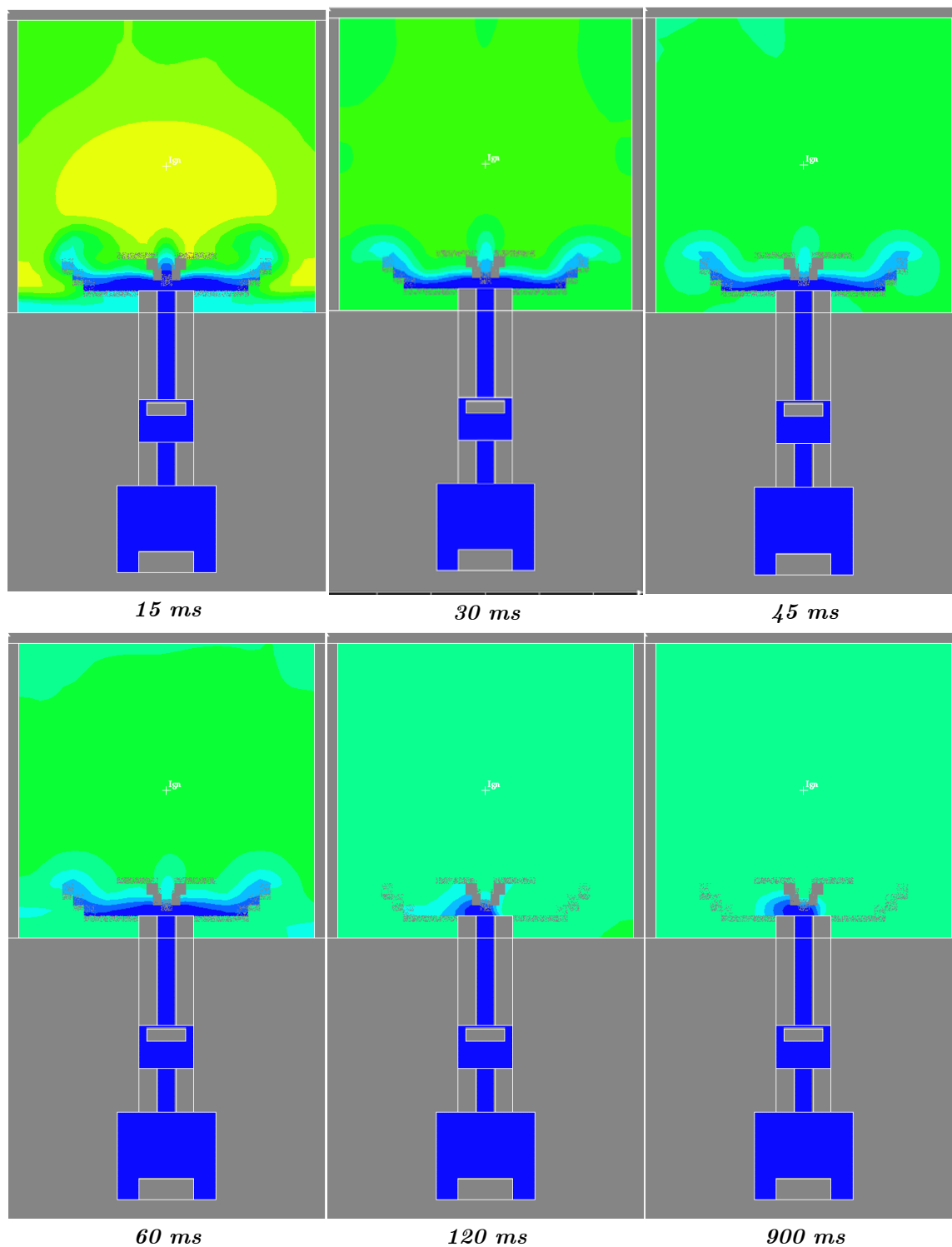


Figure E-6. Equivalence ratio as a function of time during the dispersion process. Time relative to onset of dispersion is given under each figure.

E.2.2 Pressure-Time Histories

Measured and simulated pressure-time histories for the first 150 milliseconds of the dispersion process are shown in Figure E-7. The location of the piezoelectric pressure transducers used for the experimental measurements are shown in Figure E-1, and the monitor points used in the simulations are shown in Figure E-3.

There is good agreement between simulated ($M1$) and experimental *reservoir pressure*, p_r . Initially there is a short delay in the experimental pressure decrease, due to the opening of the outlet valve. After some time the simulated reservoir pressure becomes slightly influenced by heat transfer from the walls, the pressure determined under adiabatic conditions is higher than in the non-adiabatic case. Note that the final temperature in the reservoir when the absolute pressure is reduces from 21 to 1 bar can be estimated theoretically if we assume the process isentropic:

$$T_{r,f} = T_{r,i} \left(\frac{p_{r,f}}{p_{r,i}} \right)^{\frac{\gamma-1}{\gamma}} \approx 123K \quad (D.2)$$

or about -150 °C; the specific heat ratio γ has been set to 1.4.

There are significant differences between simulated ($M2$) and experimental *nozzle pressure*, p_n . The simulation code did not support supersonic flow. This can probably explain some of the discrepancies, like the sudden “*jump*” in nozzle pressure after 30 to 40 milliseconds. This phenomenon can probably be explained by the existence of a shock in the nozzle, analogous to the classical theory for flow through a converging-diverging nozzle found in most text on gas dynamics (e.g. Shapiro, 1953). The influence of heat transfer in the simulated results is evident, non-adiabatic conditions yields results much closer to the experimental values.

Adiabatic conditions results in a much lower simulated *vessel pressure*, p_v (monitor point $M3$) than non-adiabatic conditions. This again illustrates the effect of heat conduction in heating the air inside the reservoir. Although the rate of pressure rise is lower for the simulation, the overall results in the non-adiabatic case are comparable to those found experimentally. While both the experimentally determined vessel pressure, and the simulated adiabatic vessel pressure, stabilizes after some 60 milliseconds; the pressure continues to rise in the non-adiabatic case. This is probably due to two minor limitations in the simulations:

- i)* Because it is assumed in the non-adiabatic simulations that all solid surfaces have infinite heat capacity and constant temperature of 298 K, the temperature in the remaining gas inside the reservoir will continue to rise until it reaches 298 K.
- ii)* In the simulations the outlet valve is not closed, hence there will be continued inflow long after the time when the valve is closed in the experiments (50-60 milliseconds).

Improved simulations that can imitate the closing of the outlet valve, and take into account the limited heat capacity of the reservoir and allow for supersonic flow, will probably yield better results.

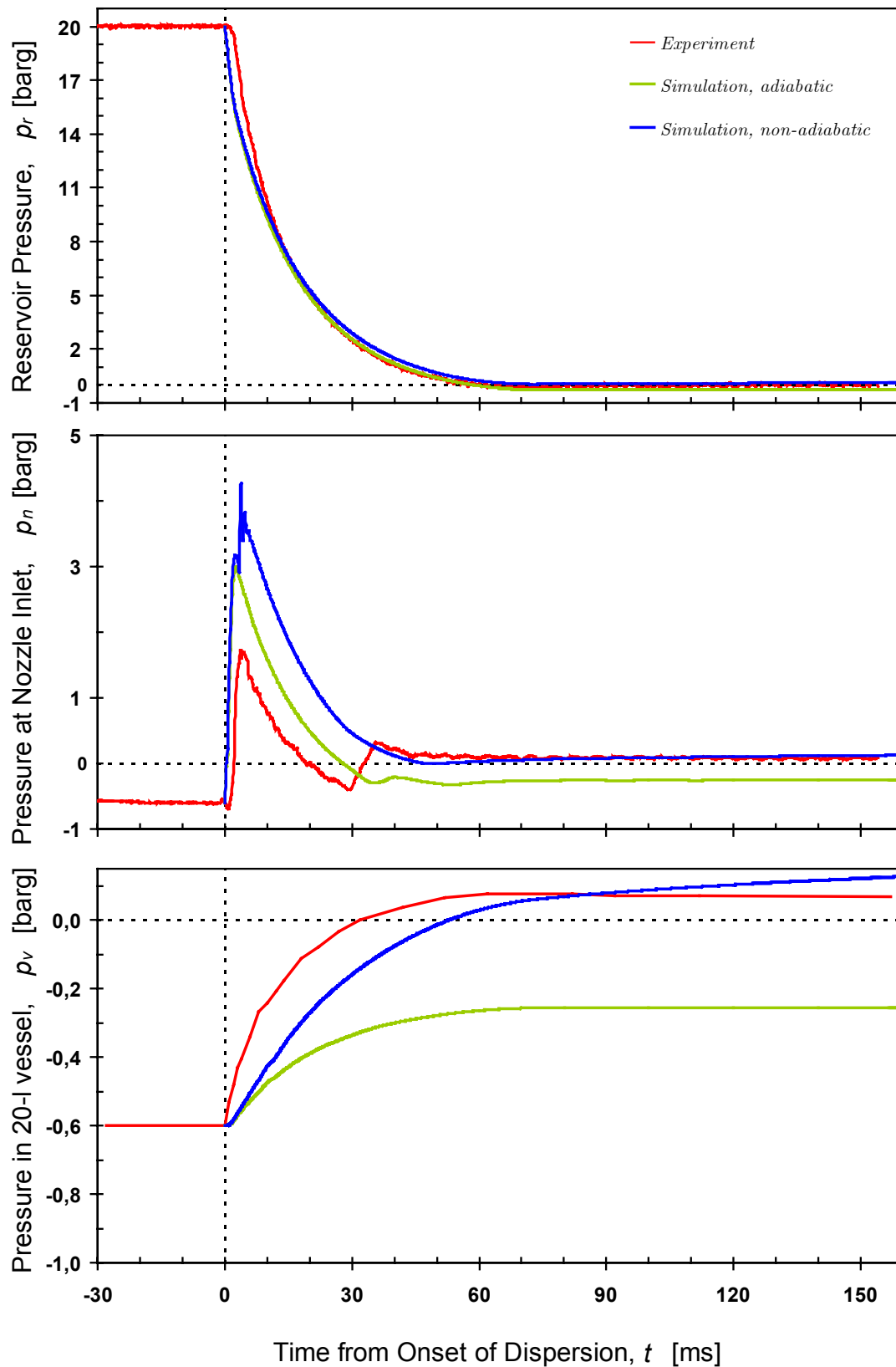


Figure E-7. Simulated and experimental pressure-time histories for dispersion experiments. The curves representing experimental values are the mean value of the five tests with the rebound nozzle described in Chapters 3 and 4. The locations of the pressure transducers are shown in Figure E-1; monitor points for simulated pressures in Figure E-3.

E.2.3 Turbulence

Decay of root-mean-square velocity

The simulated build-up and decay of turbulence will be presented through the output variable $TURB$ (*turbulence velocity*) from the FLACS-simulations:

$$TURB = \left(\frac{2}{3}k\right)^{1/2} \quad (D.3)$$

where k is the *turbulence energy* from the k - ε model. $TURB$ as a function of time in the cubical vessel is illustrated in Figure E-8.

It can be shown that the value of the variable $TURB$ should be comparable to the measured root-mean-square velocity from Appendix D. Turbulence energy is defined as:

$$k \equiv \frac{1}{2}\overline{u'_i u'_i} = \frac{1}{2}(\overline{u_1'^2} + \overline{u_2'^2} + \overline{u_3'^2}) \quad (D.4)$$

For isentropic turbulence, i.e. $\overline{u_1'^2} = \overline{u_2'^2} = \overline{u_3'^2} = \overline{u'^2}$; hence, (D.4) can be written as:

$$k = \frac{3}{2}\overline{u'^2} \quad (D.5)$$

$$k = \frac{3}{2}(TURB)^2 \xrightarrow{ISOTROPIC} TURB^2 = \overline{u'^2} \quad (D.6)$$

It follows that for isotropic turbulence we should have:

$$TURB = \sqrt{\overline{u'^2}} = u'_{rms} \quad (D.7)$$

Hence, it should be reasonable to compare the simulated parameter $TURB$ with the measured parameter u'_{rms} from Appendix D.

Experimental results are compared with results from simulations in Figure E-9. The values for the variable $TURB$ from the simulations are considerably higher than the experimentally determined root-mean-square velocity, typically by a factor of 2-3; note that both of the axes in the upper figure are logarithmic. There can be several explanations for the poor agreement between the two, i.e.:

- i)* According to Dahoe (2000), the baroclinic effect, discussed in Chapter 2, is the main source of turbulence production in the first ten milliseconds after onset of injection. The standard k - ε model used in these simulations cannot be expected to handle this effect. Thus, the initial build-up period is not reproduced properly in the simulations, as indicated in Figure E-9.
- ii)* The smoothing procedures that are used to analyse the LDA data can severely influence the experimental results.
- iii)* The turbulence production modelled by FLACS can be too high due to the poor geometrical representation of the rebound nozzle. It is also possible that the k - ε model performs better on turbulent transient gas injection if some of the fundamental constants in the model are adjusted (Ouellette and Hill, 2000).
- iv)* The fact that the simulations are limited to subsonic flow can also be an explanation, especially during the first 10 milliseconds.

It is interesting to note that the simulated and experimental results are in much better agreement when no smoothing is done prior to the calculation of the root-mean-square velocity, see Figure E-10.

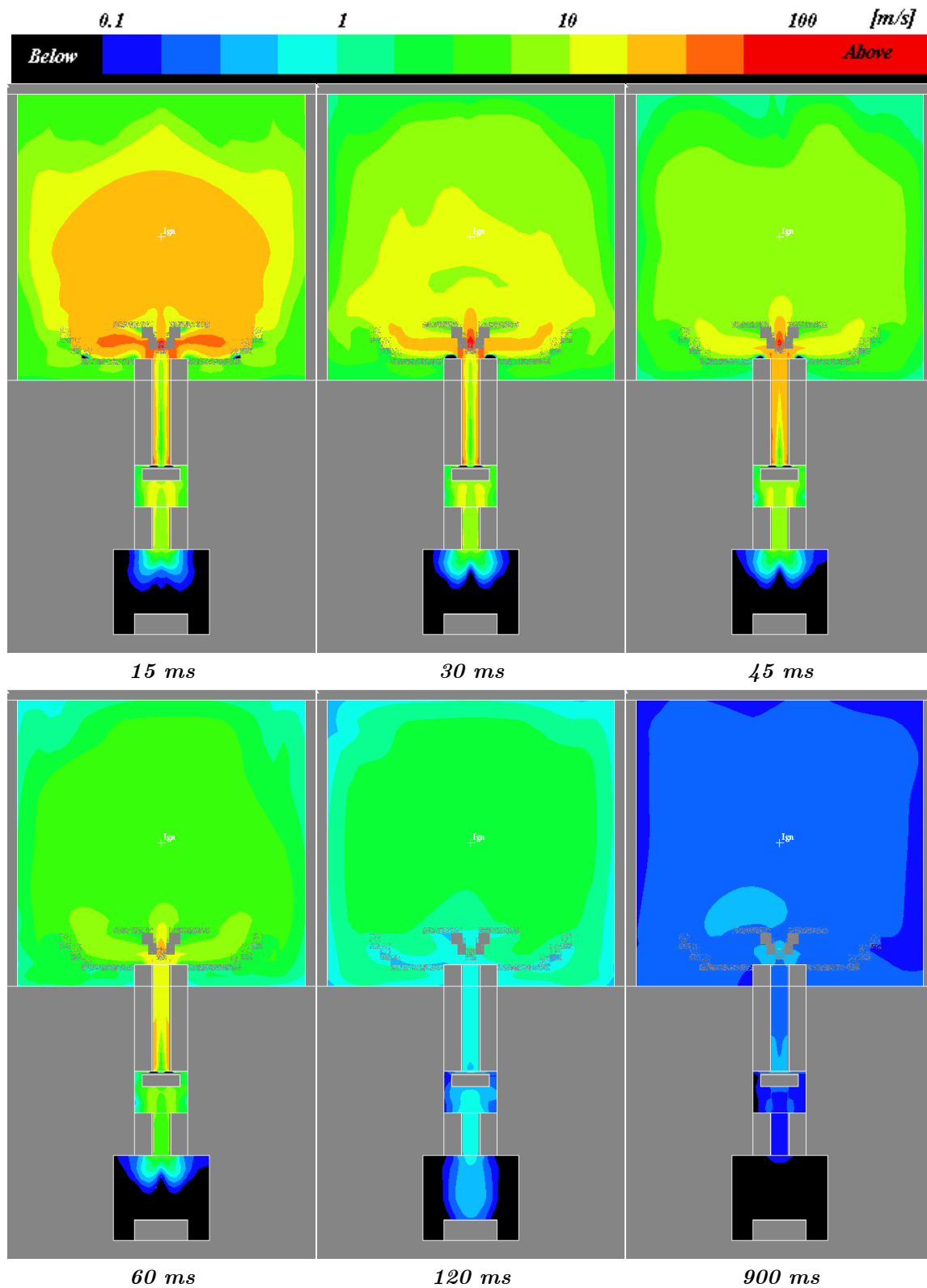


Figure E-8. Turbulence velocity (TURB) in one cross section at various time steps of the dispersion process.

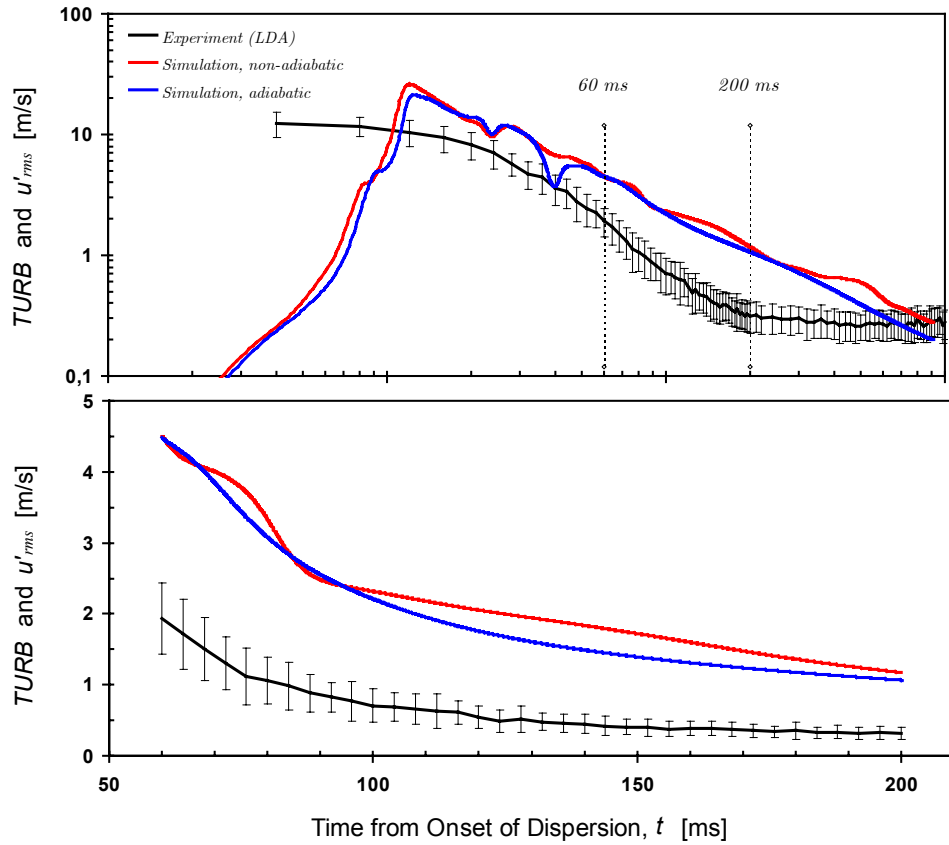


Figure E-9 Measured and simulated decay of turbulence inside the 20-l cubical vessel during the dispersion process. The experimental results are the mean value of the root-mean-square velocity for all the 60 tests with the rebound nozzle (at various positions), analysed by the moving regression algorithm described by Dahoe (2000); error bars indicate one standard deviation above and one standard deviation below the mean. The simulated results are the variable TURB from FLACS, taken at the monitor point M3; both adiabatic and non-adiabatic results are shown.

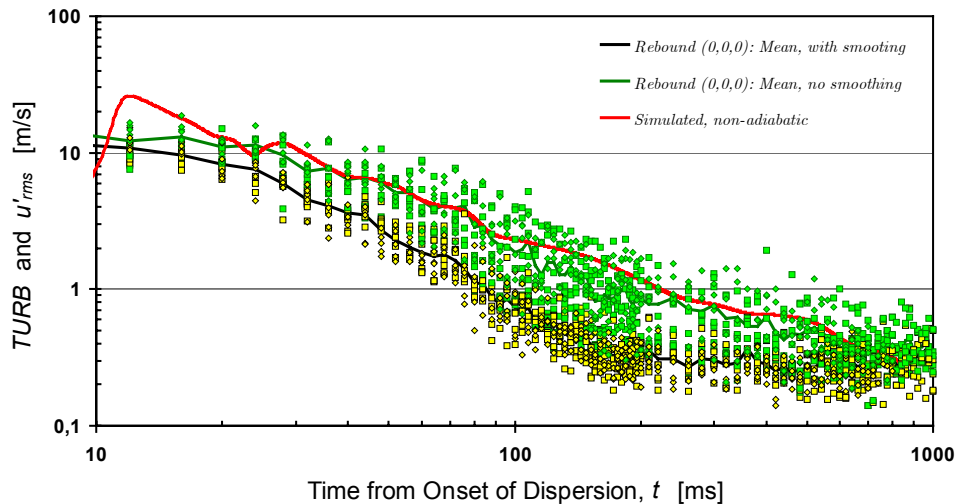


Figure E-10 Measured and simulated decay of turbulence inside the 20-l cubical vessel during the dispersion process. The experimental results are the mean value of the root-mean-square velocity for all the 20 tests with the rebound nozzle at (0,0,0); analysed by both the moving regression algorithm described by Dahoe (black/yellow), and without any smoothing (green); individual measurements are shown to indicate the spread in data. The simulated results are the variable TURB from FLACS, taken at the monitor point M3.

Turbulent length scale

Several turbulent length scales can be derived from the k - ε model (Ertesvåg, 1999), e.g. an expression for mixing length:

$$\ell_m = C_\mu^{3/4} \frac{k^{3/2}}{\varepsilon} \quad (\text{D.8})$$

where k is the turbulent kinetic energy, ε is the dissipation rate of turbulent kinetic energy, and C_μ is a constant (equal to 0.09) from the equation defining the turbulent viscosity in the standard k - ε model (Lauder and Spalding, 1974).

The length scale LT reported in FLACS is defined as:

$$LT = C_\mu \frac{k^{3/2}}{\varepsilon} = C_\mu^{-1/4} \ell_m \approx 1.8 \cdot \ell_m \quad (\text{D.9})$$

The simulated value of LT as a function of time is shown in Figure E-11.

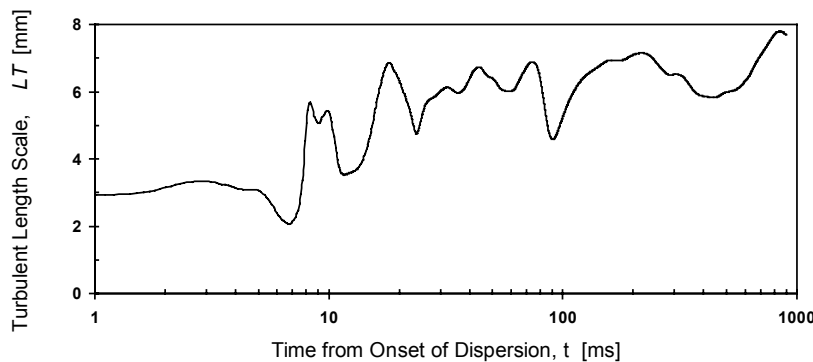


Figure E-11 Simulated turbulent length scale (LT) in the point $(0,0,0)$ during the transient dispersion process.

E.2.4 Velocity

Simulated values of the three velocity components in the point $(0,0,0)$ are shown in Figure E-12. Most conspicuous is perhaps the strong downward flow up to some 80-90 milliseconds. At the default ignition delay time of 60 milliseconds, the downward flow is in the order of 10 m/s (or 10 mm/ms); i.e. the initial flame kernel can be displaced a considerable distance away from the centre of the vessel if the initial combustion rate is slow.

The simulated flow-pattern in a vertical cross-section passing through the centre of the spark gap (yz -plane, $x=0$) is shown in Figure E-13. Most of this cross-section is dominated by downward flow. The simulated flow-pattern in a vertical cross-section next to the vessel wall (yz -plane, $x=-13$) is shown in Figure E-14. Most of this cross-section is dominated by upward flow. Figure E-15 shows the simulated flow-pattern in a vertical cross-section passing through the centre of the spark gap, but perpendicular to the cross-sections in the figures above (xz -plane, $y=0$).

It should be noted that in the real vessel, the outlet valve would close after about 50-60 milliseconds. Hence, the simulated flow pattern would be different if this effect could be included in the simulations, especially for the flow near the rebound nozzle.

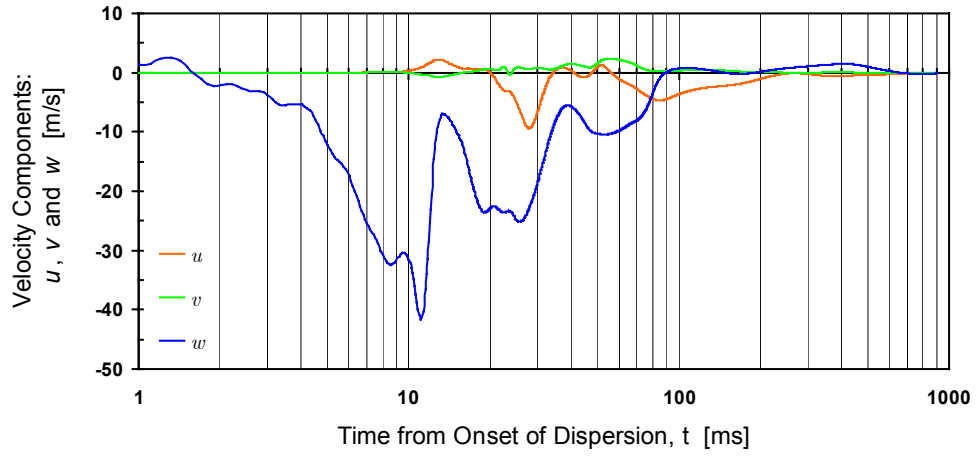


Figure E-12 Simulated values of the three velocity components in the point $(0,0,0)$ during the transient dispersion process.

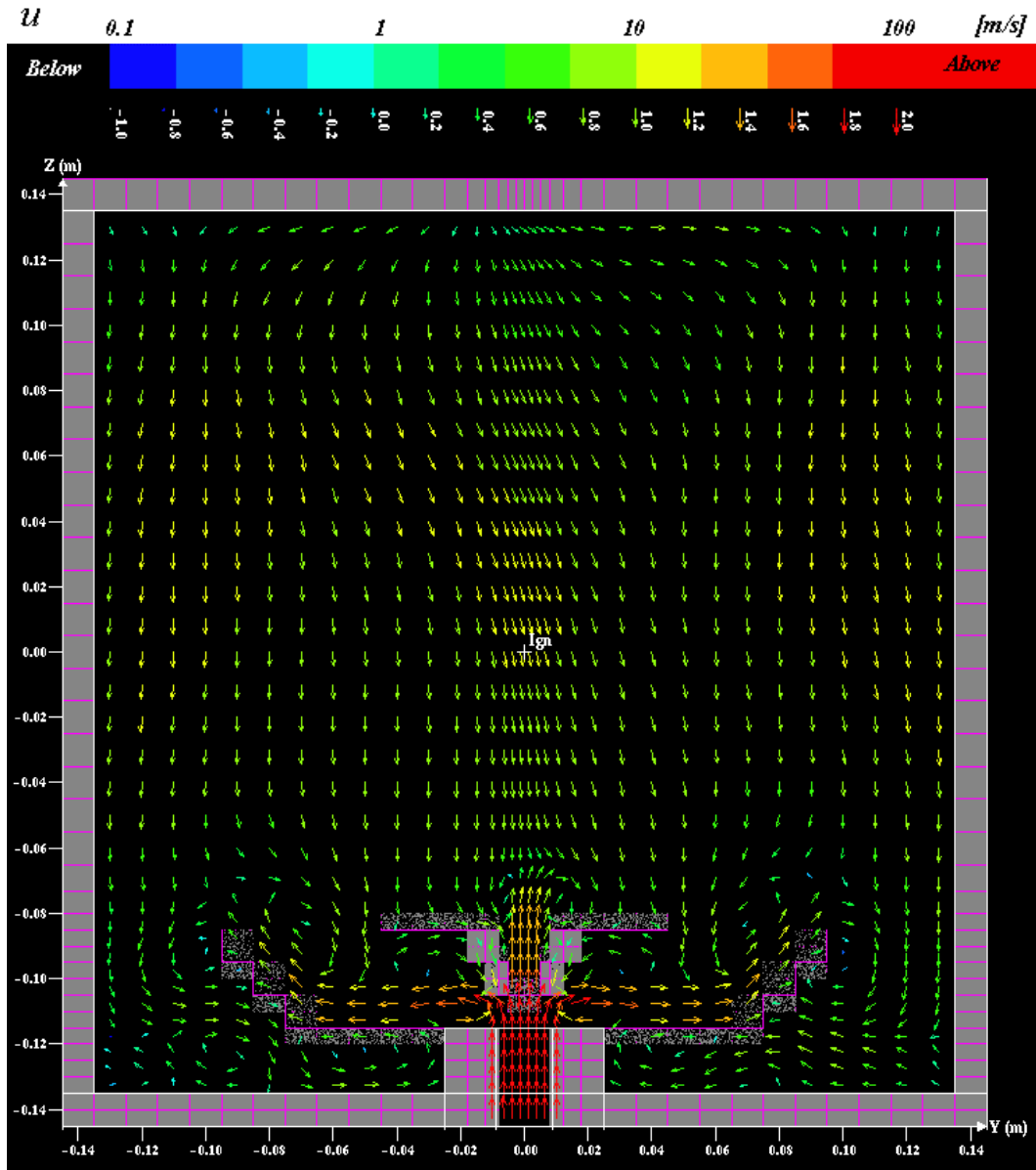


Figure E-13. Simulated velocity in yz -plane, $x=0$ cm, $t_v=60$ ms.

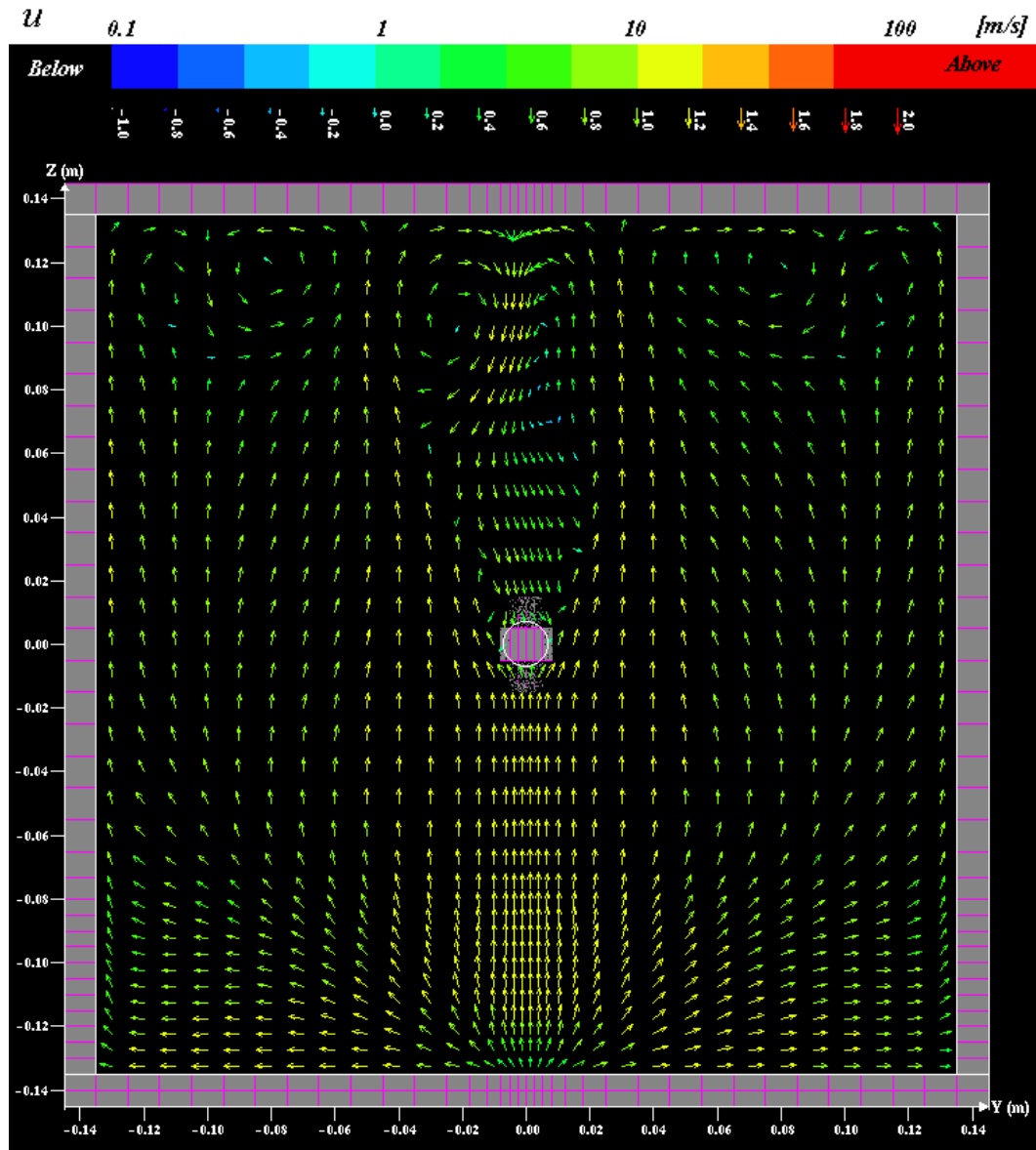


Figure E-14. Simulated velocity in yz -plane, $x=-13$ cm, $t_n=60$ ms.

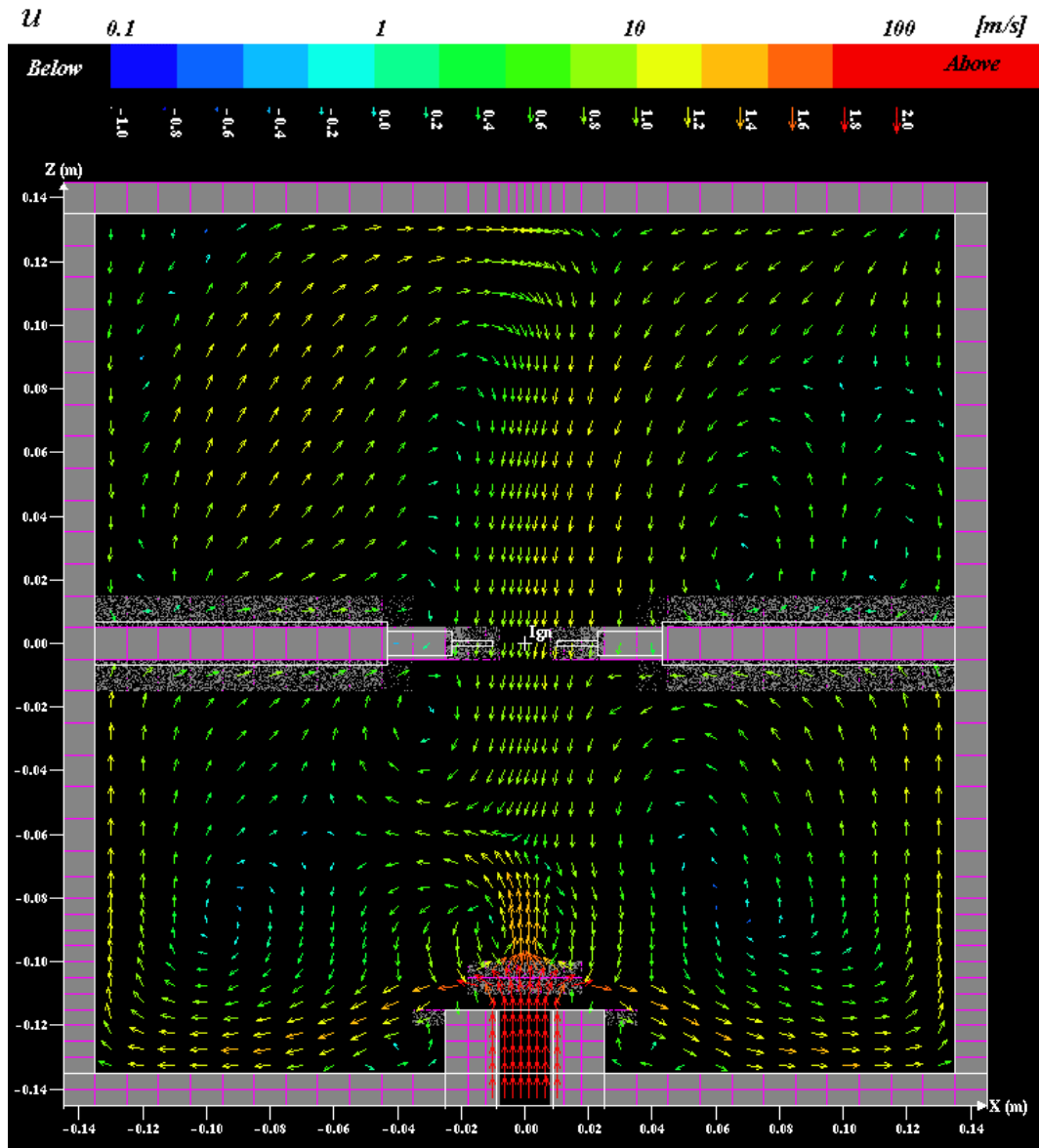


Figure E-15 Simulated velocity in xz -plane, $y=0$ cm, $t_o=60$ ms.

E.3 Explosions

Simulations of propane-air explosions have been started from dump-files generated during the dispersion process described in section E.2; the results will be compared with results from the corresponding experiments described in Chapter 4. Only the default combustion model in FLACS, the so-called *β flame model*, is used in these simulations.

Pressure-time histories for both simulations and experiments are shown in Figure E-16. It is evident that the combustion proceeds at a higher rate in the simulation compared to the experiments, increasingly so for increased ignition delay times. The slightly lower explosion pressure observed in the simulations is probably partly caused by the fact that the outlet valve is still open; thus, the reservoir serves as extra volume. The rate of pressure decrease after the explosions is more rapid for the experiments, probably because the simulations does not take into account the condensation of water on the walls of the vessel.

Figure E-17 shows the simulated and experimental rate of pressure rise as a function of ignition delay time. The simulated results are significantly higher than the ones from experiments. There can be several explanations for this, e.g.:

- i)* The initial turbulence level from the simulations can be too high. Although the results in section E.2.3 is rather ambiguous, they indicate that the simulated value of *TURB* probably is significantly higher than the measured root-mean-square velocity. One reason for this may be excessive turbulence production downstream of the rebound nozzle; it is unclear how the sub-grid models in FLACS will handle the volume porosities resulting from the poor representation of this nozzle.
- ii)* The default combustion model used by FLACS, the *β flame model*, is developed for large-scale gas explosions, especially under partly confined conditions. The flame has a fixed thickness of about three grid cells, or in this case about three cm. It is likely that another combustion model, the *Simple Interface Model (SIF)*, would have performed better. Arntzen (1998) contains a comprehensive description of the combustion models used by *FLACS*.

Some illustrations of flame surface growth for various ignition delay times are shown in Figure E-18. The initial flame kernel is displaced downwards by the flow for short ignition delay times, as would be expected from the discussion in section E.2.4.

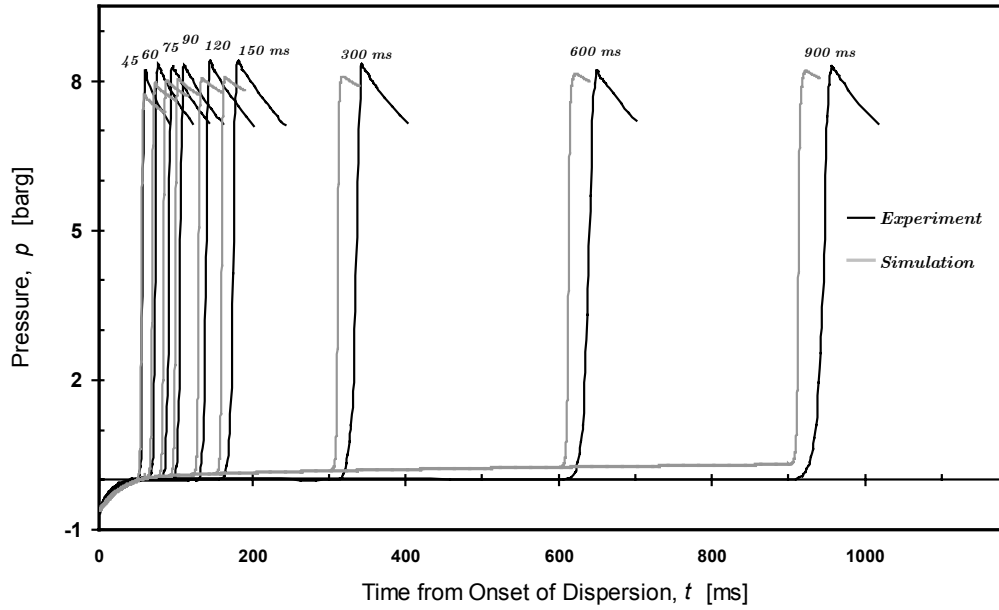


Figure E-16 Simulated and experimental pressure-time histories of propane-air explosions in the 20-litre cubical vessel. The nominal fuel concentration is 4.5 per cent propane by volume in all tests. The corresponding ignition delay time is given above each pair of curves.

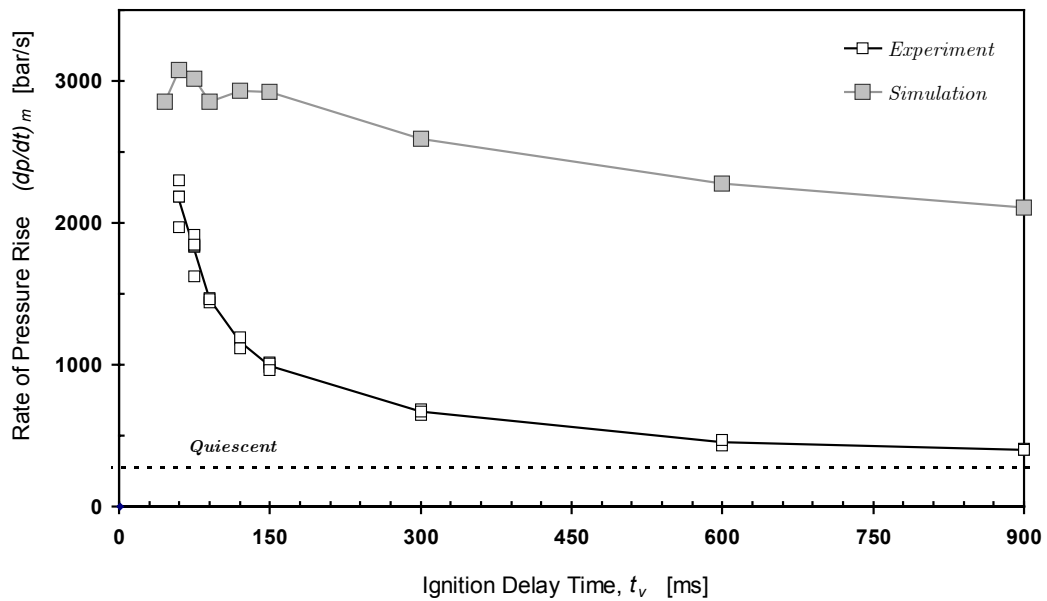


Figure E-17 Simulated and experimental rates of pressure rise for propane-air explosions in the 20-litre cubical vessel. The nominal fuel concentration is 4.5 per cent propane by volume in all tests. The dotted line represents the experimentally determined rate of pressure rise under initially quiescent conditions.

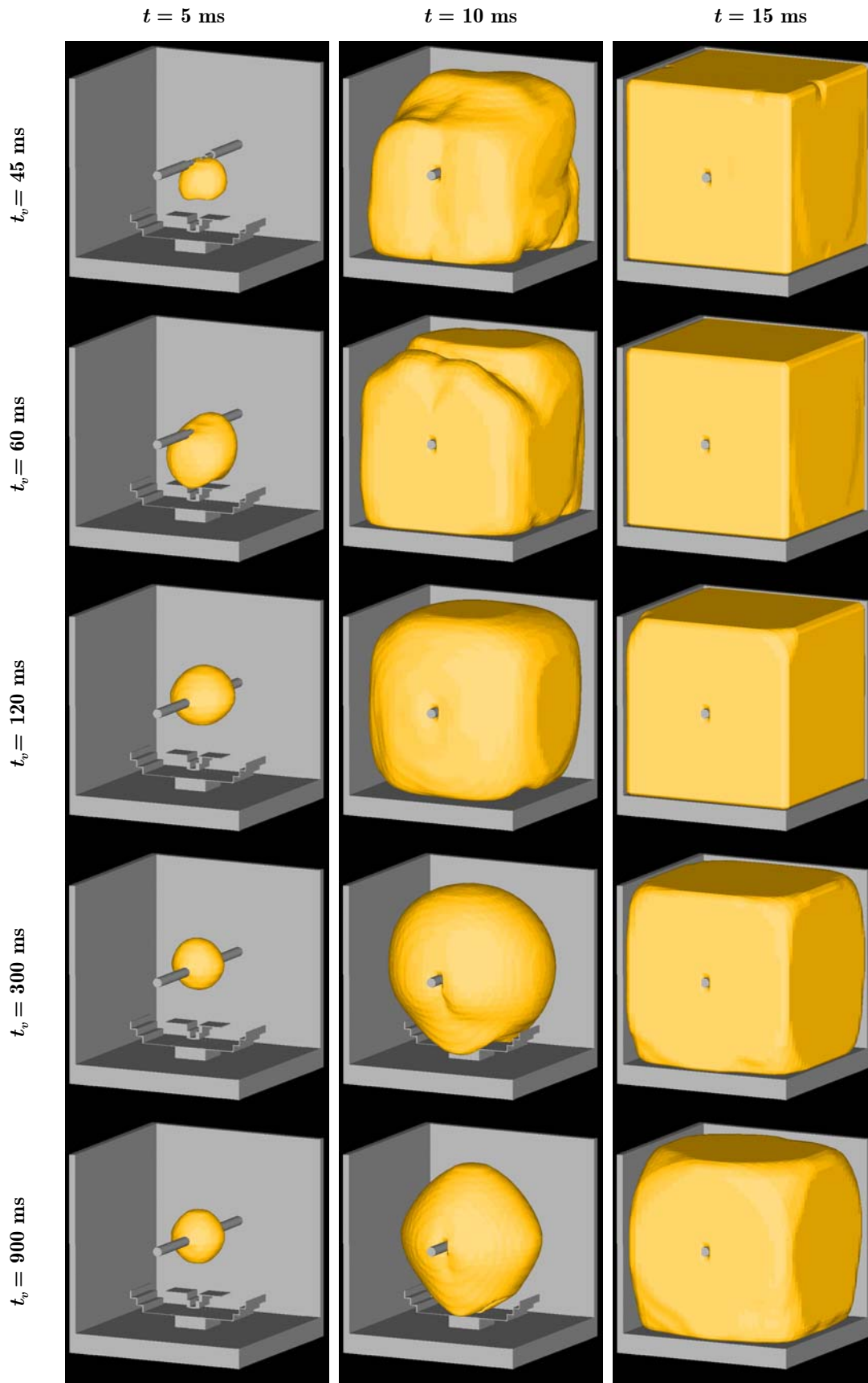


Figure E-18 Flame surface development during propane-air explosions in the 20-l cubical vessel for various ignition delay times. The yellow surface represents 15 per cent product by mass.

References

- Arntzen, B.J. (1998). *Modelling of Turbulence and Combustion for Simulation of Gas Explosions in Complex Geometries*. ISBN 82-471-0358-3. Dr. Ing. Thesis, The Norwegian University of Science and Technology (NTNU), Trondheim.
- Bjerketvedt, D., Bakke, J.R. & van Wingerden, K. (1993). *Gas Explosion Handbook*. Version 1.2, Ref. No. CMR-93-A25034, Christian Michelsen Research AS, Fantoft, Bergen.
- Ertesvåg, I.S. (2000). *Turbulent Strøyming og Forbrenning: Frå Turbulensteori til Ingeniørverktøy*. ISBN 82-519-1568-6. TAPIR Forlag, Trondheim (in Norwegian).
- Lauder, B.E. & Spalding, D.P. (1974). *The Numerical Computation of Turbulent Flows*. Computer Methods in Applied Mechanics and Engineering, **3**, pp. 269-289.
- NORSOK Standard Z-013 (2001). *Risk and Emergency Preparedness Analysis*. Rev. 2, Norwegian Technology Centre.
- Ouellette, P. & Hill, P.G. (2000). *Turbulent Transient Gas Injections*. Journal of Fluid Engineering, **122**, pp. 743-753.
- Shapiro, A.H. (1953). *The Dynamics and Thermodynamics of Compressible Fluid Flow; Vol. I*. The Roland Press Company, New York.

